Nicholas Ayache
Hervé Delingette
Maxime Sermesant (Eds.)

LNCS 5528

Functional Imaging and Modeling of the Heart

5th International Conference, FIMH 2009
Nice, France, June 2009
Proceedings

Springer

Lecture Notes in Computer Science 5528

Commenced Publication in 1973
Founding and Former Series Editors:
Gerhard Goos, Juris Hartmanis, and Jan van Leeuwen

Editorial Board

David Hutchison
Lancaster University, UK

Takeo Kanade
Carnegie Mellon University, Pittsburgh, PA, USA

Josef Kittler
University of Surrey, Guildford, UK

Jon M. Kleinberg
Cornell University, Ithaca, NY, USA

Alfred Kobsa
University of California, Irvine, CA, USA

Friedemann Mattern
ETH Zurich, Switzerland

John C. Mitchell
Stanford University, CA, USA

Moni Naor
Weizmann Institute of Science, Rehovot, Israel

Oscar Nierstrasz
University of Bern, Switzerland

C. Pandu Rangan
Indian Institute of Technology, Madras, India

Bernhard Steffen
University of Dortmund, Germany

Madhu Sudan
Massachusetts Institute of Technology, MA, USA

Demetri Terzopoulos
University of California, Los Angeles, CA, USA

Doug Tygar
University of California, Berkeley, CA, USA

Gerhard Weikum
Max-Planck Institute of Computer Science, Saarbruecken, Germany

Nicholas Ayache Hervé Delingette
Maxime Sermesant (Eds.)

Functional Imaging and Modeling of the Heart

5th International Conference, FIMH 2009
Nice, France, June 3-5, 2009
Proceedings

Springer

Volume Editors

Nicholas Ayache
Hervé Delingette
Maxime Sermesant
INRIA Sophia Antipolis
Asclepios Research Project
2004 route des Lucioles, BP 93, 06902 Sophia Antipolis CEDEX, France
E-mail: {nicholas.ayache, herve.delingette, maxime.sermesant}@sophia.inria.fr

Library of Congress Control Number: Applied for

CR Subject Classification (1998): J.3, I.6, I.3, I.2.1, I.4

LNCS Sublibrary: SL 6 – Image Processing, Computer Vision, Pattern Recognition, and Graphics

ISSN 0302-9743
ISBN-10 3-642-01931-5 Springer Berlin Heidelberg New York
ISBN-13 978-3-642-01931-9 Springer Berlin Heidelberg New York

This work is subject to copyright. All rights are reserved, whether the whole or part of the material is concerned, specifically the rights of translation, reprinting, re-use of illustrations, recitation, broadcasting, reproduction on microfilms or in any other way, and storage in data banks. Duplication of this publication or parts thereof is permitted only under the provisions of the German Copyright Law of September 9, 1965, in its current version, and permission for use must always be obtained from Springer. Violations are liable to prosecution under the German Copyright Law.

springer.com

© Springer-Verlag Berlin Heidelberg 2009
Printed in Germany

Typesetting: Camera-ready by author, data conversion by Scientific Publishing Services, Chennai, India
Printed on acid-free paper SPIN: 12686605 06/3180 5 4 3 2 1 0

Preface

FIMH 2009 was the fifth international conference on Functional Imaging and Modeling of the Heart. It was held in Nice, France, during 3-5 June 2009. This biennial scientific event presents research and development efforts in the field of cardiovascular modeling and image analysis to better understand the physiology and pathologies of the human heart. The final objective is to improve the diagnosis and therapy of cardiac diseases, which remain a major health issue in the western world and in Asia.

This international conference is fostering the collaboration between scientists in various fields (signal and image processing, biophysics, biomedical engineering, robotics, computer science, applied mathematics, etc.) and experts in cardiology, radiology, surgery, biology and physiology.

During the past 8 years, FIMH has established itself as a leading international conference on the methodological aspects of functional imaging and modeling of the heart with a strong emphasis on clinical applications and validation. The previous conferences were held in Helsinki (2001), Lyon (2003), Barcelona (2005) and Salt Lake City (2007) with an increasing number of peer-reviewed articles published in the *Lecture Notes in Computer Science* proceedings available at the time of the event. Links to current and previous meetings and associated LNCS volumes are available at http://www-sop.inria.fr/asclepios/events/FIMH09

The 2009 proceedings contain original articles selected after a competitive and rigorous peer-review process. The authors had to submit a full paper (8 pages in the proceedings format) to be reviewed in a double-blind process by 3 or 4 members of the international Program Committee composed of 55 prominent scientists in the field. For the first time this year the authors of accepted papers had to reply point by point to the remarks and suggestions of the reviewers while submitting their revised final version, which was reviewed a second time for final acceptance. To help the authors improve their original contributions, they were allowed two additional pages to include more explanations, results and/or references as requested by the reviewers.

The result of this selection is a set of 54 articles involving 200 authors and co-authors from 14 countries of 4 continents. These contributions were presented in Nice during a set of single-track oral and poster sessions. In addition, Professors R. Razavi (London, UK), R. Howe (Harvard, USA), A. McCulloch (San Diego, USA) and T. Peters (London, Canada), presented state-of-the-art advances during their keynote lectures.

We want to thank the members of the Program Committee, the additional reviewers, the organizing team and all the participants who jointly contributed to the scientific success of this memorable event.

June 2009

Nicholas Ayache
Hervé Delingette
Maxime Sermesant

Organization

The 2009 Functional Imaging and Modeling of the Heart conference (FIMH 2009) was organized by INRIA Sophia Antipolis - Méditerranée.

Conference Chairs

General Chair	Nicholas Ayache, INRIA, France
Program Chair	Hervé Delingette, INRIA, France
Publication Chair	Maxime Sermesant, INRIA, France

Program Committee

Elsa Angelini	ENST Paris, France
Simon Arridge	University College London, UK
Theo Arts	Maastricht University, The Netherlands
Leon Axel	NYU Langone Medical Center, USA
Peter Bovendeerd	Eindhoven University, The Netherlands
Dominique Chapelle	INRIA Paris - Rocquencourt, France
Patrick Clarysse	CREATIS-LRMN, University of Lyon, France
Piero Colli Franzone	Pavia University, Italy
Dorin Comaniciu	Siemens, USA
Olaf Dössel	Karlsruhe University, Germany
James Duncan	Yale University, USA
Riccardo Fenici	Rome Catholic University, Italy
Alejandro Frangi	Pompeu Fabra University, Spain
Mireille Garreau	Rennes University, France
Olivier Gérard	General Electrics, Norway
Jean-Frédéric Gerbeau	INRIA Paris - Rocquencourt, France
Arun Holden	Leeds University, UK
Robert Howe	Harvard University, USA
Peter Hunter	Auckland University, New Zealand
Peter Kohl	Oxford University, UK
Boudewijn Lelieveldt	Leiden University, The Netherlands
Cristian Lorenz	Philips Research, Germany
Isabelle Magnin	CREATIS-LRMN, University of Lyon, France
Sherif Makram-Ebeid	Philips Healthcare Research, France
Andrew McCulloch	University of California San Diego, USA
Rob MacLeod	Utah University, USA
Elliot McVeigh	Johns Hopkins University, USA
Dimitris Metaxas	Rutgers University, USA
Johan Montagnat	I3S CNRS, France
Wiro Niessen	Erasmus Medical Center, The Netherlands

Alison Noble	Oxford University, UK
Nikos Paragios	Ecole Centrale Paris, France
Terry Peters	Robarts Research Institute, Canada
Annie Raoult	Paris Descartes University, France
Johan Reiber	Leiden University, The Netherlands
Kawal Rhode	King's College London, UK
Daniel Rueckert	Imperial College London, UK
Frank Sachse	Utah University, USA
Gunnar Seemann	Karlsruhe University, Germany
Maxime Sermesant	INRIA Sophia-Antipolis—Méditerranée, France
Pengcheng Shi	Rochester Institute of Technology, USA
Nicolas Smith	Oxford University, UK
Michel Sorine	INRIA Paris - Rocquencourt, France
Jos Spaan	Academic Medical Center, The Netherlands
Larry Staib	Yale University, USA
Regis Vaillant	General Electrics HealthCare, France
Adriaan van Oosterom	CHUV Lausanne, Switzerland
Max Viergever	University Medical Center Utrecht, The Netherlands
Andreas Wahle	Iowa University, USA
Jürgen Weese	Philips Research, Germany
Graham Wright	Sunnybrook Health Sciences Centre, Canada
Chenyang Xu	Siemens, USA
Alistair Young	Auckland University, New Zealand

Organizing Team (INRIA)

Agnès Cortell
Tommaso Mansi
Monique Simonetti
Isabelle Strobant (Website Chair)

Referees (in addition to Program Committee members)

Martin Bishop	Yingliang Ma	Anna Sher
Phani Chinchapatnam	Tommaso Mansi	Marijn van Stralen
Qi Duan	John Moore	Hari Sundar
Martin Fink	Paul Novotny	Anna Vilanova i Bartrolì
Alan Garny	Jean-Marc Peyrat	Wolfgang Wein
Andrew King	Perry Radau	Liron Yatziv
Klaus Kirchberg	Normand Robert	Shelten Yuen
Cristian Linte	Steven Shea	Yuemin Zhu

Sponsoring Institutions

The FIMH 2009 conference was organized in Nice, France, by INRIA Sophia-Antipolis—Méditerranée with the major involvement of the External Relations and Valorization Events Office and the Asclepios Project Team.

The conference was also sponsored by the companies Philips Research, Siemens Corporate Research, Microsoft Research and by the European Network of Excellence VPH (Virtual Physiological Human).

Table of Contents

Cardiac Imaging and Electrophysiology

Characterization of Post-infarct Scars in a Porcine Model – A Combined Experimental and Theoretical Study 1
Mihaela Pop, Maxime Sermesant, Tommaso Mansi, Eugene Crystal, Jay Detsky, Yuesong Yang, Paul Fefer, Elliot R. McVeigh, Alexander Dick, Nicholas Ayache, and Graham A. Wright

Evolution of Intracellular Ca^{2+} Waves from about 10,000 RyR Clusters: Towards Solving a Computationally Daunting Task 11
Pan Li, Wenjie Wei, Xing Cai, Christian Soeller, Mark B. Cannell, and Arun V. Holden

Cardiac Motion Estimation from Intracardiac Electrical Mapping Data: Identifying a Septal Flash in Heart Failure 21
Oscar Camara, Steffen Oeltze, Mathieu De Craene, Rafael Sebastian, Etel Silva, David Tamborero, Lluis Mont, Marta Sitges, Bart H. Bijnens, and Alejandro F. Frangi

Extracting Clinically Relevant Circular Mapping and Coronary Sinus Catheter Potentials from Atrial Simulations 30
Frank M. Weber, Christopher Schilling, Dorothee Straub, Sandeep Gurm, Gunnar Seemann, Cristian Lorenz, and Olaf Dössel

Cardiac Architecture Imaging and Analysis

Cardiac Fibre Trace Clustering for the Interpretation of the Human Heart Architecture 39
Carole Frindel, Marc Robini, Joël Schaerer, Pierre Croisille, and Yue-Min Zhu

A Quantitative Comparison of the Myocardial Fibre Orientation in the Rabbit as Determined by Histology and by Diffusion Tensor-MRI 49
Stephen H. Gilbert, Olivier Bernus, Arun V. Holden, and Alan P. Benson

Adaptive Reorientation of Cardiac Myofibers: Comparison of Left Ventricular Shear in Model and Experiment 58
Wilco Kroon, Tammo Delhaas, Peter Bovendeerd, and Theo Arts

The Purkinje System and Cardiac Geometry: Assessing Their Influence on the Paced Heart 68
Daniel Romero, Rafael Sebastian, Bart H. Bijnens, Viviana Zimmerman, Patrick M. Boyle, Edward J. Vigmond, and Alejandro F. Frangi

Noise-Reduced TPS Interpolation of Primary Vector Fields for Fiber Tracking in Human Cardiac DT-MRI 78
Feng Yang, Xin Song, Stanislas Rapacchi, Laurent Fanton, Pierre Croisille, and Yue-Min Zhu

Comparison of Rule-Based and DTMRI-Derived Fibre Architecture in a Whole Rat Ventricular Computational Model 87
Martin J. Bishop, Patrick Hales, Gernot Plank, David J. Gavaghan, Jürgen Scheider, and Vicente Grau

Cardiac Imaging

Fixing the Beating Heart: Ultrasound Guidance for Robotic Intracardiac Surgery 97
Robert D. Howe

Lumen Border Detection of Intravascular Ultrasound via Denoising of Directional Wavelet Representations 104
Amin Katouzian, Elsa Angelini, Auranuch Lorsakul, Bernhard Sturm, and Andrew F. Laine

A Statistical Approach for Detecting Tubular Structures in Myocardial Infarct Scars 114
Camille Vidal, Hiroshi Ashikaga, and Elliot R. McVeigh

Quantitative Tool for the Assessment of Myocardial Perfusion during X-Ray Angiographic Procedures 124
Jean Liénard and Régis Vaillant

Multiview RT3D Echocardiography Image Fusion 134
Kashif Rajpoot, J. Alison Noble, Vicente Grau, Cezary Szmigielski, and Harald Becher

Cardiac Electrophysiology

Investigating Arrhythmogenic Effects of the hERG Mutation N588K in Virtual Human Atria 144
Gunnar Seemann, Paola Carillo, Daniel L. Weiss, Martin W. Krueger, Olaf Dössel, and Eberhard P. Scholz

Left to Right Atrial Electrophysiological Differences: Substrate for a Dominant Reentrant Source during Atrial Fibrillation 154
Oleg V. Aslanidi, Mark R. Boyett, and Henggui Zhang

Electrocardiographic Simulation on Coupled Meshfree-BEM Platform 162
Linwei Wang, Ken C.L. Wong, Heye Zhang, and Pengcheng Shi

HERG Effects on Ventricular Action Potential Duration and Tissue Vulnerability: A Computational Study 172
Alan P. Benson, Moza Al-Owais, Wing C. Tong, and Arun V. Holden

Voxel Based Adaptive Meshless Method for Cardiac Electrophysiology Simulation 182
Phani Chinchapatnam, Kawal Rhode, Matthew Ginks, Prasanth Nair, Reza Razavi, Simon Arridge, and Maxime Sermesant

Cardiac Motion Estimation

Local Cardiac Wall Motion Estimation from Retrospectively Gated CT Images 191
Jochen Peters, Olivier Ecabert, Holger Schmitt, Michael Grass, Jürgen Weese

Physically-Constrained Diffeomorphic Demons for the Estimation of 3D Myocardium Strain from Cine-MRI 201
Tommaso Mansi, Jean-Marc Peyrat, Maxime Sermesant, Hervé Delingette, Julie Blanc, Younes Boudjemline, and Nicholas Ayache

Coronary Occlusion Detection with 4D Optical Flow Based Strain Estimation on 4D Ultrasound 211
Qi Duan, Elsa D. Angelini, Auranuch Lorsakul, Shunichi Homma, Jeffrey W. Holmes, and Andrew F. Laine

Cardiac Motion Extraction from Images by Filtering Estimation Based on a Biomechanical Model 220
Philippe Moireau, Dominique Chapelle, and Mariette Yvinec

Active Model with Orthotropic Hyperelastic Material for Cardiac Image Analysis 229
Ken C.L. Wong, Linwei Wang, and Pengcheng Shi

Cardiac Mechanics

Personalised Electromechanical Model of the Heart for the Prediction of the Acute Effects of Cardiac Resynchronisation Therapy 239
Maxime Sermesant, Florence Billet, Radomir Chabiniok, Tommaso Mansi, Phani Chinchapatnam, Philippe Moireau, Jean-Marc Peyrat, Kawal Rhode, Matt Ginks, Pier Lambiase, Simon Arridge, Hervé Delingette, Michel Sorine, C. Aldo Rinaldi, Dominique Chapelle, Reza Razavi, and Nicholas Ayache

Ventricular Mechanical Asynchrony in Pulmonary Arterial Hypertension: A Model Study 249
Joost Lumens, Theo Arts, and Tammo Delhaas

A Hybrid Tissue-Level Model of the Left Ventricle: Application to the Analysis of the Regional Cardiac Function in Heart Failure 258
Julien Fleureau, Mireille Garreau, Erwan Donal, Christophe Leclercq, and Alfredo Hernández

Cardiac Electrophysiology

The Role of Blood Vessels in Rabbit Propagation Dynamics and Cardiac Arrhythmias 268
Matthew Gibb, Martin Bishop, Rebecca Burton, Peter Kohl, Vicente Grau, Gernot Plank, and Blanca Rodriguez

Estimation of Atrial Multiple Reentrant Circuits from Surface ECG Signals Based on a Vectorcardiographic Approach 277
Cédric Duchêne, Mathieu Lemay, Jean-Marc Vesin, and Adriaan van Oosterom

Atrial Anatomy Influences Onset and Termination of Atrial Fibrillation: A Computer Model Study 285
Nico Kuijpers, Huub ten Eikelder, and Sander Verheule

Cardiac Image Analysis

Left Ventricle Segmentation from Contrast Enhanced Fast Rotating Ultrasound Images Using Three Dimensional Active Shape Models 295
Meng Ma, Marijn van Stralen, Johan H.C. Reiber, Johan G. Bosch, and Boudewijn P.F. Lelieveldt

Free-Form Deformations Using Adaptive Control Point Status for Whole Heart MR Segmentation 303
Xiahai Zhuang, Kawal Rhode, Reza Razavi, David J. Hawkes, and Sebastien Ourselin

Integrating Viability Information into a Cardiac Model for Interventional Guidance 312
Helko Lehmann, Reinhard Kneser, Mirja Neizel, Jochen Peters, Olivier Ecabert, Harald Kühl, Malte Kelm, and Jürgen Weese

3D TEE Registration with X-Ray Fluoroscopy for Interventional Cardiac Applications 321
Ameet Jain, Luis Gutierrez, and Douglas Stanton

Multi-sequence Registration of Cine, Tagged and Delay-Enhancement MRI with Shift Correction and Steerable Pyramid-Based Detagging 330
Oscar Camara, Estanislao Oubel, Gemma Piella, Simone Balocco, Mathieu De Craene, and Alejandro Frangi

Segmentation of Left Ventricle in Cardiac Cine MRI: An Automatic Image-Driven Method 339
YingLi Lu, Perry Radau, Kim Connelly, Alexander Dick, and Graham A. Wright

Cardiac Biophysical Simulation

The Importance of Model Parameters and Boundary Conditions in Whole Organ Models of Cardiac Contraction 348
Steven Niederer, Kawal Rhode, Reza Razavi, and Nic Smith

Numerical Simulation of the Electromechanical Activity of the Heart . . . 357
Dominique Chapelle, Miguel A. Fernández, Jean-Frédéric Gerbeau, Philippe Moireau, Jacques Sainte-Marie, and Nejib Zemzemi

A Global Sensitivity Index for Biophysically Detailed Cardiac Cell Models: A Computational Approach 366
Sanjay Kharche, Niklas Lüdtke, Stefano Panzeri, and Henggui Zhang

Cardiac Motion Recovery and Boundary Conditions Estimation by Coupling an Electromechanical Model and Cine-MRI Data 376
Florence Billet, Maxime Sermesant, Hervé Delingette, and Nicholas Ayache

Atrioventricular Blood Flow Simulation Based on Patient-Specific Data 386
Viorel Mihalef, Dimitris Metaxas, Mark Sussman, Vassilios Hurmusiadis, and Leon Axel

Cardiac Research Platforms

A Software Platform for Real-Time Visualization and Manipulation of 4D Cardiac Images 396
Qi Zhang, Roy Eagleson, and Terry M. Peters

euHeartDB: A Web-Enabled Database for Geometrical Models of the Heart 407
Daniele Gianni, Steve McKeever, and Nic Smith

GIMIAS: An Open Source Framework for Efficient Development of Research Tools and Clinical Prototypes 417
Ignacio Larrabide, Pedro Omedas, Yves Martelli, Xavier Planes, Maarten Nieber, Juan A. Moya, Constantine Butakoff, Rafael Sebastián, Oscar Camara, Mathieu De Craene, Bart H. Bijnens, and Alejandro F. Frangi

Cardiac Image Analysis

Maximum Likelihood Motion Estimation in 3D Echocardiography through Non-rigid Registration in Spherical Coordinates 427
Andriy Myronenko, Xubo Song, and David J. Sahn

Large Diffeomorphic FFD Registration for Motion and Strain Quantification from 3D-US Sequences 437
Mathieu De Craene, Oscar Camara, Bart H. Bijnens, and Alejandro F. Frangi

Random Forest Classification for Automatic Delineation of Myocardium in Real-Time 3D Echocardiography 447
Victor Lempitsky, Michael Verhoek, J. Alison Noble, and Andrew Blake

Discriminative Joint Context for Automatic Landmark Set Detection from a Single Cardiac MR Long Axis Slice 457
Xiaoguang Lu, Bogdan Georgescu, Arne Littmann, Edgar Mueller, and Dorin Comaniciu

Cardiac Anatomical and Functional Imaging

Cardiac Imaging and Modeling for Guidance of Minimally Invasive Beating Heart Interventions 466
Terry M. Peters, Cristian A. Linte, John Moore, Andrew Wiles, Jennifer Lo, Danielle Pace, Chris Wedlake, Daniel Bainbridge, Douglas L. Jones, and Gerard M. Guiraudon

Computer-Assisted Open Heart CABG: Image-Guided Navigation for All Target Vessels 476
Claudia Gnahm, Christine Hartung, Reinhard Friedl, Martin Hoffmann, and Klaus Dietmayer

Extraction of Coronary Vascular Tree and Myocardial Perfusion Data from Stacks of Cryomicrotome Images 486
Pepijn van Horssen, Jeroen P.H.M. van den Wijngaard, Froukje Nolte, Imo Hoefer, Rene Haverslag, Jos A.E. Spaan, and Maria Siebes

Intravoxel Fibre Structure of the Left Ventricular Free Wall and Posterior Left-Right Ventricular Insertion Site in Canine Myocardium Using Q-Ball Imaging 495
Hans Dierckx, Alan P. Benson, Stephen H. Gilbert, Michael E. Ries, Arun V. Holden, Henri Verschelde, and Olivier Bernus

Cardiac Electrophysiology

Relationship between Maximal Upstroke Velocity of Transmembrane Voltage and Minimum Time Derivative of Extracellular Potential 505
Kwanghyun Sohn, Bonnie B. Punske, and Frank B. Sachse

Effects of Anisotropy and Transmural Heterogeneity on the T-Wave Polarity of Simulated Electrograms 513
Piero Colli Franzone, Luca F. Pavarino, Simone Scacchi, and Bruno Taccardi

From Intracardiac Electrograms to Electrocardiograms: Models and Metamodels 524
Géraldine Ebrard, Miguel A. Fernández, Jean-Frédéric Gerbeau, Fabrice Rossi, and Nejib Zemzemi

Author Index 535

Characterization of Post-infarct Scars in a Porcine Model – A Combined Experimental and Theoretical Study

Mihaela Pop[1], Maxime Sermesant[2,3], Tommaso Mansi[2], Eugene Crystal[1], Jay Detsky[1], Yuesong Yang[1], Paul Fefer[1], Elliot R. McVeigh[4], Alexander Dick[1], Nicholas Ayache[2], and Graham A. Wright[1]

[1] Sunnybrook Health Sciences Centre, University of Toronto, Canada
mihaela.pop@utoronto.ca, gawright@sri.utoronto.ca
[2] ASCLEPIOS project, INRIA Sophia Antipolis, France
[3] Division of Imaging Science, King's College, London, UK
[4] Dept of Biomedical Engineering, Johns Hopkins University, Maryland, USA

Abstract. Arrhythmias are often associated with healing infarcts and could arise from the border zone of the scars. The main purpose of this work was to characterize the infarct scars using in vivo electro-anatomic CARTO maps (recorded in sinus rhythm) and high-resolution ex-vivo MR images in a porcine model of chronic infarct. The MR images were segmented into scar, peri-infarct and healthy ventricular tissue, and, in select slices, the results of segmentation were validated against histology. Further, the segmented volumes and associated fiber directions (derived from diffusion-weighted (DW) MRI as well as from synthetic models), were used as input to a simple two-variable mathematical model that calculates the propagation of depolarization waves and isochronal maps; and these isochronal maps were compared to the measured ones. We further correlated the size of the scar measured during the electrophysiology (EP) study with scar dimensions obtained from MRI using ex-vivo DW-MRI methods. Finally, we present preliminary results from a qualitative comparison between the scar delineation from ex vivo and in vivo MR images.

Keywords: Cardiac MR imaging, electrophysiology, computer modeling.

1 Introduction

Post-infarction arrhythmias like ventricular tachycardia (VT) and fibrillation could be lethal if not diagnosed and treated properly [1]. In the majority of cases, the peri-infarct (also known as border zone) contains viable bundles (interdigitated within dense collagenous scars) forming channels that facilitate conduction of the electrical excitation wave within and around the scars [2]. This circuit facilitates an abnormal re-excitation of the tissue, resulting in dangerous, high heart rates. The danger for arrhythmias arises from the fact that the peri-infarct zones are viable but of reduced electrical coupling between the cells; this fact is accompanied by changes in myocardium anisotropy due to the deposition of collagen between surviving bundles (consequently, the electrical propagation is altered in this area in the settings of the chronic infarct, >4 weeks).

N. Ayache, H. Delingette, and M. Sermesant (Eds.): FIMH 2009, LNCS 5528, pp. 1–10, 2009.
© Springer-Verlag Berlin Heidelberg 2009

The arrhythmogenic substrate is usually identified during an electrophysiology (EP) study; however, the current clinical technology (e.g. CARTO used in the EP laboratory is limited to surfacic endocardial and/or epicardial maps obtained using long, invasive procedures performed under fluoroscopy [3]. Moreover, many patients are hemodynamically unstable and therefore the arrhythmogenic substrate is mapped only during sinus rhythm (without inducing VT); thus the substrate is often missed and hence cannot be treated via RF ablation [4].

There is a strong clinical motivation to supplement the electrophysiology measurements with accurate 3D anatomical information, as well as to characterize the infarct heterogeneity. Efforts have been made to characterize the post-infarct scars using imaging techniques like MRI and PET. For instance, using diffusion-weighted MRI methods, it was demonstrated in ex-vivo formalin-fixed porcine hearts that the regions of increased apparent diffusion coefficient (ADC) correlated very well with dense scars [5]. Similar findings were seen in patients with prior myocardial infarct. However, motion artifacts affect in-vivo imaging; thus ADC maps and fiber directions cannot be obtained accurately and with high spatial resolution [6]. Another recent study has demonstrated the excellent capabilities of delayed-enhanced MRI to delineate 3D anatomical scars, with fine differentiation between the core infarct and the peri-infarct (i.e., border zone) in ex-vivo porcine hearts. Tissue heterogeneity correlated well with the arrhythmogenic substrate identified from activation maps recorded in vivo in this model [7]. Progress has also been made on the clinical side, and it was shown in small cohorts of patients [8] that the peri-infarct zone size is a powerful predictor of infarction mortality. In this study, the areas of delayed enhancement were subdivided into "core" and "peri-infarct" zones on the basis of differences in signal intensity (core zone = signal $\geq$ 3 SD above that in remote non-infarcted myocardium, and peri-infarct zone = signal 2 to 3 SD above that in remote myocardium). Moreover, other clinical groups showed that the 3D anatomical information reconstructed from MRI [9] and PET [10] give a better delineation of the infarct/peri-infarct areas than the surfacic CARTO maps. However, these studies lack the histological validation for image measures of infarct heterogeneity [7, 8, 11]; furthermore, the thresholds associating EP measurements with infarct scar need to be better defined [3, 9].

Computer modelling has been extensively used in electrophysiology to predict the electrical activity in healthy hearts as well as in pathologic cases [12]. For instance, a simple mathematical model of cardiac electrical propagation (i.e., the two-variable model developed by Aliev & Panfilov [13]) which solves for the transmembrane potential and calculates the propagation of a depolarization wave, has been used to perform electro-mechanical simulations on a 3D healthy heart model [14] and with reentrant substrates [15]. It was also used to build maps of local apparent electrical conductivity by integrating information from measurements obtained via a multi-electrode sock in an in-vivo dog heart model [16]. Most of the cardiac models account for tissue anisotropy, and the fiber directions are often obtained via DW-MRI. Synthetic fibers derived from population data may also be useful when the DW-MRI data is not available but their accuracy remains to be tested.

Our broad aim is to characterize the post-infarction scars using electro-anatomic CARTO maps augmented with 3D information from MR imaging, and to complement this with insights from theoretical modelling. In the current work, we focus on: i)

building such a model from MRI; ii) comparing the scar dimensions in the model and anatomic CARTO maps; and iii) qualitatively comparing the theoretical predictions (e.g. isochronal maps) with those measured during the EP study. Figure 1 illustrates the workflow.

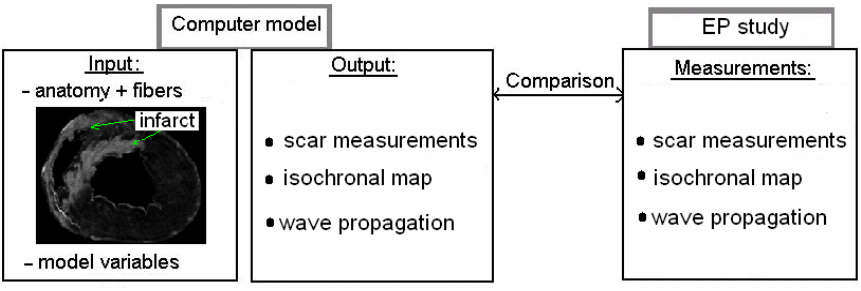

Fig. 1. Diagram of the comparison between the computer model and experiments

2 Methodology

We describe below the experimental steps following the order in which they were performed. We first completed the in vivo EP studies. We then explanted the hearts and used DW-MRI to characterize the infarct heterogeneity, as well as to derive the myocardial fiber directions. The segmented volumes were further used to construct the computer model. Next, the simulations were performed with parameters assigned by zones defined from the segmentation procedure. To validate the segmentation step, whole-mount histology was performed in select heart slices cut in short-axis.

2.1 EP Study

The animals (6 swine) had myocardial infarcts (MI) generated by a 90min coronary artery occlusion followed by reperfusion (in accordance to the animal research protocol guidelines approved by Sunnybrook Health Sciences Centre). Three animals had the left anterior descending (LAD) artery occluded, while the left circumflex (LCX) artery was occluded in the other three. The in vivo EP studies of the healing MI were performed at 4-5 weeks post-occlusion.

2.2 Magnetic Resonance Imaging and Segmentation

At the completion of the EP study, the hearts were explanted, gently preserved in formalin, and imaged using a 1.5Tesla Signa GE MR scanner for anatomy, scar characterization and myocardial fiber directions, using the MR pulse sequence described in [17]. In this work, we used the following MR parameters: TE=32ms, TR=700ms, NEX=1, *b*-value ~ 600, 7 directions for diffusion gradients, FOV/matrix =10cm, 256x256 acquisition matrix, and 2mm slice thickness. The heart anatomy was extracted from the un-weighted images (i.e., b=0) and used to generate the volumetric mesh for the mathematical model. Next, the apparent diffusion coefficient (ADC) maps were calculated using MedINRIA software and further analyzed by segmenting the heart to study the tissue heterogeneity. For segmentation, we have adapted the

expectation-maximization (EM) algorithm described in [18], which is initialized using a 3-class k-means clustering. After identification and removal of the outliers, the final segmented image contains three zones: healthy tissue, peri-infarct and infarct (dense scar). The synthetic fibers were computer generated based on well known variations of myocardial fibers from epicardium to endocardium [6, 17, 19]. The segmentation analysis, as well as the calculations of fiber directions were performed with Matlab (Mathworks, CA).

2.3 Histology

Representative slices cut in short-axis view were prepared for whole-mount histology and stained with Mason's Trichrome to enable the visualization of collagenous fibers. The samples (cut at 5μm) were scanned at 2-10μm resolution.

2.4 Computer Model

We use the cardiac mathematical model developed by Aliev and Panfilov. In the system of equations given in (1-2) we solve for the action potential (V) and recovery variable contribution (r). The term *–kV(V-a)(V-1)* controls the fast processes (initiation and upstroke of action potential) via the threshold parameter *a*, while *r,* determines the dynamics of the repolarization phase.

$$\frac{\partial V}{\partial t} = \nabla \cdot (D\nabla V) - kV(V-a)(V-1) - rV \tag{1}$$

$$\frac{\partial r}{\partial t} = -(\varepsilon + \frac{\mu_1 r}{\mu_2 + V})(ku(u-a-1)+r)\,. \tag{2}$$

Most of the parameters (i.e. ε=0.01 a=0.1, k=8, and μ_2=0.3) were set to reproduce the shape, duration and restitution of action potentials (AP) as in [15]. This model accounts for the heart anisotropy via the diffusion tensor, *D*, which depends on a tissue's conductivity, set to 1 for a normal/healthy conduction and 0 for infarct areas. The value in the anisotropy ratio (a parameter in the diffusion tensor D) is set to 0.25 for a wave propagating twice as fast along the fiber as in the transverse direction.

The heart surface mesh was created from the anatomy images using classical segmentation algorithms (thresholding, mathematical morphology, marching cubes). Then, the volumetric tetrahedral mesh was generated with the GHS3D package (INRIA, France). We solved for the transmembrane potential using the Finite Element Method, with an explicit Euler time integration scheme. The code was written in C++ and uses OpenGL libraries to display the results.

3 Results

3.1 Model Building from DW-MRI

Figure 2 shows fiber directions obtained from DW-MRI, for a heart with LAD-occlusion (a) and LCX occlusion (c), respectively. The remarkable changes in fiber directions in the settings of the chronic infarct were due to ventricular re-modelling and can be observed by direct comparison with synthetic fibers (the latter being

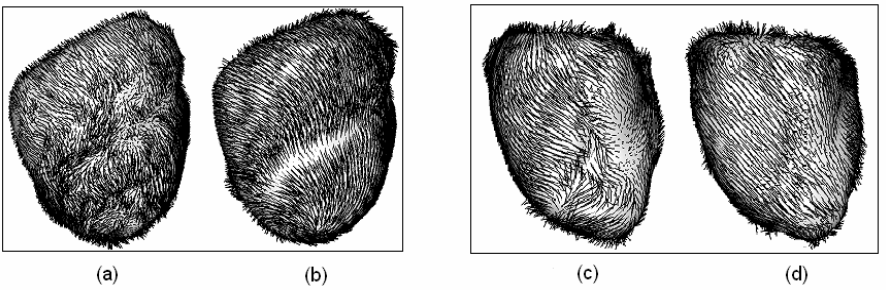

Fig. 2. Fibers reconstructed from DW-MRI (a) and (c), and synthetic fibers (b) and (d)

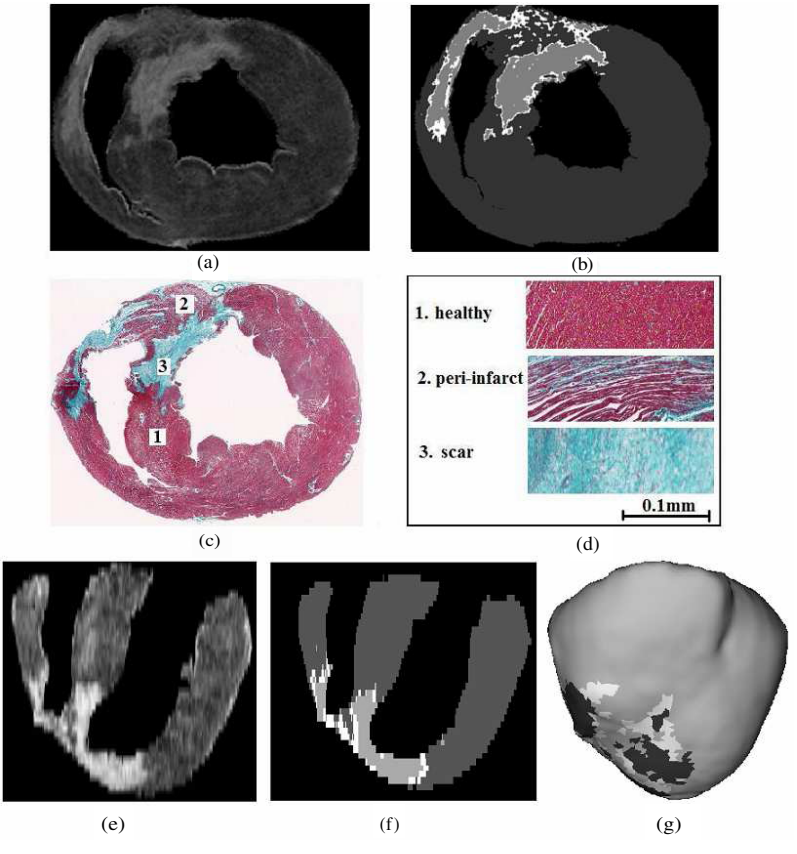

Fig. 3. A representative slice from the LAD-MI showing: short-axis ADC map from DW-MRI (a), its corresponding segmentation using the EM algorithm (b) as well as the corresponding Mason's Trichrome histology (c) with example areas from the healthy myocardium, peri-infarct, and dense/collagenous scar (d). A long axis slice of ADC map (e) and its segmentation (f) as well as the 3D volumetric reconstructed heart (g).

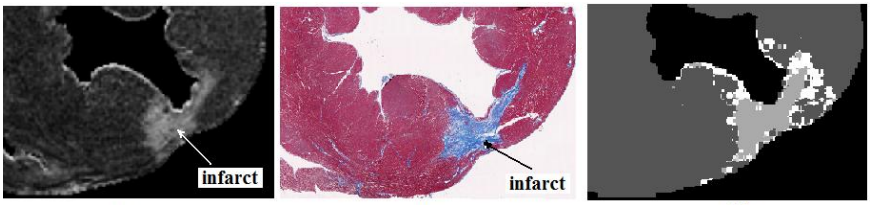

Fig. 4. A representative slice from the LCX-MI showing: ADC map from DW-MRI (a), corresponding histology (b) and the segmented slice (using the EM algorithm) (c)

generated from healthy hearts) displayed in Fig 2 b, and d, respectively. Note that for the cardiac computer model, the fiber directions were specified at the baricenter of each tetrahedral element of the computational mesh.

Figures 3 and 4 give examples of the model construction from the segmented ADC obtained in two hearts. The bright areas in Fig 3a and 4a, correspond to an expected increase in ADC values in the scar and peri-infarct. Histological analysis revealed on microscropic observation that infarct areas remodeled over time. Dense scars (stained in green/blue color in Figs 3c-d and 4b) have necrotic myocytes and large zones with myocytes replaced by dense fibrosis (in green-blue) accompanied by a complete loss of anisotropy. The peri-infarct areas have mixed islands of viable and non-viable myocytes, as well as fiber directions slightly changed due to droplets of collagen deposits between surviving cardiac myocytes (viable myocytes in red) (Fig 3d). The infarct heterogeneity was very well identified by the EM algorithm (see white areas in Figs 3b,f and 4c corresponding to peri-infarct, and light-grey areas corresponding to dense scar).

In the model, the conductivity term controls the degree of cellular uncoupling; thus, the infarct zone is modeled as a zone of zero electrical conductivity. As a result, the scar does not propagate the excitation wave regardless of the fiber directions in the scar. In the peri-infarct zone, the conductivity is reduced compared to that of normal myocardium and the wave will propagate through the peri-infarct, but at a slower rate so that direction of the wave front is influenced by the fiber orientation.

3.2 Comparison between Experiments and Theoretical Model

Voltage maps were constructed from CARTO epicardial recordings, using the usual cut-off threshold at <0.5mV for infarct (red), 0.5-1.5mV border zone (peri-infarct, green-blue) and >1.5mv healthy tissue (purple), with an example provided in Fig 5a for LAD-MI. The scar (measured on the epicardium) was 13.1cm^2 on the CARTO map vs. 11.5 cm^2 in MRI.

Moreover, the activation times can be represented by isochrones (lines connecting pixels of equal activation time). Isochronal maps can be produced over one heart beat; an example is presented in Figure 4.b-d. The isochrones calculated from the bipolar recordings (b) agreed reasonably well with those from simulated activation times (displayed on the mesh for the fibers obtained from DW-MRI (c) and the synthetic fibers (d)). For the simulations in this study, we used a computational time step of

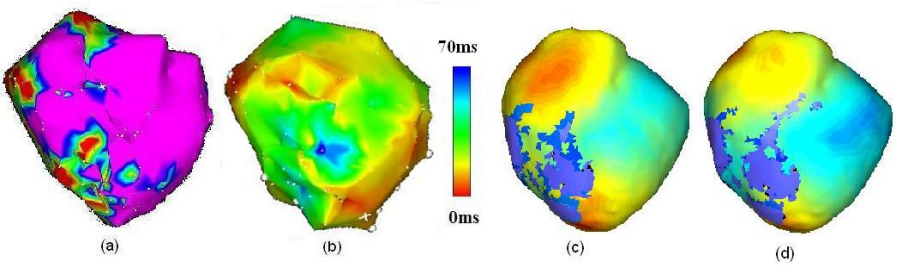

Fig. 5. Voltage map (CARTO) of the LAD-MI(a); isochronal maps generated from bipolar recordings (b) and simulated isochrones on the mesh with fibers from DW-MRI (c) and synthetically generated (d), where then red areas correspond to early activation times

$1x10^{-4}$s. The simulation time for 0.8s on a mesh of approximately 230,000 elements (~1.2mm element size) is about 1h on an Intel ® Core ™2 duo CPU, T5550 @1.83GHz, with 4Gb of RAM.

Results are also illustrated for an LCX-MI heart in Fig. 6, where the scar (in red) and border zone (in green-blue) is measured to be $<1cm^2$ using electro-anatomic CARTO voltage maps on the endocardium (a) and 2.3 cm^2 on the epicardium (b). The epicardial scar ($2.2cm^2$) from segmentation of MR images is shown on the reconstructed 3D model (c); although not shown, the endocardial scar was measured to be $2.4cm^2$ from MR images.

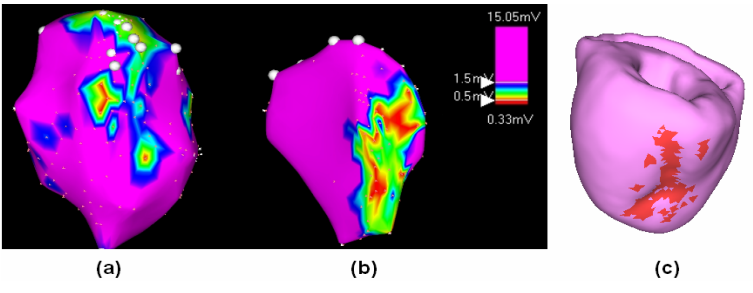

Fig. 6. Scar (red color) delineation in voltage maps (CARTO) of an LCX-MI: endocardial (a) and epicardial (b) maps, and on the 3D heart model (c)

4 Discussion and Future Work

In this work we report results for MRI characterization of post-infarct scars in a porcine model and associated electrophysiology. Experimental results obtained from ex vivo measurements demonstrated that infarct heterogeneity is well characterized by DW-MRI methods. The infarct areas can be segmented using the E-M algorithm, and good qualitative correlation was as proved by the histological analysis. Here, the logical next step will be to quantify the model-predicted scar against the Mason's Trichrome stain that we used. In particular, this stain will permit the quantification of collagen/fibrosis (which is related to the electrical uncoupling of the cells). In the

future, we will perform a comparison between the areas of these three segmented zones against corresponding identified areas in the histological images. A few methods based on color thresholding are available for microscopic image analysis and will be explored in the future. Further, the segmented images served to build a 3D volumetric model of the heart that was used to calculate the scar dimensions and compare them with measured size from CARTO voltage maps; this could help in the calibration of the voltage thresholds for infarct (which are still ambiguous in the EP study).

The model developed by Aliev&Panfilov is not a biophysical model, but rather rapidly computes, at a macroscopic scale, the propagation of depolarization wave, from which the isochronal maps can be calculated and compared with isochrones from electrical measurements. Our initial results showed good correspondence between the model and experimental measures. However, results were limited by the fact that we did not register the CARTO anatomical images with the MR images; thus localization of errors was not performed. In CARTO images we will quantify the scar and peri-infarct using either the voltage maps or isochronal maps, or a combination of both, exactly as per the method provided in [9]. An image-based model was recently successfully constructed to characterize the atrium excitation [20]; for accurate comparisons, such estimations should be included. Obviously, the in vivo MR images will help identifying the scars areas; thus the CARTO maps will be recorded with a higher density around the border zone of the infarct. Then, a registration will be performed: a) for the endocardial maps we will use anatomical markers (i.e. valves, apex) to register the model-based surfaces (RV, LV) to the CARTO endocardial surface (as per the method provided in [9]), and b) the epicardial surface will be registered to the model by a method that we have previously developed and used to register the anatomic model to epicardial surfaces derived via optical images [21]. The epicardial map is recorded during open chest procedure (in our current CARTO experiment), and that makes it easy to glue opaque markers (which are visible in the MRI) onto the exposed surface; the markers location can then be used for a rigid registration between the CARTO surface and the epicardial surface of the heart model (as in [21]).

Our efforts are also being extended to building a 3D model from in-vivo MRI data. For instance, Fig.7 presents a preliminary result comparing the left ventricle segmentations of an in-vivo MR image using multi-contrast delayed enhancement

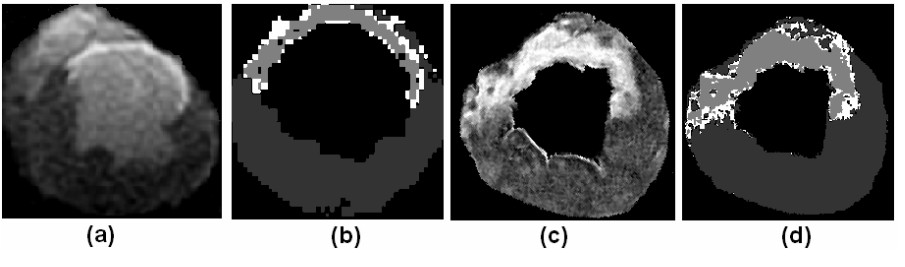

Fig. 7. Comparison between segmentation of in vivo MCDE and ex vivo DW-MR images

(MCDE) method developed in our laboratory [22] and a corresponding ex vivo DW-MR image. While good agreement was found, next steps include obtaining higher resolution in vivo images, as well as characterizing and segmenting the scars involving the right ventricle. "Heterogeneous" areas were identified in DE-MRI by Ashikaga et al [7] in ex vivo images acquired with a resolution of 0.4x0.4x0.4mm as well as by Yan [8] in humans (using a 8-mm slice thickness). In our studies we focus on regions which are more than 1 pixel wide, reducing the likelihood that partial voluming between two distinct tissue regions dominates we focus on regions which are more than 1 pixel wide, reducing the likelihood that partial voluming between two distinct tissue regions dominates. To demonstrate further that partial voluming effects do not dominate in the highlighted regions, we plan to perform experiments with a smaller slice thickness in the future (currently we are using a 2-mm slice thickness for the ex vivo DTI method and 5mm for the in vivo MCDE).

To conclude, the validation and calibration of fast computer models is ongoing; this is an important step prior to their integration into clinical applications (i.e. diagnosis and therapy planning); scar characterization obtained from ex vivo imaging data is useful in facilitating this validation / calibration phase. The goal of the these models is to be used in combination with less invasive imaging and EP diagnostic procedures, to improve the outcome of the therapy and its success rate [23]. Minimal amount of imaging time and pre-operative processing is desired; our model is highly adaptive and ultimately will be fitted to patient data. One limitation will be the lack of the fiber directions data, but models with synthetic fibers can be used instead. We also envision that MRI combined with limited information (e.g. 12-lead ECG) as in [24], together with the theoretical characterization of action potential propagation, will be enough to diagnose many of the scar-related diseases.

References

1. Kebler, A., Rudy, Y.: Basic mechanisms of cardiac impulse propagation and associated arrhythmias. Physiological Review 84, 431–488 (2004)
2. Ursell, P.C., Gardner, P.I., et al.: Structural and electrophysiological changes in the epicardial border zone of canine myocardial infarcts during healing. Circ. Research 56, 436–451 (1985)
3. Arenal, A., del Castillo, S., Gonzalez-Torrecilla, E., et al.: Tachycardia-related channel in the scar tissue in patients with sustained monomorphic VT. Influence of the voltage scar definition. Circulation 110, 2568–2574 (2004)
4. Ciaccio, E.J., Chow, A.W., Kaba, R.A., et al.: Detection of the diastolic pathway, circuit morphology, and inducibility of human postinfarction VT from mapping in sinus rhythm. Heart Rhythm 5(7), 981–991 (2008)
5. Wu, E.X., Wu, Y., et al.: MR diffusion tensor imaging study of postinfarct myocardium structural remodeling in a porcine model. Magnetic Resonance Medicine 58(4), 687–695 (2007)
6. Wu, M.T., Tseng, W.Y., Su, M.Y., et al.: Diffusion tensor magnetic resonance imaging mapping the fiber architecture remodeling in human myocardium after infarction: correlation with viability and wall motion. Circulation 114, 1036–1045 (2006)
7. Ashikaga, H., Sasano, T., Dong, J., et al.: MR based anatomical analysis of scar-related VT. Circulation Research, 1–9 (2007)

8. Yan, A.T., Shayne, A.J., Brown, K.A., et al.: Characterization of the Peri-Infarct Zone by Contrast-Enhanced Cardiac MRI is a powerful predictor of Post-Myocardial infarction mortality. Circulation 114, 32–39 (2006)
9. Codreanu, A., Odille, F., Aliot, E., et al.: Electoanatomic characterization of post-infarct scars. Comparison with 3D myocardial scar reconstruction based on MRI. Journal of the American College of Cardiology 52(10), 839–842 (2008)
10. Dickfield, T., Lei, P., Dilsizian, V., et al.: Integration of 3D scar maps for VT ablation with PET-Computed tomography. Cardiovascular Imaging 1(1), 73–82 (2008)
11. Nazarian, S., Bluemke, D.A., Lardo, A.C., et al.: Magnetic resonance assessment of the substrate for inducible VT in nonischemic cardiomyopathy. Circulation 112(18), 2821–2825 (2005)
12. Clayton, R.H., Panfilov, A.V.: A guide to modelling cardiac electrical activity in anatomically detailed ventricles. Progress in Biophysics & Molecular Biology (review) (2007)
13. Aliev, R., Panfilov, A.V.: A simple two variables model of cardiac excitation. Chaos, Soliton and Fractals 7(3), 293–301 (1996)
14. Nash, M.P., Panfilov, A.V.: Electromechanical model of the excitable tissue to study reentrant cardiac arrhythmias. Progress in Biophysics and Molecular Biology 85, 501–510 (2004)
15. Sermesant, M., Delingette, H., Ayache, N.: An Electromechanical Model of the Heart for Image Analysis and Simulation. IEEE Trans. on Med. Imag. 25(5), 612–625 (2006)
16. Moreau-Villeger, V., Delingette, H., Sermesant, M., Ashikaga, H., McVeigh, E.R., Ayache, N.: Building maps of local apparent conductivity of the epicardium with a 2-D electrophysiological model of the heart. IEEE Transactions on Biomedical Engineering 53(8), 1457–1466 (2006)
17. Helm, P., Tseng, H.J., Younes, L., McVeigh, E.R., Winslow, R.L.: Ex vivo 3D diffusion tensor imaging and quantification of cardiac laminar structure. Magn. Res. Med. 54, 850–859 (2005)
18. Van Leemput, Maes, K., Vandermeulen, F., et al.: Automated segmentation of multiple sclerosis lesions by model outlier detection. IEEE Trans. on Medical Imaging 20(8), 677–688 (2001)
19. Arts, T., Costa, K.D., Covell, J.W., et al.: Relating myocardial laminar architecture to shear strain and muscle fiber orientation. Cardiovascular Research Institute 280(5), 2222–2229 (2001)
20. Tilg, B., Fischer, G., Modre, R., Hanser, F., et al.: Model-based imaging of cardiac electrical excitation in humans. IEEE Transactions on Medical Imaging 21(9), 1031–1039 (2002)
21. Pop, M., Sermesant, M., Lepiller, D., et al.: Fusion of optical imaging and MRI for the evaluation and adjustment of macroscopic models of cardiac electrophysiology: a feasibility study. Medical Image Analysis (2008) (July 25, E-Pub. ahead of print)
22. Jay, D.S., Stainsby, J.A., Vijayaraghavan, R., Graham, J.J., Dick, A.J., Wright, G.A.: Inversion-recovery-prepared SSFP for cardiac-phase-resolved delayed-enhancement MRI. Magn. Res. Med. 58(2), 365–372 (2007)
23. Sermesant, M., Peyrat, J.M., Chinchapatnam, P., Billet, F., Mansi, T., Rhode, K., et al.: Toward patient-specific myocardial models of the heart. Heart Fail Clin. 4(3), 289–301 (2008)
24. Strauss, D.G., Wu, K.C.: Imaging myocardial scar and arrhythmic risk prediction – a role for the electrocardiogram? J. Electrocardiol. 42(2), 138.e1–8 (2009)

Evolution of Intracellular Ca^{2+} Waves from about 10,000 RyR Clusters: Towards Solving a Computationally Daunting Task

Pan Li[1], Wenjie Wei[1], Xing Cai[1], Christian Soeller[2], Mark B. Cannell[2], and Arun V. Holden[3]

[1] Center of Biomedical Computing, Simula research laboratory, 1325 Lysaker, Norway
[2] Department of Physiology, School of Medical Sciences, University of Auckland, Private Bag 92019, Auckland, New Zealand
[3] Computational Biology Laboratory, Institute of Membrane and Systems Biology, University of Leeds, Leeds LS2 9JT, United Kingdom
panli@simula.no
http://www.simula.no

Abstract. Detailed knowledge of spatial-temporal behaviours of intracellular calcium dynamics is very important in understanding excitation-contraction coupling of cardiac myocytes under both normal and pathological conditions, such as initiation and propagation of spontaneous calcium waves. A full cell simulation integrating about 10,000 Ca^{2+} release units (CRUs) in a typical cardiac myocyte is considered a multi-scale, computationally demanding problem. In this paper, we imported an experimentally obtained spatial distribution of Ryanodine Receptor (RyR) clusters into a spatially extended, stochastic model of intracellular Ca^{2+} dynamics, to investigate the role of the structural bifurcation of Z-disks on the initiation and propagation of intracellular Ca^{2+} waves from spatially symmetric Ca^{2+} sparks. Besides, we also proposed a simple parallelization strategy to increase computational speed for this chanllenging problem in cardiac modelling.

Keywords: Ca^{2+} dynamics, stochastic model, parallel computing.

1 Introduction

Intracellular Ca^{2+} signalling regulates excitation-contraction (EC) coupling in the heart. During membrane depolarization, Ca^{2+} enters the cell via L-type Ca^{2+} channel (LCC) located at T-tubule network, then evokes major Ca^{2+} release via nearby clusters of Ryanodin Receptors (RyR) located in regions of close apposition between Sarcoplasmic Reticulum (SR) and surface membranes. This process is referred as Ca^{2+} induced Ca^{2+} release (CICR), and these discrete, elemental Ca^{2+} release events from SR as Calcium sparks. The action potential triggering local elementary Ca^{2+} releases, or Ca^{2+} sparks [1], will then result in a synchronized Ca^{2+} elevation throughout the cell, leading to a contraction.

N. Ayache, H. Delingette, and M. Sermesant (Eds.): FIMH 2009, LNCS 5528, pp. 11–20, 2009.
© Springer-Verlag Berlin Heidelberg 2009

The dyadic space between T-tubule and SR, which contains locally coupled LCC and RyR clusters, is also referred as Ca^{2+} release unit (CRU), see Figure 1(A). Ca^{2+} signalling in the dyadic space is fundamentally discrete and stochastic [2], and there are about 10,000 dyadic spaces with different Ca^{2+} dynamics in a typical cardiac myocyte [3], and, in rat cardiac myocytes, between 120 and 260 RyRs per cluster [4]. It is a multiscale, computationally demanding task to study how variations of their local interactions can lead to different global Ca^{2+} wave behaviours [3], for example, the initiation and propagation of spontaneous Ca^{2+} waves, which may be linked to the genesis of cardiac arrhythmias [5]. A spatially extended, stochastic model of intracellular Ca^{2+} dynamics, that covers time scales from less than a millisecond to a few seconds, and space scales from nanometers to about 100 μm, is needed because of the spatio-temporal nature of intracellular Ca^{2+} signalling. There are a number kinetically detailed, spatially homogeneous or compartmental models of intracellular Ca^{2+} dynamics [6] [7], where spatial aspects have been neglected. This is due to both the lack of experimental measurements of spatial localization of Ca^{2+} regulating proteins, and the required computational demand. However, recent advances in high resolution imaging of cardiac proteins and high performance computing allow 3D plus time (3D+t) reconstruction of intracellular Ca^{2+} dynamics.

The spatial organization of RyR clusters has been considered to have a longitudinal spacing between neighbouring RyR clusters is at least twice wider as the

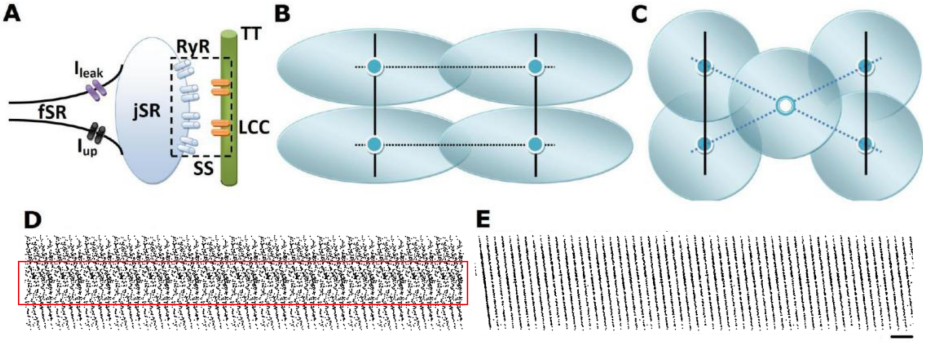

Fig. 1. (A) Schematic illustration of Ca^{2+} dynamics within a CRU, including the coupling between LCC and corresponding RyRs inside the subspace. (B) (C) Theoretical explanations of solitary Ca^{2+} wave propagation from discrete CRUs based on anisotropic (B) and isotropic (C) Ca^{2+} sparks, where anisotropic diffusion from a Ca^{2+} spark can encourage longitudinal synchronization of neighbouring CRUs to overcome the effects of larger longitudinal spacing, while isotropic Ca^{2+} spark can also lead to sustained wave propagation given that branching structure of Z-disk can bridge the gap. (D) (E) Geometric models of whole cardiac myocyte with spatial localization of RyRs reconstructed by stacking an experimentally measured data set that covers about 3.5 Z-disks repetitively in the longitudinal direction (D), aligning these RyR clusters in two-dimensional planes with an angle of 7.6 degrees to the transverse axis (E). The scale bar represents 5 μm. The red box in (D) indicates the bifurcating region.

transversal spacing, based on many previous experimental and theoretical studies [9]. Such a 2:1 organization, together with an anisotropic profile of Ca^{2+} spark diffusion, reproduced experimental observations of isotropic Ca^{2+} wave propagation. However, recent evidence shows that both of these assumptions were inappropriate [4] [8]. Although high resolution imaging of RyRs and Z-disks in rat ventricular myocytes has shown peripheral localization of RyR clusters might still seem to fit in the 2:1 fashion, it is complicated in the centre of the cell. In Soeller et al's work [4], the observation of structural bifurcation of Z-disks, which refers to the splitting of Z-disks into two branches, leads to a less independent or standalone understanding of neighbouring Z-disks, while the localization of RyR clusters were also shown to follow such a branching structure. Ca^{2+} sparks were recently reported to be isotropic instead [8]. These experimental findings might suggest that an isotropic profile of Ca^{2+} sparks, and the branching structure of the Z-disk, can provide a basis for explaining intracellular Ca^{2+} wave behaviours - see Figure 1 (C).

The aim of this study is to (i) propose a theoretical explanation for initiation and propagation of three-dimensional intracellular Ca^{2+} waves incorporating these new experimental results, and investigate the role of branching Z-disk in regulating cytoplasmic Ca^{2+} transient, and also to (ii) implement a parallelization strategy for solving this problem. Here, we focused on spontaneous Ca^{2+} release activities in a ventricular myocyte.

2 Methods

2.1 Reconstruction of RyR Distribution for Computer Simulations

RyR2 clusters were labelled using mouse monoclonal anti-RyR2 Abs in isolated rat cardiac myocytes, while the Z-disks were labelled using a mouse monoclonal Ab against alpha-actinin. Fluorescent images were obtained with a Zeiss LSM410 laser scanning confocal microscope using a Zeiss 63x NA 1.25 oil-immersion objective. The distribution of RyR clusters was determined using a cluster detection algorithm, and provided for computational simulations in the format of Cartesian coordinates with number of RyRs per cluster.

The original data set has the dimensions of 24 μm $\times$ 24 μm $\times$ 7.2 μm, that covers about three and a half Z-disks, and it was represented as a computational domain discretised into 120 $\times$ 120 $\times$ 36 voxels. Due to the repetitive nature of RyR distribution along the longitudinal axis, an extended geometric model (Realistic geometry) with dimensions of 120 $\times$ 120 $\times$ 570 containing 10830 RyR clusters, was constructed by cascading the original experimentally measured data set throughout the full length of the cell for more detailed investigation of global behaviours, see Figure 1(D). For comparison with previous studies [9] [10], a second model (Pseudo geometry), in which all RyR clusters were placed on idealized flat and non branching Z-disks based on experimentally measured data, was also constructed, and to mimic the general geometry of the experimental data, these flat planes representing Z-disks were orientated at an angle of 7.6 degrees to the transverse axis, see Figure 1(E).

The number of RyRs per cluster ranged from 8 to 500 with mean value of 174 and standard deviation of 144 (see Figure 2), and is estimated according to the methods described in [4]. For this particular dataset, it seems that the peripheral RyR clusters have more RyRs expressed than the centre of the cell.

There is a possibility that the number of RyRs on clusters in the periphery are somewhat artificially high. This could arise from the imaging geometry which would tend to cause closely spaced clusters on the sarcolemma being merged within the confocal point spread function. In the future, this limitation can be overcome by merging two data sets, one of which has high resolution sarcolemmal data to identify surface clusters correctly, the second oriented so that we estimate the t-system associated clusters correctly. In this paper we have used a data set optimized for the t-system associated clusters. Here, we assume the calcium release strength can be scaled by the number of RyRs according to [12], then, a larger Ca^{2+} release on average is expected for peripheral CRUs.

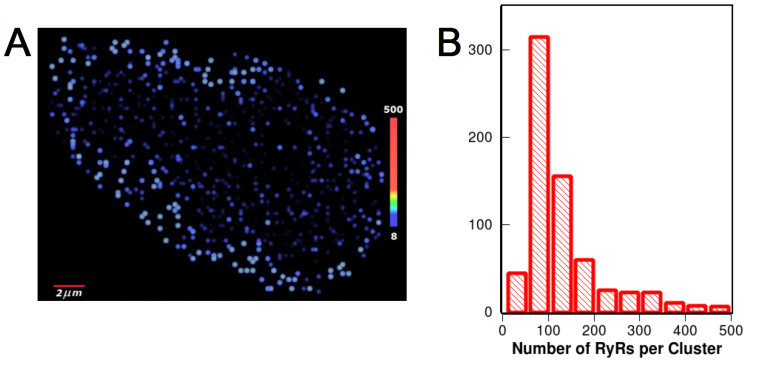

Fig. 2. (A) Projection of RyR clusters of the experimental dataset onto a 2D transversal plane of the cell, which is colour-coded according to the number of RyRs per cluster. Large RyR clusters appear to be concentrated in the peripheral region. (B) The statistical profile of number of RyRs per cluster.

2.2 Modeling Intracellular Ca^{2+} Dynamics

A spatially extended model [11] was modified to simulate intracellular Ca^{2+} dynamics, with details of stochastic triggering of Ca^{2+} release from CRU, Ca^{2+} uptake back into SR, SR leak current, cytoplasmic buffers. This modified model can be described as:

$$\frac{\partial \left[Ca^{2+}\right]}{\partial t} = \nabla \cdot \left(D_c \nabla \left[Ca^{2+}\right]\right) + N_{\mathrm{RyR}}^{\frac{1}{s}} \frac{i_{Ca}}{2F} \delta(\boldsymbol{r}) + J_{\mathrm{buffer}} - J_{\mathrm{pump}} + J_{\mathrm{leak}}, \quad (1)$$

$$J_{\mathrm{buffer}} = \sum_{n=1}^{2} \left(-k_n^+ \left[Ca^{2+}\right] \left([B_n]_T - [CaB_n]\right) + k_n^- \left[CaB_n\right]\right) \quad (2)$$

$$J_{\mathrm{pump}}\left(Ca^{2+}\right) = \frac{v_{\mathrm{pump}} \left[Ca^{2+}\right]^m}{K_{\mathrm{pump}}^m + \left[Ca^{2+}\right]^m}, \quad J_{\mathrm{leak}} = J_{\mathrm{pump}}(c_0), \quad (3)$$

where i_{Ca} is the elementary Ca^{2+} release strength from a single Ryanodine receptor. Because of local variations in CRU excitability and CRU release flux can effect global wave, the strength of elementary Ca^{2+} release from a RyR cluster is scaled by $N_{\mathrm{RyR}}^{\frac{1}{s}}$ with $s \geq 2$, where N_{RyR} is the number of RyR receptors per cluster according to [12] , rather than being considered uniform throughout the cell. Here, $s = 2$ was used. $\delta(\boldsymbol{r})$ represents the spatial discretion of RyR clusters. n identifies the cytoplasmic buffers. For Calmodulin, $k_1^+ = 100\mu M^{-1}/s$, $k_1^- = 38s^{-1}$, and $[B_1]_T = 24\mu M$; for Troponin C, $k_2^+ = 39\mu M^{-1}/s$, $k_2^- = 20s^{-1}$, and $[B_2)_T = 70\mu M$.

RyR clusters are spatially discrete, and their probability to fire is governed by a probability function P, based on the Ca2+ concentration, and also the Ca2+ sensitivity factor K_{poss}. A RyR cluster releases Ca^{2+} when

$$P_{[Ca^{2+}](\boldsymbol{r_N},t)} = P_{\max}\frac{\left[Ca^{2+}\right]^n}{K_{poss}^n + \left[Ca^{2+}\right]^n} > u_{\mathrm{rand}}, \quad T_N^M > T_N^{M-1} + \tau_R, \tag{4}$$

where T_N^M denotes the Nth sparks at site M, and u_{rand} is a uniformly distributed random number between 0 and 1. For isotropic calcium diffusion, D_c of 150 μ^2/s was used for isotropic calcium diffusion, and other detailed parameter settings were used the same as in [11]. There are seven variables in this model, while constants i_{Ca}, τ, K_{poss}, D_c were manipulated to produce various calcium wave behaviors.

Table 1. Model parameters

Parameter	Standard Value	Definition
D_c	$150\mu m^2$/s	Ca^{2+} diffusion coefficient
τ	10 ms	Open time of Ca^{2+} release unit
i_{Ca}	2pA	Amplitude of elemental Ca_{2+} release
F	96500 C/mol	Farady's constant
s	2	Scale factor for Ca^{2+} release
v_{pump}	200 μM/s	Maximum SR pump rate
K_{pump}	0.184 μM	SR pump Michaelis constant
m	4.0	Pump hill coefficient
n	1.6	Hill coefficient for $P_{Ca^{2+}}$
c_0	0.10 μM	Background Ca^{2+} concentration

2.3 Numerical Method and Parallelization

The whole geometry of a cell is of an irregualr shape and thus immersed inside a cuboid with $570 \times 120 \times 120$ grid points. The occupied volume of the cell is marked out for each point. Points outside the cell do not participate in computation. The remaining points represent either cytoplasm or CRUs. From Fig. 2 (A), one can easily see the shape of a 2D cross-section. For discretization, Forward Euler is used in the temporal direction and a standard seven-point stencil of finite difference is used in the spatial direction. The resulting numerical method

is thus fully explicit. The 2D cross-section of the cell geometry is of an irregular shape that changes very little along the z-direction. This prompted us to adopt a 1D domain partitioning along that direction, as the way of dividing the computational load among multiple processors. Comparing with a general 3D domain partitioing strategy based solely on the number of grid points, which may or may not lie inside the cell geometry, such a 1D partitioning gives better load balance. A potential disadvantage, however, is that the communication overhead may become too big, when each subdomain is too thin in the z-direction. To enable data exchange between neighboring processors, we have adopted the MPI programming standard [13].

3 Results

3.1 Effects of RyR Localization on Initiation of Ca^{2+} Wave

To investigate the effects of bifurcating Z-disks on intracellular Ca^{2+} wave propagation, RyR clusters in a small region (2μm $\times$ 12μm $\times$ 12μm) at the upper

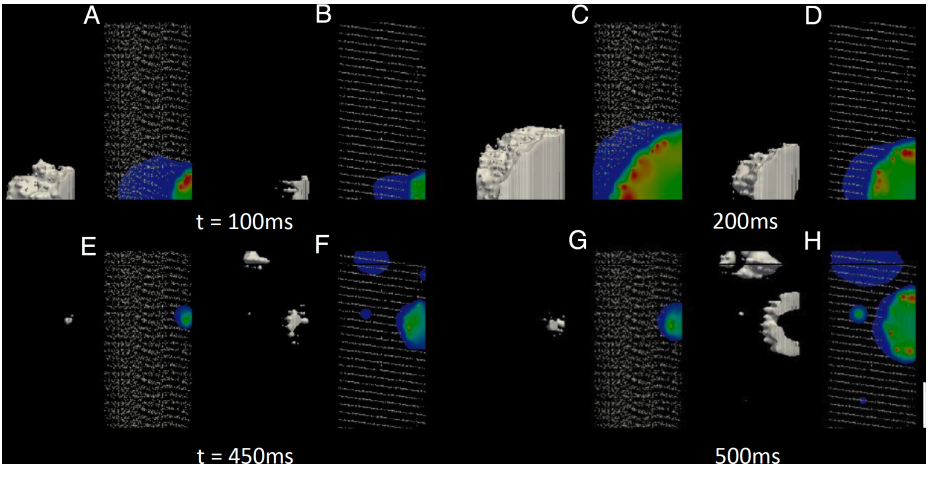

Fig. 3. Snapshots of Ca^{2+} dynamics from a movie simulating the behaviour of an evoked Ca^{2+} wave (A - D) and endogenous activity (E - H) in models of a ventricular cell with a realistic (A, C, E, G) and pseudo geometry (B, D, F, H) for the distribution of RyR clusters. In each of the snapshots each white dot indicates the spatial location of a RyR cluster. At t = 0, all the RyRs in a cuboid at the lower edge of the cell were activated. The evoked Ca^{2+} wave, visualised as the 1 μM isosurfaces (left) and colour-coded for local Ca^{2+} (right) for the realistic geometry at t = 100 and 200 ms is shown in panels (A) and (C) and for the pseudo-geoemtry in panels (B) and (D). Spontaneous activity is observed at t=450ms and 500ms for the realistic geometry (E, G) and pseudo-geometry (F, H). Note the top panel only shows the lower section of the whole cell, while the bottom panel showing the upper section, due to space limit. Color scheme from blue to red represents $[Ca]^{2+}$ from 1 to 250 μM.

left corner of the cell was activated to release Ca^{2+} at t=0ms, using both real and pseudo geometries, see Figure 3 (A). Note that the seeded region should be considered as a line stimulus instead a point stimulus, which is necessary in understanding the properties of Ca^{2+} wave propagation.

Figure 3 (A)-(D) illustrate the evoked propagating Ca^{2+} waves in realistic (A,C) and pseudo-geometries (B,D), as isosurfaces, and as a colour-coded distribution of Ca^{2+} concentration. For the realistic geometry, the isosurface appears spherical, and the 2D section through the wavefront as circular, indicating isotropic propagation, with a velocity increasing with time to 95μm/s as the wavefront curvature decreases. Propagation in the pseudo-geometry, where there is an enforced planar distribution of RyRs within planar Z-disks, is anisotropic, with propagation faster in the longitudinal than the transverse direction. Such an observation might be caused due to those larger peripheral RyR clusters. Since higher Ca^{2+} release flux can be less sensitive to small changes in neighbouring spacing between RyR clusters.

3.2 Effects of RyR Localization on Spontaneous Ca^{2+} Activities

Spontaneous Ca^{2+} activities were controlled through the probability function described in the method section, through both local Ca^{2+} concentration and Ca^{2+} sensitivity factor. With given Ca^{2+} sensitivity factor, local Ca^{2+} elevation seems to be the only factor to increase the firing probability of a RyR cluster, however, there are other less explicit factors, such as the local variation of Ca^{2+} release strength due to the size of RyR clusters, and distance to the nearest neighbouring RyR cluster. In Figure 3 (f) (h), in the same simulation, two robust spontaneous Ca^{2+} release hot spots were observed using pseudo geometry, and both of them initiated spontaneous sustaining Ca^{2+} wave to propagate, while using real geometry in Figure 3 (e) (g), only one hot spot was observed, and it struggled to survive. Such an observation tends to suggest that the realistic geometry is less encouraging in producing spontaneous Ca^{2+} activities, which is reasonable given spontaneous Ca^{2+} release is considered to be linked with cardiac arrhythmias.

3.3 Regenetive and Abortive Ca^{2+} Waves

Ca^{2+} wave is the result of collective summation of individual Ca^{2+} sparks, and a sustained or regenetive Ca^{2+} wave should be able to travel across many CRUs without losing its magnitude through the so called fire-diffuse-fire (FDF) process. An initiated Ca^{2+} wave can fail to maitain propagation, so it collapses, or is abortive. In Figure 4, both abortive and regenative Ca^{2+} waves were reproduced with slightly different parameter settings using the realistic geometry. Both of these two wave patterns revealed the spatial irregularities of Ca^{2+} wave fronts caused by the recruitment of resting CRUs nearby.

3.4 Parallelization

In order to see a complete propagation of a Ca^{2+} wave through the whole cell, the simulation time should be about 2.5 seconds. To estimate the achievale speedup,

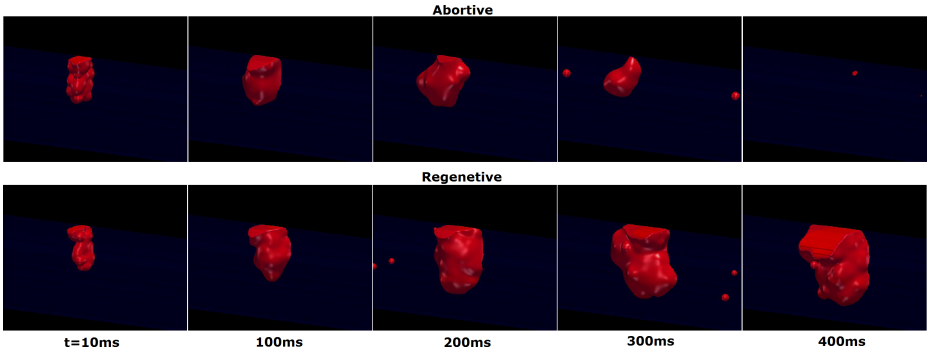

Fig. 4. Screenshots of computer simulations to reproduce both the abortive and regenetive Ca^{2+} waves using realistic geometry with parameter settings of i_{Ca}=2.0 τ=0.012ms, and i_{Ca}=1.8 τ=0.015ms respectively. The wave fonts were visualized as the red isosurface with the value of 1μM.

we first ran a serial simulation of 20ms, which took 3332.5 seconds wall time on a single core of a Xeon(R) E5420 2.5 GHz procssor. Then, we run the full-scale parallel simulation of 2500ms usnig 256 cores on a Linux cluster, where each compute node has two quad-core Xeon(R) E5420 2.5 GHz procssors. 32 computes nodes each with 8 cores were used in total. The interconnect of the cluster is gigabit ethernet. The wall time of the parallel simulation was 2501.71 seconds, which can be translated to a speedup of 166.5 (because the estimated serial wall time of a full 2.5-second simulation is $2.5/0.02 \times 3332.5 = 416562$ seconds).

4 Discussion

We have reproduced isotropic intracellular Ca^{2+} wave propagation by incorporating new experimentally defined location [4] [14] of RyR clusters together with details such as spatially symmetric profile of Ca^{2+} spark and locally varied Ca^{2+} release strength from each single CRU. The model spanned across the time scales from ms to s, and space scales from nanometers to about 100 μm.

Compared to the previous 2:1 fashion of spatial organisation of RyR clusters, the more homogeneous distribution of RyR clusters is less likely to produce spontaneous Ca^{2+} release according to our simulation. The effects of peripheral large-sized RyR clusters on regulating intracellular Ca^{2+} dynamics needs further experimental and theoretical investigations, such as, whether or not large-sized RyR clusters are always expressed away from the centre, and if they have more physiological implications, for example, in de-tubulated ventricular myocytes, calcium wave always diffuse from the surface of the cell into the centre, can large-sized peripheral RyR clusters be responsible for this behavior?

There are several limitations of the model. First of all, all the CRUs were considered as point sources without any local control mechanisms, and it is a

current challenge to construct detailed stochastic Ca^{2+} dynamics that include additional local CRU gating complexity and SR geometry. Besides, the realistic geometry used here is produced by stacking a fairly thin experimentally measured data set together, and can be improved by employing objectives combing long working distance to record more axially extended data sets.

As to the aspect of parallel computing, using a flat-MPI approach (i.e., the number of MPI processes is the same as the number of processors cores used) that was employed in the present study may not be the optimal solution on a multicore-based cluster. Instead, the possibility of using thread-based parallelism (such as OpenMP) within each compute node, combined with MPI-based parallelism between the nodes, should be investigated.

Acknowledgement

This work was supported by a Center of Excellence grant from the Norwegian Research Council to Center for Biomedical Computing at Simula Research Laboratory, and grants from the Auckland Medical Research Foundation, the Health Research Council, the Wellcome Trust and the European Union through the Network of Excellence BioSim, Contract No. LHSB-CT-2004-005137.

References

1. Cheng, H., Lederer, W.J.: Calcium sparks. Physiol. Rev. 88, 1491–1545 (2008)
2. Hake, J., Lines, G.T.: Stochastic binding of calcium ions in the dyadic cleft: continuous versus random walk description of diffusion. Biophys J. 94, 4184–4201 (2008)
3. Hinch, R., Greenstein, J.L., Winslow, R.L.: Multi-scale models of local control of calcium induced calcium release. Prog. Biophys. Mol. Biol. 90, 136–150 (2006)
4. Soeller, C., Crossman, D., Gilbert, R., Cannell, M.B.: Analysis of ryanodine receptor clusters in rat and human cardiac myocytes. PNAS 104, 14958–14963 (2007)
5. Eisner, D.A., Venetucci, L.A., Trafford, A.W.: Life, sudden death, and intracellular calcium. Circ. Res. 99, 223–224 (2006)
6. Hinch, R., Greenstein, J.L., Tanskanen, A.J., Xu, L., Winslow, R.L.: A simplified local control model of calcium-induced calcium release in cardiac ventricular myocytes. Biophys. J. 87, 3723–3736 (2004)
7. Hinch, R.: A mathematical analysis of the generation and termination of calcium sparks. Biophys. J. 86, 1293–1307 (2004)
8. Banyasz, T., Chen-Izu, Y., Balke, C.W., Izu, L.T.: A new approach to the detection and statistical classification of Ca2+ sparks. Biophys. J. 92, 4458–4465 (2007)
9. Izu, L.T., Wier, W.G., Balke, C.W.: Evolution of cardiac calcium waves from stochastic calcium sparks. Biophys. J. 80, 103–120 (2001)
10. Izu, L.T., Means, S.A., Shadid, J.N., Izu, C.Y., Balke, W.C.: Interplay of ryanodine receptor distribution and calcium Dynamics. Biophys. J. 91, 95–112 (2006)
11. Li, P., Lancaster, M., Holden, A.V.: A three dimensional ventricular E-Cell (3Dv E-Cell) with stochastic intracellular calcium handling. In: Sachse, F.B., Seemann, G. (eds.) FIMH 2007. LNCS, vol. 4466, pp. 180–189. Springer, Heidelberg (2007)

12. Thul, R., Falke, M.: Release currents of IP(3) receptor channel clusters and concentration profiles. Biophys. J. 86, 2660–2673 (2004)
13. Pacheco, P.S.: Parallel programming with MPI. Morgan Kaufmann Publishers, San Francisco (1997)
14. Soeller, C., Jayasinghe, I.D., Li, P., Holden, A.V., Cannell, M.B.: 3D high resolution imaging of cardiac proteins to construct models of intracellular Ca2+ signalling. Exp. Physiol. (2009), doi:10.1113/expphysiol.2008.043976

Cardiac Motion Estimation from Intracardiac Electrical Mapping Data: Identifying a Septal Flash in Heart Failure

Oscar Camara[1,⋆], Steffen Oeltze[2], Mathieu De Craene[1], Rafael Sebastian[1], Etel Silva[3], David Tamborero[3], Lluis Mont[3], Marta Sitges[3], Bart H. Bijnens[4,1], and Alejandro F. Frangi[1,4]

[1] Center for Computational Imaging and Simulation Technologies in Biomedicine (CISTIB) – Universitat Pompeu Fabra (UPF) and Networking Biomedical Research Center on Bioengineering, Biomaterials and Nanomedicine (CIBER-BBN), Barcelona, Spain
oscar.camara@upf.edu
[2] Institute of Simulation and Graphics, Otto-von-Guericke University, Magdeburg, Germany
[3] Cardiology Department, Thorax Clinic Institute, Hospital Clínic, Institut d'Investigacions Biomèdiques August Pi i Sunyer, University of Barcelona, Spain
[4] Institució Catalana de Recerca i Estudis Avançats (ICREA), Barcelona, Spain

Abstract. In this paper, we present a methodology to estimate cardiac motion directly from the high resolution temporal data provided by an intra-cavity electrical mapping system (CARTO). These data consist in intracardiac electrical measurements, obtained invasively through the contact of a catheter with the endocardial wall at different locations, with simultaneous recording of the position of the measuring catheter over time. The 3D displacement fields between the different timepoints obtained from the position measurements are projected onto the vector pointing from the CARTO points to the centroid of the CARTO cloud, giving a very intuitive vectorial coarse representation of the diastolic and systolic motion. Furthermore, scalar projection 1D curves can be used to identify specific motion patterns. We have applied the proposed methodology to the CARTO acquisitions of nine candidates to cardiac resynchronization therapy, identifying the specific sequence of motion and deformation (septal flash) found in LBBB, which was confirmed by visual inspection of the corresponding MR and 3D-US images.

Keywords: Electrical mapping, CARTO, septal flash, cardiac motion, left bundle branch block, cardiac resynchronization therapy.

1 Introduction

Estimation of cardiac motion is crucial for a complete understanding of cardiac (dys-)function in a wide range of cardiovascular pathologies such as left bundle

⋆ Corresponding author.

N. Ayache, H. Delingette, and M. Sermesant (Eds.): FIMH 2009, LNCS 5528, pp. 21–29, 2009.
© Springer-Verlag Berlin Heidelberg 2009

branch block (LBBB) and for the optimization of related clinical procedures such as cardiac resynchronization therapy (CRT). CRT is an innovative treatment for congestive heart failure aiming at synchronizing the electrical activation of the left ventricle (LV) in order to better coordinate its contraction, thus assuring the generation of enough force to push blood through the body. However, up to a third of the patients who are treated with CRT do not show any response to this very expensive therapy. Therefore, the development of new patient selection indices would lead to better success rates of CRT. For instance, a fast motion pattern called septal flash [1], a mechanical consequence of dyssynchronous contraction which occurs in some LBBB patients at early systole, has been related to a high probability of response to the CRT therapy.

In general, this type of motion information is obtained by applying post-processing techniques either to gray-scale images [2,3,4,5] or to acquired velocity data [6]. On the other hand, detailed electrophysiological data on the LV is also critical for a better planning of clinical procedures and patient's follow-up. However, it can only be measured invasively, using either endocardial contact mapping (CARTO, Biosense, Cordis Webster, Marlton, NJ) or non-contact mapping (Ensite, Endocardial Solutions, Saint Paul, MN) systems, or with a sock of epicardial electrodes to record epicardial electropotential data [7].

Automatic combination of the electrophysiological data given by these invasive systems with cardiac motion estimates or geometrical information obtained from medical images is not straightforward due to the different nature of the acquisitions and the use of different spatial reference systems. Registration techniques applied on data acquired in a XMR system [8] can partially solve this problem, but it is a relatively expensive solution. Another issue is that abnormal motion patterns specific to known cardiac pathologies require rich data with high spatial and/or temporal resolution to be identified. For instance, fast events such as a septal flash would be better captured with Doppler Myocardial Imaging than with MRI due to its higher frame-rate.

In this paper, we propose to estimate cardiac motion directly from the data provided by a CARTO system. Along with electrical measurements defined at a given number of acquisition points at the endocardium, a CARTO system provides, for every acquired point, the 3D spatial location of the measuring catheter over time at a high acquisition rate (100Hz). The catheter's spatial location obviously follows the motion undergone by the corresponding heart segment. Consequently, we compute a 4D displacement field from the time-varying spatial location of the catheter. The computed 3D displacement vector of every CARTO acquired point is then projected onto the vector that goes from this point to the centroid of the CARTO cloud of points, giving a very intuitive vectorial coarse representation of the diastolic and systolic motion. The associated scalar projection can be plotted over time to identify specific motion patterns.

We have applied the proposed methodology to the CARTO data of nine CRT candidates with and without a septal flash. The scalar projection curves showed significant peaks within the ECG interval defined between the contraction onsets of the earliest (septum) and latest (lateral wall) activated CARTO points in four

patients, which were confirmed by visual inspection of corresponding MR and US images.

2 Intracardiac Electrical Mapping Acquisitions

For the present study data from 9 patients showing heart failure (age 65 ± 10 years) was collected. The study protocol was accepted by the Hospital Clínic's ethics committee and written informed consent was obtained from all patients. All the patients were candidates for CRT, according to current recommendations based on the NYHA classification, the ejection fraction (EF) and the QRS length. Details about the characteristics of each patient and these indices are given in Table 1.

Table 1. Clinical Data

ID	Age	NYHA	EF [%]	QRS [ms]
1	75	II	50.9	200
2	71	III	22.8	160
3	68	III	26.2	120
4	80	III	25	200
5	66	III	25	200
6	58	III	27	200
7	55	II	24.8	120
8	68	III	9	140
9	65	III	26	120

Data of these patients consisted of endocardial electroanatomic contact mapping (CARTO, Biosense, Webster), a system that basically consist of a low-intensity magnetic field generated by a location pad under the bed of the patient, two catheters instrumented with a sensor and a graphic computer.

CARTO maps are composed by a set of intracardiac samples that contain electrical signals (recorded at $1kHz$) and position of the catheter (recorded at $100Hz$) over $2500ms$ so that ECG and trajectory data can be derived. The absolute positions of the catheter tip are given in millimeters. The electrical measurements consist of uni- and bipolar voltages where the unipolar peak-to-peak voltage refers to the potential difference between the catheter tip and a reference electrode, whereas the bipolar voltage is the potential difference between the 2 electrodes within the catheter (Ring-Tip).

For each patient, a number of point measurements ranging from 32 to 83 (mean of 49.6) were obtained. Points were taken from different areas of the LV endocardium so that the approximate geometry could be recovered. As the samples are obtained sequentially, the system uses a common reference point in the surface ECG (R wave) to start recording the electrical signals. In that way, we are able to recover and align electrical signals and to calculate the local activation maps. Analysis of the mapping data was carried out for patients in sinus rhythm.

3 Septal Flash

The identification of dyssynchrony indexes, to identify patients that could benefit from CRT, has been an issue of debate over the last years. Some simple indexes measured from echocardiographic data [9,10] have proven to have a poor prediction capability of CRT success. Recently, a fast motion pattern, called *septal flash*, which occurs in some LBBB patients at early systole, has been related to a high probability of response to the CRT therapy.

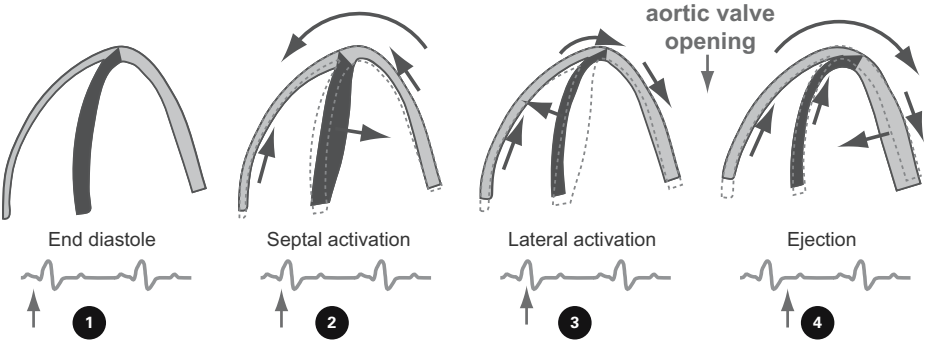

Fig. 1. Diagram showing the septal flash motion

A septal flash can be explained by unbalanced forces appearing in the septum due to a conduction delay between the activation of the septum and the lateral wall. In a normal left ventricle, all segments are activated almost simultaneously and thus deform in synchrony. In this case, the contraction that the septum exerts on the lateral wall while contracting is balanced by the symmetric contraction exerted by the lateral walls towards the septum. Because of this balance, the motion of the septum is mostly longitudinal and the apex remains stationary.

In the case of a conduction delay between the septum and the lateral wall, the interaction between the walls changes significantly. Indeed, the septum in this case contracts while the contralateral wall does not. This provokes a faster and inward motion of the septum stretching the lateral wall. Once the lateral wall is activated, it will in turn start stretching the septum which makes the septum going in the outward direction. This quick succession of inward and outward motion of the septum, happening within the (wide) QRS complex and the isovolumetric contraction time (IVCT), is illustrated in Fig. 1. The quick reversal in the septal displacement direction for the LBBB patient is the septal flash that we want to identify from CARTO data in this paper.

4 Cardiac Motion Estimation from CARTO Data

The proposed methodology for the estimation of cardiac motion from CARTO data can be divided in the following stages:

1. computation of the 4D displacement field;
2. filtering out outliers and temporal smoothing of the 4D displacement field;
3. projection of the 4D displacement field onto the unit vector pointing to the centroid of the CARTO cloud of points;
4. temporal analysis of the vector projection and the 1D scalar projection curves.

The first stage of the methodology is the estimation of the trajectory of each CARTO point over time, i.e. the computation of the 4D displacement field. For doing so, we made use of the spatial locations of the measuring catheter at consecutive timepoints, which are available every 10ms.

The resulting displacement field is quite noisy, in particular for timepoints far away from the trigger point (R peak of the last heart cycle). This is due to the uncertainty in the spatial location of the catheter when it is not in contact with the endocardium wall but rambling in the bloodstream. Nevertheless, it must be pointed out that the CARTO system provide visual signs alerting when the catheter is in contact with the wall and thus the acquisition of electrical and catheter spatial location measurements is more accurate (trigger point). In order to reduce the noise of the 4D displacement field, CARTO points are defined as outliers if they have spatial displacements in their catheter's trajectory larger than 2cm, indicating timepoints far away from the trigger point (it is always at 2000ms of the acquired 2500ms) where the catheter is not in contact with the wall. The mean and standard deviation of the percentage of outliers rejected in this filtering out stage for the nine patients are $21.34\% \pm 12.21\%$. Moreover, we applied a temporal smoothing to the remaining CARTO points, based on a binomial filter using the previous and following points in the trajectory.

The next step in the proposed methodology consisted in projecting the displacement vector of each CARTO point onto the unit vector going from its spatial location to the centroid of the cloud of CARTO points, at each timepoint of the sequence. The scalar projection (or scalar resolute), $sp_{\boldsymbol{a}}\boldsymbol{b}$, of the displacement vector $\boldsymbol{a}$ onto the centroid unit vector $\boldsymbol{b}$ is obtained as follows:

$$sp_{\boldsymbol{a}}\boldsymbol{b} = \frac{\boldsymbol{a} \cdot \boldsymbol{b}}{\mid \boldsymbol{a} \mid}. \tag{1}$$

The scalar projection of a given CARTO point will be positive when its displacement vector points towards the centroid (contraction), and is negative when moving away from the centroid (dilation). The vector projection (or vector resolute) can then be found by multiplying the scalar resolute by $\boldsymbol{b}$, resulting in a very intuitive and normalized vectorial coarse representation of the diastolic and systolic cardiac motion. The scalar resolute values can be plotted over time, deriving 1D curves with information that can be used to identify particular motion patterns for some CARTO points.

5 Identifying the Septal Flash

In this paper, we analyzed these 1D curves and the corresponding vectorial representation to identify septal flash motion. For doing so, we selected the

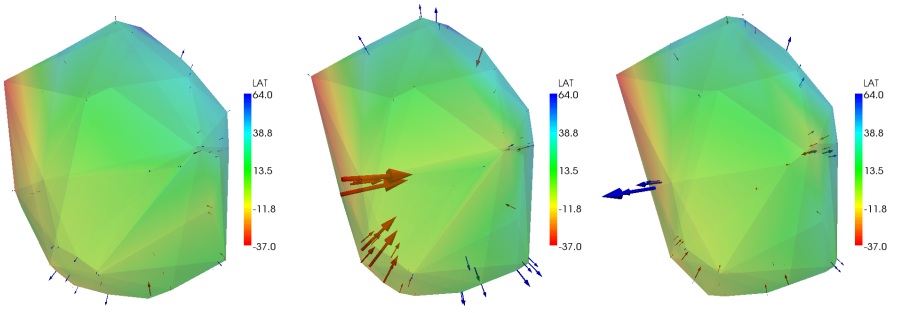

Fig. 2. Delaunay triangulations of CARTO points, colored according to the LATs (red: earliest LATs; blue: latest LATs.), together with vector projection displacements (arrows). From left to right, three different frames within the septal flash interval.

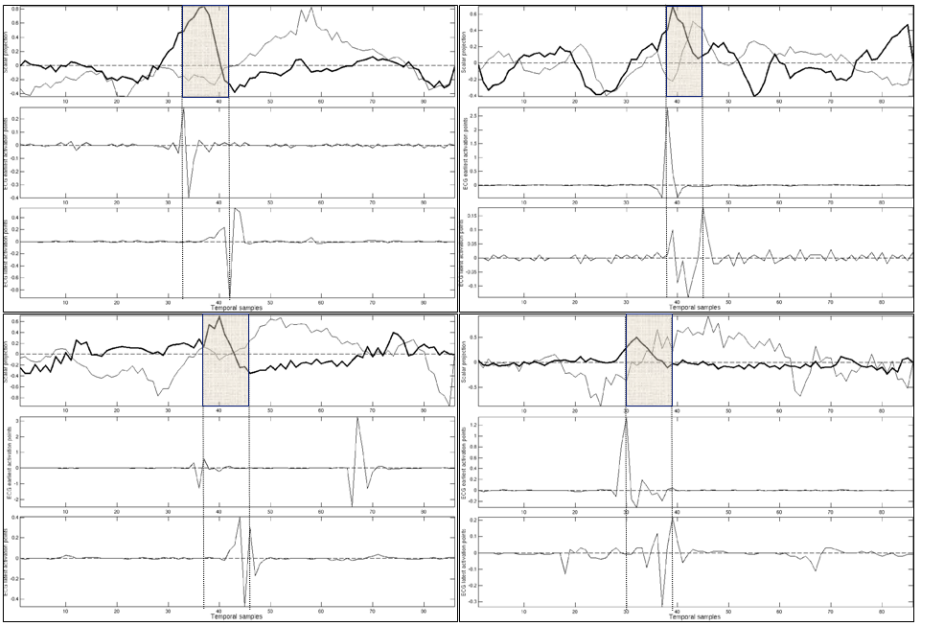

Fig. 3. Scalar projection curves (top in each subplot) and ECGs of CP_{elat} (middle in each subplot) and CP_{llat} (bottom in each subplot) for four cases with septal flash. The darker and thinner lines in the scalar projection curves corresponds to the septal and lateral wall points, respectively. The dashed markers limit the septal flash interval (shady in the scalar projection curves).

CARTO point with the earliest local activation time (LAT), CP_{elat}, and the one with the latest LAT, CP_{llat}. In LBBB patients, it is quite likely that CP_{elat} would be located at the septal wall and CP_{llat} at the lateral wall. The individual ECGs (unipolar and bipolar voltages) corresponding to CP_{elat} and CP_{llat} gave

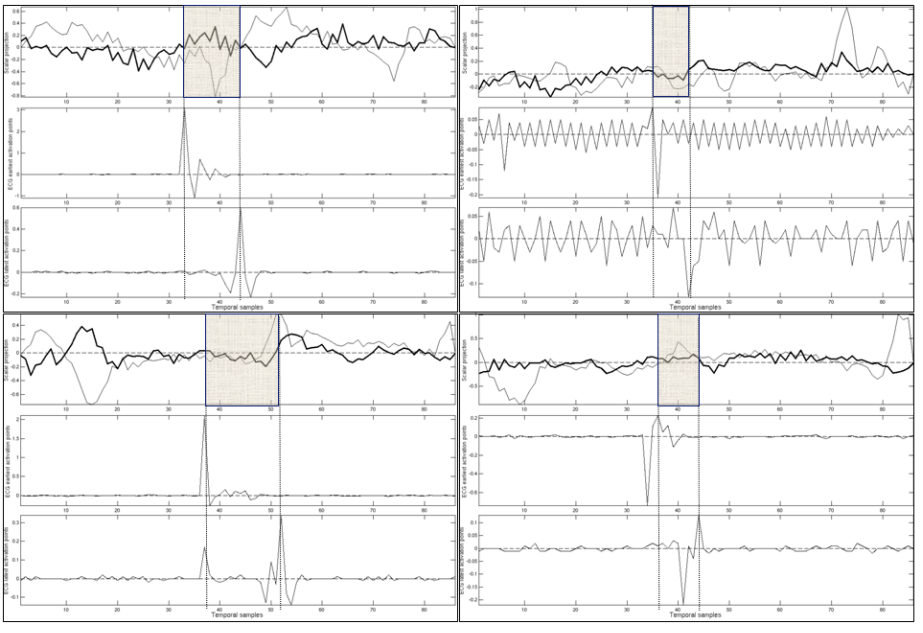

Fig. 4. Scalar projection curves (top in each subplot) and ECGs of CP_{elat} (middle in each subplot) and CP_{llat} (bottom in each subplot) for four of the five cases without septal flash. The darker and thinner lines in the scalar projection curves corresponds to the septal and lateral wall points, respectively. The dashed markers limit the septal flash interval (shady in the scalar projection curves).

us the time interval where, if present, the septal flash must occur, specifically between the R peaks of CP_{elat} and CP_{llat}. Within this septal flash interval (see shady region in Fig. 3 and Fig. 4), an abnormally large peak would show up in the scalar projection 1D curve of the CP_{elat} if a septal flash appears, representing the sudden contraction and relaxation of the septum. In other heart regions (e.g., CP_{llat}) or in patients without septal flash, no significant peaks should be present in the same time interval.

Fig. 2 shows the Delaunay triangulations of the CARTO points for three different frames within the septal flash interval for one patient having septal flash, together with the arrow representation of the vector projection. For the CARTO data displayed in Fig. 2, one can easily observe the presence of large arrows pointing towards and then going away from the centroid in some points of the septal wall, representing a fast motion that corresponds to a septal flash.

Fig. 3 and Fig. 4 show the scalar projection curves and the ECGs for patients with (four cases) and without (four of the five cases are shown for space reasons) septal flash, respectively. For each case, the top subplot presents the scalar projection curves for the CARTO points with the earliest (septum, thicker line) and latest (lateral wall, thinner line) LATs. The middle and bottom subplots correspond to the individual ECGs (bipolar voltage) of the CP_{elat} and the CP_{elat},

respectively. It is straightforward to distinguish septal flash from not septal flash cases by visual inspection of the scalar projection curves of the septal wall points within the septal flash interval. In the cases illustrated in Fig. 3, a substantial peak appears just after the activation of CP_{llat}, while no considerable event develops in cases displayed in Fig. 4. The same classification of septal/no septal flash cases was obtained by visual inspection of the corresponding MRI (including tMRI, cine MRI, delay-enhancement MR) and 3D-US data by an expert cardiologist.

6 Conclusions

To the best of our knowledge, this is the first time CARTO data is used for cardiac motion analysis, making its comparison with electrophysiological data trivial, without needing complex or manual registration techniques. Furthermore, the high acquisition rate and the 3D nature of the CARTO data (one frame each 10ms) has allowed to identify fast 3D events such as septal flash motion with simple post-processing techniques of the catheter's trajectories. Future work will be focused on automating the procedure with simple signal processing algorithms and on quantitatively comparing these results with indices provided by registration techniques applied to medical images.

Acknowledgments

This research has been partially funded by the Industrial and Technological Development Centre (CDTI) under the CENIT Programme (CDTEAM project) and the European Community's Seventh Framework Programme (FP7/2007-2013) under grant agreement n. 224495 (euHeart project). Dr. O. Camara and R. Sebastian acknowledge grant support from the Spanish Ministry of Research and Innovation, under a Ramon y Cajal and Juan de la Cierva Research Fellowship respectively.

References

1. Parsai, C., Bijnens, B., Sutherland, G., Baltavaeva, A., Claus, P., Marciniak, M., Paul, V., Scheffer, M., Donal, E., Derumeaux, G., Anderson, L.: Toward understanding response to cardiac resynchronization therapy: left ventricular dissynchrony is only one of multiple mechanisms. European Heart Journal (2008) (in press)
2. Perk, G., Tunick, P., Kronzon, I.: Non-doppler two-dimensional strain imaging by echocardiography–from technical considerations to clinical applications. Journal of the American Society of Echocardiography 20, 234–243 (2007)
3. Axel, L., Montillo, A., Kim, D.: Tagged magnetic resonance imaging of the heart: a survey. Medical Image Analysis 9(4), 376–393 (2005)
4. Ledesma-Carbayo, M., Kybic, J., Desco, M., Santos, A., Suhling, M., Hunziker, P., Unser, M.: Spatio-temporal nonrigid registration for ultrasound cardiac motion estimation. IEEE Transactions on Medical Imaging 24(9), 1113–1126 (2005)

5. Elen, A., Choi, H., Loeckx, D., Gao, H., Claus, P., Suetens, P., Maes, F., D'Hooge, J.: Three-dimensional cardiac strain estimation using spatio-temporal elastic registration of ultrasound images: a feasibility study. IEEE Transactions on Medical Imaging 27(11), 1580–1591 (2008)
6. Bijnens, B., Cikes, M., Claus, P., Sutherland, G.: Velocity and deformation imaging for the assessment of myocardial disfunction. European Journal of Echocardiography (in press, 2009)
7. Nash, M., Mourad, A., Clayton, R., Sutton, P., Bradley, C., Hayward, M.: Evidence for multiple mechanisms in human ventricular fibrillation. Circulation 114, 536–542 (2006)
8. Rhode, K., Sermesant, M., Brogan, d., Hegde, S., Hipwell, J., Lambiase, P., Rosenthal, E., Bucknall, C., Qureshi, S., Gill, J., Razavi, R., Hill, D.: A system for real-time XMR guided cardiovascular intervention. IEEE Transactions on Medical Imaging 24(11), 1428–1440 (2005)
9. Yu, C., Abraham, W., Bax, J., Chung, E., Fedewa, M., Ghio, S., Leclercq, C., León, A., Merlino, J., Nihoyannopoulos, P., et al.: Predictors of response to cardiac resynchronization therapy (PROSPECT)–study design. American Heart Journal 149(4), 600–605 (2005)
10. Chung, E., Leon, A., Tavazzi, L., Sun, J., Nihoyannopoulos, P., Merlino, J., Abraham, W., Ghio, S., Leclercq, C., Bax, J., et al.: Results of the Predictors of Response to CRT (PROSPECT) Trial. Circulation 117(20), 2608 (2008)

Extracting Clinically Relevant Circular Mapping and Coronary Sinus Catheter Potentials from Atrial Simulations

Frank M. Weber[1], Christopher Schilling[1], Dorothee Straub[1], Sandeep Gurm[1], Gunnar Seemann[1], Cristian Lorenz[2], and Olaf Dössel[1]

[1] Institute of Biomedical Engineering, Universität Karlsruhe (TH)
Kaiserstr. 12, 76131 Karlsruhe, Germany
frank.weber@ibt.uni-karlsruhe.de
http://www.ibt.uni-karlsruhe.de
[2] Philips Research, Hamburg, Germany

Abstract. Patient-specific model adaptation and validation requires a comparison of simulations with measured patient data. For patients suffering from atrial fibrillation, such data is mainly available as intracardiac catheter signals. In this work, we demonstrate the simulation of clinically relevant catheter data as measured using circular mapping catheters (such as Lasso® or Orbiter®) and coronary sinus catheters using atrial simulations on a realistic geometry. Four circular catheters are modeled using a projection technique for two distinct types of application. We show that in sinus rhythm, the choice of a distinct electrophysiological model does not impair the signal quality. Finally, we compare simulated potentials to a real clinical measurement. In the future, with patient-specific models available, such comparisons can constitute an important interface for personalizing cardiac models.

Keywords: Intracardiac Potentials, Modeling, Circular Mapping, Lasso, Orbiter, Catheter, Patient-Specific Adaptation, Atrial Fibrillation.

1 Motivation

Cardiac simulations are approaching clinical applications. In this context, patient-specific model validation and adaptation becomes more and more important. Besides anatomical modeling, physiological parameters such as conduction velocities and activation times must be adjusted based on clinical measurements. Therefore, data must be extracted from the simulations such that it can be compared to patient data acquired in standard clinical workflow.

For applications regarding atrial arrhythmia such as atrial flutter or atrial fibrillation (AF), the most significant clinical data available are intracardiac catheter measurements. Typical catheters used in clinical practice are circular mapping catheters (CMCs) such as Lasso® [1] or Orbiter® [2] and coronary sinus (CS) catheters. It is therefore desirable to perform virtual catheter measurements in the simulation model. It is further interesting to see if the results are influenced by the choice of a distinct electrophysiological (EP) model.

N. Ayache, H. Delingette, and M. Sermesant (Eds.): FIMH 2009, LNCS 5528, pp. 30–38, 2009.
© Springer-Verlag Berlin Heidelberg 2009

2 Methods

To generate catheter potentials from a simulation, an atrial excitation is simulated on a realistic anatomical dataset. From the resulting transmembrane voltage (TMV) distributions, the extracellular potential is derived using a field calculation. Finally, points in the model are selected such that their positions represent the catheter electrodes and the extracellular potential is extracted there.

2.1 Input Data Generation

This simulation study is based on the Visible Man (VM) [3] data set of the atria with an original resolution of 1 mm cubic voxel side length. As the atrial walls are not thicker than a few millimeters, the data was interpolated to a resolution of 0.33 mm.

Cardiac excitation in normal sinus rhythm was simulated using three different approaches. Firstly, a monodomain (MD) finite-element (FE) reference simulation was performed in a multi-processor C++ environment [4] using the atrial cell model by Courtemanche, Ramirez and Nattel (CRN) [5]. All cells were prepaced in single-cell simulations at 1 Hz for 10 beats. Secondly, the adaptation of a minimal four-state cell-model for reproducing atrial excitation properties [6,7] has recently been demonstrated. Due to its tunability and speed, it seems promising for the use in clinical applications. We therefore simulated the excitation of the atria using the minimal model (MM) for comparison. A third approach is a ruled-based system, a so-called cellular automaton (CA) [8]. It is parametrized using single-cell simulations with the CRN model. It is a lot faster, but suffers from stronger discretization effects than monodomain simulations. To avoid initialization artifacts, only the third simulated beat is analyzed.

The output of all three simulation approaches are the TMV distributions in the cubic voxel dataset at discrete time steps, recorded every millisecond for the MD model and 0.5 ms for the CA. The signals measured by the catheters, however, are not transmembrane voltages but extracellular potentials. These are calculated using an FE solver operating on a tetrahedron model.

Normally, a forward calculation is performed in a model of the whole thorax. However, as the endocardial surface is almost only surrounded by blood, the atrial model is placed in the center of a virtual box of blood extending 30 mm over the limits of the atria. A comparison to results obtained in the full VM torso (not shown here) did not reveal any relevant influence induced by this simplification. As no body surface electrocardiograms are investigated, this approximation appears favourable to significantly reduce the calculation time.

The TMVs V_m are interpolated onto the approximately 130,000 atrial nodes of the tetrahedral geometry. The current sources on the heart are then calculated as $I_\mathrm{imp} = -\nabla\cdot(\sigma_i \nabla V_\mathrm{m})$. Finally, the extracellular potential Φ_e at every point of the grid is derived from solving Poisson's equation $\nabla \cdot [(\sigma_i + \sigma_e)\nabla\Phi_e] = I_\mathrm{imp}$ using an FE method, where σ_i and σ_e are the intra- and extracellular conductivity.

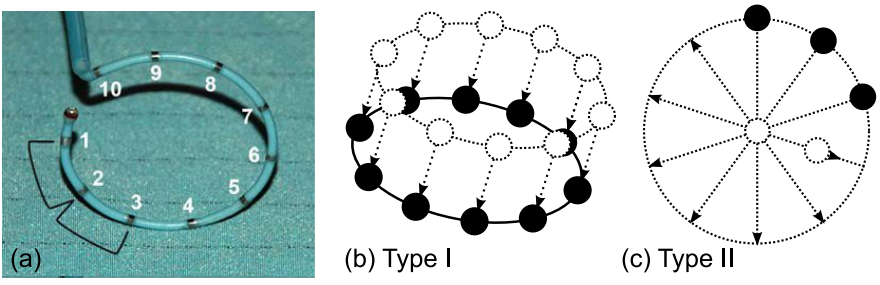

Fig. 1. Circular mapping catheter. (*a*) Example Lasso® catheter [9]. (*b*) For modeling, a type I catheter is preliminarily positioned above the endocardium and then projected onto the boundary surface. (*c*) Type II catheters placed inside cavities are radially projected outwards from the center point. In this figure, three electrodes have reached their final position while the fourth one is just being projected.

2.2 Modeling Circular Mapping Catheters

The goal of this work is to simulate clinically relevant data, with a focus on circular mapping catheter potentials. Thus, points in the model must be selected such that they represent the circular arrangement of electrodes. A clinical Lasso or Orbiter catheter typically consists of a tip containing 10, 14 or 20 electrodes at equal distances as shown in figure 1a. Exemplary dimensions are electrode widths around 1 mm and distances in the range of 4 to 10 mm. For some catheters like the Orbiter or a variable Lasso, the diameter can be adjusted.

When trying to model this geometry, two types of applications must be distinguished. Firstly, a catheter fixed at some radius is pressed against the atrial wall (here referred to as 'type I'). Secondly, a catheter is introduced into a cavity, especially the pulmonary veins (PVs), and expanded until contact to the cavity wall is established along the whole circumference ('type II').

For each type, a projection method is used to determine points in the model representing the desired catheter. For type I applications, the number of electrodes, the catheter radius and a center point at some distance from the heart wall are specified. There, a temporary set of electrodes is created. With a second point defining the direction towards the tissue, each electrode is projected onto the boundary between blood and tissue (fig. 1b). For type II catheters, a point in the cavity center and a normal vector are specified. This defines the plane in which the electrodes will be located. They will then be projected outward from the center along directions in the plane, shifted by equal angles (fig. 1c).

While a real catheter measurement also deforms the atrial wall, this cannot be accounted for in the model. However, for not too extremely curved or uneven (type I) or asymmetric (type II) regions, the projection should give a good approximation. To ensure a uniform placement, the average electrode-center and electrode-electrode distances are calculated from the final electrode positions. It must further be noted that for a real catheter, the tip length is fixed and only the radius changes. This is accounted for in the model by specifying the angle in

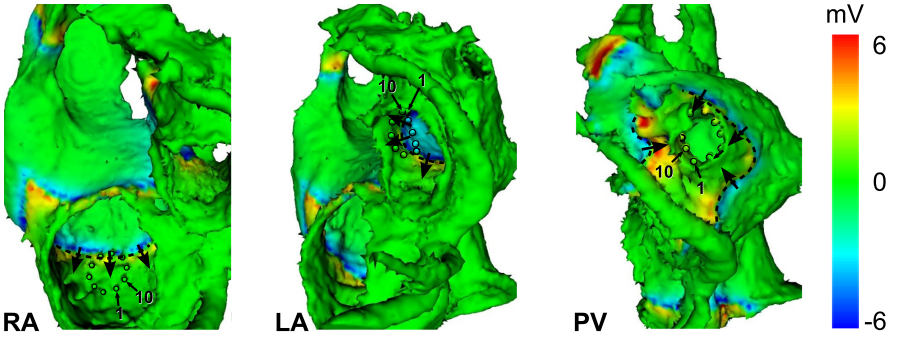

Fig. 2. Circular catheters of type I modeled in the right atrium (RA) and left atrium (LA) as well as a type II catheter in the left inferior pulmonary vein (PV). The catheters consist of 10 electrodes with a diameter of 13 mm for the type I catheters. The first and last electrodes are marked. In color, the extracellular potential as derived from the forward calculation with the Courtemanche model is shown. After stimulation in the sinus node, the wave has propagated for 60 ms (RA and LA) or 102 ms (PV), respectively. The direction of wave front propagation is marked with black arrows.

degree occupied by the catheter. Values smaller than 360° represent open circles while larger values produce overlapping catheter ends.

With this method, three virtual CMCs were placed in the atrial geometry (fig. 2). A type I catheter with a diameter of 13 mm and 10 electrodes covering 360° was placed in the RA and LA respectively. A type II catheter, also with 10 electrodes covering a full circle, was placed in the left inferior pulmonary vein (PV). In the first step, the electrode positions were determined. At this stage, the extracellular potential at the selected nodes of the tetrahedral geometry can be extracted to approximate the catheter signals. Then, a spherical metal electrode with a radius of 1 mm, consisting of approximately 150 nodes, is inserted into the tetrahedral model at each position with its center lying at 0.5 mm distance from the atrial wall. After solving Poisson's equation again for the refined geometry, the electrode potential can be extracted from the center of the sphere.

Finally, there was clinical data available for comparison. It was recorded in a 60-year old female patient who suffered from paroxysmal AF and underwent PV ablation [9]. Potentials in nomal sinus rhythm at 85 beats per minute were recorded by an Orbiter and a CS catheter and extracted from an EnSite NavX® [10] system together with 3D mapping information. According to the position of the Orbiter as depicted in fig. 3a, a type I CMC with a diameter of 12 mm and 14 electrodes covering a total angle of 670° was modeled at a similar position, close to the left atrial appendage (LAA) as shown in figure 3b.

2.3 Modeling Coronary Sinus Catheters

Besides circular mapping catheter measurements, clinical data normally also comprises data recorded in the coronary sinus [9]. A typical CS catheter consists

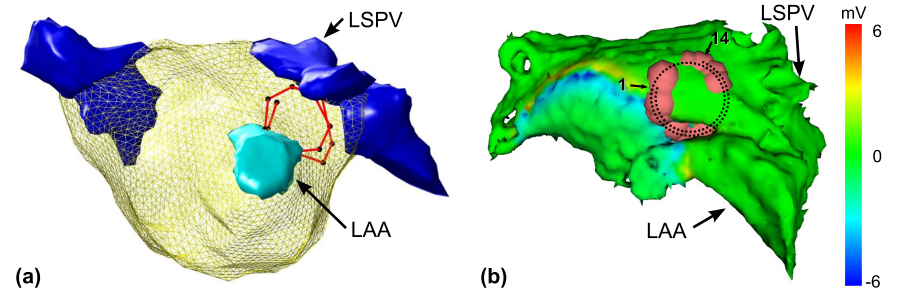

Fig. 3. Modeled Orbiter catheter used for comparison of measured and simulated data. (*a*) 3D surface model of the patient's LA, extracted from EnSite NavX mapping system. The tracked electrode positions are marked. (*b*) Modeled type I catheter close to the LAA. For comparison, the electrodes at the endocardial surface are visualized by spheres arbitrarily enlarged to penetrate the LA wall for most of the electrodes.

of four pairs of two electrodes. To allow for comparison with the available clinical data, we manually modeled a virtual CS catheter with distances of approximately 2 mm within an electrode pair and 10 mm between the pairs. At the selected positions, metal electrodes were inserted as described above.

3 Results

The modeled CMCs were analyzed in terms of their geometric setup. Therefore the catheter center point was calculated as the average of the final electrode positions. The mean distance of the electrodes from the center was 7.0 ± 0.4 mm for the RA catheter, 6.7 ± 0.2 mm for the LA Lasso, 6.0 ± 0.7 mm in the PV, and 6.9 ± 0.6 mm for the 14-electrode Orbiter close to the LAA. The mean distance between neighboring electrodes was calculated to 4.4 ± 0.4 mm (RA), 4.3 ± 0.4 mm (LA), 3.8 ± 0.4 mm (PV) and 6.2 ± 1.5 mm (LAA).

As used in clinical practice, potential differences between neighboring electrodes for the CMCs in the RA, LA and PV are considered (figure 4a). The results obtained from the MM are shifted by 1 ms to match the CRN data. For the PV catheter, the signals obtained from the cellular automaton are shifted by 7.5 ms to match the other data. This is due to the fact that the CA velocity was parametrized such that the RA and LA signals match between the models. The signals calculated from all three models are well-shaped and recognizable as catheter signals (see fig. 4b for an example of measured data). Except for minor features, there are no significant differences between the models. Also the amplitudes are approximately the same.

For type I catheters, the excitation front first hits one end of the catheter before it travels across the underlying tissue. This leads to the typical wave-like activation pattern from top to bottom. Compared to the electrode positions (fig. 2), the leading electrode pairs 6-7 and 7-8 in the RA signals match well with the direction of the first excitation. The same can be observed for 2-3 and 3-4 in

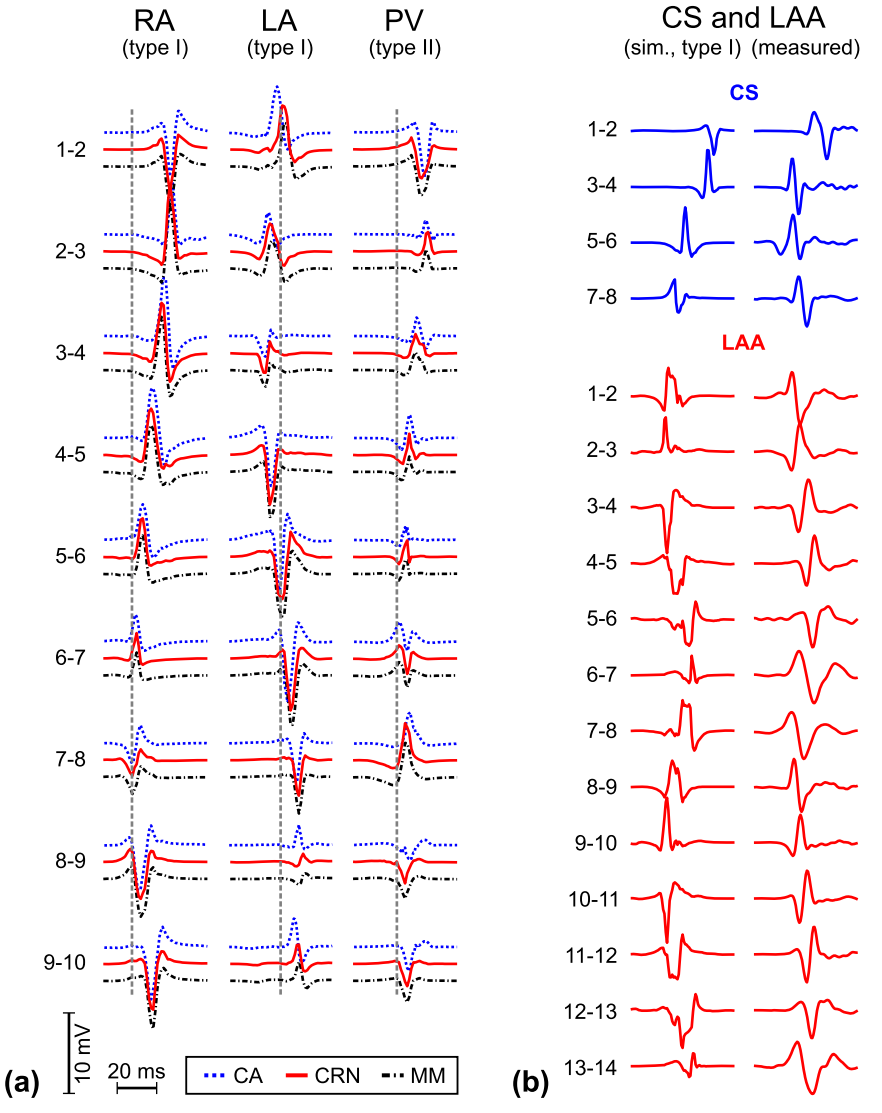

Fig. 4. (*a*) Simulated signals recorded from virtual Lasso catheters in the right atrium (*RA, left column*), left atrium (*LA, middle column*) and left inferior pulmonary vein (*PV, right column*). 1-2 depicts the signal difference between electrode 1 and 2. Simulations with the three EP models are compared, each shifted by 2 mV. Vertical lines mark the time instants shown in fig. 2. (*b*) Comparison of real clinical measurements to simulated data (CRN model) from the CS and the circular LAA catheter. The time scale is the same as in (a). The clinical signals were recorded in a 60-year old female who suffered from proxysmal AF and underwent RF ablation of the PVs. The patient was reported to be in sinus rhythm at a rate of 85 beats per minute. Signals were normalized due to large variations in amplitude.

the LA. Type II circular catheters inside cavities are not always traversed from one end to the other. Therefore, the activation sequence does not necessarily look wave-like. This is also observed in the PV signals shown in figure 4.

These results show the general feasibility of the method used for modeling virtual circular mapping catheters and simulating their measured potentials. In the next step, a first qualitative comparison of the data simulated in the generic model to measurements from an individual patient is performed as shown in figure 4b. As the clinical data signals showed large variations in amplitude, they were normalized before plotting.

The modeling of the CMC in the vicinity of the LAA was rather difficult as the tissue on the endocardial surface was very structured in this region of the VM dataset. Anyway, the simulated catheter signals are well-recognizable, although the signal forms differ. Comparing the general shape of the activation pattern between simulation and measurement, both show a similar wave pattern. There is however some difference in the activation sequence: while in the simulation electrode pair 9-10 is leading, in the measured data 7-8 is activated first.

For the CS, the simulated and measured signals are of comparable width whereas the activation pattern also is different. While in the model, the activation front travels from the proximal to the distal end of the CS, in the patient data the middle region of the CS is activated first.

4 Discussion and Conclusions

This projection placement method has some limitations. While for real catheters, the distance between two electrodes is fixed, this is only accounted for in the model by placing the electrodes at equally-spaced angles. Further, the deformation of the atrial wall induced by a real measurement cannot be modeled. If the atrial wall is very uneven, the final distances may differ. Therefore, this method requires *a posteriori* control of the final electrode positions. The calculated average electrode-center distances showed a slight increase compared to the nominal radius, namely 8 % for the RA and 3 % for the LA Lasso as well as 15 % for the LAA Orbiter. This is caused by the fact that the electrodes on the heart wall are not perfectly located on a plane. The elliptic geometry of the PV ostium causes an increased standard deviation (SD) in the PV catheter (0.7 mm) compared to the values of the RA and LA catheter (0.4 and 0.2 mm). The inter-electrode distances of the RA, LA and PV Lassos show a SD of 0.4 mm, thus one order of magnitude lower than the mean value (around 4 mm). This demonstrates the relatively uniform positioning. For the Orbiter that was modeled in a very structured tissue area, the SD is increased (1.5 mm), but still amounts to less than 25 % of the mean value (6.2 mm) and should therefore be sufficient.

Choosing a distinct electrophysiological (EP) model has only minor impacts on the signal quality of the simulated potentials. So the need for analyzing intracardiac potentials within a certain application does not impose any boundary conditions on the EP model to be used. Especially, the use of simplified and

faster models such as the minimal model and the Cellular Automaton for such applications is possible. This can dramatically decrease simuluation time which is crucial in clinical applications. If there are differences in the signals between the models, these might rather be caused by the actual activation sequence of the heart. While in the monodomain model, the excitation conduction can both be affected by wave-front curvature and wall thickness, this is not the case for the cellular automaton. However, this study is restricted to sinus rhythm. The case of AF needs further investigations.

The signals extracted from three reference catheters in the RA and LA (type I) as well as in the PV (type II) show very reasonable results regarding the activation sequence. The comparison of the simulated signals from the coronary sinus and left atrial appendage to real clinical data already showed qualitative similarities. Again, it has to be noted that no adaptation of the simulation model has been performed to get an even better matching. Several limitations and possible sources of errors must be considered. First, instead of a patient-specific atrial geometry the Visible Man dataset was used. It may differ from the patient's heart, especially in very structured and variable regions like close to the LAA. Second, the catheter position was set manually such that it represented the measurement setup as good as possible. Yet as the endocardium between the LAA and the LSPV was very structured in the VM model, the catheter was somewhat shifted towards the LA roof. Additionally, catheter size and orientation were only estimated based on the picture in fig.3. Further, it is unclear to what extent tissue structure may have impaired quality of the measured signals. As shown in fig.3, some electrodes may have been located on the LAA opening without optimal tissue contact. Therefore, more systematic comparisons between simulated and measured signals should be performed in anatomically simpler regions such as the posterior LA wall or the LA roof.

Besides, the model did neither include fiber orientation nor important structures of the atrial excitation conduction system such as the Crista Terminalis [11] or the Bachmann bundle (BB) [12]. Especially the BB has a significant impact on the excitation conduction from RA to LA, thus influencing the activation sequence of the atria. Also, the morphologic features of the CS can vary significantly between different individuals [11]. This might for example explain the difference in activation patterns of the CS. Finally, though in sinus rhythm, the clinical data was measured in a patient suffering from AF. Such an arrhythmia can lead to changes in the electrophysiology and excitation conduction (remodeling) [13] that were not taken into account here.

These results demonstrate a promising framework for the generation of clinically relevant catheter potentials from electrophysiological simulations. Even from a generic heart model, clinical measurements can in future be simulated and analyzed in terms of their information content. With patient-specific anatomical models available, comparisons between measured and simulated catheter signals can constitute an important interface for patient-specific model adaptation and validation according to individual patient data.

References

1. Biosense Webster, Diamond Bar, USA
2. Bard Electrophysiology, Lowell, USA
3. Visible human project, national library of medicine, Bethesda, USA
4. Seemann, G., Sachse, F., Karl, M., Weiss, D., Heuveline, V., Dössel, O.: Framework for modular, flexible and efficient solving the cardiac bidomain equation using petsc. In: Proceedings ECMI (2008)
5. Courtemanche, M., Ramirez, R., Nattel, S.: Ionic mechanisms underlying human atrial action potential properties: Insights from a mathematical model. Am. J. Physiol. 275, 301 (1998)
6. Bueno-Orovio, A., Cherry, E., Fenton, F.: Minimal model for human ventricular action potentials in tissue. Journal of Theoretical Biology 253, 544–560 (2008)
7. Weber, F.M., Lurz, S., Keller, D.U.J., Weiss, D.L., Seemann, G., Lorenz, C., Doessel, O.: Adaptation of a minimal four-state cell model for reproducing atrial excitation properties. In: Proc. Computers in Cardiology (2008)
8. Werner, C.: Simulation der elektrischen Erregungsausbreitung in anatomischen Herzmodellen mit adaptiven zellulären Automaten. PhD thesis (2001)
9. Schmitt, C., Deisenhofer, I., Zrenner, B. (eds.): Catheter Ablation of Cardiac Arrhythmias: A Practical Approach. Springer, Heidelberg (2006)
10. St. Jude Medical, St. Paul, USA
11. Saremi, F., Krishnan, S.: Cardiac conduction system: anatomic landmarks relevant to interventional electrophysiologic techniques demonstrated with 64-detector ct. Radiographics: a Review Publication of the Radiological Society of North America, Inc. 27, 1539–1565 (2007)
12. Saremi, F., Channual, S., Krishnan, S., Gurudevan, S., Narula, J., Abolhoda, A.: Bachmann bundle and its arterial supply: imaging with multidetector ct–implications for interatrial conduction abnormalities and arrhythmias. Radiology 248, 447–457 (2008)
13. Nattel, S.: New ideas about atrial fibrillation 50 years on. Nature 415, 219–226 (2002)

Cardiac Fibre Trace Clustering for the Interpretation of the Human Heart Architecture

Carole Frindel, Marc Robini, Joël Schaerer, Pierre Croisille, and Yue-Min Zhu

CREATIS-LRMN, CNRS UMR 5220, INSERM U630, INSA of Lyon
Bâtiment Blaise Pascal
69621 Villeurbanne cedex, France

Abstract. Cardiac fibre architecture plays a key role in heart function. Recently, the estimation of fibre structure has been simplified with diffusion tensor MRI (DT-MRI). In order to assess the heart architecture and its underlying function, with the goal of dealing with pathological tissues and easing inter-patient comparisons, we propose a methodology for finding cardiac myofibrille trace correspondences across a fibre population obtained from DT-MRI data. It relies on the comparison of geometrical and topological clustering operating on different fibre representation modes (fixed length sequences of 3-D coordinates with or without ordering strategy, and 9-D vectors for trace shape approximation). In geometrical clustering (or k-means) each fibre path is assigned to the cluster with nearest barycenter. In topological (or spectral) clustering the data is represented by a similarity graph and the graph vertices are divided into groups so that intra-cluster connectivity is maximized and inter-cluster connectivity is minimized.

Using these different clustering methods and fibre representation modes, we predict different fibre trace classifications for the same cardiac dataset. These classification results are compared to the human heart architecture models proposed in the literature.

1 Introduction

DT-MRI measures water diffusion in tissues. These MRI measurements describe the local cellular pattern in the cardiac muscle, where many cells have similar orientations. These diffusion measurements take the form of diffusion tensor maps [3]. However, due to the high complexity of the data, manual exploration of diffusion tensor maps for the purpose of segmentation, registration, diagnosis or inter-individual comparison is very difficult. In practice, one can visualize tensors directly using small glyphs, or try to reconstruct the anatomical architecture by performing tractography [2,8]. Still, detailed three-dimensional cardio-anatomical knowledge is necessary to choose a region of interest for display of the glyphs or paths.

By performing automatic classification of fibre traces (or fibre paths), one could reduce this data interaction problem to the choice of which group of paths to display. Not only would this aid in visualization of the DT-MRI data, but

N. Ayache, H. Delingette, and M. Sermesant (Eds.): FIMH 2009, LNCS 5528, pp. 39–48, 2009.
© Springer-Verlag Berlin Heidelberg 2009

also in the quantification of diffusion properties of interests such as anisotropy or fibre coherence measures.

The aim of this work is to offer insights into cardiac mechanics and pathologies by characterizing the fibre architecture, which has been proved to be important in several pathologies (e.g. hypertrophic cardiomyopathy). In this context, we propose a methodology to define a proper framework (clustering method and fibre representation mode) to perform automatic classification of the cardiac myofibres. We compare cardiac fibre paths classification results associated with three different fibre representation modes and two different clustering methods. The fibre representation modes are fixed length sequences of 3D coordinates with or without ordering strategy and mapping to an Euclidian feature space [4]. In the great variety of clustering methods, we consider a geometrical method (k-means) and a topological one (spectral clustering).

The paper is organized as follows. Section 2 describes related work in neurology and Section 3 is an overview of the proposed methodology. The results obtained within the different frameworks are exposed and compared to the human heart architecture models proposed in the literature in Section 4. Conclusions are given in Section 5.

2 Related Work

Fiber trace classification has been mainly studied in the context of neurology, where the brain regions are well identified and fibre terminations appear clearly. In this context, classification approaches attempt to identify connected brain regions. They divide the problem into two parts: the decision of how to quantify "distance" between paths, and the choice of the clustering method.

Several distance measures have been proposed in the literature. In one of the earliest approach, Ding et al. [6] compute the mean distance separating paths using pointwise correspondences between paths segments. Their method is specific to paths which have been seeded in one image slice. Other pairwise distances between paths (closest point distance, symmetric chamfer distance and symmetric Hausdorff distance) are used in [9,5,22]. Jonasson et al. [13] propose to base the computation of the path similarity measure on the number of times two paths share the same voxel. Alternatively, Brun et al. [4] introduced a 9-D vector for trace shape approximation composed of the mean and lower triangular part of the covariance matrix of the points in a path. They compute the distance between paths as the Euclidian distance between the corresponding 9-D vectors.

Three general types of clustering methods have been employed in the literature, hierarchical clustering [9,5], partitional clustering [21] and spectral clustering [4,13].

To our knowledge, there is no work on the topic of classification and quantification of cardiac myofibres using DT-MRI. In early work [12], the correspondence between the primary eigenvector and fibre orientation, and the correspondence between the combination of secondary and tertiary eigenvectors and sheet orientation has been validated by DT-MRI combined with 3-D histological reconstruction of fibre and sheet structure. In this context, the goal of classification

is to better understand the heart architecture and its underlying function. Note that cardiac fibre traces do not follow the same structure as brain fibre traces : manual exploration of cardiac fibre paths is a difficult task because the myocardium, unlike the brain, is not segmented in independent anatomical regions. However, there may be regional specializations of the myolaminar architecture within a continuum meshwork, and we believe that a myofibre classification may represent a simplification of these regions.

3 Methods

Our clustering approach is schematized in Figure 1. The different steps are detailed in the following subsections.

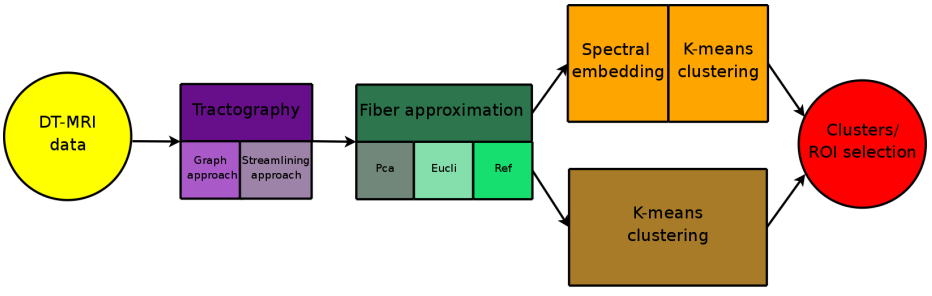

Fig. 1. Visual overview of the various studied clustering modalities

3.1 Data Acquisition

We studied one healthy *ex vivo* human heart. This one was placed in a plastic container and filled with hydrophilic gel to maintain a diastolic shape. The data were acquired with a Siemens Avanto 1.5T MR Scanner. Diffusion images were obtained using an echo planar imaging (EPI) pulse sequence with the following parameters : image reconstructed to 128×128 matrix, resolution of $2 \times 2 \times 2\,\mathrm{mm}^3$, 52 axial contiguous slices. The DT-MRI acquisition protocol is generally defined by the number N_d of diffusion sensitizing directions and the number N_e of excitations used for signal averaging: (N_d,N_e). In this work, the acquisition protocol (N_d,N_e) = (12, 4) was selected among other combinations in agreement with the acquisition protocol quality comparison conducted in [7]. The acquisition time for a 3-D dataset was $7'37''$.

3.2 Tractography

We perform tractography using the global graph-approach proposed in [8] and the streamlining approach with second-order Runge-Kutta integration [2]. Concerning the latter, we produce paths starting at all points within a region of interest covering most of the heart. Path growing stops when the fractional

anisotropy becomes too low (FA < 0.08) or when curvature becomes too high. To give an idea of the number of paths involved, there are $128 \times 128 \times 52$ voxels in our dataset, of which we extract approximately 1 500 paths with the global graph-approach and 30 000 paths with streamlining.

3.3 Fiber Representation Modes

The fibres generated by tractography are represented by either fixed length sequences of 3-D coordinates or 9-D vectors. In the case when a fibre path F is represented by a 9-D vector, the description is of the form

$$\Phi(F) = (m_x, m_y, m_z, g_{xx}, g_{xy}, g_{xz}, g_{yy}, g_{yz}, g_{zz}), \tag{1}$$

where m is the mean vector and g is the covariance matrix of the points making up the fibre trace (see [4] for details). When a fibre path is represented using a fixed length sequence of 3-D coordinates, the fibre is resampled at 20 equally spaced points using B-spline approximation.

Note that fibre representation is not an easy task. Each representation mode suffers from approximation errors. On one hand, the 9-D vector representation mode views the fibres as random point processes and ignores some features of fibre geometry. On the other hand, fixed length sequences of 3-D coordinates consider the fibres as directed objects ; which may cause two spatially adjacent fibres to be distant in the feature space. In fact, two adjacent fibres may be estimated with opposite directions. This depends on how the streamlining process is seeded or how the grid is scanned in the case of the graph approach ; it does not reflect the fibre architecture. To be independent of this phenomenon, we proposed to specify the direction of the tractographic paths with respect to a given 3-D reference point. More specifically, a given tractographic path will see its direction changed if the starting point of the fixed length sequence is not the closest endpoint to the reference point.

Below, we denote the fixed length sequence representation by **ref** or **eucli** (depending if the fibres are ordered w.r.t. a reference point or not) and the 9-D vector representation by **pca**. We investigate different fibre representation modes because they lead to different classification results and hence, some representations may lead to classifications that are more correlated to the actual human heart structure.

3.4 Similarity Measure for Fiber Paths and Spectral Embedding

Let N be the total number of fibre paths. Clustering operates on the complete graph K_N whose vertices are the fibre paths and whose edges are weighted by the similarity between vertices. The goal is to partition the graph vertices (the fibre paths) into groups so that intra-cluster connectivity is maximized and inter-cluster connectivity is minimized.

For the fixed length sequence representation (**ref** or **eucli**), we use the symmetrized Hausdorff distance as a similarity measure to compare paths. The Hausdorff distance H_{ij} is defined as the maximum of the pointwise minimum distances

between a pair of paths i and j. We symmetrize the distance by averaging H_{ij} and H_{ji}. For the 9-D vector representation (**pca**), we use the Euclidian distance E_{ij} to compare a pair of 9-D vectors i and j.

Let W be the similarity matrix of the underlying graph K_N ($W = H$ or E depending on the fibre representation used). Spectral embedding makes use of the spectrum of the similarity matrix W of the data to perform dimensionality reduction for clustering in fewer dimensions. The method used is described in [19]. The first step consists in scaling W using a diagonal matrix D whose entries are the row sums of W. This produces the laplacian L :

$$L = D^{-\frac{1}{2}} W D^{-\frac{1}{2}}. \tag{2}$$

Embedding vectors are then calculated by solving the generalized eigenproblem $(D - W)y = D\lambda y$, which minimizes the Normalized Cut [20]. The spectral embedding of the input data corresponds to the projection on the n largest scaled eigenvectors.

3.5 Clustering

The traditional Lloyd [18] algorithm converges to a local optimum of the k-means cost function. However, the clustering quality depends heavily on initialization. One idea for initializing k-means is to choose the farthest point from those picked so far. However, this is very sensitive to outliers.

Arthur and Vassilvitskii [1] suggest the following alternative procedure, called k-means++: choose each point at random with probability proportional to its minimum distance to the previously chosen points. The proposed method is computationally inexpensive and is robust against the density and the size of the clusters. In addition, formation of a spurious cluster is avoided by ensuring that the seed point is not an outlier point.

In this study, we run k-means++ clustering on the fibre paths and on the output from spectral embedding. The resulting clusters correspond to fibre bundles.

3.6 Prediction of the Number of Clusters

For spectral clustering, we note that the magnitude of the eigenvalues falls off quickly. This implies that a good approximation to the full similarity matrix W can be computed using only a subset of its spectrum. To approximate the data, the eigenvalues are plotted and those that tend to level out are ignored. The data is then projected onto the remaining r eigenvectors to get a rank-r approximation.

For k-means, we display the energy (sum of the average squared distance between fibre paths and their corresponding barycenter) as a function of the number of clusters used for classification. Above a certain amount of clusters, the energy stabilizes. We identify the beginning of the stabilization step as the optimal number of clusters to use.

4 Preliminary Results

In this section, we present results based on both synthetic and real fibre trace data to illustrate the performance of the different clustering frameworks. In section 4.1, we show simulation results designed to illustrate capabilities of the different frameworks (representation mode and clustering method). Section 4.2 compares the different frameworks in the case of real cardiac fibre trace data obtained from diffusion tensor MRI.

4.1 Synthetic Dataset

The purpose of the synthetic example – as shown in Figure 2 – is to analyze the ability of the different frameworks to cluster a 2D data set (25 fibre paths) into two bundles. When the simple k-means clustering framework is used (see Figs. 2(a)-(c)), erroneous clustering results occur. However, the spectral clustering approach with **eucli** and **ref** fibre representation modes (see Figs. 2(e) and 2(f)) cluster the input data successfully. The difference between simple k-means (i.e without spectral embedding) and spectral clustering lie in the fact that k-means is based on geometry and therefore tends to gather fibres that are close (w.r.t. a distance measure) regardless of fibre bundle topology.

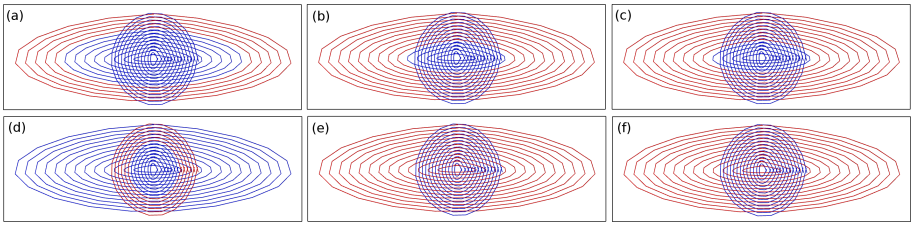

Fig. 2. Synthetic example consisting of two elliptical fibre populations. First row : Clustering results based on simple k-means. Second row : Clustering results based on spectral embedding. (a) and (d), (b) and (e), and (c) and (f) respectively use **pca**, **eucli** and **ref** fibre representation modes. The colors of fibre traces indicate cluster membership.

4.2 Fiber Traces from Cardiac DT-MRI

We now apply our methodology in partitioning the fibre traces of the human heart into anatomical bundles. Figures 3(a) and 3(b) display the results of the different frameworks for human heart fibre paths obtained from two different tractography algorithms [2,8]. The two tractography methods lead to similar results.

From the literature, we know that the human heart architecture decomposes into three levels : a primary structure defined as the predominant fibre orientation [16,14], a secondary structure defined as the organization of the myolaminae

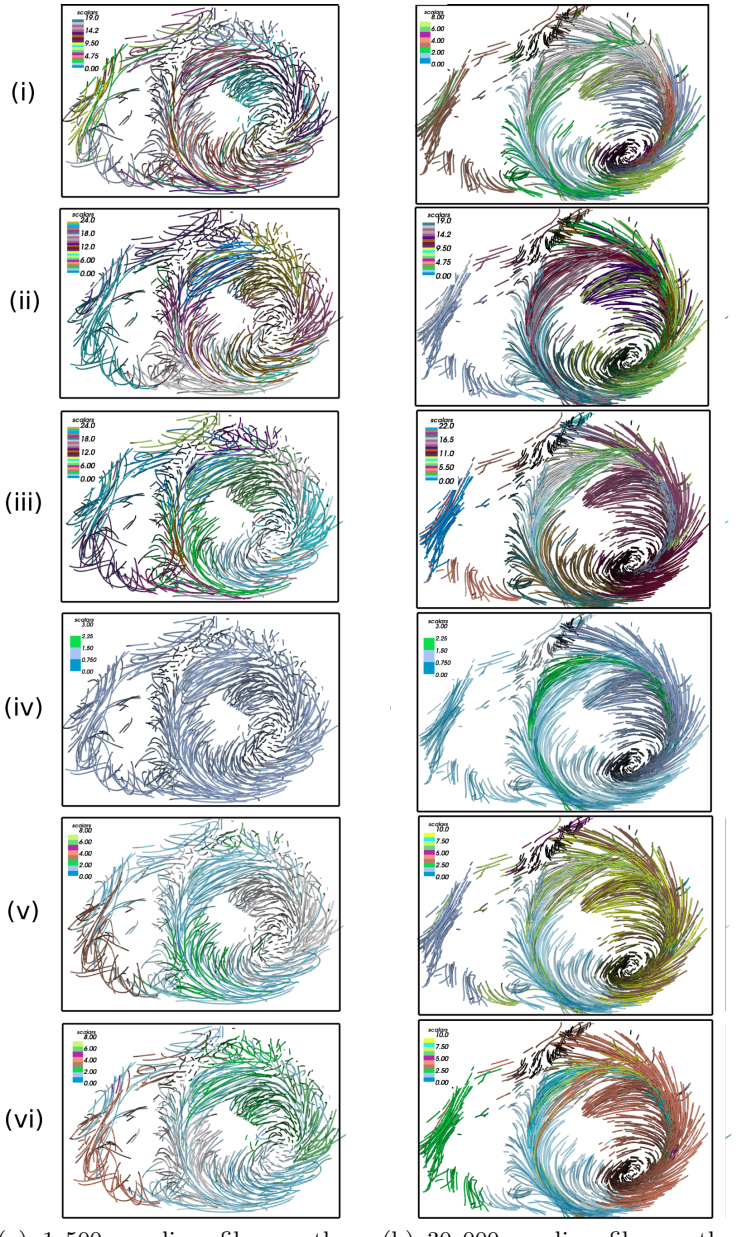

(a) 1,500 cardiac fibre paths obtained from global graph-approach

(b) 30,000 cardiac fibre paths obtained from streamlining

Fig. 3. Top view of equatorial slice. Clustering results of cardiac fibre traces are ordered as follows : (i) **pca** k-means, (ii) **eucli** k-means, (iii) **ref** k-means, (iv) **pca** spectral clustering, (v) **eucli** spectral clustering, (vi) **ref** spectral clustering. The colors of fibre traces indicate cluster membership.

through which these fibres course [11,17], and a tertiary structure defined as localized aggregations of the primary and secondary structures. Some researchers have emphasized the band-like nature of the tertiary structure [15], but some controversy exists regarding this point.

Simple k-means with **ref** and **pca** representation modes (Figs. 3(a)i, 3(a)iii, 3(b)i and 3(b)iii) decribes changes of fibre orientation through layers from epicardium to endocardium, which is detailed in models focusing on the primary cardiac structure [16,14]. The eucli representation mode (Figs. 3(a)ii and 3(b)ii) provides less accurate results because it depends on arbitrary fibre direction (cluster membership is locally less coherent : fibres with similar geometry are not always assigned to the same cluster).

Spectral clustering with **pca** representation mode (Figs. 3(a)iv and 3(b)iv) finds that the human heart is a continuum meshwork where no regional specialization of the myolaminar architecture can be identified. On the other hand, spectral clustering with **ref** and **eucli** representation modes allow the identification of radial myocardial sheets described in models focusing on the secondary and tertiary cardiac structures [11,17,10]. In accordance with these models, Figs. 3(a)v, 3(a)vi, 3(b)v and 3(b)vi display bimodal populations of sheet orientation (the clustering method identifies two main populations which are displayed here using two different colors). Both regions run adjacently in the circumferential direction with sudden change in their abutments. This is particularly visible in Figure 3(a)vi where a sharp orientation change is observed between blue and green fibre populations. This is less clear with the **eucli** representation mode (Fig. 3(a)v) : again because of fibre direction dependency.

5 Discussion and Conclusions

We provided a methodological study of different clustering frameworks for effective partitioning of cardiac fibre traces. The comparison between fibre representation modes shows that it has to be direction-independent. Orientation dependency leads to errors in the computation of similarity between fibres and in the computation of cluster barycenters. The comparison of clustering methods indicates that simple k-means accounts for fibre trace geometry (primary cardiac structure) whereas spectral clustering convey connectivity informations (secondary and tertiary cardiac structures). No method is better than the other ; choosing one over the other is a matter of the type of information to be displayed.

This suggests that clustering may allow automatic identification of myocardial regions from DT-MRI images, which could greatly ease analysis and comparison of these images for the design of patient-specific therapies. Proper grouping of myofibres could for example allow to identify and quantify dysfunctional regions for different cardiac pathologies.

Acknowledgments. This work was supported by Siemens, the French ANRT and the French Research Unit (GDR) STIC-Santé from CNRS-INSERM.

References

1. Arthur, D., Vassilvitskii, S.: k-means++: The advantages of careful seeding. In: SODA (2007)
2. Basser, P.J., Pajevic, S., Pierpaoli, C., Duda, J., Aldroubi, A.: In vivo fiber tractography using DT-MRI data. Magnetic Resonance in Medicine 44(4), 625–632 (2000)
3. Le Bihan, D., Van Zijl, P.: From the diffusion coefficient to the diffusion tensor. NMR Biomed. 15, 431–434 (2002)
4. Brun, A., Knutsson, H., Park, H.J., Shenton, M.E., Westin, C.F.: Clustering fiber traces using normalized cuts. In: Barillot, C., Haynor, D.R., Hellier, P. (eds.) MICCAI 2004. LNCS, vol. 3216, pp. 368–375. Springer, Heidelberg (2004)
5. Corouge, I., Gouttard, S., Gerig, G.: Towards a shape model of white matter fiber bundles using diffusion tensor MRI. In: ISBI, pp. 344–347 (2004)
6. Ding, Z., Gore, J.C., Anderson, A.W.: Classification and quantification of neuronal fiber pathways using diffusion tensor MRI. MRM 49, 716–721 (2003)
7. Frindel, C., Robini, M., Rapacchi, S., Stephant, E., Zhu, Y., Croisille, P.: Towards in vivo diffusion tensor MRI on human heart using edge-preserving regularization. In: Int. Conf. IEEE EMBS 2007, pp. 6007–6010 (2007)
8. Frindel, C., Schaerer, J., Gueth, P., Clarysse, P., Zhu, Y.M., Robini, M.: A global approach to cardiac tractography. In: ISBI, pp. 883–886 (2008)
9. Gerig, G., Gouttard, S., Corouge, I.: Analysis of brain white matter via fiber tract modeling. In: EMBS, p. 426 (2004)
10. Gilbert, S.H., Benson, A.P., Li, P.L., Holden, A.V.: Regional localisation of left ventricular sheet structure: integration with current models of cardiac fibre, sheet and band structure. Eur. J. Cardiothorac. Surg. 32, 231–249 (2007)
11. Harrington, K.B., Rodriguez, F., Cheng, A., Langer, F., Ashikaga, H., Daughters, G.T., Criscione, J.C., Ingels, N.B., Miller, D.C.: Direct measurement of transmural laminar architecture in the anterolateral wall of the ovine left ventricle: new implications for wall thickening mechanics. Am. J. Physiol. Heart Circ. Physiol. 288, H132430 (2005)
12. Helm, P.A., Younes, L., Beg, M.F., Ennis, D.B., Leclercq, C., Faris, O.P., McVeigh, E., Kass, D., Miller, M.I., Winslow, R.L.: Evidence of structural remodeling in the dyssynchronous failing heart. Circ. Res. 98, 125–132 (2006)
13. Jonasson, L., Hagmann, P., Thiran, J.-P., Wedeen, V.J.: Fiber tracts of high angular resolution diffusion mri are easily segmented with spectral clustering. In: ISMRM (2005)
14. Streeter Jr., D.D.: Gross morphology and fiber geometry of the heart, pp. 61–112. Williams and Wilkins, Baltimore (1979)
15. Kocica, M.J., Corno, A.F., Carreras-Costa, F., Ballester-Rodes, M., Moghbel, M.C., Cueva, C.N.C., Lackovic, V., Kanjuh, V.I., Torrent-Guasp, F.: The helical ventricular myocardial band: global, three-dimensional, functional architecture of the ventricular myocardium. Eur. J. Cardiothorac. Surg. 29, S21–S40 (2006)
16. Krehl, L.: Beiträge zur Kenntniss der Füllung und Entleerung des Herzens. Abh. Math.-Phys. Kl Saechs. Ges. Wiss. 17, 341–362 (1891)
17. LeGrice, I.J., Smaill, B.H., Chai, L.Z., Edgar, S.G., Gavin, J.B., Hunter, P.J.: Laminar structure of the heart: ventricular myocyte arrangement and connective tissue architecture in the dog. Am. J. Physiol. 269, H57182 (1995)
18. Lloyd, S.P.: Least squares quantization in PCM. IEEE Trans. Inform. Theory 28, 129–137 (1982)

19. Ng, A.Y., Jordan, M.I., Weiss, Y.: On spectral clustering: Analysis and an algorithm. In: Advances in Neural Information Processing Systems, vol. 14, pp. 849–856. MIT Press, Cambridge (2001)
20. Shi, J., Malik, J.: Normalized cuts and image segmentation. PAMI 22, 888–905 (2000)
21. Shimony, J., Snyder, A., Lori, N., Contum, T.: Automated fuzzy clustering of neuronal pathways in diffusion tensor tracking. In: ISMRM (2005)
22. Tsai, A., Westin, C.F., Hero, A.O., Willsky, A.S.: Fiber tract clustering on manifolds with dual rootedgraphs. In: CVPR, pp. 1–6 (2007)

A Quantitative Comparison of the Myocardial Fibre Orientation in the Rabbit as Determined by Histology and by Diffusion Tensor-MRI

Stephen H. Gilbert, Olivier Bernus, Arun V. Holden, and Alan P. Benson

Institute of Membrane and Systems Biology and Multidisciplinary Cardiovascular Research Centre, Faculty of Biological Sciences, University of Leeds, Leeds, LS2 9JT, UK
{s.h.gilbert,o.bernus,a.v.holden,a.p.benson}@leeds.ac.uk

Abstract. Early models of rabbit cardiac fibre structure where from fitting histological fibre orientation onto finite element models. More recently models have been produced using DT-MRI. In a quantitative comparison of these models, in a selected equatorial slice the fibre helix angle has a transmural change of -111.8±30.8º (mean linear fit ± S.D.) in the histological data [H-1]), -92.4±54.5º in DT-MRI dataset [DTI-1] and -86.3±30.7º in DT-MRI dataset [DTI-2]. Variation is large due to outlier data near the RV posterior insertion, and is less when selected anatomical transmural locations are quantified; the lateral LV has a monotonic transmural change of H-1:-87.5±3.7º (mean linear fit ± S.E of slope); DTI-1: -84.8±2.2º; DTI-2:-77.7±2.5º. There is greater variation in the transmural change of the transverse angle than the helix angle (DTI-1, 4.6±83.0º (mean linear fit ± S.D.), pooled data). Limitations in the datasets from both methodologies are discussed in the light of this analysis.

Keywords: Cardiac structure, Diffusion tensor magnetic resonance imaging.

1 Introduction

A striking feature of cardiac anatomy is the regular helical orientation of the myocytes which make up the walls of the right and left ventricles (RV, LV), sometimes referred to as "myocardial fibre-orientation" and reviewed in [1]. This conformation of myocytes is critical in cardiac function, both in the mechanics of cardiac contraction [2] and in the spread of electrical excitation which coordinates this contraction [3]. Good models of whole-heart fibre-orientation are therefore a pre-requisite for the functional modelling of the heart, both in its normal function, and its altered function in disease.

Whole heart myocardial fibre-orientation can be determined by a variety of methods: (i) following the principal direction of the fibres in gross dissections [4], (ii) through quantitative histological measuring methods using a purpose built registration rig [5] and (iii) from optical mapping studies using the diffraction of polarised light [6]. Method (i) is non-quantitative, method (ii) is laborious and method (iii) requires reconstruction of angular measurements into a volume and can only be used to measure the out-of-plane component of the fibre angle.

N. Ayache, H. Delingette, and M. Sermesant (Eds.): FIMH 2009, LNCS 5528, pp. 49–57, 2009.
© Springer-Verlag Berlin Heidelberg 2009

DT-MRI has many potential advantages over these traditional methods. It determines fibre-orientation for the whole heart volume, without the shortcomings associated with measuring the out-of-plane component of orientation and without the volume reconstruction challenges associated with histological methods. It is not labour intensive, it is relatively fast, it can be applied *in vivo* (although resolution is lower and technical hurdles still exist). It also reveals information about cardiac sheet orientation [1].

Histologically determined datasets have been used in many modelling studies [4]- both in the modelling of fibrillation and arrhythmia, of defibrillation and of electromechanics. It is only recently that DT-MRI models have been applied in simulation studies [7,8].

Validation of fibre-orientation determination by DT-MRI and comparison with histology have been carried out, but these have examined isolated blocks of tissue [9]. This study is the first comparison of whole heart models of fibre-orientation against a whole heart smoothed histologically derived model (Vetter & McCulloch, [10]). The questions addressed are i) how do these models qualitatively compare, ii) what are the advantages and drawbacks of these models, iii) how do these models quantitatively compare.

2 Methods

Two rabbit hearts where imaged by DT-MRI and these volumes were registered to the smoothed histological dataset [10]. Fibre helix and sheet angles for the three data sets were calculated with respect to an axis fitted to the centre of the left ventricle (LV).

2.1 Tissue Preparation

Two New Zealand white rabbits were euthanised with pentobarbital sodium, the thoracic cavity opened and the heart removed by incision of the great vessels. The heart was placed immediately into 4% formaldehyde/phosphate buffered saline (PBS) and stored in this at 4°C for a maximum of 7 days. The atria of the second heart (DTI-2) were removed and direct measurements of chamber dimensions made (not reported here). Heart 1 was imaged in Fomblin (Aldrich), and heart 2 was imaged in 5% polyacrylamide (Aldrich).

2.2 Imaging

The hearts were imaged using a Bruker 9.4 T MR instrument (Bruker BioSpin MRI GmbH) and a standard reduced encoding diffusion-weighted gradient echo sequence at 20°C: 500 ms TR; 18.7 ms TE; diffusion gradients with 5 ms duration and 8.9 ms separation; b = 1130 s/mm . The imaging grid was 120 x 128 x 190, with voxel dimensions 0.1833 mm x 0.1875 mm x 0.2000 mm for DTI-1 and grid 128 x 128 x 160, with voxel dimensions 0.2000 mm x 0.2000 mm x 0.2000 mm for DTI-2. For each scan a single b0 image was acquired and diffusion-weighted images sensitised in each of 12 optimised directions. The imaging sequence was based on the scheme set out by [11]. Scan time was 10 hours and 6 scans were performed and mean measurements were calculated at each voxel.

2.3 Registration

Image volume registration was carried out using the Insight Tool Kit (ITK [12]) Normalised Correlation method allowing a maximum of 300 iterations.

2.4 Calculation of the Fibre Angles and Selection of the Regions of Interest

The fibre helix and transverse angles were calculated as described in [8]. A centroid axis was fit to the LV of the Vetter & McCulloch (1998) geometry, and the fibre orientation in the DT-MRI geometries was defined with respect to this axis (Fig 1). A mid-equatorial slice was selected for detailed characterisation, and the fibre angles were extracted for comparison at 30˚ intervals around the short axis circumference from a transmural radius of voxels (Fig 2.). The transmural dimension was normalised, and angles plotted from 10% to 90% normalised transmural distance (NTD) to which linear regression fits were made.

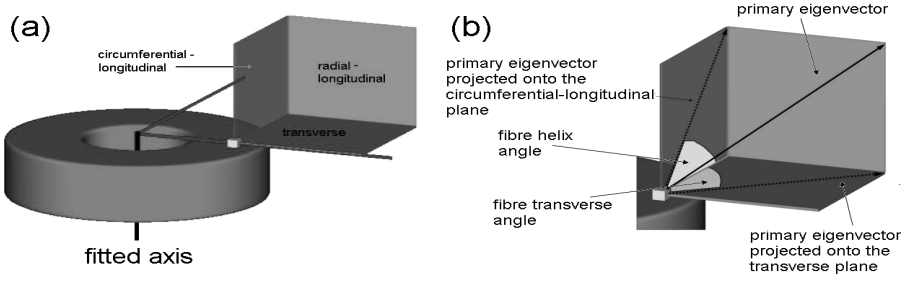

Fig. 1. (a) definition of standard planes with respect to the cardiac short-axis and the fitted LV centroid axis, (b) definition of the fibre helix and transverse angles with respect to the planes

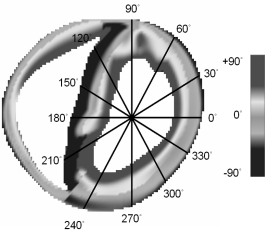

Fig. 2. The position of the circumferential transmural regions (at angle τ anti-clockwise from the lateral LV) from which the fibre angles were extracted from the selected equatorial slice

3 Results

3.1 Registration

The quality of the volume registration was assessed through visualisation of the alignment of the external cardiac geometry and the alignment of the ventricular cavities (Fig. 3.). The registration of DTI-1 to DTI-2 is closer than the registration of DTI-1 to H-1 or DTI-2 to H-1.

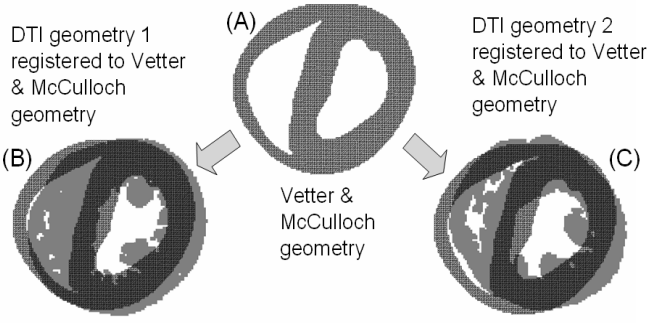

Fig. 3. The registration in the selected equatorial LV slice

3.2 Morphometric Comparison of Datasets

Measurements made directly from the geometries are compared to echocardiographic values from normal conscious rabbits (Table 1.)

Table 1. Comparison of the dataset dimensions with normal rabbit *in vivo* measurements

Measurement	Vetter & McCulloch	DT-MRI Heart 1	DT-MRI Heart 2	Normal diastole§	Normal systole§
LVID(cm)	1.0	1.0	0.98	1.540 ±0.112	1.009 ±0.091
LVAW(cm)	0.34	0.34	0.34	0.217 ±0.056	nrm
LVPW(cm)	0.38	0.38	0.39	0.274 ±0.041	nrm

LVID: LV inner diameter; LVAW: LV anterior wall; LVPW: LV posterior wall; nrm: not routinely measured; § - from [13]

3.3 Quantification of the Fibre Angles

Plots of the transmural fibre helix angle distributions are shown in Fig. 4. and of the fibre transverse angle in Fig. 5.

4 Discussion and Conclusion

The better registration between DTI-1:DTI-2 than DTI-1:H-1 or DTI-2:H-1 has not been analysed quantitatively, however, the qualitative comparison presented allows useful observations to be made on tissue preparation methods and appropriate registration methods. This less close registrations with H-1 are due to several factors: (i) the larger than physiological right ventricle (RV) in the Vetter & McCulloch model (as acknowledged in [10] this is probably due to RV distension when filling with dental rubber, (ii) the LV cavity has a non-physiological shape in the Vetter & McCulloch model, as the interventicular septum bulges convexly into the LV cavity

(again a likely consequence of RV over-distension), (iii) the apex of the Vetter et al. model is more pointed than of either DT-MRI geometry. The purpose of using a gel to fill the ventricles in [10] was to preserve their geometry during sectioning and imaging, and it is common practice to do this in DT-MRI [15], as was done for DTI-1. Here (similarly to [15]) we used a gel poured as a liquid which sets to a solid gel at room temperature, whereas in [10] dental putty was used which is a paste at room temperature. It is likely that the risk of non-physiological deformation is greater with this substance. DTI-2 was prepared without ventricular filling with gel, instead imaging was carried out in the liquid perfluorinated polyether Fomblin (as in [11]). No qualitative change in LV geometry is observed between DTI-1 and DTI-2, leading to the tentative conclusion that LV gel filling is not necessary for DT-MRI studies. If conventional non-rigid registration methods had been used then the normal physiological geometry of the ventricular cavities in the DT-MRI datasets would have been deformed towards the non-physiological conformation of the ventricular cavities in the H-1 dataset. In order to use non-rigid registration whilst avoiding such problems it will be necessary to use registration methods that limit deformation within the norms of cardiac physiological and anatomical form.

Examination of the fibre helix plots (Fig 4.) shows the well characterised [1] transmural regular angular change in profiles $\tau = 0°$, 30°,60°, 150°, 180°, 210° and 270°. The linear fits to the profiles have generally low slope standard error (S.E.) (Table 1), exemplified where $\tau = 0°$[H-1:-87.5±3.7º (mean linear fit ± S.E of slope); DTI-1: -84.8±2.2º; DTI-2:-77.7±2.5º]. If the data from the circumferential transmural radii are combined, there is marked variation: H-1:-111.8±30.8º (mean linear fit ± S.D.); DTI-1: -92.4±54.5º; DTI-2: -86.3±30.7º. This variation is largely due to the outlier transmural radius ($\tau = 120°$) where there is a large jump in helix angle in DTI-1 (i.e. a large change in angle over a short-transmural-distance), giving a positive slope linear fit with large S.E. [DTI-1: +9.2.5±30.3º]. The same effect is seen to a lesser degree in DTI-1: $\tau = 90°$, and may be as a consequence of fibre orientation complexity in the region of the posterior insertion of the RV into the LV. The reason for the lower endocardial helix angle in DTI-2 (and non-monotonic profile) at $\tau = 300°$ and the greater noise in the helix angle profile in DTI-2 at $\tau = 330°$ is not known. It is of note that for every circumferential position the transmural helix angle profile, as observed qualitatively, and as quantified by the slope of the linear fit, is closer between H-1 and DTI-1 or H-1 and DTI-2, than between DTI-1 and DTI-2. Judged on the helix angle profile (and ignoring the non-physiological chamber geometry,) the Vetter and McCulloch model is a good general model of angles obtained using DT-MRI.

The transverse angle is markedly different between hearts and it is more challenging to describe or interpret the transmural profiles. At some LV circumferential locations the three datasets have different transmural patterns of transverse angle change (at $\tau = 0°$, 90°, 120°, 150°, 180°). In other regions H-1 and DTI-2 profiles are similar ($\tau = 240°$, 330°), or H-1 and DTI-2 profiles are similar ($\tau = 30°$, 60°), or DTI-1 and DTI-2 profiles are similar ($\tau = 210°$, 270°, 300°). These observations are borne out by the linear fit statistics in Table 2, however as some profiles are complex and non-monotonic, the interpretive value of the linear fits is less than for the helix angle profiles. In simple terms (i) the transverse angle profile differs depending on circumferential position (in both histological and DT-MRI datasets), and (ii) differs at a

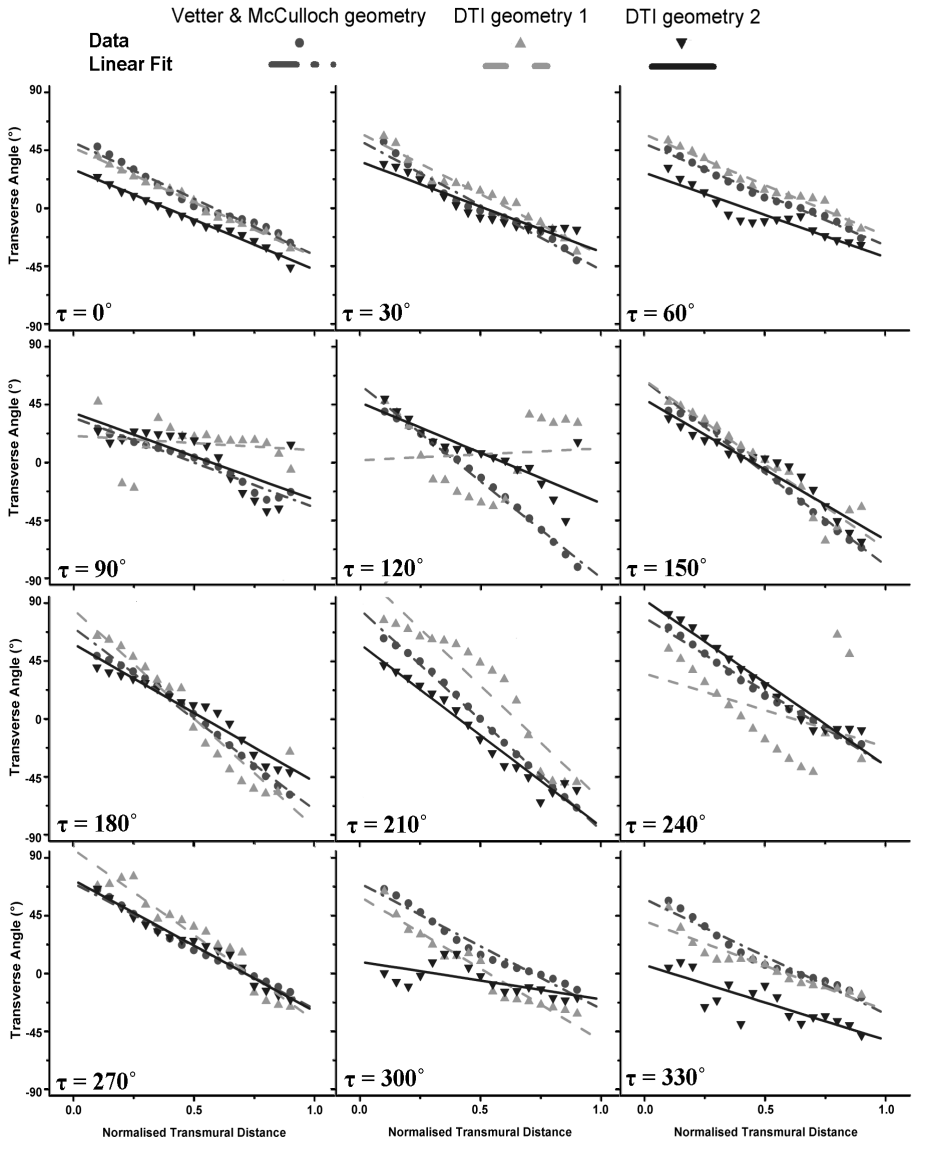

Fig. 4. Fibre helix angle plots from the circumference of the LV of the selected equatorial slice. The transmural radii (τ) are separated by 30º.

circumferential position between datasets. The first observation would not have been anticipated from the classical histological descriptions of the angle [4] which was of similar transmural angles within short-axis slices, with a change of transverse angle from positive at the base to negative at the apex. However, observation (i) was made by [16] in the rat DT-MRI data. The transmural variation reported here is greater than that reported in the normal rat were the average was ±20º, with S.D. ~25º [16]. Profiles of

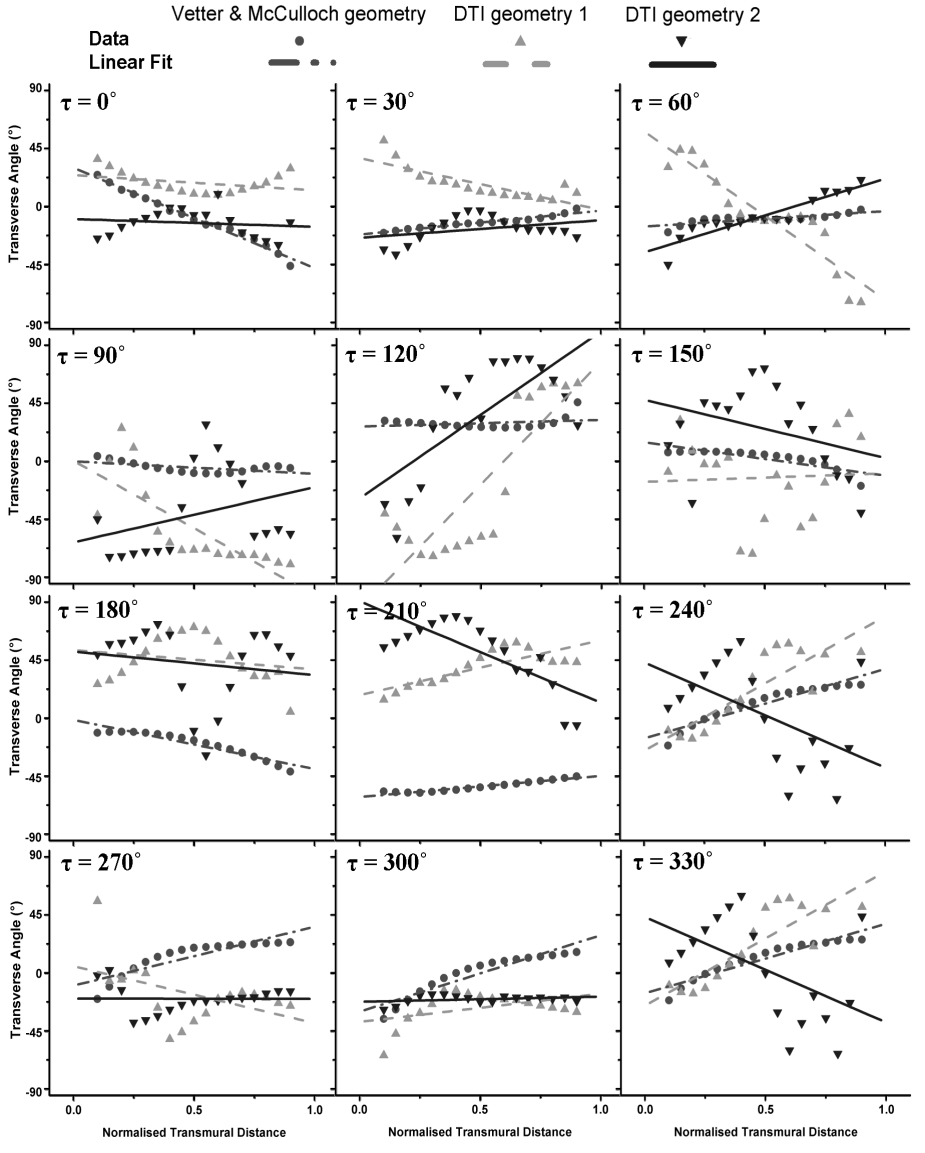

Fig. 5. Fibre transverse angle plots from the circumference of the LV of the selected equatorial slice. The transmural radii are separated by 30º.

greater transverse angle magnitude (H-1: τ = 210°) and greater transverse angle variability ((DTI-1, DTI-2: τ = 120°) are found here. The reason for this is unknown. The pattern of transmural profiles in individual rabbit hearts cannot be compared to data in [16] as only pooled data were provided.

Table 2. Comparison of linear fits to the helix and transverse angle data for the three data sets for the 30º spaced LV cirfumferential extracted radii

τ(°)	Helix Angle						Transverse Angle					
	Vetter & McCulloch		DT-MRI geometry 1		DT-MRI geometry 2		Vetter & McCulloch		DT-MRI geometry 1		DT-MRI geometry 2	
	g	**ε**	**g**	**ε**	**g**	**ε**	**g**	**ε**	**g**	**ε**	**g**	**ε**
0	-87.5	3.7	-84.8	2.2	-77.7	2.5	-77.7	2.5	-11.8	8.1	-6.0	10.9
30	-100.5	4.7	-95.0	5.3	-70.2	6.2	18.5	1.2	-40.1	7.5	13.7	9.7
60	-79.1	2.2	-78.7	3.5	-65.7	6.2	12.0	2.3	-130.6	13.4	57.2	6.8
90	-69.8	3.8	-11.2	16.8	-67.6	15.3	-9.7	3.4	-104.5	21.3	42.9	32.4
120	-150.1	3.2	9.2	30.3	-78.4	13.4	5.2	4.6	191.1	31.8	129.3	32.1
150	-143.4	3.5	-131.2	10.3	-109.2	8.0	-25.9	4.1	6.6	32.6	-45.2	32.6
180	-141.7	3.6	-169.4	14.2	-107.1	6.3	-38.2	3.2	-15.0	18.5	-18.2	30.5
210	-171.5	2.2	-177.2	16.0	-141.9	7.8	16.4	1.1	42.7	8.4	-78.8	17.4
240	-114.9	2.6	-57.0	33.0	-128.6	6.6	53.9	4.6	104.3	18.0	-81.7	34.4
270	-97.8	2.8	-132.8	9.1	-102.1	4.4	45.7	6.4	-44.1	21.5	-0.16	11.0
300	-97.6	4.6	-112.0	7.7	-29.1	8.9	59.4	5.7	21.8	11.7	4.0	3.1
330	-89.2	4.8	-69.1	6.3	-58.2	10.1	30.1	3.0	35.0	4.4	58.5	13.7
μ (g)	-111.8		-92.4		-86.3		7.5		4.6		6.3	
σ(g)	30.8		54.5		30.7		38.6		83.0		57.9	

τ: transmural radii circumferential location (see Fig 1.); g: slope of linear fit; ε: standard error of slope of linear fit; μ(g): mean of g; σ(g) : S.D. of g.

The heart preparation protocol in [10] aimed to fix and quantify the heart in diastole. Here the DT-MRI hearts were prepared by exsanguination followed by immediate immersion fixation in 4% formalin/PBS. In [10] perfusion fixation was used after arrest in diastole with hyperkalaemic cardioplegic solution. It might be expected that the Vetter & McCulloch model would be in a more diastolic state, and that the DT-MRI hearts may be more systolic due to myofibre shortening in contraction. This was assessed by comparison of lateral LV transmural fibre helix angles (panel at $\tau=0^{\circ}$ in Fig. 4) to published values for diastole and systole [14]. Although these published values are for the canine, the same pattern of fibre orientation has been reported widely in other mammalian species [4]. All hearts have transmural fibre helix angles close to the values described for diastolic dogs (lower than systolic values) and interestingly the values in the Vetter & McCulloch model are higher than for the DT-MRI hearts.

In conclusion (i) the Vetter & McCulloch model has fibre helix angles generally similar to DT-MRI determined values, (ii) both the DT-MRI models and the Vetter & McCulloch model have transverse angle profiles that vary around the LV equatorial circumference, (iii) large fibre transverse angles are found in both the DT-MRI models and the Vetter & McCulloch model, greater than that reported in rat DT-MRI [16]. The limitations of DT-MRI and the underlying complexity of the branching of cardiac myocytes (discussed in length in [1] should be considered in the interpretation of these results.

It will be necessary to quantify a large number of DT-MRI datasets to better characterise the behaviour of the transverse angle. The ventricular chamber geometry of the Vetter & McCulloch model is less physiological than those derived by DT-MRI here, but both models have thicker walls and smaller LV cavities than *in vivo* rabbit hearts.

References

1. Gilbert, S.H., Benson, A., Li, P., Holden, A.: Regional localisation of left ventricular sheet structure: integration with current models of cardiac fibre, sheet and band structure. Eur. J. Cardio.-thorac. Surg. 32, 231–249 (2007)
2. Arts, T., Costa, K.D., Covell, J.W., McCulloch, A.D.: Relating myocardial laminar architecture to shear strain and muscle fiber orientation. Am. J. Physiol. Heart Circ. Physiol. 280, H2222–H2229 (2001)
3. Clayton, R.H., Panfilov, A.V.: A guide to modelling cardiac electrical activity in anatomically detailed ventricles. Prog. Biophys. Mol. Biol. 96, 19–43 (2008)
4. Streeter Jr., D.D.: Gross morphology and fiber geometry of the heart. In: Berne, R.M., Sperelakis, N. (eds.) Handbook of physiology: section 2 The heart (American Physiology Society), pp. 61–112. Williams and Wilkins, Baltimore (1979)
5. Nielsen, P.M., Le Grice, I.J., Smaill, B.H., Hunter, P.J.: Mathematical model of geometry and fibrous structure of the heart. Am. J. Physiol. 260, H1365–H1378 (1991)
6. Jouk, P.S., Usson, Y., Michalowicz, G., Grossi, L.: Three-dimensional cartography of the pattern of the myofibres in the second trimester fetal human heart. Anat. Embryol. 202, 103–118 (2000)
7. Benson, A.P., Halley, G., Tong, W.C., Holden, A.V.: Virtual cell and tissue dynamics of ectopic avtivation of the ventricles. Chaoes 17, 015105 (2007)
8. Benson, A.P., Ries, M.E., Holden, A.V.: Effects of geometry and architecture on re-entrant scroll wave dynamics in human virtual ventricular tissues. In: Sachse, F.B., Seemann, G. (eds.) FIMH 2007. LNCS, vol. 4466, pp. 200–209. Springer, Heidelberg (2007)
9. Hsu, E.W., Muzikant, A.L., Matulevicius, S.A., Penland, R.C., Henriquez, C.S.: Magnetic resonance myocardial fiber-orientation mapping with direct histological correlation. Am. J. Physiol. 274, H1627—1634 (1998)
10. Vetter, F.J., McCulloch, A.D.: Three-dimensional analysis of regional cardiac function: a model of rabbit ventricular anatomy. Prog. Biophys. Mol. Biol. 69, 157–183 (1998)
11. Jiang, Y., Pandya, K., Smithies, O., Hsu, E.W.: Three-dimensional diffusion tensor microscopy of fixed mouse hearts. Magn. Reson. Med. 52, 453–460 (2004)
12. Insight Tool Kit, `http://www.itk.org`
13. Stypmann, J., Engelen, M.A., Breithardt, A.K., Milberg, P., Breithardt, O.A., Eckardt, L., Cordula, P.N.: Doppler echocardiography and tissue Doppler imaging in the healthy rabbit: differences of cardiac function during awake and anaesthetised examination. Int. J. Cardiol. 115, 164–170 (2007)
14. Streeter Jr., D.D., Spotnitz, H.M., Patel, D.P., Ross Jr., J., Sonnenblick, E.H.: Fiber orientation in the canine left ventricle during diastole and systole. Circ. Res. 24, 339–347 (1969)
15. Helm, P.A., Tseng, H.J., Younes, L., McVeigh, E.R., Winslow, R.L.: Ex vivo 3D diffusion tensor imaging and quantification of cardiac laminar structure. Magn. Reson. Med. 54, 850–859 (2005)
16. Chen, J., Song, S.K., Liu, W., McLean, M., Allen, J.S., Tan, J., Wickline, S.A., Yu, X.: Remodeling of cardiac fiber structure after infarction in rats quantified with diffusion tensor MRI. Am. J. Physiol. Heart Circ. Physiol. 285, H946–H954 (2003)

Adaptive Reorientation of Cardiac Myofibers: Comparison of Left Ventricular Shear in Model and Experiment

Wilco Kroon[1], Tammo Delhaas[1], Peter Bovendeerd[2], and Theo Arts[1]

[1] Maastricht University, Cardiovascular Research Institute Maastricht, 6200 MD Maastricht, The Netherlands
jw.kroon@fys.unimaas.nl
[2] Eindhoven University of Technology, Department of Biomedical Engineering, 5600 MB Eindhoven, The Netherlands

Abstract. Mechanical load plays an important role in cardiac growth and remodeling. In a previous mathematical model study the hypothesis was tested that fiber cross-fiber shear acts as a stimulus for remodeling of the pattern of myofiber orientations [7]. It was found that reorientation in response to fiber cross-fiber shear yielded realistic longitudinal and transmural components of myofiber orientation. In this study, we investigated whether circumferential-radial shear, as determined experimentally with magnetic resonance tagging, can be reproduced in the model as well. Our results show that after myofiber reorientation differences in circumferential-radial shear between model and experiment were reduced significantly. However, a complete match could not be obtained through shear-induced myofiber reorientation alone.

1 Introduction

It is well recognized that cardiac cells such as fibroblasts and myocytes respond to changes in mechanical load. For instance, stretch may significantly alter protein synthesis and enzymatic activity [9,12]. As such, mechanical load plays an important role in adaptive cardiac growth and remodeling. However, the stimulus-response relation remains unclear.

In mathematical model studies of left ventricular (LV) mechanics, it has been shown that myofiber strain during the cardiac cycle is very sensitive to orientation of the myofibers in the LV wall [2]. As such, adaptation of myofiber orientation is an effective tissue response for normalizing myofiber strains. Hypothesizing that myofiber strain would be a stimulus for adaptation of the myofiber orientations, Bovendeerd *et al.* (1998) optimized the pattern of myofiber orientations for homogeneity of myofiber strain during ejection by means of minimizing a global penalty function and found that the resulting myofiber orientations was well within the range of that determined experimentally with magnetic resonance diffusion tensor imaging (MRDTI) [3]. Unfortunately, due to inaccuracies in MRDTI measurements, experimental data on myofiber orientation has a relatively broad range [5].

N. Ayache, H. Delingette, and M. Sermesant (Eds.): FIMH 2009, LNCS 5528, pp. 58–67, 2009.
© Springer-Verlag Berlin Heidelberg 2009

Thus, direct comparison of model-predicted orientations with experimental data is not a very critical check for the model.

The pattern of myofiber orientations manifests itself in LV shear deformation. In particular, circumferential-radial shear (E_{cr}, definition is shown in Fig 1A) was found to be sensitive to the distribution of myofiber orientations [2], suggesting that comparison of E_{cr} constitutes a more critical test. Consequently, in a study by Ubbink *et al.* (2006) the optimum orientations found by Bovendeerd *et al.* (1998) were slightly changed with respect to the endo- to epicardial crossover to improve agreement between model predicted and measured E_{cr} [13].

Global optimization of myofiber orientations, as performed in Bovendeerd *et al.* (1998), is unlikely to represent a physiologic mechanism of adaptation. Instead, it is more likely that cells adjust their orientation in response to a local stimulus. In Kroon *et al.* (2008), the hypothesis was investigated that local fiber cross-fiber shear deformation, i.e., shear in the plane spanned by the fiber direction and a direction perpendicular to the fiber direction, acts as a stimulus for adaptation of the myofiber orientations [7]. Near the steady-state, this approach of local adaptation yielded longitudinal and transmural components of the myofiber orientations that were also within the range of experimental data.

In this study, we further test this candidate mechanism of adaptive myofiber reorientation by investigating whether it results in a realistic E_{cr} pattern. For that purpose, we compute E_{cr} before and after myofiber reorientation and compare the results with E_{cr} from magnetic resonance tagging (MRT) experiments in three healthy volunteers.

2 Methods

MRT data for three healthy (27-32 yrs old) humans were used as experimental reference for the model simulations. In short, tagging images were acquired in breath hold using ECG triggering, starting 20 ms after the R-wave. Using spatial modulation of the magnetization [1], grid-tagged images were acquired over a period of 80-90% of the cardiac cycle in three parallel short-axis sections of the heart located at 1/3, 1/2 and 2/3 the apex-to-base distance from the valve base. The images were analyzed off-line with custom software using Matlab 7.0 (MathWorks, Natick, MA). For further details on the data acquisition method and the method to determine E_{cr} from the MRT data sets we refer to Ubbink *et al.* (2006) and Van der Toorn *et al.* (2002) [13,15].

The applied models of cardiac mechanics and myofiber reorientation were described earlier [6,7]. In short, for the model of cardiac mechanics, the stress-free LV geometry is represented by a truncated ellipsoid (Fig 1B). The LV wall is composed of myofibers. Their orientation in the stress-free geometry is quantified by helix angle $\alpha_{h,0}$ describing inclination of the myofiber with the local circumference in local longitudinal direction, and by transverse angle $\alpha_{t,0}$ describing endo-to-epicardial crossover of the myofiber (Fig 1B). Tissue Cauchy stress is the sum of passive tissue matrix stress and active myofiber stress, uniaxially generated in the myofiber direction. The relation between deformation and the

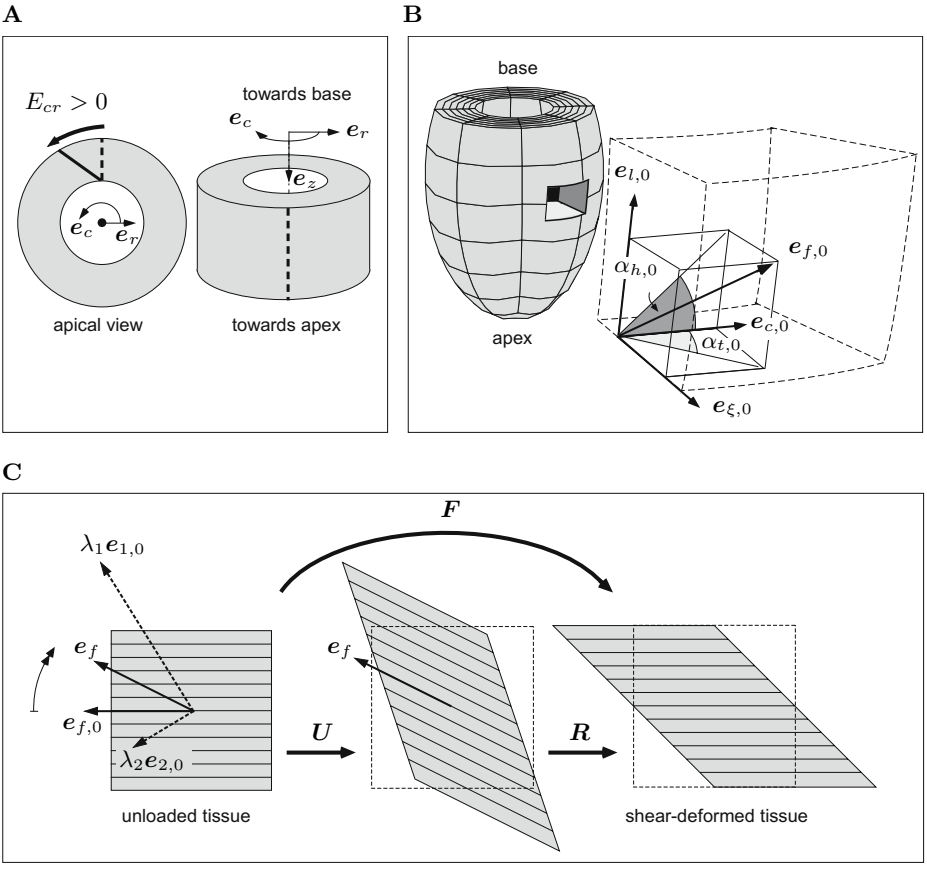

Fig. 1. A Definition of circumferential radial shear strain E_{cr} with respect to a global cylindrical coordinate system with radial direction $\boldsymbol{e}_r$, circumferential direction $\boldsymbol{e}_c$ and axial direction $\boldsymbol{e}_z$. In case the epicardium rotates more in circumferential direction than the endocardium, when viewing the heart from the apex, circumferential-radial shear strain is positive. **B** Helix angle $\alpha_{h,0}$ and transverse angle $\alpha_{t,0}$ in the stress-free model geometry to define the unloaded myofiber direction $\boldsymbol{e}_{f,0}$ with respect to a wall-bound (ellipsoidal) coordinate system having local transmural direction $\boldsymbol{e}_{\xi,0}$, circumferential direction $\boldsymbol{e}_{c,0}$, and longitudinal direction $\boldsymbol{e}_{l,0}$. **C** Illustration of the quantities involved in the adaptation of the myofiber orientation. In reality we simulate adaptation in three dimensions, but for illustrative convenience we show a 2D situation. During the cardiac cycle, the unloaded myofiber with direction $\boldsymbol{e}_{f,0}$ is subject to deformation $\boldsymbol{F}$, which involves a rigid body rotation $\boldsymbol{R}$ and a strain $\boldsymbol{U}$. Rigid body rotations are assumed irrelevant to the adaptation process. As a consequence, $\boldsymbol{e}_{f,0}$ is not adapted to the myofiber direction in the deformed tissue, but to the myofiber direction $\boldsymbol{e}_f$ in the tissue configuration that is obtained after rotation-free deformation. Notice that reorientation occurs only if the unloaded fiber direction $\boldsymbol{e}_{f,0}$ does not coincide with one of the principal deformation directions $\boldsymbol{e}_{i,0}$. This situation occurs in case of shear in the plane spanned by the fiber direction and a perpendicular direction, i.e., in case of fiber-cross fiber shear. ($\longrightarrow\!\!\!\!\!\!\blacktriangleright$) Direction in which $\boldsymbol{e}_{f,0}$ is adapted.

passive tissue stress is assumed to be non-linear and transversely isotropic [6]. Local active myofiber stress is a function of sarcomere length, sarcomere shortening velocity and time since mechanical activation. Sarcomere length in the stress-free state is constant throughout the wall and equals 1.9 μm. Mechanical activation of the LV is synchronous with a cycle time of 600 milliseconds. Hemodynamic preload and afterload as imposed on the LV by the vascular system are represented by a simple closed-loop lumped parameter (windkessel) model [7]. Deformation is computed from the balance of linear momentum using the finite element method (FEM).

Fiber cross-fiber shear strains were used to locally adapt the orientation of the myofibers $\boldsymbol{e}_{f,0}$ in the stress-free geometry according to the following evolution equation [7]:

$$\frac{\partial \boldsymbol{e}_{f,0}}{\partial t} = \frac{1}{\kappa}(\boldsymbol{e}_f(\boldsymbol{U}) - \boldsymbol{e}_{f,0}) \tag{1}$$

with κ being a time constant set to 10 s. The concept of fiber cross-fiber shear acting as stimulus for reorientation enters the evolution equation through the

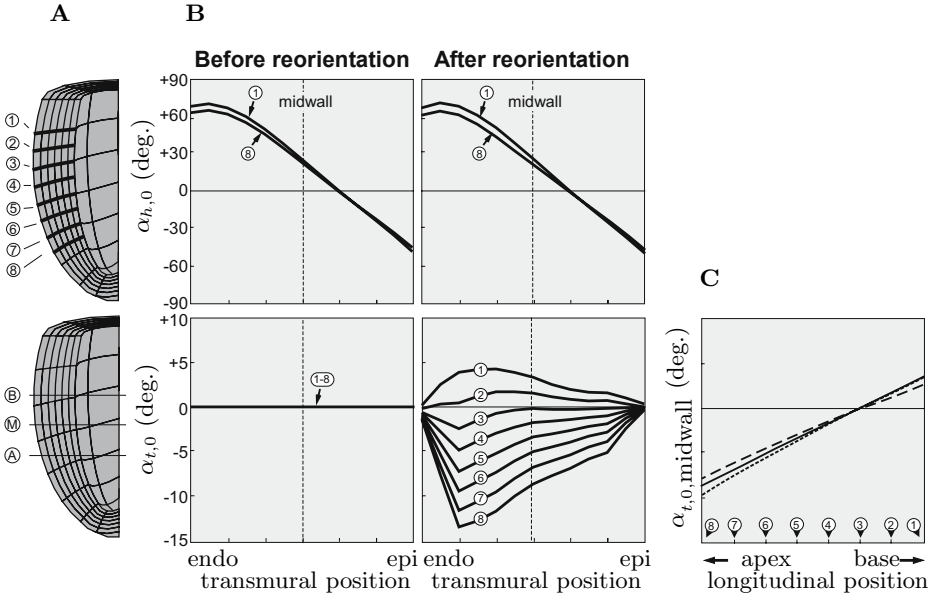

Fig. 2. **A** Top: levels for which the transmural variation in helix and transverse angle are visualized. Bottom: positions of the three short-axis slices relative to the finite element mesh; Ⓑ=basal, Ⓜ=midventricular, and Ⓐ=apical slice. **B** Top: helix angles $\alpha_{h,0}$ in the stress-free model geometry. Bottom: transverse angles $\alpha_{t,0}$. Notice that adaptation mainly affected the transverse angle. **C** Transverse angle $\alpha_{t,0}$ at midwall as a function of longitudinal position. (——) Obtained after reorientation to shear strain, this study; (– – –) Obtained after global optimization for homogeneous myofiber strain during ejection, from [3]; (--------) Obtained after multiplication of transverse angles obtained by [3] with a factor of 1.25, from [13].

definition of fiber direction $\boldsymbol{e}_f$ in the deformed tissue after having excluded rigid body rotations $\boldsymbol{R}$:

$$\boldsymbol{e}_f = \frac{\boldsymbol{U} \cdot \boldsymbol{e}_{f,0}}{|\boldsymbol{U} \cdot \boldsymbol{e}_{f,0}|} \tag{2}$$

with $\boldsymbol{U}$ the part of the deformation gradient tensor left after excluding rigid body rotations. Strain tensor $\boldsymbol{U}$ is calculated from the deformation gradient tensor $\boldsymbol{F}$ according to [10]:

$$\boldsymbol{U} = \boldsymbol{R}^{-1} \cdot \boldsymbol{F} = \sqrt{\boldsymbol{F}^T \cdot \boldsymbol{F}} = \sum_{i=1}^{3} \lambda_i \boldsymbol{e}_{i,0} \boldsymbol{e}_{i,0} \tag{3}$$

where $\boldsymbol{e}_{i,0}$ are the principal strain directions and λ_i the strain magnitudes in these directions (eigenvectors and eigenvalues of $\boldsymbol{U}$, respectively). In Fig 1C we show a two-dimensional illustration of the vector and tensor quantities involved in the adaptation process.

Initial helix angles were set to values that were determined after global optimization to achieve homogeneous myofiber strain during ejection [3]. In contrast to Bovendeerd *et al.* (1998) and Ubbink *et al.* (2006), initial transverse angles were set a non-physiological value of zero, in order to test whether adaptation could yield more physiologic (non-zero) values. Subsequently, myofiber orientations were locally adapted at time increments of 1 ms during 30 consecutive cardiac cycles [7]. The myofiber angles before and after adaptation are shown in Fig 2B.

E_{cr} was determined before and after adaptation. For comparison with MRT data, strains were determined at the level of the MR slices by interpolation from adjacent nodal points in the FEM mesh. The locations of the MR slices relative to the FEM mesh are shown in Fig 2A. Similar to the experimental procedure [13], strains were computed with respect to begin-ejection and averaged in transmural and circumferential directions.

3 Results

3.1 MRT Experiments

The time course of E_{cr} is similar for all three hearts (Fig 3)[1]; E_{cr} decreases equally in all three slices until one third of the ejection period. Thereafter, E_{cr} continues to decrease near the apex, remains about constant near the equator, and increases near the base. Throughout the isovolumic relaxation phase, E_{cr} increases in all slices, but remains negative. Notice that this negative E_{cr} implies that the subepicardium rotates in clockwise direction with respect to the subendocardium, when viewing the heart in apex to base direction. The overall amplitude in E_{cr} during the cardiac cycle increases towards the apex, having a

[1] The MRT data for subject #1 is the same as used for the right panel of Fig 3 in [13]. In [13], apex and basal slice should have been reversed. Small differences in the time course are due to the fact that analysis was redone by a different researcher.

value of about 0.08 in the apical slice. At the last available frame in the filling phase, E_{cr} is close to zero, suggesting that during isovolumic contraction changes in E_{cr} are limited.

3.2 Mathematical Model Simulations

Fig 3 shows the time course of E_{cr} as simulated with the myofiber orientations before and after adaptation to fiber cross-fiber shear.

Before reorientation, E_{cr} increases to about +0.07 during the first third of the ejection phase. During the rest of ejection, E_{cr} decreases but remains positive. During isovolumic relaxation and the first part of filling, E_{cr} decreases strongly. Thereafter, E_{cr} continues to decrease slightly. In the isovolumic contraction phase a strong increase in E_{cr} is observed. The overall amplitude of E_{cr} during the cardiac cycle increases towards the apex, having a value of about 0.40 in the apical slice.

After reorientation, the overall E_{cr} amplitude decreased fourfold to about 0.10. Basal E_{cr} decreases during ejection. For the midventricular and apical slice an increase is observed during the first third of ejection. Maximum E_{cr} during ejection is observed at the apex (+0.06). For the remaining part of ejection, E_{cr}

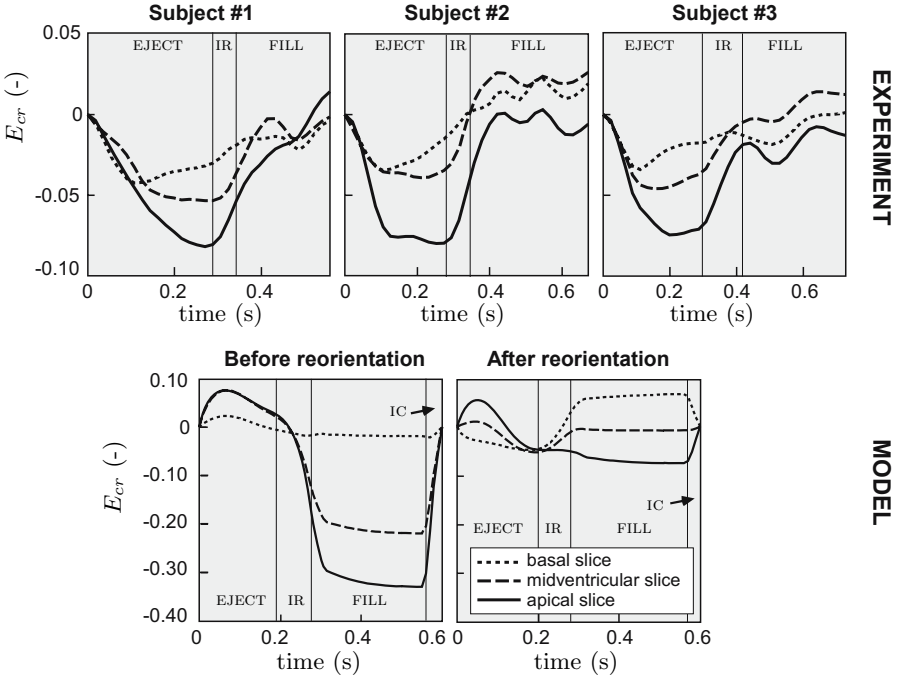

Fig. 3. Circumferential-radial shear strain (E_{cr}) during the cardiac cycle in experiment and model. For the phases in the cardiac cycle: EJECT=ejection; IR=isovolumic relaxation; FILL=filling; IC=isovolumic contraction. Note the difference in scales between the experiment and model.

decreases in all slices, having a value of about -0.05 at the start of isovolumic relaxation. During isovolumic relaxation E_{cr} increases in the midventricular and basal slice. This increase is more pronounced towards the base. In the apical slice, E_{cr} remains about constant. Consequently, E_{cr} diverges between the slices; at the end of isovolumic relaxation, E_{cr} in the basal, midventricular, and apical slice becomes about +0.05, 0, and -0.05, respectively. These differences remain similar during filling. A large change during isovolumic contraction causes E_{cr} in all slices to return to zero at the end of the cardiac cycle.

4 Discussion

In a previous study, myofiber orientations in the left ventricle (LV) were estimated with a mathematical model through shear-induced adaption of the myofiber orientations [7]. The model-estimated myofiber orientations were found to be well within the range of experimentally measured orientations. In this study, we investigated whether E_{cr}, as computed with the adapted myofiber orientations, was realistic as well.

4.1 Comparison between Model and Experiment

The MRT data show a consistent time course for E_{cr} for the three hearts. The apex-to-base gradient as well as the absolute values of E_{cr} are similar to the data presented by Young *et al.* (1994) [16] (after correcting for differences in the used coordinate system by changing the sign of E_{cr}).

Before myofiber reorientation, the model shows a positive E_{cr} during ejection, followed by a decrease during isovolumic relaxation, yielding a strongly negative E_{cr} at the end of filling. In contrast, the experiments shows a negative E_{cr} during ejection. Near the end of filling E_{cr} is close to zero. The overall amplitude during ejection is much higher in the model ($\sim$0.40) than in the experiment ($\sim$0.08).

After myofiber reorientation, the model shows a more realistic overall E_{cr} amplitude of $\sim$0.10. Furthermore, as in the experiment, E_{cr} increases during isovolumic relaxation. However, the apex-to-base gradient in E_{cr} remains opposite to that in the experiment. Although for the last part of ejection phase E_{cr} is negative, still an unrealistic positive E_{cr} is observed near begin-ejection. During isovolumic contraction, still a non-physiological large change in E_{cr} is observed.

4.2 Myofiber Orientation and Shear Strain

E_{cr} is related to the spatial and temporal pattern variation in tissue anisotropy. Therefore, differences between model and experiment mainly occur during ejection and isovolumic relaxation (Fig 3), when tissue anisotropy changes due to myofiber contraction and relaxation.

Tissue anisotropy is strongly related to the fiber orientation. To elaborate on that relation and explain the observed E_{cr} patterns, we consider a conceptual model of LV mechanics (Fig 4). Upon shortening of the myofibers in the subendocardial layers ($\alpha_h > 0$), the apex tends to rotate in clockwise direction with respect

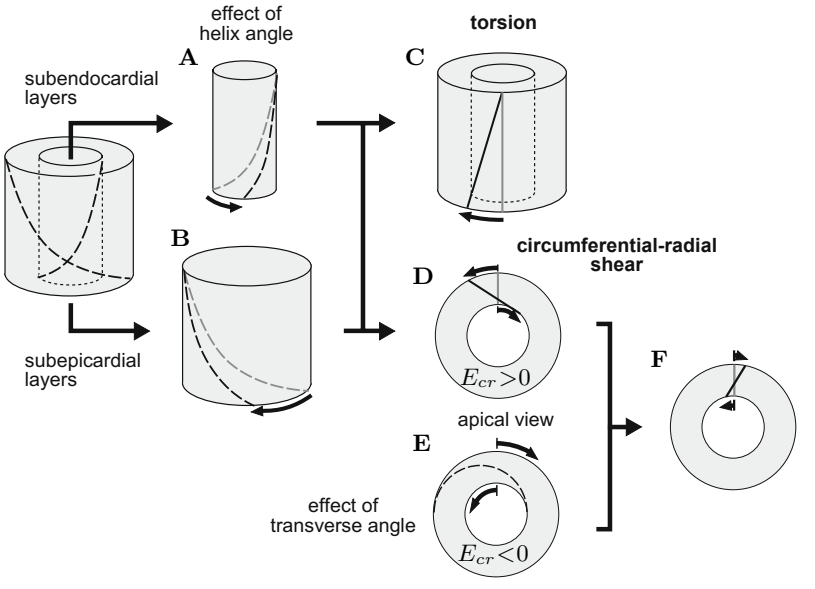

Fig. 4. Illustration of the influence of myofiber orientations on E_{cr}, which quantifies the transmural gradient in rotation with a slice. In absence of a transverse angle, shortening of the myofibers (− −) would cause (**A**) a clockwise apical rotation of the subendocardium and (**B**) a counterclockwise rotation of the subepicardium, when viewing the apex in apex-to-base direction. (**C**) The nett effect of these rotations is apparent through torsion. (**D**) The resulting transmural difference in rotation creates a transmural shear load yielding a positive E_{cr}. (**E**) In case of a negative transverse angle, myofiber contraction causes a shear load that is opposite to that induced by the transmural difference in rotation. (**F**) The final shear depends on the balance between the two opposing shear loads. Adapted from [13].

to the base, when viewing the heart from the apex. Shortening of myofibers in the subepicardial layers ($\alpha_h < 0$) tends to rotate the apex in counterclockwise direction. As a consequence a transmural difference in rotation a shear load is created. This load results in an E_{cr}. The amplitude and sign of this shear are determined by the shear stiffness of the tissue. In absence of a transmural component in orientation, i.e., with $\alpha_t = 0$, active shear stiffness is low and mechanical equilibrium is reached with a large positive E_{cr}. This explains the overestimation in E_{cr} amplitude as observed in the model before myofiber reorientation. In case $\alpha_t < 0$, an active force would counterbalance the shear load generated by the transmural difference in rotation. This explains the significant reduction in E_{cr} amplitude that is observed in the model after myofiber reorientation.

4.3 Study Assumptions and Limitations

Remaining discrepancies between shear strains in the mathematical model and those in the experiment originate from assumptions in the model of cardiac mechanics, in the model of myofiber reorientation, or in both.

Except for the myofiber orientations, tissue properties as used in the model were taken from Kerckhoffs *et al.* (2003) [6]. In order to quantitatively assess the influence of these model parameters on the computed E_{cr} (including settings of the initial conditions), a parameter sensitivity study certainly warranted. However, such a study is severely hampered by the high computational costs.

Qualitatively, we can state that passive shear stiffness may affect the transmural mechanical coupling between subsequent myocardial layers, and thus E_{cr}. Increased passive stiffness will generally yield a lower E_{cr} amplitude. Biaxial shear experiments suggest passive cardiac tissue to be orthotropic rather than transversely isotropic [4]. However, in a model study, the sensitivity of shear strains to the choice of the passive material model was found to be small [14]. We also assumed that sarcomere lengths in the externally unloaded LV are homogeneously distributed. In reality, however, the externally unloaded LV exhibits a transmural gradient in sarcomere length with epicardial sarcomeres being longer than endocardial ones [11]. Since actively generated myofiber stress is directly related to sarcomere length, a transmural gradient in sarcomere length may alter the transmural balance of forces and thus the shear strains. Shear strains may also be affected by the transmural differences in mechanical activation of the LV wall. Kerckhoffs *et al.* (2003) found that the pattern of mechanical activation affects heterogeneity in systolic myofiber strains [6]. Shear strain patterns, however, were not addressed in that study. Finally, the simplified LV geometry, the absence of mechanical interactions between the LV and the right ventricle, and simplifications in the lumped parameter model of the circulation may have affected E_{cr}, also.

In the adaptation model, myofiber orientations are determined by the shear strain pattern in the wall. As such, the assumptions described above may indirectly influence the adapted myofiber orientations. The midwall transverse angles as obtained though local adaptation in our model are close to the angles obtained by Ubbink *et al.* (2006) (Fig 2C). Yet, the E_{cr} as predicted in this study is less realistic than reported by Ubbink *et al.* (2006), which illustrates the high sensitivity of E_{cr} to the transverse angles. As such, a study is justified in which the sensitivity of the adapted myofiber orientations to values of the other tissue parameters is assessed.

Finally, we note that in reality, besides myofiber reorientation, other adaptation mechanisms are likely to be active, i.e., the above described tissue properties (e.g., passive stiffness, sarcomere lengths) may be the result of mechanically induced adaptation as well. In the future, inclusion of additional adaptive mechanisms should be considered.

5 Summary and Conclusion

In summary, we compared model predicted circumferential-radial shear strain (E_{cr}) with experimental data as obtained with magnetic resonance tagging in three healthy subjects. We found that by adapting myofiber orientations in the model on the basis of fiber cross-fiber shear strain, differences in E_{cr} between model and experiment could be reduced significantly. However, a complete match could not be obtained on the basis of myofiber reorientation alone.

References

1. Axel, L., Dougherty, L.: MR imaging of motion with spatial modulation of magnetization. Am. J. Physiol. Heart. Circ. Physiol. 171, 841–845 (1989)
2. Bovendeerd, P.H., Huyghe, J.M., Arts, T., van Campen, D.H., Reneman, R.S.: Influence of endocardial-epicardial crossover of muscle fibers on left ventricular wall mechanics. J. Biomech. 27, 941–951 (1994)
3. Bovendeerd, P.H., Rijcken, J., van Campen, D.H., Schoofs, A.J.G., Nicolay, K., Arts, T.: Optimization of left ventricular muscle fiber orientation. In: Pedersen, P., Bendsøe, P. (eds.) Proc. IUTAM Symposium on Synthesis on Bio Solid Mechanics, Copenhagen, Denmark, pp. 285–295 (1998)
4. Dokos, S., Smaill, B.H., Young, A.A., LeGrice, I.J.: Shear properties of passive ventricular myocardium. Am. J. Physiol. Heart. Circ. Physiol. 283, H2650–H2659 (2002)
5. Geerts, L., Bovendeerd, P., Nicolay, K., Arts, T.: Characterization of the normal cardiac myofiber field in goat measured with MR-diffusion tensor imaging. Am. J. Physiol. Heart. Circ. Physiol. 283, H139–H145 (2002)
6. Kerckhoffs, R.C., Bovendeerd, P.H., Kotte, J.C., Prinzen, F.W., Smits, K., Arts, T.: Homogeneity of cardiac contraction despite physiological asynchrony of depolarization: a model study. Ann. Biomed. Eng. 31, 536–547 (2003)
7. Kroon, W., Delhaas, T., Bovendeerd, P., Arts, T.: Computational analysis of the myocardial structure: Adaptation of cardiac myofiber orientations through deformation. Med. Imag. Anal. (2008), doi:10.1016/j.media.2008.06.015
8. Lin, D.H., Yin, F.C.: A mulitaxial constitutive law for mamalian left ventricular myocardium in steady-state barium contracture or tetanus. J. Biomech. Eng. 120, 504–517 (1998)
9. MacKenna, D., Summerour, S.R., Villarreal, F.J.: Role of mechanical factors in regulating fibroblast function and extracellular matrix synthesis. Cardiovasc. Res. 46, 257–263 (2000)
10. Malvern, L.E.: Introduction of the mechanics of a contious medium. Prentice-Hall Inc., Englewood Cliffs (1969)
11. Rodriguez, E.K., Omens, J.H., Waldman, L.W., McCulloch, A.D.: Effect of residual stress on transmural sarcomere length distributions in rat left ventricle. Am. J. Physiol. Heart Circ. Physiol. 264, H1048–H1056 (1993)
12. Simpson, D.G., Majeski, M., Borg, T.K., Terracio, L.: Regulation of cardiac myocyte protein turnover and myofibrillar structure in vitro by specific directions of stretch. Circ. Res. 85, e59–e69 (1999)
13. Ubbink, S.W., Bovendeerd, P.H., Delhaas, T., Arts, T., van de Vosse, F.N.: Towards model based analysis of cardiac MR tagging data: relation between left ventricular shear strain and myofiber orientation. Med. Imag. Anal. 10, 632–641 (2006)
14. Usyk, T.P., Mazhari, R., McCulloch, A.D.: Effect of laminar orthotropic myofiber architecture on regional stress and strain in the canine left ventricle. J. Elast. 61, 143–164 (2000)
15. Van der Toorn, A., Barenbrug, P., Snoep, G., Van der Veen, F.H., Delhaas, T., Prinzen, F.W., Maessen, J., Arts, T.: Transmural gradients of cardiac myofiber shortening in aortic valve stenosis patients using MRI tagging. Am. J. Physiol. Heart. Circ. Physiol. 283, H1609–H1615 (2002)
16. Young, A.A., Kramer, C.M., Ferrari, V.A., Axel, L., Reichek, N.: Three-dimensional left ventricular deformation in hypertrophic cardiomyopathy. Circ. 90, 854–867 (1994)

The Purkinje System and Cardiac Geometry: Assessing Their Influence on the Paced Heart

Daniel Romero[1,⋆], Rafael Sebastian[1], Bart H. Bijnens[1,2], Viviana Zimmerman[1], Patrick M. Boyle[3], Edward J. Vigmond[3], and Alejandro F. Frangi[1,2]

[1] Computational Imaging & Simulation Technologies in Biomedicine (CISTIB), Universitat Pompeu Fabra (UPF) and Networking Biomedical Research Center on Bioengineering, Biomaterials and Nanomedicine (CIBER-BBN), Barcelona Spain
daniel.romero@upf.edu
[2] Institució Catalana de Recerca i Estudis Avançats (ICREA), Barcelona, Spain
[3] Department of Electrical & Computer Engineering, University of Calgary, Calgary, AB, Canada

Abstract. Whole heart computer models are being widely used to assess treatment planning like Cardiac Resynchronization Therapy (CRT), a recognized treatment for heart failure. Certain aspects like cardiac geometry and the Purkinje system (PS) are still sometimes neglected on the studies. The present study includes a model of the human ventricles with incorporated anatomical structures such as myofibers orientation and Purkinje system. Two meshes representative of hypertrophic and dilated cardiomyopathies were generated from an original healthy subject mesh. In the context of (III) atrio-ventricular (AV) block, a sequential pacing protocol was tested for different device configurations. The pacing protocols were performed in models including the PS and in models lacking the PS. The results show that the Purkinje System leads to the synchronization of the septum and the left ventricle (LV) lateral wall, thus minimizing the interventricular delay. Also the modifications in the geometry resulted in changes in the activation patterns of the LV lateral wall, differing notably from physiological scenario.

Keywords: Patient-specific geometry, cardiac electrophysiology, Purkinje system, Cardiac Resynchronization Therapy, ventricular pacing.

1 Introduction

Heart modelling is starting to be frequently used to study physiological phenomena as well as to assess therapeutic treatment planning to various cardiac diseases. Furthermore, the integration of patient-specific details may help customize the design of treatments and increase their effectiveness [1,2].

However, a number of anatomical structures and properties (i.e. conductivity of the tissue), needed in the process of modelling, can not be non-invasively

⋆ Corresponding author.

N. Ayache, H. Delingette, and M. Sermesant (Eds.): FIMH 2009, LNCS 5528, pp. 68–77, 2009.
© Springer-Verlag Berlin Heidelberg 2009

extracted from existing image modalities, and population based data is used instead. This is the case of structures as myocardial fiber orientation and the Purkinje system (PS), key features in the electrical propagation and contraction of the heart. Purkinje fibers form the terminal component of the cardiac conduction system, which is a type of fast conducting cardiac tissue, responsible for synchronous activation cardiomyocytes during the cardiac cycle [3]. Nonetheless, in several electrical and mechanical simulation, and clinical oriented studies, the PS has been neglected [4,5,6,7] thus excluding from their observations and results intrinsic phenomena such as the PS retrograde activation observed in paced hearts.

Cardiac resynchronization therapy (CRT) is a pacemaker therapy used to treat heart failure patients (New York Heart Association class III and IV). It proved to improve systolic function in ventricular dyssynchrony [8], leading to improvement of functional capacity, inverse remodeling, and reduction of morbidity and mortality [9]. Aside from all the benefits, several clinical trials have demonstrated that one third of patients do not respond favourably to CRT using standard clinical selection criteria [9,10]. The use of personalized computational models for electrophysiological simulations of the heart may improve the understanding and application of CRT.

Certainly, comprehending the variations on the activation sequence related to changes in geometry and underlying structures, could help strengthening the selection criteria for CRT and also optimising the pacing protocol for the individual. Thus, the goal of this paper is to study the combined roles of anatomy and PS in the electrical activation sequence on the paced heart through computational simulations.

2 Construction of Anatomical Models

The anatomical models were built using a surface mesh previously obtained from the segmentation of a cardiac multislice computed tomography (MSCT) scan of a healthy subject [11]. For the segmentation, a heart statistical atlas trained and built with 100 MSCT patient scans, and based on point distribution and active appearance models had been used. The models used for the simulations were all biventricular (BV) since general CRT procedures require to implant a pacemaker lead in each ventricle.

The original surface mesh (see Fig. 1(a)) was mathematically transformed into two new meshes to represent dilated (DCM) and hypertrophic (HCM) cardiomyopathies. In clinical practice, dilatation is diagnosed when the ventricular diameter exceeds 117% of the expected normal, age-related, value while hypertrophy is diagnosed when wall thickness exceeds 125% of the expected maximal thickness [12]. Based on these criteria and comparing to typical patients, as seen in the Cardiology clinic, the HCM mesh was constructed by scaling the LV endocardium to achieve a 50% radial increment in wall thickness (see Fig. 1(c)). For the DCM mesh, the LV endocardial surface was radially displaced to obtain a 50% increment in diameter and the epicardial surfaces was consequently dilated

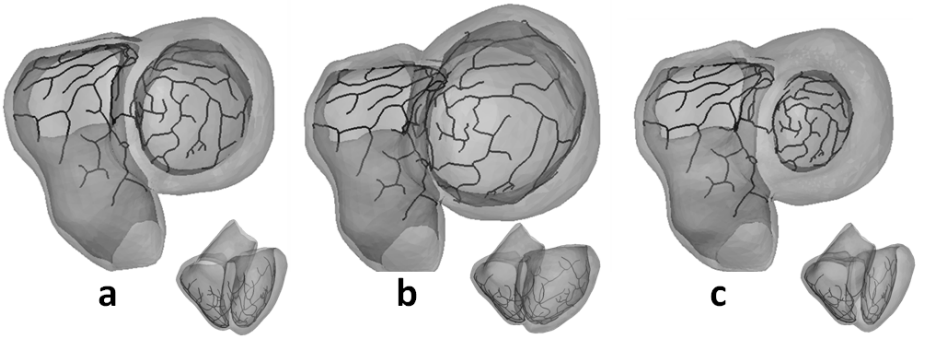

Fig. 1. Basal views of the ventricular surface models: (a) original healthy subject, (b) dilated (DCM), and (c) hypertrophic (HCM) cardiomyopathies. The lines represent the RV and LV PS branches.

to additionally achieve a 30% thinning of the average wall thickness to compensate for the lack of increase in myocardial mass in the dilating (non volume overloaded) hearts (see Fig. 1(b)).

The three surface meshes were then used to create high-resolution volumetric tetrahedral meshes needed for the numerical simulations. Volumetric mesh quality was ensured by controlling both the maximum distance between neighbouring nodes and the radius-to-edge ratio to assure regularly-shaped elements. The average inter-node distance was smaller than 500 μm, and the number of nodes and tetrahedral elements between 2.5 – 3.5 million, and 15 – 21 million, respectively. Mesh resolution was chosen based on a previous study were the influence of the mesh resolution on the electrical propagation [13] was evaluated. Following this study, tissue conductivities values recommended by Roberts [14] with mesh resolutions of the order of 500μm lead to realistic propagation velocities.

For the present study, myocardial fiber orientation was calculated for every element of the mesh, using a mathematical formulation based on the work of Streeter [15].

2.1 The Purkinje System

The Purkinje network was manually defined as an independent structure in the healthy subject surface mesh. The position of the terminals was determined following the experimental activation sequences described by Durrer [3]. The path between terminals were built using splines to form a tree structure. The structure thus obtained consists of the bundle branches and 100 branches distributed over the endocardial surface mesh. In Fig. 1 the RV and LV PS are clearly shown.

The PS in the pathological meshes were obtained using the same transformation algorithms previously described to obtain these deformed meshes. It was hypothesized that in a heart with an abnormal geometry, the number of branches in the Purkinje network is not affected, thereby no new terminals were generated.

3 Mathematical Modelling of Electrophysiology

The electrical propagation in the cardiac tissue was determined using the monodomain formulation [16], with a semi-implicit method (Crank-Nicholson) to iteratively solve the equations [17]. The Ten Tusscher et al. model [18] was chosen to simulate ionic kinetics for bulk myocardial cells, and the DiFrancesco-Noble model [19] for the PS. Both ionic models are based on experimental measurements and have proven to represent realistically the behaviour of cardiac cells.

The PS was modelled as in [20], with 1D cubic Hermite elements to ensure continuity of current at junctions and bifurcations. Purkinje fibers were isolated electrically from the myocardium, and only connected to it at the terminal points by Purkinje to myocardial junctions, which are modelled as fixed resistances. Each Purkinje cell is coupled to the n myocardial elements that lie within a specified radius. For further information see [21]. The pacemaker lead stimulus was modelled as a cube of 1 mm^3 that injects a transmembrane current of 0.05 $\mu A/cm^3$ for 1 ms.

All the numerical calculations were performed using the Cardiac Arrhythmia Research Package (CARP) [22,23].

3.1 Application to Study Electrical Activation in CRT

To assess the influence of cardiac geometry and the PS, a set of sequential pacing protocols were tested on the three cardiac models. Seven pacing scenarios determined by different time delays between the RV and LV pacing leads (interventricular delay, or VVD) were tested. The time delays ranged from 30 ms RV lead preactivation (VVD -30) to 30 ms LV lead preactivation (VVD 30) with intervals of 10 ms between pacing strategies. A (III) AV block was assumed for all these pacing scenarios. Leads were positioned on the apical endocardium (RV lead) and the lateral free wall epicardium (LV lead). As control cases a physiological activation (starting from the AV node) was also performed in the three models.

In order to further study the contribution of PS to the activation sequence all pacing simulations were repeated in the absence of the PS using physiological tissue conductivity values for the bulk myocardial tissue.

4 Results

In the physiological simulations performed for this study, the activation sequences were triggered from the AV node, starting the activation of the bundles of His at time $t = 0$. The activation on the myocardium spreads from the PS terminals to the endocardial surface, and propagates following an apex to base, and endocardium to epicardium pattern.

Figure 2 shows the 3D isochronal maps of the local activation times (LATs) obtained from the simulations, with time intervals of 10 ms. Local activation time is defined as the time, with respect to a reference (i.e. initial lead stimulus), at

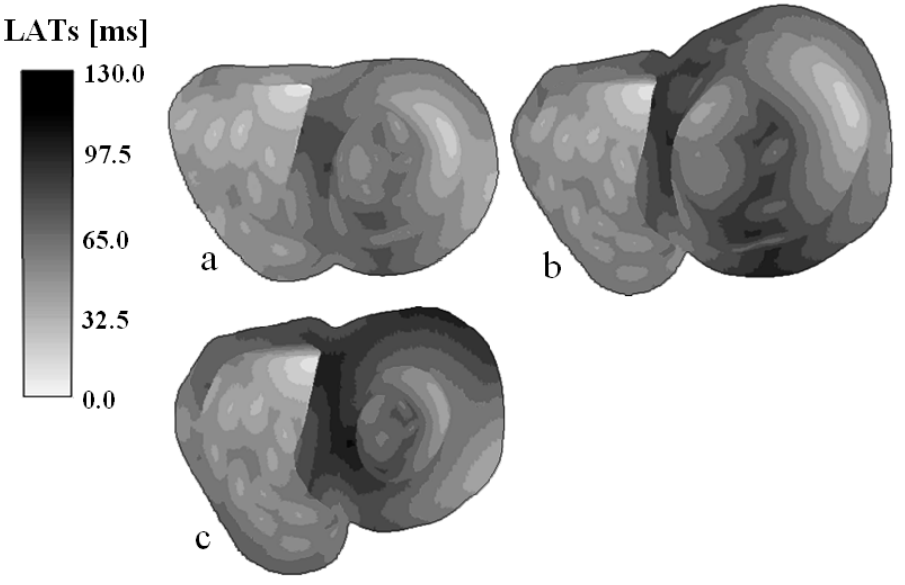

Fig. 2. Basal views showing the 3D isochronal maps of the local activation times for simultaneous pacing (VVD 0). (a) healthy subject mesh; (b) DCM mesh; (c) HCM mesh.

which a cell depolarizes. Figures correspond to activation using simultaneous pacing (VVD 0).

On the pacing scenarios there are two characteristics determining the activation sequences: wall thickness and PS density. The wall thickness, different in the three models, delayed the PS retrograde activation caused by the LV lead stimulus. The wavefront originated from this lead crossed the LV lateral wall and activated the closest Purkinje terminal fiber. Since the area of the endocardial surface varies along the models, being the HCM the smallest, followed by the healthy and the DCM, the density of Purkinje terminals per unit surface depends on the model. This density variation clearly affected the time for LV lead wavefront to find and enter the PS (see differences in late activated regions between Figures 2(a), 2(b), and 2(c)). However, once the PS was retrogradely activated, the depolarization spreaded rapidly, re-entering the bulk myocardium at the remaining terminals of the network allowing the fast activation of remote areas. Although in the models considered the LV lateral wall was mainly activated by the LV stimulus, the activation times of the septal wall were highly sensitive to the use of a PS. The stimulus given by the RV lead entered very quickly the RV PS since the lead rests on the endocardial apical region. Therefore, the activation of the RV PS was completed a few milliseconds after the initial stimulus. This effect can be observed (see Figure 2) as a large number of early activated small regions over the RV endocardium. Moreover, due to the proximity of the RV lead to the septal wall, the wavefront crossed the septum and contributed to the activation of the PS on the LV apex.

In order to further compare the activation patterns obtained for each pacing scenario and cardiac anatomy, cumulative frequency histograms were used. The histograms show the normalized percentage of LV myocardial tissue activated in time intervals, over the whole depolarization sequence.

A common initial activation rate can be observed in the histograms since the activation of the LV spread out initially only through the myocardium (see slope of the curves in Figs. 3 (a)-(c)). In the three models, increments in the activation rate are determined by the amount of myocardium activated from the PS re-entrants, which in turn are dependent on their geometry-density relation, and wavefronts generated by the leads. The LV PS is reached first in the healthy model, whereas in the HCM (solid line) due to the thicker wall, and in the DCM (dashed line) due to the lower density of PS terminals, there is a higher delay. In the case of the DCM, due to the low PS density, the wavefronts travel furthest through the myocardium before finding a PS terminal (lower slope).

Simulations with the models lacking PS show higher values of the ventricle's total activation time (TAT) (see Figs. 3 (d)-(f)). These increased values might

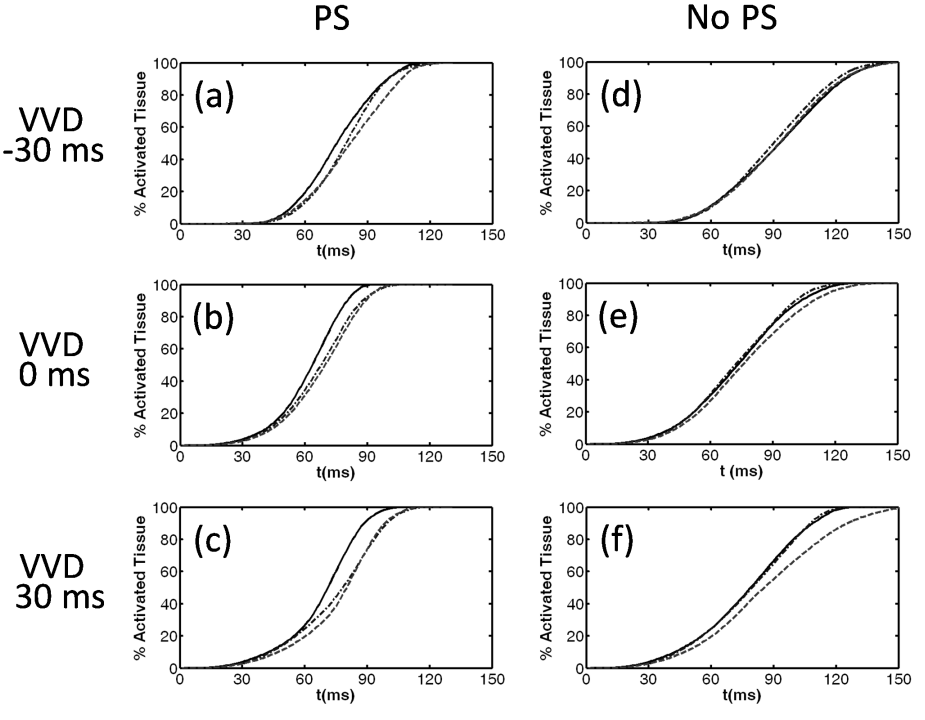

Fig. 3. Cumulative frequency histograms of the normalized percentage of activated tissue. The lines correspond to: (solid) healthy; (dashed) DCM; and (dash-dotted) HCM models. The first column correspond to the simulations with PS, and the second without PS. Rows correspond to RV lead preactivation (VVD -30 ms); simultaneous leads activation (VVD 0); and LV lead preactivation (VVD 30 ms).

lead to intraventricular dyssynchrony on the mechanical response, since different regions are depolarizing with marked delays between them. Additionally, a change in the overall activation patterns can be seen. In general, all the plots show a smaller and steady slope when compared to the PS cases. The main reason is that the wavefront has to reach remote areas travelling only through the bulk myocardium.

The American Heart Association (AHA) 17 segment division was used to analyse the mean activation time on each LV region. Some of the information thus obtained is presented as bulls eye plots in Figure 4. Comparing the figures corresponding to the different geometries (Healthy, DCM, and HCM), it can be observed that the activation sequence of the segments of the LV lateral wall change their order of activation, which in physiological cases follow an apex to base pattern and now start from the LV lead position and spread towards base and apex. Moreover, comparing the cases with and without PS, a different behaviour is observed for the septal and for the lateral wall regions. The septal regions show shorter mean activation times with PS than without PS. On the other hand, the mean values for the lateral wall do not show noticeable changes. This leads to more synchronous activations in models with PS. It was further observed (not shown in the figures presented) that the mean activation times on the LV lateral wall are mainly dependent on the timing of the LV lead activation.

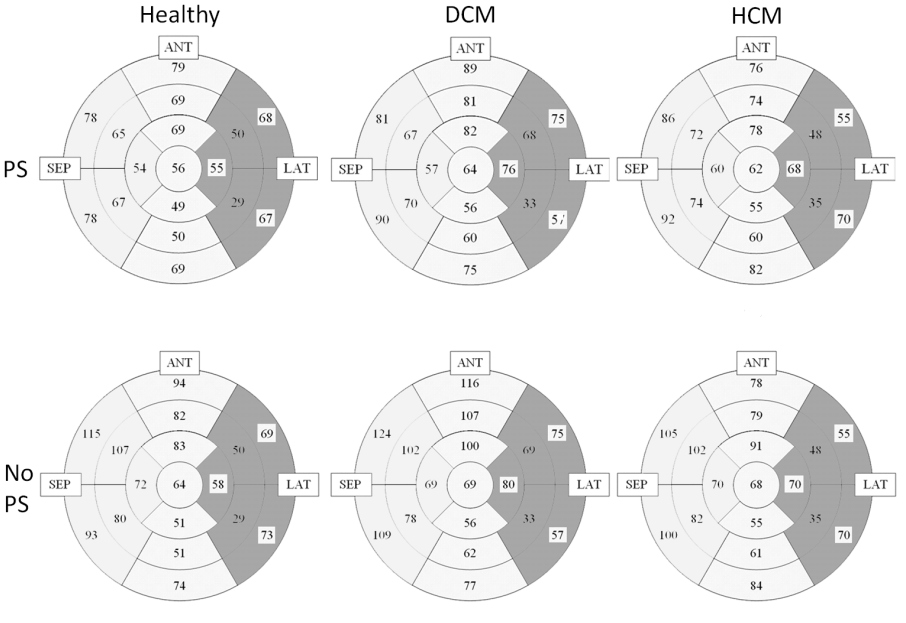

Fig. 4. Bulls eye plots of the 17 segments displaying the LV activation times for simultaneous pacing (VVD 0)

5 Conclusions

The importance of the PS in the electrical activation and its effect in CRT.

The analysis of the simulations performed on this study highlights the role of the PS and the specific cardiac geometry in the sequence of activation of the LV for different pacing strategies. The Purkinje system helps to minimize the intraventricular delay, so its appropriate activation synchronizes the septal and the LV lateral wall. Even though the importance of the PS in the electrical activation and its effect in CRT was shown, the PS model needs to be improved. The density of terminals in the system is probably low, leading to delays in the initial activation. A study to determine the accurate density of the PS is yet to be made.

The present study focused only on the electrical solution of the heart's activation, thus the mechanical feedback was neglected. Therefore, mechanical simulation should be included in the model in order to be able to refine the conclusions with regard to pacing therapies.

The influence of the geometry of the heart on the electrical activation pattern is highly relevant, as was pointed out. The wavefront generated from the LV lead, travelling from epicardium to endocardium, and the initiation of the PS retrograde conduction, are important variables on achieving an adequate pacing protocol. Structural changes that affect the LV size and thickness lead to a potential increase of intraventricular delays. Pacing on different geometries show variations in the activation sequences, specially on the LV lateral wall, in some cases differing significantly from the normal activation (apex to base).

Acknowledgments

This research has been partially funded by the Industrial and Technological Development Centre (CDTI) under the CENIT Programme (CDTEAM Project) and the European Community's Seventh Framework Programme (FP7/2007-2013) under grant agreement n. 224495 (euHeart project). Dr. R. Sebastian was funded by the Ministerio de Ciencia e Innovación (Juan de la Cierva program). Dr. B. Bijnens is an ICREA research professor at Universitat Pompeu Fabra. E. Vigmond and P.Boyle were funded by The Natural Sciences and Engineering Research Council of Canada. P. Boyle is supported by the Alberta Ingenuity Fund.

References

1. Henriquez, C., Papazoglou, A.: Using computer models to understand the roles of tissue structure and membrane dynamics in arrhythmogenesis. Proc. IEEE 84(3), 334–354 (1996)
2. Rodríguez, B., Li, L., Eason, J.C., Efimov, I.R., Trayanova, N.A.: Differences between left and right ventricular chamber geometry affect cardiac vulnerability to electric shocks. Circ. Res. 97(2), 168–175 (2005)

3. Durrer, D., van Dam, R.T., Freud, G.E., Janse, M.J., Meijler, F.L., Arzbaecher, R.C.: Total excitation of the isolated human heart. Circulation 41(6), 899–912 (1970)
4. Pollard, A.E., Burgess, M.J., Spitzer, K.W.: Computer simulations of three-dimensional propagation in ventricular myocardium, effects of intramural fiber rotation and inhomogeneous conductivity on epicardial activation. Circ. Res. 72(4), 744–756 (1993)
5. Weiss, D.L., Keller, D.U.J., Seemann, G., Dössel, O.: The influence of fibre orientation, extracted from different segments of the human left ventricle, on the activation and repolarization sequence: a simulation study. Europace 9 (suppl. 6), vi96–v104 (2007)
6. Sermesant, M., Delingette, H., Ayache, N.: An electromechanical model of the heart for image analysis and simulation. IEEE Trans. Med. Imaging 25(5), 612–625 (2006)
7. Reumann, M., Farina, D., Miri, R., Lurz, S., Osswald, B., Dössel, O.: Computer model for the optimization of av and vv delay in cardiac resynchronization therapy. Med. Biol. Eng. Comput. 45(9), 845–854 (2007)
8. Gassis, S., León, A.R.: Cardiac resynchronization therapy: strategies for device programming, troubleshooting and follow-up. J. Interv. Card. Electrophysiol. 13(3), 209–222 (2005)
9. Abraham, W.T.: Rationale and design of a randomized clinical trial to assess the safety and efficacy of cardiac resynchronization therapy in patients with advanced heart failure: the multicenter insync randomized clinical evaluation (miracle). J. Card. Fail 6(4), 369–380 (2000)
10. Chung, E.S., Leon, A.R., Tavazzi, L., Sun, J.P., Nihoyannopoulos, P., Merlino, J., Abraham, W.T., Ghio, S., Leclercq, C., Bax, J.J., Yu, C.M., Gorcsan, J., Sutton, M.S.J., Sutter, J.D., Murillo, J.: Results of the predictors of response to crt (prospect) trial. Circulation 117(20), 2608–2616 (2008)
11. Ordas, S., Oubel, E., Sebastian, R., Frangi, A.: Computational atlas of the heart. In: 15th International Symposium on Image and Signal Processing and Analysis. IEEE Computer Society, Los Alamitos (2007)
12. Camm, A.J., Lscher, T.F., Serruys, P. (eds.): The ESC Textbook of Cardiovascular Medicine. Wiley-Blackwell Publishing, Oxford (2006)
13. Sebastian, R., Ordas, S., Vigmond, E., Plank, G., Rodríguez, B., Frangi, A.: Assessing influence of conductivity in heart modelling with the aim of studying cardiovascular diseases. In: Proc. of SPIE Medical Imaging (2008)
14. Roberts, D.E., Scher, A.M.: Effect of tissue anisotropy on extracellular potential fields in canine myocardium in situ. Circ. Res. 50(3), 342–351 (1982)
15. Streeter, D.: Gross morphology and fibrous structure of the heart. In: Handbook of Physiology: The Cardiovascular System, vol. 1, pp. 61–112. Oxford University Press, Oxford (1979)
16. Plonsey, R.: Bioelectric sources arising in excitable fibers (alza lecture). Ann. Biomed. Eng. 16(6), 519–546 (1988)
17. Whiteley, J.P.: An efficient numerical technique for the solution of the monodomain and bidomain equations. IEEE Trans. Biomed. Eng. 53(11), 2139–2147 (2006)
18. Tusscher, K.H.W.J.T., Panfilov, A.V.: Cell model for efficient simulation of wave propagation in human ventricular tissue under normal and pathological conditions. Phys. Med. Biol. 51(23), 6141–6156 (2006)
19. DiFrancesco, D., Noble, D.: A model of cardiac electrical activity incorporating ionic pumps and concentration changes. Philos. Trans. R Soc. Lond. B Biol. Sci. 307(1133), 353–398 (1985)

20. Vigmond, E.J., Clements, C.: Construction of a computer model to investigate sawtooth effects in the purkinje system. IEEE Trans. Biomed. Eng. 54(3), 389–399 (2007)
21. Boyle, P., Deo, M., Vigmond, E.: Behaviour of the purkinje system during defibrillation-strength shocks. In: Proc. 29th Annual International Conference of the IEEE Engineering in Medicine and Biology Society EMBS 2007, pp. 419–422 (2007)
22. Vigmond, E.J., Hughes, M., Plank, G., Leon, L.J.: Computational tools for modeling electrical activity in cardiac tissue. J. Electrocardiol. 36(suppl.), 69–74 (2003)
23. Plank, G., Liebmann, M., dos Santos, R.W., Vigmond, E.J., Haase, G.: Algebraic multigrid preconditioner for the cardiac bidomain model. IEEE Trans. Biomed. Eng. 54(4), 585–596 (2007)

Noise-Reduced TPS Interpolation of Primary Vector Fields for Fiber Tracking in Human Cardiac DT-MRI

Feng Yang, Xin Song, Stanislas Rapacchi, Laurent Fanton, Pierre Croisille, and Yue-Min Zhu

CREATIS-LRMN, CNRS UMR 5220, Inserm U 630, INSA of Lyon, University of Lyon 1, University of Lyon, France
{feng.yang,xin.song,stanislas.rapacchi,laurent.fanton, pierre.croisille,Yue-Min.Zhu}@creatis.insa-lyon.fr

Abstract. Denoising and interpolation of primary vector fields in DT-MRI are essential for tracking myocardial fibers of the human heart. In this paper, a noise-reduced interpolation method for 3-D primary vector fields in human cardiac DT-MRI is proposed. The method consists of first localizing the noise-corrupted vectors using local statistical properties of the vector fields, then restoring the noise-corrupted vectors by means of Thin Plate Spline (TPS) interpolation method, and finally applying a global TPS interpolation to gain higher resolution in the spatial domain. Experiments and results show that the proposed method allows us to obtain higher resolution and reduce noise, while improving direction-coherence (*DC*) of vector fields, preserving details, and improving fiber tracking.

Keywords: DT-MRI, human heart, myocardial fiber, vector field, denoising, TPS interpolation, tensor field.

1 Introduction

Diffusion tensor magnetic resonance imaging (DT-MRI, or DTI) is a new technique that allows ex-vivo and/or in-vivo investigation of structural properties of fibrous tissues by measuring the relative diffusion in different directions of water molecules in each voxel of an MR image [1]. In brain or cardiac DT-MRI, to track the fibers of brain white matter or myocardium, fiber tracking or tractography is computed using the principal eigenvectors of diffusion tensors.

DT-MRI is very sensitive to noise and artifacts [2], so that the calculated primary vector fields are subject to errors, which results in harmful impacts on the quality of fiber tracking. Therefore, denoising of vector fields in DT-MRI data becomes an important step for relaxation of acquisition constraints as well as for applications like fiber tracking. On the other hand, more specifically, because of inherent acquisition problems in human cardiac DT-MRI, in some part of the myocardium, the acquired data is rather sparse, and the myocardium appears discontinuous. In order to better describe the myocardium, it is necessary to do data interpolation that can be performed at the level of diffusion weighted (DW) images, or tensor fields or still vector fields. However, in some situations, the only information we are given is the

N. Ayache, H. Delingette, and M. Sermesant (Eds.): FIMH 2009, LNCS 5528, pp. 78–86, 2009.
© Springer-Verlag Berlin Heidelberg 2009

vector fields. This is the case when we track fibers from vector fields using the most common streamline fiber tracking algorithm that is directly based on primary vector fields, or when we have no possibility to come back to tensor fields or DW images, or still when it is not necessary to come back to tensor fields or DW images. Interpolating directly noisy vector fields will also magnify and introduce errored vectors Furthermore, there don't exist methods that allow interpolating vector fields while denoising, since when interpolating noisy vectors, the noise is magnified at the same time. That has led us to propose the noise-reduced interpolation approach for vector fields.

Vector Wiener filter is the optimal vector filter in the sense of minimum mean-square error. However, it needs the noise-free image and the power of noise to be known. The most popular vector filter is the vector median filter [3], which is widely used to remove the impulse noise. To improve its performance in the suppression of additive Gaussian noise, vector median filter has been combined with linear filter [3] or extended to the weighted vector median filter [4]. In addition, vector directional filters [5] are proposed to eliminate vectors with atypical directions in the color space, and regularization method with PDE is proposed in [6] to denoise vector-valued images. Although these methods are effective in smoothing noise, they tend to remove fine details. Moreover, these methods are introduced for color images, which are different from the real DT-MRI vector fields. Considering the particularities of DT-MRI vector fields, some denoising methods have been mentioned in the regularization of DT-MRI vector fields. In [7], a PDE-based method for regularizing principal diffusion vector fields is introduced, which is based on the structure sensitive function derived from the local orientation similarity. A variational approach to restore primary eigenvector fields is addressed in [8], and is aimed to minimize a total variation based energy defined for the direction map. In [9], a vector field regularization method, focused on the non-rigid registration, is proposed by combining vector convolution filters and vectorial splines, which are deduced from isotropic differential quadratic forms of 2D deformation vector fields. In this paper, we propose a new mechanism to denoise vector fields, which only handles the noise-corrupted vectors to overcome the drawbacks caused by denoising the whole vector field in a uniform manner.

Meanwhile, vector interpolation is a useful technique often used in fiber tracking algorithms to improve fiber tracking results. In [10], primary vector components are interpolated with fractional anisotropy (FA) values used as weights. A selective eigenvector interpolation criterion is proposed in [11], which uses inner product threshold value to decide the weight for corresponding eigenvectors. These methods, however, have some drawbacks: the vector components in practical applications are generally correlated, and if each component is processed independently, this correlation is not utilized. The TPS model [12] inherently utilizes the correlation between vector components and minimizes the energy of vector fields, performing vector interpolation with some desirable properties.

In this paper, a noise-reduced TPS interpolation method for primary vector fields is proposed. The method first localizes and removes the noise-corrupted vectors using a vector homogeneity criterion, and then restores the noisy vectors using TPS interpolation. With the thus obtained noise-reduced vector fields, a global TPS interpolation for the whole vector field is implemented to obtain higher spatial

resolution. The rest of this paper is organized as follows: we present the proposed algorithm in section 2, the experimental results and discussion in section 3, and the conclusion in section 4.

2 Noise-Reduced Interpolation by TPS Model

The proposed noise-reduced interpolator includes three functions: localization of noise-corrupted vectors, restoration of these incorrect vectors, and interpolation of the whole vector field. The first function is to determine the presence of noise-corrupted vectors in a chosen window, where we have to make a reference and to search an optimal threshold value for it; the second is to restore the noise-corrupted vectors and the third to interpolate the primary vector field to get higher resolution. The flowchart of such noised-reduced interpolation for the primary vector fields using TPS interpolation is shown in Fig. 1.

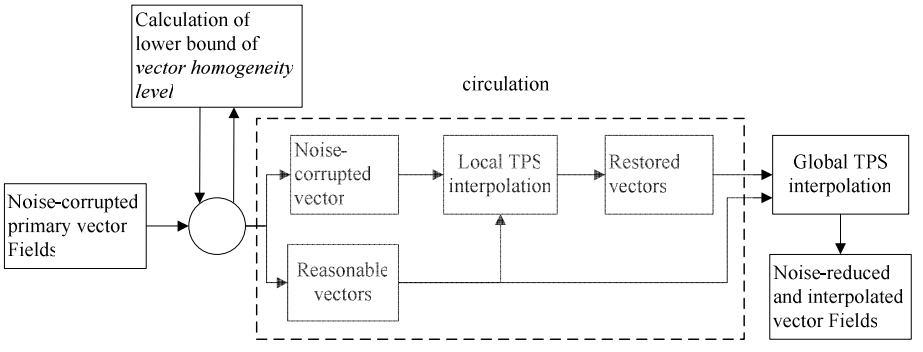

Fig. 1. Flowchart of noise-reduced interpolation of the primary vector fields. The left part stands for the inputted noise-reduced vector fields, while the output is the noised-reduced and interpolated vector fields. The dotted rectangle indicates the circulation of the denoising process and restoration of the noise-corrupted vectors.

As vectors are related to each other in a local area, given a vector, its direction shouldn't deviate greatly from the directions of its neighboring vectors [15]. We therefore introduce the notion of *vector homogeneity level*, which is determined by inner product of vectors, to define correlations between neighboring vectors. Assuming that the vector field size of one slice is $N \times N$, in a given square window $W_{i,j,k}$ at voxel (i, j, k) , the chosen vector is $v(x_0, y_0, z_0,)$, its neighboring vectors are $\{v(x_k, y_k, z_k)\}_{k=1}^{15}$, then the vector homogeneity level for the vector $v(x_0, y_0, z_0,)$ in the 4×4 square window $W_{i,j,k}$ (other window sizes are possible, but the size 4×4 gave us the best results) is defined as

$$d(x_0, y_0, z_0) = \frac{1}{15} \sum_{k=1}^{15} (x_0 x_k + y_0 y_k + z_0 z_k) \tag{1}$$

When the eigenvectors are of unity length, the inner product $x_0x_k + y_0y_k + z_0z_k$ reflects the cosine angle value between $v(x_0, y_0, z_0,)$ and $v(x_k, y_k, z_k,)$, and vector homogeneity level $d(x_0, y_0, z_0,)$ indicates the mean cosine for the angle between $v(x_0, y_0, z_0,)$ and its fifteen neighbors and will have a value between -1 and 1, as the angle between two vectors is $[0,\pi]$.

Thus, we can determine the noise-corrupted vector using the lower bound of *vector homogeneity level,* noted as L_b. When $d(x_0, y_0, z_0,)$ is smaller than L_b, the vector $v(x_0, y_0, z_0,)$ is considered as incoherent with respect to other vectors, and is regarded as a noise-corrupted vector.

Once the noise-corrupted vectors are localized, they can be restored by interpolation using the relationship of its neighbors. In this paper, we use the Thin Plate Spline (TPS) interpolation for its ability of accounting for the correlation among vector components and for its smooth property [12].

The name "thin plate spline" refers to a physical analogy involving the bending of a thin sheet of metal. TPS is initially proposed for image registration to get all the coordinates in the deformed image when knowing a number of control points in the original image and the corresponding control points in the deformed image [12][13][14]. Our purpose is to restore the noise-corrupted vectors as well as obtain higher resolution of the vector field specified by irregular points and corresponding vectors.

The function of three-dimensional (3-D) TPS interpolation can be describes as:

$$f(x, y, z) = a_1 + a_x x + a_y y + a_z z + \sum_{i=1}^{n} w_i U \mid P_i - (x, y, z) \mid \tag{2}$$

where $f(x, y, z)$ is the vector at coordinate (x, y, z), P_i stands for the coordinates of control points, and a_1, a_x, a_y, a_z in the first 4 terms are the global affine transform coefficients, while w_i in the remaining terms are the (non-global) non-linear transformation coefficients. The most important term in formula (2) is the radial basis function: $U(r) = \mid r \mid = (x^2 + y^2 + z^2)^{1/2}$, which is the fundamental solution of biharmonic equation and guarantees that the TPS function minimizes the bending energy:

$$I(f) = \iiint_{R^3} (f_{xx}^2 + f_{yy}^2 + f_{zz}^2 + 2f_{xy}^2 + 2f_{xz}^2 + 2f_{yz}^2) dxdydz \tag{3}$$

where, f_{xx}, f_{yy}, f_{zz} designate the second-order partial derivatives of function $f(x, y, z)$, and f_{xy}, f_{xz}, f_{yz} the second-order mixed derivatives of function $f(x, y, z)$. Minimizing the bending energy ensures that the vector fields are optimally smooth according to this measure [12]. For this property, we use TPS interpolation to restore the noise-corrupted vectors.

In a 4×4 window, if a vector is identified as noise, other vectors in this window are chosen as the landmarks of TPS model to restore the noise-corrupted vector. To get better denoising results, the influence of noise-corrupted vectors in the neighborhood should be reduced as small as possible. Thus, when we choose the landmarks for the restoration, we first determine whether the vector homogeneity

level of each neighboring vector is higher than the lower bound, and if it is, this neighboring vector will be chosen as one landmark for the TPS interpolation, otherwise, it will be dropped in this restoration process. Particularly, for a given window position, if the number of noisy vectors inside the window is greater than one third of total number of vectors inside the window, the neighborhood is considered as a region without clear majority. In this case, we will not denoise any vector in this window, and interpolate them directly.

With the noise-reduced vector fields, we complete the global TPS interpolation to get higher resolution as well as more information for fiber tracking. For this purpose, we use vectors in the myocardium as the landmarks of TPS model so that the vectors we get from interpolation follow the whole model determined by these landmarks. Vectors beyond the myocardium are discarded by masks gotten from the T2 images.

3 Experiments and Results

In this section, we use the proposed method to interpolate the primary vector fields of DT-MRIs while achieving their denoising. The thus noise-reduced and interpolated vector fields are then tracked by a conventional streamline fiber tracking algorithm, to better get insights into the ability of the proposed method to get higher resolution and robustness to noise.

3.1 Data Acquisition

In our experiments, the primary vector fields were calculated from cardiac DT-MRI data corresponding to six human hearts. These data has been acquired on Siemens 1.5 T Magnetom Sonata in the Hospital of Neuro-Cardiology of Lyon. The healthy human heart fixed by the gel was located in a plastic box to avoid artifacts such as susceptibility and motion during acquisition. The acquisition parameters were: TE = 98 ms, TR = 8600 ms, FOV = 256×256 mm^2, slice thickness =2 mm, slice spacing =2mm, slice duration = 142.5 ms, number of slices = 52, slice size = 128×128, diffusion sensitivity b = 1000 s/mm^2, gradient directions = 30.

3.2 Evaluation Criteria

Our algorithm is assessed at the level of vector field and in terms of fiber tracking, as well as quantitative analysis such as *direction-coherence (DC)* we define as follows

$$DC = 20\lg(C_c / C_i) \tag{4}$$

where C_c and C_i denote the number of vectors that have the same and different *vector homogeneity level* as its neighboring vectors, respectively. *DC* indicates the direction coherence of the vector fields. A greater DC value means a more coherent direction.

As cardiac DW images present a piece-wise constant feature, we applied our method to 3-D primary vector fields of each slice to study the restoration of the noise-corrupted vectors combined with high resolution through TPS interpolation. To illustrate the effect of denoising and interpolation, we compare the primary vector

fields obtained using the proposed method with both the original vector fields and the interpolated vector fields without denoising.

3.3 Results and Discussion

Figure 2 illustrates the results of noise-reduced interpolation for primary eigenvector fields corresponding to the 10th slice of a human heart dataset. Obviously, the principal eigenvector directions are more regularly oriented, and structure details (shape of myocardium and fiber orientations) of vector fields are preserved after denoising and interpolation. Since the primary eigenvector's direction corresponds to the fiber orientation at this position, with our noise-reduced interpolation, the fiber tracking of the myocardium would be better and more robust.

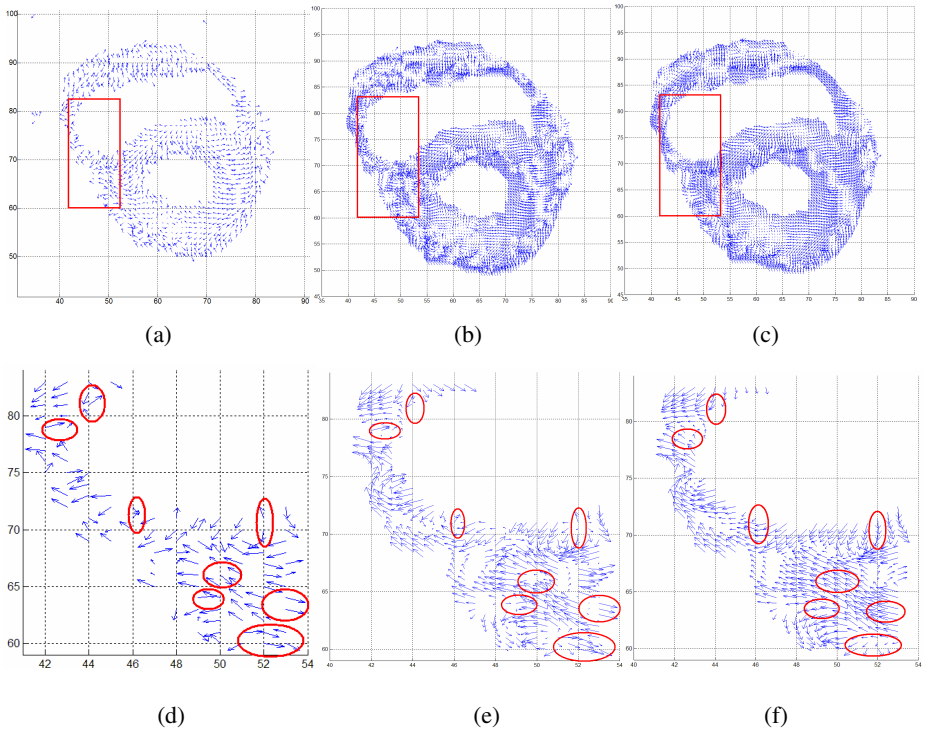

Fig. 2. Results of noise-reduced interpolation for primary eigenvector fields corresponding to the 10th slice of a human heart dataset. (a) Original primary vector fields. (b) Interpolated primary vector fields. (c) Noise-reduced interpolation of primary vector fields. (d) The sparse region marked with red rectangles in (a). (e) The sparse region marked with red rectangles in (b). (f) The sparse region marked with red rectangles in (c).

To evaluate the robustness to noise of our method, we calculated the *DC* parameter before and after noise-reduced interpolation of two different slices in the same human heart and the same slice in different human hearts, as shown in Fig. 3.

The results given in Fig. 3 show that the proposed method improves the *DC* of primary vector fields by increasing its values by a factor of 15 dB in average, with respect to the results obtained by interpolating directly the original vector fields. That implies that after noise-reduced interpolation, vectors are more coherent. At the same time, we may notice that the DC curve varies irregularly, which is caused by the fact that the shape of myocardium in the acquired images, especially for the myocardium of the right ventricle, is rather irregular and varies greatly from the slice near base to the slice near apex. It is observed from Fig. 3(a) that the values of DC from slices 10 to 20 are rather close (the blue line), due to the fact that the myocardium shapes of the corresponding slices are similar. After the noise-reduced interpolation, the slices do not have the same DC increasing. For example, the DC of the 13th slice is similar to its neighboring slices before denoising, whereas after denoising, it becomes smaller than its neighbors, which implies its DC reduction smaller than that of its neighbors. This is because the 13th slice is the most coherent and its neighboring slices less. The more coherent the slice is, the less noisy vectors there are, and consequently, the less difference between the denoised and un-denoised vector fields (so less reduction of DC values).

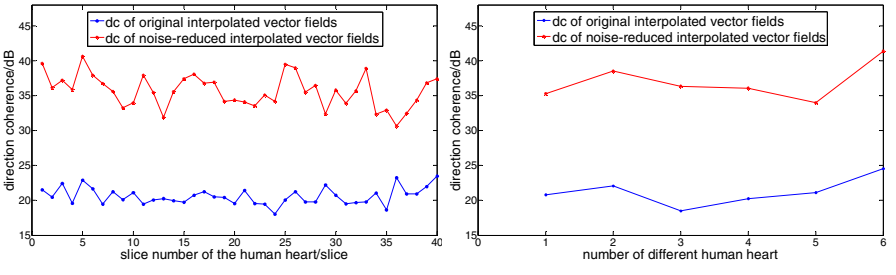

(a) (b)

Fig. 3. *DC* of primary vector fields before and after noise-reduced interpolation. (a) *DC* of different slices in the same human. (b) *DC* of the same slice in different human hearts.

Figure 4 illustrates an example of improvement in fiber tracking when using the proposed noise-reduced interpolation for primary vector fields. It concerns a human heart of 52 slices, and the conventional streamline algorithm was used to track the fibers. The visualization used a color coding representation of eigenvector's projection on each axis. It is observed that fibers sometimes become discontinuous or even disappear in some parts of the right ventricle, because the primary eigenvectors in these zones are so incoherent or so sparse that it is impossible or difficult to continue fibers using the streamline fiber tracking algorithm. Comparing the normal and sparse regions in Fig. 4 (a) and (b), we can conclude that by interpolation, fibers become denser obviously in the normal region, but for sparse region, interpolation seems not to produce effects for fiber tracking. This is because eigenvectors in the sparse regions are still incoherent after interpolation so that fibers are difficult to be formed. Nevertheless, fibers in both the normal and the sparse regions become significantly denser and smoother after noise-reduced interpolation. The reason is that the primary eigenvectors become more coherent so that more fibers can be formed or fibers become more continuous when using the streamline algorithm.

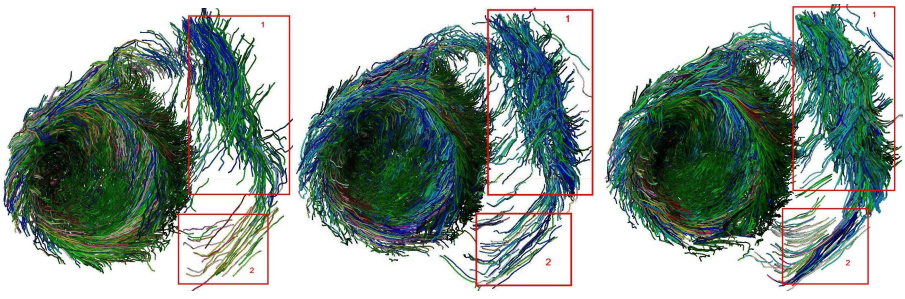

(a) (b) (c)

Fig. 4. Fiber tracking from the primary vector fields in human cardiac DT-MRI. Red rectangles marked with 1 and 2 indicate the normal and sparse regions of the right ventricle, respectively. (a) Fiber tracking from original vector fields. (b) Fiber tracking from interpolated original vector fields. (c) Fiber tracking from noise-reduced and interpolated vector fields.

4 Conclusion

We have proposed a noise-reduced interpolation method for vector fields. By first localizing the noise-corrupted vectors using local information, then restoring them using local TPS interpolation, and finally applying global TPS interpolation, the method allows us to simultaneously get higher resolution, preserving details, and obtaining better *DC*. The results demonstrate that the proposed method improves the *DC* by a factor of 15 dB in average, and yields smoother and denser fiber tracking of the myocardium.

References

1. Moseley, M.E., Cohen, Y., Mintorovitch, J., Kucharczyk, J., Weinstein, P.R.: Early Detection of Regional Cerebral Ischemia: Comparison of Diffusion and T2-weighted MRI and Spectroscopy. Magn. Reson. Med. 14, 330–336 (1990)
2. Basser, P.J., Pajevic, S.: Statistical Artifacts in Diffusion Tensor MRI (DTMRI) Caused by Background Noise. Magn. Reson. Med. 44, 41–50 (2000)
3. Astola, J., Haavisto, P., Neuvo, Y.: Vector Median Filters. Proceeding of the IEEE, 678–689 (1990)
4. Viero, T., Oistamo, K., Neuvo, Y.: Three-dimensional Median-Related Filters for Color Image Sequence Filtering. IEEE Transactions on Circuits and Systems for Video Technology 15, 129–142 (1994)
5. Trahanias, P., Karakos, D., Venetsanopoulos, A.: Directional Processing of Color Images: Theory and Experimental Results. IEEE Transactions on Image Processing 5, 868–881 (1996)
6. Tschumperlé, D., Deriche, R.: Vector-valued Image Regularization with PDE's: A Common Framework for Different Applications. In: IEEE Conference on Computer Vision and Pattern Recognition, pp. 651–656 (2003)

7. Yoruk, E., Acar, B.: Structure Preserving Regularization of DT-MRI Vector Fields by Nonlinear Anisotropic Diffusion Filtering. In: Proceedings of European Signal Processing Conference (EUSIPCO), Antalya, Turkey (2005)
8. Coulon, O., Alexander, D.C., Arridge, S.R.: Diffusion Tensor Magnetic Resonance Image Regularisation. Medical Image Analysis 8, 47–67 (2004)
9. Cathier, P., Ayache, N.: Isotropic Energies, Filters and Splines for Vector Field Regularization. J. Mathematical Imaging and Vision 20, 251–265 (2004)
10. Zhao, X., Wang, M.S., Gao, W., Liu, H.Y.: White Matter Fiber Tracking Method by Vector Interpolation with Diffusion Tensor Imaging Data in Human Brain. IEEE Engineering in Medicine and Biology Society (2005)
11. Kim, K.H., Ronne, I., Formisano, E., Goebel, R., Ugurbil, K., Kim, D.S.: Robust Fiber Tracking Method by Vector Selection Criterion in Diffusion Tensor Images. IEEE Engineering in Medicine and Biology Society, 1080–1083 (2004)
12. Davis, M.H., Khotanzand, A., Flaming, D.P., Harms, S.E.: A Physics-based Coordinate Transformation for 3-D image Matching. IEEE Transactions on Medical Imaging 16, 317–328 (1997)
13. Bookstein, F.L.: Principal Warps: Thin-plate Splines and Decomposition of Deformations. IEEE Transactions on Pattern Analysis and Machine Intelligence 11, 567–585 (1989)
14. Sprengel, R., Rohr, K., Stiehl, H.S.: Thin-plate Spline Approximation for Image Registration. In: Engineering in Medicine and Biology Society, Bridging Disciplines for Biomedicine. Proceedings of the 18th Annual International Conference of the IEEE, pp. 1190–1191 (1996)
15. Holmes, A.A., Scollan, D., Winslow, R.L.: Direct histological validation of diffusion tensor MRI in formaldehyde-fixed myocardium. Magnetic Resonance in Medicine 44, 157–161 (2000)

Comparison of Rule-Based and DTMRI-Derived Fibre Architecture in a Whole Rat Ventricular Computational Model

Martin J. Bishop, Patrick Hales, Gernot Plank, David J. Gavaghan, Jürgen Scheider, and Vicente Grau

University of Oxford

Abstract. The anisotropic electrical conduction within myocardial tissue due to preferential cardiac myocyte orientation ('fibre orientation) is known to impact strongly in electrical wavefront dynamics, particularly during arrhythmogenesis. Faithful representation of cardiac fibre architecture within computational cardiac models which seek to investigate such phenomena is thus imperative. Drawbacks in derivation of fibre structure from imaging modalities often render rule-based representations based on a priori knowledge preferential. However, the validity of using such rule-based approaches within whole ventricular models remains unclear. Here, we present the development of a generic computational framework to directly compare the fibre architecture predicted by rule-based methods used within whole ventricular models against fibre structure derived from DTMRI data, and assess how relative differences influence propagation dynamics throughout the ventricles. Results demonstrate the close overall match between the methods within the rat ventricles, and highlight regions for potential rule-adaption.

Keywords: DTMRI, cardiac electrophysiology, fibre orientation.

1 Introduction

The structure of ventricular myocardium is known to be highly heterogeneous, with the existence of a preferential cardiac myocyte orientation, commonly referred to as 'fibre orientation'. Furthermore, the myocyte fibre axis rotates through ~ 120 degrees from epicardium to endocardium. The resulting anisotropic conduction of myocardial tissue has been shown to play an important role in cardiac electrical propagation dynamics during normal activity and arrhythmias [3,4,10]. Therefore, anatomically based representations of fibre architecture within computational models are essential to faithfully represent this complex structure-function interaction of electrical conduction within cardiac tissue.

Although histology can provide accurate measurements of the transmural rotation of fibres through the myocardial wall [13], this approach is destructive, preclusively time-consuming, and it is an existing challenge to register the 2D fibre information from histology slices to provide a complete representation of 3D fibre architecture [7]. Recently, Diffusion Tensor MRI (DTMRI) has proved a

N. Ayache, H. Delingette, and M. Sermesant (Eds.): FIMH 2009, LNCS 5528, pp. 87–96, 2009.
© Springer-Verlag Berlin Heidelberg 2009

useful non-destructive means of deducing local cardiac fibre direction, agreeing with histologically-measured fibre angles [11]. However, DTMRI data is often noisy along surface boundaries due to partial volume effects [1] and is often not available for the particular geometry upon which a computational model is based (for example in simplified slab models). In addition, due to the long scan times needed, and sensitivity to motion artifacts, DTMRI is rarely used to measure myocardial fibre at a high resolution in-vivo. As a result of these drawbacks, it is often necessary to embellish computational models with parametric rule-based representations of fibre orientation using *a priori* knowledge of fibre structure throughout the myocardial wall.

Rule-based methods have been developed to parameterise changes in fibre helix angles (the angle between the circumferential direction and the projection of the fibre vector onto the plane spanned by the circumferential direction and the local longitudinal direction) through sections of the ventricular free wall based upon histological measurements [8,13]. Although such rules have been used to define fibre architecture in whole ventricular models [8], because they were derived from fibre data in isolated regions of the ventricular free wall, the validity of incorporating them into whole ventricular models remains unclear. For example, how to define the fibre orientation in the septum or close to regions where the left ventricle(LV)/right ventricle(RV)/septum meet remains an open question.

Therefore the goal of this study is to directly compare the fibre architecture predicted by rule-based parametric models used within whole ventricular computational models against DTMRI-derived fibre architecture information from the rat, and to assess how the relative differences influence propagation dynamics throughout the whole ventricles. Discrepancies between the fibre architectures is analysed, providing important information about the failings of rule-based methods as well as highlighting potential problems/errors in the DTMRI data. Although previous studies have sough to quantitatively compare DTMRI fibre vector predictions with those derived from rule-based parametric approaches, they have been restricted to analysis of wedge preparations [12,14] and thus the effect upon propagation dynamics throughout the whole volume of the ventricles has yet to be investigated.

2 Methods

2.1 Diffusion Tensor MR Image Acquisition

All experimental investigations conformed to the UK Home Office guidance on the Operation of Animals (Scientic Procedures) Act of 1986. The heart was excised from a female Sprague Dowley rat, swiftly perfused in Langendorff mode, fixed using fast-acting Karnovskys fixative, left for 12 hours, and then embedded in 1% agarose inside a 28 mm diameter glass NMR tube. All MRI data was acquired using a Varian 9.4 T (400 MHz) MR system (Varian Inc, CA) [7], comprising of a horizontal magnet (bore size 210 mm), a VNMRS Direct Drive console, and shielded gradient system (1 T/m, rise time 130 μs). A birdcage coil

with an inner diameter of 28 mm (Rapid Biomedical, Germany) was used to transmit/receive the NMR signals.

The heart was imaged using a 3D fast spin echo diffusion weighted pulse sequence, with TR= 1 s, TE (effective)= 43 ms, and 8 echoes per excitation. Unipolar trapezoidal diffusion gradients were applied in 6 non-co-linear directions, arranged according to the optimized scheme [7], resulting in a mean b-value of 703 s mm^{-2}. The data were acquired at 101.6 μm isotropic resolution with four averages, resulting in a total scan time of 64 hours. Following acquisition, the diffusion tensor was calculated on a voxel-by-voxel basis via a noise-weighted linear least squares fit method, using in house software developed in IDL (Interactive Data Language, ITT Corporation, USA). The primary eigen vector of the diffusion tensor at each voxel was then used to infer local 'fibre orientation' as has been demonsrated previously in comparision with histological data [11]. Fig. 1(c) shows the orientation of the primary eigen vector of the diffusion tensor at each voxel. A XYZ to GRB colour scheme has been used.

2.2 Computational Model Generation

Segmentation. To construct an anatomically detailed computational cardiac model, geometrical information regarding the anatomy of the heart was first extracted from the MR data-set via segmentation. In the absence of a separate anatomical MR scan, the segmentation was performed on the apparent diffusion coefficient (ADC) volume, which provided the most robust discrimination between tissue/background voxels. A level-set threshold filter (ITK, `www.itk.org`) was used to segment the ADC volume. A collection of seed points, automatically selected using a conservative threshold, was used for initialisation. A series of morphological operations was then applied to fill holes, remove isolated objects and surface artifacts. Manual edition was finally done to correct minor errors, particularly in the RV region, and to remove the papillary muscles using the Seg3D software (Scientific Computing and Imaging Institute, University of Utah, USA).

To assess the effect of different fibre architectures on propagation dynamics within the ventricular myocardium, a detailed computational model including only the ventricles was produced from the segmented data set. To achieve this, a series of points were manually selected on the surface separating the ventricles from the atria. A B-splines surface was fitted to the points and used to remove the atria. Fig. 1(a) shows a short-axis slice from the ADC volume; Fig. 1(b) shows the final segmentation.

Finite Element Mesh Generation. The final segmented voxel image stack was used directly to generate a tetrahedral finite element mesh using the meshing software Tarantula (`www.meshing.at`) [9]. The total mesh produced by Tarantula consisted of 885490 node points, making up 4926130 tetrahedral elements with 244188 bounding triangular faces, and is shown in Fig. 1(d). Parameters were adjusted in Tarantula to produce tetrahedral element edge lengths similar to the

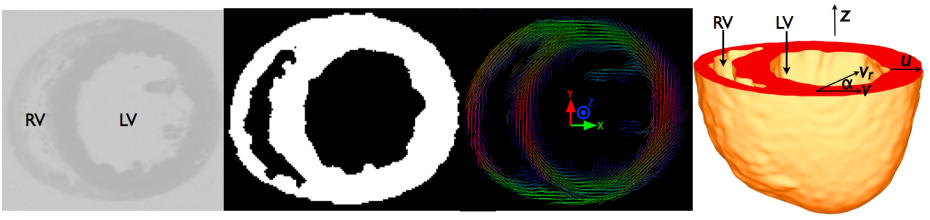

(a) (b) (c) (d)

Fig. 1. Short-axis slices through the ADC data (*a*), final segmented voxel image stack (*b*) and primary eigen vector DTMRI data (*c*). (*d*) Tetrahedral finite element mesh showing a view inside the ventricular cavities (*right*).

voxel resolution of the DTMRI data (100 μm), producing min/mean/max edge lengths of the tetrahedral elements of 25/122/205 μm, respectively.

2.3 Fibre Vector Assignment

Rule-Based Approach. The algorithm used to define fibre orientation through the ventricular finite element mesh was based upon that of [8]. Firstly, a distance map was constructed which was used to define the transmural direction at every point within the tissue. To do so, the minimum distance of each node point within the mesh to both the epicardium (d_{epi}) and endocardium (d_{endo}) was computed and used to define a normalised thickness parameter $e = \frac{d_{endo}}{d_{endo}+d_{epi}}$. In the septum, d_{epi} was taken to be the minimum distance to the endocardial surface of the RV (d^{RV}_{endo}) and d_{endo} taken to be the minimum distance to the endocardial surface of the LV (d^{LV}_{endo}), replicating the continuous fibre structure of the LV witnessed in previous studies [11]. To avoid sudden discontinuities in e at boundaries between regions, the value of e at each node was averaged with all of its immediate neighbours (termed $\bar{e}$).

The gradient of $\bar{e}$ within each tetrahedral element ($\nabla\bar{e}$) was used to define the transmural direction, **u** (see Fig. 1(d)). The vector product of **u** with a unit vector in the z-direction (the global apex-base direction, shown in Fig. 1(d)) then defined the circumferential (or latitude) direction (**v**). To account for the transmural rotation in fibre vector direction, helix angle α was defined by [8]

$$\alpha = R\,(1 - 2\bar{e}_{av})^n\,, \tag{1}$$

where $\bar{e}_{av}$ was taken to be the average of the nodal values of $\bar{e}$ making-up each tetrahdron. R was set equal to $\pi/3$ for the LV and septum, and $\pi/4$ for the RV in accordance with [8]. The power n was equal to 3 in [8]; however, other authors have also used a linear variation in α [4], which by visual inspection appeared to provide a closer comparison to our DTMRI data set. We therefore decided to test also $n = 1$ to compare linear versus cubic intramural variation. A rotation of **v** of α radians about the **u** axis further defined the real fibre vector direction ($\mathbf{v_r}$) (see Fig. 1(d)).

DTMRI Vector Assignment. Alternatively, the primary eigen vector from the DTMRI data was used to define the direction of fibre orientation within each tetrahedral finite element. A nearest neighbour approach was used to map the voxel-based DTMRI data onto the centroid of each tetrahedral element, which gave robust results due to the similarities in size imposed between the element edge lengths and the DTMRI voxel resolution.

2.4 Electrophysiological Simulations

A monodomain representation of electrical activation was used to simulate propagation throughout the ventricular finite element model using the Cardiac Arrhythmia Research Package (CARP) [7]. Membrane dynamics were modelled using a realistic rabbit ventricular ionic model [5]; although there is a species mismatch between the geometrical and ionic models, it did not affect the main goal of the study: assessment of propagation dynamics. Conductivities were taken to be 0.174 S/m parallel, and 0.019 S/m transverse, to the fibre direction [2].

3 Results

3.1 Comparison between Rule-Based and DTMRI-Derived Models

Three different definitions of fibre architecture were implemented in the finite element ventricular mesh, as described above in Section 2.3: rule-based cubic (used by [8], with $n = 3$ in Eqn. 1), rule-based linear ($n = 1$) and DTMRI-derived. Fig. 2 (top) shows a comparison between the fibre vectors assigned based upon the different approaches. It is apparent that the rule-based linear model is closer to DTMRI than the cubic one. However, although very similar, there are still some areas where the match between rule-based linear and DTMRI-derived fibres differ. The most notable areas of mis-match, highlighted by rectangular boxes in Fig. 2(c), are: (1) along the LV-side of the septum, where the rule-based linear method predicts a much smaller helix angle (less fibres with colours red/white) than the DTMRI data; and, (2) close to the epicardium within the RV free wall, where the rule-based method appears to overestimate the helix angle predicted by the DTMRI data (DTMRI has fewer fibre vectors with colour orange/red). In addition, the DTMRI directions have larger local variations than the rule-based methods in most areas, but noticeably on the RV-side of the septum, close to the corners of the RV wall where it joins the septum, as well as along much of the epicardial/endocardial surfaces. This may be due to slight errors in the segmentation in these regions, where cavity has been incorrectly labelled as tissue, meaning the primary eigen vector of the DTMRI data is poorly defined here, but it could also be due to partial volume effects [1].

These differences between the rule-based fibre vector predictions and the DTMRI-derived fibres are emphasised in the difference maps in the lower panel of Fig. 2. Here, the magnitude of the difference in the out-of-plane angle of the fibre vectors for rule-based cubic versus DTMRI-derived (panel (d)) and for rule-based linear versus DTMRI-derived (panel (e)) is plotted. In comparing the

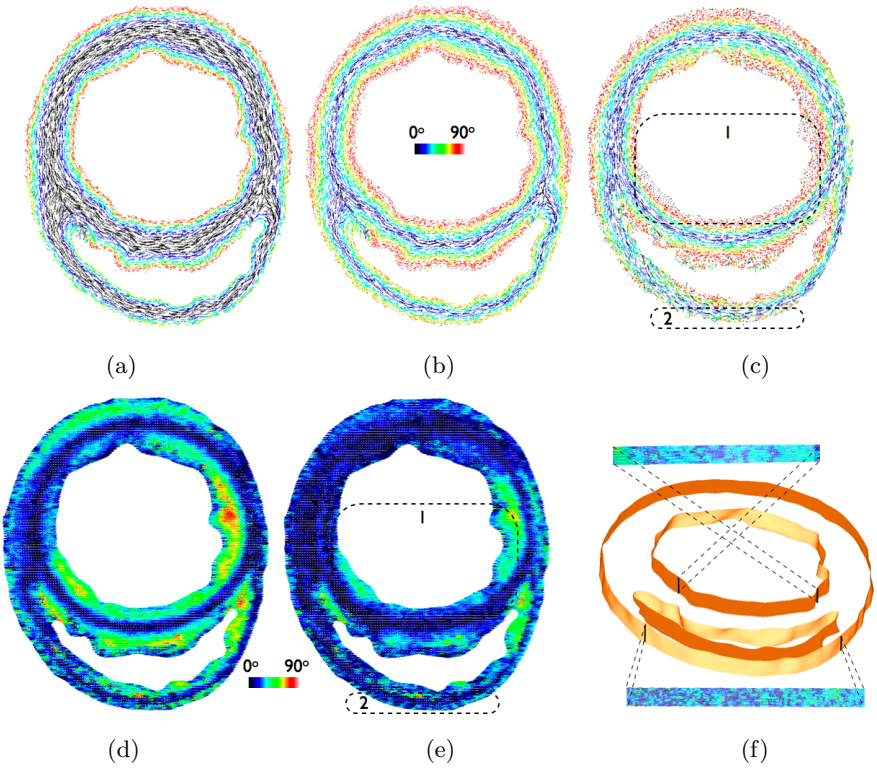

Fig. 2. (*top*) Fibres orientation vectors in a short-axis slice through the finite element ventricular model for fibres assigned by (*a*) rule-based cubic, (*b*) rule-based linear, and (*c*) DTMRI-derived methods. Colour-bar represents out-of-plane vector component. (*bottom*) Magnitude of the difference in the out-of-plane angle of the fibre vectors between rule-based cubic and DTMRI-derived (*d*) and between rule-based linear and DTMRI-derived (*e*). (*f*) Difference in the out-of-plane angle of the fibre vectors between rule-based linear and DTMRI-derived fibres along segments of the RV epicardial surface (bottom) and the LV endocardium of the septum (top).

two images of Fig. 2(d) and (e), the improved match of the rule-based linear, as opposed to the rule-based cubic, to the DTMRI-derived fibre architecture is immediately evident (mean magnitude of difference angle is $16.6 \pm 12.9°$, compared to $24.1 \pm 16.5°$, respectively). Fig. 2(e) also highlights the areas where the DTMRI data was identified as being poorly defined in Fig. 2(c) above, primarily in the RV-side of the septum and close to the corners of the RV wall where it joins the septum.

In addition, we can identify in Fig. 2(e) the two areas of consistent mis-match (i.e. not believed to be as a result of poorly defined DTMRI vectors) between the rule-based linear and the DTMRI-derived data, identified by the rectangular boxes in both Fig. 2(c) and (e): (1) along the LV-side of the septum; and, (2) close to the epicardium within the RV free wall. This difference in fibre angles

in these regions is emphasised in Fig. 2(f), where a segment of the respective endocardial/epicardial surface is visualised showing the difference in out-of-plane fibre angle between rule-based linear and DTMRI-derived fibre vectors across the surface. Similar results were seen in other short-axis slices throughout the ventricles.

3.2 Effect of Fibre Orientation Assignment Upon Propagation

The three fibre models were used to assess the impact of the specific fibre architecture upon electrical wavefront propagation dynamics throughout the volume of the ventricles. In each case, the rat ventricular model was stimulated at the apical free wall using a transmembrane current pulse of 50×10^{-4} μA/cm^3 and 1 ms duration. Fig. 3 shows snap-shots of the transmembrane potential distribution on the surface and transmurally through the ventricles at different times following stimulation. As can be seen from Fig. 3, the overall global patterns of activation are very similar in all cases. However, as in the case of the direct fibre architecture comparison in Section 3.1 above, a much closer match exists between the rule-based linear model and the DTMRI-derived model: propagation

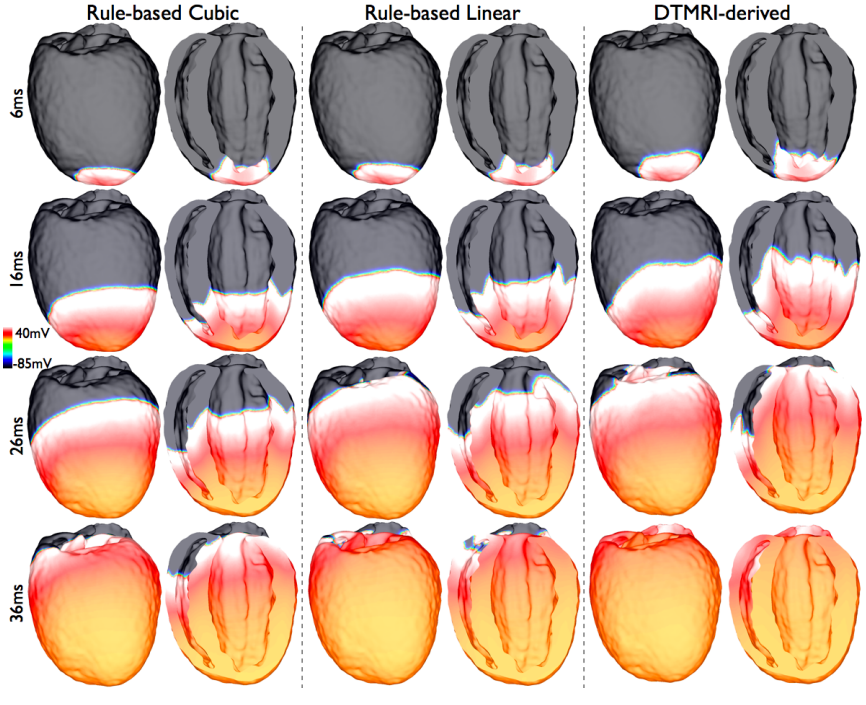

Fig. 3. Electrical propagation within the ventricular models with fibre achitecture from rule-based cubic (*left*), rule-based linear (*centre*) and DTMRI-derived (*right*) methods. For each column, snap-shots of transmembrane potential distribution are shown on the surface (*left*) and transmurally (*right*) at different times following initial stimulus.

patterns within the LV free wall appear very similar, with the characteristic 'V' shaped activation wavefront seen through the LV wall in the 16 ms image.

However, propagation within the septum does appear different between the two models, with activation propagating significantly faster up the LV side of the septum in the DTMRI-derived fibre model. This effect can be attributed to the larger helix angle seen in this region in the DTMRI data compared to the rule-based models. Consequently, the posterior wall is depolarised sooner in the DTMRI model as activation spreads from the septum. The wavefront then spreads up the posterior wall, causing the RV free-wall close to the base to depolarise faster. Finally, a slight difference in wavefront shape can also be seen in the upper RV free wall between the rule-based linear and DTMRI-derived models, which becomes apparent only in the 26 ms images. In the DTMRI model, propagation appears to be moving faster on the endocardial side of the RV wall than the epicardial side, whereas in the rule-based linear model propagation appears to move equally fast on both sides of the RV wall. This effect can be attributed to the smaller helix angle predicted by the DTMRI data for the epicardial side of the RV, described in Section 3.1 above.

These differences in activation times between the rule-based models and the DTMRI model can be seen more clearly in the activation map plots of Fig. 4 (top row). Fig. 4 (botton row) also shows differences in activation times with the DTMRI model. Here, the closer match between the rule-based linear model and the DTMRI is seen, and we can also identify the LV and RV free wall as areas where the comparison with the DTMRI model is closest, and the septum and top of the posterior wall where the match is less close.

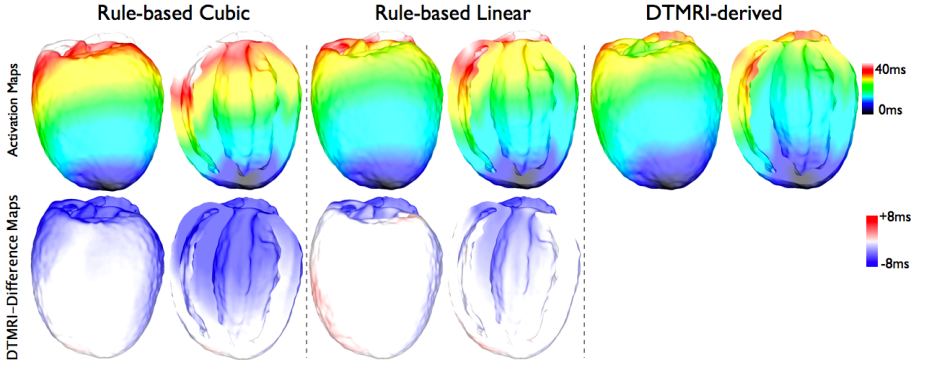

Fig. 4. (*top*) Activation map plots corresponding to propagation sequences shown in Fig. 3 for rule-based cubic (*left*), rule-based linear (*centre*) and DTMRI-derived (*right*) methods. Colour-bar represents time of activation following stimulus. (*bottom*) Activation difference maps relative to DTMRI activation map. Colour-bar indicates relative activation time difference, where white represents no difference.

4 Conclusions

In this study, we have directly compared the fibre architecture predicted by rule-based parametric methods used within whole ventricular models against fibre structure derived from DTMRI data, and, for the first time, assessed how the relative differences influence propagation dynamics throughout the volume of the ventricles. Our results have demonstrated that a rule-based linear method provides a closer match to DTMRI data than rule-based cubic approachs in the rat. However, there are areas where consistent differences appear: notably, the LV side of the septum and the epicardial side of the RV. Our results therefore provide the potential for further in-depth local analysis of the error in rule-based approaches for whole ventricular models, which will enable new sets of adapted rules to be derived for these cases, for example, by assigning an assymmetrical rotation of the fibres through the myocardial wall in parts of the RV and septum, as is suggested by our analysis.

Other discrepencies between the rule-based linear and the DTMRI-derived fibre architecture were also noted, chiefly in the endocardium of the RV and in the region where the RV cavity joins the septum, where the DTMRI data was poorly defined and appeared noisy. This artifact is thought to be due to the quality of the segmentation of the RV cavity from the ADC data, due to the poor contrast of the data in this region. Future investigations involve developing more robust segmentation techniques, including the combination of anatomical MR alongside DTMRI data for the same preparation, currently being developed in our Group [7]. However, in places where the endocardial surface is highly invaginated, partial volume effects will still cause problems [1]; an effect which will be reduced as DTMRI resolution increases [7].

Our results showed that these differences in fibre architecture described above produce small discrepencies in propagation patterns in these regions, but overall the global activation patterns are very similar for the rule-based linear and the DTMRI-derived fibre models following apical pacing. Thus, for simulations of electrical activation, the rule-based linear approach provides a robust method to incorporate faithful representation of fibre architecture throughout the ventricular myocardium. However, it is important to note that the above mentioned discrepencies in fibre structure may play a more significant role in studies of cardiac mechanics.

Finally, although restricted to the rat, our study presents the development of a generic computational framework for similar analysis to be conducted on different species, as well as in the analysis of atlas-based cardiac fibre architecture derived from DTMRI [6,7].

Acknowledgments. The authors thank Dr P. Kohl's lab for sample preparation and the financial support of the BBSRC-funded Oxford 3D Heart Project (BB E003443). MJB holds a Sir Henry Wellcome Postdoctoral Fellowship (085605/Z/08/Z), GP a Marie Curie Fellowship (MC-OIF 040190) and an Austrian Science Fund grant (SFB F3210-N18); VG is a Research Councils UK Fellow.

References

1. Alexander, A.L., Hasan, K.M., Lazar, M., Tsuruda, J.S., Parker, D.L.: Analysis of partial volume effects in diffusion-tensor MRI. Magn. Reson. Med. 45, 770–780 (2001)
2. Clerc, L.: Directional differences of impulse spread in trabecular muscle from mammalian heart. J. Physiol. 255, 335–346 (1976)
3. Fenton, F., Karma, A.: Fiber-rotation-induced vortex turbulence in thick myocardium. Phys. Rev. Lett. 81, 481–484 (1998)
4. Hooks, D.A., Tomlinson, K.A., Marsden, S.G., LeGrice, I.J., Smaill, B.H., Pullan, A.J., Hunter, P.J.: Cardiac microstructure: implications for electrical propagation and defibrillation in the heart. Circ. Res. 91, 331–338 (2002)
5. Mahajan, A., Shiferaw, Y., Sato, D., Baher, A., Olcese, R., Xie, L.H., Yang, M.J., Chen, P.S.: A rabbit ventricular action potential model replicating cardiac dynamics at rapid heart rates. Biophys. J. 94, 392–410
6. Peryat, J.-M., Sermesant, M., Pennec, X., Delingette, H., Xu, C., McVeigh, E., Ayache, N.: A computational framework for the statistical analysis of cardiac diffusion tensors: application to a small database of cannine hearts. IEEE Trans. Med. Imag. 26, 1–15 (2007)
7. Plank, G., Burton, R., Hales, P., Bishop, M.J., Mansoori, T., Bernabeau, M., Garny, A., Prassl, A.J., Bollensdorf, C., Mason, F., Rodriguez, B., Grau, V., Schneider, J., Gavaghan, D.J., Kohl, P.: Generation of histo-anatomically representative models of the individual heart: tools and application. Phil. Trans. Roy. Soc. (2009)
8. Potse, M., Dube, B., Richer, J., Vinet, A., Gulrajani, R.M.: A comparison of monodomain and bidomain reaction-diffusion models for action potential propagation in the human heart. IEEE Trans. Biomed. Eng. 53, 2425–2435 (2006)
9. Prassl, A.J., Kickinger, F., Ahammer, Grau, v.H., Schneider, J.E., Hofer, E., Vigmond, E.J., Trayanova, N.A., Plank, G.: Automatically Generated, Anatomically Accurate Meshes for Cardiac Electrophysiology Problems (2008) (under review)
10. Qu, Z.L., Kil, K., Xie, F.G., Garfinkel, A., Weiss, J.N.: Scroll wave dynamics in a three-dimensional cardiac tissue model: roles of restitution, thickness and fiber rotation. Biophys. J. 78, 2761–2775 (2000)
11. Scollan, F., Holmes, F., Winslow, R., Forder, J.: Histological validation of myocardial microstructure obtained from diffusion tensor magnetic resonance imaging. Am. J. Physiol. Heart Circ. Physiol. 275, 2308–2318 (1998)
12. Seemann, G., Keller, D.U.J., Weiss, D.L., Dössel, O.: Modelling human ventricular geometry and fiber orientation based on diffusion tensor MRI. Proc. Comp. Cardiol. 33, 801–804 (2006)
13. Streeter, D.D., Spontnitz, H.M., Patel, D.P., Ross, J., Sonnenblick, E.H.: Fiber orientation in the canine left ventricle during diastole and systole. Circ. Res. 24, 339–347 (1969)
14. Weiss, D.L., Keller, D.U.J., Seemann, G., Doessel, O.: The influence of fibre orientation, extracted from different segments of the human left ventricle, on the activation and repolarization sequence: a simulation study. Europace 9, 96–104 (2007)

Fixing the Beating Heart: Ultrasound Guidance for Robotic Intracardiac Surgery

Robert D. Howe

Harvard School of Engineering and Applied Sciences
Cambridge, MA 02138 USA
howe@seas.harvard.edu

Abstract. To treat defects within the heart, surgeons currently use stopped-heart techniques. These procedures are highly invasive and incur a significant risk of neurological impairment. We are developing methods for performing surgery within the heart while it is beating. New real-time 3-D ultrasound imaging allows visualization through the opaque blood pool, but this imaging modality poses difficult image processing challenges, including poor resolution, acoustic artifacts, and data rates of 30 to 40 million voxels per second. To track instruments within the heart we have developed a Radon transform-based algorithm, which is readily implemented in real-time on graphics processor units. For manipulation of rapidly moving cardiac tissue we have created a fast robotic device that can track the tissue based on ultrasound image features. This allows the surgeon to interact with the heart as if it was stationary. To integrate ultrasound imaging with the robotic device we have developed a predictive controller that compensates for the 50-100 ms imaging and image processing delays to ensure good tracking performance. Our in vitro studies show that this approach enhances dexterity and lowers applied forces. In vivo applications of this technology in atrial septal defect closure and mitral valve annuloplasty procedures demonstrate the potential for improved patient outcomes.

Keywords: Cardiac surgery, image-guided surgery, 3D ultrasound.

1 Introduction

Real-time 3D ultrasound (3DUS) imaging has enabled new surgical procedures within the beating heart that are not possible with current endoscopic technology [1], [2]. These procedures eliminate the need for cardiopulmonary bypass and its well documented adverse effects. They also make possible the real-time evaluation of reconstructive operations while the heart continues to function. The rapid motion of the heart, however, poses serious challenges to the surgeon. This is especially true of procedures involving intracardiac structures such as the mitral valve, which recoils rapidly with every heartbeat.

A promising solution to these problems is to employ a robotic motion compensation system to synchronize instrument motion with the heart. Operating within the heart,

N. Ayache, H. Delingette, and M. Sermesant (Eds.): FIMH 2009, LNCS 5528, pp. 97–103, 2009.
© Springer-Verlag Berlin Heidelberg 2009

though, provides significant challenges. The restricted confines make using a multi-DOF robot difficult. In addition, 3DUS must be used for guidance because it is currently the only real-time volumetric imaging technique that can image tissue through blood. Its use introduces time delays and its limited image quality can make tissue tracking difficult.

We have been working to develop a 3DUS-guided motion compensation system that overcomes these challenges to enable beating heart intracardiac procedures. Our initial efforts have been directed at mitral valve repair, particular mitral annuloplasty. The design of the present system is guided by the clinical observation that the rapid motion of the mitral annulus is dominated by translation along a single axis between the left atrium and left ventricle. This allows the use of a simplified 1 DOF motion compensation system. In the following we describe this system, including hardware design and control, and instrument and tissue target tracking from 3DUS images.

2 Mitral Annuloplasty

In many mitral valve repair procedures, an ring is attached to the annulus surrounding the valve orifice. This ring is sized to decrease the valve diameter to minimize regurgitation of blood through the valve when the ventricle contracts. In our beating heart version of the annuloplasty procedure, two instruments are introduced through the wall of the left atrium (Fig. 1). One instrument deploys an annuloplasty ring that opens into the round shape with a shape-memory-alloy frame. The other instrument deploys anchors (similar to staples) for attaching the ring to the valve annulus.

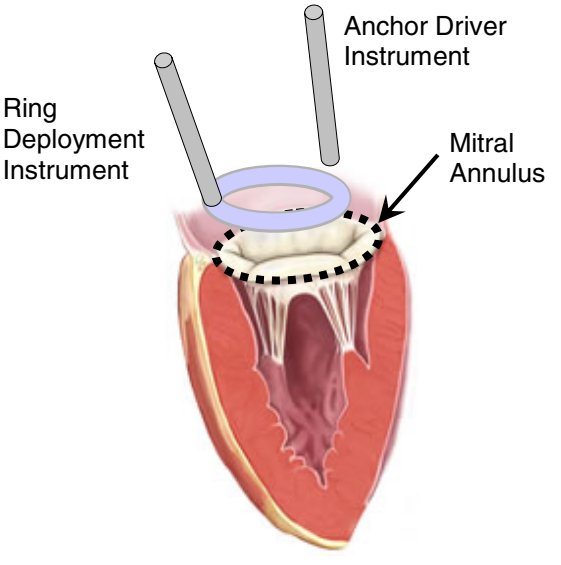

Fig. 1. Beating heart annuloplasty instruments and mitral valve apparatus

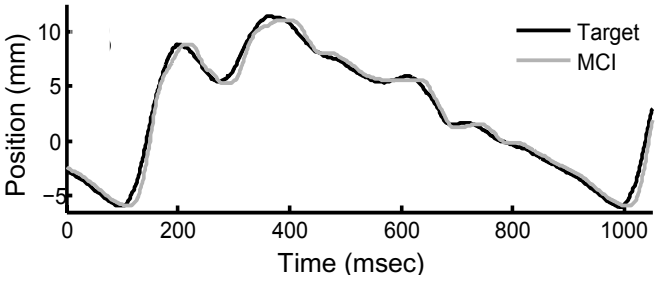

Fig. 2. Trajectory of mitral annulus centroid along principal axis ("target"), and in vitro tracking of this trajectory by the motion compensation instrument

The surgeon navigates the instruments to the desired vicinity of the annulus by observing the 3DUS image. We have developed real-time stereo visualization techniques that enhances depth perception in noisy 3DUS images and facilitates three-dimensional task execution [3]. Interacting with the annulus tissue, however, is difficult due to its fast movement: our analysis of clinical 3DUS image sequences showed annulus centroid velocity and acceleration maxima of 210 mm/s and 3800 mm/s^2 respectively, with a total travel of roughly 20 mm (Fig. 2) [4]. Fortunately, singular value analysis of the 3D trajectory shows that this motion is highly constrained to a single axis roughly parallel to the long axis of the heart, with only small excursions in the lateral directions.

This uniaxial motion permits the use of a single degree-of-freedom robotic system to track the annulus tissue motion. Such a system can help by driving the instrument to follow the fast motion of the target tissue with every heartbeat. The surgeon then operates on a "virtually stopped" heart, and can focus on selecting the appropriate locations for placing the annuloplasty ring and anchors.

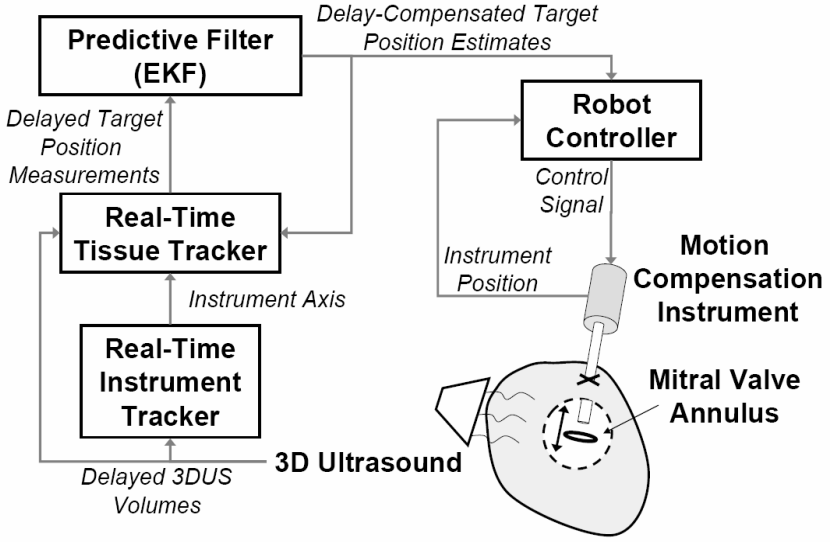

Fig. 3. Beating heart motion compensation system components

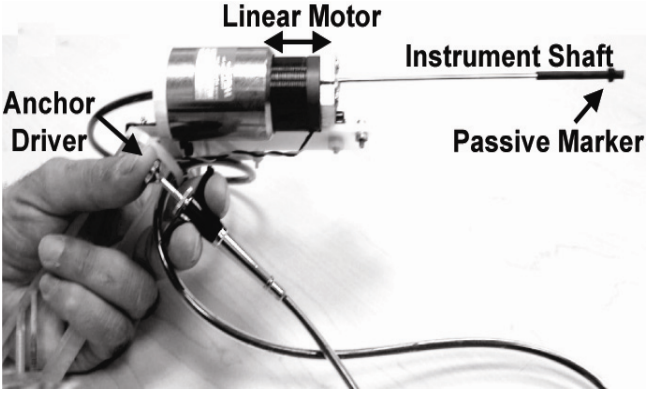

Fig. 4. Motion compensation instrument. The surgeon depresses the anchor driver plunger to push anchors into the target tissue.

Implementation of this motion compensation system requires a diverse set of functions (Fig. 3). Using 3DUS images, the system must determine the positions of the instrument and target tissue, compensate for the delays in imaging and image processing, and then drive the robotic instrument to match the target motion (Fig. 3). To track instrument positions, we take advantage of the fact that the instrument shaft is the only long, straight, bright object in the image volume. An algorithm based on a 3D generalization of the Radon transform can then detect this shape despite the high noise levels in the images [5]. Because this algorithm can be implemented as large number of projection operations, it can be executed on a graphics processor unit (GPU) in real time despite the 30-40 million voxels per second image data rate.

Tracking arbitrary tissue structures in 3DUS is challenging due to the high noise levels and poor shape fidelity. While we have had some success with texture and block-flow based techniques [6], [7], these methods cannot at present operate in real time. Fortunately, the one-dimensional constraint of the mitral annuloplasty application permits the use of a simpler "flashlight" technique [8]. During the procedure the surgeon orients the axis of the instrument towards the tissue region of interest, effectively designating the target location. The algorithm projects forward along the axis of the instrument through the 3DUS volume until it intersects the tissue surface at the target. Detection of the surface is, however, problematic due to imaging noise. We have implemented an active contour that can reliably follow the tissue surface and determine the target location.

Although instrument and tissue tracking algorithms can keep up with the image data rate, the accumulated delay from image formation, data transmission, and image processing can reach 50-100 ms. During this interval the annulus can move through most of its 20 mm range (Fig. 2), resulting in collision of the instrument with the tissue if the tracker output is used directly to command instrument motion. This can be largely alleviated by taking advantage of the near-repetitive motion of the heart from beat to beat. In our system, an extended Kalman filter estimates the future state of the system, in terms of the parameters of a Fourier decomposition of the motion [9].

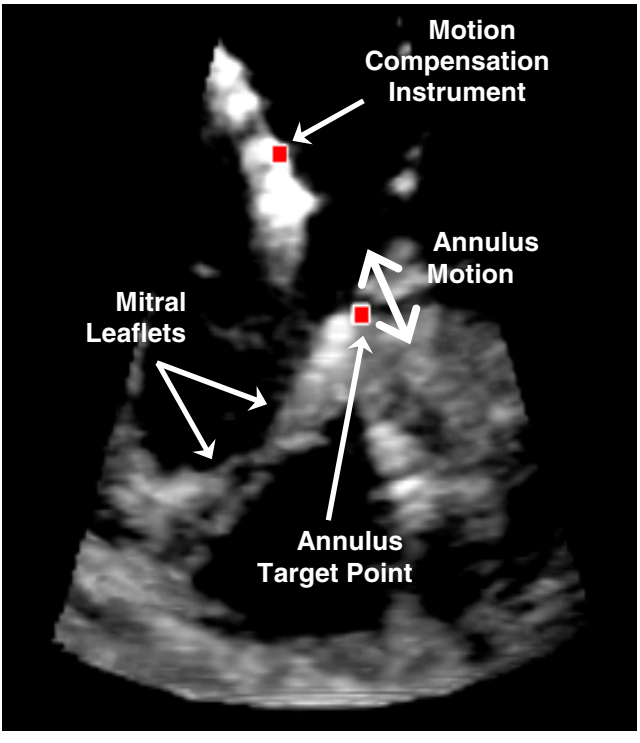

Fig. 5. Slice through 3DUS volume showing motion compensation instrument within the left atrium during an animal experiment. Dots indicate locations of instrument and annulus target determined by the real-time tracking algorithms.

The delay-compensated motion of the target tissue is then used as the input to the position controller of the motion compensation instrument (MCI). This hand-held instrument uses a voice coil actuator with a low moving mass to achieve high bandwidth and precise position control (Fig. 4). Bench tests with a target following the mitral valve trajectory confirmed that the motion compensation instrument approximately halved contact forces and doubled the precision with which surgeons can laterally position the instrument tip (Fig. 2).

Recent in vivo tests with porcine models confirm the ability of the system to accurately compensate for mitral annulus motion. Following initialization over a few heart beats, the instrument and tissue trackers lock on to their targets despite the distortion of in vivo 3DUS images. The instrument and target locations are displayed to the surgeon to facilitate navigation (Fig. 5). The motion compensation system allows the surgeon to remain in contact with the tissue while reducing peak forces. Without the motion compensation system, the ability to successfully place anchors is reduced, and the absence of tracking can result in hard contact between the instrument and annulus that produces tissue damage (Fig. 6).

These results demonstrate that it is possible to use robotic devices to perform repairs within the beating heart, using real-time 3DUS as the primary sensing modality. A

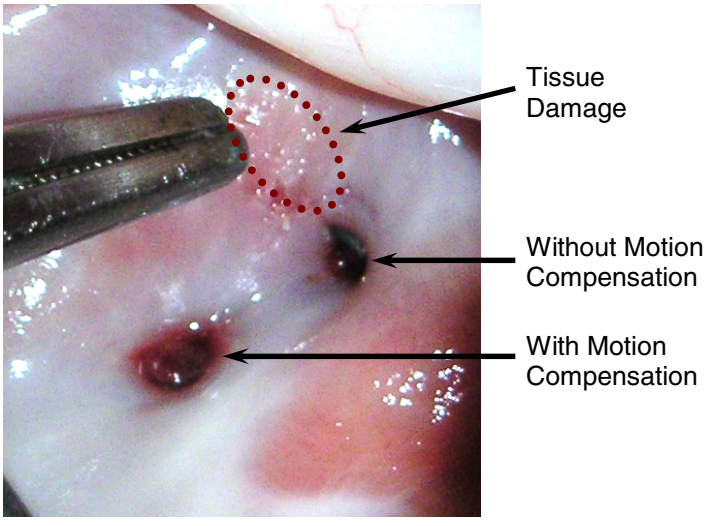

Fig. 6. Post mortem photograph of annulus showing tissue damage near site of anchor driven without motion compensation

number of additional challenges must be addressed before this technology is ready for clinical deployment. Foremost among these is safety: this system requires the use of a fast, powerful actuator in close proximity to vital cardiac structures. Promising approaches include the use of force sensing on the instrument tip to limit maximum applied forces, and ECG to provide early warning of irregular beats.

Acknowledgements

The project described here involves collaborative efforts by a large team, including Pedro del Nido and Nikolay Vasilyev of Children's Hospital Boston, Pierre Dupont and Jeff Stoll of Boston University, Ivan Salgo and Scott Settlemier of Philips Medical Systems, and Jeremy Cannon, Samuel Kesner, Daniel Kettler Paul Novotny, Douglas Perrin, and Shelten Yuen of the Harvard School of Engineering and Applied Sciences. This work is supported by the US National Institutes of Health under grant NIH R01 HL073647-01.

References

1. Cannon, J., et al.: Real-time three-dimensional ultrasound for guiding surgical tasks. Computer Aided Surgery 8, 82–90 (2003)
2. Suematsu, Y., Marx, G., Stoll, J., DuPont, P., Cleveland, R., Howe, R., Triedman, J., Mihaljevic, T., Mora, B., Savord, B., Salgo, I., del Nido, P.: Three-dimensional echocardiography-guided beating-heart surgery without cardiopulmonary bypass: a feasibility study. J. Thorac. Cardiovasc. Surg. 128, 579–587 (2004)

3. Novotny, P.M., Jacobsen, S.K., Vasilyev, N.V., Kettler, D.T., Salgo, I.S., Dupont, P.E., del Nido, P.E., Howe, R.D.: 3D ultrasound in robotic surgery: performance evaluation with stereo displays. Int. J. Med. Robotics Comput. Assist. Surg. 2, 279–285 (2006)
4. Kettler, D., et al.: An active motion compensation instrument for beating heart mitral valve surgery. In: Proc. IEEE IROS, San Diego USA (October 2007)
5. Novotny, P., et al.: GPU based real-time instrument tracking with three-dimensional ultrasound. Medical Image Analysis 11, 458–464 (2007)
6. Linguraru, M.G., Vasilyev, N., Marx, G.R., Tworetzky, W., Del Nido, P.J., Howe, R.D.: Fast Block Flow Tracking of Atrial Septal Defects in 4D Ultrasound of the Heart. Medical Image Analysis 12, 397–412 (2008)
7. Linguraru, M.G., Vasilyev, N., Del Nido, P.J., Howe, R.D.: Statistical Segmentation of Surgical Instruments in 3-D Ultrasound Images. Ultrasound in Med. & Biol. 33 (2007)
8. Yuen, S.G., Kesner, S.B., Vasilyev, N.V., Del Nido, P.J., Howe, R.D.: 3D Ultrasound-Guided Motion Compensation System for Beating Heart Mitral Valve Repair. In: Metaxas, D., Axel, L., Fichtinger, G., Székely, G. (eds.) MICCAI 2008, Part I. LNCS, vol. 5241, pp. 711–719. Springer, Heidelberg (2008)
9. Yuen, S., Novotny, P., Howe, R.: Quasiperiodic predictive filtering for robot-assisted beating heart surgery. In: Proc. IEEE ICRA, Pasadena USA (May 2008)

Lumen Border Detection of Intravascular Ultrasound via Denoising of Directional Wavelet Representations

Amin Katouzian[3], Elsa Angelini[1], Auranuch Lorsakul[3], Bernhard Sturm[2], and Andrew F. Laine[3,4]

[1] Institut TELECOM, TELECOM ParisTech, CNRS LTCI, Paris, France
[2] Volcano Corporation, Rancho Cordova, CA USA
[3] Biomedical Engineering and
[4] Radiology Departments, Columbia University, New York, NY USA
Laine@columbia.edu

Abstract. In this paper, intravascular ultrasound (IVUS) grayscale images, acquired with a single-element mechanically rotating transducer, are processed with wavelet denoising and region-based segmentation to extract various layers of lumen contours and plaques. First, IVUS volumetric data is expanded on complex exponential multi-resolution basis functions, also known as Brushlets, which are well localized in the time and frequency domains. Brushlet denoising has previously demonstrated a great aptitude for denoising ultrasound data and removal of blood speckle. A region-based segmentation framework is then applied for detection of lumen border layers, which remains a challenging problem in IVUS image analysis for images acquired with a single element, mechanically rotating 45 MHz transducer. We evaluated a hard thresholding operator for Brushlet denoising, and compared segmentation results to manually traced lumen borders. We observed good agreement and suggest that the proposed algorithm has a potential to be used as a reliable pre-processing step for accurate lumen border detection.

Keywords: Brushlet, Intravascular Ultrasound (IVUS), Denoising, Border Detection, Lumen, Thresholding.

1 Introduction

Cardiovascular disease (CVD) remains the leading cause of death worldwide. In 2004, CVD took about 800,000 lives in the United States with more than half of them due to atherosclerotic plaques [1]. There has been extensive interest in developing new imaging modalities to screen the progression and regression of atherosclerotic plaques in the past decade. Among them, intravascular ultrasound (IVUS) is the most widely used, real-time, and inexpensive imaging modality that not only provides pathological as well as morphological cross-sectional grayscale images of arterial walls but also makes atherosclerotic tissue characterization feasible, using IVUS

N. Ayache, H. Delingette, and M. Sermesant (Eds.): FIMH 2009, LNCS 5528, pp. 104–113, 2009.
© Springer-Verlag Berlin Heidelberg 2009

radiofrequency (RF) signals and images [2,3]. IVUS image segmentation has been a subject of interest for researchers due to the rapidly growing use of this imaging modality in catheterization procedures for the following two reasons. First, one important parameter during angioplasty or stent implantation procedure, is the ratio of lumen to vessel wall cross sectional area for regions of stenosis. For instance, the interventional cardiologist uses these measurements to select the appropriate type, length and diameter of a stent. Secondly, vessel walls and lumen contours are required to be traced prior to tissue characterization and plaque RF signal extraction. Pullback IVUS data files contain hundreds of cross-sectional images. The automatic extraction of vessel wall and lumen borders in those images has been the topic of various research efforts [4,5,6,7] and remains a challenging image processing problem.

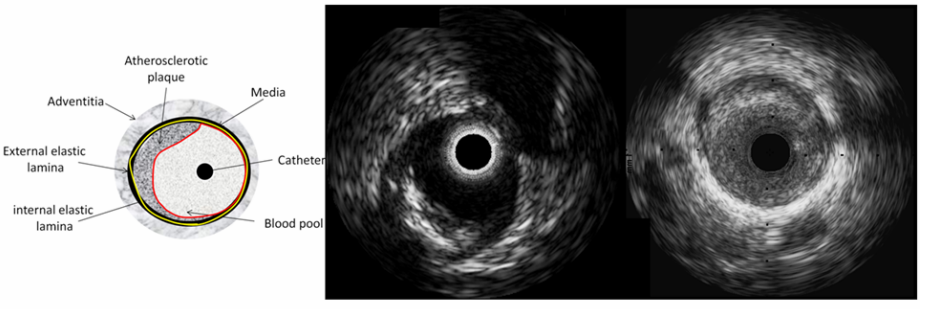

Fig. 1. Schematic cross-sectional anatomy of arterial wall and atherosclerotic plaque, the lumen border (red) and vessel wall border (yellow) (a), two distinct cross-sectional grayscale IVUS images acquired with 64-elements phased-array 20MHz (b) and single-element rotating 45MHz (c) VOLCANO transducers

Clinical application of automated segmentation methods has seen limited success due to the presence of the guide wire shadow, the arc of calcified plaques, catheter motion, cardiac motion, and the appearances of sub branches. In general, detection of the external vessel wall border is relatively easier than the internal lumen border. With IVUS ultrasound probes, the lumen border is better depicted in images acquired with a 64-element phased-array operating at 20 MHz transducer in comparison with those acquired with a single element mechanically rotating 45 MHz transducer. At higher center frequencies, the spatial resolution is improved at the cost of more scattering from red blood cells inside the lumen. Figure 1 illustrates the schematic cross-sectional anatomy of an arterial wall and atherosclerotic plaque along with two distinct cross-sectional grayscale IVUS images acquired with a 64-element 20MHz EagleEye Gold phased-array transducer (Volcano Corporation, Rancho Cordova, CA) as well as a single-element rotating 45MHz Revolution transducer (Volcano Corporation, Rancho Cordova, CA).

To improve image quality within a simple segmentation framework, we developped a three-dimensional (3D) Brushlet-based algorithm, taking into account blood flow during the pullback. The appearance of regions corresponding to plaques, vessel wall and surrounding fat is more stable within successive frames than the blood pool. Based on this observation, expansion using a brushlet basis followed by selective thresholding of brushlet coefficients was used to characterize persistent textures along the pull back dimension and remove random blood scattering and speckle. Denoising was performed in polar representation and results displayed in traditional Cartesian coordinates.

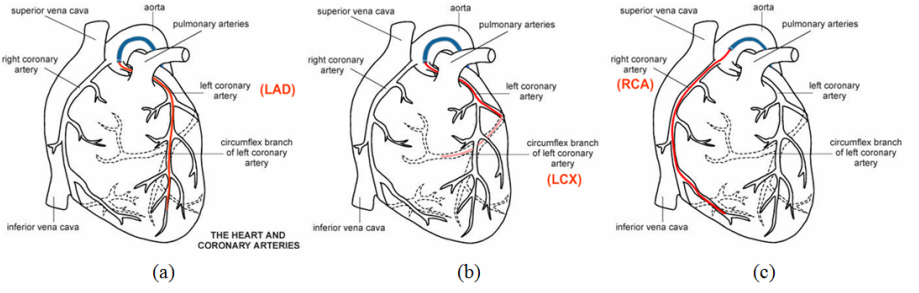

Fig. 2. The heart and coronary arteries. Schematic illustration of advanced catheter (red) into LAD (a) LCX (b) and RCA (c).

The segmentation of denoised images was then performed with region-based partitioning, Markovian regularization, and an iterated conditional mode (ICM) classification algorithm [8], based on 4 classes. Extraction of the different layers, corresponding to the ICM-classes, was finalized with a parametric deformable model.

This paper is organized as follows. Section 2 describes the acquisition system specification and data collection methodology. We then review brushlet analysis, denoising and segmentation algorithms in Section 3. The experimental results are then demonstrated in Section 4. The paper is summarized with conclusions in Section 5.

2 Data Collection

We collected IVUS grayscale images from three patients using a single element mechanically rotating 45 MHz Revolution™ transducer and s5™ imaging system manufactured by Volcano Corporation (Rancho Cordova, CA). The catheter was advanced on top of the guide wire from the femoral artery toward the site of coronary arterial occlusion (i.e. right coronary artery (RCA), left anterior descending (LAD), left circumflex (LCX)) via the aorta. Figure 2 illustrates schematically the heart, coronary arteries and the catheter path. During image acquisition, the catheter is pulled back from the distal to proximal locations with a speed of 0.5mm/sec,

acquiring 30 frames/sec. Ultimately, each grayscale IVUS frame was constructed from 256 radial lines spanning 360^{o} and 360 samples/line after decimation and interpolation in radial and lateral directions, respectively. The original images, acquired in polar coordinates, were then mapped to Cartesian coordinates to construct typical IVUS images, as shown in Figure 3.

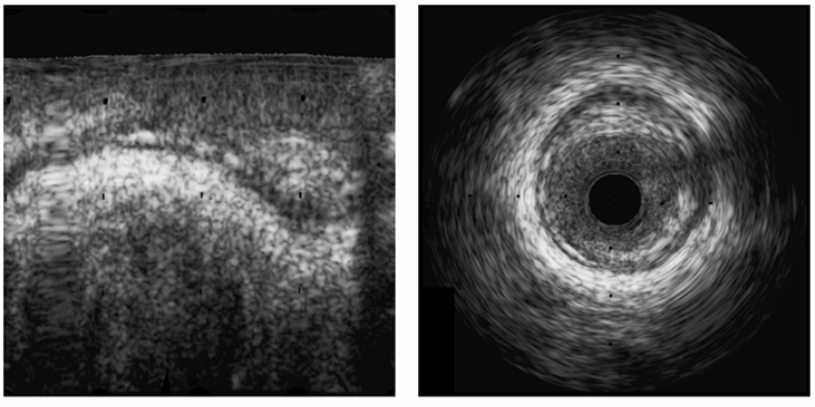

(a) (b)

Fig. 3. Grayscale IVUS image in polar (a) and Cartesian (b) domains

3 Methodology

We applied a 3D (cross-sectional image of arterial content + pull-back distance) overcomplete brushlet analysis to sub-blocks of IVUS frames in polar coordinates during each pullback. We assumed a strong spatial coherence in the appearance of plaque, arterial wall and surrounding fat within the analysis blocks. This coherence is organized in concentric circular layers and is better expressed and visualized in polar representations of the image data. Also, brushlet tiling and expansion is based on a regular square lattice which is best correlated with homogeneous textured patterns in polar (r,θ) rather than Cartesian (x,y) image representation. The presence of blood speckle within the volume of analysis is also considered to be dynamic due to blood flow. The underlying hypothesis for brushlet denoising, is that blood speckle can be removed by including the pull-back dimension in the analysis which creates "virtual textures" in the spatial-frequency domain. Finally, the results are mapped back to Cartesian coordinates for visual display.

3.1 Brushlet Basis

Brushlets are windowed complex exponential functions in the family of steerable wavelets and were introduced in [9]. They divide the real axis into subintervals $[a_n, a_{n+1}]$ of length l_n, and define a brushlet analysis function as follows

$$u_{j,n}(x) = b_n\left(x - l_n/2\right)e_{j,n}(x) + v(x-a_n)e_{j,n}(2a_n - x) - v(x-a_{n+1})e_{j,n}(2a_{n+1} - x) \quad (1)$$

The b_n and v are two windowed functions, which are defined from the ramp function. The complex orthonormal basis function $u_{j,n}$, can be constructed using these two functions along with the complex exponential function $e_{j,n}$ that is defined as $e_{j,n}(x) = \frac{1}{\sqrt{l_n}} e^{-2i\pi j\frac{(x-a_n)}{l_n}}$. Given any one-dimensional signal f in $L^2(R)$, its Fourier transform $\hat{f}$ can be projected onto the brushlet basis as $\hat{f} = \sum_n \sum_j \hat{f}_{n,j} u_{n,j}$ where $\hat{f}_{n,j}$ are the brushlet coefficients. It has been shown that the projected of $\hat{f}$ onto the brushlet basis can be implemented in an efficient fashion using a folding technique and fast Fourier transform (FFT) [10]. In the reconstruction process, the original signal can be retrieved using inverse Fourier transform and unfolding operation.

In our application, a tensor product extension was used for the volume of IVUS data frames. Consequently, such an extension would lead to the orientation selectivity in the brushlet domain, which is described next.

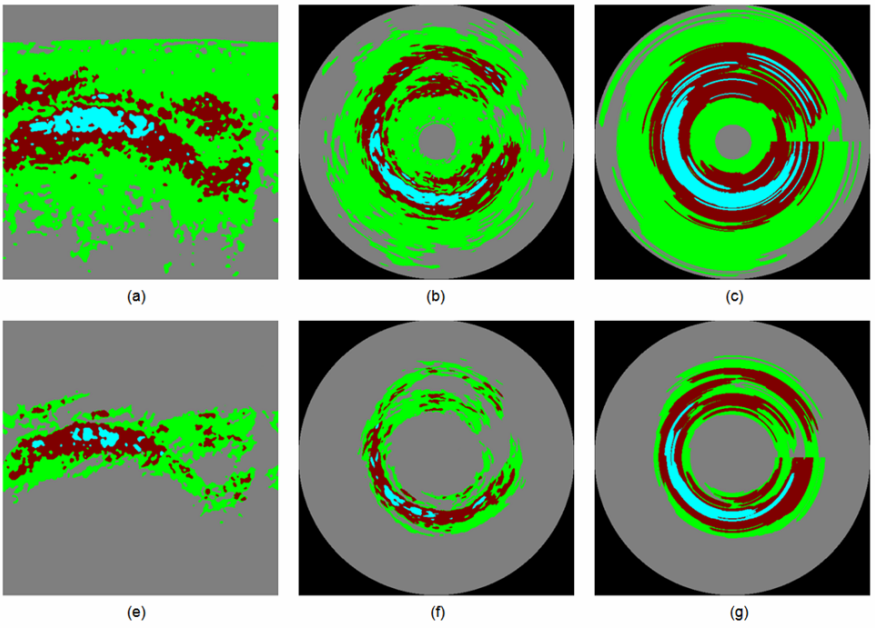

Fig. 4. ICM segmentation. 4-classes ICM results for original image in polar (a), Cartesian coordinates (b) and after dilation (c). 4-classes ICM results for denoised image in polar (d), Cartesian coordinates (e) and after dilation (f).

3.2 Frequency Tilling and Overcomplete Representation

The decomposition of the IVUS volumes onto a brushlet orthonormal basis can provide a way to capture selectable textural features of different orientations in the Fourier (brushlet) domain. Since we deal with volumetric datasets, this can be reliably performed by tilling the Fourier domain into quadrants (sub-cubes), each representing a specific size and orientation of a brushstroke, which is analogous to a wavelet scaling function.

We used an overcomplete multiscale representation of the brushlet coefficients for two reasons. First, to avoid aliasing effect and secondly, to preserve as much textural information as possible in the transform domain due to the stringent behavior of blood and plaque signals that makes the lumen border detection very challenging.

3.3 Thresholding for Removal of Blood Speckle

The purpose of this study was to offer a reliable denoising algorithm by removing blood speckle (noise), such that the resulting denoised data can be employed as an input for any 2D or 3D segmentation algorithm. We used two methods for eliminating blood noise via thresholding of the brushlet coefficients. We deployed a hard thresholding technique on real part of each brushlet coefficient.

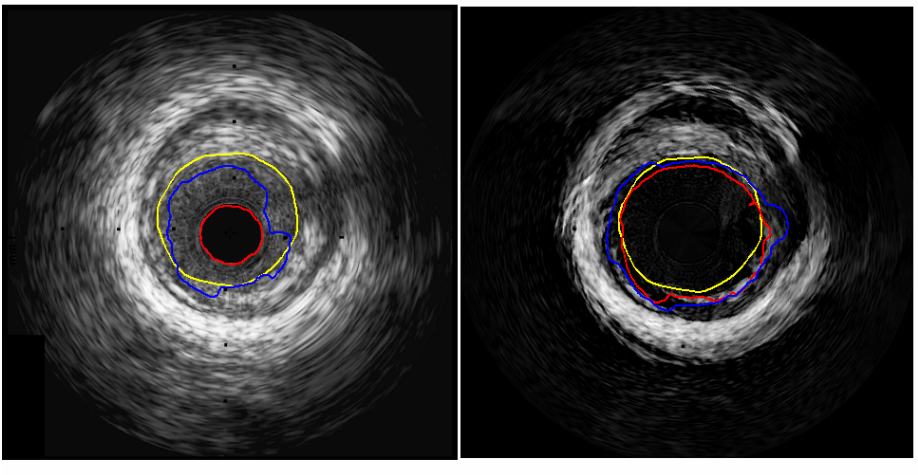

Fig. 5. Segmentation results at different layers (red, Blue) along with manually traced contour by an expert (yellow) on original (a) and denoised (b) IVUS images

3.4 Segmentation of IVUS Data

We used an iterative conditional model (ICM) segmentation framework to segment the IVUS data into 4 regions (layers), characterized by their average gray values. The

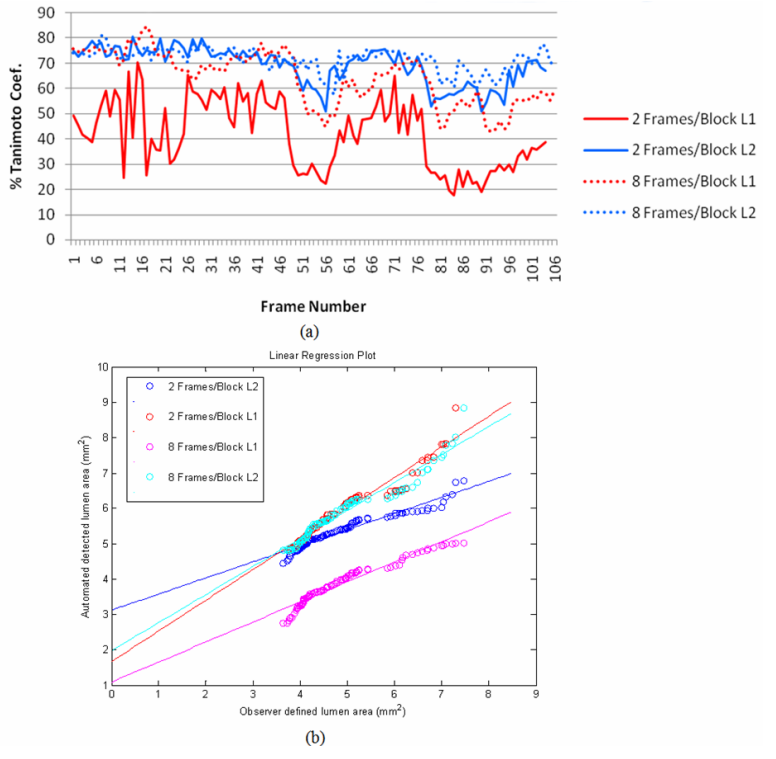

Fig. 6. Evaluation of detected contours at two layers (L1, L2) in 104 IVUS frames within a pullback with two different block sizes. Tanimoto coefficients (a), Regression analysis (b).

ICM segmentation framework corresponds to a discrete minimization of the piecewise Mumford and Shah functional energy [11] replacing curvature constraints with a Markovian regularization of the contours. The Markovian regularization provides a very efficient computational framework to control orthogonal and vertical associations of similar class labels when applied on a regular lattice corresponding to 4-neighbor pixels in 2D. Such a constraint is ideal for circular patterns such as vessel layers, when displayed in polar coordinates. We therefore applied the ICM to the IVUS original and denoised volumes in polar coordinates. Consequently, classification results were transformed to the Cartesian coordinates for visualization and extraction of the center contours with a standard parametric deformable model applied to thresholded ICM classifications for the four classes and imposing a regular growth of vessel contour areas by iteratively initializing the deformable model at the center of the image (transducer). This extraction step was performed after dilation of the ICM classification results with a horizontal line structuring element of 70 pixels, in polar coordinates. This computational step was designed to close the open and unconnected borders to obtain better results from parametric deformable model and estimate the lumen border more precisely, as illustrated in Figure 4.

4 Results and Discussion

In the first experiment, we processed IVUS volumes of size $512\times512\times2$ and the Fourier domain was tilled using four by four by two cubes in the x, y and pull-back dimensions respectively each in an overcomplete representation. We repeated the experiment using volumes of size $512\times512\times8$ to insure adequate spatial resolution in the pull-back dimension (at an 8 slice depth). Higher spatial resolution in this dimension resulted in blurred denoised data due to the effects of the motion of the catheter and heart (without ECG gating).

Figure 5 illustrates the results of our segmentation algorithm, for the second experiment, on an original IVUS image and the resulting denoised image using a hard thresholding operator. For this purpose, the thresholding was performed in each cube empirically with the threshold value set at 50% of the maximum value of real part of the coefficients. The resulting denoised coefficients were then classified into four groups with uniform gray level values for ICM initialization. However, we only extracted the contours from the first two layers since they better approximated the true lumen border. As shown in Figure 5, the segmentation algorithm outperforms well on denoised images and the automated borders at two layers (red L1 and blue L2) are well correlated and matched with manually traced lumen border (yellow), which was traced by an expert.

Table 1. Tanimoto coefficient statistics and correlation between automated and manually traced borders in 233 frames collected from three distinct cases

	Number of Frames	***Mean Tanimoto Coefficients***	***Maximum Tanimoto Coefficients***	***Minimum Tanimoto Coefficients***	***Correlation (p<0.0001)***
Case # 1	104	$L1: 64.12 \pm 10.56$ $L2: 71.34 \pm 4.74$	$L1: 84.55$ $L2: 81.02$	$L1: 42.78$ $L2: 57.53$	$L1: 79.01$ $L2: 78.74$
Case # 2	104	$L1: 71.10 \pm 9.69$ $L2: 72.70 \pm 4.05$	$L1: 84.20$ $L2: 81.09$	$L1: 48.33$ $L2: 60.87$	$L1: 0.78$ $L2: 0.80$
Case # 3	25	$L1: 69.73 \pm 4.22$ $L2: 77.08 \pm 4.63$	$L1: 77.69$ $L2: 86.93$	$L1: 60.47$ $L2: 70.14$	$L1: 0.94$ $L2: 0.95$

For both experiments regression analysis was performed to evaluate the agreement between automated and manually traced contours for 104 frames within a pullback, Figure 6(a). In addition, we computed the Tanimoto coefficients to see how well the automated and manual contours are matched throughout the pullback, Figure 6(b). The average Tanimoto coefficients for the L1 and L2 borders were found to be 41.75 ± 13.66 and 69.16 ± 7.37, respectively in the first experiment (using block size of $512\times512\times2$) and 64.12 ± 10.56 and 71.34 ± 4.74 respectively in the second experiment (using block size of $512\times512\times8$) (case #1, Table 1). The Tanimoto coefficients measure the agreement in positioning of the automated and manually traced borders. According to Figure 6(b), the higher Tanimoto coefficients were achieved for the first 50 frames, where the pullback was more consistent (minimal motion). Our results show

that non-coherent pattern of blood speckle is better captured in longer IVUS volumes. However, the changes in plaque textures or motion artifacts become more significant and can degrade the results (as shown in frames 51 and 81, Figure 6(a)). This suggests that an adaptive processing technique might help in future efforts. Table 1 summarizes the Tanimoto coefficients statistics as well as the correlation values for 233 frames extracted from three distinct cases using block size of $512\times512\times8$ IVUS frames. Overall, the extracted contours at the second layer (L2) were found to have more agreement with corresponding manually traced borders.

5 Conclusion

In this paper we presented a new 3D denoising technique based on brushlet representations to remove blood noise in IVUS images acquired with a 45MHz single- element transducer. We further used denoised volumes as input to a 3D multi-region multi-channel segmentation algorithm to estimate the lumen border. We observed that the algorithm performs reasonably well especially so in areas of consistent pullback where there is strong spatial coherence in the appearance of plaque and minimal motion. In the future, we will try to make the thresholding adaptive, correct of motion and look at other directional informative that may provide more differentiation between blood and non-blood textures.

References

[1] American Heart Association, Heart Disease and Stroke Statistics – 2006 update, American Heart Association (2006)
[2] Nair, A., Kuban, B.D., Obuchowski, N., Vince, D.G.: Assessing spectral algorithms to predict atherosclerotic plaque composition with normalized and raw intravascular ultrasound data. Ultrasound in Med. & Biol. 27(10), 1319–1331 (2001)
[3] Katouzian, A., Baseri, B., Konofagou, E.E., Laine, A.F.: An alternative Approach to Spectrum-Based Atherosclerotic Plaque Characterization Techniques Using Intravascular Ultrasound (IVUS) Backscattered Signals. In: MICCAI-CVII 2008 (2008)
[4] Cardinal, M.H.R., Meunier, J., Soulez, G., Maurice, R.L., Therasse, E., Cloutier, G.: Intravascular Ultrasound Image Segmentation: A Three-Dimensional Fast-Marching Method Based on Gray Level Distribution. IEEE Tran. Med. Imag. 25(5), 590–601 (2006)
[5] Sonka, M., Zhang, X., Siebes, M., Bissing, M.S., DeJong, S.C., Collins, S.M., Mckay, C.R.: Segmentation of Intravascular Ultrasound Images: A Knowledge-Based Approach. IEEE Tran. Med. Imag. 14(4), 719–732 (1995)
[6] Unal, G.B., Bucher, S., Carlier, S., Slabaugh, G.G., Fang, T., Tanaka, K.: Shape-Driven Segmentation of the Arterial Wall in Intravascular Ultrasound Images. IEEE Tran. Info. Tech. Biomed. 12(3), 335–347 (2008)
[7] Klingensmith, J.D., Shekhar, R., Vince, D.G.: Evaluation of Three-Dimensional Segmentation Algorithms for the Identification of Luminal and Medial-Adventitia Borders in Intravascular Ultrasound Images. IEEE. Tran. Med. Imag. 19(10) (2000)
[8] Besag, J.: On the Statistical Analysis of Dirty Pictures. Journal of Royal Statistical Society, Series B 48(3), 259–302 (1986)

[9] Meyer, F., Coifman, R.R.: Brushlets: A tool for directional image analysis and image compression. Applied and computational harmonic analysis 4, 147–187 (1997)
[10] Ausher, P., Weiss, G., Wickerhauser, M.V.: Local sine and cosine bases of Coifman and Meyer and the construction of smooth wavelets. In: Chui, C.K. (ed.) Wavelets- A tutorial in Theory and Application. Wavelet Analysis and its Applications, vol. 2, pp. 237–256. Academic Press, San Diego (1992)
[11] Mumford, D., Shah, J.: Optimal Approximation by Piecewise Smooth Functions and Associated Variational Problems. Communication on Pure and Applied Math. 42, 544–685

A Statistical Approach for Detecting Tubular Structures in Myocardial Infarct Scars

Camille Vidal[1,⋆], Hiroshi Ashikaga[2], and Elliot R. McVeigh[1]

[1] Department of Biomedical Engineering, Johns Hopkins University
[2] Division of Cardiology, Johns Hopkins School of Medicine, Baltimore, MD

Abstract. The presence of an infarct scar in the heart generates abnormal electrical pathways that may trigger the occurrence of arrhythmic episodes. While precise models of the electric propagation in the heart have been proposed, we are just starting to observe and analyze infarct scars using high-resolution imaging techniques. Recent observations have shown that the scar is a highly heterogeneous tissue, characterized by a complex interface with surrounding myocardium. For instance, the infarct scar is perforated by tunnels of live tissue, which could generate abnormal activation pathways and therefore facilitate arrhythmia episodes. In order to characterize the role of such structures, we need to first delineate them. In this paper, we propose an automatic method for the detection of these tunnels of normal tissue through scars in high resolution MR images.

Keywords: Infarct Scar, High-Resolution MR Images, Tubular Structure Detection, Image Filtering, Statistical Image Model.

1 Introduction

The mechanical contraction of the heart results from the coherent propagation of an electrical activation wave in the myocardium. Abnormal activation pathways can seriously compromise the heart's efficacy at pumping the blood. If the abnormal activation is self-sustained, it can quickly become lethal. This condition, called ventricular arrhythmia, still accounts for 30-40% of post-myocardium infarction deaths [1]. Therefore, it is common to implant a cardiac defibrillator (ICD) to patients with pre-existing infarction to monitor the heart rhythm and shock it out of arrhythmia if needed. Nevertheless, the implantation of an ICD has life-altering consequences. It may indeed happen that the ICD fires off by mistake, provoking a tremendous amount of pain to the patient and loss of consciousness. Furthermore, studies have shown that nearly 50% of the ICDs have not fired in the first years after implantation [1]. Hence, it shows that a finer stratification of the risk of post-infarction arrhythmia is needed.

⋆ This work was funded by the NIH Cardiovascular Training Grant HL007581 and by a Fellowship from the Department of Biomedical Engineering at the Johns Hopkins University.

N. Ayache, H. Delingette, and M. Sermesant (Eds.): FIMH 2009, LNCS 5528, pp. 114–123, 2009.
© Springer-Verlag Berlin Heidelberg 2009

Since the presence of an infarct scar in the heart is correlated with the occurrence of lethal arrhythmia, efforts have been pursued to understand how the infarct scar modifies the electrical pathways in the heart. Using gadolinium delayed enhancement Magnetic Resonance (MR) imaging techniques [2], it is possible to specifically mark the infarct scar. However, preliminary clinical studies have shown that simple morphological measurements, such as the relative volume of infarct and normal myocardium, do not predict accurately the risk of arrhythmia. In [3], the authors define a "gray zone," a region of the myocardium that appears darker than the infarct scar but brighter than normal myocardium. They show that the gray zone volume is correlated to some clinical markers of the risk of arrhythmia. However, there is still debate as to what the biological nature of this gray zone is. It has recently been shown that the gray zone may in fact result from partial volume effects [4]. Indeed high resolution ex-vivo MRI have revealed that the interface between the scar and the myocardium is extremely complex.

Clinical observations [5] suggest that the complex interface of the scar with the myocardium is correlated with the risk of arrhythmia. Therefore, we propose to build low-level descriptors of the infarct scar to study this correlation more precisely and identify morphological markers of risk. For instance, we have noticed that the infarct scar is frequently perforated by elongated tubular structures of normal myocardium, which we refer to as tunnels. We conjecture that the presence of such structures, which can conduct the activation across the scar, could potentially favor abnormal conduction pathways and consequently facilitate the occurrence of arrhythmic episodes. We propose in this paper a method to automatically detect these tunnels in delayed enhanced high-resolution MR images.

The detection of tubular structures in 3D images is challenging for a human observer, as one needs to examine the image volume under several orientations at each voxel to determine whether it belongs to a tunnel. However it has also been an active topic of research in computer vision and medical imaging for the delineation of blood vessels [6]. Existing methods rely on matching intensity filters [7,8], detecting parallel edges or intensity ridges [9,10], examining the Hessian of the image [11,12,13] or using combinations thereof [14]. Other approaches use non-parametric filters to find directions of low intensity variations [15,16].

In this paper, we revisit the problem of detecting tubular structures based on intensity pattern from a statistical point of view. We introduce a simple statistical model of the image intensities. Under mild assumptions of conditional independence, the intensity variation and the geometric variations can be modeled separately. This is achieved by introducing a latent image segmentation. We use the Maximum a Posteriori estimator to derive an optimal detection algorithm which can be written as a simple image convolution operation. We evaluate the performance of the proposed algorithm at detecting tubular structures on synthetic data and provide preliminary results for the detection of tunnels in a high-resolution MR images.

2 Tunnel Detector

2.1 Statistical Formulation

We model the image intensity by a real-valued random vector x, such that $x(s)$ represents the intensity value at voxel s. At each voxel of the image, we associate a discrete random variable $Y(s)$ that is equal to 0 if there are no tunnels in s is and 1 if otherwise. $Y(s)$ is obtained using the Maximum A Posteriori (MAP) estimator at each pixel:

$$\forall s, \quad \hat{Y}(s) = \underset{j=\{0,1\}}{\arg\max}\, p(Y(s) = j|x), \tag{1}$$

Equivalently, we determine the presence or absence of a tunnel as follows:

$$\hat{Y}(s) = \begin{cases} 1 & \text{if } \mathcal{C}(s) > 1 \\ 0 & \text{otherwise} \end{cases}, \text{ where } \mathcal{C}(s) = \frac{p(Y(s) = 1|x)}{p(Y(s) = 0|x)},$$

Using Bayes' rule:

$$\mathcal{C}(s) = \frac{p(x|Y(s) = 1)\, p(Y(s) = 1)}{p(x|Y(s) = 0)\, p(Y(s) = 0)}. \tag{2}$$

We assume that there exists at most one tunnel per voxel, which means that the event $\{Y(s) = 1\}$ can be written as the union of independent events $\{T(s) = 1\} \cup \{T(s) = 2\} \cup \cdots \cup \{T(s) = N\}$, where the discrete random variable T represents the type of tunnel to which voxel s belongs. We characterize a tunnel by its radius and its orientation and consider a finite set of N pairs of radii and orientations. To simplify the notations, we denote the absence of tunnel at voxel s by $T(s) = 0$, instead of $Y(s) = 0$. Equation (2) becomes:

$$\mathcal{C}(s) = \sum_{j=1}^{N} \frac{p(x|T(s) = j)\, p(T(s) = j)}{p(x|T(s) = 0)\, p(T(s) = 0)} = \sum_{j=1}^{N} \mathcal{C}(s, j) \frac{p(T(s) = j)}{p(T(s) = 0)}. \tag{3}$$

The tunnel type is estimated as follows:

$$\hat{T}(s) = \begin{cases} 0, & \text{if } \forall j, \mathcal{C}(s, j) \leq 1 \\ j, & \text{otherwise} \end{cases}, \text{ with } j = \underset{j \in \{1,N\}}{\arg\max}\, \mathcal{C}(s, j). \tag{4}$$

Equation (3) shows that the detection algorithm relies on the design of an adequate image appearance model $p(x|T(s) = j)$. In order to successfully detect tunnels, the appearance model needs to account not only for the different intensity ranges, but also for tunnels of different diameter and orientation. We will show in the following sections how this is achieved by modeling the intensity of the image as a mixture of Gaussian distributions and the tunnel geometry with a set of cylindrical templates of different orientations and diameters.

In this work, we assume that for all s, $p(T(s) = 0) = p(T(s) = 1) = \cdots = p(T(s) = j) = 1/(N + 1)$. One could argue that prior information could be obtained from the image, but in practice the proportion of tunnel and non-tunnel voxels depends on the image and is not straightforward to estimate.

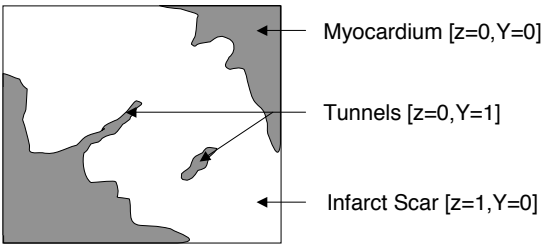

Fig. 1. Schematic of the different tissues and geometry present in the heart

2.2 Tissue-Based Image Modeling

We assume that the voxel intensities are independent given the value of $T(s)$, hence the conditional probability can be written as a product (5). In (6), we introduce a segmentation label $z(s)$ at each voxel. $z(s) = 1$ if voxel s belongs to the infarcted tissue and 0 otherwise. The ratio becomes:

$$\mathcal{C}(s,j) = \frac{\prod_t p(x(t)|T(s)=j)}{\prod_t p(x(t)|T(s)=0)}, \tag{5}$$

$$= \frac{\prod_t \sum_i p(x(t)|z(t)=i, T(s)=j)p(z(t)=i|T(s)=j)}{\prod_t \sum_i p(x(t)|z(t)=i, T(s)=0)p(z(t)=i|T(s)=0)}. \tag{6}$$

In order to simplifies further the expression of $\mathcal{C}(s,j)$, we assume that the intensity at voxel t depends only on the tissue type $z(t)$ and not on the tunnel type. It means that the intensity distribution of the normal myocardium is comparable to the intensity distribution of live tissue that forms the inner part of the tunnel. This is indeed verified in the case of our application. The ratio can therefore be rewritten:

$$\mathcal{C}(s,j) = \frac{\prod_t \sum_i p(x(t)|z(t)=i)p(z(t)=i|T(s)=j)}{\prod_t \sum_i p(x(t)|z(t)=i)p(z(t)=i|T(s)=0)}. \tag{7}$$

The distribution $p(x(t)|z(t)=i)$ represents the intensity distribution of tissue type i, while the geometry is encoded by the conditional distribution of the tissue type given the tunnel type, $p(z(t)=i|T(s)=j)$. The independence hypothesis allows us to model the intensity and the geometry separately.

2.3 Intensity Model

The computation of the ratio in (7) is quite intensive. It involves the computation at each voxel of a product of sums over all tissue types and all surrounding voxels. In order to simplify the computation of the ratio, we approximate the distribution $p(x(t)|z(t)=i)$ by its mode:

$$\forall t, i^*(t) = \arg\max_{i\in\{0,1\}} p(x(t)|z(t)=i),$$

$$\text{such that } p(x(t)|z(t)=i) = \delta(i^*(t)-i)p(x(t)|z(t)=i), \tag{8}$$

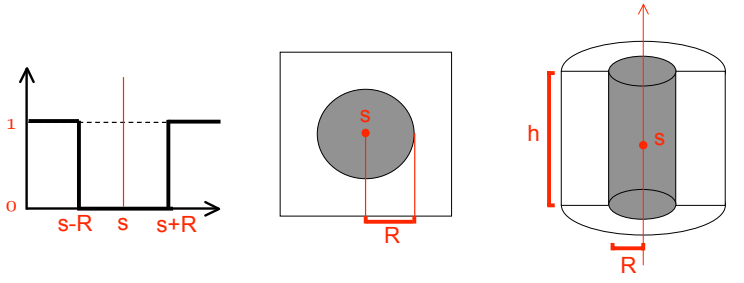

Fig. 2. Left: 1D profile of a tissue, **Middle:** 2D representation of the filter showing a cross-section of the cylinder, **Right:** 3D cylindrical filter

with $\delta(i^*(s) - i)$ the Dirac delta function. This approximation effectively segments the image based on intensity. Each voxel is assigned a label: normal or infarcted tissue. In our application we model the intensity distribution as a mixture of Gaussian distributions. The segmentation is therefore obtained by the EM algorithm [17]. However, any intensity-based segmentation technique would be suitable.

Since the intensity model is independent from the presence or absence of a tunnel, (7) becomes:

$$\mathcal{C}(s,j) = \frac{\prod_t p(z(t) = i^*(t)|T(s) = j)}{\prod_t p(z(t) = i^*(t)|T(s) = 0)}. \tag{9}$$

The resulting ratio compares the probability of observing a given tissue pattern under the hypothesis that there is a tunnel of type j at voxel s, to the probability of observing the same pattern in the absence of a tunnel.

2.4 Cylindrical Segmentation Filters

Recall that we consider N tunnel types characterized by their radii, lengths, and orientations. To each tunnel type j corresponds a unique tissue pattern that we model as a cylinder of normal tissue surrounded by infarcted tissue. We denote by f_j the 3D filter of radius R_j, orientation α_j, and length h_j, such that:

$$\forall t, \quad f_j(s,t) = \begin{cases} 0, & \text{if } t \in \text{Cyl}(s, R_j, h_j, \alpha_j), \\ 1, & \text{if } t \notin \text{Cyl}(s, R_j, h_j, \alpha_j), \end{cases} \tag{10}$$

where $\text{Cyl}(s, R_j, h_j, \alpha_j)$ denotes the cylinder centered in s, of radius R_j, height h_j and orientation α_j. If the segmentation pattern i^* observed around a voxel matches the tissue pattern in filter f_j, it is likely that this voxel belongs to a tunnel of type j. It means that $p(z(t) = i^*(t)|T(s) = j)$ should be close to 1, when $i^*(t) = f_j(s,t)$. On the contrary, if $i^*(t) \neq f_j(s,t)$, the probability $p(z(t) = i^*(t)|T(s) = j)$ should be close to 0. Recall that both $i^*(t)$ and $f_j(s,t)$ are binary quantities, thus the log-probability of observing a given tissue type at voxel t, when there is a tunnel of type j at s is, for all $j > 0$:

$$\log p(z(t) = i^*(t)|T(s) = j)$$
$$= \left(1 - [i^*(t) - f_j(s,t)]^2\right) \log(1 - \epsilon_j(s,t)) + [i^*(t) - f_j(s,t)]^2 \log \epsilon_j(s,t), \quad (11)$$

where ϵ_j controls the amount of tolerated mismatch between the image segmentation and the filter:

$$\forall t, \epsilon_j(s,t) = \begin{cases} 1/2, & \text{if } t \notin \text{Cyl}(s, \sqrt{2}R_j, h_j, \alpha_j), \\ \text{some constant} \ll 1/2, & \text{if } t \in \text{Cyl}(s, \sqrt{2}R_j, h_j, \alpha_j). \end{cases} \quad (12)$$

The rational behind the choice of ϵ_j is to limit the number of voxels contributing to $\mathcal{C}(s,j)$ and keeping a balance between the number of voxels inside and outside of the cylinder. Indeed, if $\epsilon_j(s,t) = 1/2$ the contribution of voxel t to $\mathcal{C}(s,j)$ is null.

On the other hand, if $T(s) = 0$, no specific tissue pattern is expected, hence we assume that $p(z(t) = i^*(t)|T(s) = 0) = 1/2$. Based on this assumption and Equation (11), we compute the logarithm of ratio (9):

$$\log \mathcal{C}(s,j) = \sum_t \left(1 - [i^*(t) - f_j(s,t)]^2\right) \log(1 - \epsilon_j(s,t))$$
$$+ \sum_t [i^*(t) - f_j(s,t)]^2 \log \epsilon_j(s,t) - \sum_t \log \frac{1}{2}. \quad (13)$$

This expression can be written as a convolution of the segmented image i^*:

$$\log C(s,j) = ((i^*)^2 * \lambda_j)(s) - 2(i^* * (f_j \cdot \lambda_j))(s)$$
$$+ \mathbf{1} * (\log 2 + \log(1 - \epsilon_j) + f_j^2 \cdot \lambda_j)(s), \quad (14)$$

with $\lambda_j = \log \frac{\epsilon_j}{1-\epsilon_j}$, and $\mathbf{1}$ a matrix of same dimension as filter f_j, with 1 at each entry.

In summary, the tunnel detection algorithm is carried out as follows: given a set of cylindrical filters f_j of different widths and orientations:

1. Segment the image: $\forall s, i^*(s) \leftarrow \arg\max_i \, p(x(s)|z(s) = i)$,
2. For each tunnel type j, compute the matching function $\mathcal{C}(s,j)$, cf. (14),
3. At each voxel, determine the type of tunnel using decision rule (4),
4. Reconstruct the detected tunnels, based on their detected centers, orientations and radii.

Remark: In order to filter an image, which is defined on a grid, we need to discretize the cylindrical filters (10). Since we are interested in structures of small radii (1 to 2 voxels), the discretization generates artifacts. To reduce this effect, we first build the filters at a finer resolution and downsample them, such that mixed voxels appear at the boundary of the filter, simulating the partial volume effect. In practice, the computation is unchanged, except that voxels at the tunnel boundary have a lower weight in the matching function.

3 Experimental Results

3.1 Synthetic Data

The proposed method is validated on the synthetic image proposed in [7] for different levels of noise. Since the proposed detection algorithm is meant to be used to detect thin structures in 3D, the synthetic image is first down sampled so that the synthetic tubular structures ranges between 1 and 5 pixels in width. A 3D Gaussian filter is used to build a 3D volume based on the down sampled 2D image. The performance of our method is compared to the Hessian-based detection technique implemented in the Bioimage Suite, [13]. We add a Gaussian noise whose standard deviation varies between 0 and 25 (the image ranges between 0 and 100). Figure 3 presents the detection performance of the proposed algorithm and compare them to the Hessian-based method with parameters: α=0.5, β=0.5, γ=0.25, scale varying from 1 to 5 voxels . In 3(d) the detection rate of the

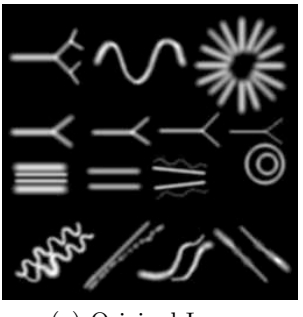

(a) Original Image

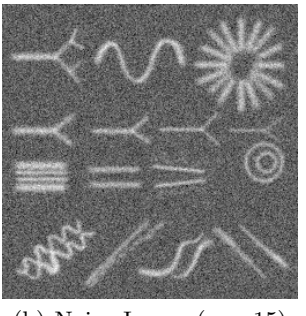

(b) Noisy Image ($\sigma = 15$)

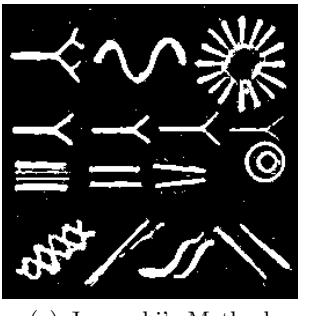

(c) Jacowski's Method

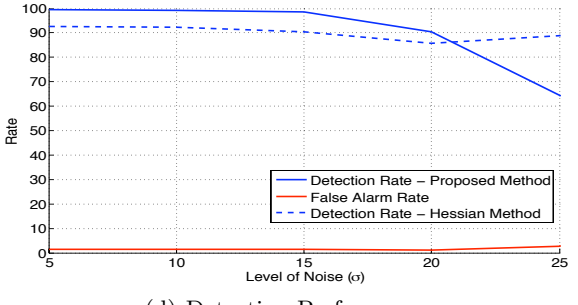

(d) Detection Performance

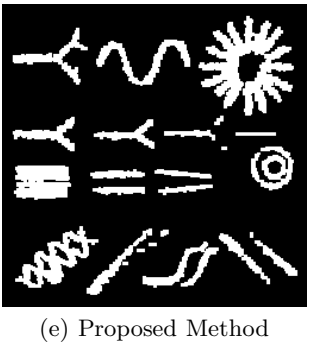

(e) Proposed Method

Fig. 3. (a) Synthetic Image, **(b)** Image with Gaussian noise, **(c)** Detection result obtained by Jackowski [13] (Detection Rate 90.4%, False Alarm 1.27 %), **(d)** Detection rate (continuous blue curve) and false alarm rate (continuous red curve) of the cylindrical segmentation filter for different levels of Gaussian noise. The dashed line represents the detection rate of the Hessian based technique for the same rate of false alarms. **(e)** Segmentation result obtained with the proposed method, (Detection Rate 98.74%, False Alarms 1.27%).

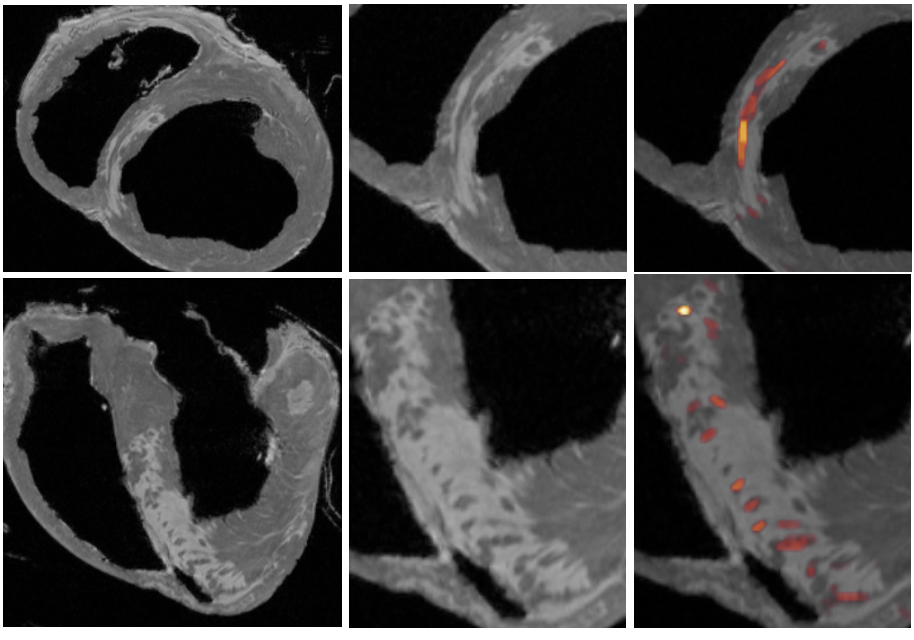

Fig. 4. Leftmost column: short and long axis view of the heart at the level of the infarct. The infarct appears at higher intensity and is punctured by many tubular structures. Central column: zoom in onto a region with many tunnels. Rightmost column: the detected tunnels superimposed onto the original image. Tunnels appearing in yellow have a higher detection score.

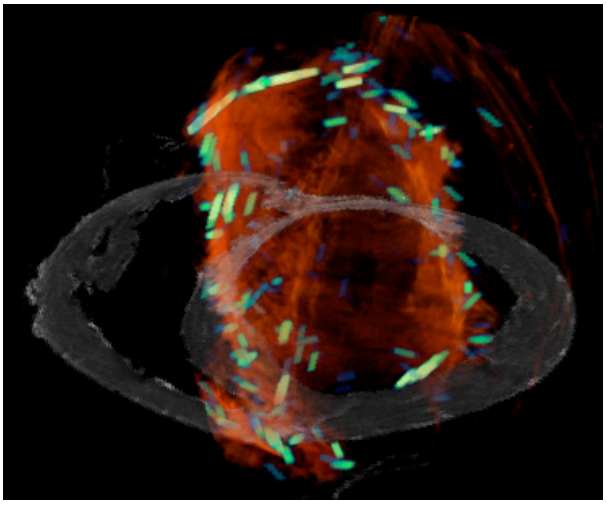

Fig. 5. 3D rendering of the infarct scar in red, superimposed on a short-axis view of the MR image. The detected tunnels are represented in blue/yellow/green depending on their detection score.

Hessian-based method is determined by looking at the performance for the same level of false alarms as we got with our method. This experiment shows that the detection rate achieved with the proposed method is very high when $\sigma \leq 20$, but diminishes significantly when the noise reaches 25%. One could probably gain in robustness to higher noise levels by refining the choice of ϵ such that the tunnels may be detected with a lower rate of false positive alarms. In this experiment the tolerance function ϵ is fixed ($\epsilon = .05$ in the center of the filter and $1/2$ in the outer part of the filter).

3.2 Tunnel Detection on Contrast-Enhanced MR Images

We use the proposed algorithm to detect tunnels in high resolution delayed enhancement MR images.The data is acquired as follow: in a male pig, the mid-left anterior descending coronary artery is occluded for 150 minutes using a balloon angioplasty catheter to create myocardium infarction. After 10 to 12 weeks, ex vivo high reslution MR Images are acquired to visualize the geometry of the infarct using Gd-DTPA (0.20 mmol/kg), to specifically mark the infarcted tissue. The heart is scanned in a 1.5-T MR scanner with a 3D gradient echo sequence (bandwidth, 130 Hz/pixel; flip angle, 20 degrees; echo time/repetition time, 4.02/9.7 ms, field of view, 100×100 mm; image matrix, 256×256; spatial resolution, 0.39×0.39×0.39 mm).

The detection proposed detection algorithm is used to detect tunnels of live myocardium in the infarct scar. We build a set of 13 filters with radius 1.5 voxels and different orientations. The cylinder has a length of 7 voxels. Figure 4 presents preliminary results of detection on two slices of the 3D volume. On both slices, numerous tunnels have been detected, which actually correspond to tunnels in the image. There are also a set of apparently false negative tunnels. In fact, using a 3D synchronized visualization tool, we examined each of the circular or elliptical cross-sections of the presented slices and noticed that the cross-sections that were not detected are valleys of complex surface elements. It is unfortunately extremely challenging to manually segment the tunnels which prevents us from getting quantitative estimate of the detection performance in the heart. False alarms occur in the fatty tissue that surrounds the heart, because fat and infarct have the similar intensity values. Figure 5 presents a 3D rendering of the infarct scar with the detected tunnels. Although most of the detected tunnels are short and located at the periphery of the infarct scar at the periphery of the infarct scar, few of them cross the infarct from side to side.

4 Future Work

The tunnel map resulting from the tubular structure detector can be easily obtained on several hearts and used as a descriptor of the infarct scar. In the future, we plan to assess the role of the tunnels in arrhythmic episodes by comparing the tunnel map of highly inducible hearts with the tunnel map of low inducible hearts.

References

1. Lombardi, F.: Timing of arrhythmic death after myocardial infarction: does it affect timing of ICD implantation? Eur. Heart Journal 26(14), 1350–1352 (2005)
2. Kim, R., Fieno, D., Parrish, T., Harris, K., Chen, E.L., Simonetti, O., Bundy, J., Finn, P., Klocke, F., Judd, R.: Relationship of MRI delayed contrast enhancement to irreversible injury, infarct age, and contractile function. Circulation 100(19), 1992–2002 (1999)
3. Klocke, F., Wu, E., Lee, D.: "Shades of gray" in cardiac magnetic resonance images of infarcted myocardium. Circulation 114, 8–10 (2006)
4. Schuleri, K., Centola, M., George, R., Amado, L., Evers, K., Kitagawa, K., Vavere, A., Evers, R., Hare, J., McVeigh, E., Lima, J., Lardo, A.: Characterization of peri-infarct zone heterogeneity by contrast enhanced multi-detector CT: Comparison with MR imaging. J. Am. Coll. Cardiol. (in press)
5. Yan, A., Shayne, A., Brown, K., Gupta, S., Chan, C., Luu, T., Carli, M.D., Reynolds, H., Stevenson, W., Kwong, R.: Characterization of the peri-infarct zone by contrast-enhanced cardiac magnetic resonance imaging is a powerful predictor of post-myocardial infarction mortality. Circulation 114, 32–39 (2006)
6. Kirbas, C., Quek, F.: A review of vessel extraction techniques and algorithms. ACM Computing Surveys 36(2), 81–121 (2004)
7. Mahadevan, V., Narasimha-Iyer, H., Roysam, B., Tanenbaum, H.: Robust model-based vasculature detection in noisy biomedical images. IEEE Trans. Inform. Technol. Biomed. 8(3), 360–376 (2004)
8. Wörz, S., Rohr, K.: A new 3D parametric intensity model for accurate segmentation and quantification of human vessels. In: Barillot, C., Haynor, D.R., Hellier, P. (eds.) MICCAI 2004. LNCS, vol. 3216, pp. 491–499. Springer, Heidelberg (2004)
9. Can, A., Shen, H., Turner, J., Tanenbaum, H., Roysam, B.: Rapid automated tracing and feature extraction from live high-resolution retinal fundus images using direct exploratory algorithms. IEEE Trans. Pattern Anal. Machine Intell. 25(2), 125–138 (1999)
10. Aylward, S., Weeks, S., Bullitt, E.: Analysis of the parameter space of a metric for registering 3D vascular images. In: Niessen, W.J., Viergever, M.A. (eds.) MICCAI 2001. LNCS, vol. 2208, pp. 932–939. Springer, Heidelberg (2001)
11. Sato, Y., Araki, T., Hanayama, M., Naito, H., Tamura, S.: A viewpoint determination system for stenosis diagnosis and quantification in coronary angiographic image acquisition. IEEE Trans. on Med. Imag. 17, 121–137 (1998)
12. Frangi, A., Niessen, W., Vincken, K., Viergever, M.: Multiscale vessel enhancement filtering. In: Wells, W.M., Colchester, A.C.F., Delp, S.L. (eds.) MICCAI 1998. LNCS, vol. 1496, pp. 130–137. Springer, Heidelberg (1998)
13. Jackowski, M., Papademetris, X., Dobrucki, L., Sinusas, A., Staib, L.: Characterizing vascular connectivity from microCT images. In: Duncan, J.S., Gerig, G. (eds.) MICCAI 2005. LNCS, vol. 3750, pp. 701–708. Springer, Heidelberg (2005)
14. Sofka, M., Stewart, C.: Retinal vessel centerline extraction using multiscale matched filters, confidence and edge measures. IEEE Trans. Med. Imag. 25(12), 1531–1546 (2006)
15. Geman, D., Jedynak, B.: An active testing model for tracking roads from satellite images. IEEE Trans. Pattern Anal. Mach. Intell. 18, 1–14 (1996)
16. Qian, X., Brennan, M., Dione, D., Dubrucki, W., Jackowski, M., Breuer, C., Sinusas, A.J., Papademitris, X.: A non-parametric vessel detection method for complex vascular structures. Med. Imag. Anal. 13, 49–61 (2009)
17. Dempster, A., Laird, N., Rubin, D.: Maximum likelihood from incomplete data via the EM algorithm. Journal of Royal Statistical Society 39, 1–38 (1977)

Quantitative Tool for the Assessment of Myocardial Perfusion during X-Ray Angiographic Procedures

Jean Liénard and Régis Vaillant

GE Healthcare, Buc, France
jean.lienard@med.ge.com

Abstract. During interventional procedures, cardiologists revascularize the ischemic heart by opening occluded arteries. Patency of the artery is assessed by selective injection of dye. Reperfusion of the myocardium is more difficult to estimate in the dim signal produced by the contrast agent in the microcirculation. Some researchers [1-2] have proposed and studied qualitative evaluations based on the observation of contrast appearance and wash-out in the heart muscle. In this paper, we describe a set of tools designed to assist the cardiologist in the assessment of myocardial perfusion. First, we apply synchronized subtraction in order to enhance the tissue opacification by removing the background. Secondly, to quantify the microcirculation temporal behavior, we compute time-density curves normalized with respect to the injection characteristics. Thirdly, we create parametric images that summarize in a single picture the dynamic information directly usable in the interventional setting.

1 Introduction

In the last years, major progresses have been made in the treatment of ischemic heart diseases and acute coronary syndromes. During revascularization by interventional procedures, angioplasty more and more substitutes thrombolysis and additive drug therapy significantly improves reperfusion and patient outcome. In order to validate these advances, the cardiologists call for quantitative and precise evaluation methods. Among them, the assessment of myocardial perfusion (MP) can play a role in the evaluation of new molecular therapy, in the treatment decision, and in the recognition of high-risk patients. In the course of coronary arteriography exams, visual grades of epicardial flow and myocardium perfusion have been proposed [1] [2] and evaluated in clinical studies. The TIMI flow evaluates the epicardial coronary flow on a scale varying from 0 (occluded artery) to 3 (normal flow). The myocardial flow is another independent factor of prognosis and mortality, also graded from 0 (inexistent blush) to 3 (normal blush). Nowadays, the validation of clinical therapeutic trials takes both ratings into account. However these subjective estimations suffer from significant observer variability and low reproducibility. Cardiologists are therefore interested in real-time methods that help them in an accurate quantification of myocardial ischemia and infarction through coronary artery blood flow and myocardial blush.

This paper describes the development, the validation and the clinical application of an X-Ray angiographic technique that visualizes the myocardial perfusion from

N. Ayache, H. Delingette, and M. Sermesant (Eds.): FIMH 2009, LNCS 5528, pp. 124–133, 2009.
© Springer-Verlag Berlin Heidelberg 2009

coronary arteriogram by means of heart phase synchronous subtraction. In addition, the tool delivers Time-Density curves (TDC) automatically generated either on selected regions-of-interest (ROI) or on a pixel-by-pixel basis to provide quantitative information or parametric images representative of the microcirculation functionality.

The plan of the paper is the following. In section Methods, we describe the aim and the implementation of the perfusion assessment methods. Section Results provides the results of validation performed on the separate components of the tool, and the results of application of the integrated tool to clinical data. We discuss the main findings, the advantages and constraints of the tool in the section Discussion, and then we conclude in the last Section.

2 Methods

Many clinical studies have demonstrated the recuperation of the heart muscle contractibility after revascularization with patients suffering from ischemic cardiomyopathy or acute myocardium infarction. However, in these cases, the improvement of left ventricle performances requires not only the restoration of the coronary blood flow but also the restitution of myocardium perfusion in the territory of the culprit artery. The objective assessment of both target results during routine interventional procedures is therefore of particular diagnostic interest.

Consequently, we developed methods, which permit online quantitative evaluation of arterial and myocardial blood flow from coronary arteriography sequences: (i) the synchronized subtraction improves the visibility of the perfused regions by removing the tissues unfilled by the contrast medium. For synchronizing cardiac images acquired before and after contrast injection, we use the existing electrocardiogram (ECG) or the kinetic cardiogram signal (KCG) automatically extracted from the images of missing ECG sequence. (ii) the Time-Density curves (TDC) represent the temporal distribution of contrast medium in various regions-of-interest selected by the operator. The application of a compartment model on TDC delivers parameters representative of vascular flow and volume. (iii) Computing the previous parameters at every pixel location provides parametric images that summarize the entire sequence into simpler physiologic information.

2.1 Synchronized Cardiac Subtraction

Digital subtraction technique based on ECG-gated acquisitions and logarithmic background subtraction has been proposed in the early 80's for enhancing the visualization of the microcirculatory phase in the whole myocardium [3]. More recently, Gibson [2] recommended applying the same concept of heartphase synchronous digital subtraction with temporally matching masks to facilitate the assessment of myocardial perfusion. For patient in breath hold, the subtracted images render only the differences due to the appearance/disappearance of the contrast medium in the coronary artery and in the muscle tissue, the "blush" (Fig. 1 shows an example).

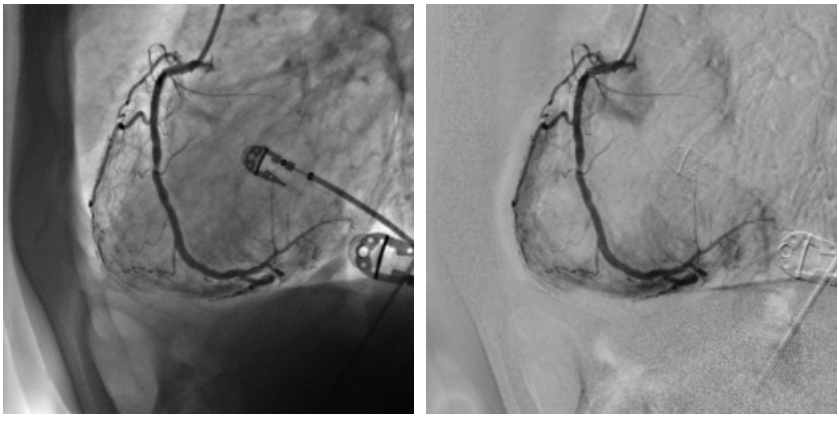

Fig. 1. The raw image (*left*) shows the opacified coronary artery surrounded by chest and diaphragm (dark regions). As a result of synchronous subtraction (*right*), the background is removed and lets appear more clearly the perfused myocardium.

During routine cardiac catheterization procedures, most of the imaging equipments perform acquisition of X-ray images and simultaneous recording of ECG signal. This protocol makes possible the mapping of opacified images I with non-opacified masks M by identifying the time acquisition of I with respect to the nearest QRS complex and selecting the frame M of the first cardiac cycle at the same ECG time slot.

For treating sequences recorded without the ECG signal, we developed an automatic analysis method for determining the requested mapping. The periodic changes of heart thickness, shape and position in the field-of-view produce X-ray exposure variations and image intensity rhythmic fluctuations. We capture this signal by measuring the mean intensity variations in two ROI on the images (one centered and one eccentric), as proposed in [4]. We also track the geometric motion of two regions-of-interest, one centered on the left side of the image and one centered on the right side, in consecutive frames along time. We determine the inter-frame displacement by using a classical multi-scale mutual information based approach. The X (resp. Y) displacement of each of these ROI along the horizontal (resp. vertical) axis is a signal linked to the phase of the beating heart. Each of the six signals (two from intensity variations and two for each of the tracked ROI) presents cyclic variations highly correlated to the cardiac motion, but possibly corrupted by interfering phenomenon (patient respiration, dye injection) we reduce by lowpass filtering. Then, we retain the most reliable signal on the criterion of highest periodicity that we quantify by the value of the first peak of its autocorrelation function. This first maximum appears at the mean period of the cardiac beats, as shown in the example of figure 2. The detection of the successive peak amplitudes, separated by that mean beat period, provides the trigger signals equivalent to the QRS ones of a physiologic ECG.

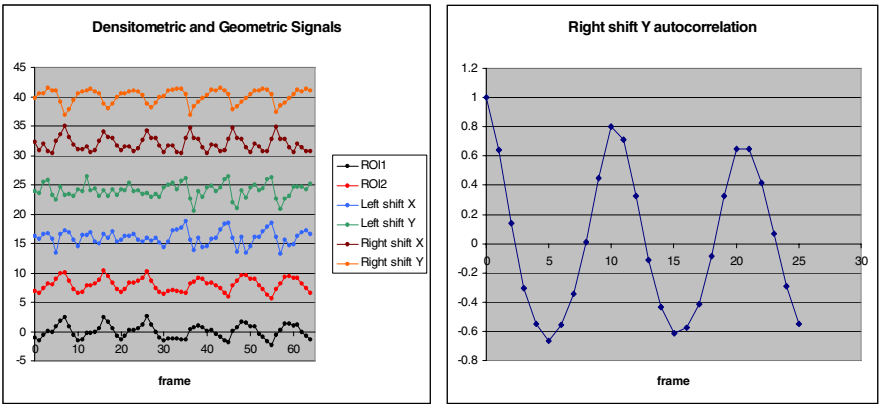

Fig. 2. Two densitometric signals, measured in a centered ROI1 and an eccentric ROI2, and 4 geometric signals, corresponding to the X and Y displacements of a left and a right ROI are measured in every frame (*left*). A cardiac beat period of 10 is determined with the Right shift Y signal, which has the highest autocorrelation score 0.8 (*right*).

2.2 Time-Density Curves

The main imaging modalities, CT scanner, MRI, SPECT, PET, Ultra-sounds currently apply the tracer kinetic models for the quantitative analysis of perfusion in organs like the brain, the kidneys or the heart. By utilizing similar indicator dilution principles in the X-ray projective imaging modality, hemodynamic parameters can be extracted from time-density curves (TDC) that represent changes in signal intensity versus time as induced by the contrast medium bolus [5]. This methodology has rather early been applied and optimized, first on animals [6-7], more recently on patient data [8-11]. Some difficulties may arise in studies of myocardial perfusion because 2D projection X-ray images of a 3D microvasculature possibly create superimposition of different circulatory regions. However, an appropriate gantry angulation depending upon the artery under exam can reduce the problem [9]. Then the major issue in densitometric measurement resides in heart motion, unless one continually relocates each ROI in order to measure the same region for all time. Another approach for avoiding movement artifacts created by both cardiac beatings and respiratory motion consists in sampling the TDC in fixed end diastolic frames acquired during a short breath-hold of the patient. An example of TDC extracted from a subtracted coronary arteriogram is given in Fig. 3. Two main parameters differentiate the TDC: the peak opacification amplitude (POP) and the time to reach the peak value (TTP). Their values characterize the flow in the region-of-interest but they significantly rely on the way the contrast medium is injected into the arterial tree. Consequently, in order to limit the parameter variability due to difference in manual dye injection, an ostial ROI located at the catheter tip provides a TDC playing the role of reference in term of POP and TTP. We then normalize the amplitude of each TDC by division with the reference POP and we convert its time of maximum TTP in transit time (TT) by subtracting the reference TTP [10]. These two parameters, normalized amplitude and transit time TT should then be independent of the main characteristics of the injection:

amount of contrast medium and starting time. For automatic injection, one could still consider other residual dependency factor, like the time of injection versus the phase of the heart beat. Further considerations should take into account the major characteristics in the formation of X-ray images, in particular the image contrast modification due to the scatter. We analyzed this matter both from a theoretical point of view and with phantom experiments as described in the Results section.

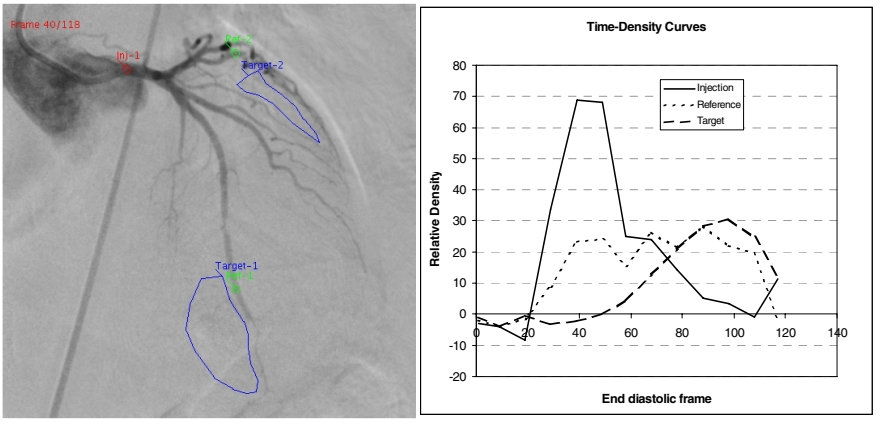

Fig. 3. Region-of-interest (ROI) are manually placed by the operator on the epicardial artery (ROI Inj-1 for Injection TDC) and on the myocardium (ROI Target-1 for Target TDC) (*left*). The corresponding densities are measured in consecutive end diastolic frames and plotted in Injection and Target Time-Density Curves (*right*).

Clinical studies have demonstrated the significant relationship between TDC parameters and myocardial flow [9-11].

2.3 Parametric Images

From the early stages of digital X-ray angiography, functional imaging has provided regional diagnostic information on arterial flow and tissue perfusion [12-13]. Indeed, parametric imaging helps the observer to visually detect regions with unexpected dynamic behavior. Similarly to manual TDC analysis, the parametric imaging algorithm considers every single pixel as a tiny ROI where it automatically measures the densitometric value in the successive diastolic frames and determines the POP and TTP parameters. In order to normalize the parameters like done with TDC, we designed an automatic detection algorithm to locate the arterial ostium where contrast injection occurs. This reference ROI is characterized by the earliest arrival of highly concentrated contrast medium in the half upper part of the field-of-view.

In the functional images, the gray-level or the color of every pixel shows either the normalized maximum value (POP) of the pixel TDC or the time for the blush to reach its maximum value with respect to the injection area (TT), or a combination of parameters, thus providing a direct visual representation of the functional impact of ischemic disease. An example of parametric images is illustrated in Fig. 4. They are

computed on a post-intervention coronary arteriogram of 184 images acquired at 15 frames/seconds on a patient admitted for acute myocardial infarction (AMI).

The TIMI myocardial blush grade (TMPG) defined by M.Gibson [2] has been estimated on a pixel-by-pixel basis by considering the POP value, the transit time TT, and the wash-out time defined as the number of cardiac cycles the blush takes to exit the microcirculation (see Fig. 4).

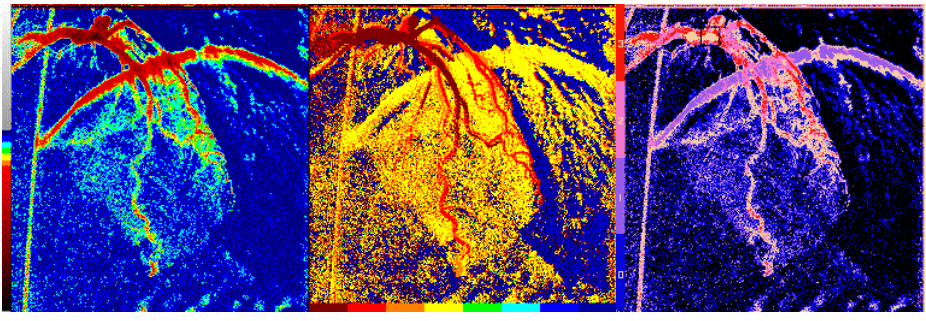

Fig. 4. Parametric image POP (*left*), TT (*center*), TMPG (*right*). The black square in the TMPG picture represents the automatic localization of the injection site. The densitometric color scales are relative. Each block in the TT color scale represents one cardiac cycle. Due to patient breathing at the end of the sequence, the diaphragm motion creates a semi-lunar artifact in the upper side of the images, without disturbing the reading of the apical myocardial area surrounding the LAD artery.

3 Results

Before processing clinical data with the complete quantification software, we separately validated the algorithmic modules.

3.1 Comparison of Kinetic-Cardiogram (KCG) and Electro-Cardiogram(ECG)

The kinetic-cardiogram algorithm makes possible the application of the synchronized subtraction on every coronary arteriogram, especially for those missing the patient ECG. To evaluate the accuracy of the KCG synchronization approach, we applied it on 28 sequences acquired with the physiologic ECG, representing a total of 435 cardiac cycles. If one tolerates a ±1 frame shift between the physiologic trigger and the estimated kinetic trigger, then they coincide in 91% of the cases (396 cycles about 435). Patient breathing and table panning during acquisition generate the divergences ≥2 frames since they alter both intensity and geometric signals.

3.1.1 Contrast Consistency on Phantom X-Ray Images

The densitometric evaluation of digitally subtracted cardiograms requires several image quality controls like the system linearity, the accuracy of measurements, and the impact of noise on precision. Therefore we performed preliminary studies with the

GE Innova system to determine the linearity of the contrast transfer function. We have found that the DSA contrast signal and the iodine concentration are linked by a linear relationship, whose coefficient of linearity varies according to some key parameters. As demonstrated in Figure 5, the 'patient' thickness plays the major role on the slope of this relationship, due to modifications of the X-ray spectrum: thicker objects request more energetic photons, generated by higher kV, leading to lower iodine mass attenuation and increased scatter.

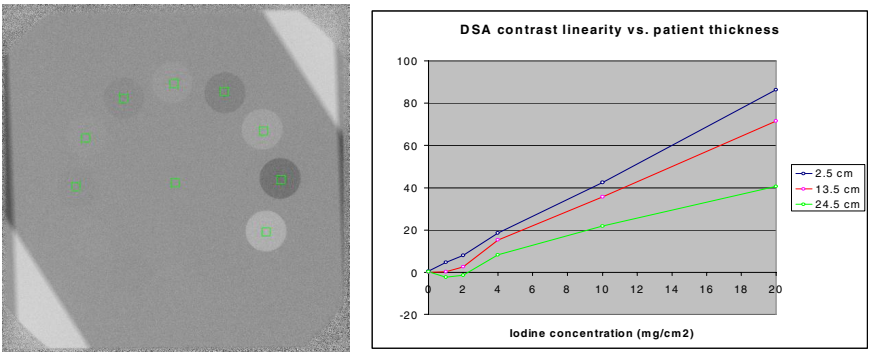

Fig. 4. The contrast wedge is a linearity insert (ref. 76-719 of Nuclear Associates); containing six iodinated discs, each with a different iodine thickness (0.5, 1, 2, 4, 10 and 20 mg/cm^2.). The phantom is acquired with two different angular positions, superimposed with different thickness PMMA block (2.5, 13.5, 24.5 cm) and images are subtracted (*left*) for assessing the linearity of the contrast signal (*right*).

In presence of scatter radiation, the logarithmic DSA low contrast signal is linearly related to the iodine thickness and concentration, but it is reduced by a factor (1+*SPR*) where *SPR* represents the secondary (scatter radiation) to primary (direct radiation) ratio. The influence of parameters like air gap or field of view is very limited.

We designed additional experiments with iodinated tubes placed over a 5 Plexiglas layers staircase block for quantitatively assessing the heterogeneity impact in the realistic case of variable density and thickness of mediastinum organs across the field of view. In this case, the relative measurements of iodine concentrations over two spatially different ROIs is impacted by local factors, like scatter ratio and mean tissue thickness. To illustrate this finding, the contrast signal of a tube filled with iodine at a concentration of 0.35 g/ml varies by 4% per centimeter of background thickness difference. For lower concentration (0.022 g/ml), the variation increases to 8%/cm. The peak amplitude of a low concentration myocardium ROI, normalized by a high concentration injection ROI can therefore vary by 12% per centimeter of thickness difference. However, in comparing the measurements at two different times t1 and t2 of an image sequence, all position-dependent factors cancel out over the same ROI. Therefore, the average value ratio obtained from an image sequence provides accurate and scatter-unaffected information on the temporal change of the contrast level in an opacified region [14]. Time parameters measured from these curves (time to peak, mean transit time) may be used in quantitative studies.

3.2 Enhancement of Blush Visibility by Synchronous DSA

Board-certified interventional cardiologists have evaluated a set of 35 subtracted sequences in term of myocardial perfusion visibility in comparison to the unsubtracted sequences. They noticed an improvement in 83% of the cases, an equal visibility in 14% of the cases, and a degraded visibility in 3% of the cases, due to motion artifact (patient breathing).

3.3 Time-Density Curves Analysis

The effectiveness of TDC for MP assessment has been evaluated in an animal experiment [10]. The study has demonstrated the substantial correlation between the TDC arterial transit time TT and the epicardial flow estimated by the TIMI frame count [2]. The normalized POP-to-TT ratio has been shown to decrease significantly ($p=0.03$) in case of total occlusion of the main left artery, and to return to a bit higher level after revascularization.

The same methodology has been applied in a clinical survey of 33 myocardial infarcted patients after reperfusion procedure in order to compare quantitative SPECT imaging data and angiographic TDC results [11]. The radionuclide activity measured in 4 pairs of AHA model segments was compared to the TDC parameters extracted from 4 ROI placed in the myocardial territory of the culprit artery. In addition to the absolute POP and TT parameters, the TDC decay slope showed the highest significant correlation with the isotopic perfusion ($p<10^{-3}$).

3.4 Injection Site Detection

We tested the reliability of the automatic detection algorithm which provides the ostium of injection. A successful detection corresponds to a location found in the artery proximal end close to the catheter tip. On 71 coronary arteriograms, the full success rate is equal to 69%. There are 14 cases (20%) where the result is located on the first bifurcation downstream of the main trunk. The algorithm fails in 11% of cases (on the catheter, on the diaphragm border, on a distal branch).

3.5 Parametric Images Analysis

A work-in-progress study is currently ongoing on 60 cases of infarcted patients for comparing the computerized TMPG parametric image with the TMPG grade visually determined by 4 independent cardiologists. Its relationship with infarction biomarkers will also be assessed.

4 Discussion

The assessment of myocardial perfusion is a clinical requirement during the interventional revascularization of infarcted hearts. Although multicenter studies have demonstrated the significant prognostic link between patient mortality rate and perfusion grade, the visual assessment of TMPG in clinical routine is not a current

practice because it requires training and it still suffers from high intra and inter-observer variability.

To obviate these limitations, the synchronous subtracted angiography provides an enhanced visibility of the myocardial blush, allowing a better reproducibility of MP grade. However, it requires the patient breath-hold all along the complete angiographic acquisition. In all the studies relative to this approach, we have observed that in more than 85% of the cases, the patients were able to hold their respiration, resulting in valuable subtracted images.

The computerized evaluation of MP by TDC analysis is an additional quantitative tool whose outcomes are in good agreement either with human observer findings or with results obtained by a different cardiac imaging technique. The gantry angulation selected for the angiographic record must be chosen with care to avoid superimposition of differently perfused regions, which could distort the amplitude and the dynamic behavior of TDC. The cardiologists involved in the mentioned studies have recommended the profile (LAO90) projection for acquiring cardiograms of left anterior descending artery and left circumflex artery. The perfused bed of the right coronary artery is better distinguished in the right anterior oblique angulation (RAO30), without overlap with the aorta.

The manual setting of ROI for TDC analysis in subtracted end diastolic frames can be aided by visualizing one of the parametric images. Indeed, the POP or the TTP picture provides a synthetic view of the arterial tree and the myocardial territory. It underlines synchronization defects and patient motion by generating artifact in regions misaligned in mask and opacified image. Beyond this usage, the TMPG parametric image displays a global overview of the heart with normal or insufficient perfusion, driving the cardiologist attention to be focused on these regions while reviewing the raw or the subtracted sequence.

5 Conclusions

In this paper, we have presented a series of tools that can be applied in the interventional setting for helping the cardiologist to assess the perfusion of the myocardium. In this approach, we have chosen to solely exploit the images available in this situation. These images demonstrate the temporal behavior of the dye in the myocardium after a selective injection done with a catheter at the ostium of the coronary. A first step, the synchronized subtraction, enables a pure qualitative assessment. More quantitative analyses are made using time-density curves. We also form parametric images by combining different parameters extracted along the sequence. In phantom experiments, we have determined the impact of the physic of the X-ray image formation on the accuracy of our measurements. A key point is also the normalization of the different computed quantities with respect to the characteristics of the injection. The evaluation of this tool has started several years ago. Animal and human data collected during the course of regular interventional have been studied. Preliminary results of the evaluation by comparison with SPECT are reported. Additional studies are on-going.

References

1. Van 't Hoff, et al.: Angiographic Assessment of Myocardial Reperfusion in Patients Treated With Primary Angioplasty for Acute Myocardial Infarction: Myocardial Blush Grade. Circulation 97(23), 2302–2306 (1998)
2. Gibson, C.M., Schomig, A.: Coronary and Myocardial Angiography. Angiographic Assessment of Both Epicardial and Myocardial Perfusion. Circulation 109, 3096–3105 (2004)
3. Radtke, W., et al.: Assessment of Myocardial Mass and Infarction Size by Digital Angiocardiography. In: Heintzen, P.H., Brenneke, R. (eds.) Digital Imaging in Cardiovascular Radiology, International Symposium Kiel (April 1982)
4. Kazmar, T., Kybic, J.: Opacity quantification in cardiac angiogram sequences. In: Jan, K., Provazn, I. (eds.) BIOSIGNAL: Analysis of Biomedical Signals and Images, Brno, Czech Republic (June 2008)
5. Schwab, A., Sandy Pang, K.: The multiple indicator dilution method and its utility in risk assessment. Environ. Health Perspect 108(suppl. 5), 861–872 (2000)
6. Pijls, N.H., et al.: Mean transit time for the assessment of myocardial perfusion by videodensitometry. Circulation 81, 1331–1340 (1990)
7. Eigler, N.L., et al.: Digital angiographic impulse response analysis of regional myocardial perfusion. Estimation of coronary flow, flow reserve, and distribution volume by compartmental transit time measurement in a canine model. Circ. Res. 68, 870–880 (1991)
8. Haude, M., et al.: X-ray densitometry for the measurement of regional myocardial perfusion. Basic Res. Cardiol. 95, 261–270 (2000)
9. Ungi, T., et al.: Vessel Masking Improves Densitometric Myocardial Perfusion Assessment. Int. J. Cardiovasc. Imaging (October 4, 2008)
10. Boyle, A.J., et al.: Quantitative Automated Assessment of Myocardial Perfusion at Cardiac Catheterization. Am. J. Cardiol. 102(8), 980–987 (2008)
11. Huttin, O.: Evaluation de la Perfusion Tissulaire au Décours de l'Infarctus du Myocarde par Angiographie Soustraite Quantitative: Correlation avec les Paramètres de Fixation en Scintigraphie au Sestamibi. MD thesis, Université Henri Poincaré, Nancy (January 2008)
12. Bursch, J.H., et al.: Arterial blood flow analysis by digital angiography. In: Heintzen, Brennecke (eds.) International Symposium Kiel, pp. 115–123. Georg Thieme Verlag (1982)
13. Liénard, J., Benchimol, C.: Imagerie paramétrique en angiographie numérique. Premier colloque image, Biarritz 1984. Gretsi Cesta, 803–808 (1984)
14. Cusma, J.T., et al.: Digital subtraction angiographic imaging of coronary flow reserve. Circulation 75, 461–472 (1987)

Multiview RT3D Echocardiography Image Fusion

Kashif Rajpoot[1], J. Alison Noble[1], Vicente Grau[1,2],
Cezary Szmigielski[3], and Harald Becher[3]

[1] Institute of Biomedical Engineering, University of Oxford, Oxford, UK
[2] Oxford e-Research Centre, University of Oxford, Oxford, UK
[3] Department of Cardiovascular Medicine, University of Oxford, Oxford, UK
{kashif,noble}@robots.ox.ac.uk, vicente.grau@oerc.ox.ac.uk,
cezary.szmigielski@cardiov.ox.ac.uk, harald.becher@orh.nhs.uk

Abstract. Real-time three-dimensional echocardiography (RT3DE) permits the acquisition and visualization of the beating heart in 3D. However, its actual utility is limited due to missing anatomical structures and limited field-of-view (FOV). We present an automatic two-stage registration and fusion method to integrate multiple single-view RT3DE images. The registration scheme finds a rigid transformation by using a multiresolution algorithm. The fusion is based on the 3D wavelet transform, utilizing the separation of the image into low- and high-frequency wavelet subbands. The qualitative and quantitative results, from 12 subjects, demonstrate that the proposed fusion framework helps in: (i) filling-in missing anatomical information, (ii) extending the FOV, and (iii) increasing the structural information and image contrast.

Keywords: Real-time 3d, RT3DE, echocardiography, image fusion, multiview.

1 Introduction

Real-time 3D echocardiography (RT3DE) utilizes a matrix-array transducer to acquire volumetric-sequence (3D+T) images of the heart. In comparison to other 3D cardiac imaging modalities, it permits simple, near real-time, low-cost, and completely harmless image acquisition to capture the true 3D nature of the heart. The images are usually acquired by positioning the ultrasound probe at the thorax and finding the acoustic window from the apical or the parasternal views. However, due to the large-sized foot-print of the ultrasound probe, it is often a problem to find a suitable acoustic window through which the complete heart or the left-ventricle (LV) chamber can be imaged. The field-of-view (FOV) of image acquisition is, therefore, limited and cannot always capture the entire heart volume. Moreover, the images contain speckle, missing boundaries, and intensity dropout.

Medical ultrasound images are constructed by the sound reflections received at the probe from the tissue interfaces in the body. It is well known that the angle between the tissue and the ultrasound wave plays an important role in the reconstruction process. Tissue interfaces perpendicular to the ultrasound wave reflect well, while the interfaces parallel to the wave may not reflect the wave at all. Thus, the single-view apical or parasternal images are often affected by limited or missing anatomical

N. Ayache, H. Delingette, and M. Sermesant (Eds.): FIMH 2009, LNCS 5528, pp. 134–143, 2009.
© Springer-Verlag Berlin Heidelberg 2009

information. Consequently, the use of any automated or manual quantitative analysis method on these images is prone to subjectivity and error.

We propose and investigate the use of acquiring apical view images from multiple probe positions at different angles (called multi-view) and fusing them together to: (i) fill-in missing information, (ii) extend the FOV of echocardiography images, and (iii) improve the image quality. The paper starts by providing a background about general and echocardiographic image fusion and presenting a summary of related work in Section 2. The registration and fusion algorithms are described in Section 3. The fusion results are evaluated in Section 4, with concluding remarks in Section 5.

2 Background and Related Work

In general, image fusion is the process of integrating several aligned source images to form a single fused image, preserving the salient features from all the source images. Image fusion is of great significance to combine images of varying focus, multiple sensor acquisition in remote sensing, and images of differing modalities in medical imaging [1].

In echocardiography, multiview RT3DE image fusion can be defined as the process of combining two or more single-view source images to form a single multi-view image which integrates the structural information from all the source images. Let $I_1(x,y,z),\cdots,I_N(x,y,z)$ be N aligned 3D single-view image frames, the fused image $I(x,y,z)$ is generated by applying a fusion rule θ on these images.

$$I(x,y,z) = \theta\big(I_1(x,y,z),\cdots,I_N(x,y,z)\big)$$

The fusion rule θ may take the form of minimum, maximum, average, or any other linear or non-linear function of the source intensities. The fusion rule θ decides how the values from source images are put together to form a single fused image.

Multiview RT3DE image fusion is related to two other common approaches found in the literature for integrating multiple acquisitions of ultrasound images: namely, spatial compounding and mosaicing. In the ultrasound literature, compounding is often employed to combine multiple ultrasound images having large overlap, with little or no angular difference in the acquisitions, to achieve the objective of improving the visual quality of the compounded image [2]. On the other hand, mosaicing [3] attempts to stitch together multiple images having little overlap, acquired with large angular separation in acquisitions, with the purpose of increasing the image information by extending the FOV. RT3DE image fusion can be considered as a combination of both compounding and mosaicing since its objectives include extending the FOV, increasing the image information, and improving the image quality. Moreover, in the fusion case, the multiple single-view images can have small or large overlap between them due to the arbitrary nature of probe movement during the image acquisition.

In Soler et al. [4], the authors employed a manual LV surface extraction procedure to assist in the single-view RT3DE image registration process. However, the LV surface extraction is a complex, time-consuming and subjective process due to the missing boundaries in the image. Moreover, the developed fusion methodology is restricted for fusion of only 2 source single-view RT3DE images. Grau & Noble [5] presented a local phase-based method for the fusion of apical and parasternal view

RT3DE images. Yao & Penney [6] extended the local phase-based compounding method of Grau & Noble [5] for up to 9 images, in an ad-hoc approach which is extremely computationally intensive. They used the local-phase based registration of Grau et al. [7] for aligning the images. In all these cases, the fusion technique is validated on only one or two subject cases. Szmigielski et al. [8] showed in a clinical work that the averaging based fusion technique significantly improves the quality and completeness of the RT3DE images.

3 RT3DE Image Fusion

We present a two-stage method for multiview RT3DE image fusion. During the first stage, the N images are aligned together using a standard multiresolution-based rigid registration algorithm. In the second stage, we develop a novel wavelet based image fusion technique to combine the aligned images. The proposed fusion approach is simple, fast and straightforward to fuse any number of single-view RT3DE images.

3.1 Automatic Rigid Image Registration

Registration aims to bring the reference volume I_{r} and floating volumes ${I_f}^i$ $(i = 2, \ldots N)$ into alignment with each other. We assume that a rigid transformation is sufficient to align I_{r} and ${I_f}^i$, as these images were acquired with ECG-gating, small probe movements, and over a gap of few minutes. There may be minor non-rigid misalignments due to the non-rigid motion of the heart, but finding a non-rigid transformation can introduce spurious deformations in the alignment process.

We followed a voxel-based registration process that attempts to find a geometrical transformation T such that the transformed floating image looks similar to the reference image by maximizing a similarity criterion C,

$$C = S\left(I_{\mathrm{r}}, T\left({I_f}^i\right)\right)$$

where S is a similarity function that measures the correspondence between the reference image and the floating image. In this work, the similarity function S was computed only for the image voxels region (i.e., excluding the region outside of acquisition pyramid in an echocardiography image). Since the images are acquired using the same modality and similar machine settings but they can have different intensity ranges, we employed the normalized cross-correlation (NCC) as the similarity function S. We followed a multiresolution registration approach with multiple initializations to avoid the local maxima of the similarity function. This ensures faster and robust estimation of the transformation T. The registration approach works through the following steps: (i) construct a 3-level multiresolution Gaussian pyramid, (ii) compute the similarity function S between the overlapping region of the reference and floating volumes, (iii) determine the transformation T at the coarsest level by maximizing the similarity criterion C, (iv) propagate T to the next finer level and refine the transformation T, and (v) iterate steps (i-iv) until it reaches the finest level on the multiresolution pyramid. For each resolution level in step (i), the image is blurred with a Gaussian kernel of variance $(\mathrm{shrink_factor}/2)^2$.

Maximization of the similarity criterion C was performed using the Powell-optimizer and tri-linear interpolation was used to approximate the transformed voxel values. The registration algorithm is applied to determine the transformation T between the end-diastolic frames of I_1 and I_i images. The spatial transformation T is then used to align the rest of the respective frames between the reference and floating sequences. A couple of example results are shown in Fig. 1, demonstrating visually the accuracy of the alignment.

3.2 Wavelets for Image Fusion

Wavelets [9] offer a simple and elegant framework of simultaneous space-frequency visualization, multiresolution analysis, and subband decomposition – permitting the separation of an image into low- and high-frequency components. The wavelet decomposition highlights interesting features in the wavelet domain which are often not visible in the spatial domain. In the 3D discrete wavelet transform (DWT), an image is divided into 8 subbands – 1 low-frequency and 7 high-frequency subbands.

We developed a wavelet based fusion scheme that is simple, efficient, fast, and extendable to fuse any number of source single-view images. Once the images are registered, the wavelet based fusion process combines the aligned single-view image volumes into a single multi-view volume that blends together the information from all the source images. The partition of an echocardiography image using wavelets into low- and high-frequency components is significant for the fusion process. In this way, we can employ suitable fusion rules for these components according to their characteristics in the image.

1. We observed in our experiments that the blood-pool speckle and the borders of the image pyramid region appear in the high-frequency wavelet components[1]. To suppress the noise[2] while still keeping the speckly appearance in the fused image similar to the original images, we average the high-frequency components.
2. On the other hand, low-frequency components are related to the more homogeneous regions of the image (e.g., myocardium). Since these regions appear brighter on ultrasound images, we choose maximum of the low-frequency components. This allows the fusion process to effectively fill-in the missing information.

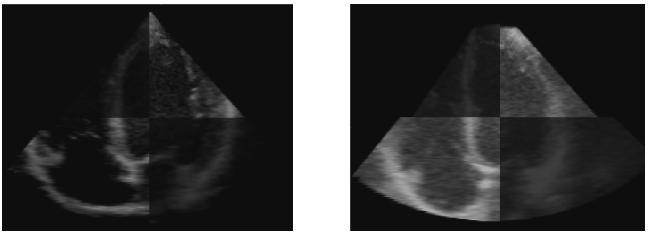

Fig. 1. Registration examples show the consistent accuracy of the registration method

[1] Note that, strictly speaking, speckle does not always have high-frequency characteristics.
[2] In this work, we define noise as highly inhomogeneous neighboring intensities.

These observations are verified by the illustration in Fig. 2, where we show the low- and high-frequency information contents of an example 2D echocardiography image slice. The 2D image, Fig. 2(a), is decomposed into low- and high-frequency wavelet components. The wavelet reconstruction from only low-frequency components is shown in Fig. 2(b), by zeroing out the high-frequency wavelet components. Fig. 2(c) depicts the wavelet reconstruction from only high-frequency wavelet components, by zeroing out the low-frequency wavelet components.

We propose the wavelet based fusion mechanism in the following 4 steps:

1. perform 1-level forward wavelet transform W^F on each single-view image I_i to separate the image into low-frequency Wav_L^i and high-frequency Wav_H^i wavelet coefficients,

$$W^F(I_i) = \left[Wav_L^i, Wav_H^i\right]$$

2. apply the maximum fusion rule θ_{max} on low-frequency coefficients Wav_L^i to obtain the fused low-frequency wavelet coefficients,

$$Wav_L^f = \theta_{max}(Wav_L^1, \cdots, Wav_L^N)$$

3. apply the mean fusion rule θ_{mean} on high-frequency coefficients Wav_H^i to obtain the fused high-frequency wavelet coefficients,

$$Wav_H^f = \theta_{mean}(Wav_H^1, \cdots, Wav_H^N)$$

4. perform inverse wavelet transform W^I from fused wavelet coefficients (Wav_L^f and Wav_H^f) to re-construct the fused image I.

$$I(x, y, z) = W^I\left[Wav_L^f, Wav_H^f\right]$$

This complete process of wavelet based fusion is graphically demonstrated in Fig. 3. We highlight the fact that the above proposed fusion strategy for the low- and high-frequency wavelet coefficients is contrary to the conventionally used wavelet based fusion of ordinary (usually non-medical) images [10]. In the conventional approach, the maximum of the high-frequency wavelet coefficients magnitude is selected to preserve the edges with the assumption that the edges lie in the high-frequency

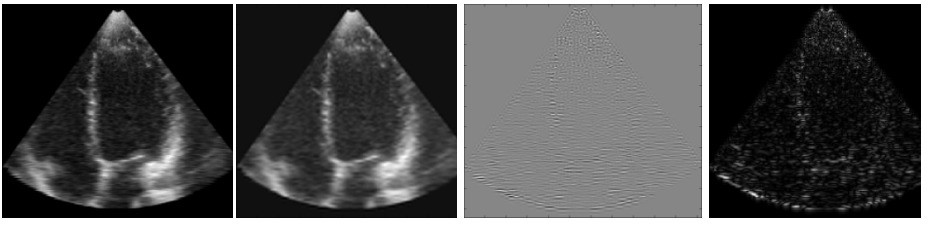

(a) (b) (c) (d)

Fig. 2. Low- and high-frequency characteristics of an echocardiography image. (a) An example 2D echocardiography image, (b) low-frequency wavelet reconstruction, (c) high-frequency wavelet reconstruction, and (d) absolute values of (c). Due to poor print quality on paper, the information of these images will be better visible in the electronic version.

components. However, this assumption is invalid for the echocardiography images which, unlike natural images, do not contain any sharp edges in the high-frequency wavelet coefficients (see Fig. 2(c) and Fig. 2(d)). Thus, the conventional approach does not yield the desired results in our application.

4 Experimental Validation

4.1 Data

Volumetric images were obtained using the Philips iE33 machine (Philips Medical Systems, Andover, USA) with a matrix-array transducer, acquiring a full volume sequence using ECG-triggering over 4 heart-beats. The usual spatial dimensions are 224x208x208 with nearly isotropic resolution of 0.82x0.84x0.76mm^3. To assess the fusion performance, the proposed method was applied on images from 12 healthy young subjects, with the number of source single-view images for each subject in the range of 3 to 6. The single-view images were recorded from different transducer positions using the following protocol. The first full-volume sequence was acquired by placing the transducer probe at the LV apex. This image was used as the reference volume for the image registration stage in 3.1. Two more full-volume sequences were acquired by translating the probe from the apex towards the lateral wall of the LV by approximately 1cm and 2cm, respectively. Another full-volume sequence was acquired by translating the probe from the apex towards the interventricular septum by approximately 1cm. Finally, two more volumes were captured by moving the probe one inter-costal space above and below the optimal apical position. We used 3 to 6 single-view images for some subjects as it was not possible to acquire all the 6 single-view images using the above protocol due to poor acoustic window.

4.2 Validation Measures

In order to evaluate the wavelet based fusion method, we computed four quantitative validation measures as defined below.

1. The % improvement in global image contrast, $\Delta(contrast)$, due to fusion is,

$$\Delta(contrast) = \left[\frac{\overline{\rho_f^{MY}} - \overline{\rho_f^{BP}}}{\frac{1}{N}\sum_{i=1}^{N}\left(\overline{\rho_i^{MY}} - \overline{\rho_i^{BP}}\right)} - 1 \right] * 100$$

where $\overline{\rho^{MY}}$ and $\overline{\rho^{BP}}$ denote the mean value in the myocardium and the blood-pool, respectively; N represents the total number of source single-view images; and i or f represent the i^{th} or fused image, respectively.

2. The improvement in SNR, $\Delta(SNR)$, in the fused image is defined as,

$$\Delta(SNR) = 20 * log\left(\frac{\frac{1}{N}\sum_{i=1}^{N}\mu_i^{BP}}{\mu_f^{BP}}\right) + 20 * log\left(\frac{\frac{1}{N}\sum_{i=1}^{N}\mu_i^{MY}}{\mu_f^{MY}}\right)$$

where μ^{MY} and μ^{BP} denote the variance in the myocardium and the blood-pool, respectively.

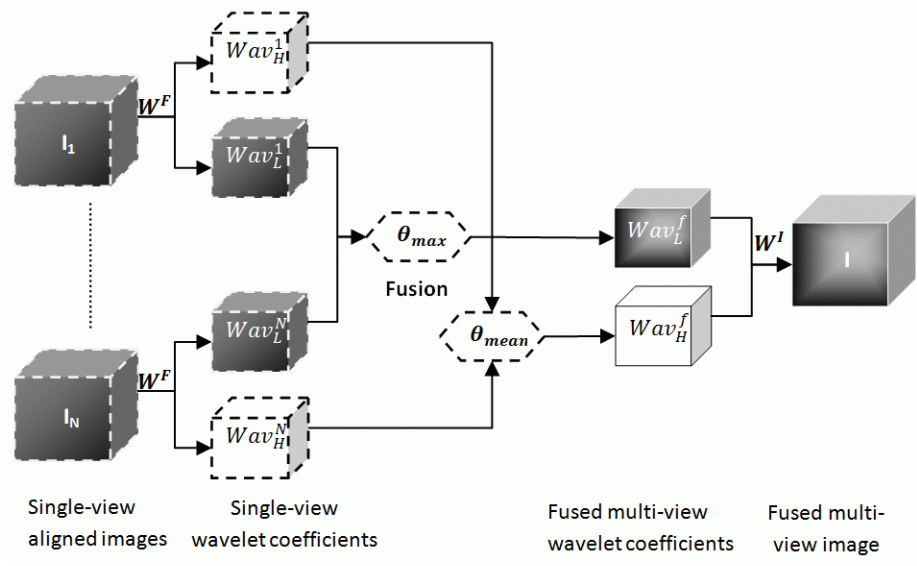

Fig. 3. Wavelet based multiview RT3DE image fusion scheme. For simplicity, only 1 high-frequency subband (Wav_H) is shown; in practice, there are 7 high-frequency subbands.

3. The quantitative change in the image's structural information is defined as the increase in the amount of total edge or feature points. The % change in feature information, $\Delta(feature)$, is computed as following,

$$\Delta(feature) = \left[\frac{nF_f}{\frac{1}{N}\sum_{i=1}^{N} nF_i} - 1\right] * 100$$

where nF represents the total number of feature points in the image. The feature map is computed using the feature detector in [11], derived from local-phase based feature asymmetry measure to detect step-like low contrast endocardial or epicardial features. These features are vital due to their potential utility in left ventricle segmentation using an active contour based algorithm, as in [12].

4. The % change in FOV, $\Delta(fov)$, due to the fusion is computed as,

$$\Delta(fov) = \left[\frac{FOV_f}{\frac{1}{N}\sum_{i=1}^{N} FOV_i} - 1\right] * 100$$

$$FOV = \sum_{i=1}^{n} vox_i$$

where vox_i denote the image voxels (1 for foreground, and 0 for background region outside the image pyramid), and n indicates the total number of voxels. The $\Delta(fov)$ is independent of the fusion technique and is a factor of image acquisition geometry.

4.3 Results and Evaluation

To assess the performance of the proposed fusion method, we implemented two other common fusion methods that use either averaging or maximum as their decision rule, respectively. The averaging fusion rule is popular in ultrasound compounding literature because of its ability to suppress noise and improve the signal-to-noise (SNR) ratio. On the other hand, the maximum fusion rule is particularly good for ultrasound images, since ultrasound images have high intensity values corresponding to important anatomical structures (e.g., myocardium). The three methods are denoted as: wavelet fusion – WAV, maximum fusion – MAX, and averaging fusion – AVG. For the computation of $\Delta(feature)$ and $\Delta(fov)$, the whole 3D volumes were used. However, in the case of computation of $\Delta(contrast)$ and $\Delta(SNR)$, representative 2D slices (apical 4-chamber plane) were used for the interactive selection of region-of-interests (ROIs) in the myocardium tissue and the blood-pool cavity (three arbitrary sized rectangle ROIs each in the myocardium and the blood-pool cavity). It was assumed that these ROIs represent the whole volume image for the computation of $\Delta(contrast)$ and $\Delta(SNR)$ measures.

Table 1 shows the mean values, over 12 images, for $\Delta(feature)$, $\Delta(contrast)$, and $\Delta(SNR)$. It shows significant contrast improvement gain with WAV (24.07%) in comparison to the popular averaging based compounding method AVG (– 5.32%). The SNR improvement with AVG ($8.01dB$) is slightly higher than WAV ($7.21dB$), because AVG involves averaging operation which achieves significantly more smoothing resulting in relatively higher SNR improvement. However, the SNR improvement with WAV is significant and comparable to AVG. The mean $\Delta(fov)$ value for 12 images is 34.15% and is independent of the image fusion technique. The amount of FOV enlargement is large, considering that an individual single-view image can already capture a big part of the heart in 3D images. The feature improvement with WAV (15.85%) and MAX (16.25%) is considerably higher than AVG (8.99%), due to the better preservation of important structures like myocardium tissue. We attribute only part of this feature improvement to be due to FOV enlargement, while the remaining is due to filling-in of missing anatomical information in the multiview combination. The above comparison demonstrates that the wavelet based fusion outperforms both of the other methods when analyzed collectively over all the quantitative evaluation measures.

Fig. 4 shows the visual results of RT3DE image fusion for a representative 2D slice. The visual results indicate that the fusion process significantly increases the structural information in the image and that every additional source single-view image, even if acquired from small probe movements, brings in some complementary feature information. The visual results show that the WAV method blends the source single-view images very well and has no stitching artifacts around the overlapping image borders as are visible on AVG fusion results. Moreover, the fusion increases the FOV, contrast and SNR of the image. Another notable gain of fusion is that it increases the density of the sampling resolution due to multiview combination. This is clearly visible on myocardium muscle tissue, papillary muscles and valves which appear thicker and have more uniform appearance after fusion.

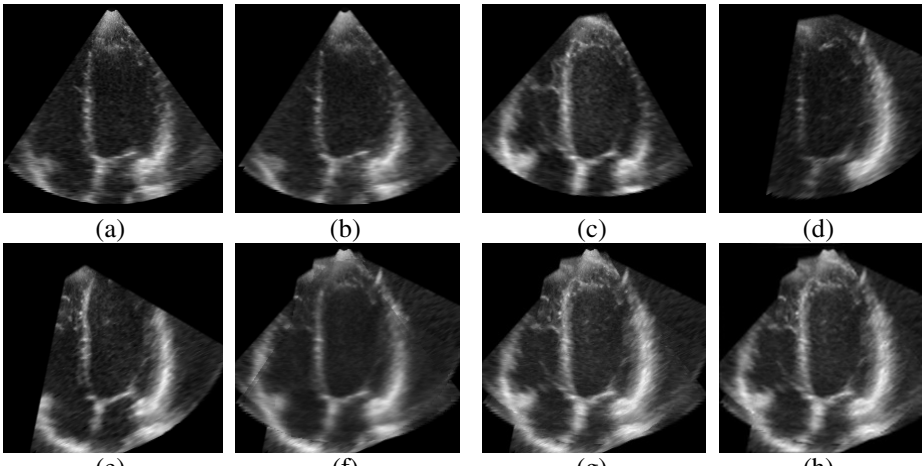

Fig. 4. Image fusion example, shows representative 2D slices. (a) – (e) 5 single-view 4-chamber images; (f) AVG fusion, (g) MAX fusion, and (h) WAV fusion.

Table 1. Comparison of AVG, MAX, and WAV fusion methods

	$\Delta(feature)$ (%)	$\Delta(contrast)$ (%)	$\Delta(SNR)$ (dB)
AVG	8.99	– 5.32	8.01
MAX	16.25	15.06	4.31
WAV	15.85	24.07	7.21

5 Conclusions

This work presented a completely automatic two stage registration and fusion method to integrate multiple single-view RT3DE apical-view images. The images were aligned using automatic multiresolution-based rigid registration algorithm, followed by wavelet based fusion method that allows the decomposition of the aligned images into low- and high-frequency components, thus permitting the use of relevant fusion rules. The quantitative validation of wavelet based fusion, against averaging and maximum based fusion methods, showed that it performs well to increase features, contrast, and SNR in the fused image.

Acknowledgement

Kashif Rajpoot is funded by a Pakistan Higher Education Commission PhD scholarship.

References

1. Goshtasby, A., Nikolov, S.: Image Fusion: Advances in the state of the art. Information Fusion, 114–118 (2007)
2. Rohling, R.N., Gee, A., Berman, L.: Three-Dimensional Spatial Compounding of Ultrasound Images. Medical Image Analysis 1, 177–193 (1996)

3. Wachinger, C., Wein, W., Navab, N.: Three-Dimensional Ultrasound Mosaicing. In: Ayache, N., Ourselin, S., Maeder, A. (eds.) MICCAI 2007, Part II. LNCS, vol. 4792, pp. 327–335. Springer, Heidelberg (2007)
4. Soler, P., Gerard, O., Allain, P., Saloux, E., Angelini, E., Bloch, I.: Comparison of Fusion Techniques for 3D+T Echocardiography Acquisitions from Different Acoustic Windows. Computers in Cardiology, 141–144 (2005)
5. Grau, V., Noble, A.: Adaptive Multiscale Ultrasound Compounding using Phase Information. In: Duncan, J.S., Gerig, G. (eds.) MICCAI 2005. LNCS, vol. 3749, pp. 589–596. Springer, Heidelberg (2005)
6. Yao, C., Penney, G.: Spatial Compounding of 3D Echocardiography: Novel Methodologies for Large Sets of Images. In: Medical Image Understanding & Analsysis (MIUA), Dundee, Scotland (2008)
7. Grau, V., Becher, H., Noble, J.A.: Registration of Multiview Real-Time 3-D Echocardiographic Sequences. IEEE Transactions on Medical Imaging 26, 1154–1165 (2007)
8. Szmigielski, C., Grau, V., Hoeschen, M., Noble, J.A., Kerber, R., Becher, H.: New Fusion Technique Significantly Improves Image Quality and Completeness of Datasets in RT3D Echocardiography. In: American Heart Association Scientific Sessions, II_401, Orlando, USA (2007)
9. Mallat, S.: A Wavelet Tour of Signal Processing. Academic Press, USA(1998)
10. Nikolov, S., Hill, P., Bull, D., Canagarajah, N.: Wavelets for Image Fusion. In: Petrosian, A.A., Meyer, F.G. (eds.) Wavelets in Signal & Image Analysis. Kluwer Academic Publishers, Dordrecht (2001)
11. Rajpoot, K., Noble, A., Grau, V., Rajpoot, N.: Feature Detection from Echocardiographic Images using Local Phase Information. In: Medical Image Understanding and Analysis (MIUA), Dundee, UK (2008), http://www.robots.ox.ac.uk/~kashif/pubs/miua2008kmr.pdf
12. Zagrodsky, V., Walimbe, V., Castro-Pareja, C., Qin, J.X., Song, J.-M., Shekhar, R.: Registration-Assisted Segmentation of Real-Time 3-D Echocardiographic Data Using Deformable Models. IEEE Transactions on Medical Imaging 24, 1089–1099 (2005)

Investigating Arrhythmogenic Effects of the hERG Mutation N588K in Virtual Human Atria

Gunnar Seemann[1], Paola Carillo[1], Daniel L. Weiss[1], Martin W. Krueger[1], Olaf Dössel[1], and Eberhard P. Scholz[2]

[1] Institute of Biomedical Engineering, Universität Karlsruhe (TH), Kaiserstr. 12, 76131 Karlsruhe, Germany
Gunnar.Seemann@ibt.kit.edu
http://www.ibt.kit.edu

[2] Dept. of Cardiology, Medical University Hospital Heidelberg, Heidelberg, Germany

Abstract. Atrial fibrillation (AF) is the most common cardiac arrhythmia in the western world. Genetic variants in the cardiac I_{Kr} channel have been identified to influence ventricular repolarization. The aim of this work is to investigate the effect of the mutation N588K on atrial repolarization and the predisposition to AF. Experimental data of N588K mutated hERG channel were incorporated in an atrial ionic model using parameter fitting. The effects of the mutation were analyzed in cell and tissue. N588K showed a gain of function effect, causing a rapid repolarization and a shortening of the action potential duration. Computer simulations of a schematic right atrial geometry were used to investigate the excitation conduction properties. The effective refractory period of mutant cells were reduced from 317 to 233 ms at 1 Hz. The conduction velocity is not significantly influenced by the mutation. Nevertheless, the wavelength of mutant cells is for all frequencies smaller, indicating that the mutation N588K predisposes the initiation and perpetuation of AF.

1 Introduction

Atrial fibrillation (AF) is the most common cardiac arrhythmia in humans [1]. The precise cellular mechanisms underlying AF are still poorly understood. AF is characterized by an abnormal rapid electrical activity in the atria resulting in a reduction of the atrial contractility. The atrial activity is normally under the control of the cardiac pacemaker function of the sinus node with 60–80 beats per minute (bpm) and is increased to 400–600 bpm during AF [1]. Sustained AF presents severe effects, like congestive heart failure, thromboembolism, ventricular arrhythmia and electrical remodeling of the atria favoring the maintenance of AF [1]. The occurrence of AF increases with age [1].

Several predisposing factors for AF have been identified, e.g. coronary artery disease, congestive heart failure, pericarditis and hypertension. However, AF has been also recognized as a heritable disorder. Recent studies have identified several genetic defects. One of the identified genetic defects is the mutation N588K in the gene *KCNH2*, which encodes the hERG protein. This protein forms the

N. Ayache, H. Delingette, and M. Sermesant (Eds.): FIMH 2009, LNCS 5528, pp. 144–153, 2009.
© Springer-Verlag Berlin Heidelberg 2009

α-subunit of the myocardial rapid delayed rectifier potassium channel responsible for I_{Kr}. The current is crucial to repolarization.

Up to now, genetic variants in this channel have been identified to modify ventricular repolarization known as long or short QT syndrome. The short QT syndrome is normally identified when the QT interval is smaller than 300 ms as measured in several different types of short QT syndrome [2]. The mutation N588K causes a gain of function effect shortening the QT interval in the ECG [3]. The reason for this is a shortening of the action potential duration (APD) and effective refractory period (ERP). Both effects could also support the initiation and perpetuation of AF by reducing the wavelength of the reentrant circuit.

The aim of this work is to investigate the effect of this mutation on atrial repolarization and the predisposition to AF. Therefore, the gating and kinetics properties of this mutant channel were implemented into the Courtemanche, Ramirez, Nattel (CRN) ionic model of human cardiomyocytes [4] using the previously presented technique of the Particle Swarm Optimization (PSO) [5]. The measured data was obtained with whole cell voltage clamp technique of wild-type (WT) and mutated hERG channels [6]. The effects were then visualized in a single-cell and in a schematic anatomic model of the right atrium. In these environments the APD, the ERP and the conduction velocity (CV) were analyzed depending on the basic cycle length (BCL). Furthermore, the possibility of inducing rotating waves in the tissue was examined.

2 Materials and Methods

In order to simulate the effects of the mutation in virtual atrial cells and tissue, an ionic model of the human atria was used as electrophysiological basis. Into this model, the measurement data was incorporated. The analysis of the mutation was then performed on a schematic geometrical model of the right atrium using the monodomain model to calculate excitation conduction.

2.1 Schematic Anatomical Model

In order to determine the CV and the ERP properties, a tissue model which represents anatomically the right atrium was used. The model included all important structures of the right atrium in a schematic way. The anatomical model includes the superior caval vein (SVC), the terminal crest (CT), some pectinate muscles (PM) and the atrial working myocardium (AWM), as shown in fig. 4 A. The sizes and locations were derived from the detailed Visible Female atrium [7]. The model consisted of 250 x 250 x 5 cubic volume elements with an edge length of 0.2 mm.

2.2 Atrial Electrophysiology and Excitation Conduction

The employed electrophysiological model of Courtemanche, Ramirez and Nattel (CRN) [4] consists of a set of coupled nonlinear ordinary differential equations in order to characterize the electrophysiological behaviour of human atrial cells.

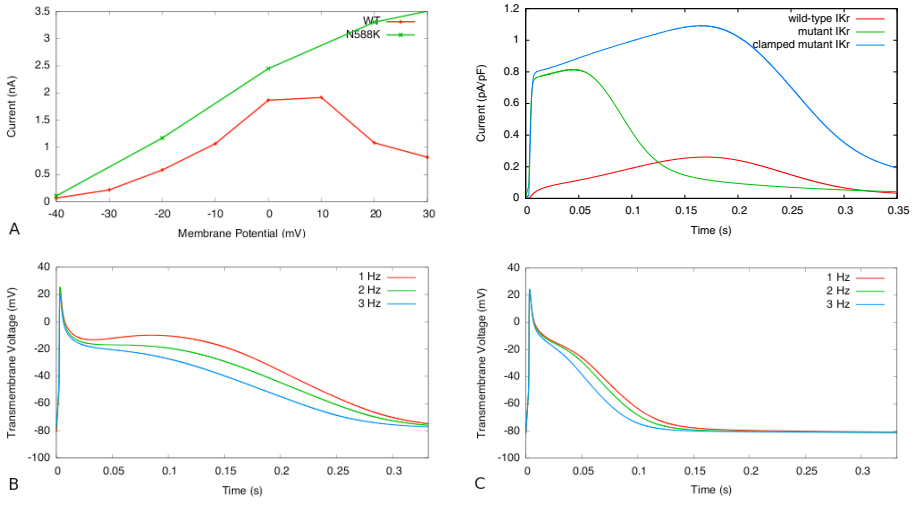

Fig. 1. (A) Steady state current-voltage relationship of the measured wild-type (red) and mutated (green) I_{Kr} channel. B: I_{Kr} for wild-type, N588K mutant and N588K mutant clamped to a wild-type action potential. The increase of I_{Kr} especially in the early phase is responsible for the shortening of the APD. Action potential of (C) physiological, and (D) mutant cells of the Courtemanche et al. model at different stimulation frequencies.

It is based on the gating concept of Hodgkin and Huxley [8]. The CRN model describes the changes of concentration and flow of ions, the kinetics of ion channels, the properties of intracellular proteins and the transmembrane voltage V_m. The equations were integrated using the Rush-Larsen scheme [9] with a time step of 20 μs. Action potential hetereogeneities of CT und PM were considered by using adapted electrophysiological parameters [7].

The monodomain model was used in order to represent the anisotropic electrical coupling of cardiomyocytes. This model calculates the intercellular current flow through the gap junctions and through the intracellular space based on Poisson's equation for stationary electrical fields:

$$\nabla \cdot (\sigma \nabla V_m) = \beta \left(C_m \frac{dV_m}{dt} + I_{mem} \right) - I_{si} \tag{1}$$

with the combined conductivity tensor σ, the membrane capacity C_m, the membrane surface to cell volume ratio β, the sum of the membrane currents I_{mem} and an externally applied current source I_{si}. The monodomain model was implemented with aid of the finite element method. For each time step of 20 μs the equation was solved.

AWM was set to isotropic, CT and PM to anisotropic conductivity. For CT and PM the anisotropy factor was adapted so that both anatomical structures presented physiological excitation velocity in longitudinal direction. The CT had an excitation velocity of 1.2 ms^{-1} and PM of 1.68 ms^{-1}. This fast longitudinal

direction was set parallel to the main axis of each CT and PM. The isotropic conductivity was set to 0.115 S/m for AWM. The transversal conductivity was set to 0.062 S/m for CT, and to 0.032 S/m for PM. The ratio for cross-axis to long-axis conductivity was set to 1:5 for CT and to 1:18 for PM.

The stimulus for the excitation conduction was set on the left side of the CT under the SCV, simulating the position of the sinus node. To investigate the predisposition for rotating waves, a S1–S2 protocol was used. During the refractory period of the first activation (S1), a second stimulus (S2) was positioned in a different place (10 mm towards the lower left corner of the model), where a part of the tissue was still refractory and the other excitable. This produced a unidirectional block in the excitation conduction.

2.3 Mutation Data and Model Adaptation

McPate et al. [6] recorded the mutant channel function by whole cell patch-clamping in hamster ovary cells. The current-voltage relationship was measured by a step protocol. Starting from $-80\,mV$ holding potential, $2\,s$ duration voltage steps were used up to $100\,mV$ in $10\,mV$ increments. The return pulse was $-60\,mV$. The mutated currents showed an inactivation at significant more positive voltages than the wild-type currents [6]. Note that in fig. 1 A the I-V-Relationship is only displayed up to 30 mV and the inactivation is not visible. The reduced plot was chosen since cells normally do not reach voltages larger than 30 mV. The inactivation at significant more positive voltages contributes to an increased repolarizing current earlier in the action potential.

Parameters of the CRN model were adjusted to the measured data using the Particle Swarm Optimization (PSO) [5]. For the wild-type model adjustment, only the maximum conductance of I_{Kr} was modified. This was necessary in order to define the ration between measured and model maximum conductance. When adjusting to the mutant data, all parameters of the ionic channel were modified by the PSO algorithm. The environmental conditions were adopted from the measurement conditions: Temperature was set to $37\,°C$ and intracellular potassium concentration was set to $4\,nM$.

3 Results

The simulations were performed in parallel on an Apple XServe with two 3 GHz Quad-Core Intel Xeon "Harpertown" processors. The simulation duration in the schematic geometrical model was approximately half an hour per second of electrophysiology. Each simulation was calculated for 20 s. The data shown in this work depict the 20^{th} beat.

3.1 Cell Simulations

The best fit of the mutant I_{Kr} to the measured data using PSO is given by:

$$I_{Kr} = \frac{g_{Kr} x_r (V_m - E_K)}{1 + exp\left(\frac{V_m + 33.13}{50.673}\right)}$$

$$x_{r(\infty)} = \left[1 + exp\left(-\frac{V_m + 0.00758}{16.93}\right)\right]^{-1}$$
$$\alpha_{x(r)} = 0.00177\frac{V_m + 0.09494}{1 - exp\left(-\frac{V_m - 0.09494}{1.4883}\right)}$$
$$\beta_{x(r)} = 7.3898 \cdot 10^{-5}\frac{V_m - 0.1346}{exp\left(\frac{V_m - 0.1346}{0.04446}\right)}$$

with a maximum conductance g_{Kr} of $0.3682\,nS/pF$, the gating variable x_r, the transmembrane voltage V_m, the Nernst potential of potassium E_K, the rate constants $\alpha_{x(r)}$ and $\beta_{x(r)}$, and the steady-state constant $x_{r(\infty)}$. These characteristics were integrated into the CRN model. The simulations showed that mutation N588K shifted inactivation of hERG towards more positive voltages, causing an increase of I_{Kr} (fig.1). This is especially visible in fig.1 B illustrating the increase in I_{Kr} in the early phase of the action potential. This results in a faster repolarization and thus to a shortening of the APD. The physiological and mutated action potentials (AP) for different frequencies are shown in fig.1 C and D. The APD_{90} of the mutant cell was reduced from $302\,ms$ to $116\,ms$ at $1\,Hz$. Both cell types showed a similar frequency adaptation.

3.2 Tissue Simulations

Since the mutation N588K caused a shortening of APD_{90} in single cell, a similar reduction of the ERP was expected. However, the ERP was only reduced from 317 ms in wild-type to 233 ms in mutant cells. As this reduction was smaller, the AP in the tissue was analyzed for both physiological and mutated case and compared to the AP of a single cell (fig.2). In the physiological case, the AP of single cell and tissue environment did not differ significantly. Only the maximum positive voltage during depolarization was decreased from $25\,mV$ to $3\,mV$ in tissue. This effect comes from the reduced upstroke velocity of the model in tissue due to electrotonic coupling. Exactly this has a significant effect in the

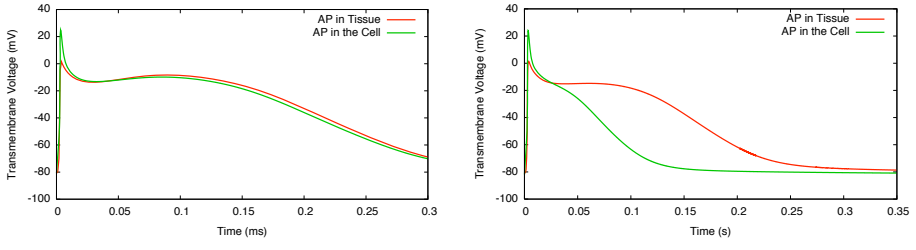

Fig. 2. Action potential in tissue of (left) physiological, and (right) N588K mutant cells of the Courtemanche et al. model. In contrast to the physiological case, the APD of the mutated case differs from the APD of the single-cell. The AP from the tissue simulation was extracted near the lower boundary of the atrial working myocardium during stimulation.

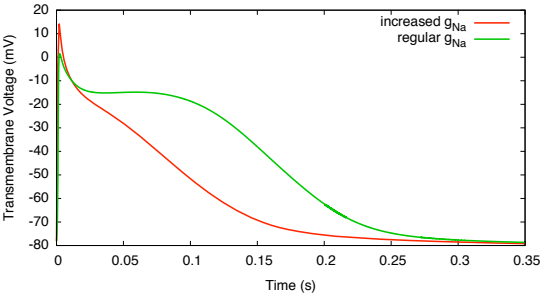

Fig. 3. AP in tissue of mutant cells with regular (green) and increased (red) Na^+ current conductivity. The larger overshoot resulting from the increase of G_{Na} caused a significant shortening of the tissue APD to 140 ms.

mutant cells since the I_{Kr} current is only significantly larger at voltages higher than $10\,mV$ compared to the physiological case. This consequently leads to a reduction of the mutant I_{Kr} in tissue and thus to a prolongation of the tissue APD of $220\,ms$ in contrast to single cell.

This behavior could result from the electrotonic interaction between cells. At negative voltages and up to 0 mV, the mutated and physiological hERG channel present similar characteristics (fig.1 A). The increase of mutated I_{Kr} is only significantly larger at voltages above +20 mV. Due to electrotonic coupling, the peak voltage in a multi-cell environment is approximately 0 mV, resulting in a smaller I_{Kr}. For that reason, the shortening of the APD in tissue is not as drastic as in a single-cell.

In order to further investigate this hypothesis, the Na^+ current conductivity G_{Na} was doubled. Fig. 3 depicts the results of this simulation. Since an increase of G_{Na} results in a larger overshoot, the mutated hERG channel could present the known effect from the single-cell, shortening drastically the APD. Hereby, an important characteristic of the mutation N588K becomes clear: it shows a dependence of the maximal voltage reached within depolarization.

The excitation propagation in the schematic model of the atrium is shown in fig.4. The CV was not modified by the mutation, only at basic cycle lengths (BCL) shorter than $200\,ms$. The main differences between wild-type and mutated case are visible in the repolarization propagation, and in the tissue APD.

Repolarization in the mutant model is faster than in the physiological one. This results in a decrease of the wavelength, which is defined as the product of ERP and CV (fig.5). The ERP describes the lowest time at which one premature beat can re-initiate an excitation. It was simulated by applying three beats with $1\,Hz$ and then a premature one. In the physiological case the ERP was $317\,ms$, whereas in the mutant model it was reduced to $233\,ms$. As ERP restitution simulations are very time consuming, we tested the ERP at 5 different frequencies. The ERP at these frequencies followed clearly the APD restitution shifted by approximately 15 ms (data not shown). Thus the APD restitution was used to calculate wavelength restitution (fig.5 C).

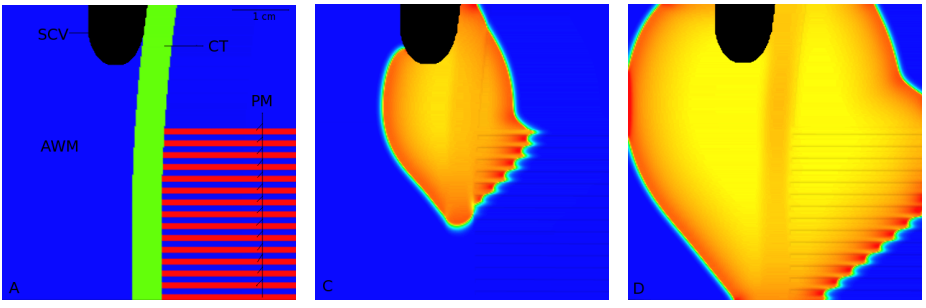

Fig. 4. (A) Schematic anatomical model of the rigth atrium. Excitation propagation during depolarization at (B) 15 ms, and (C) 30 ms after the stimulation. Red color indicates 10 mV, blue color $-80\,mV$.

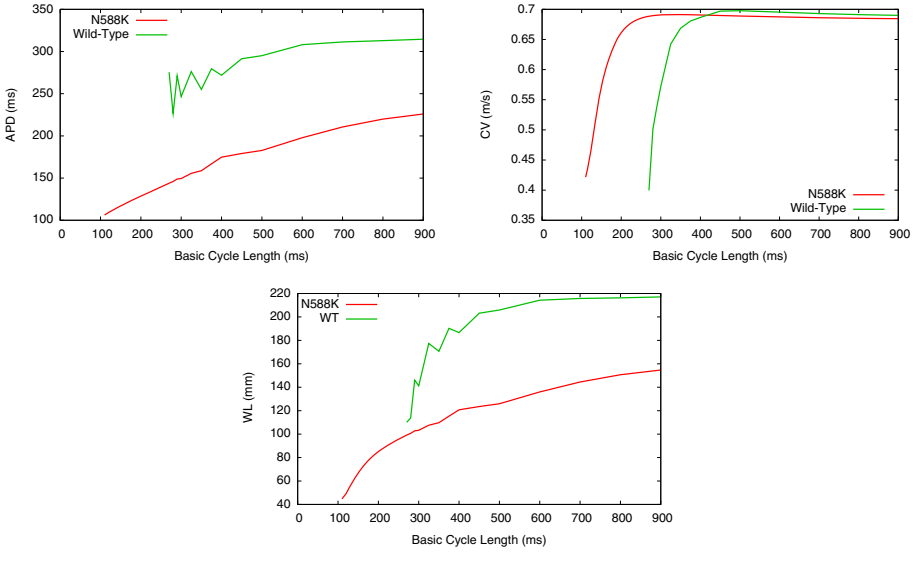

Fig. 5. Electrophysiological properties in tissue simulations depending on the BCL. (A) APD, (B) CV, (C) wavelength (WL). The wavelength is always shorter for the mutation than for wild-type.

The S1–S2 protocol was used to produced a unidirectional block in both the physiological and mutant model. In the physiological case, it was never possible to generate rotating waves with varying parameters like the size of S2 and its position (data not shown). Only in the mutant case the S1–S2 protocol led to a rotating wave (fig. 6). 135 ms after the normal stimulation (S1), a second impulse was set in a different place (S2) where a part of the tissue was refractory. The wave could propagate only in one direction, and rotated around the not excitable tissue generated by S2. The refractory period of these cells was shorter than the

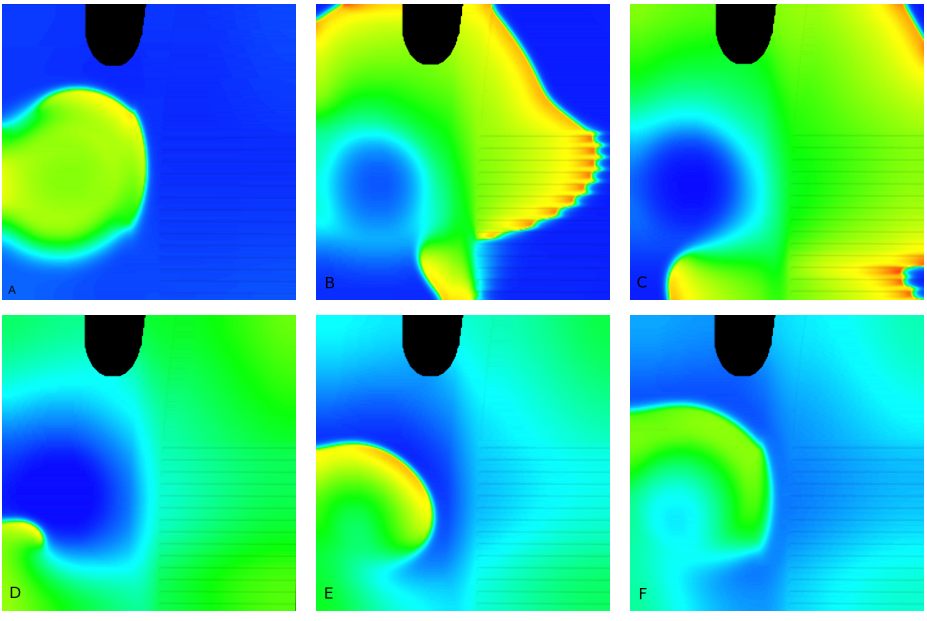

Fig. 6. Excitation propagation induced by a S1–S2 protocol. The wave can only propagate in one direction (A) and rotates around the not excitable tissue generated by S2 (B), (C). Before the wave returns to its starting point, the cells located there are no longer refractory. This leads to another propagating wave (D), (E). The re-entry dies as it encounters still refractoy tissue (F). Red indicates $10\,mV$, blue $-80\,mV$.

time that the wave needed to return to its starting point. As a result, new APs could be initiated, generating a new propagating wave. However, this new wave could not produce the same effects as the first one, as it soon encountered still refractory tissue and died out.

4 Discussion and Conclusion

The mutation N588K showed a gain of function effect of I_{Kr} caused by the shifted inactivation of hERG towards more positive voltages (fig. 1 B). In single cell, this resulted in a significant shortening of the APD to $116\,ms$. In tissue, although the effect is less, ERP is reduced by 84 ms. This factor is linked to a shortening of the wavelength, building a substrate for AF. However, our results also indicate that the behavior of the mutant channel in tissue differs from the one in a single-cell, as it depends on the maximum upstroke reached during depolarization leading to a less pronounced increase of the mutant I_{Kr} in tissue. This difference in I_{Kr} increase is due to the characteristic effect of mutation N588K on hERG channel. As shown in fig. 1, both physiological and mutant currents react in a similar way by negative voltages. The increase of I_{Kr} is significant only at more positive voltages. Due to the electrotonic coupling, the peak voltage in a multi-cell environment is $3\,mV$. As a result, mutated hERG channel does not have the

expected effect, resulting in a longer APD in tissue than in a single cell (fig. 2). This hypothesis was further supported by the experiment were the maximum conductance of I_{Na} was doubled and a reduction of the APD was observed.

Although the effect of the mutation in tissue is not as strong as in a single cell, it still differs from the physiological case, so that the predisposition for the cardiac arrhythmia is present. Furthermore, the ERP was also reduced in the tissue simulations, from 317 ms in physiological case to 233 ms in the pathological model at 1 Hz. Combined with the fact that the conduction velocity decreases by short BCL this effect builds a substrate for the initation and perpetuation of AF. As shown in the simulations, the effects of mutation N588K can produce rotating waves in contrast to the physiological case. It was never possible for the physiological case to generate a rotating wave since the wavelength was too long. This always led to the effect that the wave front was encountering still refractory tissue and died out.

The anatomical model used in this work was a schematic model of the human atrium. Factors like fiber orientation in the AWM and curvature, that play a very important role for the conduction velocity, were not considered. We expect that in a model including realistic curvature and obstacles, the conduction velocity will decrease, resulting in another shortening of the wavelength. By this way, the model could not only produce one rotating wave, but fluttery or fibrillation.

The effect of I_{Kr} significantly reducing the plateau phase might model dependent. Other human atrial models show a more triangular AP and have a more flat restitution curve. Therefore, the results generated in this work have to be investigated experimentally. Additionally, the predisposition to AF of the mutation might be overestimated with the CRN model because of its larger plateau phase compared to other model. Furthermore, the effect of the APD differences in single-cell and tissue has to be validated in a measurement study.

Other studies demonstrated in ventricular cells and tissue the effects of the mutation N588K [10,11]. Itoh et al. [10] showed that the mutation leads also to a APD reduction in ventricular cells but can also induce early after-depolarizations. Weiss and co-workers [11] illustrated the effects of N588K in a heterogeneous ventricular model. They showed that the mutation decreased the dispersion of repolarization in heterogeneous tissue. Therefore, the transmural ECG showed a shortened QT interval. This work is the first time that the effect f N588K was investigated in atrial tissue.

In a future work, we will transfer these findings into a complete anatomical model of the atria [7], in order to investigate the effects of this mutation in AF. Furthermore, this model can than be used to investigate specific treatments for patients suffering from this mutation. This includes the development of specific drugs or adapted radio frequency ablation strategies.

Acknowledgement

This research has received funding from the European Community's Seventh Framework Programme (FP7/2007-2013) under grant agreement n° 224495 (euHeart project).

References

1. Nattel, S.: New ideas about atrial fibrillation 50 years on. Nature 415, 219–226 (2002)
2. Schimpf, R., Wolpert, C., Gaita, F., Giustetto, C., Borggrefe, M.: Short QT syndrome. Cardiovasc. Res. 67(3), 357–366 (2005)
3. Cordeiro, J., Brugada, R., Wu, Y., Hong, K., Dumaine, R.: Modulation of I(Kr) inactivation by mutation N588K in KCNH2: a link to arrhythmogenesis in short QT syndrome. Cardiovascular Research 67, 498–509 (2005)
4. Courtemanche, M., Ramirez, R., Nattel, S.: Ionic mechanisms underlying human atrial action potential properties: Insights from a mathematical model. Am. J. Physiol. 275, 301 (1998)
5. Seemann, G., Lurz, S., Keller, D., Weiss, D., Scholz, E., Dössel, O.: Adaption of mathematical ion channel models to measured data using the particle swarm optimization. In: IFMBE Proceedings, vol. 22, pp. 2507–2510 (2008)
6. McPate, M., Duncan, R., Milnes, J., Witchel, H., Hancox, J.: The N588K-HERG K+ channel mutation in the 'short QT syndrome': mechanism of gain-in-function determined at 37 degrees C. Biochemical and Biophysical Research Communications 334, 441–449 (2005)
7. Seemann, G., Höper, C., Sachse, F., Dössel, O., Holden, A., Zhang, H.: Heterogeneous three-dimensional anatomical and electrophysiological model of human atria. Phil. Trans. Roy. Soc. A 364, 1465–1481 (2006)
8. Hodgkin, A.L., Huxley, A.F.: A quantitative description of membrane current and its application to conduction and excitation in nerve. J. Physiol. 177, 500–544 (1952)
9. Rush, S., Larsen, H.: A practical algorithm for solving dynamic membrane equations. IEEE Trans. Biomed. Eng. 25(4), 389–392 (1978)
10. Itoh, H., Horie, M., Ito, M., Imoto, K.: Arrhythmogenesis in the short-qt syndrome associated with combined herg channel gating defects: A simulation study. Circulation Journal 70(4), 502–508 (2006)
11. Weiss, D.L., Seemann, G., Sachse, F.B., Dössel, O.: Modelling of the short QT syndrome in a heterogeneous model of the human ventricular wall. Europace 7S2, 105–117 (2005)

Left to Right Atrial Electrophysiological Differences: Substrate for a Dominant Reentrant Source during Atrial Fibrillation

Oleg V. Aslanidi, Mark R. Boyett, and Henggui Zhang

University of Manchester, Manchester, UK
{oleg.aslanidi,mark.boyett,henggui.zhang}@manchester.ac.uk

Abstract. Experimentally observed differences in the action potential (AP) properties – primarily, refractoriness – between the left (LA) and right (RA) atria are believed to be important in maintaining atrial fibrillation. We incorporate AP models for single LA and RA cells into 2D atrial tissue models and study the role of tissue heterogeneity in global interaction between reentrant spiral waves in the LA and RA. Our simulations show that shorter refractoriness in the LA translates into a shorter period of spiral rotation, and as a result, reentry in the LA dominates the overall excitation patterns in the atria.

Keywords: Atrial heterogeneity, atrial fibrillation, spiral waves.

1 Introduction

Atrial fibrillation (AF) is the most common sustained cardiac arrhythmia seen in clinical practice, as well as the major cause of stroke [1,2,3]. Several lines of evidence point to a particularly important role of the left atrium (LA) in maintaining AF. Primarily, activation patterns mapped in isolated animal tissues [4,5] or patients [6] have revealed regular and repetitive activation in the LA, whereas activation in the RA was complex and chaotic [5,6]. Hence, it has been suggested that the LA contains "driver" regions acting as localized high-frequency excitation sources during AF.

Tissue refractoriness in the LA is shorter than in the RA [7,8,9], which can provide a potential explanation for the driving role of the LA. AF is widely associated with reentrant electrical activity in the heart [2,3], whereas the period of a reentrant spiral wave rotation is proportional to the refractoriness. If spiral waves in a heterogeneous excitable medium (such as atrial tissue) have different rotation periods, the boundary between their domains of influence will move away from the faster spiral towards the slower one [10]. As a result, the slower spiral can eventually be pushed out of the medium [11]. Shorter refractoriness in the LA means shorter period (i.e., higher frequency) of rotation than in the RA – hence, reentry in the LA should dominate the overall excitation patterns in the atria and become the high-frequency engine that maintains AF.

N. Ayache, H. Delingette, and M. Sermesant (Eds.): FIMH 2009, LNCS 5528, pp. 154–161, 2009.
© Springer-Verlag Berlin Heidelberg 2009

Relationships between atrial electrical heterogeneity and interactions of reentrant activation sources are difficult to dissect experimentally. Biophysically detailed computational models have been successfully used to dissect mechanisms of complex cardiac dynamics observed in experiments [11,12,13]. Thus, reentrant sources with the highest frequency have been shown to dominate electrical activation patterns within cardiac tissues with artificial frequency gradients [11]. However, natural interatrial heterogeneity has not been considered, whereas interactions of electrical waves with intra-atrial heterogeneities have been studied only in the context of local reentry initiation [14] and maintenance [15].

In this work we construct and study computer models accounting for well-known electrophysiological differences between the LA and RA [7,8,9], as well as within the RA [16,17,18]. AP models for single LA and RA cells [19,20] are incorporated into 2D tissue models, which are used for simulating reentrant waves and investigate the role of atrial tissue heterogeneity in global interactions between spirals in the LA and RA.

2 Methods

The dynamics of electrical processes in cardiac tissues are commonly described by the following partial differential equation (PDE) [11,12,13,19]:

$$\frac{\partial V}{\partial t} = D\left(\frac{\partial^2 V}{\partial x^2} + \frac{\partial^2 V}{\partial y^2}\right) - C_m^{-1} I_{ion}. \tag{1}$$

Here V (mV) is the membrane potential, t – time (s), D – diffusion coefficient (mm^2 ms^{-1}) that characterizes electrotonic spread of voltage via gap junctional coupling, I_{ion} – the total ionic current (pA), and C_m (pF) – the membrane capacitance. Biophysically detailed models describing individual membrane ionic currents comprising I_{ion} have been developed for rabbit atrial cells [19,20]. They accurately reproduce action potential (AP) morphologies for rabbit LA and RA myocytes (Fig. 1), as well as AP differences between the crista terminalis and pectinate muscle (PM) cells within the rabbit RA [20]. The single cell models were incorporated into 2D tissue models for the rabbit LA and RA (see below in Fig. 2), which were used in order to simulate reentrant spiral waves initiated in both atria using the standard cross-field method [13].

Equation (1) was solved for the respective 30 × 30 mm^2 LA and RA tissues using a finite-difference PDE solver based on the explicit Euler method with time and space steps $\Delta t = 0.01$ ms and $\Delta x = 0.1$ mm. The diffusion coefficient was set to the value $D = 5$ mm^2 ms^{-1}, which produced the planar AP conduction velocity of ∼0.5 m/s, as seen in experiments [21]. Computer code implementing the PDE solver was parallelized under MPI and executed on the IBM BlueGene supercomputer (Edinburgh, UK). A single run of the code simulating 1 s of activity on 128 CPUs took ∼6 hours.

3 Results

Fig. 1 shows APs simulated using the LA and RA models [19], as compared to the respective experimental recordings [7]. AP morphologies are in a very good agreement with experimental data. In LA, the AP duration (APD) is shorter and the plateau is lower than in RA – but these differences are eliminated when I_{to} in the models is completely blocked, which reproduces experimentally observed effects of 4-AP, a selective I_{to} blocker, in rabbit LA and RA [7].

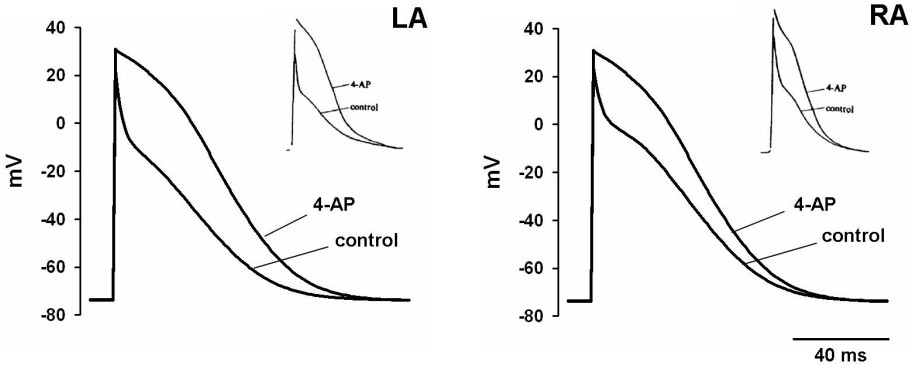

Fig. 1. Electrophysiological differences between the LA and RA. Simulated APs in the LA and RA cell models are shown in control and after 4-AP blocking of I_{to}. Insets present respective experimental recordings [7]. Pacing cycle length (CL) is 500 ms. The APD in the LA cell is 79.7 ms against 82.1 ms in the RA cell.

Fig. 2 shows initiation of reentrant spiral waves in the LA and RA tissues. The spirals arise from forced wave-breaks of the respective plane waves (i.e., propagating APs). Two resultant counter-rotating spirals in the LA and RA are shown in Fig. 3. Although both waves have developed from similar initial conditions and using similar protocols (Fig. 2), their rotation pattern is not symmetrical due to the AP differences between the LA and RA (Fig. 1). The spiral in the LA tissue (which is characterized by a shorter AP) rotates faster than that in the RA, reaching the interatrial connection first and invading into the RA. Waves from the LA reach the interatrial connection faster and faster with each period of rotation, and as a result, the boundary between domains of influence of the two spirals moves deeper into the RA (Fig. 4).

Hence, electrical patterns in the LA and RA become quite different after only several hundred ms of activity. There is a single reentrant source in the LA, whereas the patterns in the RA is more complex: apart from the reentrant wave, there is a second wave source at the interatrial junction (Fig. 4); besides waveforms emitted by both sources are more irregular that in the LA due to the intrinsic heterogeneity of the RA (Fig. 2). This is consistent with activation patterns mapped in isolated animal tissues [5] or patients [6] during AF.

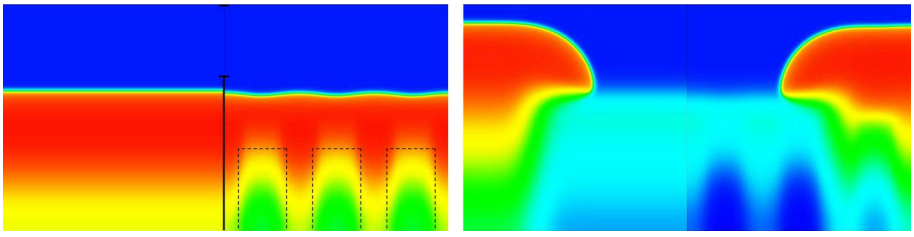

Fig. 2. Reentry initiation in the LA and RA. Plane waves are initiated simultaneously in both atria and move along the interatrial border (bottom to top in the left panel) before a phase-break is created after 30 ms, resulting in generation of two counter-rotating spirals (right panel). Here and in Figs. 3 and 4, left half of each panel is LA tissue, right half – RA tissue. Voltage distributions in the tissues are shown using the standard rainbow palette. Solid black line in the middle shows a zero-flux boundary between the atria, which corresponds to the atrial septum. Short horizontal dashes outline the interatrial connection, which corresponds to the Bachman bundle in real atria. Dotted lines indicate locations of PMs within the RA. Note that the AP in PM cells is shorter than in the rest of the RA, ∼50 ms against 82 ms at CL of 500 ms.

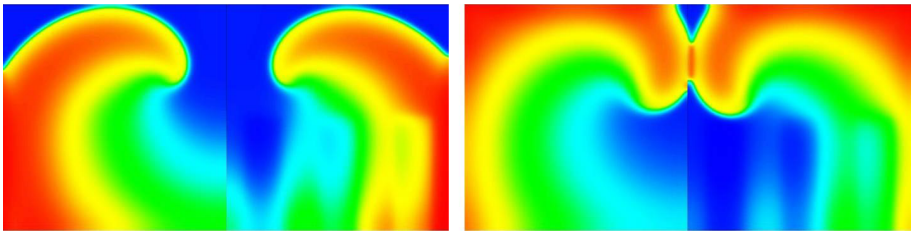

Fig. 3. Differences in spiral wave rotation between the LA and RA. Fully developed after 50 ms of movement, spirals in the LA and RA rotate with a different period (due to the differential AP morphologies – primarily, the refractoriness in these two tissues – see below). As a result, the spiral in the LA reaches the interatrial connection faster and invades into the RA (top middle of the right panel).

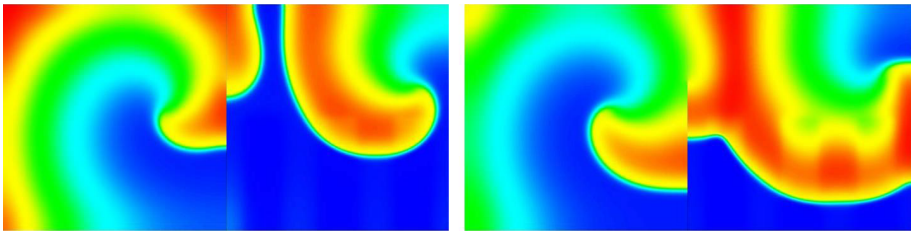

Fig. 4. Differential electrical activation patterns in the LA and RA. After 150 ms of spiral rotation in both atria, the boundary between their domains of influence moves away from the faster spiral in the LA into the RA. As a result, LA has a single spiral wave source, whereas the activation pattern within the RA is more complex. Similar patterns has been observed in experimental recordings during AF [5,6].

Electrophysiological mechanisms of faster reentrant rotation in the LA are illustrated in Fig. 5. Cellular AP restitution curves show that the APD is shorter in the LA for all rates. Hence, the refractory period – which is correlated to the APD, primarily in atrial cells [19,20] – is proportionally shorter in the LA. This difference translates into the respective difference in the reentry rotation period (normally, a reentrant spiral tries to occupy all non-refractory tissue), which is also shorter in the LA than in the RA (Fig. 5). Note that such differences hold for both homogeneous (no PM cells) and heterogeneous RA.

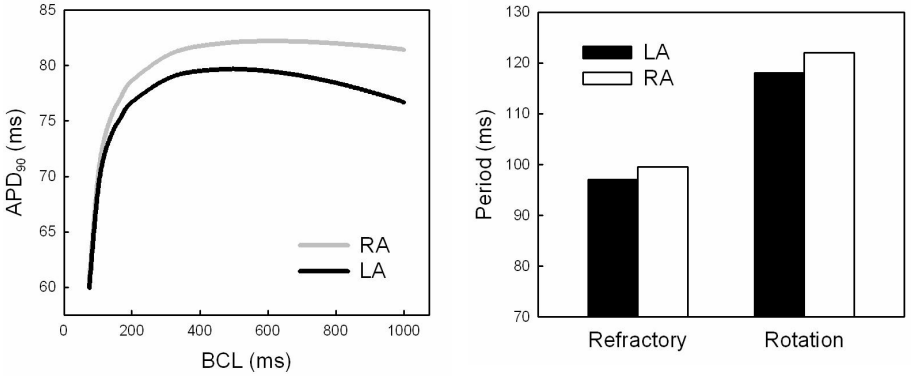

Fig. 5. Mechanisms of differential reentrant patterns in the LA and RA. Full AP restitution curves for the LA and RA cell models (left), and computed refractory periods and reentry rotation periods for the LA and RA tissues (right) are shown. The refractory period was defined as the longest S1-S2 interval that failed to initiate AP propagation [13,19] after periodic pacing of the tissue at CL of 200 ms.

4 Discussion

Despite many years of research and speculation, the mechanisms underlying maintenance of AF are poorly understood. Over the past 50 years, the multiple wavelet hypothesis has been the dominant mechanistic model of AF [1,2,3]. The hypothesis, first postulated by Moe et al. [22], states that AF is the result of randomly propagating multiple electrical wavelets that interact in very complex ways, with local excitation limited by the heterogeneous distribution of refractory periods throughout the atria. Optical mapping studies in isolated sheep hearts [5] have suggested that at least some cases of AF can be maintained by high-frequency reentrant spiral waves (rotors), usually located in the posterior LA, which result in spatially distributed frequency gradients. According to the so-called rotor hypothesis [2,3], rapidly succeeding wavefronts emanating from an ectopic focus (which is often localized near the pulmonary vein [23]) may break when conditions of heterogeneity are appropriate, and initiate two counter-rotating rotors. Eventually, only one of the rotors survives and becomes the high frequency engine that maintains AF through fibrillatory conduction to the remainder of the atria.

Thus, our study provides support to one of the most recognized theories in the rapidly evolving field of AF studies – the rotor hypothesis. Our 2D model, although geometrically simple, nevertheless captures one of the most essential and recognized features of the atria – electrophysiological heterogeneity between the LA and RA. Simulations with the model show how shorter refractoriness in the LA tissue translates into a shorter period of reentrant rotation, making reentry in the LA the dominant high-frequency wave source. Intuitive mechanisms of the role of LA to RA heterogeneity in the development of a dominant rotor have been postulated, but never properly elucidated. Our study for the first time clearly illustrates such mechanisms and quantifies the way APD differences between LA and RA generate a rotor with the dominant frequency.

Note that several essential features of atrial geometry and electrophysiology are not included in our 2D model. First, the model does not consider 3D depth of the tissue and its anisotropic bundle structure. Recent studies [20,24] have demonstrated that fibre orientation and electrical activation patterns show very little change through the depth of thin ($\sim$1 mm) atrial tissue in rabbit – however, the bundle structure is important in reentry initiation and maintenance mechanisms. Second, our model uses only few cell types (LA, RA and PM), whereas the real atria are much more heterogeneous. Various anatomical structures, such as the sinoatrial node, crista terminalis, pulmonary vein, Bachmann bundle and other interatrial connections [25,26] are not included in the current model, but may also play an important role in initiation and maintenance of AF.

Including detailed 3D geometry, electrophysiology and bundle structure of the atria is the ultimate aim in development of atrial tissue models. Such a model has been developed for human atria [27], although interatrial heterogeneity (and hence, dominant frequency) has not been considered. Our recent study [20] has developed an electrophysiologically and geometrically detailed 3D model of rabbit right atrial tissue, which included bundles of crista terminalis and pertinate muscles. Electrophysiological models of interatrial bundles has also been developed in our group recently (not published), and diffusion tensor MRI experiments aimed at reconstructing geometry of rabbit atria are in progress. The next step of our model development will be to include the detailed 3D anatomy and electrophysiology of these tissues.

Acknowledgments. This work was supported by a project grant from the Biotechnology and Biological Sciences Research Council (BBS/B/1678X).

References

1. Nattel, S., Li, D., Yue, L.: Basic mechanisms of atrial fibrillation – very new insights into very old ideas. Ann. Rev. Physiol. 62, 51–77 (2000)
2. Jalife, J., Berenfeld, O., Mansour, M.: Mother rotors and fibrillatory conduction: a mechanism of atrial fibrillation. Cardiovasc. Res. 54, 204–216 (2002)
3. Atienza, F., Jalife, J.: Reentry and atrial fibrillation. Heart Rhythm 4, S13–S16 (2007)

4. Roithinger, F.X., Steiner, P.R., Goseki, Y., Sparks, P.B., Lesh, M.D.: Electrophysiologic effects of selective right versus left atrial linear lesions in a canine model of chronic atrial fibrillation. J. Cardiovasc. Electrophysiol. 10, 1564–1574 (1999)
5. Mandapati, R., Skanes, A., Chen, J., Berenfeld, O., Jalife, J.: Stable microreentrant sources as a mechanism of atrial fibrillation in the isolated sheep heart. Circulation 101, 194–199 (2000)
6. Harada, A., Sasaki, K., Fukushima, T., Ikeshita, M., Asano, T., Yamauchi, S., Tanaka, S., Shoji, T.: Atrial activation during chronic atrial fibrillation in patients with isolated mitral valve disease. Ann. Thorac. Surg. 61, 104–111 (1996)
7. Qi, A., Yeung, J.A., Xiao, J., Kerr, C.R.: Regional differences in rabbit atrial repolarization: importance of transient outward current. Am. J. Physiol. 266, H643–H649 (1994)
8. Sih, H.J., Berbari, E.J., Zipes, D.P.: Epicardial maps of atrial fibrillation after linear ablation lesions. J. Cardiovasc. Electrophysiol. 8, 1046–1054 (1997)
9. Li, D., Zhang, L., Kneller, J., Nattel, S.: Potential ionic mechanism for repolarization differences between canine right and left atrium. Circ. Res. 88, 1168–1175 (2001)
10. Krinsky, V.I., Agladze, K.I.: Interaction of rotating waves in an active chemical medium. Physica D 8, 50–56 (1983)
11. Xie, F., Qu, Z., Weiss, J.N., Garfinkel, A.: Interactions between stable spiral waves with different frequencies in cardiac tissue. Phys. Rev. E 59, 2203–2206 (1999)
12. Gray, R.A., Pertsov, A.M., Jalife, J.: Spatial and temporal organization during cardiac fibrillation. Nature 392, 75–78 (1998)
13. Benson, A.P.,, Aslanidi, O.V., Zhang, H., Holden, A.V.: The canine virtual ventricles: a platform for dissecting pharmacological effects on propagating and arrhythmogenesis. Prog. Biophys. Mol. Biol. 96, 187–208 (2008)
14. Sampson, K.J., Henriquez, C.S.: Interplay of ionic and structural heterogeneity on functional action potential duration gradients: Implications for arrhythmogenesis. Chaos 12, 819–828 (2002)
15. Kuo, S.R., Trayanova, N.A.: Action potential morphology heterogeneity in the atrium and its effect on atrial reentry: a two-dimensional and quasi-three-dimensional study. Phil. Trans. A 364, 1349–1366 (2006)
16. Spach, M.S., Dolber, P.C., Heidlage, J.F.: Interaction of inhomogeneities of repolarization with anisotropic propagation in dog atria: a mechanism for both preventing and initiating reentry. Circ. Res. 65, 1612–1631 (1989)
17. Yamashita, T., Inoue, H., Nozaki, A., Sugimoto, T.: Role of anatomical architecture in sustained atrial reentry and double potentials. Am. Heart J. 124, 938–946 (1992)
18. Feng, J., Yue, L., Wang, Z., Nattel, S.: Ionic mechanisms of regional action potential heterogeneity in the canine right atrium. Circ. Res. 83, 541–551 (1998)
19. Aslanidi, O.V., Dewey, R.S., Morgan, A.R., Boyett, M.R., Zhang, H.: Regional differences in rabbit atrial action potential properties: Mechanisms, consequences and pharmacological implications. In: Conf. Proc. IEEE Eng. Med. Biol. Soc., vol. 1, pp. 141–144 (2008)
20. Aslanidi, O.V., Boyett, M.R., Dobrzynski, H., Li, J., Zhang, H.: Mechanisms of transition from normal to reentrant electrical activity in a model of rabbit atrial tissue: Interaction of tissue heterogeneity and anisotropy. Biophys. J. 96, 798–817 (2009)
21. de Groot, J.R., Veenstra, T., Verkerk, A.O., Wilders, R., Smits, J.P.P., Wilms-Schopman, F.J.G., Wiegerinck, R.F., Bourier, J., Belterman, C.N.W., Coronel, R., Verheijck, E.E.: Conduction slowing by the gap junctional uncoupler carbenoxolone. Cardiovasc. Res. 60, 288–297 (2003)

22. Moe, G.K., Abildskov, J.A.: Atrial fibrillation as a self-sustaining arrhythmia independent of focal discharges. Am. Heart J. 58, 59–70 (1959)
23. Haissaguerre, M., Jais, P., Shah, D.C., Takahashi, A., Hocini, M., Quiniou, G., Garrigue, S., Le Mouroux, A., Le Metayer, P., Clementy, J.: Spontaneous initiation of atrial fibrillation by ectopic beats originating in the pulmonary veins. N. Engl. J. Med. 339, 656–659 (1998)
24. Dobrzynski, H., Li, J., Tellez, J., Greener, I.D., Nikolski, V.P., Wright, S.E., Parson, S.H., Jones, S.A., Lancaster, M.K., Yamamoto, M., Honjo, H., Takagishi, Y., Kodama, I., Efimov, I.R., Billeter, R., Boyett, M.R.: Computer three-dimensional reconstruction of the sinoatrial node. Circulation 111, 846–854 (2005)
25. Sakamoto, S., Nitta, T., Ishii, Y., Miyagi, Y., Ohmori, H., Shimizu, K.: Interatrial electrical connections: the precise location and preferential conduction. J. Cardiovasc. Electrophysiol. 16, 1077–1086 (2005)
26. Platonov, P.G.: Interatrial conduction in the mechanisms of atrial fibrillation: from anatomy to cardiac signals and new treatment modalities. Europace 9, 10–16 (2007)
27. Seemann, G., Hoper, C., Sachse, F.B., Dossel, O., Holden, A.V., Zhang, H.: Heterogeneous three-dimensional anatomical and electrophysiological model of human atria. Phil. Trans. Roy. Soc. A 364, 1465–1481 (2006)

Electrocardiographic Simulation on Coupled Meshfree-BEM Platform

Linwei Wang[1], Ken C.L. Wong[1], Heye Zhang[2], and Pengcheng Shi[1]

[1] Computational Biomedicine Laboratory
Rochester Institute of Technology, Rochester, NY, USA
maomaowlw@mail.rit.edu
[2] Bioengineering Institute, University of Auckland, Auckland, New Zealand

Abstract. The foremost premise for the success of noninvasive volumetric myocardial transmembrane (TMP) imaging from body surface potential (BSP) recordings is a realistic yet efficient electrocardiographic model which relates volumetric myocardial TMP distribution to BSP distribution. With a view towards this inverse problem, the heart-torso representation and the associated TMP-to-BSP model should balance the accuracy of the model with the feasibility of TMP reconstruction. We present a novel coupled meshfree-BEM platform to this TMP-to-BSP modeling and perform electrocardiographic simulations of various cardiac conditions on personalized heart-torso structures. Simulated QRS integral maps, BSPMs and ECG leads are consistent with existent experimental studies, verifying the plausibility of the presented platform.

1 Introduction

Noninvasive imaging of volumetric myocardial transmembrane potential (TMP) dynamics aims at quantitative reconstructions of TMP dynamics inside the heart from body surface potential (BSP) sequence. The foremost premise for its success is a forward electrocardiographic model which links volumetric myocardial TMP distribution with BSP distribution. With a view towards the inverse problem of TMP reconstruction, this TMP-to-BSP model and the associated representation of the underlying heart-torso structures should emphasize the balance between the accuracy of the models with the feasibility of TMP reconstruction.

The common description of TMP-to-BSP mapping is based on the biodomain theory, where any point in the myocardium is considered to be in either the intra- or extra-cellular space [1]. Usually it is reduced to a boundary element (BE) formulation by ignoring the conductive anisotropy and inhomogeneity in both spaces [2]. As a result, it considers only TMP activity on heart surfaces. By considering the electrical anisotropy in both spaces, the finite element (FE) formulation is able to investigate volumetric electrical conduction within the myocardial mass [3]. Meanwhile it increases the problem size by considering extracellular potential in the myocardium.

This paper presents a coupled meshfree-BEM platform for TMP-to-BSP modeling to combine the advantage of BEM- and FEM-based approaches. To investigate the volumetric myocardial TMP dynamics, meshfree points are used to

N. Ayache, H. Delingette, and M. Sermesant (Eds.): FIMH 2009, LNCS 5528, pp. 162–171, 2009.
© Springer-Verlag Berlin Heidelberg 2009

detail the anatomical structure, as well as the anisotropy and heterogeneity, of the 3D myocardium. Meanwhile, to emphasize the accuracy of geometrical modeling and relax unnecessary restrictions on conductivie anisotropy or inhomogeneity of different torso tissues, we assume the torso as an isotropic and homogeneous volume conductor, represented with boundary elements on the body surface. By emphasizing the anisotropy for active current conduction but neglecting that for passive currents, this approach allows the investigation of volumetric TMP inside the myocardium while discarding irrelevant variables to reduce model complexity.

The accuracy and convergency of this approach has been verified by analytical solutions on a synthetic geometry of two concentric spheres [4]. In this paper, electrocardiographic simulations of normal cardiac conditions, ventricular pacing, bundle branch blocks (BBB) and myocardial infarction are carried out on personalized heart-torso structures. Simulated BSP map sequences, QRS integral (QRSI) maps and 12 ECG leads are compared to existent experimental studies, demonstrating the plausibility of the presented coupled meshfree-BEM platform in TMP reconstruction.

2 Methods

2.1 Personalized Heart-Torso Structures

After segmenting the short-axis cardiac MRI slice by slice and building a smoothed mesh for the heart surfaces, the 3D heart wall is represented by a cloud of points (meshfree points) inside the surface mesh. Myocardial conductive anisotropy is considered by mapping volumetric fiber structures from the fibrous structure of the canine heart in [5]. Heterogeneity of TMP shapes in the epi-, endo- and midmyocardial regions [6] is also taken into account. For a flexible control on the simulation of various cardiac conditions, the LV wall is divided into 17 segments by AHA consensus [7]. Because the torso geometry is the primary factor affecting TMP-to-BSP relationship [8], the volume conductor of torso is assumed as isotropic and homogeneous. It is described by triangulated body surface, obtained by deforming a reference torso model to match patient's image data [9].

2.2 Volumetric TMP Dynamics

Myocardial TMP dynamics is described by the 2-variable diffusion-reaction system from [10]:

$$\begin{cases} \frac{\partial u}{\partial t} = \nabla \cdot (\mathbf{D}\nabla u) + ku(u-a)(1-u) - uv \\ \frac{\partial v}{\partial t} = -e(v + ku(u-a-1)) \end{cases} \tag{1}$$

where u stands for TMP and v for recovery current. $\mathbf{D}$ is the diffusion tensor and $\nabla \cdot (\mathbf{D}\nabla u)$ accounts for the electrical propagation. Parameters e, k and a determine individual TMP shapes.

2.3 TMP-to-BSP Mapping

Potential distribution within the torso is described by the quasi-static approximation of Maxwell's equations [11]. Within the myocardium volume Ω_h, the bidomain theory [1] defines the distribution of extracellular potentials ϕ_e as a result of the gradients of TMP:

$$\nabla\cdot((\mathbf{D}_i(\mathbf{r})+\mathbf{D}_e(\mathbf{r}))\nabla\phi_e(\mathbf{r})) = \nabla\cdot(\mathbf{D}_k(\mathbf{r})\nabla\phi_e(\mathbf{r})) = \nabla\cdot(-\mathbf{D}_i(\mathbf{r})\nabla u(\mathbf{r})) \quad \forall\mathbf{r}\in\Omega_h \tag{2}$$

where $\mathbf{r}$ stands for the spatial coordinate. $\mathbf{D}_i$ and $\mathbf{D}_e$ are the effective intracellular and extracellular conductivity tensor, and their summations $\mathbf{D}_k$ is termed as the bulk conductivity tensor. In the region $\Omega_{t/h}$ bounded by the heart surfaces and body surface, potentials ϕ_t are calculated assuming that no other active electrical source exists within the torso:

$$\nabla\cdot(\mathbf{D}_t(\mathbf{r})\nabla\phi_t(\mathbf{r})) = 0 \qquad \forall\mathbf{r}\in\Omega_{t/h} \tag{3}$$

where $\mathbf{D}_t$ is torso conductivity tensor.

Because the anisotropic ratio of $\mathbf{D}_k$ is a magnitude smaller than that of $\mathbf{D}_i$, we only retain the anisotropy of $\mathbf{D}_i$ to reduce model complexity. Regarding the tissue inhomogeneity, we have justified the validity of the homogeneous torso model in TMP reconstruction [4]. Accordingly, (2, 3) is simplified into a single Poisson equation describing potential distribution $\phi(\mathbf{r})$ within the homogeneous volume conductor Ω_t:

$$\sigma\nabla^2\phi(\mathbf{r})) = \nabla\cdot(-\mathbf{D}_i(\mathbf{r})\nabla u(\mathbf{r})) \quad \forall\mathbf{r}\in\Omega_t \tag{4}$$

and it is assumed that no current leaves the body surface Γ_t: $\frac{\partial\phi_t(\mathbf{r})}{\partial\boldsymbol{n}} = 0, \forall\mathbf{r}\in\Gamma_t$.

By the *direct method* solution in BEM [12], (4) is reformulated into:

$$\begin{aligned} c(\xi)\phi(\xi) + \int_{\Gamma_t}\phi(\mathbf{r})q^*(\xi,\mathbf{r})\,\mathrm{d}\Gamma_t - \int_{\Gamma_t}(\frac{\partial\phi(\mathbf{r})}{\partial\boldsymbol{n}})\phi^*(\xi,\mathbf{r})\,\mathrm{d}\Gamma_t \\ = \int_{\Omega_t}\frac{(\nabla\cdot(\mathbf{D}_i\nabla u(\mathbf{r})))\phi^*(\xi,\mathbf{r})}{\sigma}\,\mathrm{d}\Omega_t \end{aligned} \tag{5}$$

where $c(\xi)$ is determined by surface smoothness of any point ξ on Γ_t. $\boldsymbol{n}$ is the outward normal vector of boundary surfaces. $\phi^*(\xi,\mathbf{r})$ and $q^*(\xi,\mathbf{r})$ are the so-called fundamental solution and its normal derivative [12].

The volume integral on the right hand side (rhs) of (5) is commonly approximated as a summarization of several current dipoles [13]. Instead, we introduce meshfree approximation based on moving least squares (MLS) [14] into (5) for a simpler yet more direct calculation of the volume integral. It is shown in [13] that in most cases, MLS methods are identical to kernel methods and may serve as a partition of unity. Further applying the BEM [12] to the boundary integral in (5) [4], we obtain the linear relationship between volumetric TMP and BSP:

$$\mathbf{\Phi} = \mathbf{HU} \tag{6}$$

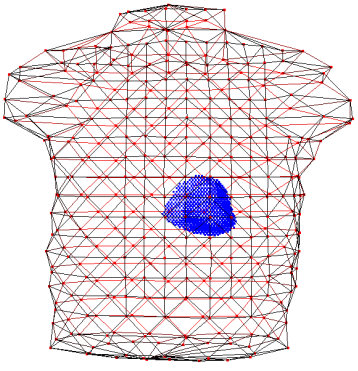

Fig. 1. Personalized heart-torso structure on coupled meshfree-BEM representation, where the ventricles are represented with a cloud of 3999 meshfree points and the torso by triangulated body surface with 370 vertices

where $\mathbf{U}$ consists of u from all meshfree points inside the myocardium and $\mathbf{\Phi}$ contains ϕ from all vertices on the body surface.

When (2) is reduced to a BE formulation [2], the conductive anisotropy and inhomogeneity in both intra- and extra-cellular spaces are ignored, and therefore only TMP activity on heart surfaces are considered. On the other side, the FE formulation considers the conductive anisotropy in both space and therefore allows the investigation of volumetric electrical conduction within the myocardial mass [3]. However, it increases the problem size by considering extracellular potentials in the 3D myocardium. This approach combines the advantages of previous BE- and FE-based efforts by emphasizing the electrical anisotropy for active current conduction but neglecting that for passive currents. It is able to study TMP activity inside the 3D myocardium and preserves the primary factors to TMP-to-BSP modeling, including 3D anisotropic heart structures and relative heart-torso positions. Meanwhile, it avoids excessive variables and focus only on TMP and BSP, the two vectors of direct interest to TMP reconstruction.

3 Results

Electrocardiographic simulations of normal cardiac conditions, ventricular pacing, BBB and MI are performed on personalized heart-torso structures. The cardiac MRIs provided by [15] contain 9 slices from apex to base, with 8mm inter-slice spacing and 1.33mm/pixel in-plane resolution. Anatomical locations of 123 electrodes on the body surface are also available. Fig 1 (b) illustrates this personalized combined heart-torso model, where the torso is represented by triangulated body surface with 736 elements and 370 vertices, and the 3D ventricular mass by 3339 meshfree points with detailed fiber structure. Simulated BSPM sequences exhibit the spatiotemporal evolution of BSP distributions. QRSI maps are generated by integrating BSPs over the QRS interval, and 12 ECG leads are calculated according to the given electrode locations. These results are compared to published experimental studies for verification.

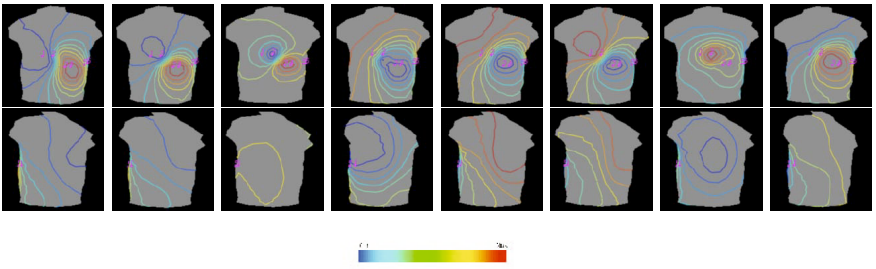

Fig. 2. Simulated BSPM isochrone sequence during normal cardiac electrical activation. The color encodes normalized BSP value.

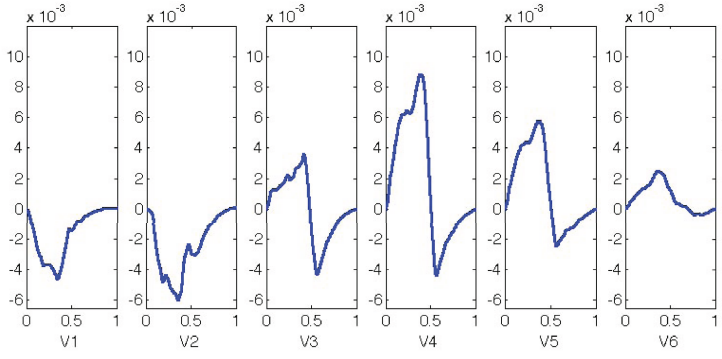

Fig. 3. Simulated normal QRS morphology of lead $V1$ - $V6$. The time course (x-axis) is normalized by the QRS interval and ECG values (y-axis) are scaled.

3.1 Normal Cardiac Conditions

Since the ventricular conduction system is not included in the current heart model, endocardial areas of earliest ventricular excitation are determined according to the experimental study of [16]. In the simulated BSPM sequence (Fig. 2), the potential maximum initially resides on the anterior thorax and the minimum on the back. The minimum then moves over the right shoulder onto the anterior region, while the positive potentials cover the back. In the end, the maximum rotate back to the superior part of the chest. Fig. 3 displays the simulated 6 precordial leads, where $V1$ shows a dominant negative defect and $V3 - V6$ display dominant positivity. Besides, since cardiac activation progresses from the thinner right ventricle across the thicker left ventricle, positive R wave increases in amplitude and duration from leads $V1$ to $V4$, while S wave is large in $V1$, larger in $V2$, and progressively smaller from $V3$ through $V6$. These results are consistent with the BSP morphology known for normal subjects [17].

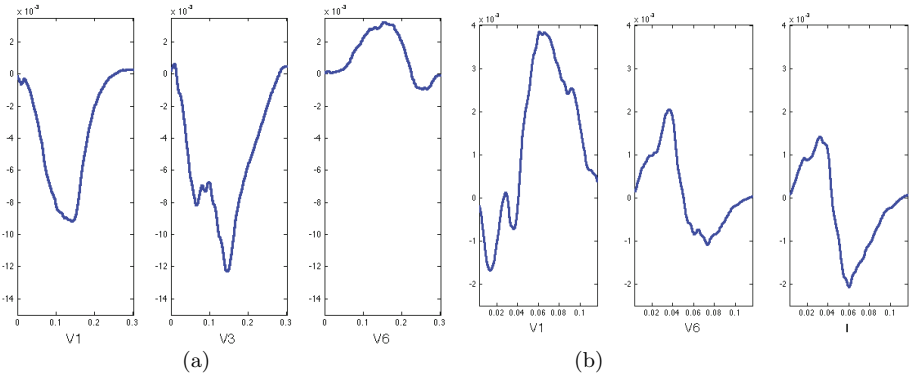

Fig. 4. Simulated QRS morphology in BBB conditions. (a) Lead $V1, V2$ and $V6$ for LBBB. (b) Lead $V1, V6$ and I for RBBB. The time course (x-axis) is normalized by the QRST interval and ECG values (y-axis) are scaled.

3.2 Bundle Branch Block (BBB)

Different BBB conditions are simulated by removing corresponding sites of earliest exitation in the ventricles. The results of ECG leads comply with standard diagnostic criteria [17]. For LBBB, since the activation proceeds sequentially from the interventricular septum to the lateral LV wall, the characteristic changes of the QRS complex are the monophasic QS morphology in $V1$, broad R wave in $V6$ and minimal R wave in $V2$ (Fig. 4 (a)). In comparison, since the RV contributes minimally to QRS complex, RBBB produces little distortion to the normal QRS morphology. As show in Fig. 4 (b), the abnormality is usually marked by the presence of a late prominent positive in $V1$, and a wide S wave in V6 and I.

3.3 Ventricular Pacing (Ectopic Activity)

The atlas of body surface QRSI map has been established for identifying ectopic ventricular activation [18]. This study simulates ventricular pacing cases in [18] for a comparison with the QRSI map atlas established therein. Fig. 5 lists examples of QRSI maps generated from ventricular pacing at 6 endocardial sites at the basal LV and the apical level. When the pacing site advances horizontally from lateral, anterior, septal to inferior part at basal LV endocardium (Fig. 5 (a)), the anticlockwise rotation of the potential maximum and minimum reported in [18] is observed. During apical pacing (Fig. 5 (b)), the minimum lies at a quite similar location on the lower anterior thorax while the maximum moves from the upper front to upper back with the pacing site moving from apical inferior to apical septal. In addition, LBBB morphology (negative QRS polarity in V1) is noted in QRSI maps for all apical pacing and LV basal septum pacing. All these observations, including the distribution, location and rotation of potential extreme, are in good accordance with the atlas [18].

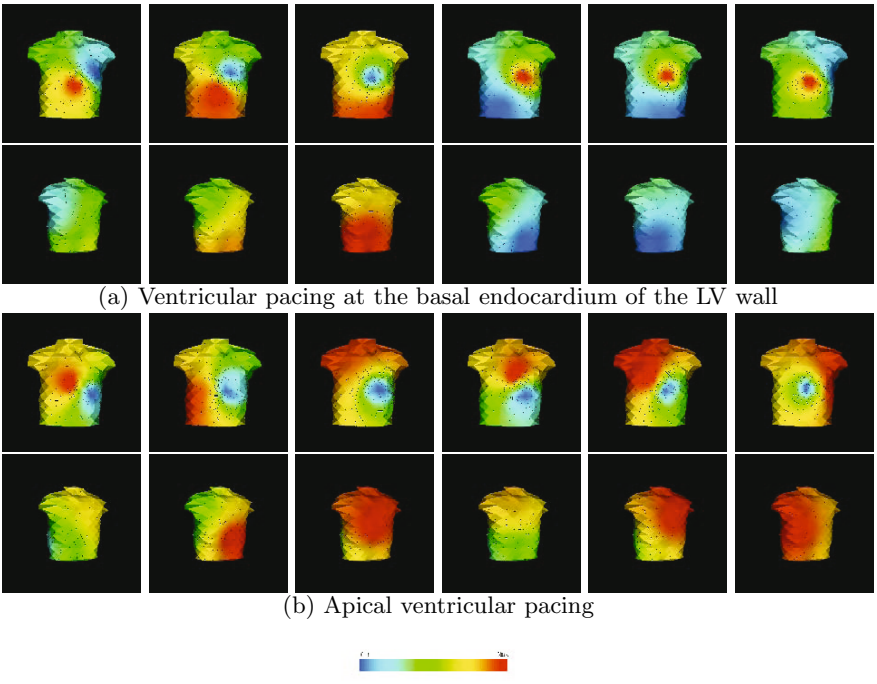

(a) Ventricular pacing at the basal endocardium of the LV wall

(b) Apical ventricular pacing

Fig. 5. Simulated QRSI maps for different ventricular pacing cases. (a) Left to right: pacing sites change horizontally from anterior-lateral, anterior, anterior-septal, inferior-septal, inferior to inferior-lateral parts of the basal LV wall. (b) Left to right: pacing sites at lateral, anterior, septal and inferior apical endocardium of the LV, LV apex and RV apex. The color encodes the integrated BSP values during QRS interval.

We have simulated BSP sequences for several typical ventricular pacing cases, and all the results are in agreement with the experimental recordings by [18]. Fig. 6 exemplifies the simulated BSP map sequence for anterior-lateral pacing at the middle LV endocardium. At the beginning, the minimum shifts from the upper right anterior thorax toward the left back while the maximum moves from the lower left anterior part to the right part of the chest. It is followed by a stable bipolar BSPM pattern featuring clockwise rotation of potential extreme. By the end of the ventricular activation, regions of positive and negative potentials appear almost vertical on the anterior and posterior torso.

3.4 Myocardial Infarction (MI)

Various locations of infarct substrates are selected from the 17 LV segments. Electrophysiological properties for infarct tissues are modified so that TMP shapes show progressively reduced action potential duration and magnitude, until no activation could be stimulated in the center of the infarcted region. Fig. 7 lists the simulated BSPMs at the beginning of the S-T segment for transmural infarction at the middle anterior, inferior and lateral walls of the LV. As reported

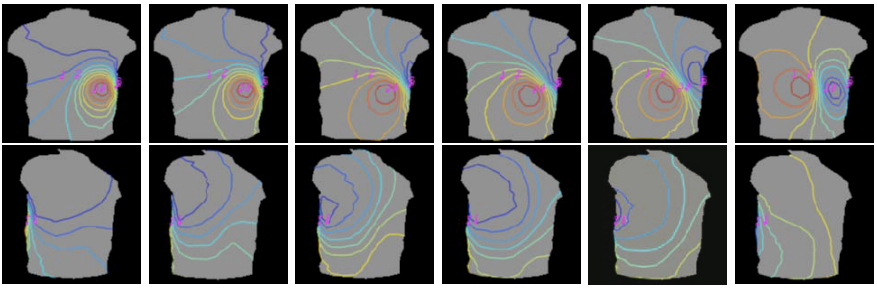

Fig. 6. Simulated BSPM isochrone sequence of the anteriorlateral pacing at the middle endocardium of LV. The color bar is the same as in Fig. 2.

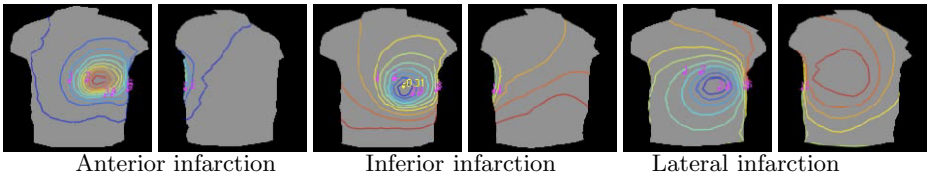

Fig. 7. Simulated BSPM isochrone map at the beginning of the S-T segment for 3 different MI conditions. The color bar is the same as in Fig. 2.

in [19], BSPMs display a potential maximum facing the infarct location and an opposite potential minimum.

4 Conclusions and Discussions

To provide an applicable heart-tosro representation and TMP-to-BSP model for noninvasive volumetric myocardial TMP imaging from BSPs, we present a novel coupled meshfree-BEM platform and verify its plausibility by electrocardiographic simulations of different cardiac conditions on realistic heart-torso structures. To improve the accuracy of simulated ECG leads, firstly, models with more complexity and detailedness are needed for a more realistic description of volumetric electrical activity of the heart. Geometrical modeling, such as the relative position between the heart and the electrodes, is another important factor on the electrocardiographic simulation. Meanwhile, a more realistic and detailed heart model would largely improve the accuracy of the simulated ECGs. For instance, the errors caused by incorrect locations of earliest ventricular excitation could be reduced by incorporating the ventricular conduction system into the heart model. By taking into account transmural electrical heterogeneity, this study avoids generating incorrect T waves as a reverse of the QRS complex. Nevertheless, more accurate divisions among the epi-, endo- and mid-myocardial

cells are desired. Besides, by including the atrium into the heart model, P wave could be generated in the simulated ECGs.

References

1. Henriquez, C.S.: Simulating the electrical behaviour of cardiac tissue using the bidomain model. Crit. Rev. Biomed. Eng. 21, 1–77 (1993)
2. Fischer, G., Tilg, B., Wach, P., Lafter, G., Rucker, W.: Analytical validation of the bem-application of the bem to the electrocardiographic forward and inverse problem. Comput. Methods Programs Biomed. 55, 99–106 (1998)
3. Fischer, G., Tilg, B., Modre, R., Huiskamp, G.J.M., Fetzer, J., Rucker, W., Wach, P.: A bidomain model based bem-fem coupling formulation for anisotropic cardiac tissue. Ann. Biomed. Eng. 28, 1229–1243 (2000)
4. Wang, L., Zhang, H., Wong, K.C., Shi, P.: Coupled meshfree-bem platform for electrocardiographic simulation: Modeling and validations. In: Dohi, T., Sakuma, I., Liao, H. (eds.) MIAR 2008. LNCS, vol. 5128, pp. 98–107. Springer, Heidelberg (2008)
5. Nash, M.: Mechanics and Material Properties of the Heart using an Anatomically Accurate Mathematical Model. PhD thesis, Univ. of Auckland, New Zealand (May 1998)
6. Yan, G.X., Shimizu, W., Antzelevitch, C.: Charactertistics and distribution of m cells in arterially perfused canine left ventricular wedge preparations. Circ. 98, 1921–1927 (1998)
7. Cerqueira, M.D., Weissman, N.J., Dilsizian, V., Jacobs, A.K., Kaul, S., Laskey, W.K., Pennell, D.J., Rumberger, J.A., Ryan, T., Verani, M.S.: Standardized myocardial segmentation and nomenclature for tomographic imaging of the heart. Circ. 105, 539–542 (2002)
8. Brandley, C.P., Pullan, A.J., Hunter, P.J.: Effects of material properties and geometry on electrocardiographic forward simulations. Ann. Biomed. Eng. 28, 721–741 (2000)
9. Cheng, L.: Non-invasive Electrical Imaging of the Heart. PhD thesis, Univ. of Auckland, New Zealand (2001)
10. Aliev, R.R., Panfilov, A.V.: A simple two-variable model of cardiac excitation. Chaos, Solitions & Fractals 7(3), 293–301 (1996)
11. Plonsey, R.: Bioelectric phenonmena. McGraw-Hill, New York (1969)
12. Brebbia, C.A., Telles, J.C.F., Wrobel, L.C.: Boundary element techniques: theory and applications in engineering. Springer, Heidelberg (1984)
13. Barnard, A.C.L., Duck, I.M., Lynn, M.L.: The application of electromagentic theroy to electrocardiology. Biophys. J. 7, 443–462 (1967)
14. Belytschko, T., Krongauz, Y., Organ, D., Fleming, M., Krysl, P.: Meshless methods: An overview and recent developments. Computer Methods in Applied Mechanics and Engineering 139(1), 3–47 (1996)
15. Goldberger, A.L., Amaral, L.A.N., Glass, L., Hausdorff, J.M., Ivanov, P.C., Mark, R.G., Mietus, J.E., Moody, G.B., Peng, C.K., Stanley, E.: Physiobank, physiotoolkit, and physionet components of a new research resource for complex physiological signals. Cric. 101, e215–e220 (2000)
16. Durrur, D., Dam, R., Freud, G., Janse, M., Meijler, F., Arzbaecher, R.: Total excitation of the isolated human heart. Comp. Methods Appl. Mech. Eng. 41(6), 899–912 (1970)

17. Wagner, G.S.: Marriott's practical electrocardiography. Lippincott williams & wilkins, Philadelphia (2001)
18. SippensGroenewegen, A., Spekhorst, H., van Hemel, N.M., Kingma, J.H., Hauer, R.N., Janse, M.J., Dunning, A.J.: Body surface mapping of ectopic left and right ventricular activation. QRS spectrum in patients without structural heart disease. Circ. 82, 879–896 (1990)
19. Miller, W.T., Geselowitz, D.B.: Simulation sutdies of the electrocardiogram. ii. ischemia and infarction. Circ. Res. 43, 315–323 (1978)

HERG Effects on Ventricular Action Potential Duration and Tissue Vulnerability: A Computational Study

Alan P. Benson[1,2], Moza Al-Owais[1], Wing C. Tong[1], and Arun V. Holden[1,2]

[1] Computational Biology Laboratory, Institute of Membrane and Systems Biology
[2] Multidisciplinary Cardiovascular Research Centre, University of Leeds, Leeds LS2 9JT, UK
a.p.benson@leeds.ac.uk
http://www.cbiol.leeds.ac.uk

Abstract. The mutations to hERG (the human Ether-a-go-go Related Gene) that cause long QT syndromes produce effects on the rapid delayed rectifier K^+ current I_{Kr} and, therefore, action potential duration (APD). These mutations can affect various properties that determine I_{Kr} kinetics. We used computational models of human ventricular myocytes to identify which of these properties, when altered, cause profound changes to APD and transmural dispersion of repolarisation (TDR). Such increases in both APD and TDR is caused by a positive shift of activation $V_{0.5}$, a negative shift of inactivation $V_{0.5}$, or by reducing maximal conductance. The largest reduction in APD is achieved by a positive shift of inactivation $V_{0.5}$. Altering the time constant of activation had relatively little effect. When two or more parameters were altered simultaneously, shifting inactivation $V_{0.5}$ had the dominant effect on APD, except for some extreme shifts of activation $V_{0.5}$ or moderate reductions of maximal conductance. HERG mutations observed clinically lie in the parameter range where maximal conductance has the dominant effect. Bifurcation analysis showed stable steady states (corresponding to physiological resting membrane potential) at all parameter values, and no APD alternans. We conclude that increased APD due to hERG mutations seen clinically are a combined effect of alterations to I_{Kr} kinetic parameters that, in isolation, cause either shortening or prolongation of the AP. Therapeutics that alter I_{Kr} conductance are potentially most beneficial.

Keywords: Cardiac, computational model, hERG, long QT syndrome, arrhythmia.

1 Introduction

Long QT syndrome (LQTS) is characterised by prolongation of the ventricular action potential and the QT interval of the ECG, and is associated with an increased risk of ventricular arrhythmias and sudden cardiac death [1]. Mutations to the human Ether-a-go-go Related Gene (hERG) cause type 2 LQTS due to

N. Ayache, H. Delingette, and M. Sermesant (Eds.): FIMH 2009, LNCS 5528, pp. 172–181, 2009.
© Springer-Verlag Berlin Heidelberg 2009

effects on the rapid delayed rectifier K^+ current I_{Kr}: reduced I_{Kr} will delay repolarisation and increase action potential duration (APD), thus increasing the QT interval.

The mutations can affect various properties that determine I_{Kr} kinetics – the voltage dependencies of activation and inactivation, channel maximal conductance, and the time constant of activation/deactivation (e.g. [2,3]). The increased APD that underlies LQTS can be achieved by a positive shift in the voltage dependence of activation of I_{Kr}, a negative shift in the voltage dependence of inactivation, decreasing channel conductance, or reducing the time constant of activation. However, studies examining hERG mutations in oocyte expression systems (e.g. [3]) have shown that the mutations can cause shifts of voltage dependence in the opposite directions, which should act to decrease APD. These effects may be counteracted by decreased channel conductance, but a computational study [4] has shown that a shift in the voltage dependence of inactivation has a dominant effect over changes to conductance. This problem is confounded by the recent identification of novel hERG mutations that have very different effects on the different aspects of I_{Kr} kinetics, with some mutations affecting only the time constant of activation and others also shifting the voltage dependence of activation and inactivation [5]. How these mutations will affect electrophysiology at the tissue level is unknown, and it is therefore unknown how the mutation would present clinically (in the ECG) and whether it would predispose to arrhythmia.

The relative roles played by alterations to the kinetic parameters underlying I_{Kr} therefore remain unclear, and thus it is not clear which aspect of channel function (conductance, gating etc.) should be targeted by pharmacological interventions, or whether pharmacological intervention will be necessary at all.

Computational models of cardiac cells and tissues can provide insights into the mechanisms underlying APD changes seen with hERG mutations, as parameters can be altered by varying amounts, either in isolation or in any combination, and their effects at the tissue level can be examined and related to clinical observations (e.g. the ECG). In this study, we used models of human cells and tissues to examine the effects that changes to the kinetic properties of I_{Kr} have on APD and tissue vulnerability to re-entrant arrhythmias.

2 Methods

For an isopotential cell, the rate of change of membrane potential V is given by

$$\frac{\mathrm{d}V}{\mathrm{d}t} = -I_{\mathrm{ion}} \ , \tag{1}$$

where t is time and I_{ion} is the sum of the transmembrane current densities. For a tissue, this equation becomes a reaction-diffusion equation of the form

$$\frac{\partial V}{\partial t} = \nabla(\mathbf{D}\nabla V) - I_{\mathrm{ion}} \ , \tag{2}$$

where ∇ is a spatial gradient operator. $\mathbf{D}$ is a diffusion coefficient tensor that characterises electrotonic spread of membrane potential, and which reduces down to a scalar D in one dimension. For I_{ion} in both cases we use the human model of Ten Tusscher & Panfilov [6] where I_{Kr} is given by

$$I_{\text{Kr}} = G_{\text{Kr}}\sqrt{\frac{\text{K}_\text{o}}{5.4}}x_{r1}x_{r2}(V - E_{\text{K}}) \ . \tag{3}$$

Here, G_{Kr} is maximal conductance, K_o is extracellular K^+ concentration and E_{K} is K^+ reversal potential given by the Nernst equation. x_{r1} and x_{r2} are dynamic activation and inactivation gating variables respectively, given by the differential equations

$$\frac{\text{d}x_{r1}}{\text{d}t} = \frac{x_{r1\infty} - x_{r1}}{\tau_{xr1}} \ , \tag{4}$$

$$\frac{\text{d}x_{r2}}{\text{d}t} = \frac{x_{r2\infty} - x_{r2}}{\tau_{xr2}} \ , \tag{5}$$

where $x_{r1\infty}$ and $x_{r2\infty}$ are the steady-state values of the gating variables, and τ_{xr1} and τ_{xr2} are time constants, all of which are functions of V and can be obtained experimentally. The steady state values correspond to activation and inactivation curves, and are described by the Boltzmann functions

$$x_{r1\infty} = \frac{1}{1 + \exp((V_{0.5,\text{act}} - V)/k_{\text{act}})} \ , \tag{6}$$

$$x_{r1\infty} = \frac{1}{1 + \exp((V - V_{0.5,\text{inact}})/k_{\text{inact}})} \ , \tag{7}$$

respectively, where $V_{0.5,\text{act}}$ and $V_{0.5,\text{inact}}$ are half activation voltages, and k_{act} and k_{inact} are slope factors. Thus, ignoring the effects of intra- and extracellular K^+ concentrations, the dynamics of I_{Kr} are determined by seven variables: the maximal conductance G_{Kr}, activation $V_{0.5}$, k and τ, and inactivation $V_{0.5}$, k and τ.

Mutations to hERG have been shown to alter both the activation $V_{0.5}$ and the inactivation $V_{0.5}$, the maximal conductance G_{Kr} and the time constant of activation τ_{xr1} (but not the slope factors or the time constant of inactivation) [2,3]. We therefore altered these four parameters in the model and examined the effects on APD at 90% repolarisation. Note that variations to the time constant τ_{xr1} were obtained by scaling the default voltage-dependend value. A 15 mm 1D heterogeneous strand model of the ventricular wall (with endocardial, midmyocardial and epicardial tissue in the ratio 3:7:5) was used to quantify the vulnerable window (VW) under control and modified conditions. The VW is a spatio-temporal region where unidirectional block of a propagating action potential can occur. Unidirectional block is one of the conditions required to initiate re-entrant arrhythmias [7] and so an increase in the VW will increase the probability that any ectopic excitation will initiate in this region, and thus the probability of re-entry is also increased. The VW is therefore a useful index of the vulnerability of tissue to arrhythmias. For details on cell and 1D model

integration, and the VW, see [8]. Limitations of using the 1D model are discussed in detail in [9]. Finally, we used bifurcation analysis to examine the stability of the model under variation of parameters. A combination of numerical integration and continuation algorithm (XPPAUT with AUTO2000 [10]) was applied, to both the full model and a reduced model with ion concentrations clamped at standard initial values, as bifurcation analysis on the full model is not trivial (see [11,12] for details).

3 Results

3.1 Altering Parameters in Isolation

Figure 1 shows the effects on midmyocardial cell APD of altering each of the I_{Kr} kinetic parameters associated with hERG mutations in isolation. As one parameter was altered, the other three parameters took on their default model values. For activation $V_{0.5}$, the shortest APD (412 ms) occurred with values more negative than −93 mV, while the longest APD (526 ms) occurred with values greater than +56 mV. The steepest part of the relationship (and so the parameter range where small shifts result in large changes to APD) is between approximately −20 and +60 mV. As the model default value for activation $V_{0.5}$ is −26 mV, a negative shift of the activation curve will cause minimal APD reduction, whereas a positive shift will increase APD by relatively large amounts. For inactivation $V_{0.5}$, the shortest APD (50 ms) occurred with values more positive than +105 mV, while the longest APD (again 526 ms) occurred with values less than −232 mV. In this case, the steepest part of the relationship was over a wider range, between approximately −200 and +50 mV. Model default inactivation $V_{0.5}$ is −88 mV, which lies roughly in the middle of the steep range, and so shifting inactivation $V_{0.5}$ in either the positive or negative directions would have large effects on APD. Scaled G_{Kr} has an approximately linear relationship with APD. When G_{Kr} was zero, APD increased to 526 ms, while doubling the model default conductance (to 0.192 nS/pF) shortened APD to 351 ms. Scaling the voltage-dependent activation time constant τ_{xr1} had the smallest effects – APD increased to only 430 ms when τ_{xr1} was scaled by 0.01, and changes to APD only occurred when τ_{xr1} was scaled by 0.5 or less. Note that the largest APD values obtained when shifting the activation and inactivation $V_{0.5}$ values (526 ms) are the same as when G_{Kr} is zero. Thus, shifting the activation $V_{0.5}$ more negative than −93 mV or shifting the inactivation $V_{0.5}$ more positive than +105 mV causes a complete block of the current. From Fig. 1, it can be seen that shifting inactivation $V_{0.5}$ can cause the largest change in APD (over a range of 476 ms), followed by altering G_{Kr} (175 ms) then shifting activation $V_{0.5}$ (114 ms), while altering τ_{xr1} has relatively little effect (16 ms). Qualitatively similar results were obtained with the endocardial and epicardial cell models (results not shown).

We performed bifurcation analysis to determine whether alterations to any of the four I_{Kr} kinetic parameters caused instability of the membrane potential. Firstly, using numerical integration, we did not observe APD alternans in any

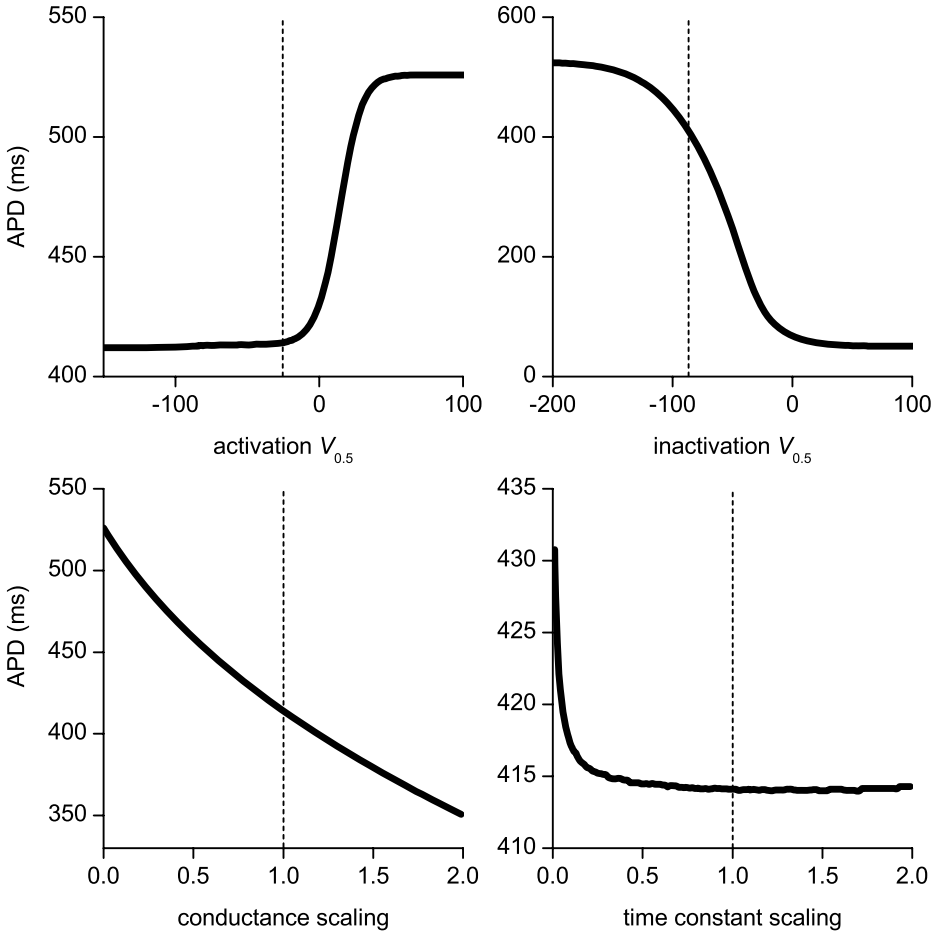

Fig. 1. Effects on midmyocardial cell APD of altering kinetic parameters associated with hERG mutations. Note the different scales on the ordinates. The dashed vertical line in each panel indicates the default value in the model, which gives an APD of 414 ms.

of the three cell models (endocardial, M or epicardial) at any of the parameter values shown in Fig. 1. Secondly, using continuation algorithms on reduced models with fixed ion concentrations, we observed a single stable steady state (corresponding to physiological resting membrane potential) at all parameter values, and two unstable steady states at only some parameter values as has been shown previously [12]. For brevity, we do not show these results.

Although an increase in APD is characteristic of LQTS, increasing the transmural dispersion of repolarisation (TDR) has been shown to be arrhythmogenic, as it increases the likelihood of conduction block and the initiation of re-entrant arrhythmias [8]. We used the maximum APD difference (usually

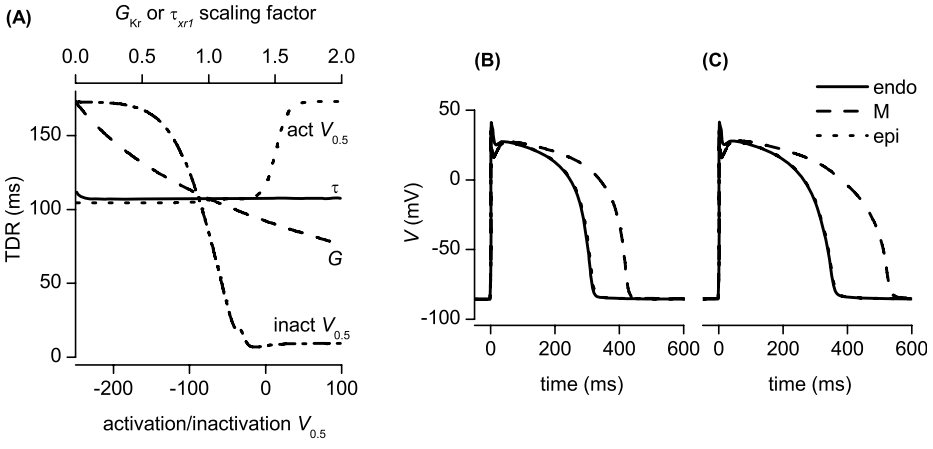

Fig. 2. (A) Effects on TDR of altering kinetic parameters associated with hERG mutations. (B) Computed action potentials with model default parameters. Here, TDR is 107 ms. (C) Computed action potentials with G_{Kr} reduced to zero. In this case, TDR is 173 ms.

between midmyocardial and epicardial) as an approximation of TDR, and examined whether TDR was changed as I_{Kr} kinetic parameters were altered. Figure 2 shows that reducing G_{Kr} to zero, shifting activation $V_{0.5}$ more negative than -93 mV or shifting the inactivation $V_{0.5}$ more positive than $+105$ mV causes the greatest TDR (173 ms in all cases). This is consistent with the results shown in Fig. 1, in that the largest TDR occured when I_{Kr} was completely blocked in all three cell types, irrespective of which parameter alteration caused the block. The increase in TDR comes about because, when I_{Kr} is blocked, the main current responsible for action potential repolarisation is the slow delayed rectifier current I_{Ks}, which has a much lower density in midmyocardial cells compared to endocardial or epicardial cells (I_{Kr} has an equal density in the three cell types). Also consistent with Fig. 1 is that shifting the inactivation $V_{0.5}$ can alter TDR the most (over a 164 ms range), followed by G_{Kr} (97 ms) then activation $V_{0.5}$ (69 ms), while altering τ_{xr1} causes little change (5 ms).

3.2 Altering Parameters Simultaneously

As altering τ_{xr1} was shown in the previous section to have little effect on APD and TDR, we omit the parameter from this section. Figure 3 shows the effects on APD of altering two of either activation $V_{0.5}$, inactivation $V_{0.5}$ or G_{Kr} simultaneously. Figure 3A shows APD as activation and inactivation $V_{0.5}$ are both altered. The inactivation $V_{0.5}$ has the dominant effect on APD, except when activation $V_{0.5}$ is more positive than approximately 0 mV. Figure 3B shows that G_{Kr} has a dominant effect on APD over activation $V_{0.5}$, except when activation $V_{0.5}$ is again more positive than approximately 0 mV. Figure 3A shows APD when inactivation $V_{0.5}$ and G_{Kr} are both altered. Inactivation $V_{0.5}$ has the dominant

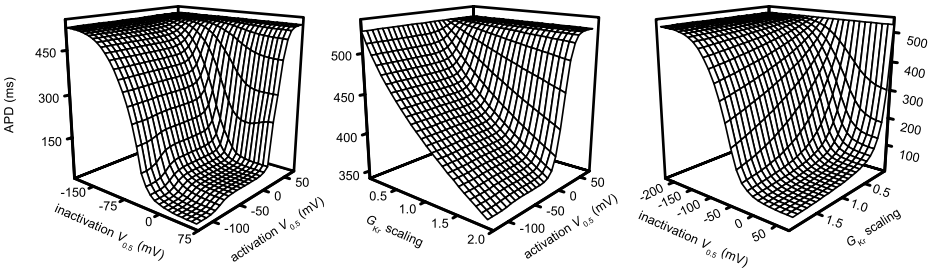

Fig. 3. Effects on midmyocardial cell APD of simultaneously altering two of the kinetic parameters associated with hERG mutations. Note the different scales on the z axes (APD).

effect on APD, except when G_{Kr} is reduced by more than half (i.e. the scaling factor is < 0.5). From these data we can conclude that activation $V_{0.5}$ will have the dominant effect on APD if it has a value more positive than approximately 0 mV, otherwise G_{Kr} has the dominant effect if it is reduced by more than half, and in all other situations inactivation $V_{0.5}$ has the dominant effect.

3.3 Vulnerable Windows

In this section we examine effects on the VW for unidirectional conduction block. Figure 4 shows VWs for the model default values (control) and two test cases. Case 1 has activation $V_{0.5}$ shifted by +15 mV, inactivation $V_{0.5}$ shifted by +10 mV, G_{Kr} scaled by 0.65, and τ_{xr1} scaled by 0.2 (all relative to control). Case 2 has activation $V_{0.5}$ again shifted by +15 mV, inactivation $V_{0.5}$ shifted by only +1 mV, G_{Kr} scaled by 0.5, and τ_{xr1} scaled by 0.2 again. These two test cases have been chosen to approximate the effects on I_{Kr} kinetic parameters for R56Q and A797K mutant hERG channels, respectively, which were expressed in oocytes where lysine mutations had been induced in residues in the cNBD domain by site directed mutagenesis [5]. The R56Q mutation has previously been implicated in type 2 LQTS [2], while A797K is a novel mutation. In each panel of Fig. 4, the black line shows time of repolarisation across the 1D tissue wall (note the heterogeneous repolarisation, which is due to spatially heterogeneous tissue type) while the grey area shows the VW, the spatio-temporal area following a preceding action potential when a localised suprathreshold excitation produces a unidirectional propagating wave. The black lines clearly show that the two test cases cause prolongation of the action potential and delayed repolarisation (and therefore LQTS), especially with case 2. This prolongation occurs even though the shift in inactivation $V_{0.5}$ is positive. Such a shift is expected to reduce APD as, from the previous section, shifting inactivation $V_{0.5}$ should have a dominant effect on APD changes. However, the shift is rather small, and G_{Kr} is just above half (case 1) or at half (case 2) of its control value. The maximum temporal width of the VW also increases in the test cases – from 7.6 ms in the control tissue to 7.7 ms with case 1 and 9.5 ms with case 2. Thus, G_{Kr} has the dominant

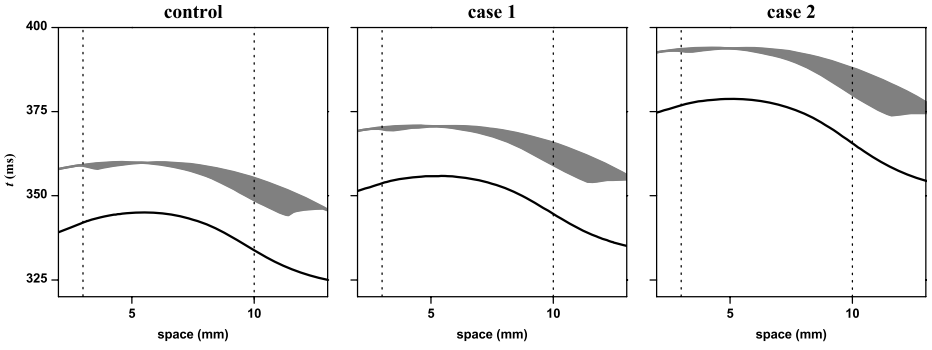

Fig. 4. VWs in the control 1D model (i.e. with default model values) and in two tissues with hypothetical hERG mutations (see text for details). The black line in each panel shows time of repolarisation along the tissue, the grey area shows the spatio-temporal extent of the VW. Because of boundary effects, we do not calculate VWs at the ends of the strands. Dashed vertical lines show the boundaries of the tissue types along the strand model - endocardial on the left (3 mm of tissue), midmyocardial in the middle (7 mm) and epicardial on the right (5 mm).

effect on APD changes (and hence the VW) when parameters are changed to those observed experimentally. We suggest from these data that therapeutic interventions aimed at increasing G_{Kr} back to a normal level can potentially have the most benefit on reducing APD (and also the VW) in type 2 LQTS. Any pharmacological intervention that did reduce the VW could therefore reduce the propensity for re-entrant arrhythmias.

4 Discussion

We have quantified the effects on APD of changing I_{Kr} kinetic parameters that have been shown to be altered with hERG mutations. Altering inactivation $V_{0.5}$ in isolation can change APD by the greatest amount, followed by G_{Kr} then activation $V_{0.5}$, while changing τ_{xr1} had little effect. This is interesting, as some hERG mutations to the N terminus region have previously been shown to exert their functional effects by increasing the rate of deactivation [13]. Our results could be model-specific, so further work to characterise hERG mutations in other models of human ventricular myocytes and tissues needs to be undertaken. When two parameters were combined simultaneously in the model, activation $V_{0.5}$ will have the dominant effect on APD if it has a value more positive than approximately 0 mV, otherwise G_{Kr} has the dominant effect if it is reduced by more than half, and in all other situations inactivation $V_{0.5}$ has the dominant effect. The effects of combining one or more parameter changes is not simply additive, and further work needs to be undertaken to examine, in detail, the relationships between each of the I_{Kr} kinetic parameters. Finally, we examined, in a 1D tissue model, effects of parameter changes of the order observed experimentally. In this situation, reductions in G_{Kr} had the dominant effect on increasing APD and the VW.

As new hERG mutations are identified and their effects on the kinetics of I_{Kr} isolated (e.g. [5]), computational studies using the framework presented in this paper can be used to predict the tissue-level effects of these mutation (in terms of TDR, the ECG and the potential for arrhythmogenesis) and identify which particular property of channel kinetics is responsible for tissue-level changes. This information can be used to inform the development of potential pharmacological interventions.

We conclude that increased APD due to hERG mutations seen clinically and experimentally are a combined effect of alterations to I_{Kr} kinetic parameters that, in isolation, cause either shortening or prolongation of the action potential. We suggest that therapeutics targeting mutant hERG subunits that alter I_{Kr} conductance are potentially most beneficial.

Acknowledgments. We thank Prof. Dennis Wray for helpful discussions. This work was supported by the European Union through the BioSim Network of Excellence (contract number LSHB-CT-2004-005137) and the Hadwen Trust for Humane Research. APB is supported by a Medical Research Council special training fellowship in biomedical informatics (G0701776).

References

1. Moss, A.J., Schwartz, P.J., Crampton, R.S., Tzivoni, D., Locati, E.H., MacCluer, J., Hall, W.J., Weitkamp, L., Vincent, G.M., Garson, A.: The long QT syndrome. Prospective longitudinal study of 328 families. Circulation 84, 1136–1144 (1991)
2. Berecki, G., Zegers, J.G., Verkerk, A.O., Bhuiyan, Z.A., De Jonge, B., Veldkemp, M.W., Wilders, R., Van Ginneken, A.C.G.: HERG channel (dys)function revealed by dynamic action potential clamp technique. Biophys. J. 88, 566–578 (2005)
3. Chen, J., Zou, A., Splawski, I., Keating, M.T., Sanguinetti, M.C.: Long QT syndrome-associated mutations in the Per-Arnt-Sim (PAS) domain of HERG potassium channels accelerate channel deactivation. J. Biol. Chem. 274, 10113–10118 (1999)
4. Peitersen, T., Grunnet, M., Benson, A.P., Holden, A.V., Holstein-Rathlou, N.-H., Olesen, S.-P.: Computational analysis of the effects of the hERG channel opener NS1643 in a human ventricular cell model. Heart Rhythm 5, 734–741 (2008)
5. Al-Owais, M., Bracey, K., Wray, D.: Role of intracellular domains in the function of the herg potassium channel. Eur. Biophys. J (2009), doi:10.1007/s00249-009-0408-2
6. Ten Tusscher, K.H.W.J., Panfilov, A.V.: Alternans and spiral breakup in a human ventricular tissue model. Am. J. Physiol. 291, H1088–H1100 (2006)
7. Jalife, J.: Ventricular fibrillation: mechanisms of initiation and maintainance. Annu. Rev. Physiol. 62, 25–50 (2000)
8. Benson, A.P., Halley, G., Li, P., Tong, W.C., Holden, A.V.: Virtual cell and tissue dynamics of ectopic activation of the ventricles. Chaos 17, 015105 (2007)
9. Benson, A.P., Aslanidi, O.V., Zhang, H., Holden, A.V.: The canine virtual ventricular wall: a platform for dissecting pharmacological effects on propagation and arrhythmogenesis. Prog. Biophys. Mol. Biol. 96, 187–208 (2008)
10. Ermentrout, B.: Simulating, analyzing, and animating dynamical systems: a guide to XPPAUT for researchers and students. SIAM, Philadelphia (2002)

11. Benson, A.P., Clayton, R.H., Holden, A.V., Kharche, S., Tong, W.C.: Endogenous driving and synchronization in cardiac and uterine virtual tissues: bifurcations and local coupling. Phil. Trans. R. Soc. A 364, 1313–1327 (2006)
12. Tong, W.C., Holden, A.V.: Bifurcation analysis of genetically engineered pacemaking in mammalian heart. J. Biol. Phys. 32, 169–172 (2006)
13. Moss, A.J., Zareba, W., Kaufman, E.S., Gartman, E., Peterson, D.R., Benhorin, J., Towbin, J.A., Keating, M.T., Prori, S.G., Schwartz, P.J., Vincent, M., Robinson, J.L., Andrews, M.L., Feng, C., Hall, W.J., Medina, A., Zhang, L., Wang, Z.: Increased risk of arrhythmic events in long-QT syndrome with mutations in the pore region of the human Ether-a-go-go-Related Gene potassium channel. Circulation 105, 794–799 (2002)

Voxel Based Adaptive Meshless Method for Cardiac Electrophysiology Simulation

Phani Chinchapatnam[1,2,⋆], Kawal Rhode[2], Matthew Ginks[2], Prasanth Nair[3], Reza Razavi[2], Simon Arridge[1], and Maxime Sermesant[2,4]

[1] Centre for Medical Image Computing, University College London, UK
p.chinchapatnam@cs.ucl.ac.uk
[2] Division of Imaging Sciences, King's College London, UK
[3] Computational Engineering and Design Group, University of Southampton, UK
[4] Asclepios Project, INRIA Sophia-Antipolis, France

Abstract. In this paper, an adaptive meshless method is described for solving the modified FitzHugh Nagumo equations on a set of nodes directly imported from the voxels of the medical images. The non-trivial task of constructing suitable meshes for complex geometries to solve the reaction-diffusion equations is circumvented by a meshfree implementation. The spatial derivatives arising in the reaction diffusion system are estimated using the Lagrangian form of scattered node radial basis function interpolant. Normal cardiac activation phenomena is fast, with a very steep upstroke and localised as compared to the size of the computational domain. To accurately capture this phenomena, a space adaptive method is presented where extra nodes are placed near the region of the activation front. The performance of the adaptive method is investigated first for synthetic geometry and then applied to a real-life geometry obtained from magnetic resonance imaging. Numerical results suggest that the presented method is capable of predicting realistic electrophysiology simulation effectively.

1 Introduction

The electrical stimulation of ventricular and atrial cells in the heart initiates the contraction and relaxation of cardiac tissue and dysfunction of this electrical command can have severe impact on cardiac function, as well demonstrated by the life-threatening ventricular fibrillation. This is the reason why the understanding of this electrical propagation and its pathologies is one of the main problems addressed by the cardiac electrophysiology community. There has been an ever growing interest in the application of computer organ-level electrophysiology simulation models to better understand and obtain novel insights from experimental and clinical observations for a generic heart [1,2], and more recently towards modelling patient-specific function [3,4]. The so-called "*forward problem*" of electrophysiology computes the electrical propagation with known physical parameters, including the source intensities and locations, material property

⋆ Corresponding author.

N. Ayache, H. Delingette, and M. Sermesant (Eds.): FIMH 2009, LNCS 5528, pp. 182–190, 2009.
© Springer-Verlag Berlin Heidelberg 2009

and boundary conditions. The state of the art of modelling electrical activity in cardiac cells can be classified into biophysical cellular models [5] and phenomenological cellular models [6,7]. Biophysical models use ion concentrations as state variables and solve for the different currents through the cell membrane. In contrast, phenomenological models directly use the resulting transmembrane potential (or extra and intra cellular potentials) as state variable. Both these type of cellular models can be introduced into a spatial diffusion framework (which may be either mono-domain or bi-domain) for simulating electrical propagation on the tissue (i.e. more than one cell).

Traditional numerical methods used to solve these multi-scale reaction diffusion systems are the finite difference method (FDM) and the finite element method (FEM). However, FDM is restricted only to model simple geometries and the FEM method requires discretisation of the physical domain of interest as a mesh of nonoverlapping elements. It is widely acknowledged in the field of medical imaging and cardiac biophysical modelling that the construction of a suitable mesh of the heart from images is a non-trivial and time consuming process. In addition, due to the specific characteristics of cardiac action potential (fast steep upstroke, plateau and steep downstroke), the activation region is very localised and in normal propagation much of the tissue is inactivate. Without any adaptivity, the integration needs to be performed on millions of nodes so as to effectively localise the propagating front [8]. For instance, "to compute a single heart beat (0.5 sec) in a realistic anatomical model (250cm^3) of the heart, about 30 million grid points and $50,000$ time steps would be required thus necessitating 50GB of disk storage and several days to compute even on the most powerful of contemporary supercomputers" [1].

Meshless methods offer an attractive alternative for solving the governing equations based solely on the representation of the domain as sampling nodes with no pre-specified connectivity constraints. A wide range of meshless schemes have been proposed in the literature; for example, element free Galerkin (EFG), meshless local Petrov Galerkin, and radial basis function (RBF) based methods [9]. In the present context of cardiac electrophysiology models, recently an EFG formulation has been successfully used to model cardiac electrical propagation in a meshless manner [10]. In this paper, we present an alternative meshless formulation based on scattered node finite difference type formulas using RBFs [11]. Further, an adaptive algorithm is described for solving the modified FitzHugh Nagumo (FHN) equation where the nodal density is automatically increased near the regions of the activation front to accurately capture the width and speed of the propagating wavefront. The convergence and stability of the adaptive meshless method is shown for a simulated case and is then applied to a geometry derived from a magnetic resonance image.

2 RBF Function Approximation

In this section, the meshless methodology for calculating the derivatives of a function at a node based on the function values on a scattered set of nodes

around the considered node is described. The methodology is based on function approximation using RBFs. Meshless methods in literature generally employ two types of basis functions for function approximation. The first one is based on variants of the least square (LS) technique, for example the EFG method. The LS technique allows an optimized approximation derived from an over-determined set of equations, and generally the resultant coefficient matrix has good properties such as positive, symmetric, and definite. Thus, the problem of singular coefficient matrix can be circumvented by means of using more local supporting points (more than the unknowns). The second basis used is the radial basis. The advantages of using RBFs instead of a polynomial basis is that RBF interpolation does not suffer from the problem of well-posedness in the case of higher dimensions [11]. Further, as RBFs are univariate functions (dependent only on the distance between two nodes), these schemes can easily be extended to higher dimensions. In this paper, we use the multiquadric RBF defined as $\phi(\|r\|) = \sqrt{(r^2+\sigma^2)}$[1]. We begin by explaining RBF interpolation and then show how the Lagrange form of RBF interpolant can be used to approximate function derivatives [11].

2.1 RBF Interpolation

Given a set of distinct scattered nodes $\mathbf{x}_i \in \mathbb{R}^d$, $i = 1, \cdots, n$, and a corresponding scalar function values $u(\mathbf{x}_i)$, $i = 1, \cdots, n$, the standard RBF interpolation problem is to find an interpolant of the form

$$u(\mathbf{x}) \approx s(\mathbf{x}) = \sum_{i=1}^{n} \lambda_i \phi(\|\mathbf{x} - \mathbf{x}_i\|) + \beta, \tag{1}$$

where $\phi(\|.\|)$ is the multiquadric RBF and β is a constant. The expansion coefficients $\{\lambda_i\}_{i=1}^n$ and β are determined by enforcing the conditions $s(\mathbf{x}_i) = u(\mathbf{x}_i)$, $\quad i = 1, \cdots, n$, and $\sum_{i=1}^n \lambda_i = 0$. Imposing these conditions leads to a symmetric block linear system of equations given by

$$\begin{bmatrix} \mathbf{\Phi} & \mathbf{e} \\ \mathbf{e}^T & 0 \end{bmatrix} \begin{bmatrix} \lambda \\ \beta \end{bmatrix} = \begin{bmatrix} \mathbf{u} \\ 0 \end{bmatrix}, \tag{2}$$

where $\mathbf{\Phi}_{i,j} = \phi(\|\mathbf{x}_i - \mathbf{x}_j\|)$, $\quad i, j = 1, \cdots, n$, and $\mathbf{e}_i = 1$, $\quad i = 1, \cdots, n$.

Lagrange Form. The RBF interpolant can alternatively be written in Lagrange form as

$$\bar{s}(\mathbf{x}) = \sum_{i=1}^{n} \chi(\|\mathbf{x} - \mathbf{x}_i\|) u(\mathbf{x}_i), \tag{3}$$

where $\chi(\|\mathbf{x}-\mathbf{x}_i\|)$ is of the form Eq. (1) and satisfies the usual cardinal conditions i.e.,

$$\chi(\|\mathbf{x} - \mathbf{x}_i\|) = \begin{cases} 1, & \text{if } \mathbf{x} = \mathbf{x}_i, \\ 0, & \text{if } \mathbf{x} \neq \mathbf{x}_i, \end{cases} \quad i = 1, \cdots, n. \tag{4}$$

[1] r denotes the Euclidean distance and σ is a free parameter known as the shape parameter.

2.2 Derivative Approximation

In the derivation that follows, we present the methodology for approximating any arbitrary linear differential operator acting on the function $u(\mathbf{x})$, denoted by $\mathcal{L}u(\mathbf{x})$. The unknown function $u(\mathbf{x})$ at any node, say $\mathbf{x}_1$, in the domain is approximated by an RBF interpolant with RBFs placed on the node itself and $n-1$ neighbouring nodes. These n nodes constitute the support region for the node $\mathbf{x}_1$. A schematic diagram of the support region for the node $\mathbf{x}_1$ is shown in Fig. 1.

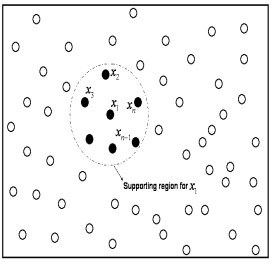

Fig. 1. Supporting region (circle) for the node $\mathbf{x}_1$

We approximate the differential operator acting on $u(\mathbf{x})$ at the node $\mathbf{x}_1$ using the Lagrangian form of the RBF interpolant i.e.,

$$\mathcal{L}u(\mathbf{x}_1) \approx \mathcal{L}\bar{s}(\mathbf{x}_1) = \sum_{i=1}^{n} \mathcal{L}\chi(\|\mathbf{x}_1 - \mathbf{x}_i\|)u(\mathbf{x}_i). \tag{5}$$

Eq. (5) can be rewritten as a FD type formula of the form

$$\mathcal{L}u(\mathbf{x}_1) \approx \sum_{i=1}^{n} w_{(1,i)}^{(\mathcal{L})} u(\mathbf{x}_i), \tag{6}$$

where the weights[2] $\{w_{(1,i)}^{(\mathcal{L})}\}_{i=1}^{n}$ are formally given by the operator $\mathcal{L}$ applied to the Lagrange form of the basis functions. In practice, the weights are computed by solving the linear system

$$\begin{bmatrix} \Phi & \mathbf{e} \\ \mathbf{e}^T & 0 \end{bmatrix} \begin{bmatrix} \mathbf{w} \\ \mu \end{bmatrix} = \begin{bmatrix} \mathcal{L}\Phi_1 \\ 0 \end{bmatrix}, \tag{7}$$

where $\mathcal{L}\Phi_1$ denotes the column vector $\mathcal{L}\Phi = [\mathcal{L}\phi(\|\mathbf{x} - \mathbf{x}_1\|)\ \mathcal{L}\phi(\|\mathbf{x} - \mathbf{x}_2\|)\ \cdots\ \mathcal{L}\phi(\|\mathbf{x} - \mathbf{x}_n\|)]^T$ evaluated at the node $\mathbf{x}_1$. Here, μ is a scalar value related to the constant β in Eq. (1) and enforces the condition $\sum_{i=1}^{n} w_{(1,i)} = 0$, which ensures that the stencil is exact for all constants. Once the weights are computed, they can be stored and used to discretise the governing partial differential equation in a similar manner as in the finite difference method.

3 Adaptive Meshless Electrophysiology Model

In this section, we describe the adaptive meshless electrophysiology model based on the RBF method described in Section 2. To model the electrical propagation, a phenomenological model [7] (modified FHN) is employed. The equations governing the dynamics of cardiac potential are given by

[2] The weights at the j^{th} supporting node of any point $\mathbf{x}_i$ with n supporting points are $\mathbf{w}_{(i,j)}^{(x)}$,$\mathbf{w}_{(i,j)}^{(y)}$, $\mathbf{w}_{(i,j)}^{(xx)}$ or $\mathbf{w}_{(i,j)}^{(yy)}$ when the operator $(\mathcal{L})$ is $\frac{\partial}{\partial x}$, $\frac{\partial}{\partial y}$, $\frac{\partial^2}{\partial x^2}$ or $\frac{\partial^2}{\partial y^2}$, respectively.

$$e\partial_\tau u = l^2 e^2 \nabla \cdot (\mathbf{D}\nabla u) + ku(1-u)(u-a) - uz,$$
$$\partial_\tau z = -(ku(u-a-1) + z), \tag{8}$$

where u is a normalised transmembrane potential and z is a secondary variable for the repolarization. k and e control the repolarization, and a the stimulation threshold and the reaction phenomenon. Parameter values are derived from [7]: $e = 0.01$, $k = 8$, $a = 0.15$. In Eq. (8), $\tau = et$ and l is the maximum distance between any two nodes in the domain. The diffusion tensor describes the effect of anisotropy due to fibres and is described in the Cartesian coordinate system as $\mathbf{D} = d_0\left((1-r)f \otimes f + r \cdot \mathbf{I}\right)$, where f denotes the fibre orientation, $\otimes$ the tensor product and $\mathbf{I}$ the identity matrix. d_0 is the conductivity in the fibre direction and r denotes the conductivity anisotropy ratio in the transverse plane.

The spatial derivatives in Eq. (8) are obtained using the RBF meshless method described in the earlier section. For example, considering a two dimensional case when the fibre direction is uniform throughout the domain the discretisation at any node $\mathbf{x}_i$ with n supporting nodes is given by

$$e\partial_\tau u = l^2 e^2 \sum_{j=1}^{n} \left(d_{11} w^{xx}_{(i,j)} + (d_{12} + d_{21}) w^{xy}_{(i,j)} + d_{22} w^{yy}_{(i,j)} \right) u_j$$
$$+ku(1-u)(u-a) - uz,$$
$$\partial_\tau z = -(ku(u-a-1) + z), \tag{9}$$

where d_{pq}, $p, q = 1, 2$ denotes the $(p,q)^{\text{th}}$ element of the conductivity tensor $\mathbf{D}$. Eq. (9) can now be solved using any of the time-stepping schemes. We employ Euler time stepping for solving Eq. (9) in this paper.

Eq. (8) is usually supplemented by the Neumann boundary condition at the boundary given by

$$\partial_n u = 0, \tag{10}$$

where $\boldsymbol{n}$ denotes the unit outward normal to the boundary. The spatial derivative can also be approximated using the RBF method in the earlier section. However, the accuracy of such a discretisation suffers as the support region consists of nodes only on one side of the boundary (interior region). In this paper, we use the conventional one sided finite difference for obtaining the boundary variables.

3.1 Adaptive Algorithm

We now describe the adaptive algorithm employed in this paper to solve the modified FHN equations. Spatial refinement is performed in the region near the propagating activation front by simply adding nodes in the region. As the spatial derivatives are obtained based on a scattered set of nodes, the addition of nodes is much easier as compared to adaptive algorithms employed by FE based methods. At every time step, active nodes are identified by $|\partial_\tau u| \geq \alpha$, where α is a pre-defined constant (set at 0.5). At each active node, we select m neighbouring nodes and then construct a local Delaunay triangulation. In each of the triangles, additional nodes are placed to increase the node density around

the active node. The function values at the additional nodes are obtained using inverse distance weighted (IDW) interpolation from the function values at the vertices of the triangle. The complete algorithm is provided below.

1. **Definitions**:
   - $Intr(X) \equiv$ interior nodes of node set X
   - $Bndry(X) \equiv$ boundary nodes of node set X
   - $\mathcal{N}(X) \equiv$ a logical array specifying to calculate weights for each $x_i \in X$
2. **Inputs**: Initial node set X_0, initial condition (u_0, z_0) and Euler time step $d\tau$
3. $X \equiv X_0$, $\tau = 0$, $\mathcal{N}(X) \equiv 1 \forall x \in Intr(X)$, $u_\tau = u_0$, $z_\tau = z_0$
4. **While** $\tau \leq \tau_{\text{final}}$
   (a) $\tau = \tau + d\tau$
   (b) Calculate Weights $\forall x \in Intr(X)$ & $\mathcal{N}(X) = 1$
   (c) Advance solution (u_τ, z_τ) $\forall x \in Intr(X)$ using Euler time stepping
   (d) Calculate solution u_τ $\forall x \in Bndry(X)$ using conventional one sided FD
   (e) Identify active nodes in X as X_{active} $(\partial_\tau u|_{X_{\text{active}}} \geq \alpha)$
   (f) $X_{\text{additional}} = \text{Null}$
   (g) **For** each $x \in X_{\text{active}}$
      i. Construct local delaunay triangulation $\mathcal{T}$
      ii. Add nodes x_a to $X_{\text{additional}}$ and interpolate function values $(u(x_a), z(x_a))$ using IDW interpolation for each triangle $\in \mathcal{T}$
   (h) $X_{\text{new}} = X \cup X_{\text{additional}}$
   (i) $\mathcal{N}(X_{\text{new}}) = 1 \forall x \in X_{\text{additional}}$ or in the neighbouring region of $X_{\text{additional}}$
   (j) $X = X_{\text{new}}$ and $\mathcal{N}(X) = \mathcal{N}(X_{\text{new}})$

From the algorithm it can be noted that the derivative weights are calculated at each node for the first iteration of the while loop and in the subsequent iterations, the weights are only calculated for all additional nodes. Additionally, for a small number of nodes which lie in the support region of these added nodes the weights are recomputed. The computational cost incurred by the algorithm depends on how efficiently the neighbours or the support nodes for a particular node are computed. In the present implementation, we follow the strategy of binning the nodes into a coarse rectangular grid and whenever the neighbours of a node $\mathbf{x}_i$ are required, we search only in the point set of the rectangular cell in which $\mathbf{x}_i$ lies, thus reducing the search time required.

4 Computational Domain and Boundary Conditions Definition Using Images

In order to simulate patient-specific electrophysiology, the computational domain must be adapted to the patient anatomy. This anatomy can be obtained with medical imaging. The idea here is to directly use the spatial information from such images in order to define the computational domain and help compute the boundary conditions.

Indeed, a segmentation of the myocardium in an image provides an indicator function for the model: when adding a point, this binary image is a direct test

whether the point is inside or outside the myocardium. Furthermore, one can compute the gradient of this binary image, and for any model point on the boundary, this gradient will provide the normal direction.

The idea is to make use of this underlying image in order to ease steps that are made difficult by the meshless formulation, like computing the normal to the surface, or knowing if a point is inside or outside the computational domain.

The methodology is illustrated for a 2D slice of the myocardium in Fig. 2. It is worth noting that obtaining an interior node along the normal to the boundary surface is trivial as one simply has to move along the normal and place an interior node at each boundary node.

a) Slice b) Gradient image c) Computational domain

Fig. 2. a) Realistic cardiac geometry image and b) gradient norm image and c) computational domain defined only by centres of the voxels

5 Numerical Experiments

The performance and stability of the algorithm is tested initially by simulating isotropic planar wave propagation in cardiac tissue. The synthetic geometry taken is a $[0, 1]^2$ two dimensional slab of tissue. Points on one side of the square are stimulated at the beginning and then the wave propagates out (Fig. 3). The node evolution w.r.t τ is shown in Fig. 4a. From Fig. 4b, it can be seen that the numerical simulation is quite stable as is evident by absence of any oscillation in the determined action potential along the horizontal centreline of the computational domain. In Fig. 4c, the wave velocity obtained using the adaptive meshless method at the centre of the domain (black line) is compared against the converged solution of a second order FD method (dashed blue line). From this subfigure, it can be seen that the adaptive method obtains a converged solution with $n \approx 4500$ nodes as compared to $n \approx 40401$ nodes required by the FD method, clearly demonstrating the effectiveness of the adaptive meshless method. Further, Fig. 4d demonstrates that the method is also able to accurately simulate anisotropic propagation with a variable fibre orientation.

The adaptive algorithm is now applied to simulate electrical propagation in a realistic geometry (2D cardiac slice) derived from medical image (see Section 4). The slice was stimulated near the right ventricular endocardium; the resultant

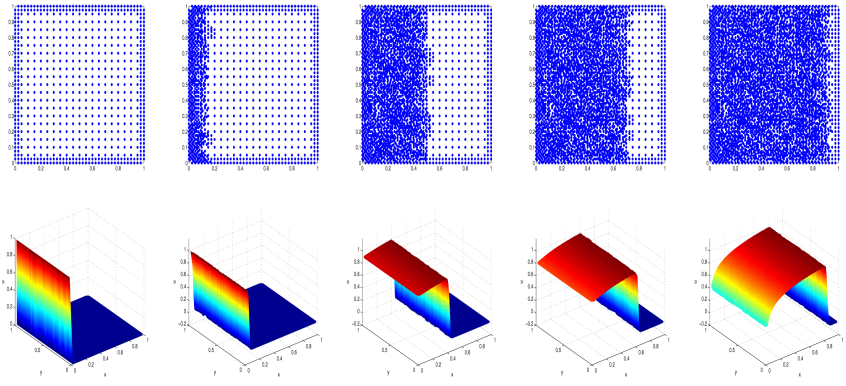

$\tau = 0$ $\tau = 0.0395$ $\tau = 0.325$ $\tau = 0.4875$ $\tau = 0.65$

Fig. 3. Node distributions and the normalised transmembrane potential $u(\tau)$ at different times for planar wave propagation; Dark red (depolarised) and Dark blue (rest)

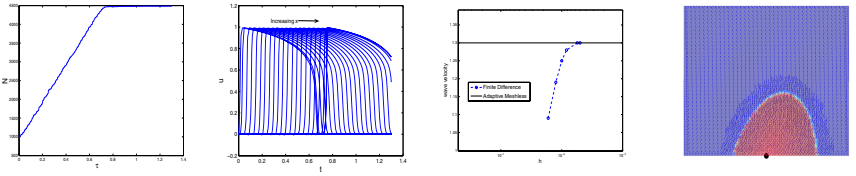

a) Node Evolution b) Stability c) Convergence d) Nonuniform fibres

Fig. 4. a) Evolution of number of nodes with respect to τ, b) u on the horizontal centre mid line, c) Convergence of wave velocity compared to second order finite difference method (blue dashed line), d) Anisotropic wave propagation ($r = 0.25$) for a variable fibre orientation ranging from $+60^o$ on the bottom surface to $+120^o$ on the top

$\tau = 0.001$ $\tau = 0.2$ $\tau = 0.55$ $\tau = 1.4$ Node Evolution (blue)

Fig. 5. $u(\tau)$ at different times for isotropic propagation

propagation and the node evolution is shown in Fig. 5. From this figure, it can be seen that the adaptive meshless method can effectively solve the cardiac electrophysiology equations on complex cardiac geometries.

6 Conclusions

A novel adaptive meshless algorithm based on RBFs has been presented to solve anisotropic cardiac electrical propagation on geometries obtained from medical images. The key advantage of the meshless method is the absence of the step of mesh construction for complex geometries. Further, the location and speed of the propagating activation front is accurately resolved by increasing the node density near the regions of the action potential wavefront. Numerical experiments conducted on synthetic geometry have shown that the methodology is stable and obtains converged results with fewer nodes as compared to the second order FD method. Application to a realistic cardiac geometry has shown that the adaptive meshless method is capable of simulating cardiac propagation effectively. Future work includes decreasing the nodal density where the gradient is small and temporal adaptivity.

References

1. Hunter, P.J., Pullan, A.J., Smaill, B.H.: Modelling total heart function. Annu. Rev. Biomed. Eng. 5, 147–177 (2003)
2. Winslow, R.L., Scollan, D.F., Holmes, A., Yung, C.K., Zhang, J., Jafri, M.A.: Electrophysiological modelling of cardiac ventricular function: from cell to organ. Annu. Rev. Biomed. Eng. 2, 119–155 (2000)
3. Kerckhoffs, R., Narayan, S., Omens, J., Mulligan, L., McCulloch, A.: Computational modeling for bedside application. Heart Failure Clin. 4, 371–378 (2008)
4. Sermesant, M., Peyrat, J.M., Chinchapatnam, P., Billet, F., Mansi, T., Rhode, K., Delingette, H., Razavi, R., Ayache, N.: Towards patient-specific myocardial models of the heart. Heart Failure Clin. 4, 289–301 (2008)
5. Luo, C., Rudy, Y.: A model of the ventricular cardiac action potential. depolarization, repolarization and their interaction. Circ. Res. 68(6), 1501–1526 (1991)
6. FitzHugh, R.: Impulses and physiological states in theoretical models of nerve membrane. Biophys. J. 1, 445–466 (1961)
7. Aliev, R.R., Panfilov, A.V.: A simple two-variable model of cardiac excitation. Chaos, Solitions and Fractals 7(3), 293–301 (1996)
8. Garny, A., Noble, D., Kohl, P.: Dimensionality in cardiac modelling. Prog. Biophysics. Mol. Biol. 87(1), 47–66 (2005)
9. Fasshauer, G.: Meshfree Methods. In: Handbook of Theoretical and Computational Nanotechnology, pp. 33–97. American Scientific Publishers (2006)
10. Zhang, H., Shi, P.: A meshfree method for solving cardiac electrical propagation. In: IEEE Eng. in Med. and Biol. 27th Annual Conference, pp. 349–352 (2005)
11. Wright, G.B., Fornberg, B.: Scattered node compact finite difference-type formulas generated from radial basis functions. J. Comput. Phys. 212(1), 99–123 (2006)

Local Cardiac Wall Motion Estimation from Retrospectively Gated CT Images

Jochen Peters[1,⋆], Olivier Ecabert[1], Holger Schmitt[2], Michael Grass[2], and Jürgen Weese[1]

[1] Philips Research Europe, Aachen, Weisshausstr. 2, 52066 Aachen, Germany
jochen.peters@philips.com
[2] Philips Research Europe, Hamburg, Röntgenstr. 24-26, 22335 Hamburg, Germany

Abstract. The heart is a dynamic organ and important characteristics about its function can be derived from 4D (3D + time) data. In this paper we present an approach for the automatic local tracking of the cardiac surfaces with sub-voxel accuracy in time series of computed tomography image volumes. First, a multi-compartment mesh is adapted to a single reconstructed image. This adapted mesh is then propagated through the whole time series. Chamber volumes and local surface motion can be estimated at arbitrary time points. Experiments on 15 time series indicate that the system is very precise and robust with respect to the selection of the start phase of the propagation. The results can be used, e.g., for dyssynchronity assessment or comparison with electromechanical models of the full heart.

Keywords: Cardiac wall motion, motion tracking, multi-slice computed tomography, image segmentation.

1 Introduction

Time series of volumetric cardiac images (i.e., 4D data) contain information about patient-specific anatomy and the dynamics of the heart. Tracking cardiac structures allows to extract their motion over the cardiac cycle. Standard functional assessment from ultrasound (US) [1], single photon emission computed tomography (SPECT) [2], magnetic resonance (MR) [3], or X-ray computed tomography (CT) [4,5] images concentrates on ventricular volumes and derived quantities such as stroke volumes and ejection fraction with a focus on the left ventricle (LV). Chamber volumes are often estimated from two images at selected cardiac phases and approximate minimum and maximum chamber filling. Measurement errors due to wrong selection of these two phases are avoided if volumes over time are available from an automatic segmentation of time series covering the complete cardiac cycle. In this paper, we present an advanced approach to *locally* track the cardiac surfaces of the *whole heart* at densely sampled points in space and time. This tracking is based on a *fully automatic* segmentation of a time series of retrospectively ECG-gated cardiac multi-slice CT images of medium resolution. Estimated displacements of the order of 0.1–2mm require

⋆ Corresponding author.

N. Ayache, H. Delingette, and M. Sermesant (Eds.): FIMH 2009, LNCS 5528, pp. 191–200, 2009.
© Springer-Verlag Berlin Heidelberg 2009

a highly consistent segmentation with sub-voxel accuracy. The resulting local wall motion estimates for the whole heart – with much finer spatial resolution than bull's eye plots characterizing 17 LV myocardial segments (American Heart Association) – enable, e.g., dyssynchronity assessment [6], analysis of contraction dynamics, comparison with predictions from electromechanical models for the complete heart [7], etc. Furthermore, high resolution image reconstruction at automatically determined local rest phases may reduce local motion artifacts (e.g., for coronaries) and improve image quality [8].

2 Method

2.1 General Segmentation Framework

To segment the cardiac surfaces we apply the shape-constrained deformable model adaptation framework of [9,4]. The endocardium of the four cardiac chambers, the left ventricular epicardium, and the truncated major vasculature (aorta, pulmonary artery and veins) are modelled by a triangulated mesh with $V = 7285$ vertices and $T = 14768$ triangles (see Fig. 1). Automatic segmentation starts by an approximate heart localization using the Generalized Hough Transform [10,4]. After positioning the mesh model, the surfaces are adapted to the corresponding image boundaries by iterating a boundary detection step and a mesh adaptation step which minimizes several energy terms. The complete method is extensively described in [4]. Briefly summarized, boundary detection defines a target point maximizing a match function along a search profile for each mesh triangle (see also Sec. 2.3). The triangles are then attracted by spring-like forces to the detected boundaries. The mesh geometry is updated to minimize the external energy associated with all spring forces. Mesh adaptation is performed in three stages. Each stage iterates boundary detection and adaptation until the mesh approaches a steady state. First, the mesh is treated as a rigid shape and only pose and size are adapted. The allowed geometric updates are translation, rotation, and scaling. In the second stage, the cardiac mesh is subdivided into 7 anatomical regions (four chambers, LV epicardium, aorta, pulmonary artery). Each region is allowed to undergo an individual affine transformation and the geometry is updated using the degrees of freedom of the 7 affine transformations. At mesh junctions, the transformations are interpolated to ensure smooth transitions. In the final stage, the mesh deforms elastically. Here, the external energy is complemented by an internal energy to regularize the deforming mesh. This internal energy penalizes deviations in length and orientation for all edges between the adapting mesh and the shape model.

2.2 Time Series Segmentation

Running the complete segmentation chain (heart localization, parametric and deformable adaptation) separately per image may reduce the consistency of the precise location of each mesh vertex on the cardiac surface. Even if the surface is quasi identical, vertices may "slide" laterally within the surface during adaptation if the initialization per image differs. To improve the geometric correspondence between the surfaces of adjacent cardiac phases, we use a progressive

adaptation: The first image volume (of phase P_0) is segmented fully automatically using all steps starting with the heart localization. Thereafter, the adapted mesh of phase P_n is used to initialize the model for the next image at phase P_{n+1}. For this new image, only the deformable adaptation is performed, and the resulting mesh serves to initialize P_{n+2} until all images have been processed. We note that our shape model is static, i.e., image information and proper boundary detection is sufficient to adapt the deformable mesh to the moving surfaces.

2.3 Improved Boundary Detection

Time series segmentation in the above framework with our *standard* cardiac model as published in [4] suffers from the limited accuracy of the boundary detection. Displacements between two successive images with phase increments of 2% range from 0.1–0.2mm up to 1–2mm (see also Sec. 3.2). To really track the cardiac surfaces for image volumes reconstructed at such small cardiac phase increments, sub-voxel accuracy is needed.

As introduced in Sec. 2.1, boundary detection maximizes the response of a triangle-specific match function F_i along a search profile perpendicular to the mesh surface. To localize the correct boundaries and to reject all (or most) misleading edges within the search range, we apply an edge detector and analyse additional image features surrounding all detected edges as detailed in [4,11]. In brief, the edge detector projects the image gradient ∇I onto the triangle normal (to suppress edges with false orientation). To encode the expected gray value transition (dark-to-bright or vice versa), the projected gradient is multiplied with ± 1. To reject false boundaries, one or several image features such as gray values on both sides of the triangle are evaluated and compared to trained acceptance intervals. If any feature value violates its interval, the edge is rejected. Training, feature selection, and triangle-specific optimization are described in [11].

Our *standard* cardiac model had been developed in order to segment CT image volumes with sub-millimeter voxel extensions. On such images, we reach an average surface-to-surface error of 0.8mm [4]. This model uses a search profile with sampling points spaced at $\delta = 1$mm and calculates the image gradient via tri-linear interpolation from the voxel data.

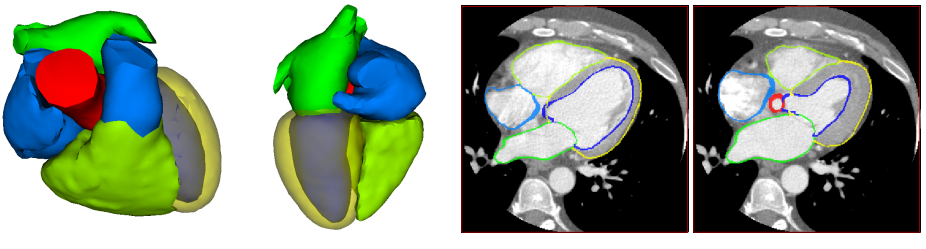

Fig. 1. Cardiac mesh (seen from top right and bottom) and segmentation examples in axial CT slice for end-diastole and end-systole of the same patient. For the left ventricle, we model both the endo- and the epicardium [dark blue inside yellow]. All other chambers are modeled by endocardial walls. Vessels are arbitrarily truncated.

To increase the accuracy of the segmentation despite reduced image resolution, an *improved* model was trained. To detect boundaries with sub-voxel accuracy, a convolution with an approximated Gauss kernel ω is applied *instead* of the trilinear interpolation scheme that is used by our standard model. We use a product of three $\cos^2$ functions extending over 3 voxels in each Cartesian direction. The image gradient is thus calculated by a convolution with the kernel gradient $\boldsymbol{\nabla}\omega$:

$$\boldsymbol{\nabla}[I * \omega](\boldsymbol{x}) = [I * \boldsymbol{\nabla}\omega](\boldsymbol{x}) \tag{1}$$

This convolution is evaluated analytically at sub-voxel positions $\boldsymbol{x}$: Each voxel's gray value is assigned to the complete voxel volume, i.e., we have a 3D gray value density (instead of gray values assigned to voxel centers). Convolution with the kernel gradient is performed by 3D integration. We do not apply a discretized convolution on the voxel grid as it is frequently done in image processing, e.g., for Sobel filters. Analytical 1D and 3D phantom studies with tissue transitions converted into a voxel image show that the gradient estimated via Eq. (1) reaches its maximum close to the true transition and is suitable to track moving edges with sub-voxel accuracy. Boundary detection in the *improved* model uses finer sampling with $\delta = 0.2$mm. To account for reduced image resolution in our test set (Sec. 3.1), the match functions F_i were re-trained for corresponding coarse images (training and test data are disjoint). Finally, the improved model applies stricter convergence checks for the mesh adaptation than our standard model.

2.4 Motion Estimation

To extract a motion vector field over the cardiac mesh surface, we track the pseudo-landmarks defined by the triangle centers $\boldsymbol{x}_i$. As a starting point, we take the time series of triangle coordinates $\boldsymbol{x}_{i,n}$ from the segmented phases P_n to obtain a "raw trajectory" over time. We synonymously use the notion of time t and cardiac phase P since they are linearly related. We note that the coordinates may exhibit some noise due to local segmentation inaccuracies that may result from the limited number of iterations during mesh adaptation or from unclear image boundaries. Furthermore, coordinates are only defined for the segmented images and the corresponding time points. To eliminate noise from the "raw trajectories" and to interpolate between segmented images, we establish local cubic fits over time. More specifically, within a time window of width $T\%$ of the cardiac cycle, a least squares fit of the form $\boldsymbol{x}(t) = \boldsymbol{a}+\boldsymbol{b}\cdot t+\boldsymbol{c}\cdot t^2+\boldsymbol{d}\cdot t^3$ is created through $\boldsymbol{x}_{i,n}$. This fit and its time derivative yields a smoothed trajectory per triangle and the triangle velocity near the center of the time window. Including the cubic term $\boldsymbol{d}\cdot t^3$ allows to approximate the trajectories for inflection points, e.g., at diastasis where motion (almost) stops and then continues along the same direction. These fits are established around densely placed evaluation times t and we use overlapping (or sliding) windows to define the contributing phases P_n and coordinates $\boldsymbol{x}_{i,n}$ per fit. To "fade out" contributions of cardiac phases P_n that are close to the borders of the sliding window, the least-squares sum down-weights contributions from more distant P_n with a factor $\cos^2(\frac{P_n - P(t)}{0.5 \cdot T\%})$ with $P(t)$ being the phase corresponding to t.

For functional indices, cardiac chamber volumes are calculated analytically from the enclosing surfaces. These volume estimates do not suffer from noise. To interpolate between segmented images, we again apply local cubic fits of the form $V(t) = a + b \cdot t + c \cdot t^2 + d \cdot t^3$ through the measured volumes V_n.

3 Experiments

3.1 Database

Our database covers time series of multi-slice computed tomography angiography (CTA) images acquired from 15 patients with 64-slice scanners in two clinics. Contrast medium is applied for coronary artery diagnosis. Bloodpool contrast in the chambers varies from patient to patient, in particular for the right chambers, and partly also within each chamber (see Fig. 2). For some time series acquired with dose modulation, SNR changes over the cardiac cycle. Heart rates vary from < 60 to 90 beats per minute. Images are reconstructed at phase increments of 2% of the RR interval using a gating window width of approximately 15%. Image resolution in the axial plane is 0.86mm (using a 256×256 voxel grid) and slice thickness is 2mm.

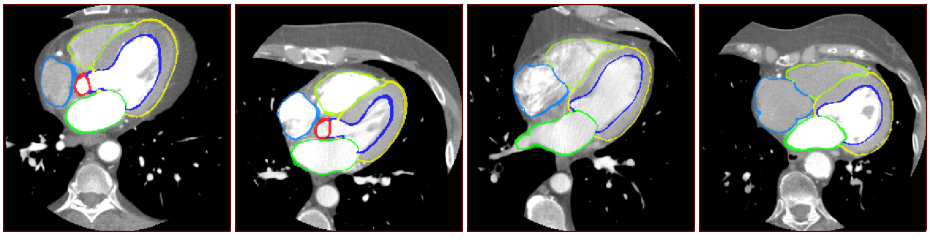

Fig. 2. Contrast variations for different patients (images around mid-disatole at 76%)

3.2 Volumes and Motion over Time

Time series segmentation and motion estimation gives access to two types of curves. First, we can plot the cardiac chamber volumes $V(t)$ over the cardiac cycle. Second, triangle velocities are estimated. To analyze the motion of certain mesh regions, magnitudes of these velocities can be averaged over a set of triangles. Both types of curves are illustrated in Fig. 3–5. As explained in Sec. 2.4, interpolated estimates can be obtained between the acquired images. The presented results evaluate volumes and motion at phase intervals of $\Delta P = 0.5\%$ and fitting windows of width $T\% = 30\%$.

Fig. 3 shows the typical behaviour of slowly beating hearts with a pronounced plateau in the volume curves at mid-diastole (diastasis) and associated low motion (see phases 70–80%). Fig. 4 shows the absense of diastasis in fast beating hearts and more complex velocity curves. Fig. 5, finally, illustrates the motion of an irregularly beating heart with small ejection fraction. Fig. 6 illustrates the local velocity distribution on the mesh surface for 10 phases over the cardiac cycle.

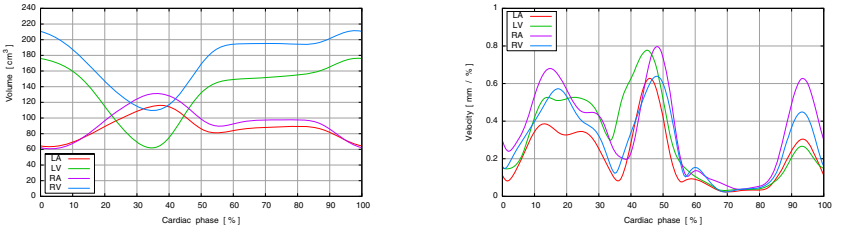

(a) (b)

Fig. 3. (a) Cardiac chamber volumes [in mm^3] and (b) triangle velocity magnitudes averaged over the chamber surfaces [in mm/%RR] for a patient with low heart rate (53bpm). (LA, RA, LV, RV = left and right atrium and ventricle; results obtained with improved model of Sec. 2.3).

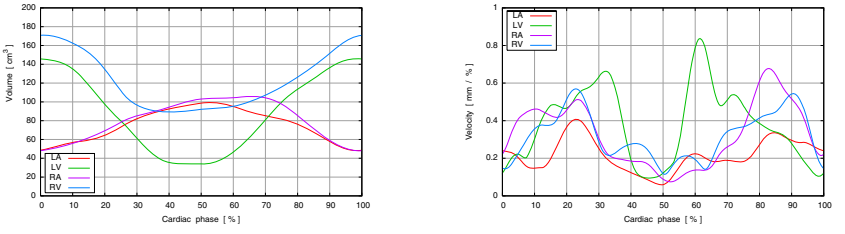

Fig. 4. As Fig. 3 for a patient with high heart rate (90bpm). Note that motion minima at mid-diastole (70–80%) have vanished.

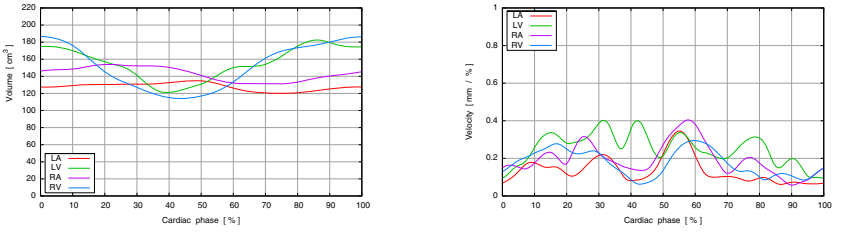

Fig. 5. As Fig. 3 for a patient with irregular cardiac rhythm (> 80bpm)

3.3 Consistency Checks

A full evaluation of 4D segmentation and derived local motion estimates poses a principle problem. Consistent ground truth segmentations with sub-voxel accuracy for 50 images per cardiac cyle are difficult to obtain. Furthermore, since the cardiac chamber surfaces are not densely covered by true anatomical landmarks that could be tracked with high accuracy, no ground truth is available for the motion fields. Using tagged MRI for tissue tracking could yield some information about motion patterns per patient but would not yield the required resolution and could not be used to accurately evaluate the segmentation of 4D images from a different modality acquired at a different time. To evaluate our

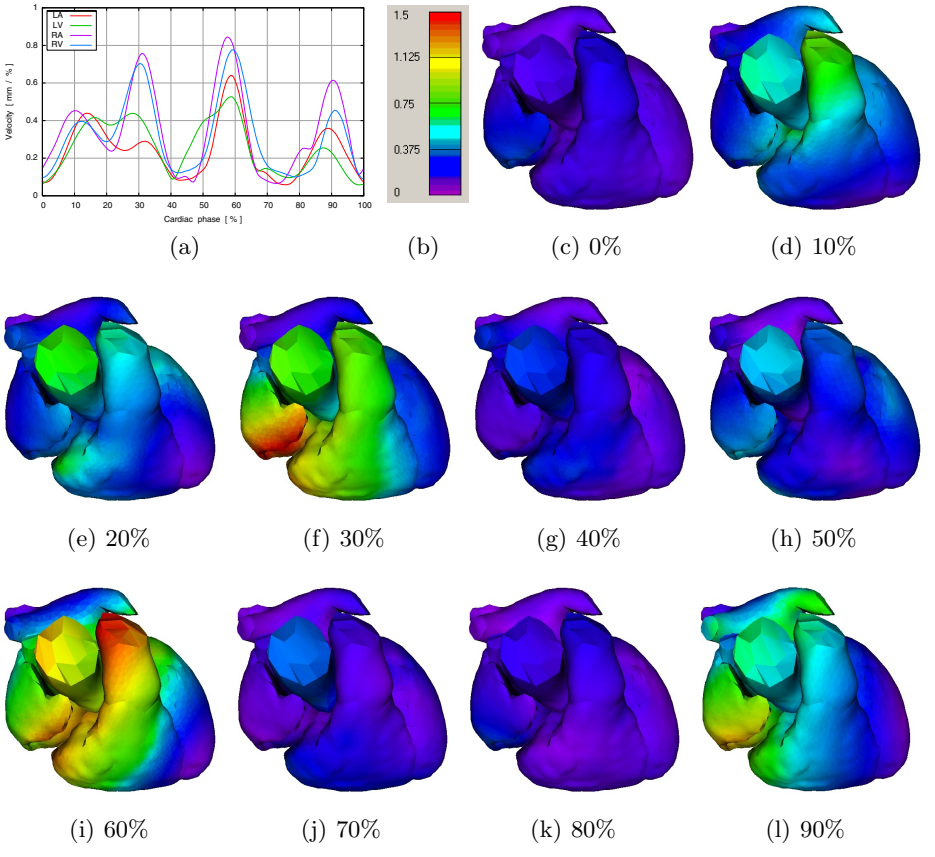

(a) (b) (c) 0% (d) 10%

(e) 20% (f) 30% (g) 40% (h) 50%

(i) 60% (j) 70% (k) 80% (l) 90%

Fig. 6. Velocities over time: (a) = velocities averaged per chamber (b) = color codes for (c)–(l) [purple = 0.0, red = 1.5mm/%RR]. (c)–(l) = color coded velocities on static mesh surface for phases at 10% intervals (perspective as Fig. 1 left).

system, we performed consistency checks to ensure that the required precision is achieved, i.e., that the system output is highly reproducible for different start conditions.

To start, we compare the segmentation of the same image before and after the progressive adaptation through one complete heart cycle. More specifically, the segmentations for phase $P_0 = 0\%$ and $P_{50} = 100\%$ are compared in terms of point-to-point distances Δ_i between corresponding triangle centers $\boldsymbol{x}_{i,n}$. We call these distances *cyclic inconsistencies*. They indicate to which extent the segmentation is reproducible after mesh adaptation with different "history". To arrive at meaningful motion estimates, these inconsistencies should be *smaller* than the minimum displacements $\boldsymbol{x}_{i,n+1} - \boldsymbol{x}_{i,n}$ between successive images from our time series, i.e., below 0.1–0.2mm for our images at 2% intervals (see Sec. 2.3 and Fig. 3–5(b)).

To check the sensitivity against variations in the start phase of the progressive adaptation, the complete time series segmentation was performed 10 times,

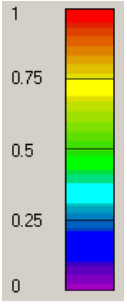

(a) red = 1.0mm

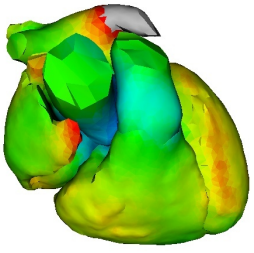

(b) Standard model

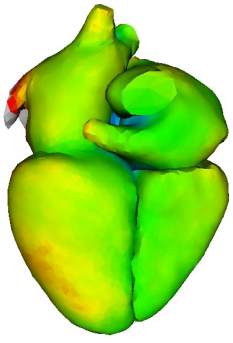

(c) Standard model

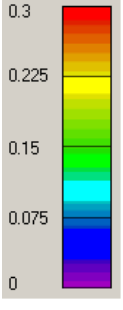

(d) red = 0.3mm

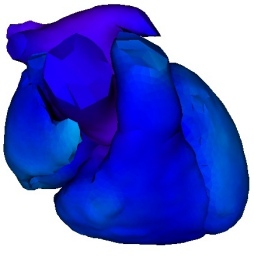

(e) Improved model

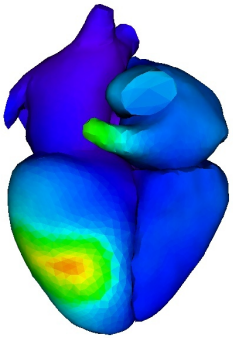

(f) Improved model

Fig. 7. Mean cyclic inconsistencies per triangle (averaged over 15 time series and 10 start phases per series). The color codes (a) for the standard model cover inconsistencies up to 1.0mm (larger values at the pulmonary veins are displayed in gray). For the *improved* model, color codes (d) represent a *smaller* interval. The region with increased inconsistencies at the bottom of the LV epicardium in (f) is due to one time series with confusing boundaries between LV epicardium, pericardium, and diaphragm (see text and last line in Tab. 1). For the improved model, mean inconsistencies at the LV endocardium are < 0.1mm (not visible).

starting at $P_0 = 0\%, 10\%, \ldots, 90\%$ and cyclic inconsistencies were measured for each start phase. In total, we get 150 measurements from the 15 time series. Table 1 summarizes the cyclic inconsistencies for the two models described in Sec. 2.3. In addition, Fig. 7 illustrates the distribution of the inconsistencies over the mesh surface.

For the *standard* model with 1mm sampling and gradients obtained from tri-linear interpolation, inconsistencies are too large for our tracking purposes. Although in the order of one voxel, we do not reach the required precision. For the *improved* model with 0.2mm sampling and convolution-based gradient calculation, the cyclic inconsistencies are drastically reduced and fulfill the requirements. Almost all triangles reach a consistency better than the sampling distance of 0.2mm. For 2 of the 15 cases, cyclic inconsistencies are a bit increased

Table 1. Cyclic inconsistencies Δ_i, averaged over the whole mesh (Δ_{mean}), and percentages of all triangles with Δ_i within different inconsistency bins. Statistics on Δ_{mean} and percentages cover 15 time series and 10 start phases per series.

Standard model [4]	Δ_{mean}	< 0.2mm	[0.2, 0.5)	[0.5, 1)	> 1mm
Mean [±SDev] (15 cases)	0.579 ±0.091 mm	20.5%	42.8%	24.2%	12.5%

Improved model	Δ_{mean}	< 0.2mm	[0.2, 0.5)	[0.5, 1)	> 1mm
Mean [±SDev] (15 cases)	0.052 ±0.008 mm	96.5%	2.1%	0.9%	0.5%
Mean [±SDev] (13 cases)	0.033 ±0.002 mm	98.8%	0.9%	0.2%	0.1%
Mean [±SDev] (2 cases)	0.178 ±0.025 mm	81.7%	9.7%	5.3%	3.3%

for some of the 10 start phases due to weak contrast near the pulmonary valve or confusing boundaries between LV epicardium, pericardium, and diaphragm. Table 1 includes a separate evaluation for these two cases. Omitting the latter case from the averages shown in Fig. 7 results in average inconsistencies for the complete LV epicardium well below 0.1mm.

Apart from measuring inconsistencies per triangle for all start phases, we compared the resulting motion curves. In general, results are very robust and the motion curves and locations of motion minima and maxima are not sensitive to the start phase. This finding is consistent with our visual impression that no gross segmentation failures did occur – neither for the initial image nor during propagation. Since initial segmentation as well as propagation are based on a shape model, we expect that the method works as long as the shape model can properly represent the anatomy. In case of hearts with pathologic anatomy (e.g., for some variants of congenital heart disease) initial segmentation may fail. In this case we expect larger inconsistencies and stronger variations for different heart phases.

4 Summary

Time series of 3D cardiac CT images can be segmented using shape-constrained deformable models. Proper gradient calculation and image sampling allows segmentation with sub-voxel accuracy. Tracking cardiac surfaces in a progressive adaptation scheme leads to consistent vertex and triangle positions that can be used to estimate local wall motion. Consistency checks indicate that the system is very precise (mean cyclic consistency = 0.05mm) and robust with respect to changing start phases for the progressive segmentation.

We note that motion occurs both along the surface normal and tangent to the surface although the latter is not explicitly tracked. Some geometric structures such as the grooves between atria and ventricles are so distinct that surface tracking should suffice to describe nearby tissue motion. In other areas – such as the locally flat ventricular epicardium – the tangential motion component may deviate from true tissue displacements. It would be interesting in future research to compare the estimated surface motion with true volumetric tissue motion

extracted from 4D US or 4D (tagged) MRI. This, however, will be challenging for the whole heart due to limited field-of-view or spatio-temporal resolution.

Access to local wall motion from 4D CT images has a potential to support a multitude of clinical and research applications, including refined functional measurements, local rest phase determination, detection and characterization of dyssynchronity, and comparison with electromechanical models of cardiac motion.

Acknowledgments. The authors would like to thank colleagues from Philips Healthcare CT for providing clinical data and continuous feedback on our cardiac segmentation system.

References

1. Gérard, O., et al.: Efficient model-based quantification of left ventricular function in 3-D echocardiography. IEEE Trans. Medical Imaging 21(9), 1059–1068 (2002)
2. Tobon-Gomez, C., et al.: Automatic construction of 3D-ASM intensity models by simulating image acquisition: Application to myocardial gated SPECT studies. IEEE Trans. Medical Imaging 27(11), 1655–1667 (2008)
3. Lynch, M., et al.: Segmentation of the left ventricle of the heart in 3-D+t MRI data using an optimized nonrigid temporal model. IEEE Trans. Medical Imaging 27(2), 195–203 (2008)
4. Ecabert, O., et al.: Automatic model-based segmentation of the heart in CT images. IEEE Trans. Medical Imaging 27(9), 1189–1201 (2008)
5. Zheng, Y., et al.: Four-chamber heart modeling and automatic segmentation for 3-D cardiac CT volumes using marginal space learning and steerable features. IEEE Trans. Medical Imaging 27(11), 1668–1681 (2008)
6. Delaunay, R., et al.: Cardiac function estimation for resynchronization therapy: Comparison between multislice-CT and speckle tracking imaging. In: Proc. ISBI, May 2008, pp. 524–527 (2008)
7. Sermesant, M., et al.: Cardiac function estimation from MRI using a heart model and data assimilation: Advances and difficulties. Medical Image Analysis 10(4), 642–656 (2006)
8. Manzke, R., et al.: Automatic phase determination for retrospectively gated cardiac CT. Medical Physics 31(12), 3345–3362 (2004)
9. Weese, J., et al.: Shape constrained deformable models for 3D medical image segmentation. In: Insana, M.F., Leahy, R.M. (eds.) IPMI 2001. LNCS, vol. 2082, pp. 380–387. Springer, Heidelberg (2001)
10. Ballard, D.H.: Generalizing the Hough transform to detect arbitrary shapes. Pattern Recogn. 13(2), 111–122 (1981)
11. Peters, J., et al.: Discriminative boundary detection for model-based heart segmentation in CT images. In: Pluim, J.P.W., Reinhardt, J.M. (eds.) Proc. SPIE Medical Imaging, March 2007, vol. 6512, pp. 65120H–1–65120H–11 (2007)

Physically-Constrained Diffeomorphic Demons for the Estimation of 3D Myocardium Strain from Cine-MRI

Tommaso Mansi[1], Jean-Marc Peyrat[1], Maxime Sermesant[1], Hervé Delingette[1], Julie Blanc[2], Younes Boudjemline[2], and Nicholas Ayache[1]

[1] INRIA-Méditerranée, Asclepios Project, Sophia Antipolis, France
[2] Assistance Publique Hôpitaux de Paris, Necker-Enfants Malades, Paris, France

Abstract. Analysing heart motion provides crucial insights on the condition of the cardiac function. Tagged-MRI and 2D-strain ultrasound enable quantitative assessment of the myocardium strain. But estimating 3D myocardium strain from cine-MRI remains attractive: cine-MRI is widely available and it yields detailed 3D+t anatomical images. This paper presents an image-based method to estimate myocardium strain from clinical short-axis cine-MRI. To recover non-apparent cardiac motions, we improve the diffeomorphic demons, a non-linear registration algorithm, by adding two physical constraints. First, myocardium near-incompressibility is ensured by constraining the deformations to be divergence free. Second, myocardium elasticity is modelled using smooth vector filters. The proposed physically-constrained demons are compared with the diffeomorphic demons and evaluated in a healthy subject against tagged MRI. The method is also tested on a patient with congenital pulmonary valve regurgitations and compared with 2D-strain measurements. In both cases, obtained results correlate well with ground truth. This method may become a useful tool for cardiac function evaluation.

1 Introduction

Analysing heart motion provides crucial insights on the condition and efficiency of the cardiac function. Myocardium strain can now be quantitatively assessed through tagged-MRI or ultrasound modalities such as 2D speckle tracking (also known as 2D-strain). Nevertheless, despite of its accuracy, tagged-MRI is still experimental [1] and while 2D-strain becomes available in clinical environment, it only provides partial evaluation of the myocardium [2]. Estimating the myocardium strain from clinical gated cine-MRI constitutes an attractive alternative. Cine-MRI is widely available and yields detailed 3D anatomical images of the beating heart with constant image quality through time. However, estimating strain from these images may result inaccurate since only the apparent motion can be extracted and slice thickness is usually large. Prior knowledge about cardiac dynamics is thus required.

N. Ayache, H. Delingette, and M. Sermesant (Eds.): FIMH 2009, LNCS 5528, pp. 201–210, 2009.
© Springer-Verlag Berlin Heidelberg 2009

Various methods have been proposed to estimate myocardium deformation from cine-MRI [3,4,5,6,7]. Some approaches drive an image registration algorithm with biomechanical finite-element models that simulate the myocardium passive properties [3,4]. These methods successfully estimate left ventricle myocardium strain. Nonetheless, they rely on specific biomechanical parameters that are difficult to determine for a given patient. Besides, such models may not apply anymore in diseases. Purely image-driven methods have thus been proposed [5,6,7]. In [5], the authors use a B-spline Free-Form Deformation (FFD) algorithm regularised using myocardium contours that are manually delineated on all time frames. The results are consistent with tagged MRI but requiring manual contours for all time frames may hamper using this approach in clinical settings. In [6], Bistoquet *et al.* present an FFD-like algorithm that ensures myocardium near-incompressibility [8]. The similarity criterion is penalised when the Jacobian of the deformation is significantly different from 1 and the dense deformation field is estimated by using divergence-free radial basis functions. However, myocardium is tracked at the nodes of the epicardium and endocardia surfaces only, the inner deformations being interpolated from the surfaces without considering possible textural hints. In [7], the authors estimate the cardiac motion using a spatio-temporal model based on FFD and Kalman filters, under the assumption of periodic motion. However, the proposed approach does not take guarantee myocardium biomechanical properties and it has been validated on 2D+t images only.

This paper presents an image-based method to estimate myocardium strain from clinical short-axis cine-MRI. Our approach relies on diffeomorphic demons [9], an efficient non-linear registration algorithm. Diffeomorphic non-linear registration [9,10,11] aims at finding a smooth, invertible, one-to-one mapping between two images, which is suited for cardiac motion analysis. Because diffeomorphic demons rely on image data exclusively, we introduce in the algorithm two physical constraints to recover plausible non-apparent cardiac motions: *i)* myocardium near-incompressibility [8] and *ii)* elasticity. Integrating incompressibility in non-linear registration algorithms has been widely studied for contrast-enhanced image registration [12,13,14]. Incompressibility can be modelled through the hard constraint Jacobian determinant of the deformation field equals 1 [12,13], or through the divergence-free approximation [6,14]. In our approach, near-incompressibility is obtained by projecting the velocity and deformation fields onto the space of divergence-free vector fields. The second physical constraint we consider is myocardium elasticity, modelled with an elastic-like regularisation. Although myocardium tissue is found visco-elastic, it can be reasonably modelled as elastic when it is analysed at the heart beat time-scale [8]. In this way, our approach is purely image-based, it evaluates the motion everywhere in the images, it does not need any mesh model and it requires very few image-based parameters. The Lagrangian finite strain tensor is finally calculated from the recovered deformation fields. The method is evaluated on a healthy subject, against tagged MRI, and on a patient suffering from congenital pulmonary valve regurgitations, against 2D-strain ultrasound.

2 Methods

2.1 Non-linear Image Registration Using Diffeomorphic Demons (DD) Algorithm

Non-linear image registration aims at providing a transformation $\phi(\mathbf{x}) = \mathbf{x} + \mathbf{u}(\mathbf{x})$, where $\mathbf{u}(\mathbf{x})$ is the displacement vector field, that aligns a template image $T(\mathbf{x})$ with a reference image $R(\mathbf{x})$. The underlying principle lies in minimising an energy $\mathcal{E}(\phi)$ that comprises a similarity criterion $\mathcal{D}(T, R, \phi)$ and a regulariser $\mathcal{R}(\phi)$ ensuring smooth transformations and integrating prior knowledge.

Diffeomorphic demons (DD) algorithm [9] minimises $\mathcal{E}(\phi)$ iteratively through two decoupled steps. A correspondence field $\mathbf{c}$ that matches the points between the two images, with a controlled uncertainty parametrised by σ_x^2, is introduced in the energy: $\mathcal{E}(\mathbf{c}, \mathbf{u}) = 1/\sigma_i^2 \ \|R - T \circ \mathbf{c}\|^2 \ + \ 1/\sigma_x^2 \ \|\mathbf{u} - \mathbf{c}\|^2 \ + \ 1/\sigma_T^2 \ \|\nabla \mathbf{u}\|^2$. In this equation, σ_i^2 is a parameter related to the noise in the images and σ_T^2 compromises between the image data term and the regularisation.

First, the correspondence field $\mathbf{c}$ is updated using the diffeomorphic update rule $\mathbf{c} \leftarrow \mathbf{u} \circ \exp(\mathbf{v})$. $\exp(\mathbf{v})$ is the exponential operator defined in the Log-Euclidian framework and $\mathbf{v}$ is the smooth stationary *velocity* field that results from the minimisation of the correspondence energy:

$$\mathcal{E}_{corr}(\mathbf{v}) = \frac{1}{\sigma_i^2}\|R - T \circ \mathbf{u} \circ \exp(\mathbf{v})\|^2 + \frac{1}{\sigma_x^2} \ \|\mathbf{u} - \mathbf{u} \circ \exp(\mathbf{v})\|^2 \qquad (1)$$

Derivating $\mathcal{E}_{corr}$ yields $\mathbf{v} = -(R - T \circ (\mathrm{Id} + \mathbf{u}))/(\|J\|^2 + \sigma_i^2/\sigma_x^2) \ J$, with $J = (\nabla R + \nabla(T \circ (\mathrm{Id} + \mathbf{u})))/2$ and $\sigma_i = |R - T \circ (\mathrm{Id} + \mathbf{c})|$ (see [9] for further details).

Second, the displacement $\mathbf{u}$ that satisfies the regulariser $\mathcal{R}(\mathbf{u})$, knowing the new correspondence field $\mathbf{c}$, is computed. The second part of the demons energy $\mathcal{E}(\mathbf{c}, \mathbf{u})$, $\mathcal{E}_{reg}(\mathbf{c}, \mathbf{u}) = 1/\sigma_x^2 \ \|\mathbf{u} - \mathbf{c}\|^2 + 1/\sigma_T^2 \|\nabla \mathbf{u}\|^2$, is minimised with respect to $\mathbf{u}$, which amounts to convoluting $\mathbf{c} = \mathbf{u} \ \circ \ \exp(\mathbf{v})$ with a Gaussian kernel.

2.2 Adding Physical Constraints to the Diffeomorphic Demons

Diffeomorphic demons (DD) algorithm is purely driven by image intensities. Therefore, it can hardly recover longitudinal shortening and circumferential twisting, which are poorly apparent in short-axis cine-MRI. To better estimate these displacements, we improve the algorithm by adding two constraints related to the myocardium tissue properties: near-incompressibility and elasticity.

Incompressibility Constraint. Contrary to [13], the incompressibility constraint is decoupled from the energy minimisation to take advantage of the two-step minimisation process offered by the demons. Since DD relies on velocity fields, fluid-dynamics laws are used to model incompressibility [14]. However, slight volume drifts may remain as the Gaussian regularisation does not preserve incompressibility. Positions are hence corrected at the end of the demons loop to further reduce volume variations.

Velocity Correction: Myocardium incompressibility can be interpreted as conservation of myocardium mass throughout the cardiac cycle [8]. Therefore, the mass continuity equation $\partial\rho/\partial t + \mathrm{div}(\rho\mathbf{v}) = 0$ applies, where ρ is the mass density, $\mathbf{v}$ is the velocity and t is the time. Assuming ρ constant and uniform, the conservation of mass becomes conservation of volume and writes as $\mathrm{div}(\mathbf{v}) = 0$.

Consequently, the incompressibility property is integrated in the DD by constraining the search space of the velocity fields $\mathbf{v}$ to the divergence-free vector space. Given the velocity field $\mathbf{v}$ computed by Equation (1), we solve the Lagrangian problem [15]:

$$\min_{\hat{\mathbf{v}}\in\{\mathbf{f}\in L^2(\Omega) \mid \mathrm{div}\ \mathbf{f}\ =\ 0\}} \max_{p\in \mathrm{H}_0^1} \left(\frac{1}{2}\|\mathbf{v}-\hat{\mathbf{v}}\|^2 + \int_\Omega p\ \mathrm{div}\ \hat{\mathbf{v}}\right) \tag{2}$$

In this equation, Ω is an open subset of $\mathbb{R}^3$ (the image space), $\mathrm{H}_0^1(\Omega)$ is the Sobolev space associated to Ω and p is the Lagrange multiplier related to the divergence-free constraint. Derivating Equation (2) gives the optimal condition:

$$\hat{\mathbf{v}} = \mathbf{v} - \mathrm{grad}\ p \tag{3}$$

under the constraint $\mathrm{div}\ \hat{\mathbf{v}} = 0$. Equation (3) is the closed-form expression of the divergence-free projector $\Pi(\mathbf{v}) = \mathbf{v} - \mathrm{grad}\ p$, where p is obtained by solving the Poisson equation $\triangle p = \mathrm{div}(\mathbf{v})$ under 0-Dirichlet boundary conditions [15].

Position Correction: Because the Gaussian regularisation may alter the obtained incompressibility, we perform a second adjustment to correct the remaining volume drifts after deformation.

For each point $\mathbf{x}$ of the image space, the Jacobian determinant $J(\mathbf{x}) = \det(\mathrm{Id} + \nabla\mathbf{u}(\mathbf{x}))$ relates to the local volume change due to the transformation $\phi(\mathbf{x}) = \mathbf{x} + \mathbf{u}(\mathbf{x})$. Hence, the volume is locally preserved if the non-linear constraint $J(\mathbf{x}) = 1$ is satisfied. However, since myocardium is *nearly* incompressible (5% of volume variation is usually observed [6,8]) and the displacements provided by the DD are smooth and derive from divergence-free velocities, the first-order approximation of $J(\mathbf{x}) = 1$, i.e. $\mathrm{div}(\mathbf{u}) = 0$, can be used to correct the remaining volume drifts. As a result, the positions are corrected like the velocities. At each iteration of the demons algorithm, the displacement field $\mathbf{u}$ is made divergence-free by using the above-mentioned projector Π (Equation (3)). It is worth stressing that the displacements are projected to reduce remaining volume drifts, whereas the velocities are projected as a result of the mass-conservation law.

Elastic-Like Regularisation. Myocardium is commonly assumed to be visco-elastic. However, at the time-scale of the heart beat, one can reasonably approximate the visco-elasticity property by elasticity [8]. In our approach, elasticity is modelled as regularisation. We substitute the diffusion-like regularisation, which is unable to model elastic deformations, by an elastic regulariser. Linear elastic regularisers have been widely studied in the past [16]. Yet, they are suitable for small displacements only and can present discontinuities in the derivatives of

the resulting deformations, which is not desirable for our application. To overcome these limitations, we regularise the deformation field using an infinite-order isotropic differential quadratic form [17]. Such regulariser behaves like elastic filters, while ensuring smooth deformations. Minimising $\mathcal{E}_{reg}(\mathbf{c}, \mathbf{u})$ with this regulariser amounts to convoluting the deformation field $\mathbf{u}$ by the 3D isotropic separable filter:

$$G_{\sigma,\kappa}(\mathbf{u}) = \frac{1}{(\sigma\sqrt{2\pi})^3(1+\kappa)} \left(\mathrm{Id} + \frac{\kappa}{\sigma^2}\mathbf{u}\mathbf{u}^T\right) \exp\left(\frac{\mathbf{u}^T\mathbf{u}}{2\sigma^2}\right) \tag{4}$$

which can be performed very efficiently by using recursive Gaussian filter [17]. In Equation (4), σ is the standard deviation of the Gaussian function and κ is a parameter that acts as a Poisson ratio coefficient. The higher is κ, the stiffer is the deformation.

Final Algorithm. Bellow we summarise the steps of the physically-constrained demons. Steps with a star (*) relates to the new physical constraints.

Physically-Constrained Demons (PCD) Algorithm

- Choose an initial spatial transformation $\phi(\mathbf{x}) = \mathbf{x} + \mathbf{u}(\mathbf{x})$
- Iterate until $\mathcal{D}(R, T; \mathbf{u})$ stops decreasing
  1. Given the current deformation $\mathbf{u}$, compute the update velocity field $\mathbf{v}$ by minimising $\mathcal{E}_{corr}(\mathbf{v})$ (Equation (1)).
  2. Fluid-like regularisation: $\mathbf{v} \leftarrow K_{fluid} \star \mathbf{v}$. K_{fluid} is typically a Gaussian kernel with standard deviation σ_{fluid}.
  3. (*) Correct the velocity to be divergence-free: $\mathbf{v} \leftarrow \Pi(\mathbf{v})$.
  4. Update the correspondence field: $\mathbf{c} \leftarrow \mathbf{u} \circ \exp(\mathbf{v})$
  5. (*) Elastic-like regularisation: $\mathbf{u} \leftarrow G_{\sigma,\kappa} \star \mathbf{c}$ (Equation (4))
  6. (*) Correct the deformation to be divergence-free: $\mathbf{u} \leftarrow \Pi(\mathbf{u})$.

About the algorithm parameters. PCD algorithm is controlled by four parameters: the maximum step length [9], σ_{fluid}, σ and κ. In all our experiments, we have used standard values according to previous experiments [9,17]: the maximum step length is 1, σ_{fluid} is 0.5, σ is 2.0 and κ is 0.5.

2.3 Estimating Strain from Cine-MRI

Strain is estimated from cine MRI by tracking the myocardium throughout the cardiac sequence. Let I_0 be the end-diastole time frame. Since DD algorithm is expressed in the Eulerian frame [16] and strain is computed in the Lagrangian frame, the tracking must be performed backwards: the strain between the images I_0 and $I_{n>0}$ is computed from the deformation obtained by registering $I_{n>0}$ to I_0. A recursive strategy is employed to take advantage of the frame-by-frame registration accuracy and to reduce tracking errors due to the changing appearance of the trabecula, papillary muscles and neighbouring

organs. Having the spatial transformation $\phi_{I_{n-1} \to I_0}$, we first compute $\phi_{I_n \to I_{n-1}}$ and then we estimate the transformation $\phi_{I_n \to I_0}$ by taking as initialisation the composed transformation $\phi_{I_n \to I_{n-1}} \circ \phi_{I_{n-1} \to I_0}$. Finally, Lagrangian finite strain tensor $\mathrm{E} = 1/2\ (\nabla \mathbf{u} + \nabla \mathbf{u}^T + \nabla \mathbf{u}^T \nabla \mathbf{u})$ is computed from the recovered deformation $\phi(\mathbf{x}) = \mathbf{x} + \mathbf{u}(\mathbf{x})$. Radial, circumferential and longitudinal strains are estimated in the heart prolate coordinate system [18].

3 Experiments and Results

The method is tested on two subjects: a healthy adult and a young patient suffering from congenital pulmonary valve regurgitations. In the two experiments, heart motion is recovered from gated short-axis cine-MRI. In the first experiment, the resulting 3D deformations are compared with tagged MRI. In the second experiment, the deformations are compared with ultra-sound 2D-strain.

Because we are mainly interested in myocardium strain and to minimise the computational overhead, diffeomorphic demons are constrained only inside a mask that delineates the cardiac muscle. As the projector Π and the elastic smoothing are decoupled from the minimisation, appearing as additive terms in the algorithm (Equations (3) and (4)), they can be added inside the mask and ignored outside (where diffeomorphic demons are still applied). It should be noted however that at the mask boundaries, the incompressibility constraint is not ensured due to the boundary conditions of the projector Π. Furthermore, discontinuities may appear at the mask boundaries when computing the displacement derivatives. These limitations are addressed by dilating the myocardium mask by one voxel, thus ensuring optimal strain estimation within the myocardium. At last, we need to segment the myocardium at the end-diastole time frame only owing to the Eulerian formulation of the demons algorithm, contrary to previous approaches which require delineations for all the cardiac sequence frames [3,5].

3.1 Left Ventricle Myocardium Strain in a Healthy Subject

Retrospective gated steady-state free precession (SSFP) cine MR and tagged MR (complementary spatial modulation of magnetisation CSPAMM) images of a healthy subject are acquired in the short-axis view covering the mid-part of both ventricles using 1.5T MR scanner (Achieva, Philips Medical System) (seven 10mm-thick slices; 1.37x1.37mm in-plane resolution, 30 frames). No longitudinal cine-MRI are available. Visual inspection of the images revealed no spatial misregistration. To improve registration performances, the resolution of the cine-MR images is made isotropic at the in-plane resolution.

First, the incompressibility constraint is evaluated by computing the Jacobian determinant of the recovered myocardium deformation at each frame of the cardiac sequence. Without any constraint, mean Jacobian equals 1.09 ± 0.07 (mean $\pm$ SD), maximum deviation from unity: 0.22. Adding the constraints yields $J(\mathbf{u}_{myo}) = 0.99 \pm 0.02$ (mean $\pm$ SD) with a maximum deviation from unity of 0.05, which relates to the observed 5% of myocardium volume variation [8].

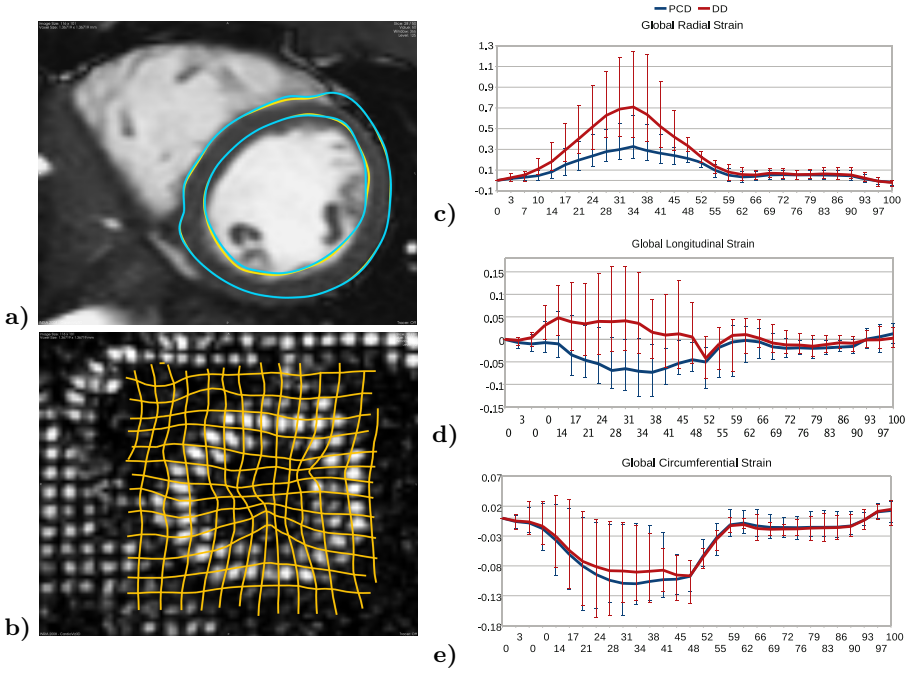

Fig. 1. a) End-systole myocardium mask propagated back to the end-diastole image using DD *(in yellow)* and PCD *(in blue)*. Both algorithms provide similar registration performances. b) Tagged-MRI at end-systole and tag grid deformed by the cine-MRI transformation estimated using PCD. c-e) Global strain with maximum and minimum zone values. Time is normalised in %.

Second, registered images provided by the physically-constrained demons (PCD) are compared with those provided by the diffeomorphic demons (DD). Available myocardium mask at end-systole is registered back to the end-diastole image using the two methods. Qualitative evaluation is satisfying (Fig. 1a). Hausdorff distance between the two registered masks is 2.23mm and average Hausdorff distance is 0.02mm, which is less than the through-plane image resolution. The physical constraints do not qualitatively decrease the registration performances.

Next, radial, longitudinal and circumferential strains are computed for the six equatorial AHA zones using DD and PCD. In this experiment, we only consider the equatorial zones since at the basal and apical regions the incompressibility assumptions may be violated due to the truncated acquisition. Fig. (1c-e) illustrate the global strains with minimum and maximum zone values. DD mainly recovers the visible radial motion of the heart, resulting in over-estimated radial strains, implausible positive longitudinal strains and weak circumferential strains. On the other hand, the physical constraints enable recovering non-apparent motions by reorienting the estimated myocardium deformations to ensure incompressibility. Radial strain is closer to clinical observations and more homogeneous across the myocardium [18], thus suggesting that the physical constraints also perform global regularisation. Longitudinal strain is clinically plausible yet slightly

under-estimated with respect to reported values, mainly because of the coarse through-plane resolution. Circumferential strain is improved but remains close to DD estimations. A probable reason is the low temporal resolution, circumferential motion occurring in few time frames.

Finally, the deformations recovered from the short-axis cine-MRI using PCD are qualitatively compared with short-axis tagged-MRI, exhibiting promising results (Fig. 1b).

3.2 Left-Ventricle Myocardium Strain in a Patient with Chronic Pulmonary Valve Regurgitations

In the second experiment we evaluate our method on a patient (age=10) with congenital pulmonary valve regurgitations. SSFP cine MRI of the heart are acquired in the short-axis view covering the entirety of both ventricles (10 9.6mm-thick slices; 1.02x1.02mm in-plane resolution; 25 frames) using a 1.5T MR scanner (Avanto, Siemens Medical Systems, Erlangen, Germany). No longitudinal cine-MRI are available. Visual inspection of the images revealed no spatial misregistration. Finally, the images are made isotropic to improve registration performances. 2D-strain measurements are performed in the short-axis and the 4-chamber views (frame-rate: 80) using Automatic Functional Imaging (Vivid7, General Electrics, Vingmed Ultrasound), as described in [2].

Lagrangian finite strain tensors are estimated from the cine-MRI. Longitudinal (L_l) and circumferential (L_c) lengthening are computed according to the relation $L_V = \sqrt{1 + \mathrm{E}_{VV}} + 1$, where E is the strain tensor and $V \in \{l, c\}$ is the

Table 1. Cine-MRI and 2D-strain (in parentheses) longitudinal lengthening. Values estimated from 3D MRI using PCD are close to the 2D measurements in spite of the different nature of the images.

Basal septal	Mid septal	Apical septal	Basal lateral	Mid lateral	Apical lateral
-0.11 (-0.19)	-0.18 (-0.19)	-0.19 (-0.09)	-0.10 (-0.11)	-0.12 (-0.11)	-0.07 (-0.11)

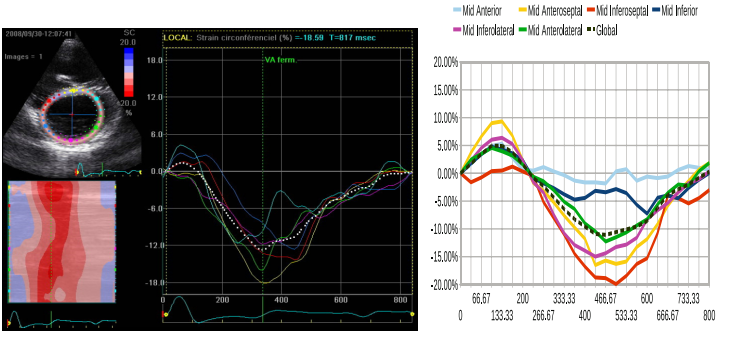

Fig. 2. Circumferential strain throughout the cardiac cycle. *Left*: 2D-strain measurement. *Right*: cine-MRI estimation. X-axis is the time in ms, Y-axis the strain in %.

considered direction. The results are compared with 2D-strain measurements. Despite of the different nature of the measurements, promising correlation is obtained. Estimated regional circumferential strains exhibit realistic variations (Fig. 2). Longitudinal strains are similar to the 2D-strain measurements in most of the heart regions visible in the acquired 2D slice (Table 1). However, as observed in the healthy subject, cine-MRI-derived longitudinal strains tend to be underestimated due to the large slice thickness. Finally, the apical septal strain has been overestimated because of the lower image quality at the apex and of the ill-defined left-right ventricles junction.

4 Conclusion

In this paper we demonstrate the effectiveness of a physically-constrained demons algorithm to recover cardiac motion from short-axis gated cine-MRI. Our approach improves the physical plausibility of the estimated myocardium deformations by constraining the registration algorithm to provide incompressible and elastic transformations. Incompressibility is modelled using divergence-free velocity fields, as defined by the mass-conservation law. A second correction is performed at the end of the demons loop to correct the positions from possible volume drifts resulting from the regularisation, which does not guarantee incompressibility. On the other hand, the second correction alone would not have been sufficient since it only approximates the strong volume-preserving constraint, thus yielding incomplete volume recovery. The physical constraints reorient the displacement vectors within the myocardium, which enables the recovery of longitudinal and circumferential motions. Compared with tagged-MRI and 2D-strain, the proposed method showed promising results for a healthy subject and a patient. Despite of the coarse longitudinal resolution, realistic through-plane motions have been recovered, yet under-estimated with respect to values reported in the literature. Future works include parameter-sensitivity study and comprehensive validation on controls and patients. This method may become a useful tool for cardiac function evaluation and retrospective studies.

Acknowledgements. The work has been partly funded by the European Commission through the IST-2004-027749 Health-e-Child Integrated Project[1]. The authors would like to thank Rado Andriantsimiavona, King's College London, Division of Imaging Sciences, for the cine and tagged MR images.

References

1. McVeigh, E.: Regional myocardial function. Cardiology Clinics 16(2), 189–206 (1998)
2. Teske, A., De Boeck, B., Melman, P., Sieswerda, G., Doevendans, P., Cramer, M.: Echocardiographic quantification of myocardial function using tissue deformation imaging, a guide to image acquisition and analysis using tissue doppler and speckle tracking. Cardiovascular Ultrasound 5, 27 (2007)

[1] http://www.health-e-child.org

3. Papademetris, X., Sinusas, A., Dione, D., Constable, R., Duncan, J.: Estimating 3D strain from 4D cine-MRI and echocardiography: In-vivo validation. In: Delp, S.L., DiGoia, A.M., Jaramaz, B. (eds.) MICCAI 2000. LNCS, vol. 1935, pp. 678–686. Springer, Heidelberg (2000)
4. Veress, A., Gullberg, G., Weiss, J.: Measurement of Strain in the Left Ventricle during Diastole with cine-MRI and Deformable Image Registration. Journal of Biomechanical Engineering 127, 1195 (2005)
5. Feng, W., Denney, T., Lloyd, S., Dell'Italia, L., Gupta, H.: Contour regularized left ventricular strain analysis from cine MRI. In: Proc. ISBI 2008, pp. 520–523 (2008)
6. Bistoquet, A., Oshinski, J., Skrinjar, O.: Myocardial deformation recovery from cine MRI using a nearly incompressible biventricular model. Medical Image Analysis 12(1), 69–85 (2008)
7. Delhay, B., Clarysse, P., Magnin, I.: Locally Adapted Spatio-temporal Deformation Model for Dense Motion Estimation in Periodic Cardiac Image Sequences. In: Sachse, F.B., Seemann, G. (eds.) FIMH 2007. LNCS, vol. 4466, p. 393. Springer, Heidelberg (2007)
8. Glass, L., Hunter, P., McCulloch, A.: Theory of Heart: Biomechanics, Biophysics, and Nonlinear Dynamics of Cardiac Function. Springer, Heidelberg (1991)
9. Vercauteren, T., Pennec, X., Perchant, A., Ayache, N.: Non-parametric diffeomorphic image registration with the demons algorithm. In: Ayache, N., Ourselin, S., Maeder, A. (eds.) MICCAI 2007, Part II. LNCS, vol. 4792, pp. 319–326. Springer, Heidelberg (2007)
10. Dupuis, P., Grenander, U., Miller, M.: Variational problems on flows of diffeomorphisms for image matching. Quaterly of Applied Mathematics 56(3), 587–600 (1998)
11. Ashburner, J.: A fast diffeomorphic image registration algorithm. Neuroimage 38(1), 95–113 (2007)
12. Rohlfing, T., Maurer Jr., C., Bluemke, D., Jacobs, M.: Volume-preserving nonrigid registration of MR breast images using free-form deformation with an incompressibility constraint. IEEE Transactions on Medical Imaging 22(6), 730–741 (2003)
13. Haber, E., Modersitzki, J.: Numerical methods for volume preserving image registration. Inverse Problems 20(5), 1621–1638 (2004)
14. Saddi, K.A., Chefd'hotel, C., Cheriet, F.: Large deformation registration of contrast-enhanced images with volume-preserving constraint. In: Proc. SPIE Medical Imaging, vol. 6512. SPIE (2007)
15. Simard, P.Y., Mailloux, G.E.: A projection operator for the restoration of divergence-free vector fields. IEEE Transactions on Pattern Analysis and Machine Intelligence 10(2), 248–256 (1988)
16. Modersitzki, J.: Numerical Methods for Image Registration. Oxford University Press, Oxford (2004)
17. Cachier, P., Ayache, N.: Isotropic energies, filters and splines for vectorial regularization. J. of Math. Imaging and Vision 20(3), 251–265 (2004)
18. Moore, C., Lugo-Olivieri, C., McVeigh, E., Zerhouni, E.: Three-dimensional systolic strain patterns in the normal human left ventricle: Characterization with tagged MR imaging. Radiology 214(2), 453–466 (2000)

Coronary Occlusion Detection with 4D Optical Flow Based Strain Estimation on 4D Ultrasound

Qi Duan[1,2], Elsa D. Angelini[3], Auranuch Lorsakul[1], Shunichi Homma[1], Jeffrey W. Holmes[4], and Andrew F. Laine[1]

[1] Columbia University, New York, NY, USA
{qd2002,al2776,sh23,laine}@columbia.edu
[2] Center for Biomedical Imaging, NYU School of Medicine, New York, NY, USA
Qi.Duan@nyumc.org
[3] Institut Telecom, Telecom ParisTech, CNRS LTCI, Paris, France
elsa.angelini@telecom-paristech.fr
[4] Department of Biomedical Engineering and Medicine, University of Virginia, Charlottesville, VA, USA
holmes@virginia.edu

Abstract. Real-time three-dimensional echocardiography (RT3DE) offers an efficient way to obtain complete 3D images of the heart over an entire cardiac cycle in just a few seconds. The complex 3D wall motion and temporal information contained in these 4D data sequences has the potential to enhance and supplement other imaging modalities for clinical diagnoses based on cardiac motion analysis. In our previous work, a 4D optical flow based method was developed to estimate dynamic cardiac metrics, including strains anddisplacements, from 4D ultrasound. In this study, in order to evaluate the ability of our method in detecting ischemic regions, coronary artery occlusion experiments at various locations were performed on five dogs. 4D ultrasound data acquired during these experiments were analyzed with our proposed method. Ischemic regions predicted by the outcome of strain measurements were compared to predictions from cardiac physiology with strong agreement. This is the first direct validation study of our image analysis method for biomechanical prediction and *in vivo* experimental outcome.

1 Introduction

Motion estimation in echocardiography has been and continues to be an active area of research. Doppler ultrasound has become widespread for imaging flow and quantifying blood and tissue velocities. However, this method is limited by angular dependency, i.e., it can only quantify the axial component of motion along the transmitted acoustic wave. Speckle tracking methods [1-4] overcome this limitation by directly tracking the backscattered echoes produced by the ultrasonic scatterers in blood and tissues. The tracking can be performed either in the image domain [2-4] or directly in the radio-frequency (RF) domain [1]. Although in theory this can be done on 1D, 2D, and 3D images, clinical applications are limited to 1D and 2D modalities. The ability of speckle tracking to estimate motion and strain has been validated against MR tagging in recent studies [5].

N. Ayache, H. Delingette, and M. Sermesant (Eds.): FIMH 2009, LNCS 5528, pp. 211–219, 2009.
© Springer-Verlag Berlin Heidelberg 2009

Development of real-time 3D (RT3D) echocardiography started in the late 1990s [6] based on matrix phased array transducers. Recently, a new generation of RT3D transducers was introduced by Philips Medical Systems (Andover, MA) in the SONOS 7500, followed by the iE33 model, which can acquire a fully sampled cardiac volume in four cardiac cycles and capture complex 4D cardiac motion well. Recently, other vendors have release their 4D ultrasound products, including GE Vivid 7 and E9, Siemens SC2000 and Toshiba Artida. However, full exploitation of three-dimensional ultrasound data for qualitative and quantitative evaluation of cardiac function remains sub-optimal due to the lack of proper 4D analysis tools. Manual tracing of myocardial borders is a tedious task that requires the intervention of an expert cardiologist familiar with the ultrasound machine and an interactive drawing interface. For this reason, myocardial motion is commonly assessed via visual inspection of B-scan images. Moreover, even though some commercial software tools now provide 3D endocardial wall motion tracking tools, to this date, there is no commercial real-time 3D ultrasound machine or software tool that can provide direct quantitative motion and strain measurements analogous to tissue Doppler or strain imaging for the entire myocardium, which has limited the application of RT3D echocardiography to anatomical measurements and visual inspection of cardiac motion.

For this reason, several image processing-based motion and strain estimation computational methods using 3D ultrasound have been proposed. Meunier [3] showed the performance of 3D speckle tracking using simulated ultrasound images. Elen *et al* [7] recently showed feasibility of using elastic registration in strain estimation. Our group [8, 9] has shown that using a correlation-based optical flow method, myocardial motion fields can be estimated, from which directional displacements and strains can be computed. In order to evaluate the values in biomechanical prediction, in this study, ischemic regions detected by our method were directly compared to cardiac physiology prediction during controlled coronary occlusion experiments.

2 Method

2.1 Correlation-Based Optical Flow

Optical flow (OF) tracking refers to the computation of the displacement field of objects in an image, based on the assumption that the intensity of the object remains constant. In this context, motion of the object is characterized by a flow of pixels with constant intensity. The assumption of intensity conservation is typically unrealistic for natural movies and medical imaging applications, motivating the argument that OF can only provide *qualitative* estimation of object motions. There are two global families of OF computation techniques: (1) Differential techniques [10-12] that compute velocity from spatio-temporal derivatives of pixel intensities; (2) Region-based matching techniques [13, 14], which compute the OF via identification of local displacements that provide optimal correlation of two consecutive image frames. Compared to differential OF approaches, region-based methods using correlation measures are less sensitive to noisy conditions and fast motion [15] but assume that displacements in small neighborhoods are similar. In three-dimensional ultrasound, this later approach appeared more appropriate and was selected for this study. Given two data

sets from consecutive time frames: $\left(I(\mathbf{x},t), I(\mathbf{x},t+\Delta t)\right)$, the displacement vector $\Delta\mathbf{x}$ for each pixel in a small neighborhoods Ω around a pixel x is estimated via maximization of the cross-correlation coefficient defined as:

$$r = \frac{\sum_{\mathbf{x}\in\Omega}\left(I(\mathbf{x},t) * I(\mathbf{x}+\Delta\mathbf{x},t+\Delta t)\right)}{\sqrt{\sum_{\mathbf{x}\in\Omega} I^2(\mathbf{x},t)\sum_{\mathbf{x}\in\Omega} I^2(\mathbf{x}+\Delta\mathbf{x},t+\Delta t)}} \tag{1}$$

In this study, correlation-based OF was applied to estimate the displacement of selected voxels between two consecutive ultrasound volumes in the cardiac cycle. The search window Ω was centered about every (5×5×5) pixel volume and was set to size (7×7×7).

2.2 Cardiac Dynamic Metrics

A flowchart of the computational framework is provided in Fig. 1 below. Three coordinate systems are involved in the computational framework (Fig. 2): pixel coordinates (i, j, k), Cartesian coordinates (x, y, z), and cylindrical coordinates (r, θ, z). The OF estimation was performed in pixel coordinates. For the computation of dynamic information, displacements in pixel coordinates were converted into Cartesian coordinates and centered inside the ventricular cavity so that the z-axis was aligned with the long axis of left ventricle. This coordinate transform is performed via a rigid transformation:

$$\begin{bmatrix} x \\ y \\ z \end{bmatrix} = R\begin{bmatrix} i \\ j \\ k \end{bmatrix} + T = \begin{bmatrix} r_{11} & r_{12} & r_{13} \\ r_{21} & r_{22} & r_{23} \\ r_{31} & r_{32} & r_{33} \end{bmatrix}\begin{bmatrix} i \\ j \\ k \end{bmatrix} + \begin{bmatrix} -O_i \\ -O_j \\ -O_k \end{bmatrix} \tag{2}$$

where R is a rotation matrix, T is a translation vector, equal to the negative pixel coordinates of the origin O of the Cartesian coordinate system. The ventricular axis was defined as the axis connecting the center of the mitral orifice and the endocardial apex. This axis has a very stable position during the whole cardiac cycle [16]. Based on the Cartesian coordinate system, a corresponding cylindrical coordinate system is established with the r-θ plane corresponding to the x-y plane and with the x-axis used as the reference for θ.

Endocardial and epicardial contours were provided by cardiologists at end-diastole, i.e. the 1st frame of the 4D ultrasound sequence, as an initialization. Based on that, myocardium voxels were segmented and automatically tracked via correlation-based optical flow algorithm through the whole cardiac cycle. Myocardial motion field (u_x, u_y, u_z) for each myocardial voxel provided by optical flow was then used to compute dynamic cardiac metrics, including:

- Displacement low magnitude $|u|$ (mm)
- Radial displacement u_r (mm)
- Circumferential displacement u_θ (mm)

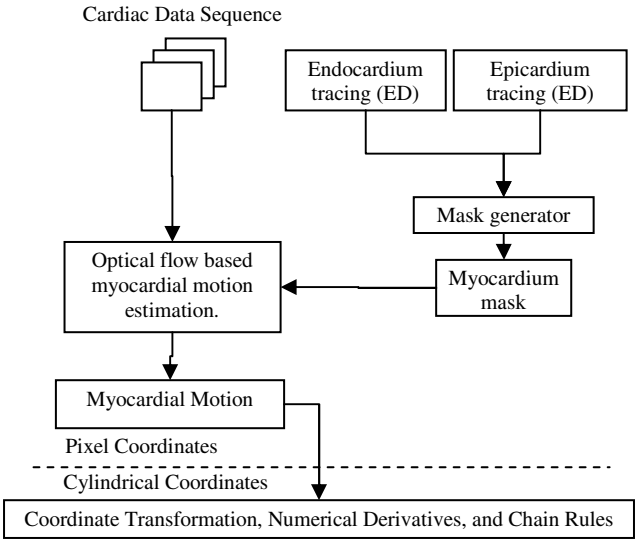

Fig. 1. Flow chart of computational framework for processing of 4D echocardiography data for measures of strain

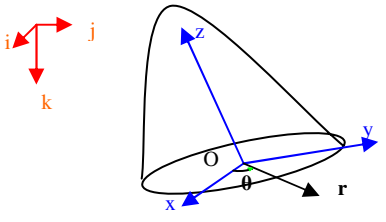

Fig. 2. Coordinate systems for data acquisition and computation

- Strain tensor $E = \left(\nabla u + \nabla u^T + \nabla u^T \nabla u\right)/2$, where the major diagonal values of E contain thickening, circumferential strain, and longitudinal strain
- Twist $\partial u_\theta / \partial z$ and cardiac torsion.

Gradient values were computed directly in pixel coordinates and converted into the cylindrical coordinate system via chain rule. Derivatives in pixel coordinates were approximated by central difference operators.

Since in clinical applications, temporal profiles of the segmental average values for displacements and strains are more valuable than ED-to-ES values, we modified our software so that it could compute temporal profiles of these cardiac dynamic metrics in segmental average fashion, according to the 16-segment model of the left ventricular myocardium according to the American Society of Echocardiography [17].

2.3 Controlled Occlusion Experiments

To validate the ability of the proposed framework in predicting ischemic regions, several controlled occlusions during open heart canine experiments were performed

under a protocol approved by Columbia University's Institutional Animal Care and Use Committee. In each experiment, 4 different occlusions, including distal and proximal LAD occlusions and distal and proximal LCx occlusions were performed. 4D ultrasound data was acquired during the experiment both for baseline and 2 minutes after occlusions with the iE33 ultrasound machine (Philips, Andover, MA), the X3-1 probe (3MHz, 25 fps) and apical screening. A gelatin pad was placed between the heart and the transducer. 4D ultrasound acquisition was acquired with 4-quadrant mode as in clinical settings. The same experiment protocol was repeated for five different dogs on five different days.

3 Results

3.1 Temporal Curves

Results of radial displacements and radial strains (thickening) on the baseline scan and after proximal LAD occlusion are shown in Fig. 3 and Fig. 4 respectively. Compared to the results of the baseline scan, radial displacement correctly indicated the outward motion of the anterior section and reduced motion for antero-septal and septal sections of the heart. Overall motion magnitudes were lower for the other three sections. The radial strain analysis results were even more interesting as: (1) negative radial strain values were observed for the anterior section throughout the whole cardiac cycle, (2) values for antero-septal segments also dropped, (3) whereas the values of lateral and posterior sections were relatively stable.

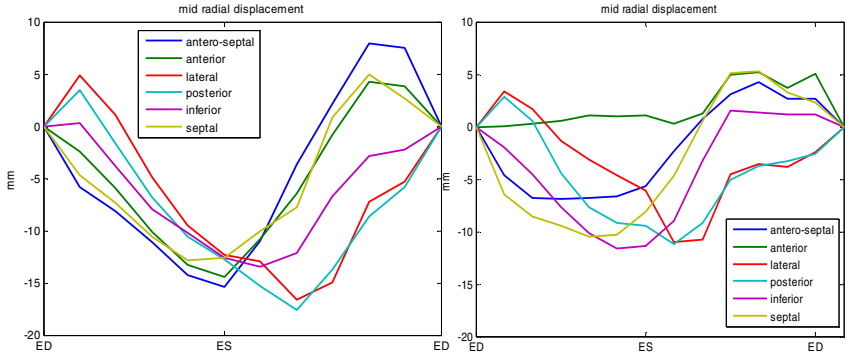

Fig. 3. Sample radial displacement estimation from 4D ultrasound analysis on (a) baseline and (b) ischemic scans in a canine experiment with proximal LAD occlusion

Similar results can also be found from the circumferential strain values in Fig. 5: Under LAD occlusion, values on the anterior segment changed from normal values (negative) to abnormal (positive); values of antero-septal segments also dropped in magnitude, whereas values of lateral and posterior sections remained relatively stable.

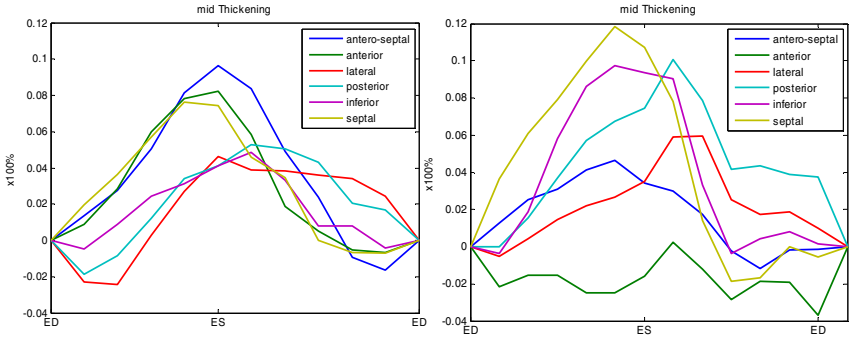

Fig. 4. Sample radial strain (thickening) estimation from 4D ultrasound analysis on (a) baseline and (b) ischemic scans in a canine experiment with proximal LAD occlusion

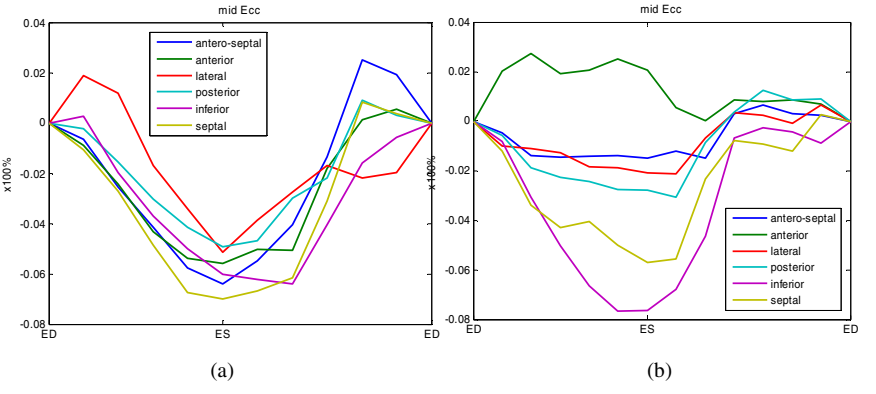

Fig. 5. Sample circumferential strain estimation from 4D ultrasound analysis on (a) baseline and (b) ischemic scans in a canine experiment with proximal LAD occlusion

3.2 ED-ES 3D Results

We also compared our findings based on optical flow strain on canine heart experimental data having a proximal LAD occlusion with predicted measures from a physiological finite element model [16] under the same occlusion status. Sample results are shown in Fig. 6. The abnormal region found by our proposed method of 4D optical flow (shown in red in Fig. 6b) were very similar to the model prediction (shown in Fig. 6a). Besides radial displacement, other metrics, such as wall thickening and cardiac torsion, have yielded similar results of agreement.

3D visualizations made with the CardioViz3D software tool [18] of selected dog studies data are shown in Fig. 7. The studies are the baseline case and the proximal LAD occlusion case from the same dog, side by side. Colors displayed on the 3D meshes are mapped to strain values rescaled between -1 and 1. From the results, the

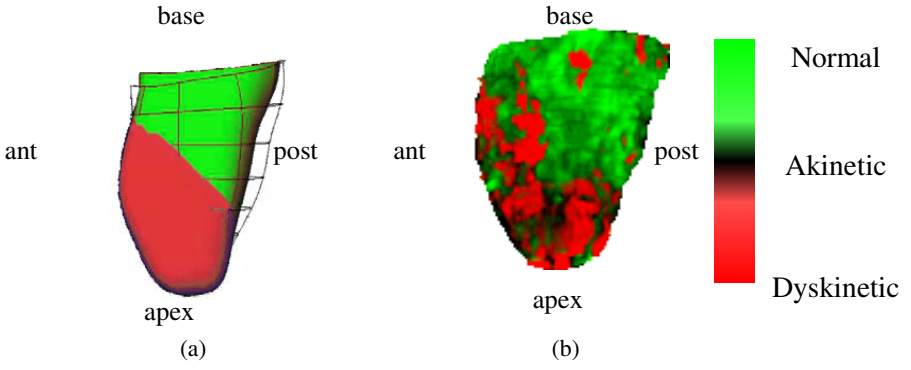

Fig. 6. (a) Anterior view of the finite element model with a large simulated LAD occlusion. Wire frame represents the endocardial surface at end diastole, solid surface the endocardial surface at end systole, and the red portion corresponds to the deactivated (ischemic) region. (b) 3D visualization of ED-to-ES radial displacement metric of a canine heart experiment with proximal LAD occlusion, which is very similar to predicted values of the physiological model under the same color mapping.

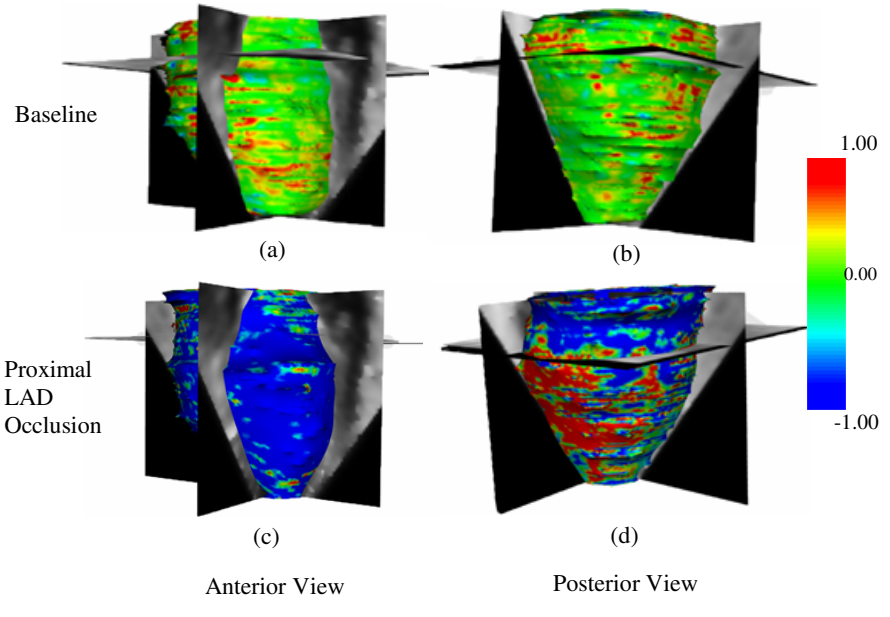

Fig. 7. 3D visualization of dog (canine) cardiac study (a) Anterior view of the baseline case (b) Posterior view of the baseline case (c) Anterior view of the proximal LAD occlusion (d) Posterior view of the proximal LAD occlusion

normal case on anterior and posterior views in Fig. 7a and 7b shows mostly a green color mapping, while in the proximal case regions of blue color are shown in specific areas. In this example, we can therefore easily localize the abnormal area on the

posterior view in Fig. 7d. This result was compared to standard views for two-dimensional echocardiography, and can indicate abnormal regions due to ischemia. These results also coincide with cardiac physiology findings for each case.

4 Conclusion

A correlation-based optical flow (OF) method was applied to myocardial tracking on 4D ultrasound data. Based on the estimated motion fields, several dynamic cardiac metrics, including displacements and strain, were derived. The proposed method was applied to 4D ultrasound data acquired via controlled coronary artery occlusion. Ischemic regions predicted by temporal profiles of strain as well as ED-ES strain maps were aligned with predictions from a cardiac physiological model, simulated with the same occlusion position and extent. In the future, a finite-element based fitting could further improve both the accuracy and robustness of our proposed computational framework. The ability to derive strain measurement from real-time 3D ultrasound is of great clinical and practical importance. Thus, our method could provide a novel diagnostic tool that would allow researchers and clinicians to use 4D strain estimation based on echocardiography.

Acknowledgements

This work was partially funded by the American Heart Association grant #0640005N, NIH 1R01HL08516-01A2, and NIH/NHLBI 1R01HL086578-01A2. The authors also would like to thank Katherine M. Parker (Department of Biomedical Engineering, University of Virginia, USA) for her contribution on processing canine experiment data.

References

1. Lubinski, M.A., Emelianov, S.Y., O'Donnell, M.: Speckle Tracking Methods for Ultrasonic Elasticity Imaging Using Short-Time Correlation. IEEE Transactions on Ultrasonics, Ferroelectrics, and Frequency Control 46, 82–96 (1999)
2. Kaluzynski, K., Chen, X., Emelianov, S.Y., Skovoroda, A.R., O'Donnell, M.: Strain Rate Imaging Using Two-Dimensional Speckle Tracking. IEEE Transactions on Ultrasonics, Ferroelectrics, and Frequency Control 48 (2001)
3. Meunier, J.: Tissue motion assessment from 3D echographic speckle tracking. Physics in Medicine and biology 43, 1241–1254 (1998)
4. Bohs, L.N., Geiman, B.J., Anderson, M.E., Gebhart, S.C., Trahey, G.E.: Speckle tracking for multi-dimensional flow estimation. Ultrasonics 38, 369–375 (2000)
5. Notomi, Y., Lysyansky, P., Setser, R.M., Shiota, T., Popovic, Z.B., Martin-Miklovic, M.G., Weaver, J.A., Oryszak, S.J., Greenberg, N.L., White, R.D., Thomas, J.D.: Measurement of Ventricular Torsion by Two-Dimensional Ultrasound Speckle Tracking Imaging. Journal of the American College of Cardiology 45, 2034–2041 (2005)
6. Ramm, O.T.V., Smith, S.W.: Real time volumetric ultrasound imaging system. Journal of Digital Imaging 3, 261–266 (1990)

7. Elen, A., Choi, H.F., Loeckx, D., Gao, H., Claus, P., Suetens, P., Maes, F., D'hooge, J.: Three-dimensional cardiac strain estimation using spatio-temporal elastic registration of ultrasound images: a feasibility study. IEEE Trans. Med. Imaging 27, 1580–1591 (2008)
8. Duan, Q., Angelini, E., Gerard, O., Homma, S., Laine, A.: Comparing optical-flow based methods for quantification of myocardial deformations on RT3D ultrasound. In: IEEE International Symposium on Biomedical Imaging (ISBI) (2006)
9. Duan, Q., Angelini, E., Herz, S.L., Ingrassia, C.M., Gerard, O., Costa, K.D., Holmes, J.W., Homma, S., Laine, A.: Dynamic Cardiac Information From Optical Flow Using Four Dimensional Ultrasound. In: 27th Annual International Conference IEEE Engineering in Medicine and Biology Society (EMBS), Shanghai, China (2005)
10. Lucas, B.D., Kanade, T.: An iterative image registration technique with an application to stereo vision. In: International Joint Conference on Artificial Intelligence (IJCAI) (1981)
11. Horn, B.K.P., Schunck, B.G.: Determining optical flow. Artificial Intelligence 17 (1981)
12. Nagel, H.: Displacement vectors derived from second-order intensity variations in image sequences. Computer Vision Graphics Image Processing 21, 85–117 (1983)
13. Anandan, P.: A computational framework and an algorithm for the measurement of visual motion. International Journal of Computer Vision 2, 283–310 (1989)
14. Singh, A.: An estimation-theoretic framework for image-flow computation. In: International Conference on Computer Vision (1990)
15. Barron, J.L., Fleet, D., Beauchemin, S.: Performance of optical flow techniques. Int. Journal of Computer Vision 12, 43–77 (1994)
16. Herz, S., Ingrassia, C., Homma, S., Costa, K., Holmes, J.: Parameterization of left ventricular wall motion for detection of regional ischemia. Annals of Biomedical Engineering 33, 912–919 (2005)
17. Cerqueira, M., Weissman, N., Dilsizian, V., Jacobs, A., Kaul, S., Laskey, W., Pennell, D., Rumberger, J., Ryan, T., Verani, M.: Standardized myocardial segmentation and nomenclature for tomographic imaging of the heart. Circulation 105, 539–542 (2002)
18. Toussaint, N., Mansi, T., Delingette, H., Ayache, N., Sermesant, M.: An Integrated Platform for Dynamic Cardiac Simulation and Image Processing: Application to Personalised Tetralogy of Fallot Simulation. In: Proc. Eurographics Workshop on Visual Computing for Biomedicine (VCBM), Delft, The Netherlands (2008)

Cardiac Motion Extraction from Images by Filtering Estimation Based on a Biomechanical Model

Philippe Moireau[1], Dominique Chapelle[1], and Mariette Yvinec[2]

[1] INRIA, Macs Project-Team, B.P. 105, 78153 Le Chesnay cedex, France
[2] INRIA, Geometrica Project-Team, B.P. 93, 06902 Sophia Antipolis cedex, France

Abstract. Starting from the presentation of a unified perspective of segmentation with deformable models and data assimilation with images, we propose a data assimilation procedure designed to dynamically estimate 3D positions and velocities of the myocardium along the heart cycle, using data consisting of contours extracted from image sequences. We assess this procedure with a test problem based on a realistic computational heart model, and with synthetic data produced from reference simulations by creating binary images of the myocardium. The automatic meshing library CGAL is then employed to create contour meshes for each snapshot, and these meshes are directly used in the model-measurement comparisons. This approach gives very satisfactory qualitative and quantitative results.

1 Introduction

One of the main difficulties in extracting useful segmentations from moving organs such as the heart [1] or the respiratory system [2] is to ensure dynamical consistency in the sequence [3]. A new method was recently proposed in [4] to estimate the state of a mechanical system from a sequence of contour surfaces. Whereas variational formulations arising from optimal control are widely used in estimation [5], our method was focused on devising a filtering approach [6] for estimation, which allows to integrate the measurements directly in a single simulation. However, estimation by filtering – e.g. Kalman filtering – has long been restricted to dynamical systems limited in size, due to the costs induced by the computation of the filter, both in terms of storage and CPU time. In particular, although it can be formulated in theory [6], optimal filtering for partial differential equations (PDEs) gives rise to untractable computations in practice, when considering discretized versions of the system, unless the model is overly simplified as the 2D heart model in [7].

To overcome these difficulties the estimation strategy originally introduced in [8] is based on feedback control concepts, thus well-adapted to systems modeled by partial differential equations (PDEs). In mechanics, in particular, collocated feedback is known to provide robust – as can also be mathematically substantiated – and easily implementable control laws for large classes of systems. When

N. Ayache, H. Delingette, and M. Sermesant (Eds.): FIMH 2009, LNCS 5528, pp. 220–228, 2009.
© Springer-Verlag Berlin Heidelberg 2009

taking the feedback operator as a filter, it can be shown for linear systems that the estimation error obeys the closed-loop dynamics associated with this feedback, hence enjoys the same convergence properties. In [4], these principles were then adapted to the case where only displacement measurements are available, with a non-linear extension when the measurements are restricted to boundary contours. This formalism provides a theoretical background to analyze the convergence of the estimation, and the proposed corresponding time discretization scheme ensures that the numerical complexity of the algorithm is comparable to a simple mechanical direct simulation.

In the present paper we demonstrate how this data assimilation approach can be used in combination with automatic mesh generation from images as proposed in [9] to directly employ a sequence of binary cardiac images and – with an adapted mechanical model of the heart – provide kinematic and physical consistency in the segmentation.

In the next section we consider the dynamic segmentation and data assimilation problems in a unified perspective. Then, in Section 3 we specialize our discussion to measurements given by a sequence of images. This whole approach is then put to work using a cardiac test problem described in Section 5, with a summary of the automatic mesh generation procedure adapted to binary images. We finally give some concluding remarks in Section 6.

2 From Segmentation by Deformable Models to Data Assimilation

One of the classical approaches in the segmentation of images – in particular in cardiac imaging – consists in using a so-called "deformable model" in order to regularize the segmentation optimization problem in the form

$$\min \{\mathcal{E}_{\text{Im}} + \epsilon\, \mathcal{E}_{\text{Int}}\}, \tag{1}$$

where the potential $\mathcal{E}_{\text{Im}}$ characterizes the discrepancy between the model and the image, while $\mathcal{E}_{\text{Int}}$ represents an internal deformation energy of the model, and ϵ a weighting coefficient. In a standard deformable model, the internal energy is a function of a set of displacement vectors which characterize the motion of the deformable model with respect to a given reference configuration. Denoting by Y the array that stores these displacement components – e.g. as for degrees of freedom in a finite element model – and invoking the stationarity associated with the above minimization problem we have

$$\mathcal{F}_{\text{Int}}(Y) = \tfrac{1}{\epsilon} F_{\text{Im}}, \quad \text{with } \mathcal{F}_{\text{Int}} = \tfrac{\partial \mathcal{E}_{\text{Int}}}{\partial Y}, F_{\text{Im}} = -\tfrac{\partial \mathcal{E}_{\text{Im}}}{\partial Y}. \tag{2}$$

When the deformable model corresponds to linearized elasticity, $\mathcal{F}_{\text{Int}}(Y)$ is a linear function of Y, which leads to

$$KY = \tfrac{1}{\epsilon} F_{\text{Im}}, \tag{3}$$

where K is the so-called stiffness matrix, hence (2) can be interpreted as the balance equation of a "spring-like" system under the effect of "image forces" which typically tend to bring the model boundaries close to the image contours.

When an image *sequence* is considered, the same segmentation procedure can – of course – be statically repeated for each image. Nevertheless, in order to effectively deal with time sampling the idea of exploiting the intrinsic dynamic consistency of the sequence by using a model which also incorporates some dynamical effects is natural and attractive. In particular, in the case of a linear elastodynamical system, this approach would give the following extension of (3), considered in [10]

$$M\ddot{Y} + C\dot{Y} + KY = \tfrac{1}{\epsilon} F_{\mathrm{Im}}, \tag{4}$$

where dot symbols denote time derivatives, while M and C denote the so-called mass and damping matrices – usually symmetric positive definite matrices, as for K.

There appears to be a strong similarity between a dynamical deformable model as described by (4) and a dynamical system considered in sequential data assimilation – also known as filtering procedures. Indeed, sequential data assimilation also considers dynamical models whose trajectories are corrected by terms reflecting the discrepancy between the model and the associated available measurements. In data assimilation, however, the model is supposed to adequately represent the "true" physical behavior of the system which is observed in the measurements, and the corrections are intended to dynamically estimate some quantities that cannot be exactly determined *a priori*, typically physical parameters and initial conditions in the dynamics. This means that the applied corrections should become small over a reasonably short time period, after which the model can be used without any further measurement-related input in a purely predictive mode, such as in weather forecasting.

Of course, in segmentation by deformable models some degree of physical adequacy may also be sought, and in data assimilation no mathematical model is ever exact, so there is no strict border between these methodologies, but rather a "continuum of approaches". Nevertheless, as already mentioned the degree of physical predictivity is a crucial criterion to assess data assimilation, hence to categorize these approaches. In the sequel, we will further explore sequential data assimilation procedures adapted to the cardiac setting, among which we will show that the natural candidate inspired from (4) is not an effective approach as such.

3 Data Assimilation in a Mechanical Model Using Position Measurements

Although our heart model will be nonlinear, in order to present the estimation principles without undue technicalities (see [4] for such details) we consider a mechanical system obeying the simple linear dynamics

$$M\ddot{Y} + C\dot{Y} + KY = R(t), \tag{5}$$

where $R(t)$ represents the external loading, which is supposed to be known. The initial condition is partly unknown, which we translate into

$$\begin{pmatrix} Y(0) \\ \dot{Y}(0) \end{pmatrix} = \begin{pmatrix} Y_0 \\ \dot{Y}_0 \end{pmatrix} + \zeta_X, \tag{6}$$

where Y_0 and $\dot{Y}_0$ denote some *a priori* on the initial positions and velocities, respectively, and ζ_X the uncertainty to be estimated.

In order to perform this estimation, we can use measurements which are modeled in the form

$$Z = HY + \chi, \tag{7}$$

where H denotes an observation operator – assumed to be linear at this stage – and χ the measurement noise. We emphasize that these two quantities *together* make up the measurement model, with χ which can be taken either in a deterministic or probabilistic setting. As an example of measurements which could be modeled by such a linear observation operator, we can mention tagged MRI with adequate post-processing to extract the 3D material displacements [11], in which case the operator H simply reduces to an interpolation between the tag-grid points and the computational nodes.

We may then as in [10] introduce a tentative data assimilation system inspired from the above image-force strategy in the form

$$M\ddot{\hat{Y}} + C\dot{\hat{Y}} + K\hat{Y} = R(t) + \gamma H^T S(Z - H\hat{Y}), \tag{8}$$

in which S represents some suitable norm in the measurement space, and γ is a gain parameter. This is the direct translation of the image-force strategy because we apply forces which are proportional to the discrepancy between the simulated and measured displacements to correct the trajectory. Defining the estimation error

$$\tilde{Y} = Y - \hat{Y}, \tag{9}$$

a simple subtraction of (8) from (5) combined with (7) yields

$$M\ddot{\tilde{Y}} + C\dot{\tilde{Y}} + (K + \gamma H^T S H)\tilde{Y} = -\gamma H^T S \chi. \tag{10}$$

In this equation we can see that the consequence of the filtering term is an added stiffness effect in the error dynamics compared to the reference system (5). This is not what we expect from an effective data assimilation procedure since it does not ensure that the error will decrease and tend to zero. In other words, in the dynamical system terminology (10) does not feature any improved stability property, in particular in the sense of asymptotic stability.

In order to employ the same type of correction term in a better dynamical setting, we rewrite the dynamics in the equivalent first-order form

$$\begin{cases} \dot{X}^d = X^v \\ M\dot{X}^v + CX^v + KX^d = R \end{cases} \tag{11}$$

with $(X^d, X^v) = (Y, \dot{Y})$. Introducing the data assimilation system

$$\begin{cases} K\dot{\hat{X}}^d = K\hat{X}^v + \gamma H^T S(Z - H\hat{X}^d) \\ M\dot{\hat{X}}^v + C\hat{X}^v + K\hat{X}^d = R \end{cases} \tag{12}$$

we then have for the error $\tilde{X} = (\tilde{X}^d, \tilde{X}^v)^T = (X^d - \hat{X}^d, X^v - \hat{X}^v)^T$

$$\frac{d}{dt}\tilde{X}^T N\tilde{X} = -\gamma(\tilde{X}^d)^T H^T SH\tilde{X}^d - (\tilde{X}^v)^T C\tilde{X}^v - \gamma(\tilde{X}^d)^T H^T S\chi. \tag{13}$$

where $\tilde{X}^T N\tilde{X} = 1/2((\tilde{X}^v)^T M\tilde{X}^v + (\tilde{X}^d)^T K\tilde{X}^d)$ represents the total energy – given by the sum of kinetic and elastic energies – of the estimation error. As discussed in [4] this shows that the corresponding dynamical system enjoys an enhanced stability, with the positive term $\gamma(\tilde{X}^d)^T H^T SH\tilde{X}^d$ representing an *added damping effect*. This effect can be further optimized by adjusting the operator S, and in our analysis we have identified as a particularly effective choice the filter named "Schur Displacement Feedback" (SDF) corresponding to

$$H^T S = \kappa K\big(K + \kappa H^T W^{-1} H\big)^{-1} H^T W^{-1}, \tag{14}$$

where W^{-1} denotes some measurement norm – or inverse of a noise covariance matrix – and κ a penalization parameter intended to be "large".

4 Measurements Provided by Images

When dealing with image measurements, in general the available data cannot be modeled in the simple form (8). Instead, in the case of segmented images, we can typically compare the boundary of the deformed model with the segmented surfaces and quantify the error by computing the distance fields between these computed and measured surfaces. Denoting by $\mathrm{dist}(\hat{X}^d, S)$ the distance field of the boundary of the deformed simulated model to a given measured surface S, we will thus be led to substituting this quantity for the difference $Z - H\hat{X}^d$ used in the linear framework. Note that we can deal with time sampling, meaning that we only have a discrete number of measured contours S_k corresponding to the successive time steps $k\Delta T$, $1 \leq k \leq N_{\Delta T}$, by using the interpolated distance fields

$$\begin{aligned} W_d(\hat{X}^d, t) = \alpha_k(t)\,\mathrm{dist}(\hat{X}^d, S_k) + (1 - \alpha_k(t))\,\mathrm{dist}(\hat{X}^d, S_{k+1}), \\ \text{with } \alpha_k(t) = \tfrac{(k+1)\Delta T - t}{\Delta T}, \end{aligned} \tag{15}$$

for $t \in [k\Delta T, (k+1)\Delta T]$ *provided that* we use a signed distance.

The natural extension of (12) in this framework is now

$$\begin{cases} K\dot{\hat{X}}^d = K\hat{X}^v - \gamma \left(\dfrac{\partial W_d}{\partial Y}\right)^T SW_d(\hat{X}^d, t) \\ M\dot{\hat{X}}^v + C\hat{X}^v + K\hat{X}^d = R \end{cases} \tag{16}$$

where it appears that the correction term bears some resemblance with image force methods, see [4]. Here, however, we emphasize that we include this term

as a correction in the first equation of the dynamics and not as a force. In this case, as also demonstrated in [4] the linearized system of the estimation error takes the same form as in Section 3 with $H = -\frac{\partial W_d}{\partial Y}(X^d, t)$. Therefore, when this time-varying linearized system is exponentially stable, by classical results of dynamical systems theory, we can infer that the original system itself can be adequately observed for initial conditions which are "sufficiently close" to the a priori considered. This also motivates our previous analysis of a linear observation operator.

5 Data Assimilation for the Cardiac System

In order to accurately model the biomechanical behavior of the heart, a nonlinear model is required, with a control term representing the electrical activation, and we considered the model presented in [12]. We used the approach described in [4] to extend our estimation strategy to a nonlinear mechanical model – with both geometric and material nonlinearities – and to formulate an adequate time discretization scheme. In practice, the electrical activation field should be concurrently estimated – since it is only indirectly measured through the ECG – and the blood pressures in the heart cavities should also be estimated unless they are accurately measured, which is only possible by invasive procedures. Nevertheless, we here demonstrate the performance of our estimation approach by focusing on mechanical estimation, using the heart model of [12] with a prescribed activation field and without blood coupling – namely with empty cavities – and considering realistic synthetic measurements, i.e. measurements produced by numerical simulations. Note that using synthetic measurements allows to circumvent modeling error issues and focus on the validation of the estimation procedure. Nevertheless, it is crucial that such synthetic data feature the same essential characteristics – including uncertainties – of the real data at hand.

These measurements consist of surface meshes extracted from binary images themselves obtained by processing – by a rasterization procedure [13]– the results of a reference simulation, with time and space sampling comparable with medical imaging specifications (we used a time sampling of 30 ms and space sampling of 0.5 mm in all directions). From each binary image, a surface mesh has been produced using the CGAL library [14]. The CGAL library includes a mesh generator based on the Delaunay refinement paradigm. The meshing algorithm builds, in a greedy way, a dense sampling of the surface to be meshed [15] while maintaining an approximating surface mesh. The approximating surface mesh is the restricted Delaunay triangulation of the sampling, i.e. the subcomplex of the three dimensional Delaunay triangulation formed by facets whose dual Voronoi edge intersects the surface. The refinement process is guided by a control over the size and shape of mesh elements and over the approximation accuracy. Upon termination, the sampling is dense enough and the restricted Delaunay triangulation is known to be homeomorphic to the original surface and geometrically close to it, for instance in term of Hausdorff distance. A notable feature of this mesh generation software is that the surface needs to be known only through

an intersection oracle that, given a line segment, can tell whether the segment intersects the surface or not and, in the affirmative case, returns an intersection point. The meshing algorithm has been extended to work with bipolar oracle able to detect and compute intersections, only when the number of intersection points is odd. The version of the oracle that we have been using in the present case is designed to answer the intersection queries directly from a segmented three dimensional image [9].

We summarize the measurement processing strategy in Figure 1.

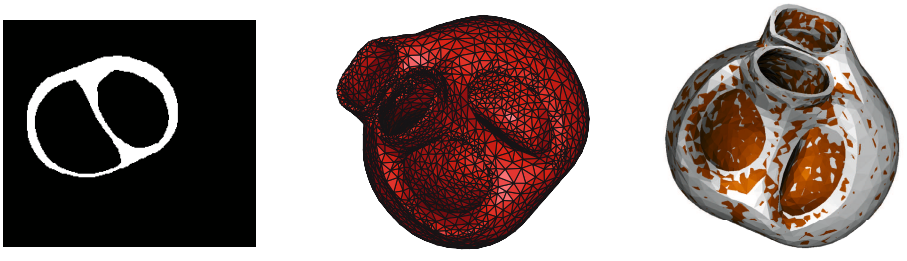

Fig. 1. Measurements used: binary images (left), meshes produced by `CGAL` (center) and comparison with reference surfaces (right)

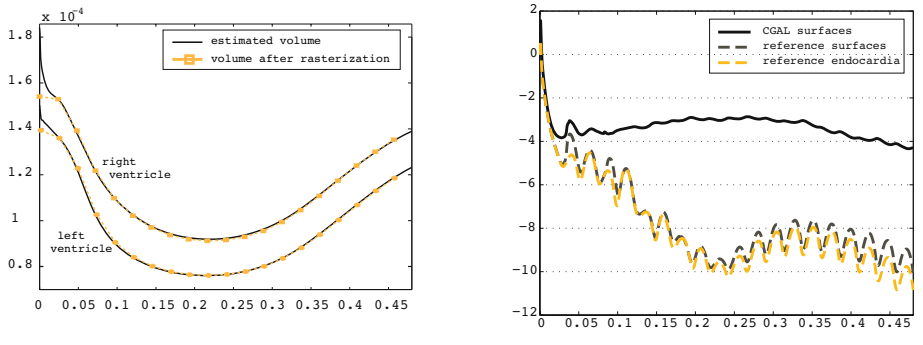

Fig. 2. Estimation errors obtained with CGAL meshes and reference surfaces, in SI units: computed volumes (left) and estimation errors in energy norm (right)

We show in Figure 2 and 3 the estimation results obtained when starting the data assimilation with a significant initial condition error, assessed by means of computed volumes of the ventricles, and estimation errors for the complete state in the energy norm (namely, kinetic plus strain energies). In the correction term we have only used the distances corresponding to the epicardium located below the valve plane, which required some adequate prior referencing – as is standard in image segmentation. As seen in the error energy, the error decreases very fast before reaching an asymptote corresponding to the error level associated with

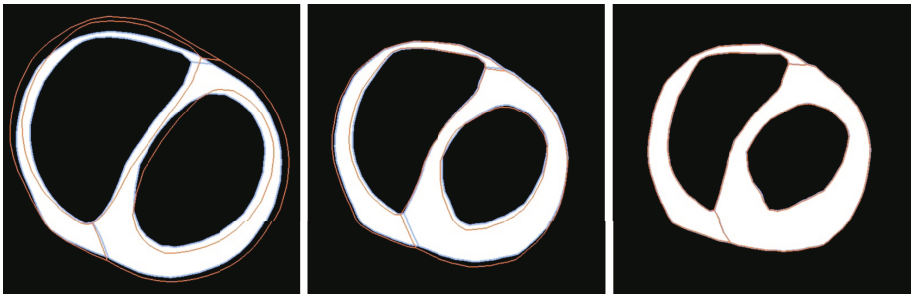

Fig. 3. Estimated contours (orange) compared with image at $t = 0$, 100, 200 ms

the space sampling resulting from the combined effect of rasterization, automatic mesh generation and distance interpolation between snapshots. Then the error fluctuates along the asymptote with a period corresponding to time sampling. As a comparison we also performed the estimation using "perfect data" – namely, the contour meshes of the reference simulation for the complete boundary and for the epicardium only – and the estimation errors are shown in Fig.2-right. This shows the effectiveness of the SDF estimation for ideal measurements, but the error obtained with realistic synthetic data and reconstructed meshes is very satisfactory.

6 Concluding Remarks

A most valuable advantage of our image-based mechanical estimator is that we can extend the state estimation to perform joint state-parameter estimation. This extension is quite straightforward by following the methodologies proposed in [8,16]. This suggests that – beyond kinematic consistency – a suitable mechanical model can offer an accurate mechanical estimation and parameter identification. The method is therefore more related to data assimilation than to image processing, and can be seen as a future tool to assist diagnosis and prognosis.

Of course, using the proposed methodology with real data – namely, real cardiac imaging measurements – remains a major challenge. Indeed, we have demonstrated the effectiveness of the estimation procedure *per se*, whereas achieving estimation with real data also crucially relies on modeling adequacy. Nevertheless, although some progress is probably still needed in the modeling validation, estimation can also be a valuable tool in the assessment of models, as the model-measurement distance is then a meaningful indicator of unmodelled errors.

Acknowledgments. The authors wish to warmly thank Jean-Daniel Boissonnat and Laurent Rineau (both from INRIA, Geometrica Project-Team) for some useful discussions regarding mesh generation.

References

1. Peters, J., Ecabert, O., Meyer, C., Schramm, H., Kneser, R., Groth, A., Weese, J.: Automatic whole segmentation in static magnetic resonance image volumes. In: Ayache, N., Ourselin, S., Maeder, A. (eds.) MICCAI 2007, Part II. LNCS, vol. 4792, pp. 402–410. Springer, Heidelberg (2007)
2. von Berg, J., Barschdorf, H., Blaffert, T., Kabus, S., Lorenz, C.: Surface based cardiac and respiratory motion extraction for pulmonary structures from multi-phase CT. In: Manduca, A., Hu, X. (eds.) Medical Imaging 2007: Physiology, Function, and Structure from Medical Images, vol. 6511, p. 65110Y. SPIE (2007)
3. Sermesant, M., Forest, C., Pennec, X., Delingette, H., Ayache, N.: Deformable biomechanical models: Application to 4D cardiac image analysis. Medical Image Analysis 7(4), 475–488 (2003)
4. Moireau, P., Chapelle, D., Le Tallec, P.: Filtering for distributed mechanical systems using position measurements: Perspective in medical imaging. Inverse Problems 25(3), 035010–035035 (2009)
5. Blum, J., Le Dimet, F., Navon, I.: Data assimilation for geophysical fluids. In: Temam, R., Tribbia, J. (eds.) Handbook of Numerical Analysis: Computational Methods for the Atmosphere and the Oceans. Elsevier, Amsterdam (2008)
6. Bensoussan, A.: Filtrage Optimal des Systèmes Linéaires. Dunod (1971)
7. Tong, S., Shi, P.: Cardiac motion recovery: Continuous dynamics, discrete measurements, and optimal estimation. In: Larsen, R., Nielsen, M., Sporring, J. (eds.) MICCAI 2006. LNCS, vol. 4190, pp. 744–751. Springer, Heidelberg (2006)
8. Moireau, P., Chapelle, D., Le Tallec, P.: Joint state and parameter estimation for distributed mechanical systems. Computer Methods in Applied Mechanics and Engineering 197, 659–677 (2008)
9. Pons, J., Ségonne, F., Boissonnat, D., Rineau, L., Yvinec, M., Keriven, R.: High-quality consistent meshing of multi-label datasets. In: Karssemeijer, N., Lelieveldt, B. (eds.) IPMI 2007. LNCS, vol. 4584, pp. 198–210. Springer, Heidelberg (2007)
10. Billet, F., Sermesant, M., Delingette, H., Ayache, N.: Cardiac motion recovery by coupling an electromechanical model and cine-MRI data: First steps. In: Miller, K., Nielsen, P. (eds.) Proc. MICCAI 2008 (September 2008)
11. Axel, L., Montillo, A., Kim, D.: Tagged magnetic resonance imaging of the heart: a survey. Med. Image Anal. 9, 376 (2005)
12. Sainte-Marie, J., Chapelle, D., Cimrman, R., Sorine, M.: Modeling and estimation of the cardiac electromechanical activity. Computers & Structures 84, 1743–1759 (2006)
13. Bresenham, V.: Algorithm for computer control of a digital plotter. IBM Systems Journal 4(1), 25–30 (1965)
14. CGAL, Computational Geometry Algorithms Library, http://www.cgal.org
15. Boissonnat, J.D., Oudot, S.: Provably good sampling and meshing of surfaces. Graphical Models 67, 405–451 (2005)
16. Chapelle, D., Moireau, P., Le Tallec, P.: Robust filtering for joint state-parameter estimation in distributed mechanical systems. DCDS-A 23(1–2), 65–84 (2009)

Active Model with Orthotropic Hyperelastic Material for Cardiac Image Analysis

Ken C.L. Wong, Linwei Wang, and Pengcheng Shi

Computational Biomedicine Laboratory
Rochester Institute of Technology, Rochester, New York, USA
{kenclwong,maomaowlw}@mail.rit.edu, pengcheng.shi@rit.edu

Abstract. Meaningful physiological models are important for studying cardiac physiology. For cardiac image analysis, the models used should be detailed enough to describe the macroscopic physiological behaviors, but should not be too complicated for the inverse problems. To achieve this goal, we propose to use an orthotropic hyperelastic biomechanical model, which has only seven parameters but was reported as the best among the five tested well-known models in a comparative study. Combining with the active contraction forces provided by electromechanical models, the cyclic cardiac dynamics can be available to provide the physiological foundation for cardiac image analysis. To facilitate the complicated inverse problems, the system is implemented under the Cartesian coordinate system, and we propose the corresponding cardiac specific boundary conditions for anatomically realistic deformations. Experiments with analytical solutions were performed to verify the correctness of the implementation, and cardiac cycles were simulated to verify the physiological plausibility of the proposed model.

1 Introduction

Realistic cardiac models are important for studying cardiac physiology, such as quantitative assessments in pathology studies via changes in model parameters, and recovering information from medical images [1]. For cardiac image analysis, the models used should be detailed enough to describe the macroscopic physiological behaviors, but should not be too complicated for the inverse problems. In general, an active cardiac model comprises an electrical propagation model (E model), an electromechanical coupling model (EM model), and also a biomechanical model (BM model), among which the BM model plays a crucial role for realistic stress-strain relation. In [2,3], a cardiac electromechanical model was introduced for image analysis and simulation, whose E, EM, and BM models were built for computationally efficiency and the system was implemented under the Cartesian coordinate system. Although the computational cost was low, the BM models used were either transversely isotropic but linear, or nonlinear but isotropic. According to biomechanical literatures [4,5], the cardiac tissue is almost incompressible and possesses nonlinear stress-strain relation. Furthermore, microscopy showed that cardiac fibers are bundled together by collagen

N. Ayache, H. Delingette, and M. Sermesant (Eds.): FIMH 2009, LNCS 5528, pp. 229–238, 2009.
© Springer-Verlag Berlin Heidelberg 2009

into fibrous-sheet structures, thus the cardiac tissue should be modeled as locally orthotropic [6]. In consequence, the use of linear or isotropic models affects the physiological plausibility. On the other hand, an anatomically accurate cardiac model was proposed in [7] with more realistic biomechanical properties. The model comprised a nonlinear orthotropic pole-zero strain energy function characterized by 18 material parameters, and the system was described under the prolate spheroidal coordinate system so that the heart geometry could be best expressed. This model provides physiologically plausible deformation, but the large number of material parameters and the complicated mechanical formulations under the curvilinear coordinate system increase the theoretical and computational difficulties of the inverse problems, especially in the cases of statistical cardiac image analysis [8,9].

In view of these problems, we utilize the hyperelastic orthotropic material model described in [10,11]. This model comprises a nonlinear strain energy function with only seven material parameters, but was reported as the best among the five tested well-known constitutive laws in a comparative study [12]. While the model was implemented in the prolate spheroidal coordinate system in [10], we have implemented the model in the Cartesian coordinate system to facilitate the inverse problems of medical image analysis. One of the difficulties of implementing the model in the Cartesian coordinate system is to enforce anatomically realistic displacement boundary conditions of the pericardium, which are relatively easy to handle in the prolate spheroidal coordinate system because of its compatibility with the cardiac geometry. To overcome this problem, we propose a simple but effective boundary condition which can be enforced through the generalized penalty method, and can incorporate motion information from medical images. With the active contraction components provided by the E and EM models described in [9], the active cardiac dynamics can be provided as the foundation for medical image analysis. Experiments with analytical solutions were performed to verify the correctness of the implementation, and cardiac cycles were simulated to verify the physiological plausibility of the proposed model.

2 Methodology

The biomechanically accurate material model and also the cardiac specific boundary conditions are essential for realistic cardiac deformation. With the cardiac system dynamics connecting these components with the kinematic quantities and contraction forces, physiologically plausible cardiac dynamics can be achieved.

2.1 Active Contraction Components

To provide the active contraction components, the E model in [13] has been used to simulate the electrical propagation pattern through the meshfree framework described in [14]. The action potentials are then converted to contraction stresses using the EM model in [2], providing the deformation pattern through the BM model described in the next section.

2.2 Hyperelastic Orthotropic Material Model

Strain Energy Function. The nonlinear myocardial stress-strain relation can be described by hyperelastic orthotropic material models [7,10]. In a study of optimizing constitutive parameters of pig cardiac tissues, the material model described in [10,11] was reported as the best among the five tested nonlinear constitutive laws, thus it has been chosen as our material model. With also the decoupled representation of nearly incompressible materials, the strain energy function of the model is given as [15]:

$$\Psi(\boldsymbol{\epsilon}) = \Psi_{\text{vol}}(J) + \Psi_{\text{iso}}(\overline{\boldsymbol{\epsilon}}) = \kappa(J \ln J - J + 1) + \frac{1}{2}a(e^{Q} - 1) \tag{1}$$

where

$$\begin{aligned} Q =& b_{ff}\overline{\epsilon}_{ff}^2 + b_{ss}\overline{\epsilon}_{ss}^2 + b_{nn}\overline{\epsilon}_{nn}^2 \\ &+ b_{fs}\left(\overline{\epsilon}_{fs}^2 + \overline{\epsilon}_{sf}^2\right) + b_{fn}\left(\overline{\epsilon}_{fn}^2 + \overline{\epsilon}_{nf}^2\right) + b_{sn}\left(\overline{\epsilon}_{sn}^2 + \overline{\epsilon}_{ns}^2\right) \end{aligned} \tag{2}$$

The strictly convex function Ψ_{vol} describes the volumetric elastic response and Ψ_{iso} associates with the isochoric elastic response of the hyperelastic material. $J = \det \mathbf{F}$, with $\mathbf{F}$ the deformation gradient, and $J = 1$ when there is no volume change. $\kappa > 0$ is the penalty factor for enforcing incompressibility, the larger its value, the more incompressible the material. $\overline{\epsilon}_{\alpha\beta}$ are the components of the modified Green-Lagrange strain tensor $\overline{\boldsymbol{\epsilon}}$ defined under the local coordinate system (f,s,n; fiber, sheet, sheet normal), which is the isovolumetric part of the Green-Lagrange strain tensor $\boldsymbol{\epsilon}$. a and $b_{\alpha\beta}$ are the seven constitutive material parameters of the tissue, with the unit of a as Pa and $b_{\alpha\beta}$ have no unit. The f-s-n coordinate system represents the fibrous-sheet structure, which orientation can be different at different locations.

Stress Tensor. The second Piola-Kirchhoff (PKII) stress tensor is given as $\mathbf{S} = \partial\Psi/\partial\boldsymbol{\epsilon}$ under the f-s-n basis [15]:

$$\mathbf{S} = \mathbf{S}_{\text{vol}} + \mathbf{S}_{\text{iso}} = Jp\mathbf{C}^{-1} + \frac{\partial\Psi_{\text{iso}}}{\partial\boldsymbol{\epsilon}} \tag{3}$$

where $p = \mathrm{d}\Psi_{\text{vol}}/\mathrm{d}J = \ln J$ is the hydrostatic pressure, and $\mathbf{C} = \mathbf{F}^{\mathrm{T}}\mathbf{F}$ is the right Cauchy-Green tensor. $\mathbf{S}_{\text{iso}} = J^{-2/3}\mathbb{P} : \overline{\mathbf{S}}$, where $\mathbb{P} = \mathbb{I} - \frac{1}{3}\mathbf{C}^{-1} \otimes \mathbf{C}$ with $(\mathbb{I})_{ijkl} = \delta_{ik}\delta_{jl}$, and $\overline{\mathbf{S}} = \partial\Psi_{\text{iso}}/\partial\overline{\boldsymbol{\epsilon}}$ with components $\overline{S}_{\alpha\beta} = ae^{Q}b_{\alpha\beta}\overline{\epsilon}_{\alpha\beta}$. Thus $\mathbf{S}$ is nonlinear with respect to the deformation.

Elasticity Tensor. The problems of finite elasticity are nonlinear and usually have no closed-form solution, thus incremental solution techniques of Newton's type are required. In consequence, the elasticity tensor $\mathbb{C}$ which provides the linearized stress-strain relation at a particular stain state is given as [15]:

$$\mathbb{C} = \frac{\partial\mathbf{S}}{\partial\boldsymbol{\epsilon}} = \frac{\partial^2\Psi}{\partial\boldsymbol{\epsilon}\partial\boldsymbol{\epsilon}} \quad \text{or} \quad C_{\alpha\beta rs} = \frac{\partial^2\Psi}{\partial\epsilon_{\alpha\beta}\partial\epsilon_{rs}} \tag{4}$$

$\mathbb{C}$ possesses the major symmetries ($C_{\alpha\beta rs} = C_{rs\alpha\beta}$) and the minor symmetries ($C_{\alpha\beta rs} = C_{\beta\alpha rs} = C_{\alpha\beta sr}$), thus it has only 21 independent components.

Defining $[\Delta\mathbf{S}]_{\text{local}} = [\Delta S_{ff}, \Delta S_{ss}, \Delta S_{nn}, \Delta S_{fs}, \Delta S_{fn}, \Delta S_{sn}]^{\text{T}}$ and $[\Delta\boldsymbol{\epsilon}]_{\text{local}} = [\Delta\epsilon_{ff}, \Delta\epsilon_{ss}, \Delta\epsilon_{nn}, 2\Delta\epsilon_{fs}, 2\Delta\epsilon_{fn}, 2\Delta\epsilon_{sn}]^{\text{T}}$ for the incremental stresses and strains. Then the stress-strain relation is given as $[\Delta\mathbf{S}]_{\text{local}} = [\mathbb{C}]_{\text{local}}[\Delta\boldsymbol{\epsilon}]_{\text{local}}$, with:

$$[\mathbb{C}]_{\text{local}} = \begin{bmatrix} C_{ffff} & C_{ffss} & C_{ffnn} & C_{fffs} & C_{fffn} & C_{ffsn} \\ C_{ffss} & C_{ssss} & C_{ssnn} & C_{ssfs} & C_{ssfn} & C_{sssn} \\ C_{ffnn} & C_{ssnn} & C_{nnnn} & C_{nnfs} & C_{nnfn} & C_{nnsn} \\ C_{fffs} & C_{ssfs} & C_{nnfs} & C_{fsfs} & C_{fsfn} & C_{fssn} \\ C_{fffn} & C_{ssfn} & C_{nnfn} & C_{fsfn} & C_{fnfn} & C_{fnsn} \\ C_{ffsn} & C_{sssn} & C_{nnsn} & C_{fssn} & C_{fnsn} & C_{snsn} \end{bmatrix} \tag{5}$$

This matrix is symmetric because $\mathbb{C}$ possesses major symmetries. Note that $[\mathbb{C}]_{\text{local}}$ must be multiplied with incremental *engineering* shear strain components ($2\Delta\epsilon_{rs}, r \neq s$) to obtain the proper incremental PKII stress tensor components.

To transform $[\mathbb{C}]_{\text{local}}$ into the global Cartesian coordinate system:

$$[\mathbb{C}]_{\text{global}} = [T][\mathbb{C}]_{\text{local}}[R][T]^{-1}[R]^{-1} \tag{6}$$

with $[T]$ the transformation matrix which is a function of f-s-n orientations, and $[R]$ is a diagonal matrix responsible for the transformation between strain and engineering strain components, with elements $\{1, 1, 1, 2, 2, 2\}$.

2.3 Cardiac System Dynamics under Finite Deformation

The material model can be related to contraction forces and kinematic quantities through the cardiac system dynamics to provide the physiologically plausible deformation. The displacement-based total-Lagrangian system dynamics under finite deformation is utilized, whose matrix representation is given as [9]:

$$\mathbf{M}\ddot{\mathbf{U}} + \mathbf{D}\dot{\mathbf{U}} + (\mathbf{K} + \mathbf{K}_b)\,\Delta\mathbf{U} = \mathbf{R}_c - \mathbf{R}_i + \mathbf{R}_b \tag{7}$$

where $\mathbf{M}$ is the mass matrix, $\mathbf{D}$ is the damping matrix, $\mathbf{K}$ is the strain incremental stiffness matrix containing the material and deformation properties, and $\mathbf{K}_b$ is related to displacement boundary conditions. The hyperelastic material properties and incompressibility are embedded in $\mathbf{K}$ as it comprises $[\mathbb{C}]_{\text{global}}$ in (6). $\mathbf{R}_c$ is the force vector containing the active forces obtained through the E and EM models, $\mathbf{R}_i$ is the nodal force vector for finite deformation only and is related to the internal stresses, and $\mathbf{R}_b$ is the force vector for enforcing boundary conditions. $\ddot{\mathbf{U}}$, $\dot{\mathbf{U}}$ and $\Delta\mathbf{U}$ are the respective nodal acceleration, velocity and incremental displacement vectors. By using the Newmark method for temporal integration, (7) can be solved for the active cardiac deformation.

2.4 Enforcing Cardiac Specific Displacement Boundary Conditions

Various structures constraining the cardiac deformation, among which the pericardium, which is a conical sac of fibrous tissue surrounding the heart, plays an important role in limiting the movement of the epicardium [16]. As fluid is filled

between the two layers of the pericardium, the movement of the epicardium is less constrained along the surface direction while more constrained normal the surface direction. It is relatively easy to simulate this boundary condition under the prolate spheroidal coordinate system by limiting the corresponding displacement variables [7]. Nevertheless, it is not trivial under the Cartesian coordinate system, and we propose the boundary condition:

$$\mathbf{u}(\bar{\mathbf{x}}) \cdot \mathbf{n}(\bar{\mathbf{x}}) = g \tag{8}$$

to simulate the constraint normal the surface direction. $\mathbf{u}(\bar{\mathbf{x}}) = [u_x \ u_y \ u_z]$ and $\mathbf{n}(\bar{\mathbf{x}}) = [n_x \ n_y \ n_z]$ are the displacement and normal on the epicardial surface under the Cartesian coordinate system at coordinate $\bar{\mathbf{x}}$. g controls the displacement along the normal direction, whose values can be zero if displacement is forbidden, or can be the signed displacement magnitude provided by image information such as the those extractable using the method described in [2].

Eq. (8) can be enforced using the generalized penalty method through [17] [1]:

$$\left(\mathbf{K} + \kappa_b \mathbf{G}^{\mathrm{T}}\mathbf{G}\right) \Delta\mathbf{U} = \mathbf{R}_c - \mathbf{R}_i + \kappa_b \mathbf{G}^{\mathrm{T}}\mathbf{V}; \tag{9}$$

$$\mathbf{G} = [\phi_1 n_x, \ \phi_1 n_y, \ \phi_1 n_z, \ \ldots, \ \phi_n n_x, \ \phi_n n_y, \ \phi_n n_z]; \quad \mathbf{V} = g \tag{10}$$

with $\phi_I = \phi_I(\bar{\mathbf{x}})$ the shape function of node I, n the number of nodes, and κ_b the penalty factor.

For the base and the apex, we have $\mathbf{G} = \mathbf{\Phi}_i, i = x, y, z$, and $\mathbf{V} = 0$, where

$$\begin{aligned}
\mathbf{\Phi}_x &= [\phi_1, \ 0, \ 0, \ \ldots, \ \phi_n, \ 0, \ 0]; \\
\mathbf{\Phi}_y &= [0, \ \phi_1, \ 0, \ \ldots, \ 0, \ \phi_n, \ 0]; \\
\mathbf{\Phi}_z &= [0, \ 0, \ \phi_1, \ \ldots, \ 0, \ 0, \ \phi_n]
\end{aligned}$$

Thus the base and the apex can be viewed as being limited by springs with stiffness controllable by κ_b. By adjusting the values of κ_b, the apex can be fixed while the base can still be movable but constrained, so that the base can move towards the apex during cardiac contraction. With these constraints defined, (7) is ready to provide the foundation for cardiac image analysis.

3 Experiments

3.1 Cubical Object

To verify the correctness of the derived equations and the implementation, experiments with analytical solutions were performed on a cubical object. The tests were static, and the object was isotropic and incompressible, i.e. $b_{\alpha\beta} = \bar{b}$, and $J = 1$.

[1] The parts related to accelerations and velocities are ignored for tidiness.

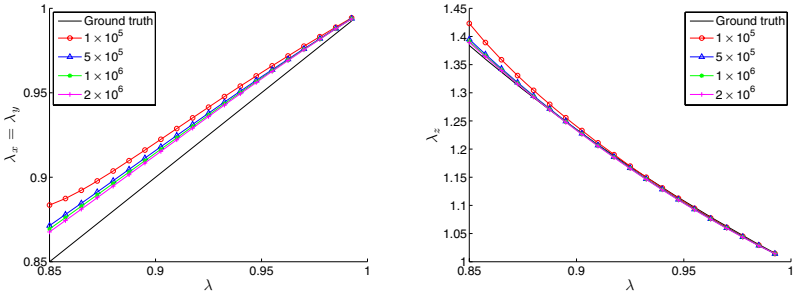

Fig. 1. Experimental results of simple extension. x-axis represents the state used for calculating the input force, and y-axis represents the resulted deformation. The legends represent different values of κ.

A simple extension was studied. For simple extension along the z-direction, the deformation gradient tensor can be given as:

$$\mathbf{F} = \begin{bmatrix} \lambda_x & 0 & 0 \\ 0 & \lambda_y & 0 \\ 0 & 0 & \lambda_z \end{bmatrix} = \begin{bmatrix} \lambda & 0 & 0 \\ 0 & \lambda & 0 \\ 0 & 0 & \frac{1}{\lambda^2} \end{bmatrix} \tag{11}$$

because $J = \det \mathbf{F} = \lambda_x \lambda_y \lambda_z = 1$ for incompressibility, and $\lambda_x = \lambda_y$ for isotropy. λ is the stretch ratio. The corresponding first Piola-Kirchhoff (PKI) stress tensor $\mathbf{P}$ can be derived using (3) and the relation $\mathbf{P} = \mathbf{FS}$, and its only nonzero component is along the z-axis:

$$P_{zz} = \frac{1}{2} a \bar{b} e^{Q} \left(\frac{1}{\lambda^6} - \lambda^6 + \lambda^4 - \frac{1}{\lambda^2} \right) \tag{12}$$

The PKI stresses were applied to the cubical object to test if the corresponding deformations could be obtained. $\lambda = 0.85$, $a = 0.88$ kPa, and $\bar{b} = 6.0$, with the stresses applied in 20 steps. Different values of κ were also tested, and the numerical results are shown in Fig. 1. The resulted λ_z were very close to the ground truth, which means that the derived stress-strain relation is accurate. The deviations of λ_x and λ_y were larger, and this is related to the incompressibility of the model. We can see that the deviations decrease with increasing κ. When κ equals to infinity, the incompressibility can be fully enforced, but this is impossible as the system matrices become ill-conditioned when κ becomes large. Nevertheless, as the myocardium is not completely incompressible, using the penalty method for incompressibility can still provide a good enough approximation.

3.2 Canine Heart Architecture

To verify the physiological plausibility of the proposed model, simulations were performed on the canine heart architecture of the University of Auckland, which provides both cardiac geometry and fibrous-sheet structure [7] (Fig. 2). The

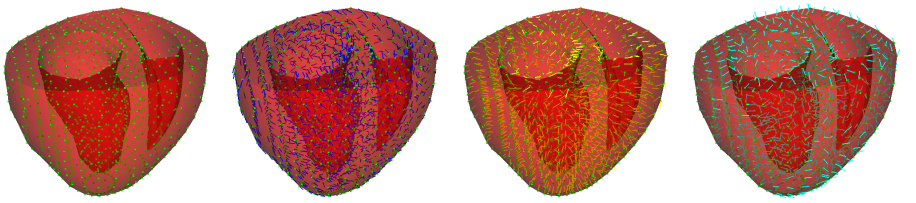

Fig. 2. Canine heart architecture. Left to right: a set of nodes (green) bounded by surfaces (red) representing the cardiac boundaries, fiber orientations (blue lines), sheet orientations (yellow lines), and sheet normal orientations (cyan lines).

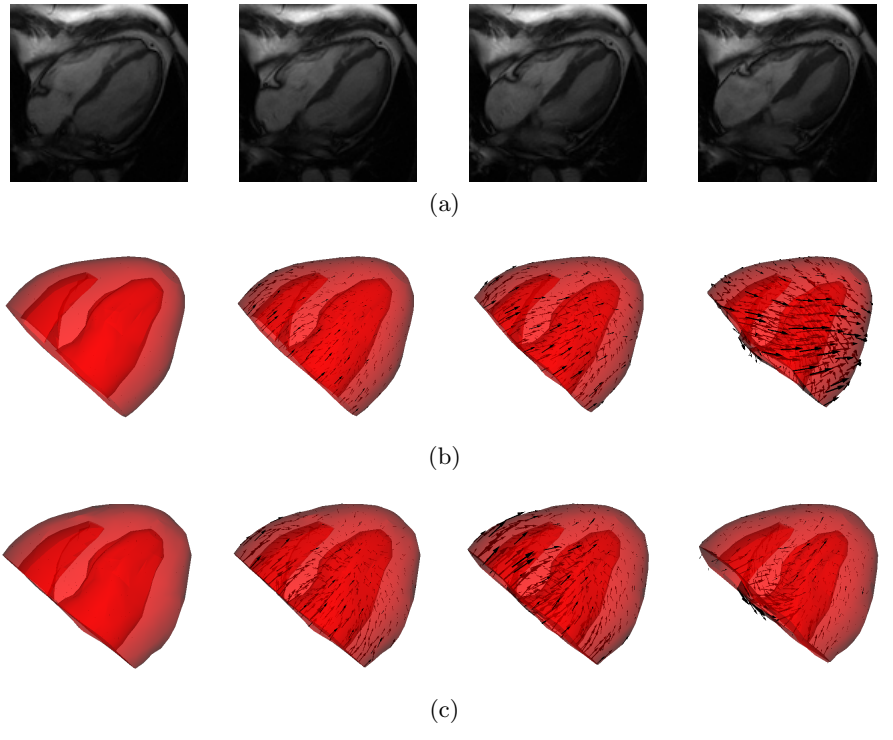

Fig. 3. Cardiac deformations during systole, from the end of diastole to the end of systole. (a) MRI sequence of a healthy human heart. (b) and (c) Simulated cardiac cycles, with black arrows representing the incremental displacement vectors. (b) With pericardial boundary conditions. (c) Without pericardial boundary conditions.

values of the material parameters were adopted from [10] ($a = 0.88$ kPa, $b_{ff} = 6.0, b_{ss} = 7.0, b_{nn} = 3.0, b_{fs} = 12.0, b_{fn} = 3.0, b_{sn} = 3.0$), except κ for which different values were tested. Active forces were simulated through the E and EM models [9], and blood pressures were applied to the left and right ventricles (LV and RV) to approximate the blood filling process. Deformations of one cardiac

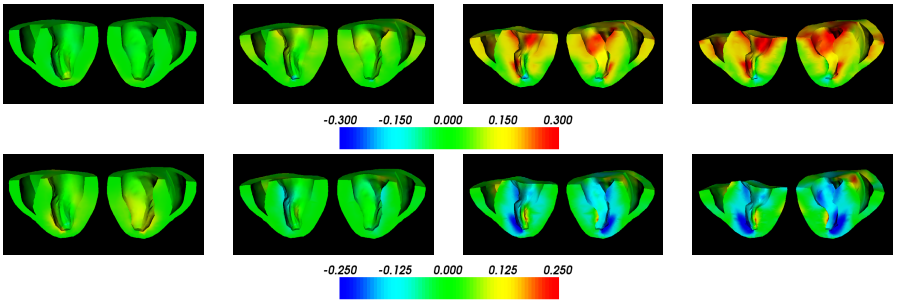

Fig. 4. Strain maps of simulated cardiac cycle. Top to bottom: radial and circumferential strains, defined under a cylindrical coordinate system with the long axis of the LV as the long axis. Left to right: the end of diastole to the end of systole. Positive values represent extensions and negative values represent contractions.

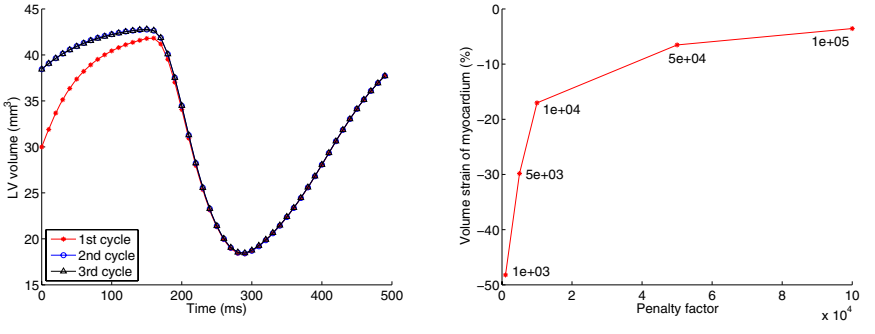

(a) (b)

Fig. 5. (a) Change of LV volume in simulated cardiac cycles. (b) Volume strain of myocardium versus penalty factor κ. Values of κ at sample points are shown.

cycle in 500 ms were computed, and three cycles were run for each simulation to alleviate the improper initial conditions.

Fig. 3 provides visual comparisons between the simulations and magnetic resonance images (MRI). The MRI show that when the heart contracts, the apex is almost fixed, the base moves towards the apex, and the motion of the epicardium is limited by the pericardium (Fig. 3(a)). Similar pattern can be observed in the simulation in Fig. 3(b). Furthermore, we can see the twisting motions of the myocardium from the incremental displacements represented by black arrows, which are specific cardiac motions observable in tagged MRI and described in literatures. Moreover, to demonstrate the importance of the proposed pericardial displacement boundary condition in Section 2.4, we have also performed another simulation without this constraint. The resulted deformations were less realistic, and the twisting motions also disappeared (Fig. 3(c)). Fig. 4 shows the deformation pattern of the myocardium through strain maps, where the negative values and positive values represent contractions and extensions respectively. The color

patterns show that the myocardium extended along the radial direction while contracted along the circumferential direction during systole, with radial and circumferential strains of 30% and -25% respectively at the end of systole, which are consistent with the descriptions in the literatures [4].

Fig. 5(a) shows the LV volume change of the simulated cardiac cycles. In the simulation, the heart contraction began at 150 ms. The LV volume at 0 ms of the first cycle was the stress-free volume without any blood pressure and active contraction forces. The volume increased before the contraction because of the applied blood pressures. The LV volume change of the second cardiac cycle is almost the same as the third cycle, which means that the cardiac deformation converged at the second cardiac cycle. The stroke volume of the converged cycle is 57.1%. The shape of the curve and the stroke volume are similar to those reported in literatures.

Fig. 5(b) shows the volume strain of the myocardium versus the change of the penalty factor κ for tissue incompressibility. The volume strain is defined as $(V_{\mathrm{ES}} - V_0)/V_0$, where V_{ES} and V_0 are the myocardial volume at the end of systole and the stress-free myocardial volume respectively. The volume strain of a completely incompressible material should be zero. It can be seen that the myocardium became increasing incompressible with the increase of κ. κ of values 5×10^5 and 1×10^6 were also tested, with volume strains -1.04% and -0.53% respectively. Nevertheless, the system became unstable and could not even complete the first cycle. In consequence, total incompressibility cannot be enforced using penalty methods, and a proper choice of κ is important for enforcing reasonable incompressibility while keeping the system stable.

4 Conclusion

In this paper, we propose an active cardiac model for cardiac image analysis, which comprises a realistic orthotropic hyperelastic material model with only seven parameters, but was reported as the best among the five tested well-known constitutive laws. To facilitate the complicated inverse problems, the system is implemented under the Cartesian coordinate system, and we propose the corresponding displacement boundary conditions of the pericardium for the anatomically realistic constraints of the cardiac deformation. Experiments with analytical solutions were performed on a cubical object, which verified the correctness of the derived formulations and the implementation, and the results show also the possible pitfalls when enforcing material incompressibility. Simulations on a canine heart architecture were done to verify the physiological plausibility of the proposed model. Through the visual comparisons of the simulated cardiac deformations to those of MRI, the strain maps of the simulated contraction patterns, and also the plot showing the quantitative temporal change of the LV volume, the proposed model has been shown to be physiologically plausible.

References

1. Hunter, P.J.: Modeling human physiology: The IUPS/EMBS physiome project. Proceedings of the IEEE 94(4), 678–691 (2006)
2. Sermesant, M., Delingette, H., Ayache, N.: An electromechanical model of the heart for image analysis and simulation. IEEE Transactions on Medical Imaging 25(5), 612–625 (2006)
3. Sermesant, M., Moireau, P., Camara, O., Sainte-Marie, J., Andriantsimiavona, R., Cimrman, R., Hill, D.L.G., Chapelle, D., Razavi, R.: Cardiac function estimation from MRI using a heart model and data assimilation: advances and difficulties. Medical Image Analysis 10, 642–656 (2006)
4. Glass, L., Hunter, P., McCulloch, A. (eds.): Theory of Heart: Biomechanics, Biophysics, and Nonlinear Dynamics of Cardiac Function. Springer, Heidelberg (1991)
5. Humphrey, J.D.: Cardiovascular Solid Mechanics: Cells, Tissues, and Organs. Springer, Heidelberg (2001)
6. LeGrice, I., Hunter, P., Young, A., Smaill, B.: The architecture of the heart: a data-based model. Philosophical Transactions of the Royal Society A 359(1783), 1217–1232 (2001)
7. Nash, M.: Mechanics and Material Properties of the Heart using an Anatomically Accurate Mathematical Model. PhD thesis, The University of Auckland (1998)
8. Hu, Z., Metaxas, D., Axel, L.: In vivo strain and stress estimation of the heart left and right ventricles from MRI images. Medical Image Analysis 7(4), 435–444 (2003)
9. Wong, K.C.L., Zhang, H., Liu, H., Shi, P.: Physiome-model-based state-space framework for cardiac deformation recovery. Academic Radiology 14(11), 1341–1349 (2007)
10. Usyk, T.P., Mazhari, R., McCulloch, A.D.: Effect of laminar orthotropic myofiber architecture on regional stress and strain in the canine left ventricle. Journal of Elasticity 61, 143–164 (2000)
11. Costa, K.D., Holmes, J.W., McCulloch, A.D.: Modelling cardiac mechanical properties in three dimensions. Philosophical Transactions of the Royal Society A 359(1783), 1233–1250 (2001)
12. Schmid, H., Nash, M.P., Young, A.A., Hunter, P.J.: Myocardial material parameter estimation — a comparative study for simple shear. Journal of Biomechanical Engineering 128, 742–750 (2006)
13. Rogers, J.M., McCulloch, A.D.: A collocation-Galerkin finite element model of cardiac action potential propagation. IEEE Transactions on Biomedical Engineering 41(8), 743–757 (1994)
14. Zhang, H., Shi, P.: A meshfree method for solving cardiac electrical propagation. In: 27th Annual International Conference of the IEEE-EMBS, pp. 349–352 (2005)
15. Holzapfel, G.A.: Nonlinear Solid Mechanics: A Continuum Approach for Engineering. John Wiley & Sons, Inc., Chichester (2000)
16. Germann, W.J., Stanfield, C.L.: Principles of Human Physiology. Pearson Benjamin Cummings, London (2005)
17. Bathe, K.J.: Finite Element Procedures. Prentice-Hall, Englewood Cliffs (1996)

Personalised Electromechanical Model of the Heart for the Prediction of the Acute Effects of Cardiac Resynchronisation Therapy

Maxime Sermesant[1,3], Florence Billet[1], Radomir Chabiniok[2], Tommaso Mansi[1], Phani Chinchapatnam[4], Philippe Moireau[2], Jean-Marc Peyrat[1], Kawal Rhode[3], Matt Ginks[3], Pier Lambiase[6], Simon Arridge[4], Hervé Delingette[1], Michel Sorine[7], C. Aldo Rinaldi[5], Dominique Chapelle[2], Reza Razavi[3], and Nicholas Ayache[1]

[1] INRIA, Asclepios project, 2004 route des Lucioles, Sophia Antipolis, France
[2] INRIA, Macs project, Rocquencourt, Le Chesnay, France
[3] King's College London, Division of Imaging Sciences, London, UK
[4] University College London, Centre for Medical Image Computing, London, UK
[5] Department of Cardiology, St Thomas' Hospital, London, UK
[6] The Heart Hospital, University College London Hospitals, London, UK
[7] INRIA, Sysiphe project, Rocquencourt, Le Chesnay, France

Abstract. Cardiac resynchronisation therapy (CRT) has been shown to be an effective adjunctive treatment for patients with dyssynchronous ventricular contraction and symptoms of the heart failure. However, clinical trials have also demonstrated that up to 30% of patients may be classified as non-responders. In this article, we present how the personalisation of an electromechanical model of the myocardium could help the therapy planning for CRT. We describe the four main components of our myocardial model, namely the anatomy, the electrophysiology, the kinematics and the mechanics. For each of these components we combine prior knowledge and observable parameters in order to personalise these models to patient data. Then the acute effects of a pacemaker on the cardiac function are predicted with the *in silico* model on a clinical case. This is a proof of concept of the potential of virtual physiological models to better select and plan the therapy.

1 Introduction

Cardiac resynchronisation therapy (CRT) involves implanting a pacemaker to improve the synchronicity of cardiac contraction. It has recently been shown to be an effective method of treating patients with dyssynchronous ventricular contraction and symptoms of heart failure. However, clinical trials have also demonstrated that up to 30% of patients may be classified as non-responders. There remains major controversy surrounding patient selection and optimisation of this expensive treatment (e.g. lead positioning, pacemaker settings). Therefore, new approaches are needed for improved patient selection and a better planning and delivery of the therapy.

N. Ayache, H. Delingette, and M. Sermesant (Eds.): FIMH 2009, LNCS 5528, pp. 239–248, 2009.
© Springer-Verlag Berlin Heidelberg 2009

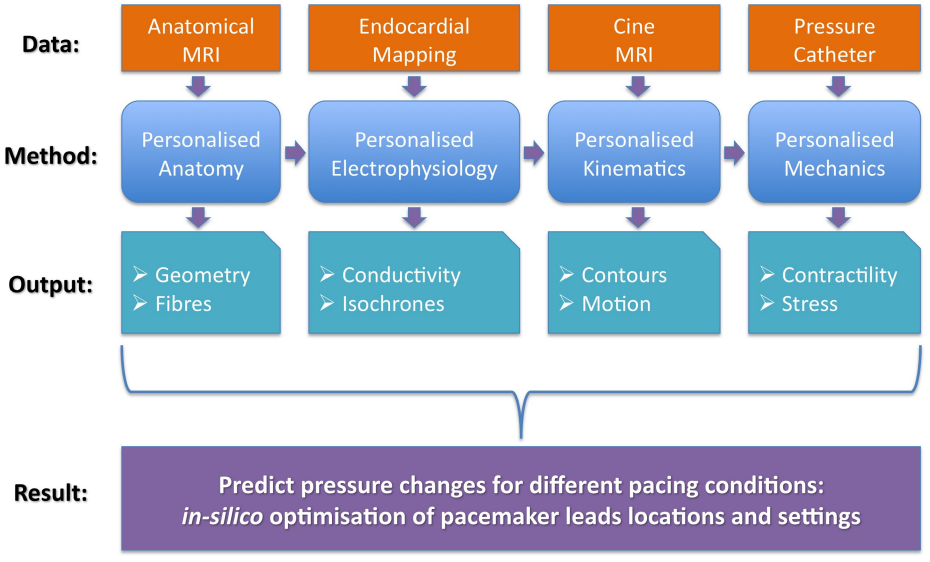

Fig. 1. Global scheme of the clinical data used for the personalised models, the generated output maps and parameters, and the resulting predictions

In this article, we demonstrate a proof of concept on a first case study of the personalisation of an electromechanical model of the heart for prediction of the changes in cardiac function due to changes in pacing (see Fig. 1). Such predictions can be used to quantify the improvement in cardiac function that can be expected from CRT and also to optimise the pacemaker implantation and settings. In this work we only focus on the acute effects of resynchronisation.

Recently, complex models have been used to simulate CRT on a generic anatomy and compared with animal experiments [1,2] which provides important insights on the pathophysiology of dyssynchrony. However, in order to translate to the clinic and impact the patient management and the therapy planning, such models need to be personalised to the specific parameters of each patient, which remains very challenging.

The proposed approach involves models whose complexity is directly related to the phenomena observed in clinical data. This is the reason why these models are often simplified compared to the very detailed models available in the literature. Involving a limited number of parameters can allow their identification from clinical measurements on a specific patient. We illustrate in this article the personalisation of several components (Fig. 1). A preliminary section details the clinical context, the data acquisition, and the data fusion. We then present the four sections concerning the personalisation of the anatomy, the electrophysiology, the kinematics and the mechanics. Finally we demonstrate this first proof of concept on the prediction of the cardiac function for two different pacing conditions.

Due to the limited space, the details of each model and their personalisation algorithms are not given in this article, but can be found in the references.

2 Clinical Context, Data Acquisition and Fusion

For cardiac modelling, the fusion of anatomical, mechanical, and electrical data is of primary importance. We use here a real-time registration solution as described in [3] that allows the spatial integration of MRI-based anatomical and functional data with X-ray-based catheter data, such as intracardiac electrical and pressure signals. The MR examination involves bSSFP Cine imaging for the estimation of ventricular function and volumes, and late enhancement images with gadolinium contrast agent for scar anatomy. The non-contact mapping is performed using the Ensite 3000 multi-electrode array catheter system (St Jude, Sylmar, CA).

The patient of this first case study is a sixty year old woman with NYHA class III symptoms (NYHA classes stand for the stages of heart failure according to the New York Heart Association. Patients with NYHA III are comfortable at rest but any other activity causes fatigue, palpitation, or dyspnea). The aetiology of heart failure is thought to be dilated cardiomyopathy although cardiac MRI did show two non-viable areas of a moderate size corresponding to the drainage area of the left anterior descending (in the apical and mid-inferoseptal segments, see Fig. 2) and of the left circumflex coronary artery (mid-inferolateral segment of the left ventricle, see Fig. 2), which are consistent with a previous subendocardial infarction. However, there was no flow-limiting disease on coronary angiography. Ejection fraction of the left ventricle was around 30% on maximal tolerated medication. The patient suffers from a left bundle branch block (LBBB). Echocardiography, including Tissue Doppler, confirmed significant mechanical dysynchrony in keeping with the ECG findings, with in particular a QRS duration of 144 ms.

3 Personalised Anatomy

3.1 Myocardial Shape

There is an important literature on the segmentation of the heart from medical images. However, to cope with extreme and variable anatomies due to pathologies, we developed a simple yet efficient method which combines specific image processing tools to extract the biventricular myocardium from Cine-MRI. The approach is made of three steps: 1) image preparation, in order to enhance image quality; 2) interactive segmentation of the myocardial boundaries at mid-diastole; and 3) construction of the volumetric anatomical model. For regional personalisation of the simulation, each tetrahedron is automatically labelled according to the anatomical region it belongs to (LV+septum, RV, scar tissue, see Fig. 2). The scar label is based on the expert manual delineation on late enhancement MRI.

3.2 Cardiac Fibre Orientation

The complex fibre architecture has an important role in the electrical and mechanical functions of the heart. We use the statistical atlas of the cardiac fibre

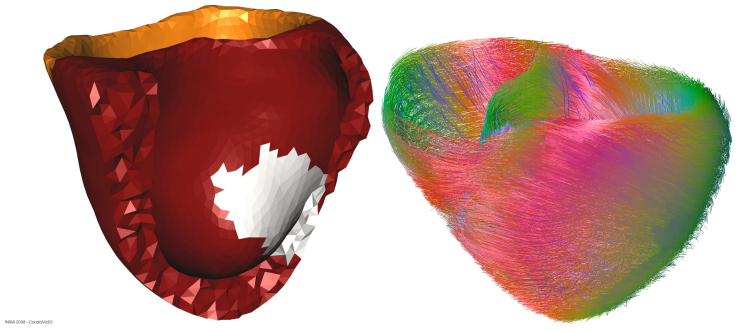

Fig. 2. (Left) 3D anatomical model of patient myocardium: left ventricle *(in red)*, right ventricle *(in orange)* and scar *(in white)*. (Right) personalised muscle fibres from registered atlas.

architecture and the methodology described in [4]. This atlas was computed from a population of *ex vivo* canine hearts but was shown to be consistent with human hearts. We first globally align the atlas with the patient's heart using a constrained affine registration. Then, a non-linear registration algorithm is performed. The resulting deformation field is used to resample and reorient the atlas of DT-MRIs to fit the patient geometry.

4 Personalised Electrophysiology

Clinical electrophysiologic data currently available only reliably describe the depolarisation times, and not the extracellular or transmembrane potentials. So we chose the Eikonal electrophysiology model accordingly. The Eikonal equation is static, and the front can be observed at a larger scale, resulting in much faster computations. An anisotropic multi-front fast marching method was developed in order to solve the Eikonal model equations very efficiently. We base our model on the Eikonal diffusion (ED) equation [5].

To personalise this electrophysiology model, there are two important adjustments to perform: the onset of the electrical propagation, and the local conduction velocity. To adjust the electrical onset, we use the earliest activation from the Ensite map. For the conduction velocity, we estimate it in the Eikonal model by matching the simulated propagation times of the model to the clinically measured propagation times of the patient. An automatic adjustment method of the apparent conductivity (AC) has been designed for surfaces [5]. We currently use a manual adjustment in order to extrapolate this to the volumetric model, in order to obtain isochrones within the muscle and in the right ventricle.

5 Personalised Electromechanical Models

The myocardium constitutive law is active, non-linear, anisotropic, incompressible and visco-elastic. Numerous laws were proposed in the literature, see e.g.

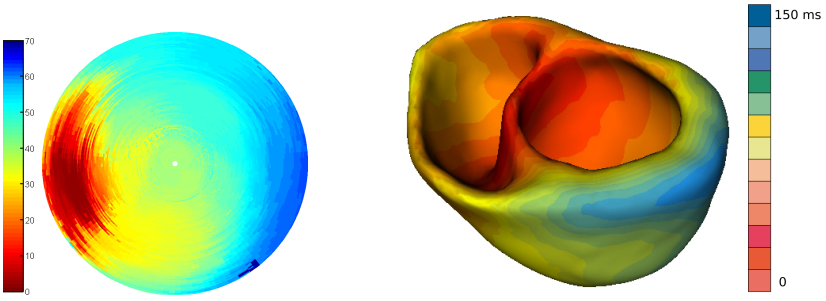

Fig. 3. (Left) LV endocardium Ensite isochronal map in sinus rhythm (in ms), (Right) simulated volumetric isochrones for extrapolation of endocardial data

[6,7,8,9,10] and references therein. The models used in our study were designed to have a complexity compatible with the clinical data used for the personalisation.

We use two different electromechanical models for the muscle contraction, depending on the application. We first introduce a simplified model as a deformable model in order to extract the motion and contours from the dynamic images (Personalised Kinematics, Subsection 5.1). We then use this information with additional pressure data in order to personalise a more complex model of the myocardial mechanics, which allows to adjust contractility and estimate pressures (Personalised Mechanics, Subsection 5.2). These models are detailed in [11] and [12]. To carry out simulations, additional needs are Windkessel models and valve laws to represent the blood flows and adequate finite element and energy-preserving time discretisation strategies.

5.1 Personalised Kinematics

In this subsection, we outline a deformable model approach to estimate the motion of the heart using Cine-MRI data and an electromechanical model. The model used here is a pro-active deformable model designed for cardiac image analysis and simulation [11]. This approach consists of adding image forces to the vertices belonging to the surface of an electromechanical model. This method is related to a sequential data assimilation approach [13], as detailed in [14]. Fig. 4 shows the MR images at end-systole. The superimposed lines represent the endocardial and epicardial surfaces of the estimated mesh. Colours correspond to the intensity of the images forces.

We can observe that despite the limited quality of routine clinical images, the estimation of the myocardial contours is relatively good, especially for the left ventricle. Due to the lack of contrast on the epicardium and the small thickness of the right ventricle, achieving a good dynamic segmentation of the RV is still very challenging. Finally, even if Cine-MRI only shows the radial motion, this

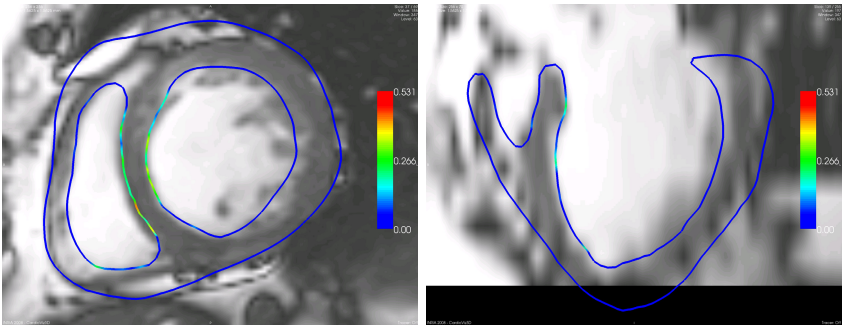

Fig. 4. Results of the motion tracking: delineation of the estimated mesh superimposed with Cine-MRI at end-systole in short- and long-axis views. Colour encodes the intensity of the image forces (blue: small, red: large).

approach estimates a complete 3D motion, interpolating with the electromechanical model for the circumferential and longitudinal motion.

5.2 Personalised Mechanics

We use this estimated motion to personalise the mechanical parameters of a more complex model, in particular to ensure a realistic simulation of the stresses. The model used here, and detailed in [12], was built from a physiological point of view and is consistent with essential thermomechanical requirements (energy balances in particular), preserved from the continuous dynamical equations to the discrete versions used for simulations. We demonstrate here that the personalisation steps presented above and a proper calibration of the mechanical parameters using the pressure-volume indicators can already provide satisfactory predictability in the direct simulation of the cardiac function.

In order to take into account the infarct, the scar tissue (segmented in the anatomical personalisation) has contractility parameters decreased by a factor of 5. We then obtained a simulated motion relatively close to the one from the personalised kinematics. While there are still discrepancies, the general behaviour is very similar. However, the automatic adjustment of local parameters is needed in order to be able to improve the fitting. The work in progress on this automatic identification is very promising [15,13]. This personalised mechanical model produces simulated pressure in very good agreement with the catheter measurement in systole (see Fig. 5, Left). Note that the slope of the simulated pressure curve is not very accurate in the diastolic phase. Although this could be adjusted by changing the parameter corresponding to active relaxation, the slope is also highly affected by the synchronicity of the repolarisation wave. As the repolarisation wave cannot be effectively detected in the measurements, due to the small amplitude and gentle slope of the T wave, we instead used action potential durations based on the ECG. This of course does not accurately represent the synchrony of repolarisation, hence we did not seek the calibration of

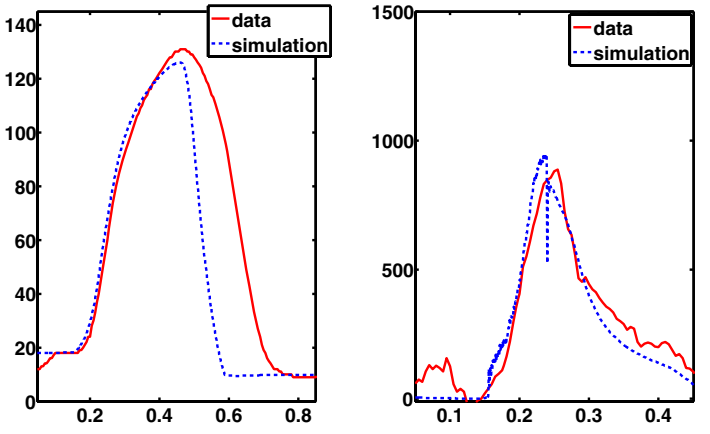

Fig. 5. (Left) Measured (solid red) and simulated (dashed blue) left ventricular pressure curves (in mmHg) in sinus rhythm (time in s). (Right) Measured (solid red) and simulated (dashed blue) left ventricular dP/dt curves (in mmHg/s) during systole in sinus rhythm (time in s).

the diastolic pressure slope. This is the reason why we only show the systolic phase in the dP/dt curves (see Fig. 5, Right).

6 Prediction of the Acute Effects of Pacing

During the electrophysiology study, different pacing conditions are tested to evaluate the effect of different pacing lead locations and delays. In this section, we test the ability of our personalised electromechanical model of the myocardium to predict the changes in the heart for two different pacing conditions. First, we simulate atrial pacing, by using ventricular isochrones similar to sinus rhythm but with a higher heart rate. We also test biventricular pacing with simultaneous endocardial left ventricular pacing (called here P1TRIV). We use the actual Ensite mapping of this pacing case to adjust the volumetric isochrones, incorporating the location of the pacing electrodes from the XMR registration.

Then, we use the mechanical model personalised in section 5.2, without changing any parameter. We input the new electrical command corresponding to the atrial and P1TRIV pacing and observe the resulting simulated pressure curves (see Fig. 7, Left), allowing to test in particular predictions on the slope of this pressure during isovolumetric contraction. As this is the major cardiac phase that is sought to be optimised by CRT, we mainly focus on the model predictive power during this phase, and early ejection. When simulating the atrial and P1TRIV pacing with the model personalised from baseline measurements, we observe a very good agreement of the pressure curve with the recorded data

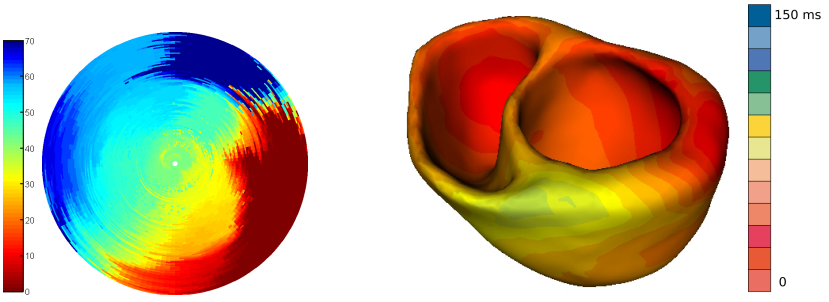

Fig. 6. (Left) LV endocardial Ensite isochronal map for P1TRIV pacing (in ms), (Right) simulated volumetric isochrones for extrapolation of endocardial data

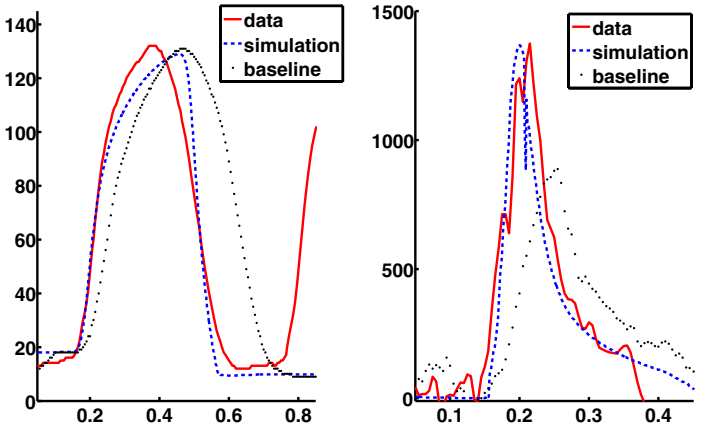

Fig. 7. (Left) Measured (solid red) and simulated (dashed blue) left ventricular pressure curves (in mmHg) with P1TRIV pacing along the cardiac cycle (time in s). (Right) Measured (solid red) and simulated (dashed blue) left ventricular dP/dt curves (in mmHg/s) during systole (time in s) with P1TRIV pacing. Baseline measurements are the dotted line.

from the pressure catheter, and the dP/dt curve is also very similar (see Fig. 7, Right, for the P1TRIV case).

One important index of the effectiveness of the contraction is the maximum of the pressure time-derivative, $(dP/dt)_{max}$. It describes how the pressure builds up during the isovolumetric contraction.

$(dP/dt)_{max}$ in $mmHg/s$	Sinus Rhythm	Atrial Pacing	P1TRIV
Measured	**930**	**950**	**1381**
Simulated	**950**	**980**	**1370**

We can see that the improvement of the cardiac function brought by the two different pacing conditions is well predicted by the *in silico* simulations.

7 Conclusion

We presented the personalisation of a complete electromechanical model of the myocardium using XMR interventional data and how this personalised model could be used to predict the effects of therapy. This model has been tested on the left ventricular pressure resulting from different depolarisation maps. The behaviour of the model in sinus rhythm as well as the predictions of the model under two pacing conditions compare well with the measured data, which make such an approach very promising. This is the first case study demonstrating how models of the heart can be adjusted to be patient-specific and a first proof of concept of how this approach can be useful for planning of therapy.

While several steps still require interactive adjustment, the methodology for automatic parameter estimation is becoming available [15,13,5]. In the case of CRT, such predictions could help optimise the pacemaker settings *in silico*, which may include the pacing lead locations and delays between chamber stimulation.

Acknowledgements

Part of this research was funded by the INRIA Research Action CardioSense3D, by the Technology Strategy Board's Collaborative Research and Development programme (grant number 17352) with Philips Healthcare, Best, the Netherlands, and by the EPSRC grant EP/D061474/1.

References

1. Kerckhoffs, R.C., Lumens, J., Vernooy, K., Omens, J.H., Mulligan, L.J., Delhaas, T., Arts, T., McCulloch, A.D., Prinzen, F.W.: Cardiac resynchronization: Insight from experimental and computational models. Prog. Biophys. Mol. Biol. 97(2-3), 543–561 (2008)
2. Kerckhoffs, R.C., McCulloch, A.D., Omens, J.H., Mulligan, L.J.: Effects of biventricular pacing and scar size in a computational model of the failing heart with left bundle branch block. Med. Image Anal. (July 2008)
3. Rhode, K., Sermesant, M., Brogan, D., Hegde, S., Hipwell, J., Lambiase, P., Rosenthal, E., Bucknall, C., Qureshi, S., Gill, J., Razavi, R., Hill, D.: A system for real-time XMR guided cardiovascular intervention. IEEE Transactions on Medical Imaging 24(11), 1428–1440 (2005)
4. Peyrat, J.M., Sermesant, M., Pennec, X., Delingette, H., Xu, C., McVeigh, E.R., Ayache, N.: A computational framework for the statistical analysis of cardiac diffusion tensors: Application to a small database of canine hearts. IEEE Transactions on Medical Imaging 26(11), 1500–1514 (2007)
5. Chinchapatnam, P., Rhode, K., Ginks, M., Rinaldi, C., Lambiase, P., Razavi, R., Arridge, S., Sermesant, M.: Model-based imaging of cardiac apparent conductivity and local conduction velocity for diagnosis and planning of therapy. IEEE Transactions on Medical Imaging 27(11), 1631–1642 (2008)

6. Humphrey, J., Strumpf, R., Yin, F.: Determination of a constitutive relation for passive myocardium: I. A new functional form. ASME Journal of Biomechanical Engineering 112, 333–339 (1990)
7. Nash, M.: Mechanics and Material Properties of the Heart using an Anatomically Accurate Mathematical Model. PhD thesis, University of Auckland (1998)
8. Caillerie, D., Mourad, A., Raoult, A.: Cell-to-muscle homogenization. Application to a constitutive law for the myocardium. Math. Mod. Numer. Anal. 37(4), 681–698 (2003)
9. Hunter, P., McCulloch, A., ter Keurs, H.: Modelling the mechanical properties of cardiac muscle. Progr. Biophys. Mol. Biol. 69, 289–331 (1998)
10. Smith, N., Nickerson, D., Crampin, E., Hunter, P.: Computational mechanics of the heart. from tissue structure to ventricular function. J. of Elasticity 61(1), 113–141 (2000)
11. Sermesant, M., Delingette, H., Ayache, N.: An Electromechanical Model of the Heart for Image Analysis and Simulation. IEEE Transactions in Medical Imaging 25(5), 612–625 (2006)
12. Sainte-Marie, J., Chapelle, D., Cimrman, R., Sorine, M.: Modeling and estimation of the cardiac electromechanical activity. Computers & Structures 84, 1743–1759 (2006)
13. Moireau, P., Chapelle, D., Le Tallec, P.: Joint state and parameter estimation for distributed mechanical systems. Computer Methods in Applied Mechanics and Engineering 197, 659–677 (2008)
14. Billet, F., Sermesant, M., Delingette, H., Ayache, N.: Cardiac motion recovery by coupling an electromechanical model and Cine-MRI data: First steps. In: Workshop Computational Biomechanics for Medicine III (MICCAI 2008) (2008)
15. Sermesant, M., Moireau, P., Camara, O., Sainte-Marie, J., Andriantsimiavona, R., Cimrman, R., Hill, D.L., Chapelle, D., Razavi, R.: Cardiac Function Estimation from MRI Using a Heart Model and Data Assimilation: Advances and Difficulties. Medical Image Analysis 10(4), 642–656 (2006)

Ventricular Mechanical Asynchrony in Pulmonary Arterial Hypertension: A Model Study

Joost Lumens[1,2], Theo Arts[2], and Tammo Delhaas[1]

[1] Department of Physiology
[2] Department of Biomedical Engineering, Maastricht University,
Universiteitssingel 50, 6200 MD, P.O. Box 616, Maastricht, The Netherlands
j.lumens@fys.unimaas.nl

Abstract. In pulmonary arterial hypertension (PH), increase of myofiber contraction duration in the right ventricular (RV) free wall as compared to that in the left ventricular (LV) free wall leads to mechanical asynchrony. We used the lumped TriSeg model describing ventricular mechanics to determine effects of increasing pulmonary resistance and of changing time of RV free wall activation on ventricular pump mechanics and on myofiber mechanics in the ventricular walls. Simulated circumferential strain in the ventricular walls under normal and PH conditions agreed with measurements in patients. When the RV free wall was early activated with respect to the LV free wall and septum, simulations showed decreased RV volume and decreased myofiber work in the RV free wall whereas LV free wall and septal myofiber work increased. This suggests that RV free wall pacing in PH improves RV pump function and increases homogeneity of myofiber load in the ventricular walls.

Keywords: Ventricular interaction, myofiber mechanics, stress, strain, pacing, pump work.

1 Introduction

In patients suffering from pulmonary arterial hypertension (PH), right ventricular (RV) pressures are chronically elevated due to increase of pulmonary peripheral resistance. In these patients, increase of RV afterload prolongs circumferential shortening of the RV free wall as compared to that of the septum and left ventricular (LV) free wall. The delay of the RV free wall contraction appeared strongly correlated with severity of disease in PH patients [1]. Measurements of circumferential strain in the ventricular walls showed a delay of peak shortening of the RV free wall relative to that of the LV free wall and septum while onset of shortening happened simultaneously in the three ventricular walls [2]. RV free wall shortening even continued after pulmonary valve closure leading to leftward septal motion during passive LV relaxation, thus hindering early LV filling [2]. Therefore, mechanical interaction of the ventricular walls determines pump efficiency in PH. The precise mechanisms behind this phenomenon are poorly understood since it is hard to quantify the load and energetic contribution of each ventricular wall to total pump work.

N. Ayache, H. Delingette, and M. Sermesant (Eds.): FIMH 2009, LNCS 5528, pp. 249–257, 2009.
© Springer-Verlag Berlin Heidelberg 2009

In the present study, the lumped TriSeg model of ventricular interaction [3] was used to quantify the effect of increase in pulmonary resistance on ventricular pump mechanics and contractile myofiber mechanics in the three ventricular walls. Furthermore, the moment of RV free wall activation was changed with respect to those of the LV free wall and septum to study how these changes affect pump mechanics of both ventricles and myofiber mechanics in the three ventricular walls.

2 Methods

2.1 Model Design

The TriSeg model of ventricular mechanics, previously described in more detail by Lumens *et al.* [3], incorporates mechanical interaction of the LV free wall (LW), RV free wall (RW), and septal wall (SW) resulting in a strong coupling of LV and RV pump function. Three thick-walled spherical segments representing the LW, SW, and RW are coupled in a common junction thereby encapsulating the left and right ventricular cavity (Fig. 1). Midwall area and curvature are calculated for all three wall segments, given instantaneous volumes of left and right ventricular cavity and an estimate of septal curvature and area. From midwall area and curvature of each wall, sarcomere extension is calculated using the one-fiber model that relates global

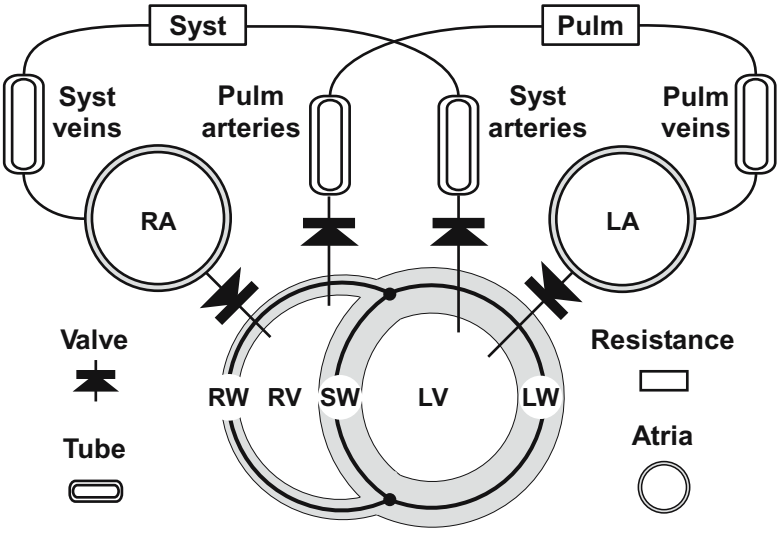

Fig. 1. The TriSeg model of the ventricular walls (shaded) incorporated in the modular CircAdapt model of the whole circulation [3, 5]. Three thick-walled spherical segments representing the left ventricular free wall (LW), right ventricular free wall (RW), and septal wall (SW) are coupled mechanically at the midwall junction (dots), thereby forming a left (LV) and a right (RV) ventricular cavity. Cardiac valves connect the left (LA) and right (RA) atrium to the ventricles (chamber module) and the ventricles to the systemic (Syst) and pulmonary (Pulm) circulations, containing nonlinear tube and resistance modules.

ventricular geometry to sarcomere length [4]. Myofiber stress is calculated with constitutive equations of sarcomere mechanics incorporating Hill's sarcomere force-velocity relation and Starling's sarcomere length-contractility relation, as described in more detail by Arts *et al.* [5]. Radial and axial force components of midwall tension, as exerted by each wall segment on the common junction, are calculated from segment geometry and myofiber stress. Thus, force balance in the junction provides two equations, which are solved numerically by proper variation of septal curvature and area. With the thus obtained solution for ventricular geometry, LV and RV pressures are calculated from wall tensions.

The TriSeg model of ventricular mechanics is implemented in the existing CircAdapt model of the whole circulation [5], which supplies the required hemodynamic boundary conditions for the ventricles. The CircAdapt model is designed as a network of modules representing cardiac chambers, valves, large blood vessels, and resistances (Fig. 1). Extended with the TriSeg model, the CircAdapt model allows beat-to-beat simulation of time-dependent ventricular mechanics and hemodynamics, e.g., volumes and pressures of the ventricular cavities, geometries and myofiber mechanics of the three ventricular walls, and flows through valves. The number of independent parameters is reduced tremendously by incorporating adaptation of size and mass of cardiac walls and blood vessels to mechanical load so that stress and strain in the walls of heart and blood vessels are normalized to tissue-specific physiological standard levels [3, 5, 6].

The core of the CircAdapt model is a set of first-order differential equations in state-variables, which has been solved numerically using the ODE113 function in Matlab 7.1.0 (MathWorks, Natick, MA) with a temporal resolution of 2 ms.

2.2 Simulations

The following simulations of ventricular mechanics and hemodynamics under normal and pathological right ventricular loading conditions were performed with constant resting values of cardiac output (85 ml s^{-1}), cardiac cycle length (0.85 s), and mean arterial pressure (12.2 kPa). A control simulation (Contr) was performed under normal cardiac loading conditions. Adaptation was performed under exercise conditions (mean systemic flow 3x normal, heart rate 2x normal) rendering size and mass of the ventricular walls. In the second simulation (PHAd), pulmonary resistance was elevated to a level resulting in a mean arteriovenous pressure drop of 3.5 kPa over the pulmonary circulation and subsequently adaptation was applied following the same procedure as used for the Contr simulation. This PHAd simulation represented mild PH fully compensated by load adaptation. Then, using the PHAd simulation as point of departure, pulmonary resistance was elevated acutely to two levels associated with pressure drops of 6.5 and 9.5 kPa across the pulmonary circulation without applying further load adaptation (PH1 and PH2, respectively). To study the effect of timing of RV free wall activation on ventricular mechanics in PH, two acute interventions were applied to the PH2 simulation. The RV free wall was activated 50 ms earlier (PH2Early) and 50 ms later (PH2Late) than the septal and LV free wall.

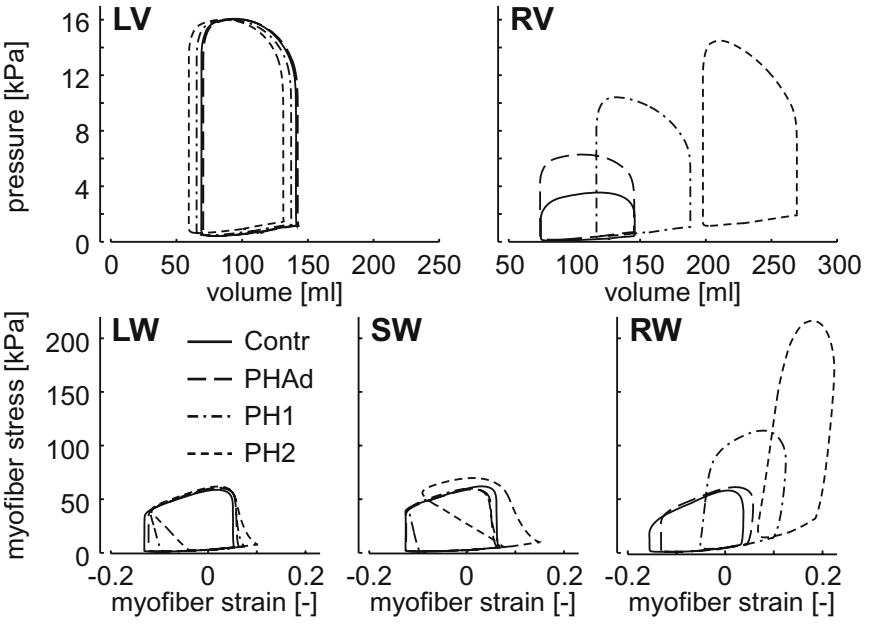

Fig. 2. Simulated ventricular pressure-volume loops and myofiber stress-strain loops. With control (Contr) and with mild PH after adaptation (PHAd) left and right ventricular pump functions were normal and myofiber load was distributed homogeneously over the walls. Acute increases of pulmonary resistance without further adaptation (PH1 and PH2) resulted in RV dilatation, increase of RV pump work, and increase of myofiber work density in the RV free wall. Abbreviations: LV, left ventricular; LW, left ventricular free wall; PH, pulmonary arterial hypertension; RV, right ventricular; RW, right ventricular free wall; and SW, septal wall.

For all simulations, global LV and RV pump functions were assessed by analysis of cavity pressure-volume relations. Contractile myofiber functions in the three ventricular walls were assessed by analysis of myofiber Cauchy stress-natural strain relations. Simulated circumferential strain patterns were compared with strain patterns as measured in chronic PH patients [2]. In our simulations, circumferential strain was derived from the Lagrangian strain tensor as the change of sarcomere length relative to reference sarcomere length at the moment of pulmonary valve opening.

3 Results

Figure 2 shows simulated pressure-volume loops of the left and right ventricular cavity and myofiber stress-strain loops of the three ventricular walls under control and PH conditions. For PH with load adaptation (PHAd), increase of pulmonary resistance resulted in increased RV pressure and 60% increase of RV free wall thickness, whereas LV free wall and septal thicknesses hardly changed. Ventricular volumes and myofiber stress-strain relations were similar for control (Contr) and PHAd. Adaptation resulted in a homogeneous distribution of myofiber load over the three ventricular walls. Increasing

pulmonary peripheral resistance without applying further adaptation resulted in large increase of RV cavity volume and relatively small decrease of LV cavity volume. Myofiber work density, i.e., myofiber work per unit tissue volume, was quantified as the area of the myofiber stress-strain loop. In the RV free wall, myofiber work density was increased primarily as a result of increased systolic myofiber stress. Myofiber work densities in the septum and LV free wall decreased primarily as a result of increasing myofiber strain during passive relaxation.

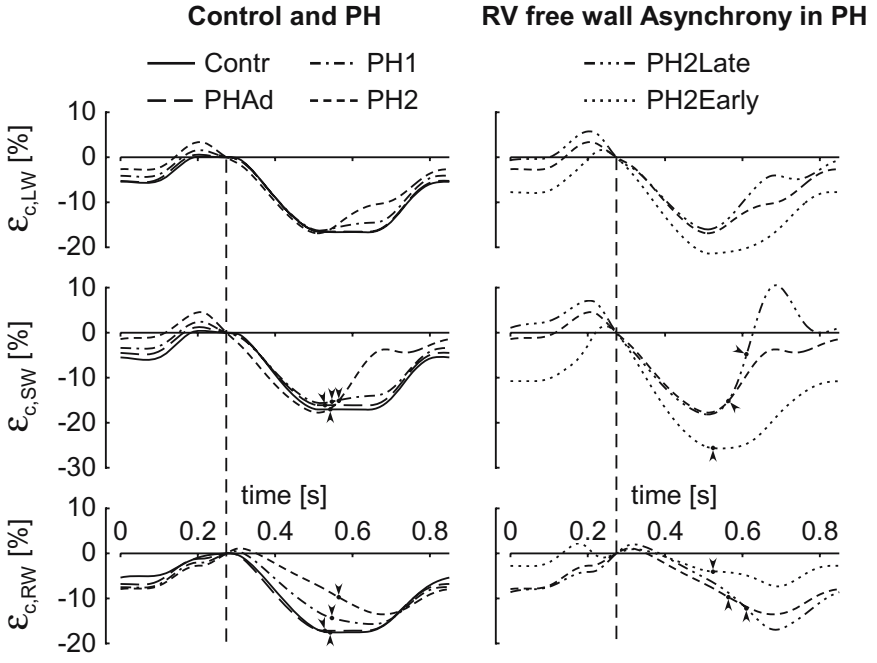

Fig. 3. Simulated time courses of circumferential strains in the LV free wall, septum, and RV free wall ($\varepsilon_{c,LW}$, $\varepsilon_{c,SW}$, and $\varepsilon_{c,RW}$, respectively). Strain patterns were similar in the ventricular walls in control (Contr) and pulmonary hypertension with adaptation (PHAd). Further increase of pulmonary resistance without further adaptation (PH1 and PH2) resulted in decrease of RW peak shortening and prolongation of RW shortening. RW shortening continued after pulmonary valve closure. Timing of RW mechanical activation significantly affected circumferential strains in the ventricular walls (PH2Late and PH2Early). Vertical dashed lines indicate time of zero strain (reference length). Arrows indicate time of pulmonary valve closure.

In Fig. 3, simulated time courses of circumferential strain in the ventricular walls are shown. In the Contr and PHAd simulations, circumferential strain patterns were similar in the three walls and appeared unaffected by increase of pulmonary resistance. As soon as pulmonary resistance was increased acutely without further adaptation (PH1 and PH2), onset of LV free wall and septal circumferential shortening occurred earlier than pulmonary valve opening while onset of RV free wall shortening was delayed. Peak RV free wall circumferential shortening decreased and duration of RV free wall circumferential shortening increased. RV free wall shortening continued

after pulmonary valve closure, while the LV free wall and septal wall already lengthened. RV isovolumic relaxation lasted double as long and was delayed by 22 ms in the PH2 simulation as compared to Contr. A 50 ms delay of mechanical activation of the RV free wall with respect to that of the septum and LV free wall (PH2Late) resulted in a 3.4% increase of RW peak shortening and in increased circumferential lengthening of the septum and LV free wall during LV isovolumic relaxation. When mechanical activation of the RV free wall occurred 50 ms earlier than that of the septum and LV free wall (PH2Early), RW peak shortening decreased 6.2% while peak shortening of the septum and LV free wall increased 8.0% and 4.5%, respectively.

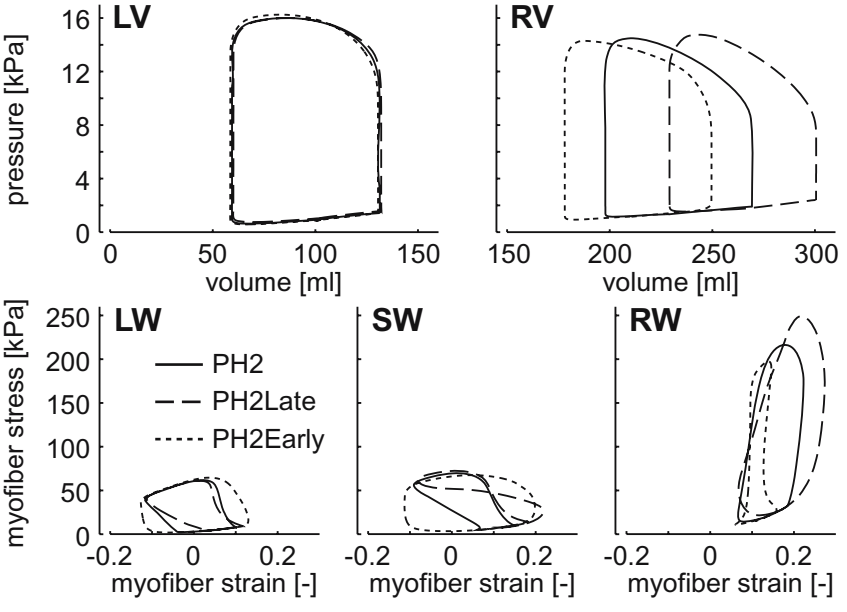

Fig. 4. Simulated ventricular pressure-volume loops and myofiber stress-strain loops. In PH, a 50 ms delay of RV free wall activation with respect to that of the LV free wall and septum (PH2Late) was associated with increase of RV volume, increase of RV free wall myofiber work density, and decrease of myofiber work densities in the septum and LV free wall. Early RV free wall activation (PH2Early) was associated with decrease of RV volume, decrease of RV free wall myofiber work density, and increase of myofiber work densities in the septum and LV free wall. Abbreviations: similar as in Fig. 2.

In Fig. 4, RV cavity volume and myofiber stress-strain relations in the walls appeared sensitive to changes in timing of RV free wall mechanical activation. As compared to the simulation of PH with simultaneous mechanical activation of the ventricular walls (PH2), late RV free wall activation (PH2Late) was associated with a 30 ml increase of RV end-diastolic volume and no change of LV volume. Peak RW myofiber stress was increased by 33 kPa and myofiber work was distributed less homogeneously over the walls, i.e., RW myofiber work density increased while LW and SW myofiber work densities decreased. Early RV free wall activation (PH2Early), however, was associated with a 20 ml decrease of RV end-diastolic volume and no change of LV volume. RW

myofiber work density decreased due to decrease of peak RW myofiber stress by 18 kPa and decrease of myofiber ejection strain. LW and SW myofiber work densities increased primarily as a result of increase of myofiber ejection strain. Finally, these changes resulted in a more homogenous distribution of mechanical myofiber load over the walls while total ventricular pump work remained unchanged.

4 Discussion and Conclusions

In this study, a mathematical model describing mechanics of ventricular interaction was used to simulate ventricular mechanics and hemodynamics in severe pulmonary hypertension. Mild pulmonary hypertension (PHAd simulation) was simulated by moderate increase of pulmonary peripheral resistance and applying structural load adaptation that normalized myofiber stress and strain in the walls to physiological standard levels. Similarly as observed in experimental animals with mild chronic RV pressure overload, the RV free wall hypertrophied, while resting LV and RV end-diastolic volumes and average sarcomere length in the RV free wall did not change [7, 8]. Increasing pulmonary resistance without further adaptation (PH1 and PH2 simulations) resulted in RV dilatation, small decrease of LV volume, and prolonged and delayed RV isovolumic relaxation. All these changes are in agreement with measurements obtained in patients with pulmonary arterial hypertension [9, 10]. Furthermore, the model was used to quantify the effect of early and late RV free wall activation on ventricular pump mechanics in severe pulmonary arterial hypertension. With early activation of the RV free wall, RV end-diastolic volume decreased. Furthermore, myofiber work density decreased in the RV free wall, whereas it increased in the LV free wall and septum resulting in a more homogeneous distribution of myofiber load in the ventricular walls. Late activation of the RV free wall resulted in opposite effects on ventricular mechanics and pump function.

In a study by Marcus *et al.* [2] among patients with severe PH, circumferential strain was measured noninvasively in the three ventricular walls using magnetic resonance tagging and strain analysis. A large delay of time to peak shortening in the RV free wall with respect to that in the LV free wall was observed. According to our simulations, this delay was primarily caused by prolongation of RV free wall shortening instead of delayed onset of mechanical activation. RV free wall shortening continued during left and right ventricular isovolumic relaxation, while the septum and LV free wall were stretched. All these changes measured in PH patients were also observed in our PH1 and PH2 simulations.

In advanced stages of PH, mechanical asynchrony of ventricular contraction finally leads to heart failure and patient death [1]. Manipulating timing of ventricular contraction by pacing has been suggested as a potential therapy to improve ventricular pump efficiency in patients with PH [2, 11]. In PH patients with concomitant delay of RV free wall activation (e.g., right bundle branch block), resynchronizing RV free wall activation by pacing may enhance RV pump efficiency (Fig. 4). RV volume and myofiber work in the RV free wall decreased significantly when simulating early activation of the RV free wall. The decrease of RW myofiber work was compensated by increase of myofiber work in the septum and LV free wall. When assuming the adaptive capacity of these latter two walls to be adequate in PH patients, our model simulations suggest that RV free wall pacing in PH improves RV pump function and increases homogeneity of myofiber load in the ventricular walls.

In the TriSeg model, each ventricular wall is lumped into a spherical wall segment containing a single contractile fiber describing average passive and active sarcomere properties of the entire wall [3-5]. Although this simplified setup allows inhomogeneity of material properties to some extent, i.e., between ventricular walls, it does not allow local inhomogeneities of material properties within a single wall. In our simulations with changed RV free wall activation times, the effect of activation spread within a single wall was not included. In all simulations, mechanical activation time of each wall represented average activation time.

In absence of adaptation, the effect of increased RV afterload on LV end-diastolic volume (Fig. 2) was qualitatively similar to measurements in PH patients. However, quantitatively our PH2 simulation appeared to underestimate the effect. In patients with severe pulmonary arterial hypertension, LV end-diastolic volume appeared significantly smaller (≥25%) than in healthy controls [2, 9]. In our PH2 simulation, only a 7% decrease of LV end-diastolic volume was observed with respect to the Contr simulation. Most probably this underestimation resulted from the assumption of constant cardiac output for all simulations though it is measured that cardiac output is significantly decreased in PH patients, whereas their LV end-systolic volume and heart rate are not significantly changed as compared to healthy controls [9]. This effect on cardiac output was not included in our simulations in order to study the isolated effect of increased pulmonary peripheral resistance on ventricular mechanics.

In conclusion, incorporation of the TriSeg module in the closed-loop CircAdapt model of the whole circulation resulted in a tool enabling realistic simulation of ventricular mechanics during the whole cardiac cycle under normal as well as pulmonary hypertensive conditions. Mechanical interaction of the three ventricular walls was related to global LV and RV pump mechanics using the principle of conservation of energy. Simulations of pulmonary hypertension showed similar changes of RV and LV pump functions and mechanical tissue load in the walls as measured in patients, i.e., prolonged RV free wall shortening associated with circumferential lengthening of the septum and LV free wall during LV isovolumic relaxation. Furthermore, simulations showed that early mechanical activation of the RV free wall may have beneficial effects on tissue load and pump efficiency in pulmonary arterial hypertension.

Acknowledgments. We gratefully acknowledge the financial support of Actelion Pharmaceuticals Nederland B.V. (Woerden, The Netherlands) and the Netherlands Heart Foundation (Grant 2007B203).

References

1. Lopez-Candales, A., Dohi, K., Rajagopalan, N., Suffoletto, M., Murali, S., Gorcsan, J., Edelman, K.: Right ventricular dyssynchrony in patients with pulmonary hypertension is associated with disease severity and functional class. Cardiovasc Ultrasound 3, 23 (2005)
2. Marcus, J.T., Gan, C.T., Zwanenburg, J.J., Boonstra, A., Allaart, C.P., Gotte, M.J., Vonk-Noordegraaf, A.: Interventricular mechanical asynchrony in pulmonary arterial hypertension: left-to-right delay in peak shortening is related to right ventricular overload and left ventricular underfilling. J. Am. Coll. Cardiol. 51(7), 750–757 (2008)

3. Lumens, J., Delhaas, T., Kirn, B., Arts, T.: Modeling ventricular interaction: a multiscale approach from sarcomere mechanics to cardiovascular system hemodynamics. In: Pac. Symp. Biocomput., pp. 378–389 (2008)
4. Arts, T., Bovendeerd, P.H., Prinzen, F.W., Reneman, R.S.: Relation between left ventricular cavity pressure and volume and systolic fiber stress and strain in the wall. Biophys. J. 59(1), 93–102 (1991)
5. Arts, T., Delhaas, T., Bovendeerd, P., Verbeek, X., Prinzen, F.W.: Adaptation to mechanical load determines shape and properties of heart and circulation: the CircAdapt model. Am. J. Physiol. Heart Circ. Physiol. 288(4), H1943–H1954 (2005)
6. Arts, T., Prinzen, F.W., Snoeckx, L.H., Rijcken, J.M., Reneman, R.S.: Adaptation of cardiac structure by mechanical feedback in the environment of the cell: a model study. Biophys. J. 66(4), 953–961 (1994)
7. Minami, S., Onodera, T., Okazaki, F., Miyazaki, H., Ohsawa, S., Mochizuki, S.: Myocyte morphological characteristics differ between the phases of pulmonary hypertension-induced ventricular hypertrophy and failure. Int. Heart J. 47(4), 629–637 (2006)
8. Olivetti, G., Ricci, R., Lagrasta, C., Maniga, E., Sonnenblick, E.H., Anversa, P.: Cellular basis of wall remodeling in long-term pressure overload-induced right ventricular hypertrophy in rats. Circ. Res. 63(3), 648–657 (1988)
9. Gan, C.T., Lankhaar, J.W., Marcus, J.T., Westerhof, N., Marques, K.M., Bronzwaer, J.G., Boonstra, A., Postmus, P.E., Vonk-Noordegraaf, A.: Impaired left ventricular filling due to right-to-left ventricular interaction in patients with pulmonary arterial hypertension. Am. J. Physiol. Heart Circ. Physiol. 290(4), H1528–H1533 (2006)
10. Stojnic, B.B., Brecker, S.J., Xiao, H.B., Helmy, S.M., Mbaissouroum, M., Gibson, D.G.: Left ventricular filling characteristics in pulmonary hypertension: a new mode of ventricular interaction. Br. Heart J. 68(1), 16–20 (1992)
11. Beyar, R.: Heart inefficiency in pulmonary hypertension: a double jeopardy. J. Am. Coll. Cardiol. 51(7), 758–759 (2008)

A Hybrid Tissue-Level Model of the Left Ventricle: Application to the Analysis of the Regional Cardiac Function in Heart Failure

Julien Fleureau[1,2,⋆], Mireille Garreau[1,2], Erwan Donal[1,2,3], Christophe Leclercq[1,2,3], and Alfredo Hernández[1,2]

[1] INSERM, U642, Rennes, F-35000, France
[2] Université de Rennes 1, LTSI, Rennes, F-35000, France
[3] CHU Rennes, Service de Cardiologie et Maladies Vasculaires, Rennes, F-35000, France
julien.fleureau@gmail.com,
{alfredo.hernandez,mireille.garreau}@univ-rennes1.fr,
{erwan.donal,christophe.leclercq}@chu-rennes.fr
http://www.ltsi.univ-rennes1.fr/

Abstract. This work contributes to the systemic interpretation of clinical data for the analysis of the regional cardiac function in the context of heart failure. A two-step patient-specific approach, combining a realistic geometry and a hybrid, tissue-level electromechanical model of the left ventricle is proposed. For the first step, a fast framework to extract a realistic geometry of the left ventricle from MSCT data is proposed. This geometry is then applied to a tissue-level model of the left ventricle, coupling a discrete electrical model, a mechanical model integrating a visco-elastic law, solved by a finite element method and a hydraulic model. A set of simulations carried out with the model are shown and preliminary results of the parameter identification approach, based on real patient data, are presented and discussed.

Keywords: Heart failure, cardiac MSCT segmentation, cardiac model.

1 Introduction

Cardiovascular diseases are a major health concern all over the world and, especially, heart failure (HF) has gained more importance in the recent years. Improving diagnosis and therapy is therefore critical. Advances have been made over years in the design of drugs, but some of them have been associated with side effects and negative outcomes. Technological solutions can rely on revascularization in case of ischemic cardiomyopathy and coronary disease, but also on Cardiac Resynchronization Therapy (CRT) in heart failure patients who remain

⋆ This work was financed by the European ALFA IPECA project and is part of the IMOP research project n° 04 T 187-188-189-190 CITH supported by the French Research Minister.

N. Ayache, H. Delingette, and M. Sermesant (Eds.): FIMH 2009, LNCS 5528, pp. 258–267, 2009.
© Springer-Verlag Berlin Heidelberg 2009

highly symptomatic, despite optimized pharmacological treatment. One interesting approach to improve diagnosis and therapy is based on the development and identification of patient-specific physiological cardiac models.

Many mathematical models of cardiac electromechanics have been proposed in the literature (see [3] for a review). They are usually built by coupling a set of components representing the anatomy and the electrophysiological, mechanical and hydraulic activities of the heart. These components can be represented at different levels of detail. On the one hand, the simplest models do not take into account the cardiac anatomy and are based on a dynamic elastance which is able to reproduce whole-organ pressure-volume loops [2]. These 0-D models require very low computational resources and are often coupled with rather detailed models of the circulation and autonomic regulation. However, they are, by definition, not useful to analyze the regional function of the heart. On the other hand, the most detailed models integrate: i) realistic anatomy, including regional fiber orientation, ii) cell-level models of the electrical activity, iii) a mechanical model with realistic passive tissue properties and electromechanical and mechano-electrical couplings, driving the active properties of the myocardial tissue and iv) a hydraulic model including a minimal circulatory loop and an algorithm for estimating the intra-ventricular pressure. Although this kind of models have shown to be useful in a number of situations, their computational complexity and the significant number of parameters make them difficult to be used in a patient-specific clinical application. Between these two extreme levels of detail, some of electromechanical models have been proposed and applied to the regional strain function analysis [6,8], providing encouraging results and showing the interest of such model-based approaches in this application.

The objective of this work is therefore to propose a simplified, tissue-level model to assist on the interpretation of regional myocardial function, measured by means of echocardiographic strain signals. This model should present a level of detail allowing fast simulations and the possibility to perform parameter identification. This work is part of the IMOP project (IMaging for Optimisation of biventricular Pacing) which purpose is to define a CRT optimization method based on the fusion of mechanical, electrical and anatomical data. The aim of this project is to better plan the placement of CRT leads and to optimize the parameters of the stimulator, using both advanced 3D dynamic cardiac imaging modalities (including MultiSlice Computed Tomography (MSCT) acquisitions, Magnetic Resonance Imaging (MRI) and Ultrasound imaging) and electrophysiological data (including in particular activation delay maps).

This paper is structured as follows. In a first section, a brief description of the proposed model, including its anatomical, electrical, mechanical and hydraulic components is given with a description of the associated parameter identification methodology. A second section presents simulation results and preliminary results for the parameter identification phase on real strain data.

2 Model Description

2.1 Anatomical Model

In the context of our study, the 3D MSCT images acquired at one instant of the MSCT sequence (General Electric Lightspeed VCT 64 system) is used for each analysed patient. A geometrical surfacic model is derived from these MSCT cardiac volumes, by applying a specific semi-interactive segmentation procedure, composed of the following four main steps:

- A local spatial frame of the left ventricle (directed through the long axis of the organ - used in short axis view) is obtained by an iteractive selection of directions and planes in the volume.
- The automatic extraction of the endocardium and mesh construction is then realized by 2D region growing processes regularly spaced along the ventricular axis (48 slices). A circonferential subsampling of the extracted contour thus leads to a 48 by 48 points regular mesh of the wall (48 points by each 2D contour).
- A corresponding regular mesh of the epicardium is then obtained by the detection of the local myocardial thickness in each point of the interior mesh (this detection process uses the statistical test of cumulated sum).
- Those two meshes are finally smoothed by a B-Spline interpolation to remove the potential irregularities of the shapes (due to papillar muscles or trabecular structures for example).

A smoothed geometry matching the patient data and compatible with a future integration in a mesoscopic numerical cardiac model is thus obtained (Figure 1) with very low computational loads (segmentation time lower than 10 seconds).

This muscle model is spatially and anatomically divided into 18 segments (Figure 1) with homogeneous mechanical (stiffness, viscosity) and electrical (electrophysiological timings) properties to fit the model resolution to the one used

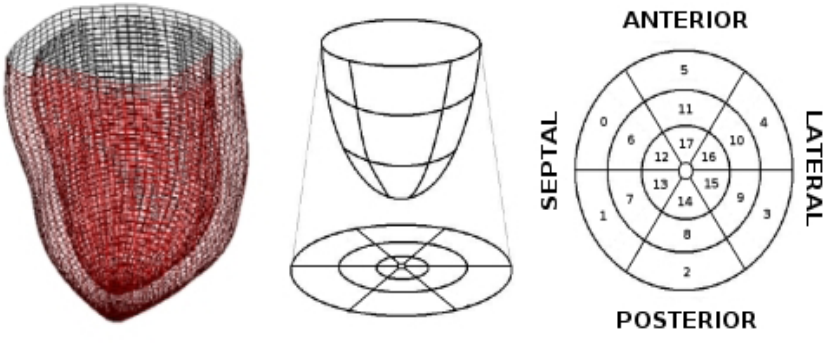

Fig. 1. On the left, anatomical model of the left ventricle obtained after the segmentation process. On the middle and on the right, division of the anatomical model into 18 segments.

by the clinician in cardiac function analysis. In this paper, only one slice has been defined along the transmural direction. We have thus made the approximation of using a constant mean fiber orientation for each segment, instead of a more realistic fiber orientation representation.

2.2 Electrophysiological Model

The propagation of the cardiac electrical activity is implemented with an automata network [4]. For each segment of the model, an automaton jointly models the local electrical potential and an analytical Electro-Mechanical Driving Function (EMDF) that represents, in a simplified manner, the complex processes involved in the electro-mechanical coupling at a tissue level (e.g. calcium dynamics of each cell composing the tissue, effect of the heterogeneous mechanical activation of each cell, etc.). The propagation properties of each automaton are mainly controlled by a parameter representing the duration of the depolarization phase (T_{UAP}). A truncated sine wave, with its peak value occurring at time T (elapsed since the electrical activation of each segment), was chosen for the EMDF, in a similar way as in [1]. Each automaton is initially at rest and is excited by one of its neighbors. An external stimulation regularly initiates the depolarization from the antero septo basal segment.

2.3 Mechanical Model

The passive mechanical component of the model is represented by a linear isotropic visco-elastic law as in classical Hill-Maxwell rheological models. The stiffness and viscosity of each segment are set to 1e6 Pa and 5e-2 s, as proposed in the literature.

The active tension is computed at each simulation time, for the 18 segments, by applying a spatially homogenized Nash relation [5], using as input the EMDF generated by the automata and including one scaling parameter (EMR) for each segment. The active tension is directed along the local fiber angle (homogeneous in each segment and set to mean values observed in the literature [7]). It appears in the model as a regional exterior stress applied to each segment. The only other exterior stress applied to the model is due to the intraventricular pressure, which is given by the hydraulic model (we recall that the right ventricle is not considered for the moment).

The previously defined mechanical system is solved at each instant thanks to a low resolution P2 finite element method where each mesh matches with a parallepipedical approximation of one of the 18 segments. Provided the regularity of the mesh obtained after the segmentation process and the linearity of the mechanical law that was employed, a model with just 18 elements has been thus designed in a first step. Such choices have been made independently of a complete mesh dependence analysis but were motivated by previous works (see [4]) where similar decisions led to encouraging results in a mesoscopic level of resolution.

The assembly step is then performed via a Galerkine method. Temporally, a Newmark scheme (well known for its numerical stability) is adopted and a Lagrangian approach is chosen to spatially fix the left ventricle (and more precisely the center of gravity of its upper segments).

2.4 Hydraulic Model

The blood inside the cavity is modeled by the variation of a homogeneous pressure inside the endocardium which reproduces a characteristic Pressure/Volume cycle during one beat. The endocardiac pressure is computed during the ejection and filling phases by means of a simple analytical model of the aortic and mitral valves. This model simulates the valves opening and the pressure balancing between the ventricle and the atrium and aorta, but they are not able to reproduce the end diastolic pressure decrease at this stage. During the isovolumic phases, a first order relation between the volume and pressure variations inside the ventricle (due to the use of a linear mechanical model) is applied in a prediction-correction scheme, to keep the blood volume constant. The phase switches controlling, for example, valve opening and closure, are realized thanks to the use of simplified models including stationary values for preload and afterload, because no circulation model is taken into account.

The proposed approach is thus a hybrid tissue-level model of the left ventricle characterized by three parameters (T_{UAP}, T and EMR) for each segment (i.e $18 \cdot 3 = 54$ parameters). Its low resolution is compatible with a light implementation, offering interesting performance as one cardiac cycle can be simulated in less than 10 seconds on a standard personal computer. A complete framework dedicated to the muscle segmentation but also to the simulation and the 3D+T visualization of the complete model has been developed and it is thus possible to observe the nodes displacements of the model during simulation and the associated endocardiac pressure and volume.

2.5 Parameter Identification

As a first approach for a patient-specific model definition, we are interested in evaluating the capability of the proposed parametric model to reproduce clinical observations from a heart failure patient. We dispose of 3D MSCT images and echocardiographic radial displacement signals (for the 18 segments of the model) from patients of the IMOP study, as well as other clinical indicators of their cardiac function. A parameter identification phase has thus been formalized as the determination of the model parameters minimizing the squared error between the simulated radial displacements and those observed from the patient. This is a complex global optimization problem because of the model non-linearities (due to the automata) but also because of the approximations made during the model design. The cost function not only contains multiple local minima, but several solutions, mathematically equivalent but physiologically different, may also exist. Aware of these difficulties, a distributed evolutionary algorithm, adapted to real-valued genomes, has been chosen for the identification of the model parameters

described previously. For each one of the 18 segments, parameters T_{UAP}, T and EMR were optimized, leading to a global identification process where each individual of the population includes $3 \times 18 = 54$ genes. A population of 200 individuals have been chosen and a maximum number of 300 generations have been set for the genetic algorithm. A priori knowledge has been introduced for the creation of the initial population, by defining the T_{UAP} parameters with a uniform random distribution centered at values corresponding to a characteristic desynchronized ventricle. Standard genetic operators of arithmetic crossover and gaussian mutation have been then applied with probabilities equal to 0.5 during the whole process.

3 Results

This section presents results from the sensitivity analysis of the model and from a first approach of patient-specific parameter identification, which compares the model with real clinical echocardiographic data.

Once the numerical stability of the model has been checked, verification and sensitivity analysis have been performed. Results from two of the sensitivity analysis tests performed (sensitivity to the influence of the model geometry and sensitivity to the parameter values of the mechanical law), evaluated in terms of the obtained pressure/volume loops, are presented here. Figure 2-a highlights the slight influence of shifting from a realistic geometry to an ellipsoidal geometrical model. Figure 2-b shows the sensitivity of the model to the a lower Young modulus that implies, logically, a larger resulting stroke volume.

Figure 3 presents Pressure/Volume loops obtained by applying: i) a significant electrical desynchronization between the septal and lateral walls, obtained by increasing the electrical propagation delay for specific segments (Figure 3-a) and ii) a complete mechanical inactivation of one region, obtained by modifying the electromechanical coupling parameter EMR for the corresponding model segment (Figure 3-b). A significant decrease of the intraventricular stroke volume is obtained as expected.

After this verification of the global consistency of the model, a parameter identification step has been applied to evaluate the capacity of the model to reproduce real radial displacements. The identification step previously described was consequently performed on echocardiographic radial displacement signals from one patient of the IMOP study. Results presented in this paper have been obtained after 300 generations of the identification algorithm (Figure 4), corresponding to around 8 hours of computation time on a six-processors cluster. The first results are presented in Figure 5.

These results highlight the positive aspects but also the limits of the current model (N.B.: radial displacements are only presented here for the upper segments of the ventricle but they are very similar for the two others levels). Despite the model simplifications, a relative consistency in the morphologies, amplitudes and timings of the real and simulated displacements can be observed, especially for segments 2, 3, 4 and 5. Some complex biphasic morphologies, corresponding to

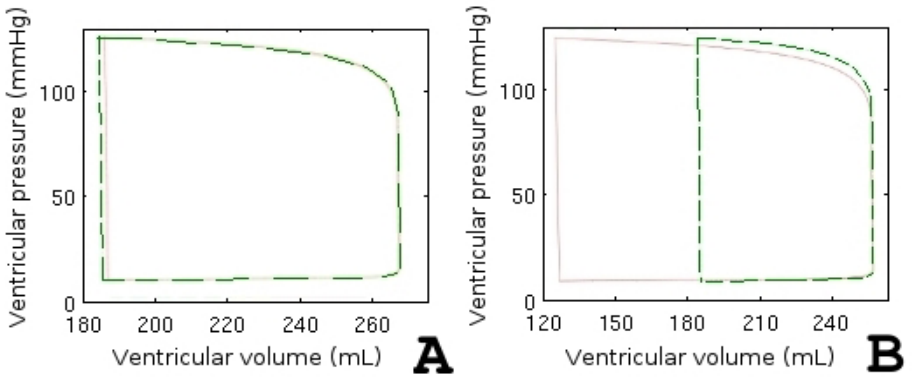

Fig. 2. Pressure/Volume loops simulated for different configurations of the model. a) Simulation of a ventricle configured with an "ellipsoidal" geometry (continuous line). b) Simulation of a ventricle with lower Young modulus $\sim$ 5e5 Pa (continuous line). In both figures, dotted lines represent the results obtained from a reference, "physiological" case.

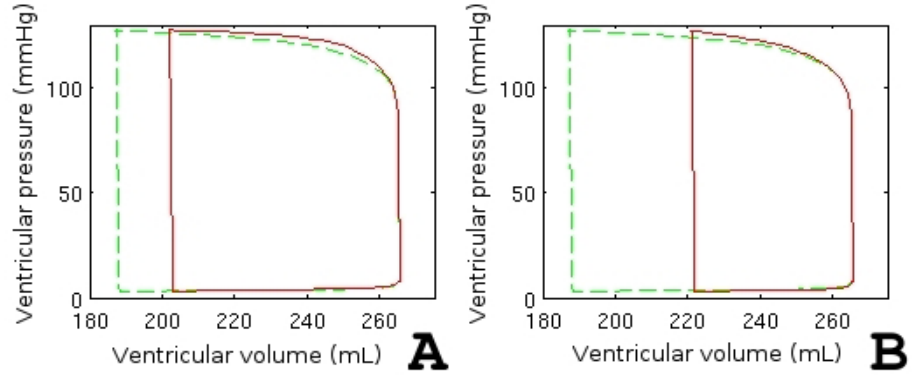

Fig. 3. Pressure/Volume loops simulating pathological conditions. a) Simulation of a strongly desynchronized ventricle (with an electrical delay of 180 ms between the septal and lateral walls). b) Simulation of a ventricle suffering from a local loss of contractility in its lateral wall (EMR= 0 for segments 3, 4, 9, 10, 15 and 16). In both figures, dotted lines represent the results obtained from a reference, "physiological" case.

a premature forward motion of the septal segments and then to a backward motion of those same segments under the pressure developed by the lateral wall contraction, are reproduced (segments 1, 2 and 3). The reduced stroke volume (15 mL) obtained by the simulation after parameter identification (shown on Figure 5) is consistent with the real volume obtained from MRI (10 mL) for this patient which suffers from severe heart failure and is a candidate for a cardiac resynchronization therapy. Moreover, the significant electrical desynchronization between the septal and lateral walls, suggested by the bull's eye representation of the electrical propagation parameters (around 180 ms) is similar to the QRS

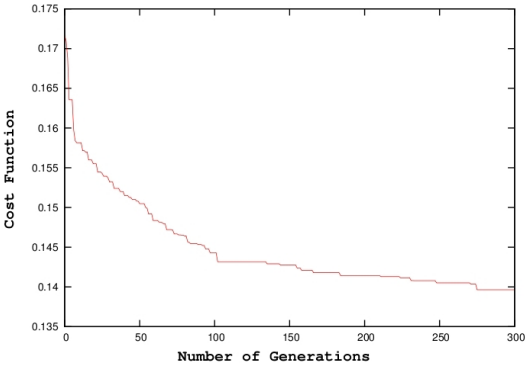

Fig. 4. Convergence of the evolutionary algorithm

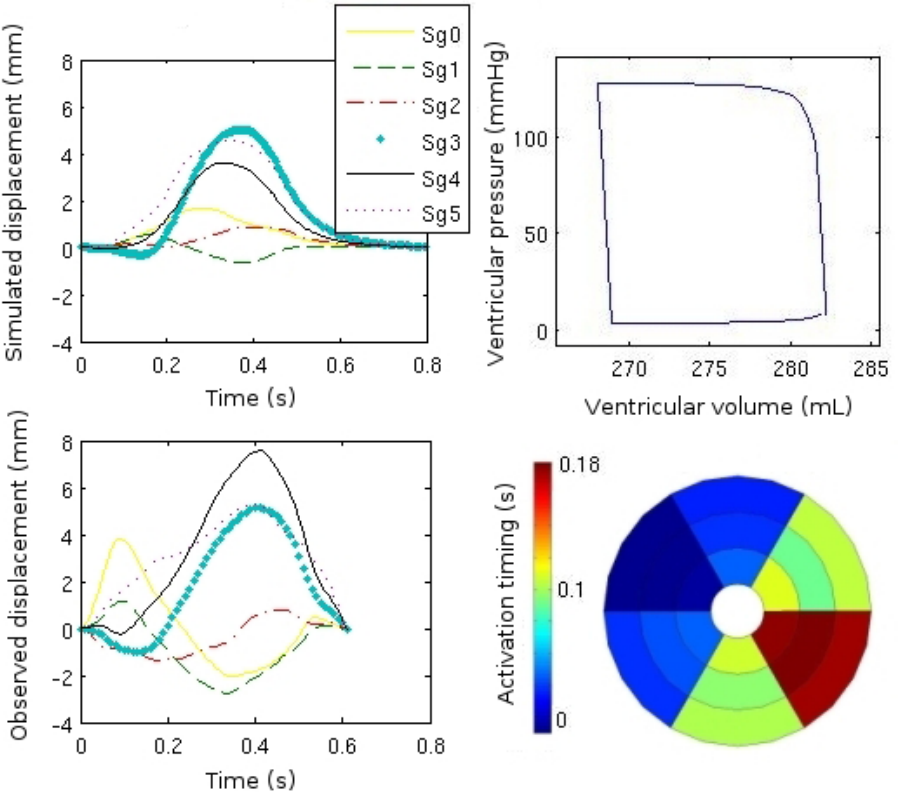

Fig. 5. On the left, radial displacement signals of upper segments of the ventricle simulated by the identified model (top) and measured in echography (bottom). On the right, Pressure/Volume cycle simulated by the identified model (top) and bull's eye diagram of the simulated electrical activation timing for each of the 18 segments (bottom).

duration observed from the patient's ECG (around 160 ms). Nevertheless, some other phenomena like the premature contraction of the septal wall (under the influence of the right ventricle and clearly observable in the displacement of segments 0 and 1), and, more generally, the behavior of the septal segments are not satisfactorily reproduced. The absence of the right ventricle but also the fixation of numerous degrees of freedom in the model (Young's modulus - stiffness - and viscosity, which are homogeneous for all segments) may explain these problems. The fact that no a priori knowledge has been included in the identification phase and also the variability of the echocardiographic data should also influence the quality of these first results on parameters identification. However, we consider these results as encouraging and they show the level of feasibility of a low-resolution approach in this context.

4 Conclusion and Perspectives

This paper introduced and described the first results obtained with a hybrid, tissue-level model of the left ventricle, dedicated to the analysis of observed echocardiographic regional displacement signals. The relevance of the multi-formalism approach and the interest of using an adapted level of resolution in the modeling step have been studied. A first identification step was also presented, giving encouraging results. The current limits of the proposed model were also pointed out. Our current efforts are directed to integrate the influence of the right ventricle and to add problem-specific knowledge into the evolutionary algorithm, in order to identify other parameters, such as regional Young's modulus. In parallel, increasing mesh resolution should be an interesting step to do to take into account inhomogeneities of both electrical propagation, fiber orientation but also mechanical properties. Finally, the identification stage is now planned to be launched on more patients to evaluate the "elasticity" and the relevancy of the mesoscopic proposed model in the targeted context of application.

References

1. Bovendeerd, P.H., Borsje, P., Arts, T., van De Vosse, F.N.: Dependence of intramyocardial pressure and coronary flow on ventricular loading and contractility: a model study. Annals of Biomedical Engineering 34(12), 1833–1845 (2006)
2. Guarini, M., Urzua, J., Cipriano, A., Gonzalez, W.: Estimation of cardiac function from computer analysis of the arterial pressure waveform. IEEE Transactions on Biomedical Engineering 45(12), 1420–1428 (1998)
3. Kerckhoffs, R.C.P., Healy, S.N., Usyk, T.P., McCulloch, A.D.: Computational methods for cardiac electromechanics. Proceedings of the IEEE 94(4), 769–783 (2006)
4. Le Rolle, V., Hernández, A.I., Richard, P., Donal, E., Carrault, G.: Model-based analysis of myocardial strain data acquired by tissue doppler imaging. Artificial Intelligence in Medicine 44(3), 201–219 (2008)
5. Nash, M.: Mechanics and Material Properties of the Heart using an Anatomically Accurate Mathematical Model. PhD thesis, University of Auckland (1998)

6. Sermesant, M., Moireau, P., Camara, O., Sainte-Marie, J., Andriantsimiavona, R., Cimrman, R., Hill, D.L., Chapelle, D., Razavi, R.: Cardiac function estimation from mri using a heart model and data assimilation: Advances and difficulties. Medical Image Analysis 10(4), 642–656 (2006)
7. Streeter, D.D., Hanna, W.T.: Engineering mechanics for successive states in canine left ventricular myocardium: I. cavity and wall geometry. Circ. Res. 33, 639–655 (1973)
8. Ubbink, S.W., Bovendeerd, P.H., Delhaas, T., Arts, T., van de Vosse, F.N.: Towards model-based analysis of cardiac mr tagging data: Relation between left ventricular shear strain and myofiber orientation. Medical Image Analysis 10(4), 632–641 (2006)

The Role of Blood Vessels in Rabbit Propagation Dynamics and Cardiac Arrhythmias

Matthew Gibb, Martin Bishop, Rebecca Burton, Peter Kohl, Vicente Grau, Gernot Plank, and Blanca Rodriguez

University of Oxford

Abstract. Recent experimental findings have suggested the important role played by blood vessels within the heart in stabilising arrhythmias. However, this link has yet to be explored computationally. In this paper, we develop a computational framework to model fibre orientation around structural inhomogeneities in myocardial tissue based on information obtained from high-resolution histological and MRI images. This framework allows the simulation of cardiac wavefront propagation for a generalised vessel orientation and position within the ventricular wall and transmural fibre architecture around it. We simulate propagation following different stimulation protocols around a transmural and a sub-epicardial vessel, using both bidomain and monodomain representations. We demonstrate the importance of accurately modelling the fibre structure around blood vessels relative to a simplistic transmurally varying fibre orientation model and suggest how this may impact pro-arrhythmic electrical dynamics.

Keywords: Cardiac electrophysiology, arrhythmias, cardiac vasculature, fibre orientation.

1 Introduction

Sudden cardiac death is the leading cause of mortality in Western society, with ventricular fibrillation being a central aspect to many of these fatalities. However, many of the fundamental mechanisms underlying these lethal arrhythmias are poorly understood.

Recently, advances in MR and histological imaging techniques [1] have provided high resolution data on histo-anatomical myocardial structure. Experimental studies suggest that micro-structure, and specifically vascular and myocardial fibre structure, may be important in arrhythmia mechanisms. Both optical [2] and electrical mapping studies [3] have not only illuminated a close colocalisation of phase singularities (the organising centres of ventricular fibrillation [4]) with sub-epicardial vessels, but have gone further to demonstrate that the meandering of an individual singularity is largely determined by these structural irregularities; sub-epicardial vessels have been observed to stabilise singularities and thus sustain fibrillation for up to 2 hours. However, it is worth noting that

N. Ayache, H. Delingette, and M. Sermesant (Eds.): FIMH 2009, LNCS 5528, pp. 268–276, 2009.
© Springer-Verlag Berlin Heidelberg 2009

these studies were limited. The 2-D mapping data obtained do not offer any insight into wavefront dynamics below the epicardium or the role played by intramural blood vessels in these dynamics. Computational modelling techniques can provide a unique window of inference into true 3-D propagation [5] and the most up-to-date models [1], [6] are now including a wealth of geometrical and structural information derived from high resolution MRI and histology imaging datasets. However, those models do not yet include accurate representation of the vascular tree and how it impacts myocardial fibre orientation.

In this study, we have developed a computational framework to investigate the role of microstructure, and in particular blood vessels and fibre orientation in their vicinity, in wavefront propagation across the ventricular wall. A detailed mathematical model of fibre orientation around the blood vessels has been developed based on information obtained from highly detailed histological and MRI datasets images [1]. A 3D MRI rabbit ventricular dataset was segmented to obtain the 3D vascular tree. The position and orientation of blood vessels within the ventricular wall was analysed to guide the placement of vessels during simulation. Using the model, computer simulations were carried out to analyse ventricular wavefront propagation for different orientations and positions of the blood vessels. Our results demonstrate that the presence of the blood vessels encourages the development of curvature of the activation wavefront around the blood vessels, which may have important implications in further analysis of arrhythmia mechanisms.

2 Methods

Fig. 1(a) shows a finite element rabbit ventricular mesh and extracted coronary vascular tree. The main blood vessels were obtained directly from a high-resolution MRI rabbit heart data-set, segmented using a level-sets approach, which was also used to generate the finite element ventricular mesh. Further details of the MR data acquisition and segmentation pipeline can be found in [6]. The complexity of the vascular tree would impair a systematic investigation of the importance of blood vessels in electrical wavefront propagation using a 3D ventricular model. Therefore, as a first step, we developed a cuboid segment of tissue, with dimensions 10mm x 10mm x 4mm, which represents a histological section of left-ventricular rabbit tissue. We examine the electrophysiological effect of 2 types of vasculature: a vertical (sub-)epicardial vessel (i.e. one that runs predominantly in the global apex-base direction close to the epicardium) and a transmural vessel (i.e. one which runs predominantly in the global epi-endocardium direction). These were the main two types of vasculature observed in the 3D MRI dataset.

2.1 Fibre Orientation Model

Fig. 1(b) shows a histological image of the fibre structure of a rabbit heart in the vicinity of a blood vessel. Fibres can clearly be observed negotiating

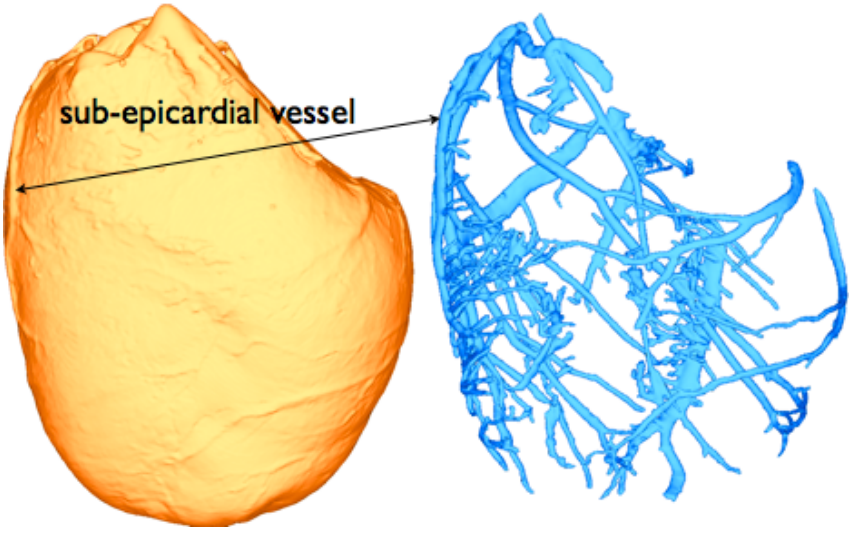

(a)

(b)

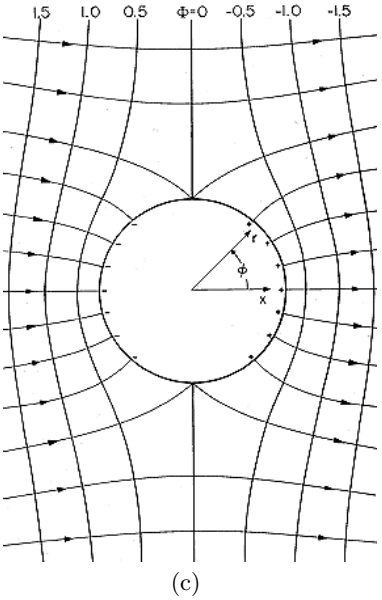

(c)

Fig. 1. (a) Finite element rabbit ventricular mesh (*left*) and extracted coronary vascular tree (*right*) obtained from a segmented high-resolution MR rabbit data-set [6]. **(b)** Histological image of rabbit mid-myocardial wall long-axis slice, provided by [1]. **(c)** The equipotentials (vertical lines) and field lines (horizontal with arrow heads) of a conducting circle in an infinite uniform field derived from the analytical solution to Eq. 11.

around blood vessels, both large and small. A new mathematical model of fibre orientation varying both transmurally across the ventricular wall and around blood vessels was developed. Every point in the tissue model was assigned to a myocardial sheet (i.e. a curved surface containing contiguous muscle fibres), which can be mathematically represented as the isosurfaces of a scalar potential field (Φ). The potential outside a conducting cylinder in a uniform field provides a useful starting point for blood vessels, and takes the form

$$\Phi = -aE_0 \left(\frac{r}{a} - \frac{a}{r} \right) \cos\theta \ , \tag{1}$$

where a is the cylinder radius, E_0 is the field strength far away from the cylinder and r and θ are 2-D polar coordinates. A plot of the analytical solution to Eq. 1 is depicted in Fig. 1(c). Every point on the circle in Fig. 1(c) is at an equal potential; equipotentials close to the circle run parallel to it and any fieldline starting or terminating on the circle must do so perpendicularly.

The following dependency of overall fibre direction on myocardial tissue depth has been implemented previously computationally [7]. Let e be a thickness parameter $e = \Phi_{\text{endo}}/(\Phi_{\text{endo}} + \Phi_{\text{epi}})$, where Φ_{endo} and Φ_{epi} are the potentials held across the endo- and epicardium, respectively, then $\alpha = \frac{\pi}{3}(1 - 2e)^3$, where α is the fibre angle from the horizontal. Thus, fibre direction is calculated as the vector lying tangential to its sheet at an angle α from the horizontal. When the vessel intersects the sheet, a different approach must be taken. The isolines of Fig. 1(c) are projected onto each sheet, oriented such that the central vertical line in (c) forms an angle α with the horizontal. The methods described above for assigning fibre orientation around blood vessel structures were generalised to an arbitrary vessel position, dimension and direction.

Fig. 2(a) shows how the modelled myocardial sheets deform around an epicardial vessel. Sheets close to the red cylindrical vessel boundary are seen to deform to accommodate it, similarly to the isopotentials in Fig. 1(c). Fig. 2(b) also shows the downwards fibre angle close to the epicardium, due to the transmurally varying fibre direction described above [7]. When the vessel intersects the sheets perpendicularly, (as shown in Fig. 2(b)) it is assumed that the sheets and their containing fibres are not perturbed in the transmural direction (i.e. the sheets are flat planes of constant myocardial depth). Again, note the upward trend in fibre angle within the endocardial sheet, due to the same variation as above. It is clear from the enlarged right-hand picture that fibres negotiate around the vessel where it intersects the sheet as shown in Fig. 2. For comparison, an additional 'simplistic' representation of fibre orientation was also implemented in which only the transmural rotation of fibres was modelled [7], but no account was made for a realistic modelling of fibre architecture around the blood vessels.

2.2 Simulation of Electrical Activation

The geometrical model described above was used to generate a tetrahedral finite element mesh using the meshing software Tarantula (`www.meshing.at`). The

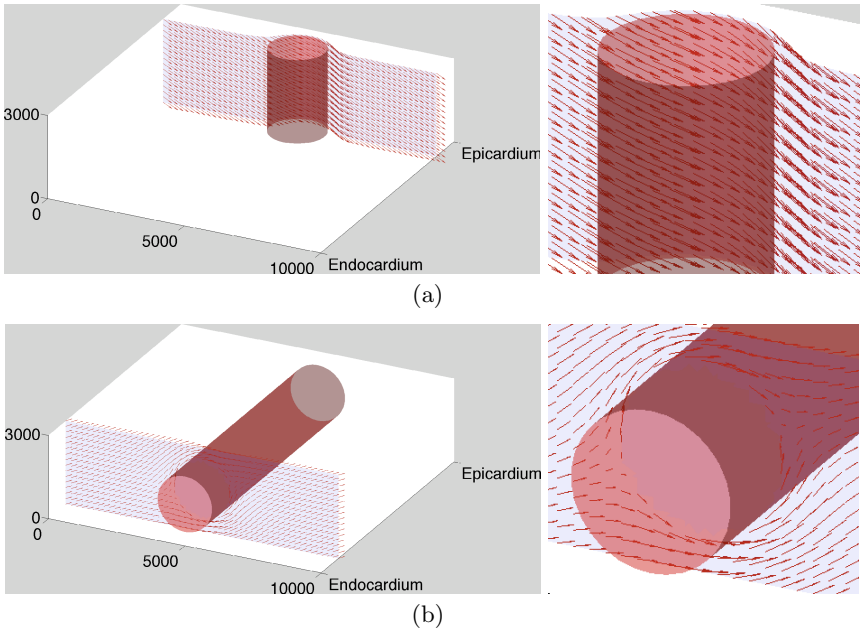

Fig. 2. Two plots of an example myocardial sheet (in translucent gray) around an epicardial **(a)** and a transmural **(b)** vessel, respectively. The red arrows, plotted at regular intervals on the surface of each sheet, represent local fibre direction. All arrows lie tangential to the sheet containing them.

centre of each tetrahedron was assigned a fibre direction, calculated as discussed above. Finally, the Cardiac Arrhythmias Research Package (CARP) [6] was used to simulate propagation of electrical activation throughout the volume of the myocardial mesh. Membrane dynamics were modelled using a detailed rabbit ionic model [8].

Electrical propagation was initiated in the slab model with both an epicardial vessel and a transmural vessel following two stimulation protocols: (1) 'transmural': stimulation of the endocardial face, to elicit propagation in the endo-/epicardial (transmural) direction; (2) 'axial': stimulation of a cut transmural face of the slab, to elicit propagation in the direction roughly parallel to the epi-/endocardium (axial direction). For all model set-ups and stimulation protocols, both monodomain and bidomain simulations were performed.

3 Results

Fig. 3 shows the distribution of transmembrane potential at different times following stimulation within the tissue (left) and activation time maps (right) from the bidomain simulations for each of the protocols outlined in Section 2.2 above. In this case the accurate model of fibres propagating around the blood vessel was

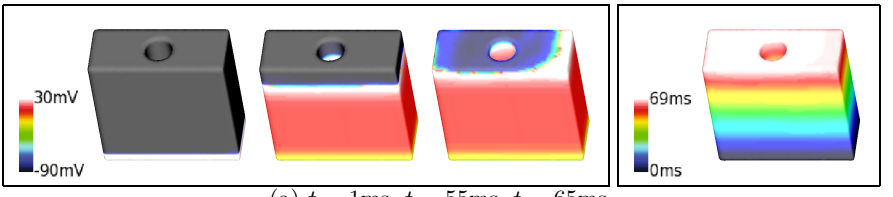

(a) $t = 1$ms, $t = 55$ms, $t = 65$ms.

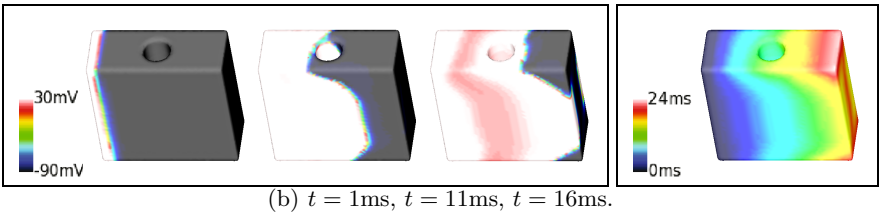

(b) $t = 1$ms, $t = 11$ms, $t = 16$ms.

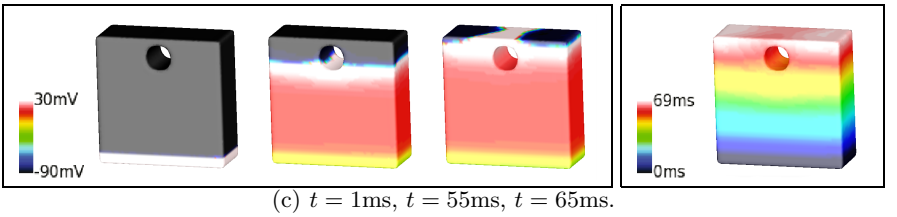

(c) $t = 1$ms, $t = 55$ms, $t = 65$ms.

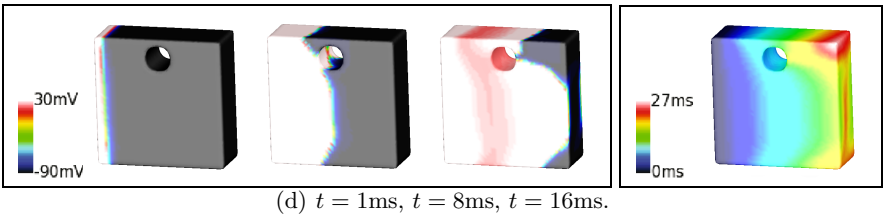

(d) $t = 1$ms, $t = 8$ms, $t = 16$ms.

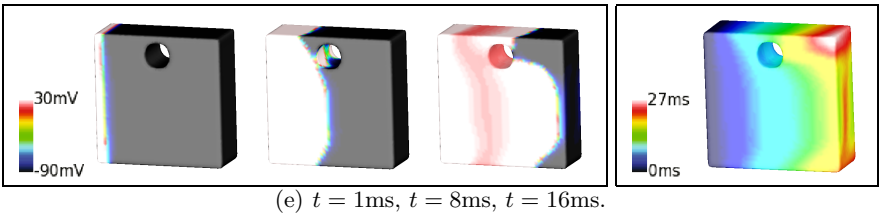

(e) $t = 1$ms, $t = 8$ms, $t = 16$ms.

Fig. 3. Distribution of transmembrane potential in the model at listed times following stimulus (*left*) and activation time maps (*right*) obtained from bidomain simulations. The top surface is epicardial in each diagram. Four regimes were simulated: **(a)** transmural propagation around a transmural vessel; **(b)** axial propagation around a transmural vessel; **(c)** transmural propagation around an epicardial vessel; **(d)** and axial propagation around an epicardial vessel. **(e)** Transmembrane potential distribution from the same protocol as in (d) obtained from monodomain simulation.

implemented (Fig. 2). Panel (e) shows results from the same simulation as in panel (d) but obtained from monodomain simulations. During transmural propagation (panels (a) and (c)), where the wave propagates largely perpendicularly

to the fibres, the wavefront deviates only slightly from planar propagation. However, the vessel has a noticeable retarding effect on propagation during axial propagation in panels (b) and (d), deforming the wavefront significantly. The wavefront morphology in the monodomain simulation of panel (e) is very similar

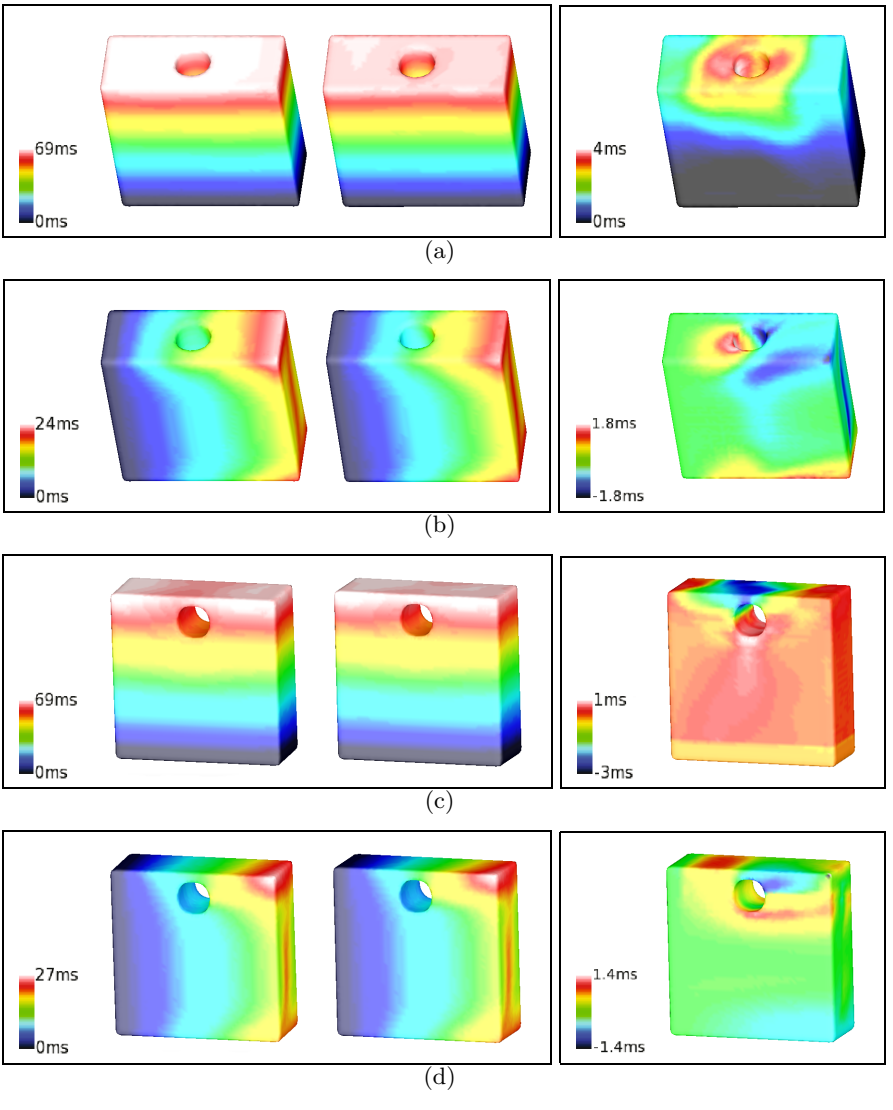

Fig. 4. Activation maps from the previous bidomain simulations detailed in Fig. 3 (column 1) compared to those generated with only a simplistic transmurally varying fibre model (no accounting for fibre displacement around a vessel, column 2), and the time difference maps between the two (column 3). Positive difference values correspond to a longer activation time in the first column.

to (d). A maximum activation time difference of 1.3ms between monodomain and bidomain simulations is observed. This is due to the conduction load interaction imposed on the wavefront by the extracellular 'bath' residing within the vessel in the bidomain model.

Fig. 4 (left) shows activation maps for the same bidomain simulations detailed above in Fig. 3 (column 1) as well as corresponding activation maps for the same protocols but generated with only a simplistic transmurally varying fibre model (column 2) i.e not including the accurate modelling of fibres flowing around the blood vessel. Activation difference maps between the two cases are shown in column 3. Positive difference values correspond to a longer activation time in the first column. Note that for (b), (c) and (d), where the propagation direction is perpendicular to the vessel, the simple fibre model wave reaches the vessel first but is last to leave; fibres lead straight to the vessel boundary instead of meandering around them, but then terminate on the surface, stopping the propagation of that section of wavefront to the other side of the vessel. This is represented in the difference maps by redder colours on the stimulated side of the vessel and more blue colours on the far side. Time difference ranges as a proportion of maximum activation times are: 5.5%, 15.1%, 5.4% and 10.4% for (a), (b), (c) and (d) respectively. Thus, the most significant effects of realistic fibre modelling are seen in propagation along muscle fibres, especially around transmural blood vessels.

4 Discussion and Conclusions

In this study we have shown the development of a generic computational framework to faithfully model fibre orientation around structural inhomogeneities in myocardial tissue, such as blood vessels. Applying the model with different stimulation protocols we were able to analyse the effects of activation wavefronts propagating around both (sub-)epicardial and transmural vessels.

The results of all of our simulations demonstrate the important role played by blood vessels in myocardial tissue in enhancing wavefront curvature in passing wavefronts, which could act as a mechanism to trigger arrhythmias. Furthermore, our results showed that the impact of our histologically-driven fibre model was greatest when activation waves propagated along myocardial fibres; both proportional time differences and wavefront distortion are much greater than in perpendicular propagation. The negotiation of fibres around blood vessels slightly smoothes the retarding effect of blood vessels by channelling waves around the vessel perimeter. The timings of an axial wave incident on a transmural vessel are affected by more than 15% (relative to a simplistic fibre model), and the largest of these changes are concentrated very close to the vessel boundary (in all cases, a vessel 'wake' is clearly visible in the difference maps of Fig. 4), underlining the importance of accurate fibre description in this region. Differences between mono- and bidomain simulations were also assessed; only minor differences (less than 1.3 ms) in activation times were observed and morphological disparities were all but imperceptible. One application of this study is to assess directly the

role of the complex fibre structure around blood vessels in the maintenance of arrhythmias.

References

1. Burton, R.A.B., Plank, G., Schneider, J.E., Grau, V., Ahammer, H., Keeling, S.L., Lee, J., Smith, N.P., Gavaghan, D.J., Trayanova, N., Kohl, P.: Three-dimensional models of individual cardiac histoanatomy: Tools and challenges. Ann. N.Y. Acad. Sci. 1080, 301–319 (2006)
2. Valderrábano, M., Chen, P., Lin, S.: Spatial distribution of phase singularities in ventricular fibrillation. Circulation 108, 354–359 (2003)
3. Qin, H., Huang, J., Rogers, J.M., Walcott, G.P., Rollins, D.L., Smith, W.M., Ideker, R.E.: Mechanisms for the maintenance of ventricular fibrillation: The nonuniform dispersion of refractoriness, restitution properties, or anatomic heterogeneities? J. Cardiovasc. Electrophysiol. 16, 888–897 (2005)
4. Gray, R.A., Pertsov, A.M., Jalife, J.: Spatial and temporal organization during cardiac fibrillation. Nature 392, 75–78 (1998)
5. Bernabeu, M., Bishop, M., Pitt-Francis, J., Gavaghan, D., Grau, V., Rodriguez: High performance computer simulations for the study of propagation dynamics in realistic heart models. In: Proceedings of the Computers in Cardiology Meeting (2008)
6. Plank, G., Burton, R., Hales, P., Bishop, M., Mansoori, T., Bernabeau, M., Garny, A., Prassl, A., Bollensdorf, C., Mason, F., Rodriguez, B., Grau, V., Schneider, J., Gavaghan, D., Kohl, P.: Generation of histo-anatomically representative models of the individual heart: tools and application. Phil. Trans. Roc. Soc. (accepted, 2009)
7. Potse, M., Dubé, B., Richer, J., Vinet, A., Gulrajani, R.M.: A comparison of monodomain and bidomain reaction-diffusion models for action potential propagation in the human heart. IEEE Trans. Biomed. Eng. 53(12), 2425–2435 (2006)
8. Mahajan, A., Shiferaw, Y., Sato, D., Baher, A., Olcese, R., Xie, L., Yang, M., Chen, P., Restrepo, J., Karma, A., Garfinkel, A., Qu, Z., Weiss, J.: A rabbit ventricular action potential model replicating cardiac dynamics at rapid heart rates. Biophys. J. 94, 392–410 (2008)

Estimation of Atrial Multiple Reentrant Circuits from Surface ECG Signals Based on a Vectorcardiographic Approach

Cédric Duchêne[1], Mathieu Lemay[1], Jean-Marc Vesin[1], and Adriaan van Oosterom[2]

[1] Institute of Electrical Engineering, Ecole Polytechnique Fédérale de Lausanne, Lausanne, Switzerland
[2] Department CardioMet, Centre Hospitalier Universitaire Vaudois, Lausanne, Switzerland

Abstract. This paper presents a simulation study on the identifiability of multiple reentrant circuits on the basis of the vectorcardiogram. The methods involved include an advanced tracking of the basic frequencies of the dominant rotors and a supporting identification based on the observed loops of their vectorcardiogram. The vector cardiogram was derived from body surface potentials spatially sampled by different lead systems. The results indicate that up to three independent circuits can be identified reliably.

1 Introduction

The onset and maintenance of supraventricular arrhythmias require an initiating event and an anatomic substrate. In atrial flutter (AFL), a single, macro reentrant circuit triggers the electrical atrial activity (AA). In contrast, during atrial fibrillation (AF) the situation is more complex and available data support a "focal" mechanism [1] involving automaticity, or multiple reentrant wavelets [2]. The wavelets may be initiated by a single wavelet named mother-rotor [3] or by any other activation wave simultaneously present in the tissue [4].

If no appropriate substrate is present, supraventricular arrhythmia, once initiated, will not be maintained and terminates spontaneously [5]. The presence of sources such as a focal activity, macro re-entries, and/or mother-rotors represent "stable" triggers of sustained supraventricular arrhythmias. The management of sustained supraventricular arrhythmias requires the elimination or isolation of their sources by curative ablation procedures [5]. The identification and localization of such "stable" triggers present challenges in current ablation procedures. This paper relates to macro re-entries that are assumed to exhibit some stability regarding location and frequency of revolution. For the sake of convenience these are referred to as rotors.

The surface 12-lead electrocardiogram (ECG) is currently the standard non-invasive source of information used in the diagnosis of supraventricular arrhythmia. So far, the complexity of the electrical AA has mainly been assessed through frequency or time-frequency analysis of the ECG signals [6,7]. To obtain a more

N. Ayache, H. Delingette, and M. Sermesant (Eds.): FIMH 2009, LNCS 5528, pp. 277–284, 2009.
© Springer-Verlag Berlin Heidelberg 2009

precise understanding of arrhythmias, it would be desirable to extract information about the underlying spatiotemporal dynamics.

Of late [8], the spatial complexity of the different AA dynamics was expressed by means of the atrial vectorcardiogram (VCG). A biophysical model of the dynamics of AA was used to generate electrophysiologically realistic source descriptions during sinus rhythm (SR), AFL, and episodes of AF arising in different substrates. The atrial VCGs resulting from these sources were computed. This study has allowed us to evaluate the potential of the atrial VCG for characterizing AA dynamics.

The VCG estimates the first-order spatial moment of the cardiac source distribution, represented by a single current dipole. As such, it can be expected to be non-specific in the presence of multiple, dominant rotors, each having a distinct location and basic frequency. The analysis of our simulated data as well as clinical recordings [9,10] strongly suggested that multiple dominant sources could be identifiable on the basis of body surface potentials (BSPs).

In the present simulation study, we explored the feasibility of identifying multiple rotors based on observed body surface potentials. Rather than using a single dipole, as in the VCG, the source description involved entails individual dipoles at each of the set of locations that have been identified in our simulations as well as clinical studies as being the most likely sites of such reentrant activity (Fig.1).

The individual rotor frequencies $f = f_{\mathrm{rev}}$ (number of revolutions per second) were identified by a mono-lead frequency tracking algorithm [11]. These were used subsequently to identify the corresponding contribution in the BSP data as represented by an individual vector for each rotor considered.

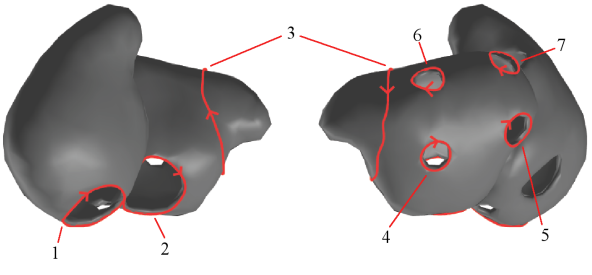

Fig. 1. Trajectories of seven reentrant circuits drawn on the geometry of an atrial model (left: anterior view, right: posterior view), revolving around: tricuspid valve (1), mitral valve (2) and left appendage (3). Those marked 4, 5, 6, and 7 refer to lower left, lower right, upper right and upper left pulmonar veins, respectively.

2 Methods and Materials

2.1 Simulating Body Surface Potentials

For each of the rotors revolving along the contours of the trajectories indicated in Fig. 1, body surface potentials were generated as follows. A single dipole $\boldsymbol{d}$

was used to represent the entire electrical activity at the wave front of the rotor. Its position revolved along the trajectory $\boldsymbol{r}(t)$ at a uniform velocity, orientated tangentially to the trace, while retaining a uniform strength. For any rotor k of a total of K considered, $\boldsymbol{d}_k(t) = \boldsymbol{d}(\boldsymbol{r}_k(t))$.

The body surface potential field $\boldsymbol{\Phi}_k(\boldsymbol{r}', t)$ generated by this source at location $\boldsymbol{r}'$ on the thorax at time t were computed, while assuming σ, the conductivity of the medium, to be uniform. The effect of the zero current flow at the boundary of the thorax was computed by means of the Boundary Element Method (BEM). Accordingly, by first computing the infinite medium potentials as [12]

$$\boldsymbol{\Phi}_{k,\infty}(\boldsymbol{r}', t) = \frac{1}{4\pi\sigma} \frac{\boldsymbol{d}(\boldsymbol{r}_k(t)) \cdot [\boldsymbol{r}' - \boldsymbol{r}_k(t)]}{R^3}, \tag{1}$$

where R is the length of the vector $\boldsymbol{r}' - \boldsymbol{r}_k(t)$, the bounded medium potentials were computed as

$$\boldsymbol{\Phi}_k(\boldsymbol{r}', t) = \boldsymbol{B}\ \boldsymbol{\Phi}_{k,\infty}(\boldsymbol{r}', t), \tag{2}$$

in which $\boldsymbol{B}$ denotes the BEM operator [13].

In their numerical application, the source locations were specified at equidistant time steps n along the trajectory. Atrial geometry, location and orientation were derived from magnetic resonance imaging of a healthy subject, as was the geometry of the thorax [14]. The latter was a closed, triangulated surface, specified at L=670 vertex locations that included the positions of the electrodes of the standard 12-lead ECG as a subset. In this situation the right-hand side of (2) denotes a multiplication of matrices $\boldsymbol{B}$ of size $(L \times L)$ and $\boldsymbol{\Phi}_{k,\infty}$ of size $(L \times N)$, with N the number of time samples considered.

If multiple rotors were assumed to be active simultaneously, the linearity of the medium permits the application of the superposition, hence, in this case the thorax potential was computed as the sum of the contributions of the individual rotors:

$$\boldsymbol{\Phi} = \sum_k \boldsymbol{\Phi}_k = \boldsymbol{B} \sum_k \boldsymbol{\Phi}_{k,\infty}. \tag{3}$$

2.2 The Inverse Approach

The solution to the inverse procedure implied in the objective of the present study would, ideally, identify the full specification at all time instants considered of all source elements on the basis of the observed potential field. However, the blurring effect of the spreading out of the electric currents prohibit this. It is because of this that source-volume conductor models have to be postulated, but even then additional measures have to be taken to safeguard the quality of the estimated sources [12]. Within the context of the forward simulation described in the previous sub-section, the inverse problem would demand the localization throughout time of all dipole trajectory $\boldsymbol{r}_k(t)$ for all K contours. This constitutes solving a non-linear parameter estimation problem because of the non-linearity in (1), which forms another barrier to finding a useful solution. In such situations additional simplifying constraints have to be incorporated. This motivates the following steps of the procedure.

Rotation round a fixed location. In the inverse procedure, the electric sources of the rotor were represented by a single dipole located at the center of gravity of the contour. The cyclic orientation in space of the dipole during a period of near-stationarity of the rotor then carves out a trajectory similar to that of the true trajectory of the rotor. Having taking this center as known *a priori*, the non-linearity of the inverse problem vanished and a linear problem remained to be solved.

Filtering data in the frequency domain. When multiple reentrant circuits are active simultaneously, the periodicity of the contributions of individual rotors offers the possibility of imposing additional constraints. The frequency spectrum of the contribution of a single rotor will be dominated by its basic frequency, in particular if observed at a distance. With K rotors active, each revolving at an individual f_k, spectral analysis from the source yields their values. The estimations of each instantaneous component frequency f_k were based on the signal of lead V_L, which was analyzed by a single frequency tracker (SFT) [15]. SFT is composed of a single pole bandpass filter with an adaptive transfer function and a feedback mechanism that adapts the central frequency of the filter based on its output signal. A problem with this scheme is the possible cross-talk between the various SFTs, due to the fact that the corresponding filters are not perfect bandpass ones. A solution to this problem is to use all-zero filters (AZFs) in a cross-coupled fashion to suppress interferences from other frequency components in each SFT [11]. The algorithm provides frequency estimates $\{\widehat{f}_k\}_{k=1}^{K}$ of the sources, which are in fact the center frequencies of the bandpass filters. Subsequently, K bandpass filters having center frequencies set to these estimates were designed. The estimate $\widehat{\boldsymbol{\Phi}}_k$ of the body surface potential map $\boldsymbol{\Phi}_k$ as defined in (3) was obtained by applying the k^{th} element of the bandpass filter bank to the complete body surface potential map $\boldsymbol{\Phi}$.

Estimating $\boldsymbol{d_k(t)}$. For any of the lead systems studied, estimates of the dipoles $\boldsymbol{d}_k(n)$ were derived at time instant n from the corresponding $\widehat{\boldsymbol{\Phi}}_k(n)$ in the following manner:

$$\widehat{\boldsymbol{d}}_k(n) = \boldsymbol{T}\,\widehat{\boldsymbol{\Phi}}_k(n), \tag{4}$$

where the matrix of reconstruction $\boldsymbol{T}$ is the $3 \times L$ transfer matrix determined as in (2) and (3) for a single stationary dipole. The origin of the vector $\widehat{\boldsymbol{d}}_k(n)$ was set at the center of gravity of the k^{th} contour (*a priori* information). The estimate of the complete k^{th} reentrant circuit was obtained by linking points indicated by the $\widehat{\boldsymbol{d}}_k(n)$ vector over the estimated complete cycle length $1/\widehat{f}_k$.

2.3 Evaluation Procedure

The performance of the approach was tested by an experimental protocol on three different source configurations.

In the first configuration a single reentrant circuit was taken to be present, with frequency of revolution f_1. The sense of rotation was chosen as clock-wise

when viewed from outside the atria. Next, two reentrant circuits, at frequencies f_2 and f_3, were added in the second and third configuration, respectively. The frequencies of the reentrant circuits were set at 5.88Hz (f_1), 4.5Hz (f_2) and 7.35Hz (f_3), values inspired by the frequencies observed on a clinical AF database, which were 5.88 ± 1.33Hz [16].

For the first configuration, all of the seven locations indicated in Fig. 1 were scanned. Subsequently, two (K=2) as well as three (K=3) simultaneously active sources were tested, involving a total of 42 and 210 permutations, respectively.

The performance of the proposed approach was evaluated while using the complete set of body surface potentials at the nodes of the triangulated thorax (670 electrodes), the standard 12-lead ECG system (9 electrodes), and a 12-lead system dedicated to the analysis of atrial signals [17]. The dedicated system includes electrodes sensing VR, VL, VF, V1 and V4 of the standard 12-lead system as well as four additional electrodes placed at: one intercostal space above V1 (V1S), to the right of V1S (V2RS), just below the left clavicle (VLC), and on the back at the same level as V1.

The results are specified by listing the means and standard deviations of the differences between 1) the original f_k values and their estimates $\widehat{f}_k$, 2) the $\boldsymbol{d}_k(n)$ and $\widehat{\boldsymbol{d}}_k(n)$ components after gravity center correction, and 3) the directions between normals to the surface carrying the reentrant circuits and their estimates.

3 Results

In Table 1 the results of the frequency estimation of the tracking algorithm with a tracking lead located in V_L are listed. The error of reconstructions obtained based on the entire body surface potential map (670 electrodes) as well as when using the potentials at the electrodes of the standard and the adapted 12-lead systems are summarized in Table 2. It lists the averages of the normalized mean square error (nMSE) values between $\boldsymbol{d}(n)$ and estimated $\widehat{\boldsymbol{d}}(n)$ for the x-, y-, z-components are represented for lone sources ($K = 1$) at all of the seven contours and all combinations of 2 and 3 sources ($K = 2$ and $K = 3$, respectively) out of the seven contours considered. The mean and standard deviation θ of the angles between the normals to the surface of the original circuits and their estimates circuits are shown in the last column.

Table 1. Performance of the frequency estimation (mean ± standard deviation) in Hz. The number of reentrant circuits to be estimated is denoted by K. The frequencies of the reentrant circuits were set at 5.88Hz (f_1), 4.5Hz (f_2) and 7.35Hz (f_3).

K	$\widehat{f}_1$	$\widehat{f}_2$	$\widehat{f}_3$
1	5.88 ± 0.00	—	—
2	5.88 ± 0.01	4.51 ± 0.02	—
3	5.83 ± 0.36	4.42 ± 0.27	7.35 ± 0.02

Table 2. Comparison between the reconstruction errors with respect to the x, y, z components (mean ± standard deviation) obtained by the entire set of body surface potentials (L=670), the standard 12-lead system and the adapted 12-lead system. The mean and standard deviation θ of the angles between the normals to the surface of the original circuits and their estimates circuits are indicated in degrees (°).

system	K	$d_x - \widehat{d}_x$	$d_y - \widehat{d}_y$	$d_z - \widehat{d}_z$	θ (°)
all leads	1	0.08 ± 0.05	0.06 ± 0.08	0.03 ± 0.01	2.06 ± 1.22
	2	0.08 ± 0.05	0.07 ± 0.06	0.04 ± 0.02	2.26 ± 1.22
	3	0.18 ± 0.33	0.16 ± 0.40	0.12 ± 0.41	6.47 ± 16.06
standard 12-lead	1	0.13 ± 0.08	0.53 ± 0.95	0.29 ± 0.21	21.17 ± 9.44
	2	0.15 ± 0.08	0.72 ± 0.07	0.28 ± 0.18	21.46 ± 9.09
	3	0.27 ± 0.52	0.73 ± 1.26	0.33 ± 0.22	24.78 ± 18.44
adapted 12-lead	1	0.30 ± 0.24	0.07 ± 0.10	0.15 ± 0.11	14.84 ± 6.90
	2	0.36 ± 0.26	0.06 ± 0.08	0.16 ± 0.09	14.90 ± 6.47
	3	0.41 ± 0.44	0.14 ± 0.31	0.19 ± 0.27	18.28 ± 16.60

In all of the cases considered, the sense of rotation of the estimate rotors were found to be correct.

4 Discussion

The results shown in section 3, show that the proposed approach was able to identify and characterize multiple simultaneously active reentrant circuits on the basis of potentials observed on the body surface. The accuracy of the average frequency estimates was to 0.11 Hz. If the frequencies of the different rotors are sufficiently separated ($\geq$ 1 Hz) the approach permits their correct identification.

Interestingly, the method correctly identified the sense of revolution of each rotor. This holds promise for the identification of the sense of revolution in atrial flutter in clinical cases.

The accuracy of the reentrant circuit reconstruction was characterized by high values when using the entire body surface potential; with an average nMSE value of 0.09 ± 0.16 for the three components and an average angular error $3.60 \pm 6.17°$. The lowest values were obtained when using the standard 12-lead system: an average nMSE value of 0.38 ± 0.40 for the three components and an average angular error of $22.47 \pm 12.32°$. With the same number of leads, the adapted 12-lead system yields an average nMSE value of 0.20 ± 0.21 for the three components and an average angular error of $16.01 \pm 9.99°$. The difference between the two 12-lead systems performances is mainly due to the reconstruction error of the y-component which is more accurately estimated in the adapted 12-lead system owing to the inclusion one lead located on the back.

When the reentrant circuits revolved in a plane, the accuracy of reconstruction proved high: for sources located around the pulmonary veins and sources

located on the tricuspid and mitral valves, the average nMSE for the three components was 0.04 ± 0.03. In contrast, when the reentrant circuits were more complex, the accuracy of reconstruction was lower: the average nMSE for the three components was 0.15 ± 0.11 for source 3, located at the left appendage.

The present study obviously needs to be classed as feasibility study, the results as a proof of principle. It remains to be seen if principal assumptions of the approach: the *a priori* knowledge of the number of reentrant circuits in the separation source step (presented in section 2.2) and the *a priori* knowledge of the gravity center of each source will stand up well in the application to clinical data. This is to be tested in the continuation of this project. This will further include the optimization of the frequency tracking procedure, and studying the option of simultaneously incorporating multiple leads, e.g. for the minimization of the impact of strong, confounding harmonics of the atrial signals.

Acknowledgements

This study was made possible by grants from the Theo- Rossi-Di-Montelera Foundation and the Swiss Governmental Commission of Innovation Technologies (CTI).

References

1. Haisaguerre, M., Jais, P., Shah, D.C., Takahashi, A., Hocini, M., Quiniou, G., Garrigue, S., Le Mouroux, A., Le Metayer, P., Clementy, J.: Spontaneous initiation of atrial fibrillation by ectopic beats originating in the pulmonary veins. N. Eng. J. Med. 339, 659–666 (1998)
2. Allessie, M.A., Konings, K., Kirchhof, C., Wijffels, M.: Electrophysiologic mechanisms of perpetuation of atrial fibrillation. Am. J. Cardiol. 77(3), 10A–23A (1996)
3. Jalife, J.: Rotors and spiral waves in atrial fibrillation. J. Cardiovasc. Electrophysiol. 14, 776–780 (2003)
4. Xie, F., Garfinkel, A., Weiss, J.N.: Electrical refractory period restitution and spiral wave reentry in simulated cardiac tissue. Am. J. Physiol. (Heart Circ. Physiol.) 283, H448–H460 (2003)
5. Wharton, J.: Ablation of atrial fibrillation: a procedure come of age? Curr. Control Trials Cardiovasc. Med. 2, 67–70 (2001)
6. Stridh, M., Sörnmo, L., Meurling, C.J., Olsson, S.B.: Sequential characterization of atrial tachyarrhtyhmias based on ECG time-frequency analysis. IEEE Trans. Biomed. Eng. 51(1), 100–114 (2004)
7. Bollmann, A., Husser, D., Mainardi, L., Lombardi, F., Langley, P., Murray, A., Rieta, J.J., Millet, J., Olsson, S.B., Stridth, M., Sörnmo, L.: Analysis of surface electrocardiograms in atrial fibrillation: techniques, research, and clinical applications. Europace 8(11), 911–926 (2006)
8. Lemay, M., Vesin, J.M., Forclaz, A., Kappenberger, L., van Oosterom, A.: Spatial dynamics of atrial activity assessed by the vectocardiogram: from sinus rhythm to atrial fibrillation. Europace 9(6), vi109–vi118 (2007)
9. Lemay, M., Jacquemet, V., Vesin, J.M., van Oosterom, A.: Mean firing rate of atrial fibrillation as estimated from the ECG: Evaluation using a biophysical model. In: Computers in Cardiology 2007, vol. 34, pp. 37–40 (2007)

10. Lemay, M., Dang, L., Vesin, J.M.: Quasi-periodic atrial activity components in the ECG used to predict the success of electrical cardioversion of atrial fibrillation. In: Computers in Cardiology 2008, pp. 125–128 (2008)
11. Uldry, L., Duchêne, C., Prudat, Y., Murray, M.M., Vesin, J.M.: Adaptive tracking of EEG components. In: Advanced Biosignal Processing. Springer, Heidelberg (in press, 2009)
12. Gulrajani, R.M.: Bioelectricity and Biomagnetism. John Wiley & Sons, Chichester (1998)
13. Oostendorp, T., van Oosterom, A.: Source parameter estimation in inhomogeneous volume conductors of arbitrary shape. IEEE Transactions on Biomedical Engineering 36(3), 382–391 (1989)
14. van Oosterom, A., Jacquemet, V.: Genesis of the P wave: atrial signals as generated by the equivalent double layer source model. Europace 7(suppl. 2), S21–S29 (2005)
15. Liao, H.E.: Two discrete oscillator based adaptive notch filters OSC ANFs for noisy sinusoids. IEEE Transactions on Acoustics, Speech, and Signal Processing 53(2), 528–538 (2005)
16. Lemay, M., Prudat, Y., Jacquemet, V., Vesin, J.M.: Phase-rectified signal averaging used to estimate the sominant frequencies in ecg signals during atrial fibrillation. IEEE Trans. Biomed. Eng. (2008) TBME.2008.2001296
17. Ihara, Z., van Oosterom, A., Jacquemet, V., Hoekema, R.: Adaptation of the standard 12-lead electrocardiogram system dedicated to the analysis of atrial fibrillation. J. Electrocardiol. 40(1), e1–e68 (2007)

Atrial Anatomy Influences Onset and Termination of Atrial Fibrillation: A Computer Model Study

Nico Kuijpers[1], Huub ten Eikelder[2], and Sander Verheule[1]

[1] Cardiovascular Research Institute Maastricht (CARIM), Maastricht University, Universiteitssingel 50, 6229 ER Maastricht, The Netherlands
[2] Department of Biomedical Engineering, Eindhoven University of Technology, Den Dolech 2, P.O. Box 513, 5600 MB Eindhoven, The Netherlands
nico.kuijpers@bf.unimaas.nl

Abstract. Vulnerability to atrial fibrillation (AF) is increased in acutely dilated atria and is related to stretch-activated channels (SACs). To investigate the role of atrial anatomy in AF, we apply a computer model of human atrial electromechanics that includes SACs and contraction of the sarcomeres. Trabecular bundle structures are modeled by varying atrial wall thickness in a triangular mesh representing the human atria. Vulnerability to AF is investigated by application of overall stretch, while stimulating near the pulmonary veins. Due to contraction of some areas, stretch increases in other areas, leading to a variation in effective refractory period (ERP). Onset and perpetuation of AF in our model is explained by an increased dispersion in ERP, conduction slowing, and local conduction block. Atrial contraction attributes to the termination of AF through mechanoelectric feedback. We conclude that onset and termination of AF episodes under stretch are related to atrial structure and mechanoelectric feedback.

Keywords: Atrial anatomy, atrial fibrillation, mechanoelectric feedback, stretch-activated channels.

1 Introduction

Experimental studies indicate an increased vulnerability to AF in acutely dilated atria [1,2,3,4]. In acutely dilated rabbit atria, an inhomogeneous distribution of conduction slowing and block was observed, which was related to the trabecular structure of the atria [5]. Acute stretch induces changes in electrophysiological behavior, which is explained by the stretch-activated channel (SAC) hypothesis [6]. In this simulation study, we investigate the hypothesis that, under stretch, the trabecular structure of the atria leads to inhomogeneity in conduction velocity and effective refractory period (ERP), which increases the vulnerability to AF. In addition, we investigate the effect of atrial contraction on the termination of an AF episode.

N. Ayache, H. Delingette, and M. Sermesant (Eds.): FIMH 2009, LNCS 5528, pp. 285–294, 2009.
© Springer-Verlag Berlin Heidelberg 2009

2 Methods

To investigate the effect of stretch and trabecular bundle structure on atrial electrophysiology, we apply the well-known bidomain equations [7]. Our model describes active membrane behavior as well as intracellular coupling and interstitial currents, and has been extended to describe a stretch-activated membrane current and cardiac mechanics.

2.1 Atrial Electrophysiology

To model atrial electrophysiololgy, we apply the Cellular Bidomain Model [8,9], which is a discrete version of the continuous bidomain equations [7]. In our model, the atrial tissue is subdivided in segments. Each of the segments represents a small portion of atrial tissue, including interstitial fluid. Ionic membrane currents and intracellular calcium handling is described by the Courtemanche-Ramirez-Nattel model of the human atrial action potential [10].

In this study, the human atria are represented by a triangular mesh created from MRI data [11]. To incorporate a trabecular bundle structure, thickness of the tissue is varied as is shown in Figure 1. The triangular mesh is refined by subdividing the triangles in smaller segments as described by Virag *et al.* [12]. The electrophysiological state of each segment is defined by the intracellular potential (V_{int}), the extracellular potential (V_{ext}), and the state of the cell membrane, which is expressed in gating variables and ion concentrations. The membrane potential is defined by $V_{\text{mem}} = V_{\text{int}} - V_{\text{ext}}$. Exchange of current between the intracellular and extracellular domains occurs as transmembrane current (I_{trans}),

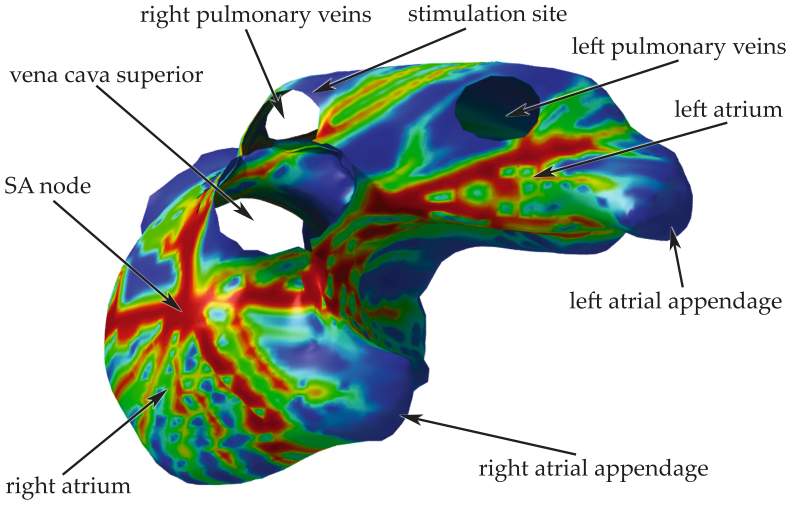

Fig. 1. Trabecular bundle structures are modeled by varying wall thickness. Red is thick tissue, green is tissue of medium thickness, and blue is thin tissue. The stimulation site is located near the right pulmonary veins.

which consists of ionic membrane currents (I_{ion}) and capacitative currents, and is defined by

$$I_{\text{trans}} = \chi \left(C_{\text{mem}} \frac{\mathrm{d}V_{\text{mem}}}{\mathrm{d}t} + I_{\text{ion}} \right), \tag{1}$$

where $\chi = 2000\ \text{cm}^{-1}$ is the ratio of membrane surface to tissue volume and $C_{\text{mem}} = 1.0\ \mu\text{F/cm}^2$ is membrane capacitance per unit membrane surface.

Intracellular and extracellular currents between adjacent segments are related to intracellular and extracellular conductivities (g_{int} and g_{ext}). In the present study, $g_{\text{int}} = g_{\text{ext}} = 6.25$ mS/cm, in all directions, i.e., the non-stretched atrial tissue is assumed to be isotropic. Anisotropy is incorporated by decreasing the conductances between adjacent segments with increasing stretch ratio as described in Kuijpers *et al.* [13]. The effect of adjusting electrical coupling in this way leads to a faster conduction along the bundles than across.

2.2 Atrial Mechanics

Mechanical behavior of a single segment is modeled by a series elastic (SE), a contractile (CE), and a parallel elastic (PE) element with parameters obtained from Solovyova *et al.* [14]. Contractile tension depends on intracellular Ca^{2+} concentration, sarcomere length, and the velocity of sarcomere shortening. Active force generated by the sarcomeres is described by *model 4* of Rice *et al.* [15] and is related to intracellular Ca^{2+} concentration and sarcomere length as previously described [13,16].

Stretch ratio (λ) of a segment is defined by $\lambda = l_s/l_{s0}$, with l_s the actual sarcomere length and $l_{s0} = 1.78\ \mu$m the reference sarcomere length. Overall stretch ratio of the atria is defined as the average of the stretch ratios of all segments. To simulate atrial dilatation, it is assumed that the same amount of force is applied to each segment. During the simulation, the amount of force applied to the atria is adjusted, such that the overall stretch ratio remains constant (isometric simulation). Since the model allows for the redistribution of strain throughout the geometry, contraction of early-activated regions may induce more strain in later-activated regions and influence membrane behavior and conduction. Since thicker tissue is harder to deform, variation in thickness will lead to differences in local strain and increases heterogeneity in electrical coupling.

2.3 Stretch-Activated Current

To model the response of the ionic membrane currents to changes in stretch, we extended the Courtemanche-Ramirez-Nattel model [10] with a stretch-activated current (I_{sac}). The current size of I_{sac} depends on V_{mem} and stretch ratio λ by

$$I_{\text{sac}} = \frac{G_{\text{sac}}(V_{\text{mem}} - E_{\text{sac}})}{1 + K_{\text{sac}} \exp(-\alpha_{\text{sac}}(\lambda - 1))}, \tag{2}$$

where $G_{\text{sac}} = 0.5$ nS/pF is the maximum membrane conductance, $E_{\text{sac}} = 0$ mV is the reversal potential, $K_{\text{sac}} = 100$ is a parameter to define the amount of

current when $\lambda = 1.0$, and $\alpha_{\text{sac}} = 3$ is a parameter to describe the sensitivity to stretch [17]. Intracellular Na^+, K^+, and Ca^{2+} concentrations are adjusted as described in Ref. [13].

2.4 Simulation Set-Up

Influence of stretch on impulse propagation was simulated in a single fiber with a length of 1 cm that was composed of segments with a length of 0.01 cm. The effect of the atrial bundle structure on the vulnerability to AF was evaluated by repetitively stimulating (interval 0.6 s) near the pulmonary veins. This site of stimulation was chosen, because focal activity triggering atrial arrhythmia often originates in the pulmonary veins [18,19]. Overall stretch was kept constant during a simulation, but was varied in between simulations ranging from 0 to 10%.

2.5 Numerical Integration Scheme

The Cellular Bidomain Model can be written as a coupled system of differential equations and linear equations [9]. To compute V_{mem}, the differential equations are solved using a forward Euler scheme. The system of linear equation is solved each time step using an iterative method as described in Kuijpers *et al.* [9].

When simulating electromechanics in the mesh of the human atria, two levels of coarseness were distinguished. Mechanics computation was performed on the coarsest level (3800 segments), while electrophysiology was simulated on the finer level (33754 segments). The average distance between the centers of adjacent segments on the coarsest level was 0.27 cm and on the finest level 0.09 cm. Under the assumption that the atria are isotropic with $g_{\text{int}} = g_{\text{ext}} = 6.25$ mS/cm, the length constant is in between 0.19 and 0.24 cm. To obtain accurate simulation results, the distance between the centers of adjacent segments should be at most 0.03 cm, which is still 3 times smaller than the average distance on the finest level. To obtain accurate results without further refinement of the mesh, computation of the transmembrane current I^n_{trans} for segment n was done by spatially "smoothing" the ionic membrane current I_{ion}. In our numerical integration scheme, Equation (1) is replaced by

$$I_{\text{trans}} = \chi \left(C_{\text{mem}} \frac{\mathrm{d}V_{\text{mem}}}{\mathrm{d}t} + (1-\alpha) I^n_{\text{ion}} + \frac{\alpha}{M_n} \sum_{m=1}^{M_n} I^m_{\text{ion}} \right), \tag{3}$$

where $0 \leq \alpha \leq 1$, I^n_{ion} represents the membrane current of segment n, and $\frac{1}{M_n} \sum_{m=1}^{M_n} I^m_{\text{ion}}$ the *average* value of I_{ion} of the M_n surrounding segments. This method can be interpreted as a way to "smooth" I_{ion} such that the spatial distribution of I_{ion} corresponds better to the coarser mesh. To evaluate accuracy, simulations of normal atrial depolarization were performed and compared with results obtained using a finer mesh with distance 0.03 cm (302320 segments). Conduction velocity θ on the finest mesh was 0.90 m/s, while θ was 0.57, 0.76, 0.89, and 1.06 for $\alpha = 0.0$, 0.2, 0.3, and 0.4, respectively, on the coarser mesh. In this study, we used $\alpha = 0.3$.

Ionic currents were computed as described in Ref. [10] with a time step of 0.02 ms. Computation time was reduced by locally increasing the simulation time step for the ionic currents to 0.1 ms during repolarization and rest. Both the Ca^{2+}-force relation and cardiomechanics were computed using a forward Euler method with a time step of 0.1 ms.

When computing atrial mechanics, overall stretch ratio was set as boundary condition. The mechanical state of each segment was computed from the state obtained during the previous time step and the boundary condition as described in Kuijpers *et al.* [13]. At the start of the simulation, no force was applied and each segment had stretch ratio 1.0. During the first 200 ms, overall stretch was increased until the desired value was reached. Electrical stimulation began after 200 ms.

3 Results

3.1 Effect of Stretch on Impulse Propagation

In Figure 2, the influence of stretch on the propagating action potential along a fiber is illustrated. With increasing fiber stretch, the action potential duration (APD) increased, while I_{Na} decreased. The reduced I_{Na} resulted in a lower maximum upstroke velocity and is explained by inactivation of Na^+ channels as a consequence of the increased V_{mem} during rest. Conduction velocity decreased from 0.4 m/s without stretch to 0.2 m/s with 20% stretch ($g_{\mathrm{int}} = 1.74$ mS/cm and $g_{\mathrm{ext}} = 6.25$ mS/cm).

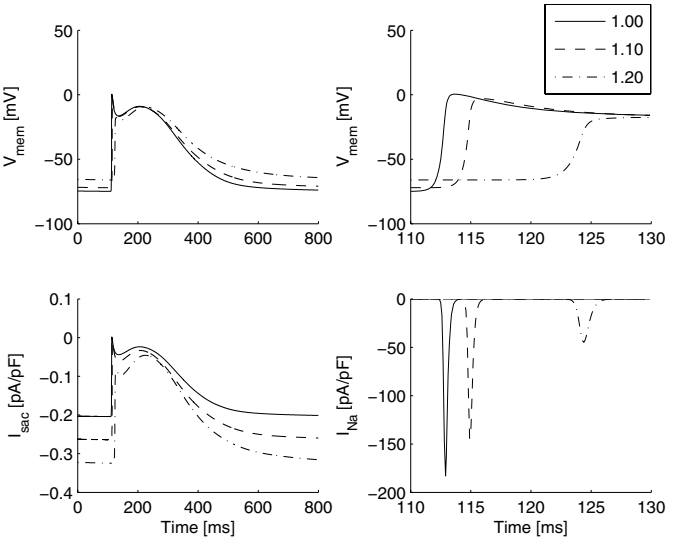

Fig. 2. Effect of stretch on the action potential (AP) and impulse propagation in a single fiber. Left: membrane potential (V_{mem}) and stretch-activated current (I_{sac}). Right: V_{mem} and fast Na^+ current (I_{Na}) during AP upstroke. A stimulus current was applied at 100 ms. Data are plotted for fiber stretch 1.00, 1.10, and 1.20 for a segment located 0.5 cm from the stimulation site.

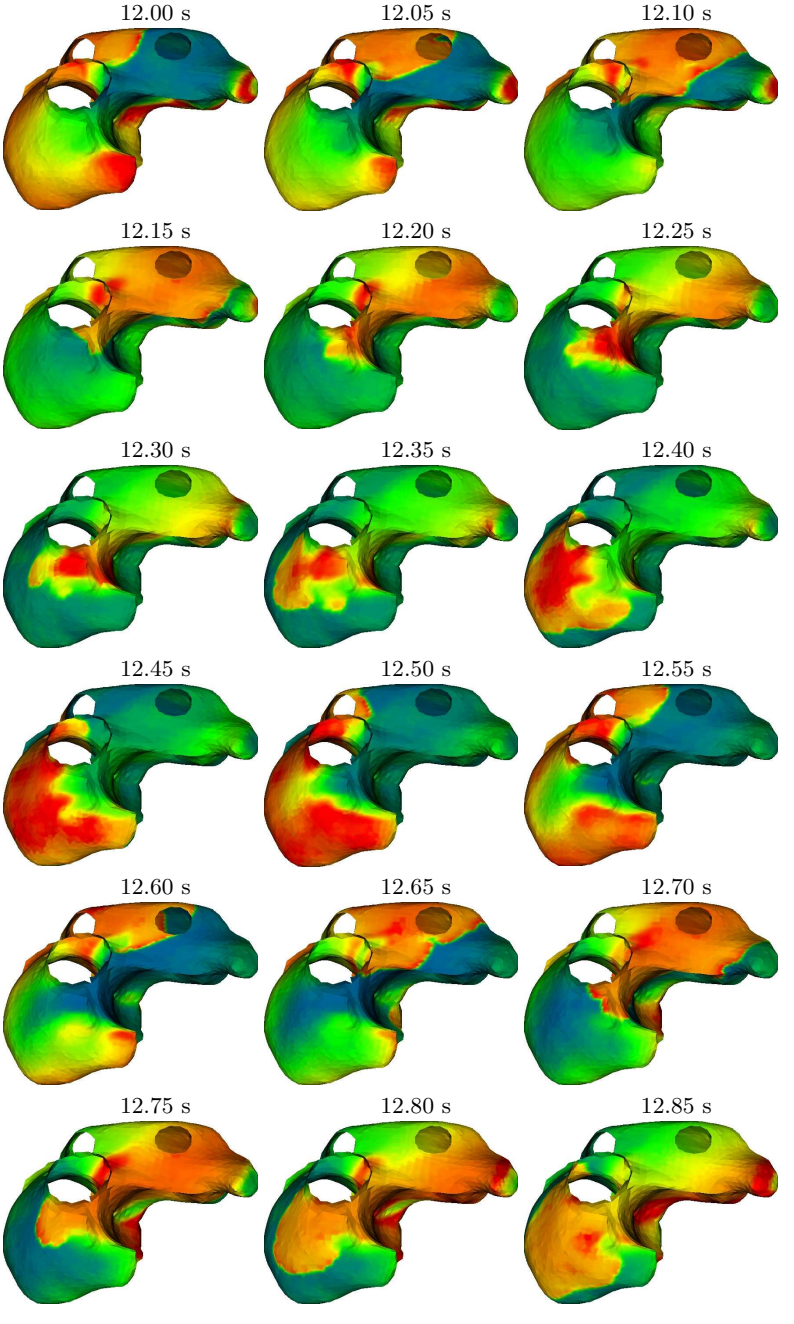

Fig. 3. Atrial fibrillation with 10% stretch. Membrane potential (V_{mem}) is shown between 12.0 and 12.85 s with intervals of 0.05 s. Red is depolarized tissue, green is tissue with increased V_{mem}, and blue is recovered tissue.

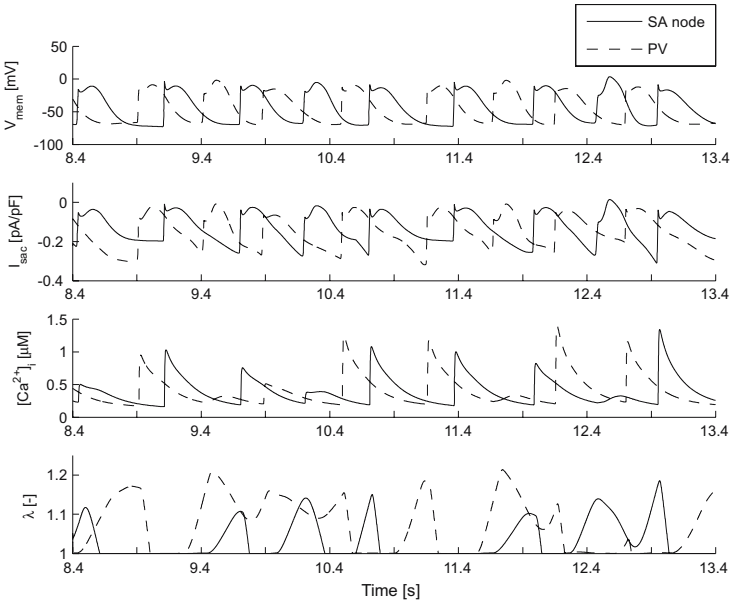

Fig. 4. Membrane potential (V_{mem}), stretch-activated current (I_{sac}), intracellular Ca^{2+} concentration ($[Ca^{2+}]_i$), and stretch ratio (λ) for a segment near the sino-atrial node (SA node) and a segment near the pulmonary veins (PV) during an episode of atrial fibrillation with 10% stretch (simulation time 8.4 - 13.4 s)

3.2 Effect of Anatomy on the Vulnerability to AF

To investigate the influence of the atrial bundle structure on the vulnerability to AF, ectopic activity was simulated by applying a stimulus current near the pulmonary veins with an interval of 0.6 s. Without stretch, conduction was normal and with 5% stretch, conduction was significantly slower. With 10% stretch, local conduction block occurred, which lead to a reentrant depolarization wave after 3 s. The path of the depolarization wave changed over time and the arrhythmia stopped after 14 s. In Figure 3, the atrial arrhythmia is shown after 12 s of simulation time. In Figure 4, V_{mem}, I_{sac}, intracellular Ca^{2+} concentration ($[Ca^{2+}]_i$), and stretch ratio (λ) are shown for a segment near the sino-atrial (SA) node and a segment near the pulmonary veins (PV) between 8.4 and 13.4 s. λ changes due to contraction of the segment and is influenced by contraction of other parts of the atria. Changes in λ affect I_{sac}, V_{mem}, and $[Ca^{2+}]_i$, and contribute to the irregularity in impulse propagation.

3.3 Effect of Contraction on AF

To investigate the influence of atrial contraction on arrhythmic behavior, the simulation with 10% stretch was continued after 13.4 s with and without sarcomere contraction. In Figure 5, it is shown how the arrhythmia terminated after

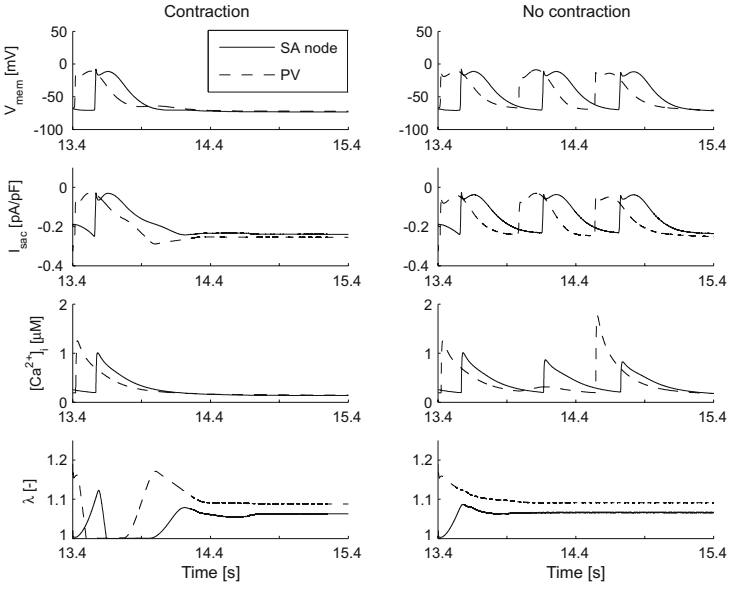

Fig. 5. V_{mem}, I_{sac}, $[\mathrm{Ca}^{2+}]_{\mathrm{i}}$, and λ for a segment near the sino-atrial node (SA node) and a segment near the pulmonary veins (PV) during an episode of atrial fibrillation with 10% stretch (simulation time 13.4 - 15.4 s). Left: with sarcomere contraction. Right: without sarcomere contraction.

14 s with sarcomere contraction, while it continued for another second without sarcomere contraction. With contraction, V_{mem} was increased at 14 s in the thin region near the pulmonary veins due to an increase in λ. The increase in V_{mem} resulted in reduced membrane excitability and block of the reentrant depolarization wave. Without contraction, the depolarization wave was not blocked and continued to reenter.

4 Discussion

Atrial dilatation is simulated by the application of overall stretch to the atria. Trabecular bundle structures lead to an inhomogeneous distribution of stretch, which influences membrane excitability, impulse propagation, action potential duration (APD), and effective refractory period (ERP). Dispersion in APD and ERP is further enhanced by the contraction of active parts of the atria and can influence both the onset and the termination of atrial arrhythmia.

Conduction slowing and block in our model is explained by a decreased membrane excitability caused by I_{sac}. Satoh and Zipes [4] measured an increased ERP both in the thin atrial free wall and in the crista terminalis under stretch. The ERP of the thin free wall was increased more than the ERP in the thicker crista terminalis, which they explain by the assumption that the thin free wall was

more stretched compared with the thicker bundles [4]. Eijsbouts *et al.* [5] found, in addition to conduction slowing, an increased occurrence of intra-atrial block. Our simulation results are in agreement with these experimental observations and explain the vulnerability to AF under acute stretch.

When reducing atrial contraction, we found that the arrhythmia continued for one more second before it was terminated. Thus, atrial contraction may influence the termination of AF.

4.1 Model Validity and Limitations

Validity of our model largely depends on the validity of the underlying models and parameters. Validity and limitations of the models for the ionic membrane currents, cross-bridge formation, and cardiomechanics are extensively discussed elsewhere [10,14,15,17]. Validity and limitations of the integrated cell model and the model of I_{sac} is discussed in Refs. [13,16].

A possible limitation of our model is the assumption that the amount of overall stretch applied to the atria remains constant throughout the simulation, i.e., there is no blood flowing to and from the atria. With respect to the mechanical part of the model, it is assumed that tension applied to the segments is homogeneous, while, according to Laplace's law, tension is related to local curvature. Another limitation is the assumption of a uniaxial state in the atrial wall, i.e., segments are only stretched in the direction of the fiber. In reality, segments will also experience force in the direction perpendicular to the fiber axis in the plane of the atrial wall. This force tends to reduce strain along the fiber direction, which results in an overestimation of stretch in our model.

In conclusion, overall stretch of about 10% significantly influences the vulnerability to AF. Termination of AF episodes is not only related to the amount of stretch, but also to atrial structure and contractility.

Acknowledgements. The authors would like to thank Peter van Dam and Adriaan van Oosterom for providing the triangular mesh of the human atria.

References

1. Bode, F., Katchman, A., Woosley, R.L., Franz, M.R.: Gadolinium decreases stretch-induced vulnerability to atrial fibrillation. Circulation 101, 2200–2205 (2000)
2. Bode, F., Sachs, F., Franz, M.R.: Tarantula peptide inhibits atrial fibrillation. Nature 409, 35–36 (2001)
3. Ravelli, F.: Mechano-electric feedback and atrial fibrillation. Progr. Biophys. Mol. Biol. 82, 137–149 (2003)
4. Satoh, T., Zipes, D.P.: Unequal atrial stretch in dogs increases dispersion of refractoriness conducive to developing atrial fibrillation. J. Cardiovasc. Electrophysiol. 7, 833–842 (1996)
5. Eijsbouts, S.C.M., Majidi, M., van Zandvoort, M., Allessie, M.A.: Effects of acute atrial dilation on heterogeneity in conduction in the isolated rabbit heart. J. Cardiovasc. Electrophysiol. 14, 269–278 (2003)

6. Kohl, P., Sachs, F.: Mechanoelectric feedback in cardiac cells. Phil. Trans. R Soc. Lond. 359, 1173–1185 (2001)
7. Henriquez, C.S.: Simulating the electrical behavior of cardiac tissue using the bidomain model. Crit. Rev. Biomed. Eng. 21, 1–77 (1993)
8. Kuijpers, N.H.L., Keldermann, R.H., Arts, T., Hilbers, P.A.J.: Computer simulations of successful defibrillation in decoupled and non-uniform cardiac tissue. Europace 7, S166–S177 (2005)
9. Kuijpers, N.H.L., Keldermann, R.H., ten Eikelder, H.M.M., Arts, T., Hilbers, P.A.J.: The role of the hyperpolarization-activated inward current I_f in arrhythmogenesis: a computer model study. IEEE Trans. Biomed. Eng. 53, 1499–1511 (2006)
10. Courtemanche, M., Ramirez, R.J., Nattel, S.: Ionic mechanisms underlying human atrial action potential properties: insights from a mathematical model. Am. J. Physiol. Heart Circ. Physiol. 275, H301–H321 (1998)
11. van Dam, P.M., van Oosterom, A.: Atrial excitation assuming uniform propagation. J. Cardiovasc. Electrophysiol. 14 (suppl. 10), S166–S171 (2003)
12. Virag, N., Jacquemet, V., Henriquez, C.S., Zozor, S., Blanc, O., Vesin, J.M., Pruvot, E., Kappenberger, L.: Study of atrial arrhythmias in a computer model based on magnetic resonance images of human atria. Chaos 12, 754–763 (2002)
13. Kuijpers, N.H.L., ten Eikelder, H.M.M., Bovendeerd, P.H.M., Verheule, S., Arts, T., Hilbers, P.A.J.: Mechanoelectric feedback leads to conduction slowing and block in acutely dilated atria: a modeling study of cardiac electromechanics. Am. J. Physiol. Heart Circ. Physiol. 292, H2832–H2853 (2007)
14. Solovyova, O., Katsnelson, L., Guriev, S., Nikitina, L., Protsenko, Y., Routkevitch, S., Markhasin, V.: Mechanical inhomogeneity of myocardium studied in parallel and serial cardiac muscle duplexes: experiments and models. Chaos, Solitons and Fractals 13, 1685–1711 (2002)
15. Rice, J.J., Winslow, R.L., Hunter, W.C.: Comparison of putative cooperative mechanisms in cardiac muscle: length dependence and dynamic responses. Am. J. Physiol. Heart Circ. Physiol. 276, H1734–H1754 (1999)
16. Kuijpers, N.H.L., ten Eikelder, H.M.M., Bovendeerd, P.H.M., Verheule, S., Arts, T., Hilbers, P.A.J.: Mechanoelectric feedback as a trigger mechanism for cardiac electrical remodeling: a model study. Ann. Biomed. Eng. 36, 1816–1835 (2008)
17. Zabel, M., Koller, B.S., Sachs, F., Franz, M.R.: Stretch-induced voltage changes in the isolated beating heart: importance of timing of stretch and implications for stretch-activated ion channels. Cardiovasc. Res. 32, 120–130 (1996)
18. Haïssaguerre, M., Jaïs, P., Shah, D.C., Takahashi, A., Hocini, M., Quiniou, G., Garrigue, S., Le Mouroux, A., Le Métayer, P., Clémenty, J.: Spontaneous initiation of atrial fibrillation by ectopic beats originating in the pulmonary veins. New Engl. J. Med. 339, 659–666 (1998)
19. de Bakker, J.M.T., Ho, S.Y., Hocini, M.: Basic and clinical electrophysiology of pulmonary vein ectopy. Cardiovasc. Res. 54, 287–294 (2002)

Left Ventricle Segmentation from Contrast Enhanced Fast Rotating Ultrasound Images Using Three Dimensional Active Shape Models

Meng Ma[1], Marijn van Stralen[2], Johan H.C. Reiber[1], Johan G. Bosch[2], and Boudewijn P.F. Lelieveldt[1]

[1] Division of Image Processing, Department of Radiology, Leiden University Medical Center, Leiden, The Netherlands
[2] Department of Experimental Echocardiography, Thoraxcenter, Erasmus MC, Rotterdam, The Netherlands

Abstract. In this paper we propose a novel segmentation technique for quantification of sparsely sampled single-beat 3D contrast enhanced echocardiographic data acquired with a Fast Rotating Ultrasound transducer (FRU). The method uses a 3D Active Shape Model of the Left Ventricle (LV) in combination with local appearance models as prior knowledge to steer the segmentation. From a set of semi-manually delineated contours, 3D meshes of the LV endocardium are constructed for different cardiac phases. Mesh surfaces are partitioned into a fixed number of regions, each of which is modeled by a local image appearance. During segmentation, model update points are generated based on similarity matches with these local appearance models in multiple curved 2D cross-sections, which are then propagated over a dense 3D mesh. The Active Shape Model effectively constrains the shape of the 3D mesh to a statistically plausible cardiac shape. Leave-one-out cross validation was carried out on single-beat contrast enhanced FRU data from 18 patients suffering from various cardiac pathologies. Experiments show that the proposed method generates segmentation results that agree with the ground truth contours with average Point to Point (P2P) error of 4.1±2.0 mm and average Point to Surface (P2S) error of 2.4±2.1mm. Convergence tests show that the proposed method is capable of producing acceptable segmentation results (with less than 1.5X error compared to favorable initialization) within the range of 18~22 mm of in-plane displacement and 12~14 degrees of long-axial orientation error.

1 Introduction

As a non-invasive 3D cardiac imaging modality, 3D echocardiography has recently drawn much attention from clinical practice. This is due to its capability of generating high temporal resolution 3D images with free viewing angles in a fast and patient friendly way. Particularly, the use of contrast agent significantly enhances imaging in routine echocardiography and stress echocardiography. Compared to non-contrast ultrasound modalities, contrast enhanced ultrasound provides better image quality in most patients and, more importantly, spares the patients from further invasive investigations as stated in [1]. Among all types of 3D ultrasound transducers, the Fast Rotating Ultrasound (FRU) transducer developed by Erasmus MC shows some unique

N. Ayache, H. Delingette, and M. Sermesant (Eds.): FIMH 2009, LNCS 5528, pp. 295–302, 2009.
© Springer-Verlag Berlin Heidelberg 2009

characteristics that lead to faster image acquisition with higher in-plane resolution and good quality harmonic imaging [2], which is advantageous for contrast imaging. Using microbubble agents, the FRU is able to generate image sequences with signal enhancement from blood pool, which better defines the borders of the left ventricular cavity and thereby improves the viewer's ability to assess ventricular chamber dimensions and both global and regional systolic function, see Figure 1.

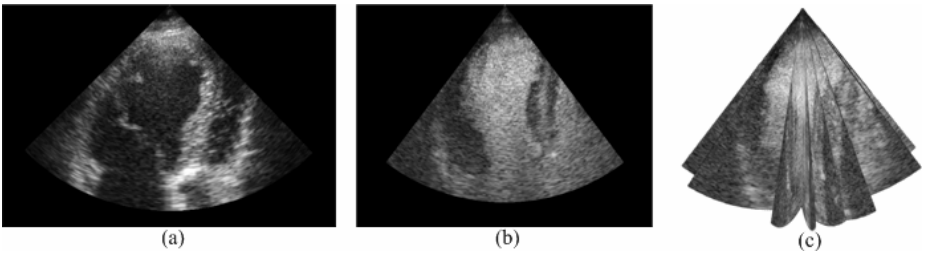

Fig. 1. (a) A 2D image generated from regular FRU; (b) A 2D frame from contrast FRU; (c) Multiple contrast FRU frames aligned in 3D space

Manual analysis of echocardiographic images in general is difficult especially when using contrast enhanced imaging. In combination with the huge amounts of data in 3D echocardiography, it makes the analysis cumbersome, labor intensive and therefore high inter-observer variabilities are common. Automation of the analysis can reduce the amount of work in the analysis tremendously and also eliminate the interobserver variability.

Although many automatic analysis approaches have been proposed for all types of 2D and 3D echocardiography modalities as listed in Noble et al. [3], automatic analysis of contrast enhanced images has been widely acknowledged as a challenging problem [4]. Only a limited number of methods has been reported for contrast ultrasound imaging. Noble et al. [5] adapted a nonrigid registration technique originally from contrast MR for aligning contrast-enhanced echocardiography sequences. Zwirn et al. [6] presents an algorithm that automatically detects endocardium in myocardial opacificated echocardiography based on converting the frames, given in Cartesian coordinates, into polar coordinates, and applying a set of filters in order to compute the initial estimation of the endocardial boundary. However, these methods concern 2D contrast echocardiography and, to the authors' knowledge, segmentation method for 3D contrast echocardiography has not been reported.

The goal of this work is to develop 3D segmentation method for *contrast enhanced* FRU sequences. To realize this, we adapted the method from an automatic segmentation solution for sparse MR data [7], and also from our previously proposed segmentation method for non-contrast FRU sequence [8]. We retrained the appearance component and modified the previous method to a contrast ultrasound oriented approach that is able to automatically quantify LV function. Leave-one-out cross validation and robustness tests were carried out to measure the performance of the method.

2 Methods

2.1 Overview

Statistical shape models have shown to be a powerful tool for segmentation both in 2D and in 3D. Combined with the local appearance models, dynamic programming and an update propagation scheme, 3D Active Shape Models have demonstrated the capability of segmenting echocardiographic data with high sparsity, particularly for regular FRU [8]. As for contrast enhanced ultrasound, the challenges are usually the rapidly changing contrast levels, attenuation, shadowing etc. To overcome these drawbacks, we propose a shape model guided method with the assistance of locally sampled intensity information and a contour tracking approach with inter-landmarks consistence.

In this work, we construct the 3D shape models from expert semi-manually annotated contours for end-diastolic (ED) and end-systolic (ES) phases from a set of contrast FRU. Apart from shape models, local intensity models are also constructed to serve as the appearance prior. The matching of the LV model is an iterative process driven by update points detected in the 2D images using pre-trained local appearance patches and propagated to the model surface, but regularized by shape constraints imposed from the 3D shape model, as shown in Fig. 2. Due to the sparse nature of the data, the 3D model is not only used for regularizing the intermediate shapes generated from each step, but also serves as the population based shape reconstruction in areas of data sparsity.

2.2 Model Construction

From an expert annotated subset of 2D contours in the FRU cross-sections, a full set of planar contours is generated using the semi-automatic method of van Stralen et al. [9] with manual adjustments to achieve complete expert acceptance. Based on the planar contours, 3D LV meshes of all cardiac phases were generated. Point correspondence was achieved by sampling each training sample in an LV specific coordinate frame that was defined as follows. First, the mitral valve plane (MVP) and the left ventricular long axis (LAX) are reconstructed by mapping the contours from the 2D curved planes into the 3D coordinate space. The MVP is defined as a best-fit plane through the mitral valve points; the LAX is defined as the straight line through the center of the MVP and the center of gravity (CoG) of the apical region of the LV. The azimuthal direction is defined by the position of the center of the aortic valve. Then, the mesh points are determined from the interpolated LV surface by a regular spherical sampling for the apical region (top 25% of LAX) and a regular cylindrical sampling of the non-apical LV section, resulting in 901 mesh vertices. See Fig. 3.

From the set of 3D meshes, the LV statistical shape model was constructed using standard Active Shape Modeling, as introduced by Cootes [10]. The point correspondent training samples are Procrustes aligned to eliminate pose and scale differences between training samples. Subsequently, Principal Component Analysis (PCA) is deployed to model the residual shape variation. In this study, because we are mostly interested in measuring the ED and ES phase (and consequently the ejection fraction), separate shape models for ED and ES are built.

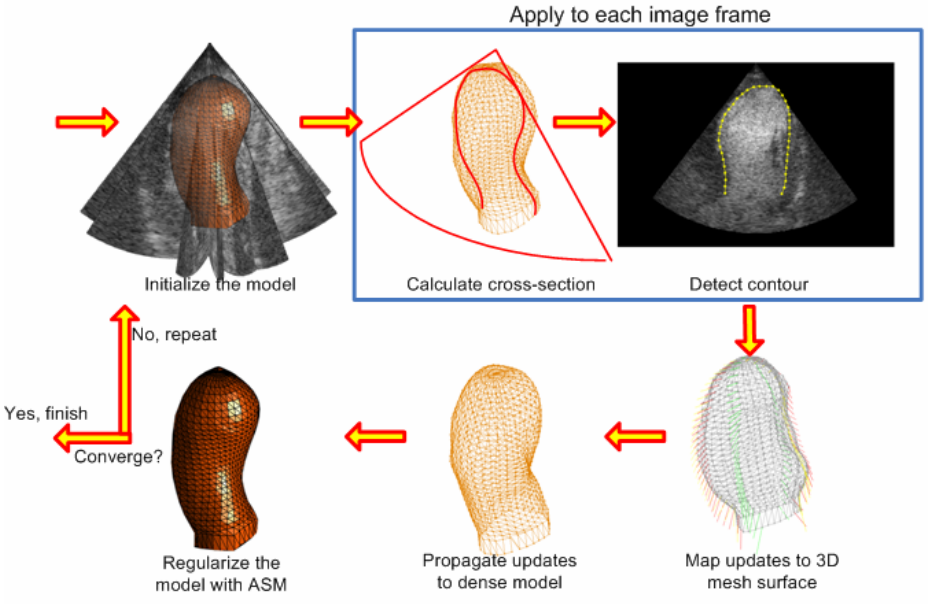

Fig. 2. Method overview: First, a mean shape is positioned to the sparse image frames. For each frame, a cross-section between image slice and the model is computed and updated based on the intensity information in the image. The updated nodes are then mapped back to 3D model and propagate throughout the whole model surface. The subsequent regularization using the ASM model constrains the propagated shape into the plausible range.

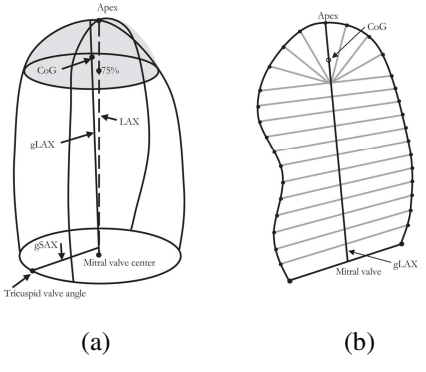

Fig. 3. (a) The definition of the long axis of the LV. (b) A schematic 2D representation of the 3D point correspondence.

Local intensity models are constructed to serve as templates for the model matching. To accomplish this, the 3D model surface is partitioned into a fixed number of regions. For each region, a local mean patch and its variances are generated for the computation of Mahalanobis distance to the intensity patches from the matching frame. These local patches capture the intensity features around the LV endocardial

border regarding the opaicfied blood pool that usually appears as high intensity region in the image and thus can guide the segmentation process during matching.

2.3 Model Matching

From the initial model position, the intersection between the 3D model and the multiple curved image planes is calculated to form a contour for each slice. For each landmark of this contour, a scan line perpendicular to the contour defined the search space. We search for the contour location on this line on X candidate positions, equally spaced symmetrically with respect to the current contour. The trained image patch corresponding to the 3D surface partition in the 2D landmark is then compared to the patch centered along the scan lines on the 2D FRU image. The Mahalanobis distances between the trained patch and scanline patch are computed and stored in a cost matrix. Using dynamic programming [11], an optimal continuous path (contour) through this cost matrix is calculated, which is subsequently mapped back to the 3D space as a set of candidate points for the 3D ASM.

The update points on the model surface are propagated over the entire model surface to fill in regions without updates using a Gaussian propagation mechanism. Each source is convolved with a Gaussian with kernel, thus the magnitude of update from a single source can be defined as

$$M(\lambda,\omega)=\begin{cases} e^{\frac{\|\lambda-\omega\|^2}{2\sigma p^2}} & if\ \|\lambda-\omega\|\le\chi \\ 0 & if\ \|\lambda-\omega\|>\chi \end{cases} \quad (1)$$

where, $M(\lambda,\omega)$ is the update magnitude for the receiving node λ, ω is the source node, $\|\lambda\text{-}\omega\|$ is the geodesic distance between these nodes. σ_p determines the width of the Gaussian kernel, and χ defines the update region and was set to $3\sigma_p$. In case the receiving node falls in the update regions from multiple source nodes, the update magnitude is determined by the source node with the highest magnitude.

The model update point configuration does not necessarily maintain the shape of the LV wall. Therefore, the projected shape eigenvectors of the shape model are constrained to a range of ±3SD along each principal axis. The constrained model serves as input for the next iteration if the conditions of convergence are not yet fulfilled.

3 Experimental Results

3.1 Data

Apical contrast enhanced image sequences were acquired using the FRU transducer from 18 patients suffering from different degrees of myocardial infarction and ischemic cardiomyopathy. The FRU transducer [2] consists of a linear phased array which is capable to rotate at 240 ~ 480 rpm and acquire cardiac apical images at about 100 frames per second, which results in 5 ~ 8 frames per cardiac phase (depending on the heart rate and the desired number of phases). The probe is able to produce image frames in around 100 fps with approximately 80 to 120 ultrasound beams per cone/frame. In the raw image, each ultrasound beam is represented by around 500

pixels. The working image data (with coordinates conversion) are image frames with 600x400 pixels. The ECG signals were acquired simultaneously. For the validation of this study, images from a single cardiac cycle that start from the ED phase to the next ED phase were used. The cardiac cycle was divided into 16 cardiac phases, ED phase was determined using the ECG signals, and the ES phase was manually defined as the moment before the mitral valve opens. From this single-beat data, the clinically important parameters ED and ES volume and EF were automatically measured using the proposed method. Each phase typically contained 5 ~ 8 2D image frames.

3.2 Cross Validation

Leave-one-out cross validation was performed to evaluate the segmentation accuracy of the proposed method. The segmentation results were compared to ground truth contours that were generated from a semi-manual method described in [9]. The LV surface was divided into 25 regions (apex plus 4 levels with each level contains 6 sectors) for intensity patch training and matching. This division was configured empirically to capture the heterogeneity in intensities over the surface, while in the mean time, minimizing the number of segments. Besides the average Point to Point (P2P), Point to Surface (P2S) errors of the vertices, the validation also considered the signed volume and EF error to observe the global bias of these measures. For all the validation indices, the medians were also recorded to detect a possibly non-symmetrical distribution of the validation results due to outliers. The results of the validation are shown in Table 1 and Fig. 4 illustrates two final segmentation results together with the contrast enhanced data in 3D renderings.

Table 1. Cross validation results (18 patients)

	Avg. ± St. Dev.		*Median*	
	ED	ES	ED	ES
P2P (mm)	4.2 ± 2.1	3.9 ± 1.8	4.1	3.9
P2S (mm)	2.3 ± 2.3	2.5 ± 2.1	2.2	2.4
Volume (signed error in percentage)	3.0 ± 7.7%	-4.0 ± 8.5%	2.6%	-2.8%
EF (signed error)	4.7 ± 10.8%		3.6%	

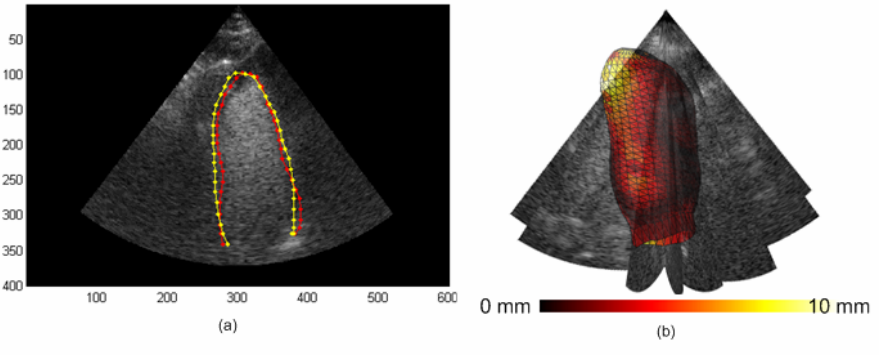

Fig. 4. Examples of 3D segmentation: (a) an individual frame segmentation results (red) compared to manual annotation (yellow); (b) 3D segmentation with P2P error color-coded on the surface from ES phase (For clear visibility, refer to the digital copy of this paper)

3.3 Convergence Test

To evaluate the robustness of the proposed method with respect to less favorable initializations, a range of model initializations was tested. The initial model was intentionally misplaced along horizontal, vertical and rotational directions to test the tolerance to initialization errors. The same measurements (P2P, P2S, volume, EF) were carried out for each initialization. Fig. 5 shows the P2S errors of the ED phase under different initializations. From the convergence validation we conclude that within the interval of 18mm - 22 mm of in-plane displacement and 10 - 14 degree long-axial orientation misalignment with respect to the favorable initial position, the model still converges to a similar error of at most 150% of the minimum error.

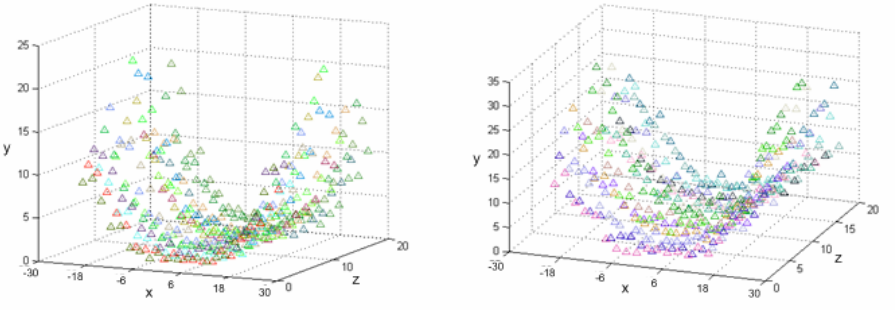

Fig. 5. Convergence test results for in-plane initial displacements. The x-axis is the initial in-plane misalignment (in mm), the y-axis is the final P2S error (in mm) and the z-axis is for different patients (coded in different colors). (a) Horizontal displacements and error measures. (b) Vertical displacements and error measures.

4 Discussion and Conclusion

In this study, we adapted a segmentation method that combines active shape models and local appearance models to application in contrast enhanced FRU data. The proposed method is able to automatically segment 3D left ventricle endocardium from sparsely sampled contrast enhanced FRU images. The method incorporates an appearance model and dynamic programming techniques to consistently trace the LV endocardium, together with a Gaussian propagation scheme to distribute the sparse updates over the 3D model surface and ASM models to constrain the border detection to plausible shapes. In this way, the method is designed to be tolerant to high data sparsity and initialization misalignments.

From the validation results, average P2P error of 4.1±2.0 mm and more importantly the P2S error of about 2.4±2.2 mm indicate a fairly accurate segmentation and clinical importance. However, from the signed error measures of ED, ES volumes and EF, global biases of overestimation of ED volume and underestimation of ES volume (thus also overestimation in EF) were observed. This is mostly due to the fact that blood pool is hardly visible at ES phase so the detected contours tend to shrink due to

the absence of contrast agent, resulting in smaller ES volume. Also, it is apparent that the median values for all measures are evidently different from the average, which indicates a skewed error distribution because of outliers.

In conclusion, we investigated the possibility of generalizing the segmentation method for FRU to contrast enhanced FRU. The method is adapted from a previous work with contrast oriented modifications and retrained appearance components. Though the automatic segmentation of the contrast enhanced sequences has been widely known as a difficult problem, the proposed method is able to generate similar segmentation results to regular FRU data (average P2P=3.8±2.4 mm and P2S=2.0±1.8 mm), which indicates that the presence of contrast agents in the FRU data does not hamper the proposed automatic segmentation method. Furthermore, convergence tests show that the method is capable of generating relatively accurate segmentations with acceptable in-plane and orientation misalignments, which indicates that the method is robust with respect to initialization.

Acknowledgements

This research is supported by the Dutch Technology Foundation STW (grant 06666), applied science division of NWO and the Technology Program of the Ministry of Economic Affairs. The authors also thank Esther K.Y. Leung and Marco M. Voormolen for the preparation of patient data and tracing manual contours.

References

[1] Bhatia, V.K., Senior, R.: Contrast echocardiography: evidence in clinical uses. Journal of the American Society of Echocardiography 21(5), 513–514 (2008)
[2] Voormolen, M.M., et al.: Harmonic 3-D echocardiography with a fast-rotating ultrasound transducer. IEEE Trans. Ultrason. Ferroelectr. Freq. Control 53(10), 1739–1748 (2006)
[3] Noble, A.J., Boukerroui, D.: Ultrasound image segmentation: A survey. IEEE Trans. Med. Imag. 25(8), 987–1010 (2006)
[4] Becher, H., Burns, P.N.: Handbook of contrast echocardiography: Left ventricular function and myocardial perfusion. Springer, Berlin (2000)
[5] Noble, A.J., et al.: Automated, nonrigid alignment of clinical myocardial contrast echocardiography image sequences: comparison with manual alignment. Ultrasound in Medicine & Biology 28(1), 115–123 (2002)
[6] Zwirn, G., et al.: Automatic endocardial-boundary detection in low mechanical-index contrast echocardiography. IEEE Trans. Biomed. Eng. 53, 2310–2322 (2006)
[7] van Assen, et al.: SPASM: A 3D-ASM for segmentation of sparse and arbitrarily oriented cardiac MRI data. Medical Image Analysis 10(2) (2006)
[8] Ma, M., et al.: Model Driven Quantification of Left Ventricular Function from Sparse Single-beat 3D Echocardiography. In: Proc. SPIE Medical Imaging (in press, 2009)
[9] van Stralen, M., et al.: Semi-automatic border detection method for left ventricular volume estimation in 4D ultrasound data. In: Proc. SPIE Medical Imaging 2005, vol. 5747, pp. 1457–1467 (2005)
[10] Cootes, T.F., et al.: Active Shape Models - their training and application. Computer Vision and Image Understanding 61(1), 38–59 (1995)
[11] Dijkstra, E.W.: A note on two problems in connexion with graphs. Numerische Mathematik 1, 269–271 (1959)

Free-Form Deformations Using Adaptive Control Point Status for Whole Heart MR Segmentation

Xiahai Zhuang[1], Kawal Rhode[2], Reza Razavi[2], David J. Hawkes[1], and Sebastien Ourselin[1]

[1] Centre for Medical Image Computing, Medical Physics Department, University College London, WC1E 6BT, UK
x.zhuang@ucl.ac.uk
[2] Division of Imaging Science, King's College London, SE1 7EH, UK

Abstract. Whole heart segmentation from cardiac MRI is useful in clinics but challenging due to the large shape variation of the heart and many indistinct boundaries commonly presented in the MR images, especially in pathological cases. Image registration for whole heart MR images has been developed and applied to atlas propagation based segmentation [1]. In this paper, we base on this segmentation framework and propose a new non rigid registration, a free-form deformations (FFDs) registration using adaptive control point status, for the segmentation refinement. This method activates and optimises control points according to the combined information of the deformation field and the heart surface from the atlas to improve the registration performance. The segmentation framework using this registration demonstrates a RMS accuracy of 1.8 ± 0.2 mm in 10 pathological data.

Keywords: Whole heart segmentation, free-form deformations, atlas propagation, registration.

1 Introduction

Whole heart segmentation [1,2] is an important technical development, providing delineations of a set of local regions of the heart on diagnostic images, especially based on magnetic resonance imaging (MRI). The segmentation of these local regions, mainly the anatomical substructures of the heart such as the atria and the ventricles, are crucial for specific functional analysis. In addition, whole heart functional analysis requires an accurate whole heart segmentation to enable the detection of subtle functional changes of the organ. Such analysis can lead to earlier diagnosis of cardiac diseases and better management of treatments. However, the segmentation from magnetic resonance (MR) images are still challenging due to the indistinct boundaries among local regions and the large shape variation of the heart. Atlas propagation using image registration for segmentation has shown good robustness and potential of being applicable to a wide range of pathological cases [1]. Unlike the segmentation using a statistical shape model, which needs a training phase from a large dataset [2], this propagation framework does not

N. Ayache, H. Delingette, and M. Sermesant (Eds.): FIMH 2009, LNCS 5528, pp. 303–311, 2009.
© Springer-Verlag Berlin Heidelberg 2009

require such training for different pathologies to perform the segmentation of an unseen case. Instead, it only requires the manual segmentation of one cardiac MR image as a template to perform the segmentation propagation. This propagation employs three image registration steps [1]. Firstly, a global affine registration is performed to obtain an automatic localisation of the global heart structure. Then, a locally affine registration is applied to ensure a good local correspondence of the anatomical substructures of the heart, such as the four chambers and major vessels. Finally, a non rigid registration based on the fluid algorithm [9] is performed to refine the segmentation propagation. However, the fluid registration used in [1] can be challenged for many pathological cases where the local shape of the heart is more variable and the images are more likely to be corrupted by noise and artefacts. To deal with such cases, we propose a new adaptive free-form deformations (FFDs) registration, extending and generalising the non-uniform FFDs proposed by Schnabel *et al.* [4]. The control points in the FFDs are associated with a status, active or passive. Active control points are then optimised, allowed to move (e.g. be active) during some specific step(s) of the registration process, while passive control points will not be optimised (e.g. remain fixed). This active-passive selection is based on the *a priori* information coming from a cardiac MR atlas. We demonstrate that this adaptive control points scheme performs well in the ten pathological data and improves the registration performance compared to the traditional standard FFDs.

This paper is organised as follow. Section 2 presents the methodology of the FFDs registration with adaptive control point status. Section 3 describes the proposed segmentation framework. Section 4 presents the segmentation results on ten pathological cases using both the proposed adaptive FFDs and standard FFDs. Section 5 draws the conclusion and highlights the potential future work.

2 Adaptive Control Point Status

2.1 Related Work

FFDs registration employs a or a series of B-splines mesh(es) to estimate the deformation field from the target image to the source image [3,6]. Schnabel *et al.* associated a status, active or passive, to each control point of the FFDs to simulate Non-Uniform Rational B-splines (NURBS) [4]. Such status is priorly computed before optimising the FFDs of each level, using either the *reference image measures* such as local entropy, or the *joint image pair measures* such as the gradient of the associated cost function [4]. Also, the status stays constant during the registration process at each level. This method, embedded into a multi-resolution registration scheme, improved the performance and significantly reduced the run-time compared to a standard FFDs scheme [4]. However, there are two potential challenges in terms of applying this framework to cardiac MR image registration.

Firstly, in the context of cardiac MR image segmentation, the adjacent tissues of the heart such as the lung and the liver, should be considered as background information. In other words, they should not influence the registration

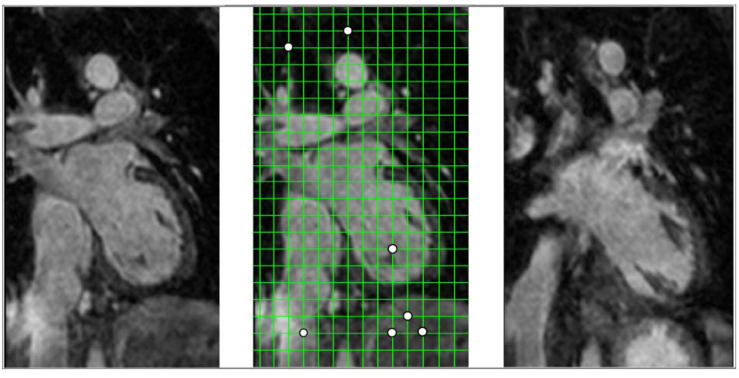

Fig. 1. Left: the target image; middle: the FFDs mesh in the target space with unnecessary active control points (white dots); right: the source image

process. However, using the status setting in [4], these areas will be taken into account, because they present relevant information for the status determination measures. For example, Fig. 1 demonstrates such situation, the control points located around the liver or papillary muscle (white dots) will also be considered as active. Hence, during the registration, the liver in the target image is likely to register to the myocardium in the source image due to their similar intensity value, while the papillary muscle in the source image is also likely to register to the myocardium in the target image. As a result, the deformation in these regions will bias the segmentation propagation of the endocardial and epicardial surfaces and generate erroneous outcomes.

Secondly, if the status is pre-set and remains constant, some control points could be inactivated, leading to diminishing the modelling ability of the FFDs meshes. For example, as shown in Fig. 2, the control points (white dots in middle row of (a)) around the contour of the ellipse will not be activated by using proposed measures in [4]. This is because the local supports of these control points are linked to the uniform regions in the source image, where the intensity gradient is low. Such low gradient results in the low value of the local entropy of the uniform region or the derivative of the intensity-based cost functions, and thus inactivates the associated control points. Instead, only the control points mapped to the boundary of the circle in the source image will be activated, as the black dots shown in the top row of Fig. 2 (b). If the status is not adaptively updated but remains constant, then the ellipse in the target image will not be able to deform appropriately to match the circle in the source image.

2.2 Adaptively Updated Status of Control Points

Due to the two challenges, we propose to set the status of control points adaptively for each registration iteration. As shown in Fig. 2 (c), after each registration iteration, the resultant deformation T_i inversely transforms or resamples

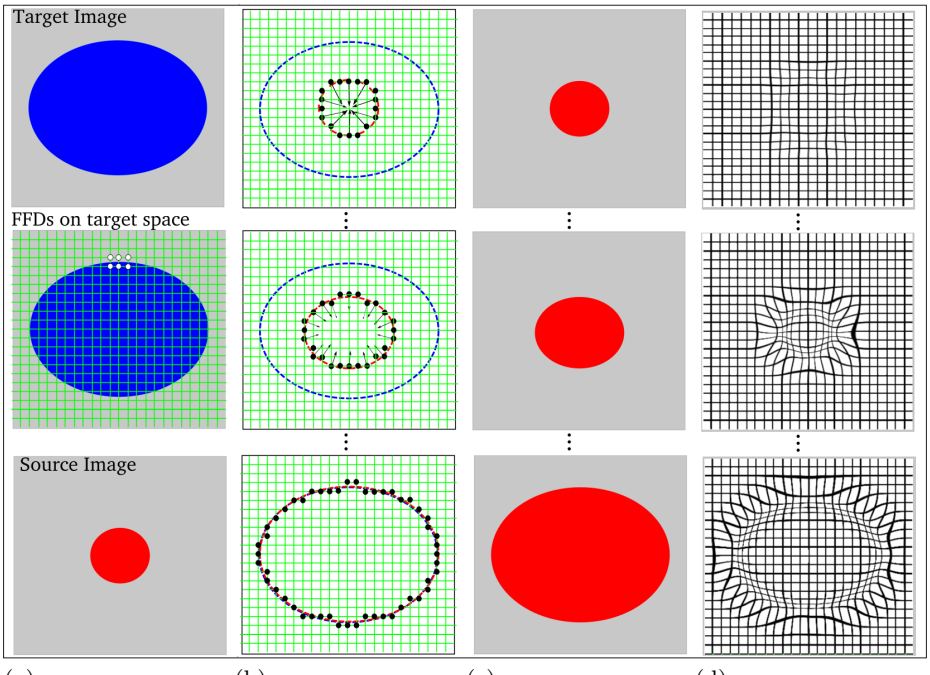

Fig. 2. Registration of an ellipse, the target image, and a circle, the source image, using adaptive FFDs where the control point status is adaptively updated for each registration iteration. The white dots in (a) are special control points explained in the text. (b) shows the FFDs meshes, the contour of the ellipse, and the contour of the inverse-transformed source image. The black dots are activated control points and the arrows demonstrate the registration driving forces. (c) gives the source image inversely transformed into the target space at different registration steps. (d) demonstrates the deformed FFDs meshes at different registration steps whose concatenation gives the resultant transformation field.

the source image I_s into the coordinate of the target image space (referred as target space) to get I_s^i. Hence, the status of the control points should be updated based on the updated information from I_s^i given the shape of the source image is priorly known, as shown in Fig. 2 (b). Based on this idea, we can extend the two measures in [4] as follows.

For the *joint image pair measures* such as the gradient of associated cost function, the status can be updated based on the updated derivative of the cost function with respect to each control point at each iteration. However, this is inefficient because the computation of the derivative of a passive control point is expensive and unnecessary.

For the *reference image measures* such as the local entropy or local intensity variance, the status can be updated based on computing the measures using the updated information from the inversely transformed source image I_s^i at each

iteration. However, this scheme is still not suitable for the registration task in the context of cardiac MR image segmentation where the control points linked to the liver are supposed to be passive, though it should work well for images with uniform background.

Therefore, we extend this idea to embed the shape of the source image into the status-setting process. As Fig. 2 (b) demonstrates, given the contour of the circle is priorly known, we only activate the control points within a certain distance to the updated circle contour at each registration step. Such update is achieved by inversely transforming the source image into the target space:

$$\text{Status}(\phi_j) = \begin{cases} active, & \text{if } ||\Phi_j - T_i^{-1}(\mathcal{C}_s)|| \leq l \\ passive, & \text{if } ||\Phi_j - T_i^{-1}(\mathcal{C}_s)|| > l \end{cases} , \tag{1}$$

where, Φ_j is the coordinate of the control point ϕ_j, $\mathcal{C}_s$ is the boundary of the source image and l is the distance threshold, which is related to the local support of the control points.

Since the segmentation of the atlas is priorly known indeed in the whole heart segmentation framework, this status-setting is suitable for the non rigid registration step in the refinement. Practically, we choose 5 to 15 mm for l, depending on the spacing of the FFDs mesh, to simulate irregular shaped B-spline meshes around the endocardial and epicardial surfaces. This not only avoids unnecessary computation of the derivative of a large number of passive control points, but also avoids activating control points in the adjacent tissues.

2.3 Directional Optimisation

Since intensity non-uniformity and artefacts are commonly presented in cardiac MR images, we further propose to constrain the active control points to move within the perpendicular direction of the inverse-transformed atlas surface. This constraint can help avoid optimising the control points along the biased gradient of the cost function due to intensity non-uniformity or artefacts. Similar to the perpendicular adaptation of vertices in active contour model [5], this directional optimisation can improve the robustness of the segmentation propagation.

Given the boundary surface $\mathcal{C}_s$ of the atlas from the source image space, let $\boldsymbol{v}_Y^s$ be a vector perpendicular to surface $\mathcal{C}_s$ at coordinate Y, $\boldsymbol{v}_X^t$ be the corresponding vector in the target space at coordinate X, T be the transformation and $Y = T(X)$. $\boldsymbol{v}_Y^s$ can be priorly computed from the normalised gradient of $\mathcal{C}_s$:

$$\boldsymbol{v}_Y^s = \text{Normalise } \nabla\mathcal{C}(Y) \ . \tag{2}$$

Therefore, the direction $\boldsymbol{v}_X^t$ for moving control point ϕ_j in target space can be computed from the inverse-transformed atlas surface at coordinate $X = \Phi_j$:

$$\begin{aligned} \boldsymbol{v}_X^t &= \text{Normalise } \nabla(T^{-1}(\mathcal{C}_s)(X)) \\ &= \text{Normalise } \nabla(\mathcal{C}_s(T(X)) \\ &= \text{Normalise } \nabla\mathcal{C}_s(Y) \cdot \nabla T(X) \ , \end{aligned} \tag{3}$$

because $T^{-1}(\mathcal{C}_s)(X) = \mathcal{C}_s(Y)$, where $Y = T(X)$.

3 Segmentation Framework

The segmentation framework in [1], which propagates the segmentation in the source image (atlas) to the target image (unseen image), has four steps:

- A cardiac MR atlas with all regions of interest segmented;
- A global affine registration to localise the heart in the atlas to that in the unseen cardiac MR image;
- A locally affine registration to further initialise the substructures such as four chambers and major vessels between the atlas and the unseen image;
- A non rigid registration to refine the propagation.

Registration. In this paper, we use the same initialisation registrations, including the global affine registration and the locally affine registration as in [1]. For the refinement registration, we employ the proposed adaptive FFDs registration to fine-tune the segmentation. Furthermore, we use both the multi-level FFDs in [4] and the maximal displacement constraint of FFDs and concatenation in [6] to guarantee a diffeomorphic registration, because the diffeomorphism preserves the topology of the heart and is desired in this segmentation framework. For the similarity measure, we use the normalised mutual information [7].

Atlas. The atlas we used in the experiment was constructed from ten healthy volunteer MR images using the same acquisition sequence, of resolution $2 \times 2 \times 2$ mm. Firstly of all, we resampled all the MR images into $1 \times 1 \times 1$ mm and normalised the intensity to the same scale. Then, we manually segmented the four chambers and major vessels of the MR images to construct the corresponding label images, as the image in Fig. 3 (right). Finally, we registerred all the label images to a common space using the global affine registration, the locally affine registration, and the fluid registration [9]. The resultant transformations were used to deform the corresponding MR images into the common space to achieve an intensity mean image. The common space is not a mean shape, but a manually constructed label image with enlarged distances between the superior regions and ventricles, as shown in Fig. 3. These enhanced features help avoid overlapping of local regions and hence can improve the registration robustness [8]. Fig. 3 shows the resultant images.

Fig. 3. The heart atlas: the intensity image (left) and the label image (right). In the label image, different chambers are assigned with different label values.

4 Results

Finally, we evaluate the segmentation framework using 10 pathological MR cases, which displayed a variety of heart abnormalities such as ventricular hypertropy and other anatomical abnormalities from Tetralogy of Fallot and myocardial ischemia diseases. They were acquired at St. Thomas' Hosptial, London, using the balanced SSFP sequence for whole heart imaging with acquisition resolution $2 \times 2 \times 2$ mm at the end-diastolic phase. The images were reconstructed or resampled into $1 \times 1 \times 1$ mm voxel size. The manual segmentations, regarded as gold standard, have been done by a technician with cardiac anatomy knowledge slice by slice using Analyze 8.1. The segmentation error is computed from the root mean squared (RMS) surface distance between the segmented surface and the gold standard.

Table 1 presents the RMS error for each anatomical sub-structures, including epicardial surface of left ventricle (EpiLV), endocardial surface of left and right ventricles (EndoLV and EndoRV), endocardial surface of left and right atria (EndoLA and EndoRA) and all these local surfaces as a whole measure (Whole), using both the proposed adaptive FFDs and the standard FFDs for segmentation refinement. The adaptive FFDs almost outperforms the standard FFDs in all categories, except for EndoRV. Especially at EpiLV, the adaptvie FFDs achieves a significantly improved accuracy, 2.3 ± 0.7 mm RMS error, which compares with 3.1 ± 1.1 mm by the standard FFDs. This is because aligning the adjacent liver, lung tissues, and papillary muscles can bias the registration of the myocardium in the standard FFDs. Such bias makes the registraiton more likely to step into local minima and produce unrealistic deformations, as the examples shown in Fig. 4.

Table 1. The segmentation error, RMS surface distance, and the percentage (%) of the error distribution: < 2 mm, $2 \sim 5$ mm, and > 5 mm

	RMS (mm)	< 2mm (%)	$2 \sim 5$mm (%)	> 5mm (%)
Segmentation using adaptive FFDs				
EpiLV	2.3 ± 0.7	75.3 ± 6.2	19.9 ± 4.2	4.8 ± 3.7
EndoLV	1.6 ± 0.3	83.8 ± 7.8	14.9 ± 7.3	1.3 ± 0.9
EndoRV	1.9 ± 0.6	82.2 ± 5.7	14.5 ± 4.0	3.3 ± 3.2
EndoLA	2.3 ± 0.6	71.5 ± 10.4	24.0 ± 9.0	4.5 ± 5.3
EndoRA	1.8 ± 0.4	80.6 ± 6.7	16.9 ± 5.0	2.5 ± 2.7
Whole	1.8 ± 0.2	81.1 ± 4.0	16.7 ± 3.9	2.2 ± 1.2
Segmentation using standard FFDs				
EpiLV	3.1 ± 1.1	72.5 ± 5.9	20.2 ± 4.2	7.4 ± 5.2
EndoLV	1.8 ± 0.7	81.2 ± 8.4	16.7 ± 7.1	2.1 ± 2.7
EndoRV	1.9 ± 0.6	80.0 ± 7.9	16.7 ± 5.8	3.2 ± 3.1
EndoLA	2.5 ± 1.0	68.2 ± 9.9	25.0 ± 6.3	6.8 ± 7.3
EndoRA	2.2 ± 0.7	74.2 ± 7.1	21.5 ± 5.7	4.3 ± 4.0
Whole	2.0 ± 0.3	77.0 ± 4.2	20.3 ± 4.0	2.7 ± 1.5

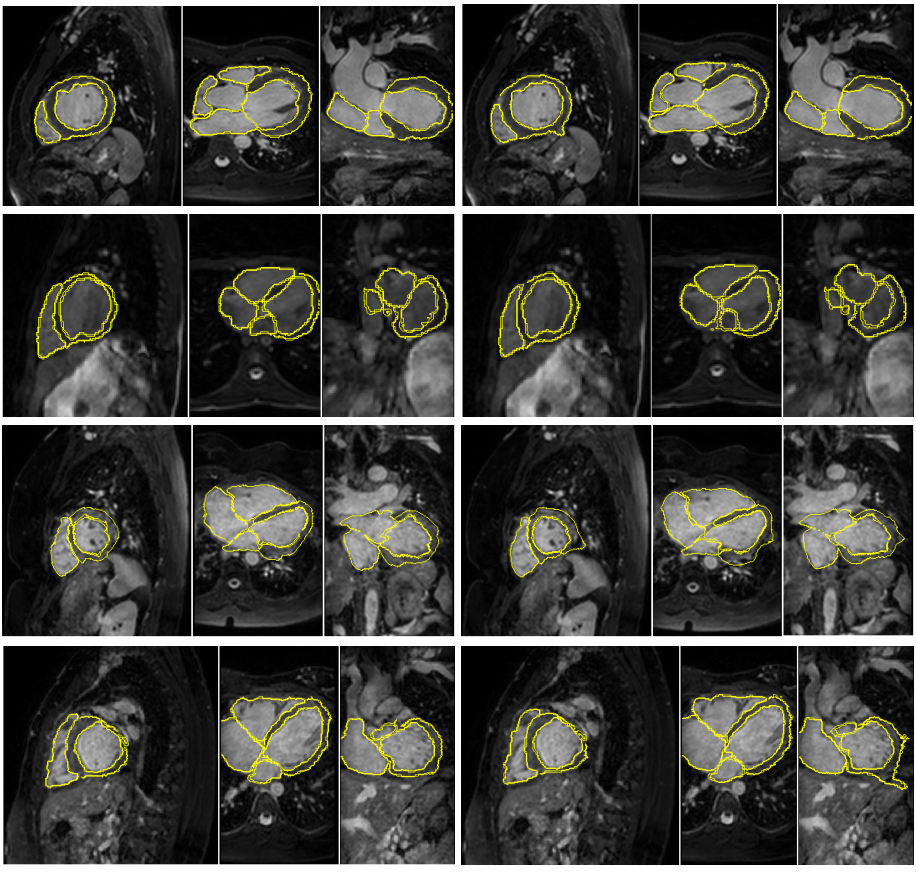

Fig. 4. Four random examples of using the adaptive FFDs registration (left) and the standard FFDs registration (right) for segmentation refinement

Table 1 also gives the error distribution for each category. The proposed FFDs achieves 1.8 ± 0.2 RMS error for the whole heart surface (Whole), and over 80% error is within 2 mm and more than 97% is within 5mm. The segmentation of EpiLV and EndoLA have demonstrated bigger errors than other categories. The major error source for EpiLV comes from the region between the left ventricle and liver tissue where boundary is not always clear from cardiac MR images; while for EndoLA, it is due to the inconsistent definition of the boundary between the left atrium and the pulmonary veins and left auricula.

5 Conclusion

We have presented a new FFDs registration for the refinement in the atlas propagation based whole heart segmentation. This registration adaptively activates the control points within the *a priori* selective regions and restricts their moving directions to constrain the deformation of the FFDs mesh, and improves

the optimisation efficiency. We applied this method to the segmentation framework and evaluated its performance on 10 pathological cases. The results have demonstrated a RMS accuracy of 1.8 ± 0.2 mm and an improved performance compared to the registration using standard FFDs. For the future work, we will validate our segmentation framework using a wider range of pathological data; and consider alternative similarity measures such as the phase registration [10] to extend it for echocardiography.

Acknowledgement

The work was funded by EPSRC grant GR/T11395/01. The authors would like to thank colleagues Yipeng Hu and Marc Modat for their valuable discussion.

References

1. Zhuang, X., Rhode, K., Arridge, S., Razavi, R., Hill, D., Hawkes, D.J., Ourselin, S.: An atlas-based segmentation propagation framework using locally affine registration–application to automatic whole heart segmentation. In: Metaxas, D., Axel, L., Fichtinger, G., Székely, G. (eds.) MICCAI 2008, Part II. LNCS, vol. 5242, pp. 425–433. Springer, Heidelberg (2008)
2. Peters, J., Ecabert, O., Meyer, C., Schramm, H., Kneser, R., Groth, A., Weese, J.: Automatic whole heart segmentation in static magnetic resonance image volumes. In: Ayache, N., Ourselin, S., Maeder, A. (eds.) MICCAI 2007, Part II. LNCS, vol. 4792, pp. 402–410. Springer, Heidelberg (2007)
3. Rueckert, D., Sonoda, L.I., Hayes, C., Hill, D.L.G., Leach, M.O., Hawkes, D.J.: Nonrigid registration using free-form deformations: Application to breast MR images. IEEE Trans. Med. Imag. 18(8), 712–721 (1999)
4. Schnabel, J.A., Rueckert, D., Quist, M., Blackall, J., Castellano-Smith, A., Hartkens, T., Penney, G., Hall, W., Liu, H., Truwit, C., Gerritsen, F., Hill, D.L.G., Hawkes, D.J.: A generic framework for non-rigid registration based on non-uniform multi-level free-form deformations. In: Niessen, W.J., Viergever, M.A. (eds.) MICCAI 2001. LNCS, vol. 2208, pp. 573–581. Springer, Heidelberg (2001)
5. Lobregt, S., Viergever, M.: A discrete dynamic contour model. IEEE Trans. Med. Imag. 14(1), 12–24 (1995)
6. Rueckert, D., Aljabar, P., Heckemann, R., Hajnal, J., Hammers, A.: Diffeomorphic registration using B-Splines. In: Larsen, R., Nielsen, M., Sporring, J. (eds.) MICCAI 2006. LNCS, vol. 4191, pp. 702–709. Springer, Heidelberg (2006)
7. Studholme, C., Hill, D.L.G., Hawkes, D.J.: An overlap invariant entropy measure of 3D medical image alignment. Pattern Recognition 32, 71–86 (1999)
8. Zhuang, X., Hawkes, D.J., Crum, W.R., Boubertakh, R., Uribe, S., Atkinson, D., Batchelor, P., Schaeffter, T., Razavi, R., Hill, D.L.G.: Robust registration between cardiac MRI images and atlas for segmentation propagation. In: Proceedings of SPIE. Medical Imaging 2008: Image Processing, vol. 6914, p. 7 (2008)
9. Crum, W., Hill, D., Hawkes, D.: Information theoretic similarity measures in non-rigid registration. In: Taylor, C.J., Noble, J.A. (eds.) IPMI 2003. LNCS, vol. 2732, pp. 378–387. Springer, Heidelberg (2003)
10. Zhang, W., Noble, A., Brady, M.: Adaptive non-rigid registration of real time 3D ultrasound to cardiovascular MR images. In: Karssemeijer, N., Lelieveldt, B. (eds.) IPMI 2007. LNCS, vol. 4584, pp. 50–61. Springer, Heidelberg (2007)

Integrating Viability Information into a Cardiac Model for Interventional Guidance*

Helko Lehmann[1], Reinhard Kneser[1], Mirja Neizel[2], Jochen Peters[1], Olivier Ecabert[1], Harald Kühl[2], Malte Kelm[2], and Jürgen Weese[1]

[1] Philips Research Laboratories, Aachen, Germany
[2] Medical Clinic I, University Hospital of the RWTH Aachen, Germany

Abstract. It has been demonstrated that 3D anatomical models can be used effectively as roadmaps in image guided interventions. However, besides the anatomical information also the integrated display of functional information is desirable. In particular, a number of procedures such as the treatment of coronary artery disease by revascularization and myocardial repair by targeted cell delivery require information about myocardial viability. In this paper we show how we can determine myocardial viability and integrate the information into a patient-specific cardiac 3D model. In contrast to other work we associate the viability information directly with the 3D patient anatomy. Thus we ensure that the functional information can be visualized in a way suitable for interventional guidance. Furthermore we propose a workflow that allows the nearly automatic generation of the patient-specific model. Our work is based on a previously published cardiac model that can be automatically adapted to images from different modalities like CT and MR. To enable integration of myocardial viability we first define a new myocardium surface model that encloses the left ventricular cavity in a way that suits robust viability measurements. We modify the model-based segmentation method to allow accurate adaptation of this new model. Second, we extend the model and the segmentation method to incorporate volumetric tissue properties. We validate the accuracy of the segmentation of the left ventricular cavity systematically using clinical data and illustrate the complete method for integrating myocardial viability by an example.

Keywords: Scar tissue, papillary muscles, endocardial trabeculae, model-based segmentation, late enhancement, MRI, cardiac, interventional guidance.

1 Introduction

While the real-time images acquired during an image guided intervention such as a revascularization procedure provide some means for orientation and navigation they often do not display all the information required for therapeutic decisions and outcome control. In [4] and [9] it has been demonstrated that many interventions may benefit

* The research leading to these results has received funding from the European Community's Seventh Framework Programme (FP7/2007-2013) under grant agreement n° 224495 (euHeart project).

N. Ayache, H. Delingette, and M. Sermesant (Eds.): FIMH 2009, LNCS 5528, pp. 312–320, 2009.
© Springer-Verlag Berlin Heidelberg 2009

from the display of an accurate anatomical 3D model as an overlay on the fluoroscopy image stream. However, besides the anatomical information the display of additional functional information is often desirable. For example, an infarcted myocardial region can only regenerate following a revascularization of the blood supplying coronary arteries if sufficient viable tissue is present in the region [6]. Similar viability information is required for myocardial repair, where drugs or cells are applied targeted to the infarcted tissue.

In this paper we show how we can determine myocardial viability and integrate the information into a patient-specific cardiac 3D model suitable for interventional guidance. To increase efficiency and to decrease inter-observer variability we propose a workflow that allows fully automatic generation of the patient-specific cardiac model and semi-automatic integration of viability information. Our approach requires the following application-specific extensions of the general comprehensive cardiac model of [3] and [8]:

- As motivated in [7], to increase the robustness of the viability estimation, we systematically exclude the endocardial trabeculae and papillary muscles from the myocardium model of [8]. Furthermore, we extend the segmentation process to interpolate a smooth surface in areas of the myocardium where these structures are attached.
- To provide the functional information in a way that is suitable for image guided interventions we associate the viability information directly with the 3D patient anatomy represented by the cardiac model. To this end we extend the part of the model describing the myocardium by a volumetric mesh. Other methods have been developed for visualization and diagnosis of viability [5] [12]. However in contrast to our approach they do not maintain the 3D anatomical context and are therefore less suitable for interventional guidance.
- To integrate the viability information, we adapt the cardiac model to a whole heart 3D MRI data set that matches a late enhancement 3D MRI data set of the same patient (similar approach to [2] for cine data). Thereby we avoid an additional segmentation step of the ill-defined myocardium contours in the late enhancement data. We finally employ a gray-value thresholding method to classify volumetric mesh elements representing myocardium tissue into viable and non-viable.

The paper is structured as follows. In Section 2 we describe the workflow from data acquisition to a patient-adapted integrated model for interventional guidance. In Section 3 our technical extensions to the cardiac model and the associated model-based segmentation process of [3] and [8] are described in detail. We validate the improved myocardium segmentation in Section 4 and illustrate the complete method by an example. In Section 5 we conclude and give an outlook on the next steps and other applications of the cardiac model.

2 Clinical Workflow

An MRI study of a patient with suspected acute myocardial infarction consists of a number of different imaging steps to establish both anatomy and function. For our approach we assume that the patient is undergoing a non-contrast enhanced

steady-state free-precession scan of the whole heart (WH) to examine anatomical properties. To determine myocardial viability a 3D late enhancement (LE) technique with phase sensitive inversion recovery (PSIR) is employed (see Fig. 1). During the image acquisitions it is ensured that both the whole heart image and the LE image are acquired in the same heart phase and breathing phase by employing a navigator technique. Thereby misregistrations between the WH image and the LE image due to heart motion and respiratory motion can be avoided.

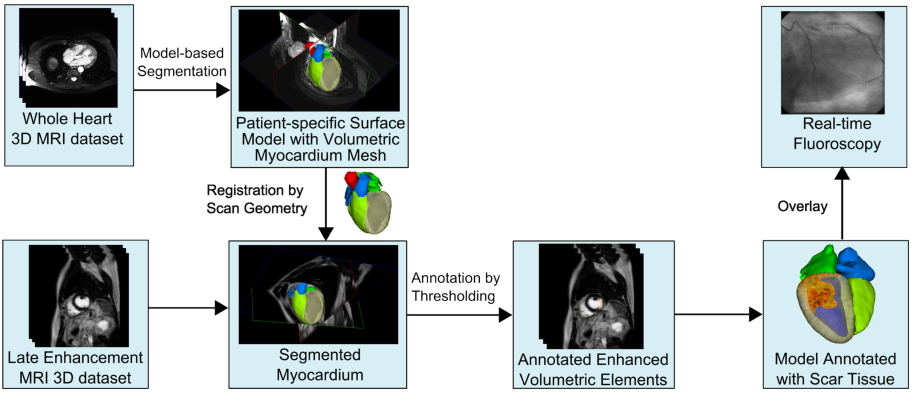

Fig. 1. Illustration of the workflow

The acquired whole heart data set is automatically segmented using a comprehensive cardiac surface model where the myocardium component comprises additionally a fine volumetric mesh of tetrahedrons. The resulting adapted model represents the patient's cardiac anatomy as well as a complete covering of the myocardium by volumetric mesh elements. Since the WH image and the LE image have been acquired in the same heart phase and breathing phase, the model adapted to the WH image can be mapped to the LE image using the common patient coordinate system. However, misalignments between the WH image and the LE image are possible and can be primarily attributed to patient movement. They can be corrected in an additional registration step if required. Mapping of the model results in a segmentation of the myocardium and the left ventricular (LV) cavity in the LE image. Then the volumetric mesh elements of the myocardium model are annotated if the contained voxels in the LE image are classified as scar tissue. Since in LE images the scar tissue appears hyperintense in contrast to dark normal myocardium tissue, voxels in the LE image can be classified as scar if they exceed a certain intensity threshold. Here we assume this threshold to be manually selected. The annotated model is finally displayed during intervention, e.g. as an overlay over a real-time fluoroscopy image.

3 Integration of Scar Tissue Information into a Cardiac Model

In the above described workflow we rely heavily on the segmentation of the heart in the WH image as described in [3] and [8]. However our envisioned application requires specific improvements, which we describe in this section.

3.1 Model-Based Whole Heart Segmentation

The essential idea of the model-based segmentation of [3] and [8] is to adapt a triangular surface mesh to an image while additionally considering a shape constraint. The adaptation is performed by iterating a boundary detection step and a mesh deformation step.

During the boundary detection step for each mesh triangle i a new target point x_i^{target} is searched in the neighborhood of the current location by maximizing a triangle specific image feature response function. At the same time a reliability function w_i is computed which increases with the feature response and decreases with the distance of the target point to the original triangle. During the mesh deformation step the mesh is modified such that

$$E_{tot} = \underbrace{\sum_{i=1}^{V} \sum_{j \in N(i)} \sum_{k=1}^{K} \omega_{i,k} ((v_i - v_j) - (T_k[m_i] - T_k[m_j]))^2}_{E_{int}} + \alpha \cdot \underbrace{\sum_i w_i \cdot D(x_i^{target}, c_i)^2}_{E_{ext}} \quad (1)$$

is minimized.

The shape constraint is modeled by the internal energy function E_{int}, which increases if the vector $(v_i - v_j)$ between a model point with index i and a neighboring model point with index $j \in N(i)$ deviates from the corresponding vector of a transformed mean shape. The respective transformation models the variability of the mean shape m_i and is defined via the affine transformations $T_k[m_i]$ and the weights $\omega_{i,k}$. The external energy E_{ext} describes how well the mesh fits to the image. To this end, for all triangles i the deviations D of the triangle center c_i from the corresponding image target point x_i^{target} of the boundary detection step are accumulated.

While the mean shape is determined from a set of reference meshes the image feature response functions are learned from a set of reference meshes with corresponding images, for details see [3]. In the following we refer to a model as a triangle mesh together with the associated image feature response functions.

3.2 Robust Model-Based Myocardium Segmentation

To quantify scar tissue in the myocardium an accurate distinction of the myocardium tissue from the LV cavity is required since in LE images the intensity of the LV blood pool is very similar to contrast enhanced scar tissue in the myocardium. However, the exact segmentation of the blood pool from other tissue in WH images is difficult and may result in large inter-observer variability as small structures such as trabeculae and papillary muscles cannot be accurately identified. More robust results can be achieved by considering trabeculae and papillary muscles to be part of the LV cavity during segmentation [7]. To achieve similar robust results using model-based segmentation we follow this approach and modify the model M_{Ref} and adaptation of [8] accordingly.

The segmentation model is the result of an automatic learning process based on image data annotated with reference meshes. Therefore, as a first step we modify these meshes such that, in contrast to the reference meshes used to train the model M_{Ref}, the submesh representing the LV cavity encloses all the trabeculae and papillary muscles (see Fig. 2). Based on the new reference meshes both the mean shape model and the new image feature response functions are learned, resulting in the new cardiac model M_{PT}.

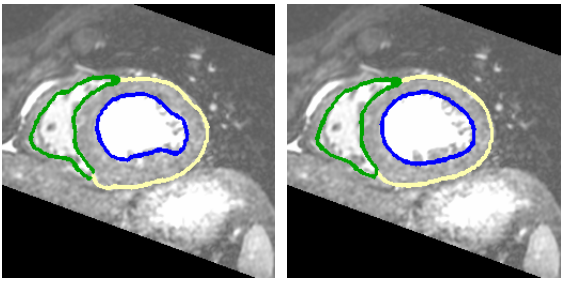

Fig. 2. Reference meshes used to train models M_{Ref} (left) and M_{PT} (right)

However, adapting the model M_{PT} to image data still results in larger deviations of the adapted meshes to the desired segmentation result, particularly in areas where trabeculae and papillary muscles are attached to the myocardium. This is due to the fact that in these areas boundaries are searched and detected although the segmentation cannot be supported by boundaries in the image.

Based on the assumption that trabeculae and papillary muscles distract the segmentation only in certain areas of the left ventricle, we identify these critical regions automatically during the model training and modify the segmentation process to rely in critical regions on the shape model. More precisely, we first use the model M_{PT} to segment the training images and calculate from this segmentation for each triangle of the model and each image the error as the distance between the reference triangle and the adapted triangle (see Fig. 3a). If this distance is larger than some threshold T_d the segmentation at this triangle is regarded as unreliable in the particular image. A triangle of the model is defined as *critical* if it was classified as unreliable for at least T_N training images (the resulting critical triangles for suitable parameters are highlighted in Fig. 3b).

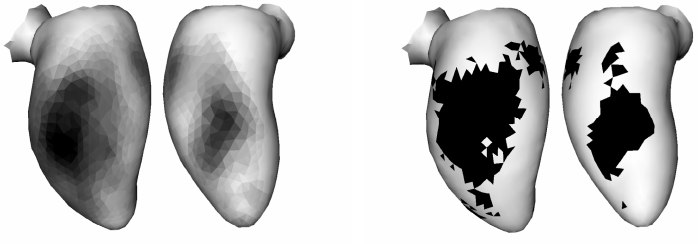

(a) (b)

Fig. 3. a) Mean error over all images (large error dark) b) Critical triangles (dark)

To allow for the accurate adaptation of critical triangles the model-based segmentation procedure is extended by performing two different iteration cycles instead of one. During the deformation step of the first cycle the influence of the boundary detection is disabled for all critical triangles by setting w_i in (1) to 0. Thereby critical triangles are geometrically interpolated from neighboring triangles only based on the

shape model. During the deformation step of the second cycle, w_i is determined as in [8] for all triangles but the boundary detection step is modified to detect boundaries only in a very small neighborhood of each triangle. Hence, both critical as well as non-critical triangles may adapt to nearby image boundaries, e.g. if a boundary is present in the current image that has not been reliably present in the training data.

3.3 A Volumetric Mesh for the Myocardium

The meshes in M_{Ref} and M_{PT} are surface meshes that allow vertices, edges and triangles to be annotated and used for quantification of geometrical properties such as a distance between anatomical landmarks and the surface area of a sub-mesh. We may also represent a tissue type as the volume enclosed by a surface mesh if the tissue types can be separated by a well defined surface. However, if the tissue types are not separable in this way, such as viable and non-viable myocardium tissue, other means have to be considered. Hence, to enable classification and representation of these tissue types we propose to cover the volume enclosed by the myocardium surface with a volumetric mesh of tetrahedrons.

Since the covering of the myocardium volume with a volumetric mesh is not driven by image characteristics but only shape characteristics of the myocardium surface, the volumetric mesh should not influence the result of the surface adaptation. Hence, to enable integration with the model-based segmentation the volumetric mesh must fulfill the surface constraints of the myocardium, i.e. surface vertices and edges must not be altered. Thereby, no new points (*Steiner points*) should be generated on the myocardium surface, i.e. additional vertices may only be introduced within the volume of the myocardium. To allow a homogeneous resolution of the tissue characterization the volume elements should be similar in size and approximately regular.

Furthermore, a correspondence between volumetric mesh elements of cardiac models adapted to different patients is desirable, as it allows a mapping of volumetric mesh elements to standard anatomical regions of the myocardium, e.g. according to the American Heart Association [1]. Consequently, we generate the volumetric mesh only once for the mean model by constrained Delaunay tetrahedralization [11]. During the adaptation of the mean model to the patient image data, first the surface model is deformed as explained in Section 3.2. Second, the deformation of the volumetric mesh is performed by interpolating the vertex coordinates of all vertices located inside the myocardium from the vertex coordinates on the myocardium surface. This is realized by interpolating for each Steiner point a transformation from the transformations T_k computed for the adapted surface. Then, the external energy in equation (1) is set to 0, the vertex coordinates of surface points in the internal energy term are fixed to the values resulting from the surface adaptation, and the resulting (internal) energy function is minimized for the Steiner points only.

4 Results

We evaluate the improved segmentation of the left ventricle on 43 WH images acquired from ischemic disease patients to inspect the coronary arteries. The images

have been acquired on Philips Intera and Achieva 1.5T scanners at end-diastolic phase over various cardiac cycles and breathing compensated. For all 43 data sets manually corrected reference meshes have been created enclosing the trabeculae and papillary muscles in the LV cavity as described in Section 3.2. A subset of 20 of these reference meshes have been created with special care by averaging the annotations of 5 technical and clinical experts. These datasets serve in the following as ground truth. Image feature response functions are trained using all 43 images and remain unchanged for all experiments. The other components of the models, i.e. the respective mean shape and critical triangle set are trained and evaluated on the subset of 20 patients in a leaving-one-out fashion using respectively one data set for evaluation and 19 sets for training. Evaluation is performed by comparing the automatically adapted meshes to the ground truth meshes. Both the symmetrized mean Euclidean "surface-to-patch" distance as described in [8], averaged over all triangles of the left ventricle, and the distribution of these distances serve as error measures. They are shown in Table 1.

We compare the three models M_{Ref}, M_{PT}, M_{PT} + *2 cycle segm*. The models M_{Ref} and M_{PT} are both trained in the same setup where the only difference is that the old uncorrected reference meshes are used to train M_{Ref} while M_{PT} is trained using the new reference meshes enclosing the trabeculae and papillary muscles in the LV cavity. For M_{PT} + *2 cycle segm* critical triangles are determined automatically and additional segmentation cycles are added as described in Section 3.2.

Note that for a large range of values for the parameters defining the set of critical triangles similar errors can be obtained. We achieved best results using $T_d = 0.8$mm and $T_N = 15$. These parameters are also used to generate the error values presented in Table 1 and Fig. 3b.

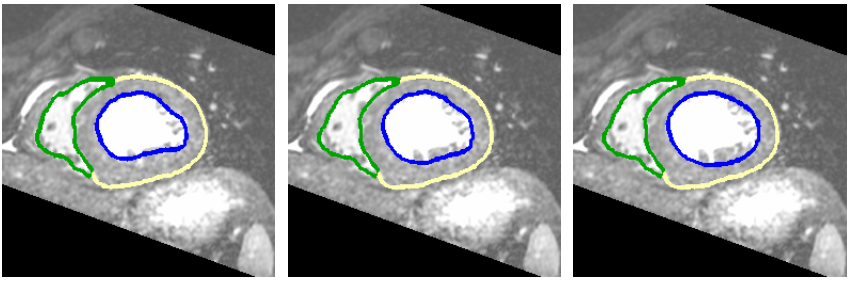

Fig. 4. Typical segmentation results (left to right: M_{Ref}, M_{PT}, M_{PT} + *2 cycle segm*)

Typical segmentation results are displayed in Fig. 4. The experiments show that the adapted model M_{Ref} inaccurately follows trabeculae and papillary muscles resulting in a mean error of 0.75 mm and a large amount of distant triangles. The distances decrease if model M_{PT} is used but the segmentation results are still unsatisfying. The model M_{PT} + *2 cycle segm* provides good results, both in terms of error and from visual inspection.

Table 1. Mean errors and distribution for the left ventricle

Model/Segm.	Mean Error (mm)	Percentage of Triangles with error range (%)		
		< 1.0 mm	1.0 – 2.0 mm	> 2.0 mm
M_{Ref}	0.75	69.7	29.3	1.0
M_{PT}	0.65	83.1	16.9	0.0
M_{PT} + *2 cycle segm.*	0.56	97.4	2.6	0.0

To illustrate the annotation of viability information in the new cardiac model we follow the workflow described in Section 319. To classify myocardial tissue into viable and non-viable we employ a simple thresholding algorithm. Thereby the tissue covered by a tetrahedron is considered non-viable if a number of samples acquired within the volume of the tetrahedron have intensities larger than a manually adjusted threshold (see Fig. 5).

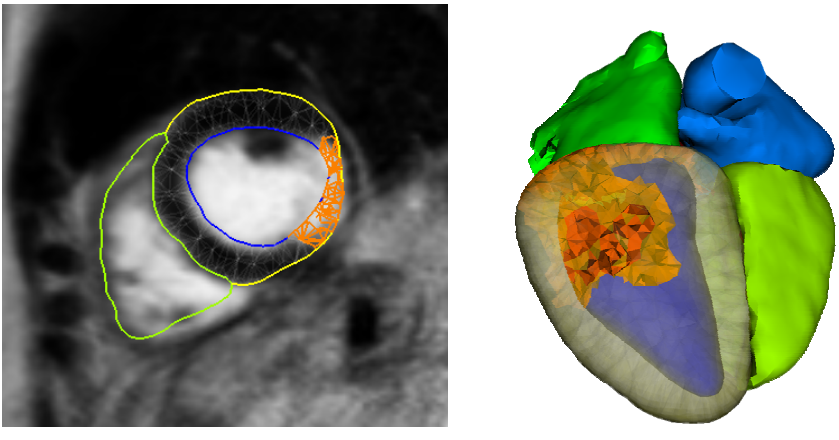

Fig. 5. A cut through the model-annotated LE data (left) and the model (right)

5 Conclusion

We have presented a workflow that allows the integration of viability information into a patient-specific cardiac model. By associating the viability information directly with the 3D patient anatomy we ensure that the model is suitable for interventional guidance, e.g. for revascularization procedures as a roadmap overlaying a real-time fluoroscopy stream.

As we aim to generate the model automatically we have extended a model-based segmentation method for the heart. In particular, we have improved the segmentation of the myocardium tissue in whole heart MR images to allow more robust automatic delineation of myocardium tissue. We have validated the improvements using clinical data from patients with ischemic disease. Furthermore, we have integrated the automatic adaptation of a volumetric mesh covering the myocardium into the segmentation process. We have shown how this volumetric mesh is used to associate functional information such as viability with the patient-specific anatomical model. Thereby we have demonstrated that we can perform viability measurements based on

a mapping of the patient-specific model to an appropriate 3D late enhancement data set and the application of a threshold-based method.

For clinical use, an improved registration between the adapted cardiac model and the LE image may be required. Furthermore the manual threshold used to differentiate between non-viable and viable tissue may be replaced by an automatic tissue classification. Future work may also address the integration of further information such as myocardial perfusion data and supply territories into the cardiac model.

The volumetric mesh model of the myocardium can also be used to perform biomechanical simulations, if mechanical properties are associated with each volumetric element

Acknowledgements

We thank M. Breeuwer, P. Ermes, G. Hautvast, F. Gerritsen of Philips Medical Systems Healthcare Informatics (Best, The Netherlands) for providing MR data and modified ground truth.

References

1. Cerqueira, M.D., et al.: Standardized myocardial segmentation and nomenclature for tomographic imaging of the heart: A statement for healthcare professionals from the Cardiac Imaging Committee of the Council on Clinical Cardiology of the American Heart Association. J. of the American Society of Echocardiography: official publication of the American Society of Echocardiography 15(5), 463–467 (2002)
2. Dikici, E., O'Donnell, T., Setser, R., White, R.D.: Quantification of Delayed Enhancement MR Images. In: Barillot, C., Haynor, D.R., Hellier, P. (eds.) MICCAI 2004. LNCS, vol. 3216, pp. 250–257. Springer, Heidelberg (2004)
3. Ecabert, O., et al.: Automatic Model-Based Segmentation of the Heart in CT Images. IEEE Trans. Med. Imaging 27(9), 1189–1201 (2008)
4. Gutiérrez, L.F., et al.: Technology Preview: X-ray Fused With Magnetic Resonance During Invasive Cardiovascular Procedures. Catheterization and Cardiovascular Interventions 70(6), 773–782 (2007)
5. Hennemuth, A., et al.: A Comprehensive Approach to the Analysis of Contrast Enhanced Cardiac MR Images. IEEE Trans. Med. Imaging 27(11), 1592–1610 (2008)
6. Kim, R.J., et al.: The Use of Contrast-Enhanced Magnetic Resonance Imaging to Identify Reversible Myocardial Dysfunction. N. England J. Med. 343(20), 1445–1453 (2000)
7. Papavassiliu, T., et al.: Effect of Endocardial Trabeculae on Left Ventricular Measurements and Measurement Reproducibility at Cardiovascular MR Imaging. Radiology 236(1), 57–64 (2005)
8. Peters, J., et al.: Automatic Whole Heart Segmentation in Static Magnetic Resonance Image Volumes. In: Ayache, N., Ourselin, S., Maeder, A. (eds.) MICCAI 2007, Part II. LNCS, vol. 4792, pp. 402–410. Springer, Heidelberg (2007)
9. Rhode, K.S., et al.: A system for real-time XMR guided cardiovascular intervention. IEEE Trans. Med. Imaging 24(11), 1428–1440 (2005)
10. Sermesant, M., et al.: Cardiac function estimation from MRI using a heart model and data assimilation: Advances and difficulties. Medical Image Analysis 10(4), 642–656 (2006)
11. Si, H., Gaertner, K.: Meshing Piecewise Linear Complexes by Constrained Delaunay Tetrahedralizations. In: Proc. of the 14th International Meshing Roundtable, pp. 147–163 (2005)
12. Termeer, M., et al.: CoViCAD: Comprehensive Visualization of Coronary Artery Disease. IEEE Trans. Vis. Comput. Graph 13(6), 1632–1639 (2007)

3D TEE Registration with X-Ray Fluoroscopy for Interventional Cardiac Applications

Ameet Jain, Luis Gutierrez, and Douglas Stanton

Philips Research North America,
Briarcliff Manor, New York

Abstract. Live 3D trans-esophageal echocardiography (TEE) and X-ray fluoroscopy provide complementary imaging information for guiding minimally invasive cardiac interventions. X-ray fluoroscopy is most commonly used for these procedures due to its excellent device visualization. However, its challenges include the 2D projection nature of the images and poor soft tissue contrast, both of which are addressed by the use of live 3D TEE imaging. We propose to integrate 3D TEE imaging with X-ray fluoroscopy, providing the capability to co-visualize both the interventional devices and cardiac anatomy, by accurately registering the images using an electro-magnetic tracking system. Phantom trials validating the proposed registration scheme indicate an average accuracy of 2.04 mm with a standard deviation of 0.59 mm. In the future, this system may benefit the guidance and navigation of interventional cardiac procedures such as mitral valve repair or patent foramen ovale closure.

Keywords: 3D TEE, X-ray, EM tracking, Image fusion.

1 Introduction

Cardiovascular disease is the single largest source of death in the US, accounting for about 871,500 deaths in 2004. It is estimated that about 37% of the adult population, or over 80 million people, has some form of the disease. Minimally invasive interventions, such as percutaneous transluminal coronary angioplasty, are a feasible option for many patients. Around 1.3 million such procedures were performed in the US alone in 2005 [1]. X-ray fluoroscopy is the standard modality for guiding these catheter-based cardiac interventions due to excellent device visualization - and in spite of poor cardiac anatomy visualization and 3D context. However, more complex procedures such as pulmonary vein isolation, patent foramen ovale closure, and mitral valve prolapse repair, are growing in case numbers, and these require additional imaging information for successful guidance and navigation.

To help overcome the current limitations of interventional X-ray imaging, attempts have been made to integrate 3D imaging like CT/CBCT (Cone Beam Computed Tomography) [2,3]. Various XMR (Xray Magnetic Resonance) platforms for fusing MR images with X-ray have also been proposed [4,5,6]. Electroanatomic mapping has also been integrated with these XMR suites [7], or with

N. Ayache, H. Delingette, and M. Sermesant (Eds.): FIMH 2009, LNCS 5528, pp. 321–329, 2009.
© Springer-Verlag Berlin Heidelberg 2009

MR alone [8]. One of the hurdles for the adoption for these technologies has been the higher cost of treatment involved. The recent availability of live 3D transesophagal echocardiography (TEE) offers soft tissue contrast and volumetric imaging, enabling easy visualization of complex cardiac anatomy and valvular function that is complementary to X-ray fluoroscopy (Figure 1). Fusion of these two modalities may allow physicians to simultaneously visualize interventional devices and their cardiac targets in a manner that is not routinely possible today. This kind of a visualization can be beneficial in a variety of procedures in electro physiology or structural heart repair procedures, where currently the cardiac anatomy is not visible and the procedures are done blindly. This multimodality image guidance has the potential for improving the clinical outcomes and reducing the time of these challenging procedures.

Previous reports have shown the utility of combining live US images with CT/MR for general interventional guidance [9,10]. Purely US-guided cardiac interventions without the aid of X-ray, have also been proposed [11,12], though they require a departure from the current clinical paradigm. 2D intra-cardiac echocardiography images have been fused with CB-CT datasets [3], while 2D intra-vascular US slices have also been registered to live fluoroscopy [13]. In contrast, live 3D ultrasound (US) offers an advantage to these 2D techniques since orienting the imaging slice in a 2D scan can be challenging in an interventional setting. In this spirit, 3D TTE (Trans-Thoracic Echocardiography) US volumes have been registered to X-ray fluoroscopy [14]. However, TTE imaging does not lend itself smoothly to interventional cardiac use due to sterility and ergonomic issues, while TEE is a more common platform.

In this publication, we propose to integrate 3D TEE volumes with X-ray fluoroscopy images, providing the capability for the visualization of both interventional devices and live cardiac anatomy. We propose to do so with the aid of an electromagnetic (EM) tracking system and present the performance.

Fig. 1. Left: A contrast enhanced cine X-ray with the left ventricular chamber visible; the rest of the heart's only faintly visible (courtesy UC-Denver, Cardiac Cath-Lab). Middle: Sample en-face view of the mitral valve acquired with the Philips X7-2t live 3D TEE probe. Right: Color doppler flow image displaying regurgitation of valve as reverse flow from the left ventricle into the left atrium, also acquired with the X7-2t probe.

2 Methods

As shown in Figure 2, to achieve intra-operative registration and fusion, we propose to use an EM tracking system. Both the TEE and the X-ray coordinate frames are independently calibrated to the tracking system. We rigidly attach sensors on the TEE probe, and perform a one-time calibration to determine the 6-DOF (degree-of-freedom) rigid body transform between the TEE image coordinates and the EM sensors attached to the TEE probe (${}^{teeSensor}F_{teeVolume}$). Similarly, a tracking sensor is rigidly mounted to the patient table, and the transformation between the X-ray coordinate frame & this tracking sensor is evaluated using a one-time calibration algorithm (${}^{xrayFrame}F_{emTable}$).

$$
\begin{aligned}
{}^{xrayImage}F_{teeVolume} = {} & {}^{xrayImage}F_{xrayFrame} \times {}^{xrayFrame}F_{emTable} \\
& \times {}^{emTable}F_{teeSensor} \times {}^{teeSensor}F_{teeVolume}
\end{aligned}
$$

The equation above combines the transformation matrices and allows us to spatially relate the 3D TEE and X-ray information. ${}^{teeSensor}F_{teeVolume}$ and ${}^{xrayFrame}F_{emTable}$ are pre-computed transforms, while ${}^{emTable}F_{teeSensor}$ is provided in real-time by the tracking system. ${}^{xrayImage}F_{xrayFrame}$ is the projection transformation that projects any 3D object location on to its corresponding 2D location in the X-ray image, and can be computed using the C-arm pose & intrinsic calibration (both available in the image headers). Together, they estimate ${}^{xrayImage}F_{teeVolume}$, a 3D to 2D transformation matrix that can overlay any voxel from a 3D TEE volume on its corresponding pixel location on the 2D X-ray projection image. Note that, since $F_{emTable}$ is EM-tracked, it allows us to (a) move the EM field generator whenever desired; & (b) keep the suite permanently pre-calibrated (cardiology tables are usually motion encoded). Both these are critical from a clinical ease-of-use perspective.

Sensor Mounting on TEE. As illustrated in Figure 3 (left), two EM sensors were experimentally fixed on the TEE probe, with one on each side of the transducer array and inclined at approximately 40^o from each other. The

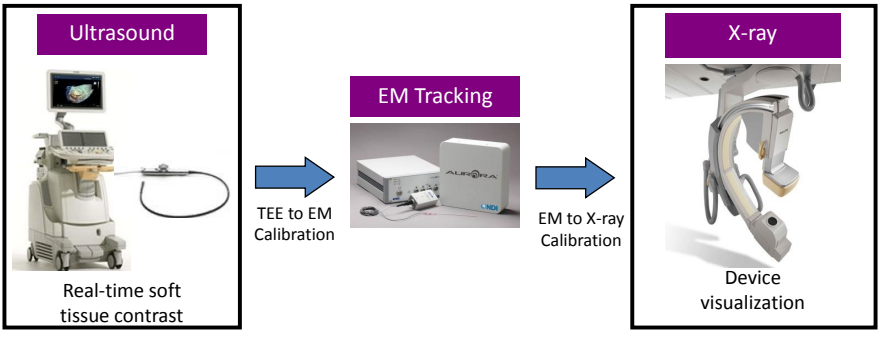

Fig. 2. The proposed overall approach to integrate the TEE and X-ray images for real-time visualization of both the cardiac anatomy and the interventional devices

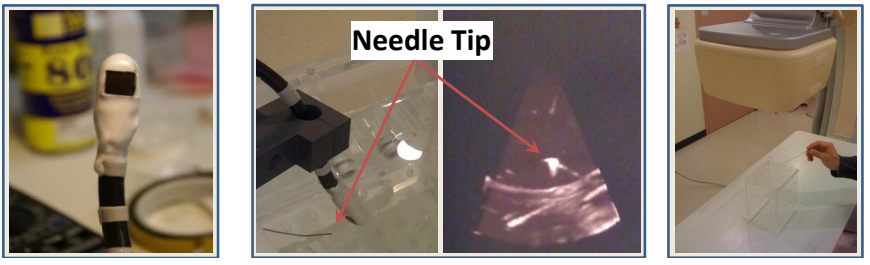

Fig. 3. Close-up of the TEE probe after the sensors have been mounted. The white material is the liquid plastic layer covering the sensors (left). Physical setup for EM-TEE calibration, showing the EM-tracked needle with the TEE probe in a water bath, and the corresponding US image (middle). The water was not doped with any solvent to change the speed of sound. The X-ray to EM calibration phantom with the EM based localization of each fiducial marker (right).

sensors were taped to the probe with thin silicone self vulcanizing tape and the assembly was coated with a liquid plastic layer. The wires for the sensors were passed through a thin catheter sheath. A window to the surface of the matrix array was preserved. The assembly is intended to keep the sensors rigid relative to the probe. Using the vendor software (NDI 6D Architect), we consolidated the relative measurements from the two sensors into a single 6-DOF reference for real-time tracking.

3 Experiments, Results and Discussion

We quantitatively evaluated the proposed registration framework on phantom experiments. Live 3D TEE imaging was performed with a Philips X7-2t probe and an iE33 ultrasound system (Philips Healthcare, Andover, MA). The TEE probe was used in the live 3D mode at an imaging depth of 10 cm, generating volumes about $10.5 \times 10.5 \times 4.7$ cm at 30 fps and a spatial resolution of $0.74 \times 0.74 \times 0.74$ mm. Note that for the purposes of these experiments, 3D streaming capability of the US machine have not been employed. Instead the validation has been done using static data capture on the machine. X-ray fluoroscopy was performed on a Philips Allura Xper FD-10 (Philips Healthcare, Andover, MA). Images were acquired as rotational runs with pre-calibrated view geometry for images acquired at 30 fps for 4 seconds, RAO 55^o to LAO 55^o. The Aurora system (Northern Digital Inc.) was used for EM tracking.

EM to TEE Calibration. As shown in Figure 3 (middle), an EM-tracked needle-tip was imaged in multiple poses using the TEE probe, and the tip locations were manually segmented in each volume. These locations relate to their corresponding EM tracked locations by the calibration matrix [15], which was computed by an iterative point-cloud registration algorithm that minimized the L_2 norm. Though 3 such points are sufficient to compute the 6-DOF calibration,

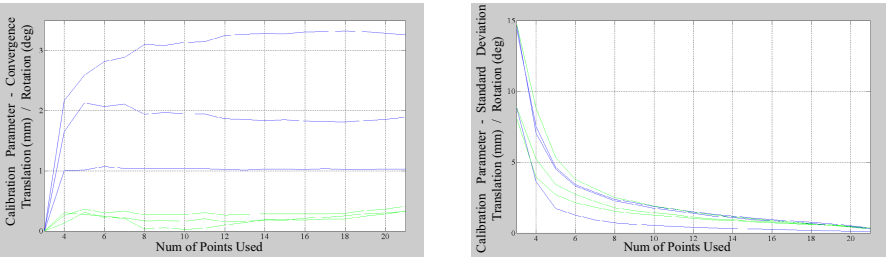

Fig. 4. The convergence of the calibration parameters (left) and the standard deviation across multiple runs (right) as a function of number of points used

in practice more are needed owing to inherent errors. Results from randomized leave-some-out tests are plotted in Figure 4, suggesting that 15 points are sufficient to calibrate the probe and for the parameters to stabilize (translation - blue, rotation - green). 15 points provide a calibration with a mean residual error of 1.42 mm (STD 0.35 mm) and a mean accuracy of 1.84 mm (STD 0.44 mm).

To further estimate the accuracy of the calibration, an additional 25 EM tracked needle-tips (5 batches of 5 individual locations each) were imaged using the TEE probe. The validation is intrinsically tricky, as the TEE sensors can only be measured by the (error-prone) tracking system. The manually segmented needle tips from TEE were transformed into EM coordinates using the calibration, which were compared to the corresponding EM tracked measurements of the tips. As shown in Table 1, the mean EM to TEE calibration accuracy as measured by this experiment is 3.01 mm (± 1.28 *mm*). Note that datasets 3 & 5, which were relatively further in distance to the EM field generator when compared to datasets 1, 2 & 4, exhibit a 2.14 *mm* greater error. This is due to the fact that the needle is tracked using only a single 5-DOF sensor, making it sensitive to EM tracking errors, and the ground truth less accurate. Nevertheless, it provides an estimate for the expected ballpark accuracy.

EM to Xray Calibration. To register the EM tracking system to the X-ray reference frame, a custom-built phantom with 12 embedded steel beads (Figure 3 - right) was imaged using the X-ray rotational run. Each bead was identified manually on two well-separated X-ray images and the epipolar constraint was used to reconstruct their 3D coordinates in the X-ray reference frame. The same beads were identified in the EM frame by touching them with a calibrated EM-tracked pointer. A point-based registration algorithm matched the corresponding points, computing the rigid transform between the EM and X-ray coordinate frames.

The mean residual errors from 23 independent calibrations was 1.58 mm $\pm$ 0.69 mm. To further estimate the calibration accuracy, 5 batches of 5 EM tracked needle-tips were reconstructed using X-ray runs, and transformed into the EM frame. Comparing these locations to those measured by the EM tracking system provided an accuracy of 2.90 mm ± 1.23 *mm* (Table 1). Again, inherent errors

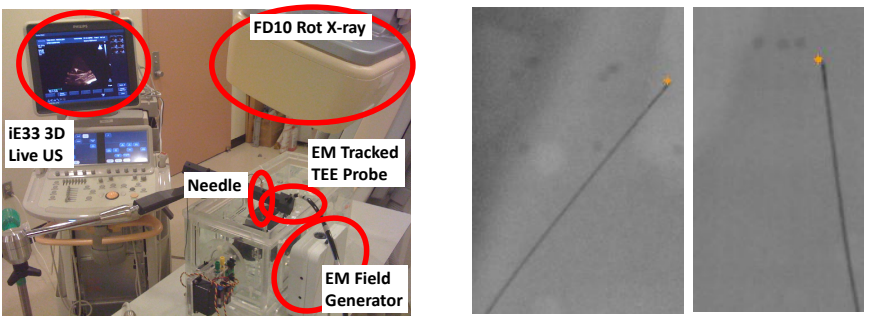

Fig. 5. The full experimental setup with both X-ray & 3D TEE modalities (left). A sample needle tip from a TEE volume is superimposed on two X-ray images separated by 55 deg (right).

of tracking system affect the EM measurements of the needle, with datasets 3 & 5 exhibiting 2.11 mm greater average error than datasets 1, 2 & 4.

TEE to X-ray Registration Accuracy. As shown in Figure 5, we imaged 5 batches of 5 needle-tips with both the TEE and X-ray imaging systems. The needle tips were manually segmented in each TEE volume, and projected into the X-ray reference frame using the computed ${}^{xrayFrame}F_{teeVolume}$ registration transform. The X-ray rotational run provided accurate ground truth location of each tip. The needles were manually segmented in two selected X-ray frames (with about 45^o separation) in each rotational run and their 3D positions reconstructed. In each dataset, both the needle and TEE positions were randomly altered to reasonably cover the workspace. Calibration transforms were chosen so as to compute a representative TEE to X-ray registration, the result being tabulated in Table 1. The average performance of the system was 1.92 mm $\pm$ 0.48 mm. Note that the X-ray-to-TEE error is lower than the tracker-to-TEE or tracker-to-Xray errors. This is due to the fact that the tracker measurements of the needle (single EM sensor) have a much greater error than the tracker measurements of the probe (two EM sensors), especially when they go further away from the EM field generator. This is also reflected in the higher STDs that the tracker-to-TEE and tracker-to-Xray experiments exhibit. It can be observed that this is a significant improvement over what has been reported in the literature. 3.14$\pm$3.13 mm was the reported accuracy for the registration of 2D ICE to CBCT volumes [3] and a mean accuracy of 8.81 mm was reported for the registration of 3D TTE with X-ray [14]. Our experiments demonstrate that an EM-guided approach to register 3D-TEE to X-ray images has the potential to provide accuracies in the order of 2 mm.

Robustness. To evaluate the sensitivity of the EM-based registration approach to the individual calibration protocols, 15 different EM to X-ray and 2 different EM to TEE calibrations were performed for datasets 2 & 3. This was

Table 1. Overall system accuracy, as evaluated using five independent trails. The accuracies of the individual calibrations are also shown.

Dataset Number	EM to TEE Accuracy (mm)	EM to X-ray Accuracy (mm)	X-ray to TEE Accuracy (mm)	EM Workspace
1	1.84	1.48	1.54	near-field
2	1.67	2.26	1.42	near-field
3	4.33	3.87	2.43	mid-field
4	2.94	2.42	2.41	near-field
5	4.28	4.46	1.80	mid-field
Average	3.01 ($\pm$1.28)	2.90 ($\pm$1.23)	1.92 ($\pm$0.48)	-

Table 2. The overall system accuracy (batches 2 & 3 only) as a function of 15 different EM-Xray calibrations and 2 different EM-TEE calibrations is reported in the first 2 rows. It shows that system is stable with respect to both the EM-TEE and EM-Xray calibrations. The bottom 2 rows show that the system is stable with respect to the region of use of the TEE probe around the EM field generator.

		EM to X-ray Calibration Trial														
		1	**2**	**3**	**4**	**5**	**6**	**7**	**8**	**9**	**10**	**11**	**12**	**13**	**14**	**15**
EM to TEE Calibration	**1**	1.2	1.2	1.2	1.9	3.4	2.1	1.5	2.8	2.0	1.8	1.9	1.5	1.8	1.6	1.5
	2	1.8	1.8	1.6	2.1	3.9	2.6	2.0	3.1	2.3	2.5	2.4	2.0	2.0	1.7	1.5
Near Field		2.1	2.1	1.9	2.2	2.9	2.2	2.5	3.1	2.4	2.6	2.5	2.4	1.8	1.7	1.3
Mid Field		1.5	1.6	1.3	2.1	4.9	3.0	1.5	3.2	2.1	2.4	2.4	1.6	2.1	1.8	1.6

done by varying the needle orientations and number of beads used during the calibration process. Table 2 details these results, indicating the overall stability of the approach. Similar registrations were performed for batches 1, 4 & 5 as well. Results from a total of 88 such TEE-Xray registration trials suggest an average performance of 2.04 $\pm$ 0.59 mm for the registered system. The sensitivity of the system was also tested as a function of the distance of the TEE probe to the EM field generator. Datasets 1, 2 & 4 were collected in the near-field (6-10 cm from the generator), while datasets 3 & 5 were collected in the mid-field (17-22 cm) of the EM workspace. Results from Table 2 suggest that the method is stable both in the near-field & the mid-fields, and the choice of the calibration protocol. Though not evaluated quantitatively here yet, it has empirically been observed that EM tracking exhibits large errors in the far-field (30-40 cm). We anticipate that the near and the mid-fields will be the regions of common use, with the near field being more desirable.

TEE to X-ray experiments on a realistic heart phantom. The phantom consists of a flexible tank system having large windows for ultrasound imaging on the sides. A realistic heart phantom [16] is mounted in this tank, with various servomechanisms and actuators that can drive cardiac motion (compression and

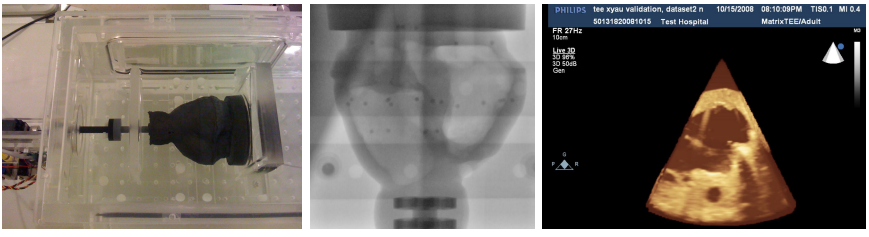

Fig. 6. A custom heart phantom (left) has been employed for in vitro experimentation. The phantom is visible under both X-ray (center) and US (right).

rotation). The heart is a replica of a human heart and has faithful external and internal detail. The replica is constructed of polyvinyl alcohol (in the cryogel form), which is suitably doped to provide realistic and/or enhanced visibility in various imaging modalities. For the purpose of studying organ morphology and its related medical imaging, the material mimics cardiac tissue very well. Furthermore, the doping levels allows us to control the level of contrast that each modality provides. Synchronization of the Phantom is achieved to external imaging equipment by data outputs which are directly connected to ECG or respiratory inputs of these machines. The servos are controlled by animation software from a P.C., or from a stand alone microprocessor. As shown in Figure 6, experimental data using this cardiac phantom has been collected using both rotational X-ray & 3D TEE, the results of which should be available by the conference.

4 Conclusion, Limitations and Future Work

Registration and fusion of real-time 3D TEE data with live fluoroscopy imaging has a significant potential for a plethora of procedures in interventional cardiology. We present an approach for achieving this registration with an average accuracy of 2.04 mm. The advantage of the proposed pre-calibrated approach is that it does not require additional registration protocols during intra-operative workflow. Shortcomings include dependence on EM tracking, which is known to be sensitive to field distortions. We will be further evaluating the robustness of such an approach, together with alternative approaches that could intra-operatively detect & correct for any potential distortions. In the future, table tracking and real-time rendering needs to be evaluated. Moreover, the work needs to be extended to fuse live 3D US images together with live 2D X-ray images to create a clinically usable tool. The clinical feasibility of combining these modalities together for guiding minimally invasive cardiac interventions can then be evaluated through *in vivo* trials. We anticipate that such an X-ray/US fusion system can eventually lead toward an excellent intra-operative planning and execution tool for cardiac guidance.

References

1. American Heart Association: Heart disease and stroke statistics, 2008 update at a glance. Technical report (2008)
2. Sra, J., Krum, D., Malloy, A., Vass, M., Belanger, B., Soubelet, E., Vaillant, R., Akhtar, M.: Registration of three-dimensional left atrial CT images with projection images obtained using fluoroscopy. Circulation 112, 3763–3768 (2005)
3. Sun, Y., Kadoury, S., Li, Y., John, M., Resnick, J., Plambeck, G., Liao, R., Sauer, F., Xu, C.: Image guidance of intracardiac ultrasound with fusion of pre-operative images. In: Ayache, N., Ourselin, S., Maeder, A. (eds.) MICCAI 2007, Part I. LNCS, vol. 4791, pp. 60–67. Springer, Heidelberg (2007)
4. Silva, R., Gutierrez, L., Raval, A., McVeigh, E., Ozturk, C., Lederman, R.: X-ray fused with MRI to target endomyocardial injections: validation in a swine model of myocardial infarction. Circulation 114, 2342–2350 (2007)
5. Yu, H., Fahrig, R., Pelc, N.J.: Co-registration of x-ray and MR fields of view in a hybrid XMR system. Journal of Magnetic Resonance Imaging 22, 291–301 (2005)
6. Rhode, K., Sermesant, M., Brogan, D., Hegde, S., Hipwell, J., Lambiase, P., Rosenthal, E., Bucknall, C., Qureshi, S., Gill, J., Razavi, R., Hill, D.: A system for real-time XMR guided cardiovascular intervention. IEEE TMI 24, 1428–1440 (2005)
7. Ector, J., Buck, S., Adams, J., Dymarkowski, S., Bogaert, J., Maes, F., Heidbühel, H.: Cardiac 3D MRI and fluoroscopy merging: a new approach for electroanatomic mapping to assist catheter ablation. Circulation 112, 3769–3776 (2005)
8. Reddy, V., Malchano, Z., Holmvang, G., Schmidt, E., Avila, A., Houghtaling, C., Chan, R., Ruskin, J.: Integration of cardiac MRI with 3D electroanatomic mapping to guide left ventricular catheter manipulation. J. Am. Coll. Cardiol. 44 (2004)
9. Penney, G., Blackall, J., Hamady, M., Sabharwal, T., Adam, A., Hawkes, D.: Registration of freehand 3D ultrasound and magnetic resonance liver images. Med. Image. Anal. 8, 81–91 (2004)
10. Wein, W., Brunke, S., Khamene, A., Callstrom, M., Navab, N.: Automatic CT-Ultrasound registration for diagnostic imaging and image-guided intervention. Medical Image Analysis 12, 577–585 (2008)
11. Linte, C., Moore, J., Wiles, A., Wedlake, C., Peters, T.: Virtual reality-enhanced ultrasound guidance: a novel technique for intracardiac interventions. JCAS 13, 82–94 (2008)
12. Vasilyev, N., Novotny, P., Martinez, J., Loyola, H., Salgo, I., Howe, R., Nido, P.: Stereoscopic vision display technology in real-time 3D echocardiography-guided intracardiac beating-heart surgery. JTCS 135, 1334–1341 (2008)
13. Wahle, A., Prause, G., Birgelen, C., Erbel, R., Sonka, M.: Fusion of angiography and ivus in-vivo: Establishing the absolute 3-D frame orientation. Transactions on Biomedical Engineering 46, 1176–1780 (1999)
14. Gutierrez, L., Shechter, G., Stanton, D., Dalal, S., Elgort, D., Manzke, R., Chan, R., Zagorchev, L.: Multimodality image guidance system integrating x-ray fluoroscopy and US image streams with EM tracking. In: SPIE Medical Imaging (2007)
15. Zhang, H., Banovac, F., White, A., Cleary, K.: Freehand 3D ultrasound calibration using an electromagnetically tracked needle. In: SPIE Medical Imaging, pp. 775–783 (2006)
16. Shelley Medical Imaging Technologies: Multi-modality Dynamic Heart Phantoms, http://www.simutec.com/dynamic_hearts.html

Multi-sequence Registration of Cine, Tagged and Delay-Enhancement MRI with Shift Correction and Steerable Pyramid-Based Detagging

Oscar Camara[1,⋆], Estanislao Oubel[1], Gemma Piella[1], Simone Balocco[1], Mathieu De Craene[1], and Alejandro Frangi[1,2]

[1] Center for Computational Imaging and Simulation Technologies in Biomedicine (CISTIB) - Universitat Pompeu Fabra (UPF) and Networking Biomedical Research Center on Bioengineering, Biomaterials and Nanomedicine (CIBER-BBN), Barcelona, Spain
[2] Institució Catalana de Recerca i Estudis Avançats (ICREA), Barcelona, Spain
oscar.camara@upf.edu

Abstract. In this work, we present a registration framework for cardiac cine MRI (cMRI), tagged (tMRI) and delay-enhancement MRI (deMRI), where the two main issues to find an accurate alignment between these images have been taking into account: the presence of tags in tMRI and respiration artifacts in all sequences. A steerable pyramid image decomposition has been used for detagging purposes since it is suitable to extract high-order oriented structures by directional adaptive filtering. Shift correction of cMRI is achieved by firstly maximizing the similarity between the Long Axis and Short Axis cMRI. Subsequently, these shift-corrected images are used as target images in a rigid registration procedure with their corresponding tMRI/deMRI in order to correct their shift. The proposed registration framework has been evaluated by 840 registration tests, considerably improving the alignment of the MR images (mean RMS error of 2.04mm vs. 5.44mm).

1 Introduction

Magnetic Resonance Imaging (MRI) allows to study different aspects of the heart anatomy and function depending on the acquisition settings. Different MR sequences, providing complementary data, are available such as cine (cMRI), tagged (tMRI) or delay-enhancement of Gadolinium (deMRI) MR imaging modalities. The combination of information on anatomy, cardiac function, global mobility, local deformations, strain maps and infarcted tissue given by these sequences could have a major impact on the knowledge about the heart. For instance, biomechanical cardiac models developed for simulation purposes will considerably improve their realism considering all these integrated data through data assimilation techniques.

The combination of MR-derived information asks for a registration procedure in order to have a common reference space where establishing correspondences

⋆ Corresponding author.

N. Ayache, H. Delingette, and M. Sermesant (Eds.): FIMH 2009, LNCS 5528, pp. 330–338, 2009.
© Springer-Verlag Berlin Heidelberg 2009

and finding correlations between complementary data. However, this MR image registration procedure is a challenging task due to the different quality and nature of the different MR acquisitions. Two major problems need to be dealt with: the presence of tags in tMRI and artifacts caused by respiration in all sequences. The former interferes in any registration involving tMRI since tags are not present in all modalities except in tMRI. Several works are available in the literature for the detagging of tMRI, mostly using Gabor filters [1] or 2D band-stop filters [2]. In this paper, we propose the use of a steerable pyramid image decomposition for detagging purposes since this technique is appropriate to extract high-order oriented structures by directional adaptive filtering. The second problem produces a shift between the 2D slices of a 3D volume since the patient cannot control the amount of air taken in each breath-hold acquisition. This issue could, for instance, lead to innaccurate strain analysis since these shift misalignments will have a strong influence on regional parameter and local direction estimations in the strain maps. Some authors have proposed shift correction algorithms for cMRI [3,4] that are based on maximizing the similarity between Long Axis (LA) and Short Axis (SA) acquisitions. Nevertheless, these algorithms need to be adapted to tMRI and deMRI since respiration artifacts are uncorrelated between different acquisitions and they have lower image quality than cMRI. Furthermore, in the case of tMRI, these shift correction algorithms will lead to tag misalignment, resulting in suboptimal anatomical structure correspondences. Finally, the SA and LA set of images are not always available in deMRI acquisitions.

In this work, we present a registration framework for the combination of information derived from cMRI, tMRI and deMRI, where the presence of tags and respiration artifacts are taken into account, as shown in Fig. 1. To the best of our knowledge, this is the first time that both problems are dealt with in the context of cMRI, tMRI and deMRI registration. The proposed method is based on using

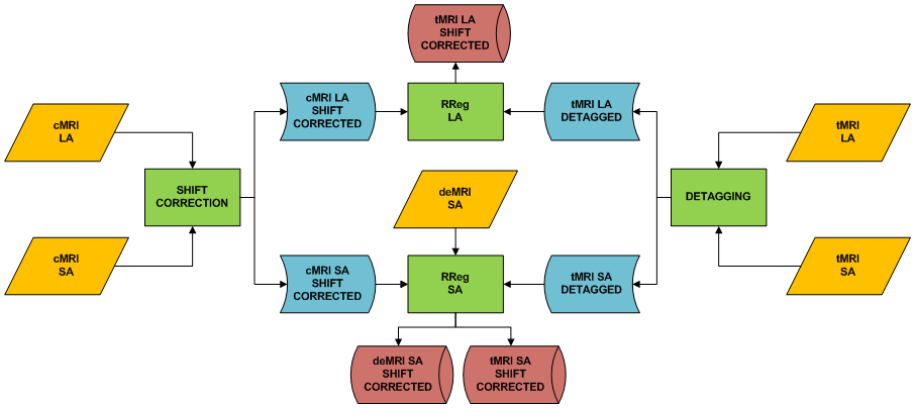

Fig. 1. Scheme of the proposed methodology. cMRI: cine MRI; tMRI: tagged MRI; deMRI: delay-enhancement MRI; LA: Long Axis; SA: Short Axis; RReg: Rigid Registration.

shift-corrected cMRI data as target images in a rigid registration with tMRI or deMRI. Cine MR images are shift-corrected with an alignment algorithm [3] that maximizes the similarity between the LA and SA images (left part of Fig. 1). As a pre-processing step, the tag lines in tMRI are removed using a steerable pyramid image decomposition (right part of Fig. 1). The detagged LA and SA tMRI will then be registered to its corresponding LA or SA shift-corrected cMRI (middle part of Fig. 1). Finally, the deMRI can also be registered to its corresponding LA and SA shift-corrected cMRI. The proposed registration framework has been evaluated with an experiment composed of 840 registration tests with known shifts.

2 Method

2.1 Shift Correction in cMRI

The shift correction of the cMRI is achieved with an algorithm proposed by Lotjonen et al. [3] for the correction of patient movements during the MR acquisition. Their method is based on maximizing the Normalized Mutual Information (NMI) between the LA and SA acquisitions by optimizing 3D slice-wise translations, thus neglecting rotations. Nevertheless, the optimization stage used in our implementation is slightly different since we make use of the analytical derivatives of the cost function, thus being able to use more efficient optimization algorithms such as the L-BFGS [5].

The transformation parameter vector, $\mathbf{p}$, includes 3D translations for every slice in SA and LA. Nevertheless, it must be pointed out that only in-plane translations are allowed due to the highly anisotropic dimensions of our data. Hence, the first $3n_s^{sa}$ values correspond to translations of SA slices, and the remaining $3n_s^{la}$ to translations in LA, where n_s^{sa} and n_s^{la} are the number of slices in SA and LA, respectively. Considering this order of parameters, the Jacobian $\partial x_i^{la}/\partial p_j$ representing the derivative at a given point of the LA image, $\mathbf{x}^{la}$, with respect to the transformation parameters, can be computed as:

$$\mathbf{J}(\mathbf{x}^{la}) = \partial x_i^{la}/\partial p_j = \begin{cases} a_{ik}, & j = 3Z(\mathbf{x}^{sa}) + k,\ k = 0:2 \\ 1, & j = 3n_s^{sa} + 3Z(\mathbf{x}^{la}) + i,\ i = 0:2 \\ 0, & otherwise \end{cases} \tag{1}$$

where a_{ik} are the components of the 3x3 matrix, $\mathbf{A}_{sl}$, defining the rigid transformation, $\mathcal{T}_{sl}$, from SA to LA, and $Z(\mathbf{x}^*)$ is the slice number corresponding to $\mathbf{x}^*$.

2.2 Detagging in tMRI

Tag lines appear in tMRI as dark stripes on the imaged tissue in a spatially encoded pattern (see Fig. 2) and undergo the same deformation as the tissue does, thus allowing temporal deformation analysis of 4D cardiac sequences. However, for inter-modal registration, the presence of tags in tMRI leads to a lack of correspondences with other imaging modalities. Therefore, a tag removal preprocessing step could be very beneficial for the cMRI-tMRI registration stage.

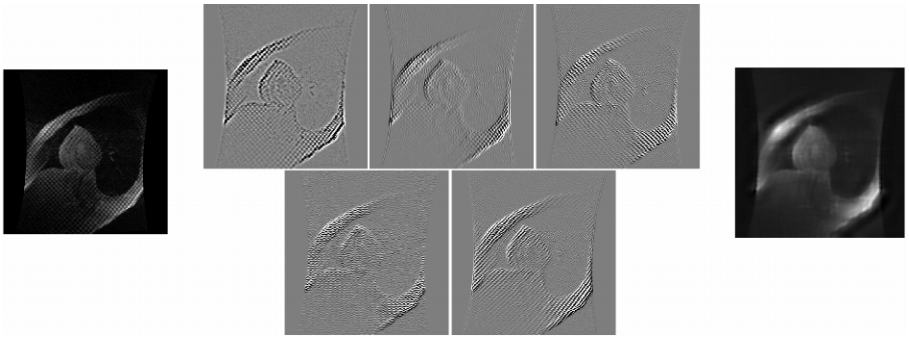

Fig. 2. Detagging results. Left: input tMRI; Centre: the five detail bands after one level of decomposition; Right: output detagged tMRI.

Qian et al. [2] developed a tag removal method based on 2D band-stop filtering to attenuate the harmonics energy peaks (modeled as 2D Gaussians) in the 2D frequency domain. Their method requires the generation of a different set of filters for each individual image, thus being computationally demanding when processing several images.

We propose the use of a steerable pyramid for detagging purposes. A steerable pyramid is an over-complete, linear, multi-resolution and multi-orientation image decomposition where the analysis and synthesis operators are derivative operators with different supports and orientations. The associated filters generate self-inverting (i.e., synthesis filters are just a reflected version of analysis filters) as well as translation and rotation invariant transforms. The steerable pyramid has some of the advantages of the orthogonal wavelet transform (e.g., good localization in both space and frequency) while improving some of its drawbacks (e.g., wavelet representations are heavily aliased and are not efficient with oblique orientations). Due to its orientation selectivity, this type of transform is suitable to extract high-order oriented structures such as edges and lines, thereby offering an efficient manipulation of the tagging lines in tMRI by directional adaptive filtering. In our application, the steerable pyramid coefficients are selectively kept or suppressed to minimize the reconstruction of tag information while preserving the non-tagged underlying image. Hence, the tagging pattern will be removed after applying the inverse steerable transform. We briefly describe below our implementation of the steerable pyramid, but more details about this type of transform can be found in [6].

Initially, the image is split into low and high-frequency bands. The low-frequency band is then divided into a set of P oriented detail images and one approximation image. The detail images are obtained using the band-pass filters $(B_1, \ldots, B_P)$ while the approximation signal is obtained using a low-pass filter followed by a dyadic downsampling. The process of splitting into P detail and one approximation images is iterated on the approximation image.

The angular constraint on the band-pass filters requires these filters to produce a steerable basis [6]. It must be pointed out that a set of filters forms a steerable

basis if: they are rotated versions of each other; and a version of these filters at any orientation may be synthesized as a linear combination of the basic filters. The simplest example of a steerable basis is a set of P directional derivatives of order $P-1$, in which the angular constraint can be expressed as

$$B_p(u,v) = B(u,v)\big(-i\cos(\theta-\theta_p)\big)^{P-1}, \tag{2}$$

where u and v are the frequency variables corresponding to the two spatial directions, $i=\sqrt{-1}$, $\theta=\arctan(v/u)$, $\theta_p=\pi\frac{p-1}{P}$ for $p=1,\ldots,P$, and

$$B(u,v) = \left(\sum_{p=1}^{P}\|B_p(u,v)\|^2\right)^{1/2}. \tag{3}$$

The pyramid can be designed to produce any number of orientation bands P, resulting in an overcomplete transform with a redundancy factor of $4P/3$. The number of orientation bands depends on the tag pattern orientation, thus P determines how many directions can be discriminated. For instance, if the tags were vertically oriented, one would need two orientation bands in order to distinguish between horizontal and vertical directions. The orientation bands obtained from a tMRI after one level of decomposition ($P=5$) are shown in Fig. 2.

The first step in the tag removal procedure consists in transforming the tMRI into its steerable pyramid with five orientation bands. Then, the oblique orientations corresponding to the tag lines are thresholded, setting to zero the coefficients whose magnitude is above a given threshold $T>0$. The threshold value can be determined as a function of the energy within the band. Alternatively, a soft-thresholding [7] technique (setting the detail coefficients to the threshold value instead of setting them to zero) can be used. Compared to the use of 2D band-stop filters [2], the proposed approach is theoretically simpler in terms of computational cost (miliseconds for 512x512 2D slices using the Matlab (The Mathworks, MA, USA) PyrTools library[1]). Furthermore, this detagging strategy is robust to noise and scale invariant due to its multiresolution nature, additionally offering a high degree of tag-orientation adaptability while reasonably preserving the edges and sharpness of the underlying image even in extreme cases with low image quality such as the tMRI available in our experiment.

2.3 Shift Correction in tMRI and deMRI

The shift correction of tMRI and deMRI is based on the principle of using the shift-corrected cMRI as target images in a rigid registration procedure. Slice-wise rigid transformations are defined by the set of translation parameters (three per slice), $\mathbf{p}=\{p_j\}_{j=0:3n_s-1}$, where n_s is the total number of slices, and the Jacobian of these transformations is:

$$\mathbf{J}(\mathbf{x}) = \frac{\partial x_i}{\partial p_j} = \begin{cases} 1\ , \text{ if } j=3Z(\mathbf{x})+i \quad i=0:2 \\ 0\ , \text{ otherwise.} \end{cases} \tag{4}$$

[1] http://www.cns.nyu.edu/~lcv/software.html

Table 1. Root mean square (RMS) of the shift correction errors (in mm) without registration (no reg) and with registration using the original tagged tMRI (tagging) and the detagged data as source images

	RMS		
	no reg	tagging	detagged
vol1	6.22±0.62	6.15±0.77	2.81±0.72
vol2	6.14±0.31	5.29±1.44	1.33±0.38
vol3	5.78±0.66	5.73±0.58	1.52±0.62
vol4	5.72±0.32	4.35±0.55	0.64±0.74
vol5	6.02±0.44	5.31±0.52	1.65±0.41
vol6	5.81±0.98	5.79±0.90	3.07±1.32
vol7	6.39±0.33	5.46±0.51	3.28±1.21
Mean	**6.01±0.25**	**5.44±0.57**	**2.04±1.00**

where $Z(\mathbf{x})$ is the slice number corresponding to $\mathbf{x}$. Manually obtained regions of interests (ROI) were available for the cMRI data, and were consequently used to constrain the parameter search at the optimization stage of the tMRI/deMRI shift correction step. Finally, linear interpolation was used for the resampling in order to fill gaps between slices due to the shift correction stage.

3 Results

3.1 Materials and Evaluation Experiment

We propose an evaluation experiment to assess the accuracy of the cMRI and tMRI registration, similar to the one designed by Lotjonen et al. [3]. We applied random 2D displacements, uniformly distributed between [-15,15]mm to tMRI corresponding to a set of 7 healthy volunteers with manually corrected shift. Similarly, the corresponding cMRI have also been manually shift-corrected. The phase corresponding to end diastole was chosen for cMRI and tMRI for optimal tag visualization. The experiment was repeated 10 times for each subject, thus the resulting generated data is composed of the original set of manually shift-corrected MRI sequences and a cohort of 140 tMRI (70 tMRIs and 70 detagged tMRIs) with different degrees of shift between their slices (around 12 slices per volume), resulting in 840 registration tests with known shifts.

For the set of 7 volunteers, we acquired cMRI and tMRI sequences in breath-hold using a General Electric Signa CV/i, 1.5 T scanner (General Electric, Milwaukee, USA). The slice thickness was 8 mm with an in-plane resolution of 0.78mm × 0.78mm and no gaps between slices. For cMRI and tMRI, data sets contained SA (12-15 slices) and LA (8-12 slices) image stacks and 30 phases per cardiac cycle. The cMRI and tMRI were acquired with the volunteers (approximately) in the same position since they did not move between different acquisitions.

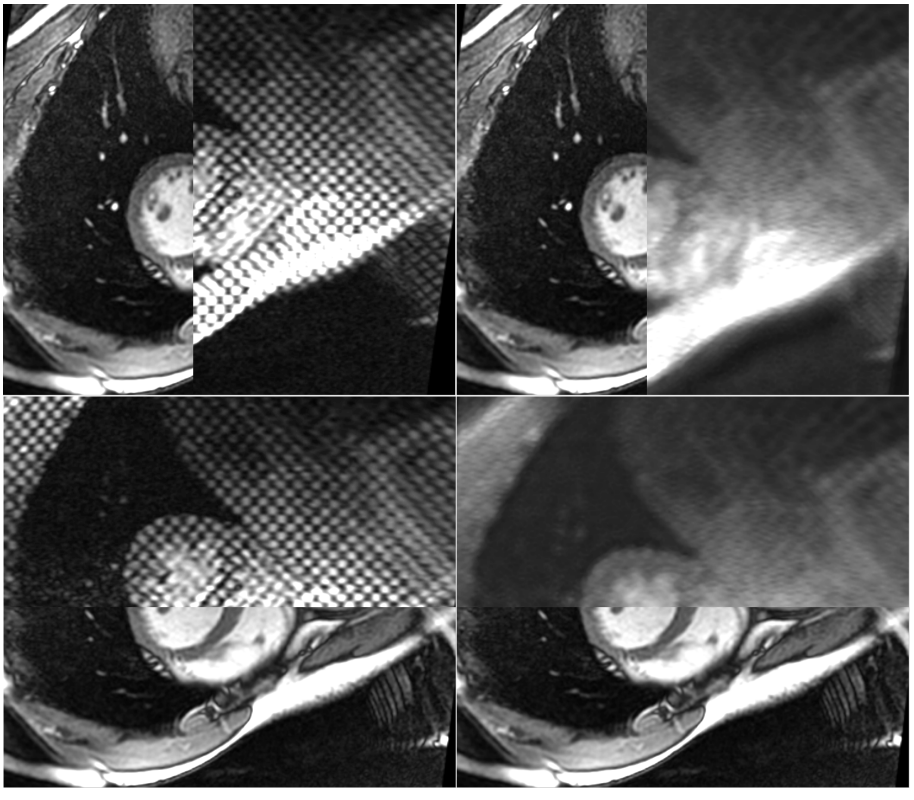

Fig. 3. Results of shift correction with tagged (left) and detagged MRI (right). Results are mixed (top: vertical; bottom: horizontal) with the corresponding shift-corrected cMRI that was used as target image.

Two different registration scenarios, using the shift-corrected cMRI as target images, were tested to assess the influence of the detagging and the tMRI shift correction methods, having the following source images: a) tMRI with known shift; b) detagged tMRI with known shift. Table 1 shows the mean and standard deviation (in mm) of the root mean square (RMS) values of the shift correction errors (averaged over 10 runs of the algorithm) for the different scenarios of the experiment. We can observe a substantial improvement (mean RMS error of 2.04mm vs. 5.44mm) when removing the tags from the tMRI in all volunteers, as shown in Fig. 3. In this figure, we can also observe that translational differences are more critical than rotational or non-rigid ones in this application.

We have also applied different shifts (from 2.5mm to 20mm) to a single case in order to identify the limits of the proposed framework. Obtained results are shown in Fig. 4, where the detagging scenario again outperforms the tagged one, which does not converge in some cases due to the low image quality of some tMRI. The proposed registration framework has sub-voxel accuracy with applied shifts under 10mm, which is convenient since artifacts due to respiration

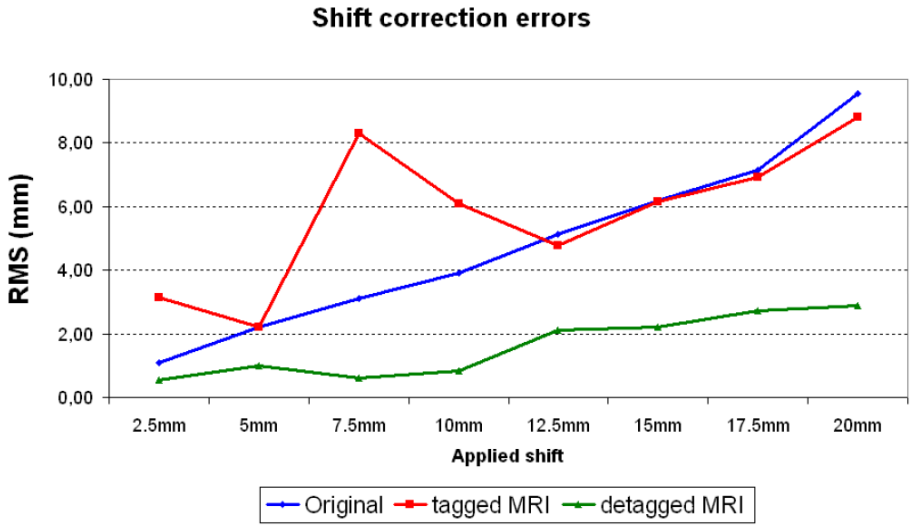

Fig. 4. Root mean square (RMS) of shift correction errors with respect to different amounts of applied known shift for a volunteer case

are typically lower than 10mm in cardiac images (typically 3-4mm and up to 7mm in some cases in the study of McLeish et al. [8]).

4 Conclusions

We have presented a registration framework to combine information provided by cMRI, tMRI and deMRI, in which the presence of tags and artifacts due to respiration are taken into account. Results demonstrated a substantial improvement of the alignment of the MR images when applying the detagging procedure and using the cMRI as target images for shift correction purposes. The proposed registration framework has been quantitatively evaluated only on tMRI. Nevertheless, deMRI should theoretically present less problems than tMRI since deMRI have better image quality and do not have tag lines. Future work will be focused on a quantitative assessment of this improvement comparing information provided by strain analysis from tMRI and infarcted regions from deMRI.

Acknowledgments

This research has been partially funded by the Industrial and Technological Development Centre (CDTI) under the CENIT Programme (CDTEAM project) and the European Community's Seventh Framework Programme (FP7/2007-2013) under grant agreement n. 224495 (euHeart project). Dr. O. Camara and Dr. G. Piella acknowledge grant support from the Spanish Ministry of Research and Innovation under a Ramon y Cajal Research Fellowship.

References

1. Manglik, T., Axel, L., Qian, Z., Pai, W., Kim, D., Dugal, P., Montillo, A.: Use of bandpass gabor filters for enhancing blood-myocardium contrast and filling-in tags in tagged mr images. In: Proceedings of the International Society for Magnetic Resonance in Medicine (ISMRM 2004), pp. 364–367 (2004)
2. Qian, Z., Huang, R., Metaxas, D., Axel, L.: A novel tag removal technique for tagged cardiac MRI and its applications. In: Proceedings of the IEEE International Symposium on Biomedical Imaging (ISBI 2007), pp. 364–367 (2007)
3. Lötjönen, J., Pollari, M., Kivistö, S., Lauerma, K.: Correction of movement artifacts from 4-D cardiac short- and long-axis MR data. In: Barillot, C., Haynor, D.R., Hellier, P. (eds.) MICCAI 2004. LNCS, vol. 3217, pp. 405–412. Springer, Heidelberg (2004)
4. Chandler, A.G., Pinder, R.J., Netsch, T., Schnabel, J.A., Hawkes, D.J., Hill, D.L.G., Razavi, R.: Correction of misaligned slices in multi-slice MR cardiac examinations by using slice-to-volume registration. In: Proceedings of the IEEE International Symposium on Biomedical Imaging (ISBI 2006), pp. 474–477 (2006)
5. Byrd, R., Lu, P., Nocedal, J.: A limited memory algorithm for bound constrained optimization. SIAM Journal on Scientific and Statistical Computing 16(5), 1190–1208 (1995)
6. Simoncelli, E.P., Freeman, W.T., Adelson, E.H., Heeger, D.J.: Shiftable multi-scale transforms. IEEE Transactions on Information Theory 38(2), 587–607 (1992)
7. Donoho, D.: De-noising by soft-thresholding. IEEE Transactions on Information Theory 41(3), 613–627 (1995)
8. McLeish, K., Hill, D., Atkinson, D., Blackall, J., Razavi, R.: A study of the motion and deformation of the heart due to respiration. IEEE Transactions on Medical Imaging 21(9), 1142–1150 (2002)

Segmentation of Left Ventricle in Cardiac Cine MRI: An Automatic Image-Driven Method

YingLi Lu[1], Perry Radau[1], Kim Connelly[1,2], Alexander Dick[3], and Graham A. Wright[1]

[1] Imaging Research, Sunnybrook Health Sciences Centre, Toronto, ON, Canada
[2] Cardiology, St Michael's Hospital, Toronto, ON, Canada
[3] Cardiology, Sunnybrook Health Sciences Centre, Toronto, ON, Canada
yinglilu@gmail.com, perry.radau@gmail.com, connellyka@yahoo.ca, Alexander.Dick@sunnybrook.ca, gawright@sten.sunnybrook.utoronto.ca

Abstract. This study investigates a fully automatic left ventricle segmentation method from cine short axis MR images. Advantages of this method include that it: 1) does not require manually drawn initial contours, trained statistical shape or gray-level appearance model; 2) provides not only endocardial and epicardial contours, but also papillary muscles and trabeculations' contours; 3) introduces a roundness measure that is fast and automatically locates the left ventricle; 4) simplifies the epicardial contour segmentation by mapping the pixels from Cartesian to approximately polar coordinates; and 5) applies a fast Fourier transform to smooth the endocardial and epicardial contours. Quantitative evaluation was performed on 41 subjects. The average perpendicular distance between manually drawn and automatically selected contours over all slices, all studies, and two phases (end-diastole and end-systole) was 1.40 ± 1.18 mm for endocardial and 1.75 ± 1.15 mm for epicardial contours. These results indicate a promising method for automatic segmentation of left ventricle for clinical use.

Keywords: Cardiac, left ventricle, segmentation, MRI.

1 Introduction

To quantitatively analyze global and regional cardiac function from cine magnetic resonance (MR) images, clinical parameters such as ejection fraction (EF), left ventricle volume, peak ejection rate, and filling rate are required. Calculations of these parameters depend upon accurate delineation of endocardial and epicardial contours of the left ventricle (LV). Manual delineation is time-consuming and tedious and has high inter-observer variability. Moreover, in clinical practice the manual delineation is typically limited to the end-diastolic (ED) and end-systolic (ES) phases, which can not be used to compute the peak ejection and filling rates. Thus, fully automatic LV segmentation on all of the phases is desirable.

The automatic segmentation of the LV in cine MR typically faces four challenges: 1) the overlap between the intensity distributions within the cardiac regions; 2) the lack of edge information; 3) the shape variability of the endocardial and epicardial

N. Ayache, H. Delingette, and M. Sermesant (Eds.): FIMH 2009, LNCS 5528, pp. 339–347, 2009.
© Springer-Verlag Berlin Heidelberg 2009

contours across slices and phases; and 4) the inter-subject variability of 1), 2) and 3). A number of methods have been proposed for (semi-) automatic LV segmentation, including using a probability atlas [1], dynamic programming [2-3], fuzzy clustering [4], a deformable model [5], an active appearance model [6], a variational and level set [7-10], graph cuts [11-12] and an image-driven approach [13]. For a complete review of recent literature describing cardiac segmentation techniques, see [14]. Although the segmentation results have improved, accurate LV segmentation is still acknowledged as a difficult problem.

In this work, we investigated a novel image-driven method for the accurate, robust, and fully automatic LV segmentation from short axis (SAX) cine MR images. The method is expected to give accurate segmentation of papillary and trabecular muscles, as well as endocardial and epicardial contours in all the phases. Main contributions of the work are that it: 1) introduces a roundness-measure-based fast and automatic LV location technique; 2) simplifies the epicardial contours segmentation by mapping the pixels from Cartesian to approximately polar coordinates; and 3) applies a fast Fourier transform to smooth the endocardial and epicardial contours.

2 Materials and Methods

2.1 Datasets

For this study, data from 41 patients were analyzed (8 female, 33 male; age: 60.3 ± 12.2). Cine steady state free precession (SSFP) MR short axis (SAX) images were obtained with a 1.5T GE Signa MRI. All the images were obtained during 10-15 second breath-holds with a temporal resolution of 20 cardiac phases over the heart cycle, and scanned from the ED phase. Six to 12 SAX images were obtained from the atrioventricular ring to the apex (thickness=8mm, gap=8mm, FOV=320mm$\times$ 320mm, matrix= 256×256). In these SAX MR acquisitions, endocardial and epicardial contours were drawn by a cardiologist in all slices at ED and ES phases, following the convention of including papillary muscles and endocardial trabeculations in the ventricular cavity. These manually drawn contours were used as the "gold standard" for evaluation purposes.

2.2 LV Location

This section presents method based on a roundness metric to automatically locate the LV blood pool's centroid on the middle slice in the ED phase. This method is based on the following assumptions: 1) the heart is approximately in the centre of the original image; 2) the left ventricle blood pool is more circular than the right ventricle blood pool; and 3) the blood has higher signal intensity than the myocardium (i.e., bright blood imaging). This procedure consists of five steps (refer to Fig.1):

1. Choose the middle (normally in the mid-cavity level) slice image in the ED phase as the target image.
2. Specify a centered, fixed rectangular region of interest (ROI) on the target image. The size of the rectangular is 110×110pixels (Fig.1a, b).

3. Apply the optimal threshold method of Otsu[15] to convert the ROI to a binary image (Fig.1c).
4. Remove all objects smaller than a predefined threshold (40 pixels) and compute the convex hull of the surviving objects (Fig.1d).
5. Compute the roundness metric $R = \frac{4\pi A}{P^2}$ of each survived convex-hulled object, where, A is area and P is perimeter length. R is equal to 1 for a circle. The object with the largest roundness metric is recognized as the LV blood pool, and its centroid coordinate (x, y) is utilized for following segmentation (Fig.1d).

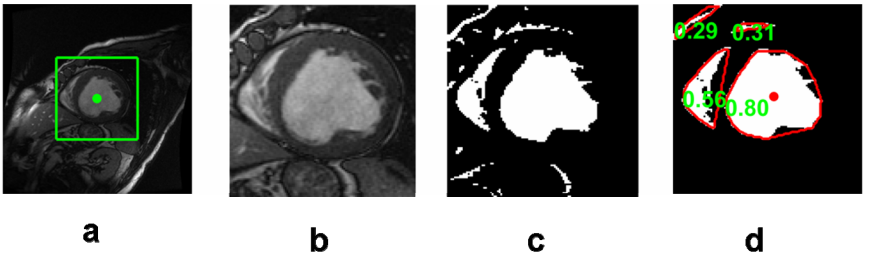

Fig. 1. LV location procedure. (a) Target image with rectangular ROI (green box) and image center(green point), (b) ROI image, (c) Binary image, (d) Surviving objects' convex hulls (red) and the corresponding roundness metric(green). The detected LV blood pool centroid is labeled as a red point.

2.3 LV Segmentation

For each 2D image, the LV blood pool contour, endocardial contour, papillary muscles' and trabeculations' contours, and epicardial contour will be detected sequentially. Given a 2D image, the first problem is how to specify a ROI that includes the LV. Our method uses a fixed size rectangle centered on the predetermined centroid (x, y) of the LV blood pool to determine an ROI. This is based on the assumption that the central part of the LV blood pool does not move much across slices and phases.

The blood pool contour is detected by the following steps (refer to Fig.2a-g):

1. Specify a rectangular ROI centered on the previously identified LV blood pool centroid coordinate (x, y) (see Section 2.2). The size of the rectangle is 110×110pixels (Fig.2a, b);
2. Apply the optimal threshold method of Otsu[15] to convert the ROI to a binary image (Fig.2c);
3. The LV blood pool object is identified by choosing the object that has maximum overlap with a predefined mask (20×20 pixels) centered on the LV blood pool centroid (Fig.2d);
4. Dilate the LV blood pool object by a disk-shaped structuring element with radius of 20 pixels to produce a refined, smaller ROI (Fig.2e);
5. Repeat steps 2-3 based on the refined ROI. This will give a refined blood pool mask (Fig.2f).

The endocardial contour is detected by the following steps (refer to Fig.2h, i):

1. Compute the convex hull of the refined blood pool (Fig.2h);
2. Smooth the convex hull's contour by applying the 1D fast Fourier transform (FFT) [16]. We first compute the FFT of the x coordinate of the contour point index, multiply the result by a low pass filter transfer function (keep only the four lowest frequency components), then take the inverse transform to produce the smoothed x coordinate. Repeat for y coordinates (Fig.2i).

The papillary muscles' and trabeculations' contours are detected by these steps:

1. Subtract the convex-hull mask of the refined blood pool from the refined blood pool mask to calculate the mask image of the papillary muscles and trabeculations (Fig.2j);
2. Trace the exterior boundaries of the objects in the mask image to determine the papillary muscles' and trabeculations' contours (Fig.2k).

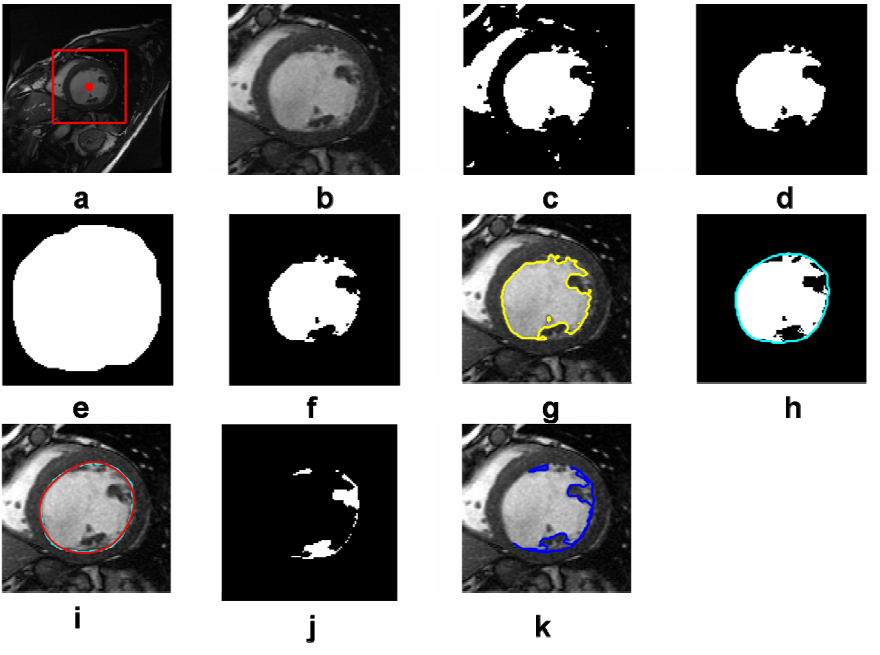

Fig. 2. LV contour calculation procedure. (a) Image with rectangular ROI and previously identified LV blood pool centroid (red), (b) ROI image, (c) Binary image, (d) Coarse LV blood pool, (e) Dilated mask, (f) Refined LV blood pool, (g) LV blood pool contour, (h) Convex hull of the LV blood pool (cyan), (i) Smoothed endocardial contour (red), (j) Papillary muscles and trabeculations' mask, (k) Papillary muscles and trabeculations' contours (blue).

The epicardial contour is calculated by the following steps (refer to Fig.3a-f):

1. Map the pixels from Cartesian to approximately polar coordinates. An outer boundary is calculated by dilation of the endocardial contour. The two contours

are interpolated to the same number of points, and paired to derive scan lines, each of a predefined length (20 pixels) (Fig. 3a). The result is a rectangular image that extends from the endocardial contour (top row) outward (bottom row) (Fig.3b).

2. Use each top-row pixel as a region growing seed, with all grown regions added and converted to a binary image (Fig.3c). For region growing, intensities are normalized by the original image maximum, and pixels added to a grown region must meet the intensity criterion (difference from mean of the grown region less than 0.04).
3. Fill image holes by morphological operations (Fig.3d).
4. The end point of each column's grown region determines an edge point (Fig.3e).
5. Inverse transform the edge point coordinates to the original coordinate space to determine the epicardial contour (Fig.3f).
6. Smooth the contour by applying the FFT technique as described earlier (Fig.3f).

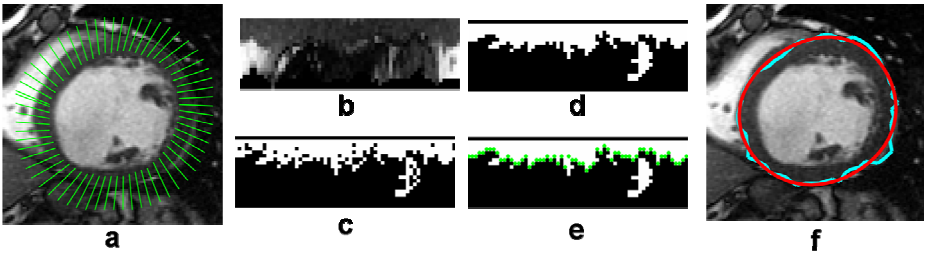

Fig. 3. LV segmentation procedure for epicardial contour. (a) Scan lines for mapping the pixels from Cartesian to polar coordinates. (b) Result of image transform. (c) Region growing binary image. (d) Image after filling holes. (e) Edge points (green). (f) Epicardial contour before (blue) and after FFT smoothing (red).

2.4 Evaluation

In order to quantitatively evaluate the automatically detected endocardial and epicardial contours of the ED and ES phases of all slices, three quantitative measures were assessed. First, the average perpendicular distance measures the distance from the automatically segmented contour to the corresponding manually drawn expert contour, averaged over all contour points. Second, the Dice metric [8]

$$DM = 2A_{am}(A_a + A_m)^{-1}$$

is a measure of contour overlap utilizing the contour areas automatically segmented (A_a), manually segmented (A_m), and their intersection (A_{am}). *DM* is always between 0 and 1, with higher *DM* indicating better match between automatic and manual segmentations. Third, the ejection fractions determined by the manual and automatic methods were compared by correlation analysis. In addition, the average perpendicular distance and Dice metric were compared with those calculated for a commercial automatic segmentation technique (Qmass MR 6.2.3, Medis[17]).

3 Results

The automatic segmentation methods were tested on 41 clinical MR exams. The averaged perpendicular distance and Dice metric over all subjects and slices in the ED and ES phases calculated for our method and QMass are shown in Tables 1 and 2. The automatically determined ejection fractions were highly correlated (0.95) with those from manual contours. Representative results for one dataset are shown in Fig. 4. Note that the segmentation method failed on three images because those images included the valve joining the atrium and ventricle.

Table 1. Averaged perpendicular distances (mm)

	QMass	Our Method
Endocardial Contour	1.75 ± 1.13	1.40 ± 1.18
Epicardial Contour	4.11 ± 2.72	1.67 ± 1.15

Table 2. Dice metric

	QMass	Our Method
Cavity Area	0.92 ± 0.07	0.93 ± 0.06
Epicardial area	0.89 ± 0.08	0.95 ± 0.04

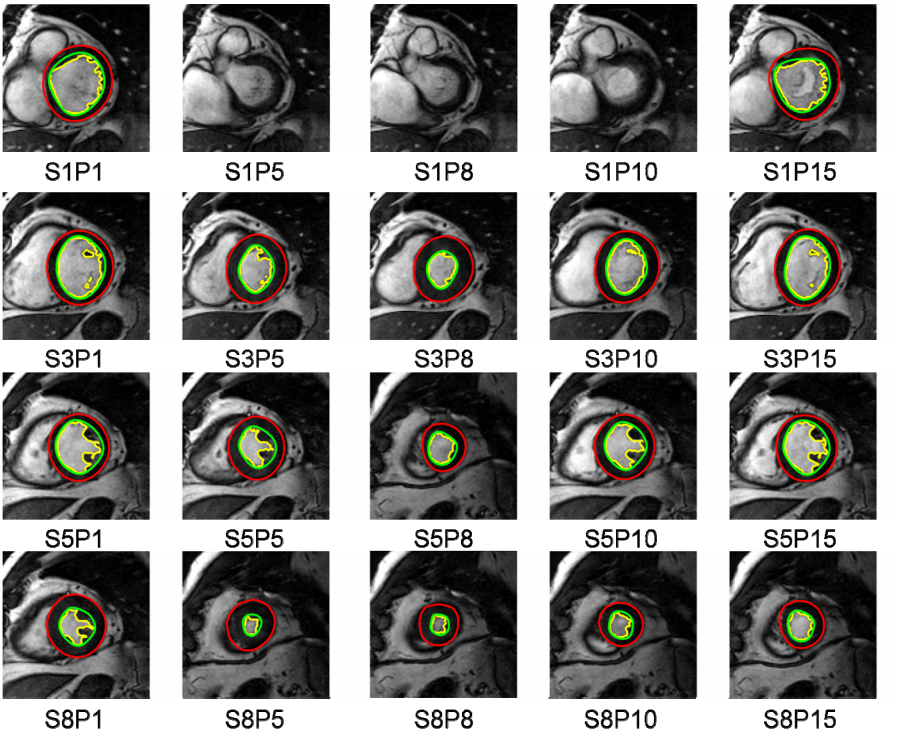

Fig. 4. Representative segmentation results. SxPy indicates the image for slice x and phase y. The contours of the blood pool (yellow), endocardium (green), and epicardium (red) are shown.

The average computation time of LV location is 0.085 ± 0.013s per subject. The average computation time of the segmentation of the proposed method is 53.7 ± 14.0s per subject (8 slices, 20 phases). The computation time was tested on consumer hardware (2×2.8GHz Quad-core Intel Xeon Mac Pro, Apple) with a non-optimized Matlab code (Mathworks) implementation.

4 Discussion and Conclusions

The proposed method for automatic segmentation has good accuracy, and was found to be superior in direct comparison with the automated technique of QMass. For further comparison, the perpendicular distance evaluations from other recent LV segmentation methods are provided in Table 3. Although dataset specifics are not uniform and thus hinder direct comparison, this meta-analysis provides additional confidence in our method.

Table 3. Averaged perpendicular distances (mm) of recent reported results

	Lorenzo-Valdés M.[1]	Uzümcü M.[3]	Fradkin M.[9]	Van Assen H.C.[18]	Our Method
Endocardial Contour	1.88	1.86	1.27	1.97	1.40
Epicardial Contour	2.75	1.77	1.56	2.23	1.67

The proposed segmentation method does not need initialization by manually drawn contours, prior statistical shape model, or gray-level appearance model. The proposed method is an image-driven method with only the assumption that the LV blood pool in a short axis image is approximately circular. Therefore it should be suitable for datasets with a wide range of anatomy, function, and image contrast as required for routine clinical use.

Previous methods of LV location have two steps: locate the entire heart and then the LV. For instance, standard deviation of the pixel values [19] and FFT based average and first harmonic magnitude image methods [22] have been used to locate the heart, and the Hough transformation [2, 6] has been proposed to locate the LV by detecting the circular region in the heart ROI. The proposed roundness metric method provides another available option for locating LV. And, it is very fast, requiring only 0.085 ± 0.013s per subject.

A difficult challenge of LV segmentation is the accurate delineation of the epicardial contours. The typical problem is ballooning epicardial contours at the junction between myocardium and lung parenchyma and subdiaphragmatic tissues. The main reason is the small intensity difference between these tissues. By mapping the pixels from Cartesian to polar coordinates, the irregular, ring-shaped ROIs are transformed to rectangular images. In this way, the epicardial contour detection problem was simplified.

Smoothing the contours by the FFT is a very fast and effective technique. The main merit of the FFT technique is to provide smoothed contours by removing outliers of the detected edge points without changing the overall shape.

The proposed method can provide contours of papillary muscles and trabeculations. Clinical studies have employed different quantification methods for calculation of LV volume, mass and ejection fraction by including or excluding

papillary muscles and trabeculations in the ventricular cavity [20, 21]. Recent studies have shown that the papillary muscles and trabeculations have a significant impact on calculation of LV volume and mass [20] and ejection fraction [21]; therefore the proposed method provides additional important options for daily clinical application.

A limitation of the proposed method is that it can not segment the LV from the right ventricle if the SAX slice includes the atria, as indicated in Fig. 4. Future research will extend the algorithm to handle these cases.

Future work will include testing the robustness of the algorithm with images acquired with different pulse sequences, contrast, and SNR characteristics, to validate our preliminary evidence of robustness. In addition, further evaluation is required with a spectrum of pathologies including ischemic and non-ischemic heart failure cases, and hypertrophic cases.

In summary, the proposed fully automated segmentation technique is fast, accurate and robust and should be of benefit for quantification of cine cardiac MR in clinical practice.

References

1. Lorenzo-Valdés, M., Sanchez-Ortiz, G.I., Elkington, A.G., Mohiaddin, R.H., Rueckert, D.: Segmentation of 4D cardiac MR images using a probabilistic atlas and the EM algorithm. Med. Image Anal. 8(3), 255–265 (2004)
2. Pednekar, A., Kurkure, U., Muthupillai, R., Flamm, S., Kakadiaris, I.A.: Automated left ventricular segmentation in cardiac MRI. IEEE Trans. Biomed. Eng. 53(7), 1425–1428 (2006)
3. Uzümcü, M., van der Geest, R.J., Swingen, C., Reiber, J.H., Lelieveldt, B.P.: Time continuous tracking and segmentation of cardiovascular magnetic resonance images using multidimensional dynamic programming. Invest. Radiol. 41(1), 52–62 (2006)
4. Rezaee, M.R., van der Zwet, P.J., Lelieveldt, B.E., van der Geest, R.J., Reiber, J.C.: A multi-resolution image segmentation technique based on pyramidal segmentation and fuzzy clustering. IEEE Trans. Image Process 9(7), 1238–1248 (2000)
5. Kaus, M.R., von Berg, J., Weese, J., Niessen, W., Pekar, V.: Automated segmentation of the left ventricle in cardiac MRI. Med. Image Anal. 8(3), 245–254 (2004)
6. Mitchell, S.C., Lelieveldt, B.P., van der Geest, R.J., Bosch, H.G., Reiber, J.H., Sonka, M.: Multistage hybrid active appearance model matching: segmentation of left and right ventricles in cardiac MR images. IEEE Trans. Med. Imaging 20(5), 415–423 (2001)
7. Paragios, N.: A level set approach for shape-driven segmentation and tracking of the left ventricle. IEEE Trans. Med. Imaging 22(6), 773–776 (2003)
8. Lynch, M., Ghita, O., Whelan, P.F.: Segmentation of the left ventricle of the heart in 3-D+t MRI data using an optimized nonrigid temporal model. IEEE Trans. Med. Imaging 27(2), 195–203 (2008)
9. Fradkin, M., Ciofolo, C., Mory, B., Hautvast, G., Breeuwer, M.: Comprehensive segmentation of cine cardiac MR images. Med. Image. Comp. Comp. Assist. Interv. 11(pt 1), 178–185 (2008)
10. Ben Ayed, I., Lu, Y., Li, S., Ross, I.: Left ventricle tracking using overlap priors. Med. Image. Comp. Comp. Assist. Interv. 11(pt 1), 1025–1033 (2008)
11. Boykov, Y., Jolly, M.P.: Interactive Organ Segmentation Using Graph Cuts. In: Delp, S.L., DiGoia, A.M., Jaramaz, B. (eds.) MICCAI 2000. LNCS, vol. 1935, pp. 276–286. Springer, Heidelberg (2000)

12. Lin, X., Cowan, B., Young, A.: Model-based Graph Cut Method for Segmentation of the Left Ventricle. In: Conf. Proc. IEEE Eng. Med. Biol. Soc., vol. 3, pp. 3059–3062 (2005)
13. Cocosco, C.A., Niessen, W.J., Netsch, T., Vonken, E.J., Lund, G., Stork, A., Viergever, M.A.: Automatic image-driven segmentation of the ventricles in cardiac cine MRI. J. Magn. Reson. Imaging 28(2), 366–374 (2008)
14. Frangi, A.F., Niessen, W.J., Viergever, M.A.: Three-dimensional modeling for functional analysis of cardiac images: a review. IEEE Trans. Med. Imaging 20(1), 2–25 (2001)
15. Otsu, N.: A Threshold Selection Method from Gray-Level Histograms. IEEE Transactions on Systems, Man, and Cybernetics 9(1), 62–66 (1979)
16. Gonzalez, R.C., Woods, R.E.: Digital Image Processing, 2nd edn., ch. 4. Prentice-Hall, New Jersey (2001)
17. http://www.medis.nl/index.htm
18. van Assen, H.C., Danilouchkine, M.G., Frangi, A.F., Ordás, S., Westenberg, J.J., Reiber, J.H., Lelieveldt, B.P.: SPASM: a 3D-ASM for segmentation of sparse and arbitrarily oriented cardiac MRI data. Med. Image Anal. 10(2), 286–303 (2006)
19. Sorgel, W., Vaerman, V.: Automatic heart localization from 4D MRI datasets. SPIE: Med. Imag. 3034, 333–344 (1997)
20. Papavassiliu, T., Kühl, H.P., Schröder, M., Süselbeck, T., Bondarenko, O., Böhm, C.K., Beek, A., Hofman, M.M., van Rossum, A.C.: Effect of endocardial trabeculae on left ventricular measurements and measurement reproducibility at cardiovascular MR imaging. Radiology 236(1), 57–64 (2005)
21. Weinsaft, J.W., Cham, M.D., Janik, M., Min, J.K., Henschke, C.I., Yankelevitz, D.F., Devereux, R.B.: Left ventricular papillary muscles and trabeculae are significant determinants of cardiac MRI volumetric measurements: effects on clinical standards in patients with advanced systolic dysfunction. Int. J. Cardiol. 126(3), 359–365 (2008)
22. Lin, X., Cowan, B.R., Young, A.A.: Automated detection of left ventricle in 4D MR images: experience from a large study. Med. Image Comp. Comp. Assist. Interv. 9(pt 1), 728–735 (2006)

The Importance of Model Parameters and Boundary Conditions in Whole Organ Models of Cardiac Contraction

Steven Niederer[1], Kawal Rhode[2], Reza Razavi[2], and Nic Smith[1]

[1] University of Oxford, Computing Laboratory Wolfson Building, Parks Road, Oxford OX1 3QD, UK
steven.niederer@comlab.ox.ac.uk
[2] King's College London, Division of Imaging Sciences, The Rayne Institute 4th Floor, Lambeth Wing, St Thomas' Hospital, London, SE1 7EH, UK

Abstract. We have developed a model of active contraction in the whole heart, using an anatomical geometry of a failing human heart, fitted to MRI data. Deformation in this model was driven by a model of active tension generation in human ventricular myocytes. By perturbing model parameters and boundary conditions we have predicted which metrics of cardiac function are sensitive to different parameters or boundary conditions. This allows us to begin to identify parameters that can be determined from different diagnostic modalities.

1 Introduction

The application of multi-scale computational models in the clinic poses a number of new challenges for cardiac modelling. In many pathologies the already significant physiological variations between individuals is amplified, necessitating the need for patient specific models to provide clinically relevant predictions of function and insight into disease mechanisms. However, cardiac models routinely have extensive parameter sets which, despite advances in diagnostic techniques, can not be readily identified *in vivo*. As each parameter will not be able to be uniquely determined for each patient, a key step in the development of patient specific models will be to identify which parameters have the greatest impact on model predictions. For example how significant is the role of fibre angle in determining cardiac function? Is a generic approximation of the fibre angle sufficient to provide accurate predictions or must the fibre angle be characterised for each patient? Having identified the important model parameters it is then necessary to identify metrics of cardiac function that are readily available in a clinical setting. These metrics can then in turn be used to determine model parameters for individual patients.

2 Methods

The model developed in this study simulates a contracting human heart. The cardiac ventricular model is described below by the geometry and fibre structure,

N. Ayache, H. Delingette, and M. Sermesant (Eds.): FIMH 2009, LNCS 5528, pp. 348–356, 2009.
© Springer-Verlag Berlin Heidelberg 2009

mechanics model and boundary conditions. Deformation is simulated using the finite elasticity equations [1]. The model is defined and solved within the CMISS (Continuum Mechanics, Image processing, Signal processing and System identification) software package, written in FORTRAN and developed at the University of Auckland (www.cmiss.org). The code was compiled using the INTEL FORTRAN compilers for XEON CPUs and solved using 2 Quad cor CPUs and 16Gb RAM. All visualisations are generated using the freely availably CMGUI graphical user interface.

2.1 Anatomical Model

Clinical MRI images of a heart failure patient were obtained via St Thomas Hospital. These images were manually segmented to identify three surfaces: the epicardium, left ventricle endocardium and right ventricle endocardium. Two dimensional bi-cubic Hermite finite elements were fit to each of the three surfaces. The two dimensional surface meshes were then converted into tri-cubic Hermite volume elements. The fitted mesh has 105 nodes and 64 elements, resulting in 2640 degrees of freedom. The mesh was then refined in the apex-base direction to give a final mesh with 183 nodes, 112 elements and 4608 degrees of freedom. The material properties of the myocardium are aligned with the laminar tissue microstructure. To describe this structure within the ventricular geometry the fibre orientation is defined relative to the material coordinates of the ventricular mesh, as described previously [2]. The method of defining the fiber orientation results in a geometry specific fiber field, however, it reflects the type of assumption used in models to define fiber orientation in the absence of patient or geometry specific information [21,22].

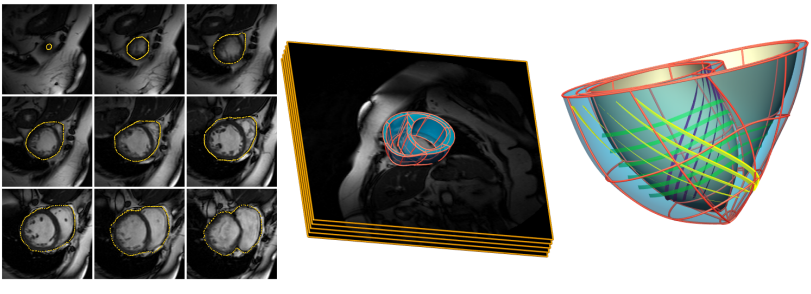

Fig. 1. A) Epicardium segmentation of MRI images at diastasis B) Ventricle volume mesh fitted to MRI images and C) Epicardium (yellow), midwall (green) and endocardium (purple) fibres varying across the wall of the heart

2.2 Mechanics Model

The model of contraction has been formulated to directly link to experimental measurements. In an initial approximation, the calcium transient is assumed to be homogenous across the heart and is defined at each Gauss point by

$$[Ca^{2+}]_i = [Ca^{2+}]_d + ([Ca^{2+}]_{max} - [Ca^{2+}]_d)\frac{t}{\tau_{Ca}} e^{1-\frac{t}{\tau_{Ca}}}. \quad (1)$$

By assuming that Ca^{2+} binds rapidly with troponin and ignoring tension dependent binding of Ca^{2+} to troponin, $[Ca^{2+}]_i$ values can be mapped onto Ca^{2+} bound to troponin concentrations using

$$Ca_{trpn50} = \frac{Ca_{50}}{Ca_{50} + K_{trpn}} \qquad [Ca^{2+}]_{trpn} = \frac{[Ca^{2+}]_i}{[Ca^{2+}]_i + K_{trpn}} \quad (2)$$

where K_{trpn} has been derived previously as 2.0μM [3]. γ acts as a nonlinear length dependent scalar, which captures the length dependent Ca^{2+} sensitivity component of the Frank Starling Law by

$$\gamma = \left(\frac{[Ca^{2+}]_{trpn}}{Ca_{trpn50}}\right)^{nh}. \quad (3)$$

The fraction of activation sites is defined by the differential equation

$$\frac{dz}{dt} = \alpha_0(\gamma(1-z) - z), \quad (4)$$

where z is the level of activation, and corresponds to the portion of crossbridges bound to actin. The level of active tension generated is assumed to be proportional to the fraction of crossbridges bound to actin, giving

$$T_a = zF_{max}, \quad (5)$$

where T_a is the level of active tension. The values of F_{max} and Ca_{50} have been proposed as being dependent on the sarcomere length [4]. This length dependence is characterised by the following simple linear functions:

$$Ca_{50} = Ca_{i50}(1 + \beta_{Ca_{50}}(\lambda - 1)) \quad (6)$$

$$F_{max} = F_{imax}(1 + \beta_{F_{max}}(\lambda - 1)) \quad (7)$$

Limited data is available to parameterise models of contraction in human cardiac myocytes. To determine the model parameters we have combined data from multiple data sets to characterise the different parameters and approximate the effects of changes in temperature and skinning on experimental measurements. The $[Ca^{2+}]_i$ transient parameters were fitted to experimental measurements by Beuckelmann et al., [5], giving $[Ca^{2+}]_{max}$ = 746mM, $[Ca^{2+}]_d$ = 96mM and $\tau_{Ca} = 120ms$.

We have fit the length dependent Ca^{+2} sensitivity of the model to steady state force Ca^{+2} curves at 21^{o}C in human skinned papillary muscle with a resting sarcomere length of 2.0 μm. The steady state force Ca^{+2} relationship is characterised by the Ca^{+2} at half activation and Hill coefficient. The half activation was 1.9, 1.43 and 1.46 at 100%, 120% and 130% slack length [6]. Fitting the steady state model to these parameters resulted in $Ca_{i50} = 1.8621$, $\beta_{Ca_{50}} = -0.8554$, $nh_i = 3.8384$.

To account for the effects of skinning and temperature the Ca_{50} and nh values were refitted to steady state force Ca^{+2} curves (half activation is 0.58 and 0.56 μM and the Hill coefficient is 5.0 and 5.21) in intact trabeculae at 30^{o}C [7,8], giving Ca_{i50} and nh_i values of 0.6650 and 7.0, respectively.

No human data was available to characterise the length dependence of peak isometric tension. Thus, F_{imax} and $\beta_{F_{max}}$ were fit to 73.47 and 2.019 and 58.045kPa and 1.871 using peak isometric data recorded by Kentish et al., [4] and Dobesh et al [9], respectively. We chose a $\beta_{F_{max}}$ value of 2.0, which falls between these measurements from these two data sets. F_{imax} was then adjusted to 100kPa to achieve tensions consistent with values of 108kPa [10] and 151kPa [11] at sarcomere lengths of 2.19 and 2.25-2.45μm in human ventricle myofibrils, respectively.

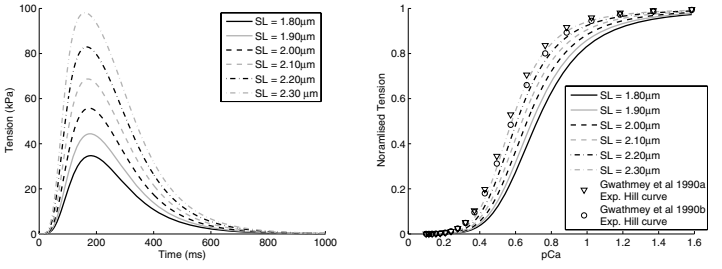

(a) **(b)**

Fig. 2. A) Isometric Tension transients and B) steady state force-calcium curves, calculated using the simple model of human cardiac myocyte active tension

The value of α_0 is 0.008ms^{-1}. This value was fitted to achieve a time to peak tension of 180ms [12,13,14] for an isometric twitch with a sarcomere length of 2.2 μm. Fig. 2 demonstrates isometric tension transients and the steady state F-pCa curves at increasing sarcomere lengths predicted by the model. The model is constructed such that each parameter can be uniquely determined directly from specific experimental data, thus allowing a unique parameter set to be determined based on the available experimental data. The passive properties of the myocardium are modelled using the Costa law fitted by Schmid et al. [15] to porcine experimental data from Dokos et al. [16]. In the following sensitivity analysis the stiffness of the constitutive law is increased by scaling the strain energy function. The Costa law fitted by Schmid et al. is transversely orthotropic. We tested the importance of considering the different stiffness's in the sheet and sheet normal directions by performing simulations where the material law was assumed to be transversely isotropic.

2.3 Boundary Conditions

The model of the heart developed in this study only represents the ventricles and does not include any representation of the atria, valves or valve plane. The

absence of these structures results in the base of the ventricle being free to deform. In simulations aiming to replicate specific imaging data it may be possible to record the movement of the base and use this to define boundary conditions. However, to use the model in its predictive capacity will require generic boundary conditions that approximate these absent structures on the ventricle. To test if the choice of boundary conditions plays a significant role in determining model predictions we have tested three different approximations of the effect of the absent structures on the base of the myocardium. The first case assumes that the absent structures have a nominal effect on left ventricle deformation. Specifically, the boundary conditions are described to limit buckling of the base by fixing all the base nodes to remain in plane and to restrict free body rotation by fixing the red and gold nodes (Fig. 3A) in one and two in plane directions, respectively. Case 1 was taken as the default boundary condition. The second boundary condition case was similar to case 1 except that instead of two base nodes being fixed the base left ventricle endocardium, as indicated by the red line in Fig. 3B, was fixed in all directions. Similarly, in case 3 the two fixed base nodes are replaced by fixing the left ventricle epicardium and right ventricle septum base (as indicated by the red line in Fig. 3C) in all directions.

Three types of boundary conditions are applied to the left and right ventricle endocardium. During isovolumetric contraction (IVC) and relaxation (IVR) the left and right ventricle cavity volumes are fixed. Ejection begins when left ventricle pressure reaches 12kPa. During ejection a three element Windkessel model [17] is used to predict the changes in pressure as a function of the flow rate. The peripheral resistance, characteristic impedance and the arterial compliance were set to 0.0543 kPa ms mm^{-3}, 0.0279 kPa ms mm^{-3} and 12000 mm^3 kPa^{-1}, respectively. During diastole a transient cavity pressure was defined to represent

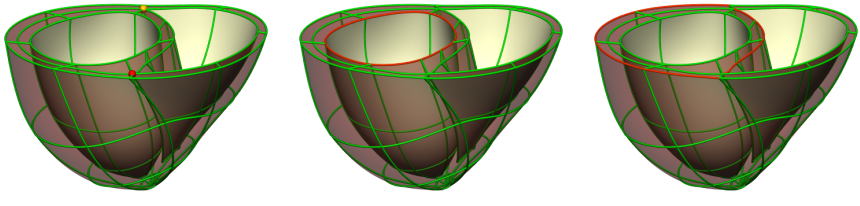

(a) **(b)** **(c)**

Fig. 3. A) Case 1, the default boundary conditions the base plane of the heart is fixed to remain in plane and not move in the apex-base direction. The red node and gold node are fixed in one and two in plane directions, respectively, to inhibit free body rotation B) Boundary condition case 2 where as in case 1 the base nodes are fixed in the apex-base direction but the endocardial base nodes, as indicated by the red line are all fixed in space C) Case 3 boundary conditions are similar to case 2 except that, as indicated the red lines the base left ventricle epicardium and right ventricle septum nodes are fixed in all directions.

initial filling, diastasis and the atrium contracting. The transient is taken from a Wiggar's plot [18] and is scaled to start at 2.25kPa, finish at 3kPa and span the duration between end IVR and IVC. Diastole begins when the pressure during IVR reaches 0.25kPa and finishes at the end of the current pacing cycle.

3 Results

Simulations of a single beat at 1Hz were performed. The ejection fraction of the heart model is less than expected for a healthy individual but the particular patient is suffering from heart failure and the expected ejection fraction is less than 35%. The model results from the default boundary conditions, and mechanics model parameters and with fibre orientation varying from $+60^o$ to -60^o ($\pm 60^o$) across the heart wall are shown in Fig. 4. To test the sensitivity of the model predictions to perturbations in model parameters and boundary conditions a set of simulations were performed, as listed in Table 1. The effect of these changes

Table 1. Dependence of metrics of cardiac function on model parameters and boundary conditions. All perturbations are from a reference heart with no fixed boundary conditions at the base (Case 1, Fig. 3) and default contraction model parameters. EDV: end diastolic volume, ESV end systolic volume and EF ejection fraction.

Parameter or boundary condition	EDV (ml)	ESV (ml)	EF	Peak Pressure (kPa)
Fibre ($\pm 60^o$)	278.144	231.026	17.0%	15.63
Fibre ($\pm 70^o$)	280.073	232.618	16.9%	15.6
Fibre ($\pm 50^o$)	275.793	228.417	17.4%	15.66
α_0 +25%	278.144	237.355	14.7%	16.41
F_{imax} +25%	278.144	223.945	19.6%	17.94
Bdy Cnd case 1	256.720	211.268	17.5%	15.63
Bdy Cnd case 2	267.654	220.633	18.1%	15.54
Stiffness +25%	272.693	225.476	17.4%	15.46
Transversely Isotropic	278.621	230.779	17.1%	16.0

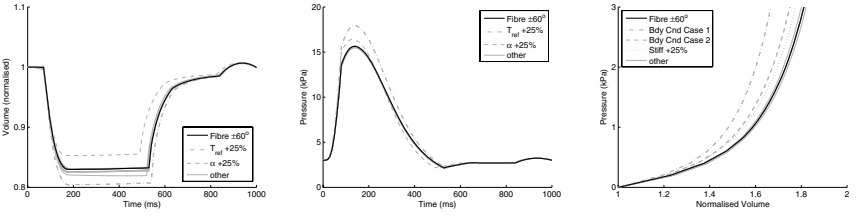

(a) **(b)** **(c)**

Fig. 4. Panels A, B and C show the volume and pressure transients and the passive inflation properties calculated by the model, respectively. The black lines correspond to results from the default model, grey dash lines correspond to specific perturbations and the remaining grey lines represent all other results from the simulations listed in Table 1.

to the model on the pressure and volume transients during a contraction are shown in Fig. 4A-B. The effect these perturbations have on passive inflation are shown in Fig. 4C.

4 Discussion

We have simulated a beating human heart using a simplified model of contraction to generate an active tension field to drive deformation. A model of contraction parameterised using human data has been embedded within a complex model of deformation, including nonlinear anisotropic constitutive laws, an isolvolumetric material, finite elasticity equations and an anatomically accurate geometry. The model is able to replicate the phases of contraction, generate physiological systolic pressures and can be solved on a high end desk top computer.

4.1 Limitations

The model is unable to fully capture the timing of each phase of contraction. In particular the period of systole is only 190ms in the model, which is likely to be a result of homogenous contraction. During a normal heart beat the wave of electrical excitation propagates over the heart over a period of 70ms. This dispersion of contraction times is likely to increase the duration of systole motivating the need for including excitation contraction coupling. Secondly, IVR is considerably slower than expected. The specific mechanism for this slow relaxation is not known but it is possibly due to the absence of a velocity dependent component in the contraction model [3]. Although more complicated models of contraction are readily available they are less able to be re-parameterised for a specific human patient. Adaptation of the model represented here may be able to address this challenge without adding excessive complexity to the model.

4.2 Sensitivity

Results in Table 1 show that the boundary conditions and stiffness of the constitutive law constrain the diastolic filling of the heart, having the largest effect on end diastolic volume and altering passive filling as shown in Fig. 4C. The cellular properties, in the form of α_0 and F_{imax} are the dominant regulators of systole. In particular a 25% increase in the reference tension caused a significant increase in the ejection fraction and decreased end systolic volume. This study confirms results from previous studies [19,20] that predicted that fibre orientation has a limited effect on organ scale metrics of cardiac function. The results shown here suggest that in the case of human contractile models there may not be a need to determine patient specific fibre orientations. However, once again, models of coupled electromechanics may increase the sensitivity of model results to fibre orientation. In particular the propagation of activation and hence timing of contraction is governed by the velocity of propagation along the fibres the role of the fibre orientation may be significantly increased.

References

1. Nash, M.P., Hunter, P.J.: Computational mechanics of the heart - From tissue structure to ventricular function. Journal of Elasticity 61, 113–141 (2000)
2. LeGrice, I.J., Smaill, B.H., Chai, L.Z., Edgar, S.G., Gavin, J.B., Hunter, P.J.: Laminar structure of the heart: Ventricular myocyte arrangement and connective tissue architecture in the dog. Am. J. Physiol. 269, 571–582 (1995)
3. Niederer, S.A., Hunter, P.J., Smith, N.P.: A Quantitative Analysis of Cardiac Myocyte Relaxation: A Simulation Study. Biophys. J. 90, 1697–1722 (2006)
4. Kentish, J.C., Terkeurs, H., Ricciardi, L., Bucx, J.J.J., Noble, M.I.M.: Comparison between the Sarcomere Length-Force Relations of Intact and Skinned Trabeculae from Rat Right Ventricle - Influence of Calcium Concentrations on These Relations. Circ. Res. 58, 755–768 (1986)
5. Beuckelmann, D.J., Erdmann, E.: Ca(2+)-currents and intracellular [Ca2+]i-transients in single ventricular myocytes isolated from terminally failing human myocardium. Basic Res. Cardiol. 87(suppl. 1), 235–243 (1992)
6. Schwinger, R.H., Bohm, M., Koch, A., Schmidt, U., Morano, I., Eissner, H.J., Uberfuhr, P., Reichart, B., Erdmann, E.: The failing human heart is unable to use the Frank-Starling mechanism. Circ. Res. 74, 959–969 (1994)
7. Gwathmey, J.K., Hajjar, R.J.: Effect of protein kinase C activation on sarcoplasmic reticulum function and apparent myofibrillar Ca2+ sensitivity in intact and skinned muscles from normal and diseased human myocardium. Circ. Res. 67, 744–752 (1990)
8. Gwathmey, J.K., Hajjar, R.J.: Relation between Steady-State Force and Intracellular Ca-2+ in Intact Human Myocardium - Index of Myofibrillar Responsiveness to Ca-2+. Circulation 82, 1266–1278 (1990)
9. Dobesh, D.P., Konhilas, J.P., de Tombe, P.P.: Cooperative activation in cardiac muscle: impact of sarcomere length. Am. J. Physiol. 282, H1055–H1062 (2002)
10. Piroddi, N., Belus, A., Scellini, B., Tesi, C., Giunti, G., Cerbai, E., Mugelli, A., Poggesi, C.: Tension generation and relaxation in single myofibrils from human atrial and ventricular myocardium. Pflügers Archiv. European Journal of Physiology 454, 63–73 (2007)
11. Stehle, R., Kruger, M., Scherer, P., Brixius, K., Schwinger, R.H.G., Pfitzer, G.: Isometric force kinetics upon rapid activation and relaxation of mouse, guinea pig and human heart muscle studied on the subcellular myofibrillar level. Basic Res. Cardiol. 97, 1435–1803 (2002)
12. Hermann, H.-P., Zeitz, O., Lehnart, S.E., Keweloh, B., Datz, N., Hasenfuss, G., Janssen, P.M.L.: Potentiation of beta-adrenergic inotropic response by pyruvate in failing human myocardium. Cardiovascular Research 53, 116–123 (2002)
13. Janssen, P.M.L., Zeitz, O., Keweloh, B., Siegel, U., Maier, L.S., Barckhausen, P., Pieske, B., Prestle, J., Lehnart, S.E., Hasenfuss, G.: Influence of cyclosporine A on contractile function, calcium handling, and energetics in isolated human and rabbit myocardium. Cardiovascular Research 47, 99–107 (2000)
14. Hasenfuss, G., Mulieri, L.A., Leavitt, B.J., Allen, P.D., Haeberle, J.R., Alpert, N.R.: Alteration of contractile function and excitation-contraction coupling in dilated cardiomyopathy. Circ. Res. 70, 1225–1232 (1992)
15. Schmid, H., Nash, M.P., Young, A.A., Hunter, P.J.: Myocardial material parameter estimation-a comparative study for simple shear. J. Biomech. Eng. 128, 742–750 (2006)

16. Dokos, S., Smaill, B.H., Young, A.A., LeGrice, I.J.: Shear properties of passive ventricular myocardium. Am. J. Physiol. 283, H2650–H2659 (2002)
17. Stergiopulos, N., Meister, J.J., Westerhof, N.: Determinants of stroke volume and systolic and diastolic aortic pressure. Am. J. Physiol. 270, H2050–H2059 (1996)
18. Katz, A.: Physiology of the heart. Raven Press, New York (1977)
19. Vendelin, M., Bovendeerd, P.H.M., Engelbrecht, J., Arts, T.: Optimizing ventricular fibers: uniform strain or stress, but not ATP consumption, leads to high efficiency. Am. J. Physiol. 283(3), H1072–H1081
20. Bovendeerd, P.H.M., Arts, T., Huyghe, J.M., van Campen, D.H., Reneman, R.S.: Dependence of local left ventricular wall mechanics on myocardial fiber orientation: A model study. J. Biomech. 25(10), 1129–1140
21. Ten Tusscher, K.H.W.J., Hren, R., Panfilov, A.V.: Organization of Ventricular Fibrillation in the Human Heart. Circ. Res. 100(12), 87 (2007)
22. Chinchapatnam, P.P., Rhode, K.S., King, A., Gao, G., Ma, Y., Schaeffter, T., Hawkes, D.J., Razavi, R.S., Hill, D.L.G., Arridge, S., Sermesant, M.: Anisotropic Wave Propagation and Apparent Conductivity Estimation in a Fast Electrophysiological Model: Application to XMR Interventional Imaging. In: Ayache, N., Ourselin, S., Maeder, A. (eds.) MICCAI 2007, Part I. LNCS, vol. 4791, pp. 575–583. Springer, Heidelberg (2007)

Numerical Simulation of the Electromechanical Activity of the Heart

Dominique Chapelle[1], Miguel A. Fernández[1], Jean-Frédéric Gerbeau[1], Philippe Moireau[1], Jacques Sainte-Marie[1,2], and Nejib Zemzemi[1,3]

[1] INRIA, Rocquencourt B.P. 105, 78153 Le Chesnay cedex, France
[2] LNHE/CETMEF, 6 quai Watier, 78401 Chatou cedex, France
[3] Univ. Paris 11, Laboratoire de mathématiques d'Orsay, 91405 Orsay cedex, France

Abstract. We present numerical results obtained with a three-dimensional electromechanical model of the heart with a complete realistic anatomy. The electrical activity of the heart-torso domain is described by the bidomain equations in the heart and a Laplace equation in the torso. The mechanical model is based on a chemically-controlled contraction law of the myofibres integrated in a 3D continuum mechanics description accounting for large displacements and strains, and the main cardiovascular blood compartments are represented by simplified lumped models. We considered a normal case and a pathological condition and the medical indicators resulting from the simulations show physiological values, both for mechanical and electrical quantities of interest, in particular pressures, volumes and ECGs.

1 Introduction

We present a complete numerical simulation of the electromechanical activity of the heart based on an integrated three-dimensional (3D) mathematical model of the cardiac electrophysiology and mechanics considered jointly. In this respect, we follow the standard approach of electromechanical modeling with "one-way coupling", namely, the electrical simulation is used as an input in the mechanical model without mechano-electrical feedback, see [12] and [13] for surveys on this approach.

The major contribution of this paper is to demonstrate that we are now able to obtain accurate simulations of the main electromechanical phenomena with a procedure integrating anatomical and physical models. We show that these simulations provide meaningful medical indicators, in particular pressures, volumes and ECGs, and this validation with *both mechanical and electrical indicators* is a pioneering result. This allows to investigate various pathological scenarii with predictive capabilities, namely, without any recalibration of the model parameters other than those directly affected by the pathology. Furthermore, the simulations give access to other physical quantities which cannot be measured – such as local values of the stresses in the tissue – which can be very valuable for clinicians to better assess a pathological condition and its possible evolutions.

N. Ayache, H. Delingette, and M. Sermesant (Eds.): FIMH 2009, LNCS 5528, pp. 357–365, 2009.
© Springer-Verlag Berlin Heidelberg 2009

The paper is organized as follows. In Section 2 we introduce the mathematical electromechanical model and describe the anatomical model. Section 3 is devoted to the numerical simulations, and we present the results obtained for both a normal and a pathological case. Some conclusions are given in Section 4.

2 An Electromechanical Model of the Heart

In this section we summarize the electromechanical model considered in this work. We assume that the electrical activity of the heart is independent of the mechanical activity, *i.e.* we do not consider mechano-electrical feedback.

2.1 Mechanical Model

The mechanical heart model that we consider was described in details in [20], and here we only summarize its key ingredients for completeness. The contractile behavior relies on a chemically-controlled constitutive law of cardiac myofibre mechanics introduced in [3] based on Huxley's model [11]. This law dynamically relates the active stress and the strain along the sarcomere, respectively denoted by τ_c and e_c, by the following set of ordinary differential equations:

$$\begin{cases} \dot{\tau}_c = k_c \dot{e}_c - (\alpha|\dot{e}_c| + |u|)\tau_c + \sigma_0 |u|_+ & \tau_c(0) = 0 \\ \dot{k}_c = -(\alpha|\dot{e}_c| + |u|)k_c + k_0 |u|_+ & k_c(0) = 0 \end{cases} \tag{2.1}$$

where the parameters k_0 and σ_0 are respectively the maximum value for the active stiffness k_c and for the stress variable τ_c, while μ is a viscosity parameter. The quantity u represents the electrical input – corresponding to a normalized concentration of calcium bound on the troponin-C – with $u > 0$ during contraction and $u < 0$ during active relaxation (we use the notation $|u|_+ = \max(u, 0)$). Following [20], we assume an affine relation between u and the transmembrane potential V_m, *i.e.* $u = \alpha V_\mathrm{m} + \beta$. This simplification is justified by the observed waveform similitudes of the transmembrane potential and the calcium concentration. The modeling of V_m is further developed in Section 2.2 below.

The overall tissue behavior combines this active law with passive components using a rheological model of Hill-Maxwell type [10] compatible with large displacements and strains. In the parallel branch of this rheological model we considered a viscoelastic behavior, with a hyperelastic potential given by the Ciarlet-Geymonat volumic energy [7,14]

$$W^e = \kappa_1(\tilde{I}_1 - 3) + \kappa_2(\tilde{I}_2 - 3) + K(J-1) - K \ln J,$$

where $\tilde{I}_1$, $\tilde{I}_2$ and J denote the reduced invariants of the Cauchy-Green strain tensor $\underline{\underline{C}}$. Regarding the viscous behavior of the parallel branch, we used the following dissipation pseudo-potential

$$W^v = \frac{\eta}{2} \dot{\underline{\underline{e}}} : \dot{\underline{\underline{e}}},$$

where $\underline{\underline{e}} = \frac{1}{2}(\underline{\underline{C}} - \underline{\underline{I}})$ denotes the Green-Lagrange strain tensor.

This combination of constitutive relations gives an expression of the second Piola-Kirchhoff stress tensor $\underline{\underline{S}}$. Note that the resulting behavior is *non-isotropic*, since the contraction law (2.1) operates in the fibre direction. We then invoke the principle of virtual work – namely the dynamical balance equation – using a total Lagrangian formulation. Denoting by Ω_{H} the reference domain corresponding to cardiac tissue, and by Γ_{endo} the left and right ventricle endocardium surfaces with outgoing unit normal vector $\underline{n}$, we have

$$\int_{\Omega_{\mathrm{H}}} \rho\, \underline{\ddot{y}} \cdot \underline{v}\, d\Omega + \int_{\Omega_{\mathrm{H}}} \underline{\underline{S}} : d_y \underline{\underline{e}}.\underline{v}\, d\Omega + \int_{\Gamma_{\mathrm{endo}}} P_{\mathrm{v}}\, \underline{n} \cdot \underline{\underline{F}}^{-1} \cdot \underline{v} J\, d\Gamma = 0, \tag{2.2}$$

for any test function $\underline{v}$ taken in a suitable displacement space, and with associated infinitesimal strain variation $d_y \underline{\underline{e}}.\underline{v}$. In this expression, ρ denotes volumic mass in the inertia term, and $\underline{\underline{F}}$ the deformation gradient. The quantity P_{v} represents the blood pressure inside the ventricles, itself directly related to the pressures in the arterial compartments, which we represented by adequate Windkessel models, see *e.g.* [15,20].

2.2 Electrical Model

As a mathematical model of the electrical activity of the heart we consider the bidomain equations (see *e.g.* [17,21,22]) and a Laplace equation for the torso.

The bidomain equations in Ω_{H} are given by:

$$\begin{cases} A_{\mathrm{m}}\big(C_{\mathrm{m}} \dot{V}_{\mathrm{m}} + I_{\mathrm{ion}}(V_{\mathrm{m}}, w)\big) - \operatorname{div}\big(\underline{\underline{\sigma}}_{\mathrm{i}} \underline{\nabla} V_{\mathrm{m}}\big) = \operatorname{div}\big(\underline{\underline{\sigma}}_{\mathrm{i}} \underline{\nabla} u_{\mathrm{e}}\big) + I_{\mathrm{app}}, & \text{in} \quad \Omega_{\mathrm{H}}, \\ -\operatorname{div}\big((\underline{\underline{\sigma}}_{\mathrm{i}} + \underline{\underline{\sigma}}_{\mathrm{e}}) \underline{\nabla} u_{\mathrm{e}}\big) = \operatorname{div}(\underline{\underline{\sigma}}_{\mathrm{i}} \underline{\nabla} V_{\mathrm{m}}), & \text{in} \quad \Omega_{\mathrm{H}}, \\ \dot{w} + g(V_{\mathrm{m}}, w) = 0, & \text{in} \quad \Omega_{\mathrm{H}}, \\ \underline{\underline{\sigma}}_{\mathrm{i}} \underline{\nabla} V_{\mathrm{m}} \cdot \underline{n} = -\underline{\underline{\sigma}}_{\mathrm{i}} \underline{\nabla} u_{\mathrm{e}} \cdot \underline{n}, & \text{on} \quad \Sigma. \end{cases} \tag{2.3}$$

Here, u_{i}, u_{e} stand for the intra- and extra-cellular potentials, A_{m} for the rate of membrane surface per unit of volume, I_{app} for a given external current, C_{m} for the membrane capacitance, and V_{m} for the transmembrane potential ($V_{\mathrm{m}} = u_{\mathrm{i}} - u_{\mathrm{e}}$). The heart-torso interface is denoted by Σ.

The intra- and extracellular (anisotropic) conductivity tensors, $\underline{\underline{\sigma}}_{\mathrm{i}}$ and $\underline{\underline{\sigma}}_{\mathrm{e}}$, are given by $\underline{\underline{\sigma}}_{\mathrm{i},e} = \sigma^{\mathrm{t}}_{\mathrm{i},e} \underline{\underline{I}} + (\sigma^{\mathrm{l}}_{\mathrm{i},e} - \sigma^{\mathrm{t}}_{\mathrm{i},e}) \underline{a} \otimes \underline{a}$, where $\underline{a}$ is a unit vector parallel to the local fibre direction and $\sigma^{\mathrm{l}}_{\mathrm{i},e}$ and $\sigma^{\mathrm{t}}_{\mathrm{i},e}$ are, respectively, the longitudinal and transverse conductivities of the intra- and extra-cellular media. The variable w, possibly vector valued, and the functions g and I_{ion} depend on the considered membrane ionic model, see *e.g.* [17,18,21]. Following [4,5], here we consider the Mitchell–Schaeffer ionic model [16].

Remark 2.1. Note that the bidomain equations (2.3) are written on the reference configuration Ω_{H} and that the local fibre directions $\underline{a}$ are independent of the myocardium displacement $\underline{y}$. This is a consequence of the above mentioned one-way coupling assumption.

The torso electrical potential u_T is described by the Laplace equation in the torso domain Ω_T

$$\begin{cases} \mathrm{div}(\underline{\underline{\sigma}}_T \underline{\nabla} u_T) = 0, & \text{in} \quad \Omega_T, \\ \underline{\underline{\sigma}}_T \underline{\nabla} u_T \cdot \underline{n}_T = 0, & \text{on} \quad \Gamma_{\text{ext}}. \end{cases} \tag{2.4}$$

where $\underline{\underline{\sigma}}_T$ stands for the torso conductivity tensor and $\underline{n}_T$ is the outward unit normal to the torso external boundary Γ_{ext}.

As regards the heart-torso coupling, standard coupling conditions generally adopted in the literature enforce both the continuity of potentials and currents on the interface Σ (see *e.g.* [17,21]). Numerical experiments reported in [4,5] have shown that this kind of full heart-torso coupling can be relaxed without seriously affecting the quality of the ECG, by imposing

$$\begin{cases} u_T = u_e, & \text{on} \quad \Sigma, \\ \underline{\underline{\sigma}}_e \underline{\nabla} u_e \cdot \underline{n} = 0, & \text{on} \quad \Sigma. \end{cases} \tag{2.5}$$

This corresponds to the so-called isolated heart assumption, which allows a decoupled solution of heart-torso problems (2.3) and (2.4). Indeed, we first solve for u_e by enforcing $(2.5)_2$ in (2.3) and, then, we recover u_T by imposing $(2.5)_1$ in (2.4). Therefore, at the discrete level, the instantaneous computation of the 12-lead ECG from the interface extracellular potential $u_{e|\Sigma}$ reduces to a simple matrix-vector operation, with an off-line computation of the corresponding transfer matrix. We refer to [4] for further details on the computation of the ECG.

2.3 Anatomical Model and Computational Meshes

The computational meshes were produced starting from the Zygote[1] heart model – a geometric model based on actual anatomical data – using the `3-matic`[2] software to obtain computationally-correct surface meshes, and the `Yams` [8] and `GHS3D` [9] meshing softwares to further process the surface meshes and generate the 3D final computational meshes, respectively. These computational meshes are displayed in Figures 1-2 and the heart meshes correspond to the diastolic stage immediately before atrial contraction, as this is assumed to provide a stress-free reference configuration. Note that the electrophysiological simulations require a finer mesh to adequately represent the propagative behavior of the depolarization and repolarization waves, hence we computed an interpolation operator to use the electrical simulations as a prescribed input at the nodes of the coarser mechanical mesh.

As regards fibre directions, since they are not provided in the original anatomical model we used an *automatic* procedure to prescribe them in the meshes. We first computed a 3D distance map [2] from any point in the tissue to the epicardium and endocardium, see Figure 1. This distance was then employed to

[1] `www.3dscience.com`
[2] `www.materialise.com`

Fig. 1. Computational heart meshes for mechanical (left, about 20,000 nodes) and electrical (center, about 110,000 nodes) simulations - Fibre directions (right)

prescribe fibres with elevation angles (with respect to the circumferential direction given by the cross product of the distance gradient and the long axis) varying linearly across the wall thickness from -65 to +65 degrees from epicardium to endocardium. We applied an additional smoothing and interpolation procedure to take into account some specific physiological direction prescriptions on the boundary resulting from tissue truncation and around the valves [19], see the final fibre directions visualized with `MedINRIA`[3] in Figure 1.

The distance map was also used to prescribe left-ventricle transmural action potential duration (APD) heterogeneity within the ionic model, which allows to obtain a correct T-wave orientation in the ECG, see *e.g.* [4,5].

3 Numerical Experiments

The variational formulations of the electrical and mechanical problems are both discretized in space using $\mathbb{P}_1$ Lagrangian finite elements, (see *e.g.* [5,4,20]). For the time discretization, a Newmark scheme is used for the solid part and a semi-implicit second order Backward Differentiation Formula (BDF) scheme for the electrical part.

In the next paragraphs we present the results of the electromechanical simulations performed in a normal and a pathological situation. For the meshes considered, each mechanical simulation takes about one hour on a standard PC for a complete heartbeat. As regards the electrical simulation, about four hours of computations are required on a recent workstation. In each case a convergence study with respect to the meshes was performed, see [6] for details.

3.1 A Healthy Case

In Figure 3 we display the simulated 12-leads ECG obtained with the electrical model in the healthy case (in black lines). We can observe that the QRS-complex

[3] `www-sop.inria.fr/asclepios/software/MedINRIA/`

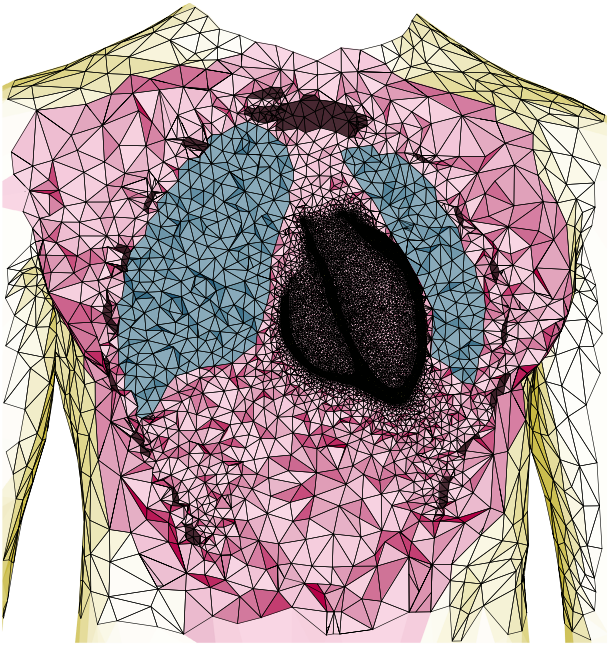

Fig. 2. Computational heart-torso mesh (cross-section) for ECG simulations

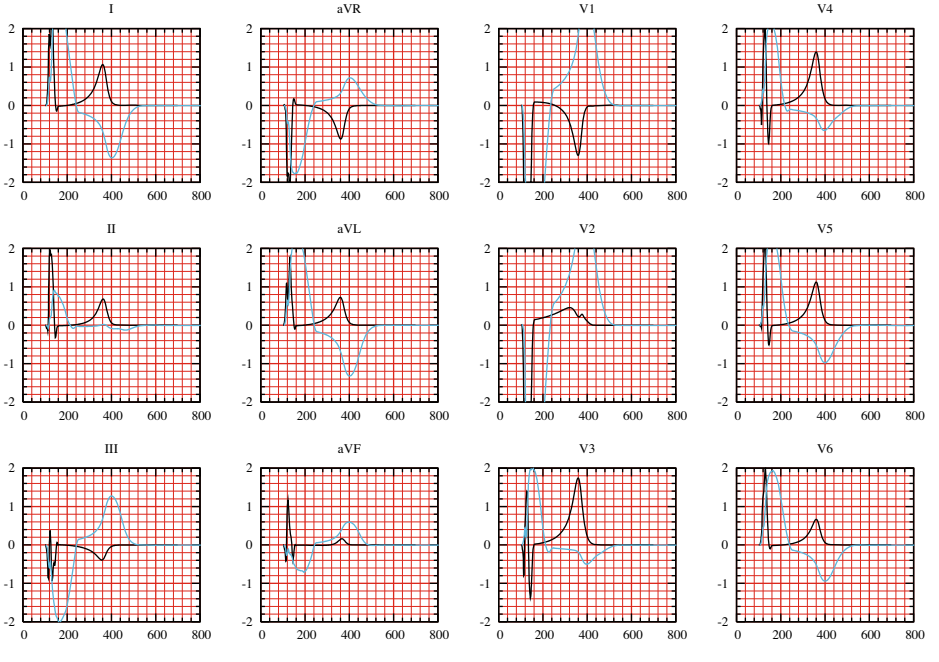

Fig. 3. Simulated 12-leads ECGs for a healthy case (black) and LBBB condition (blue)

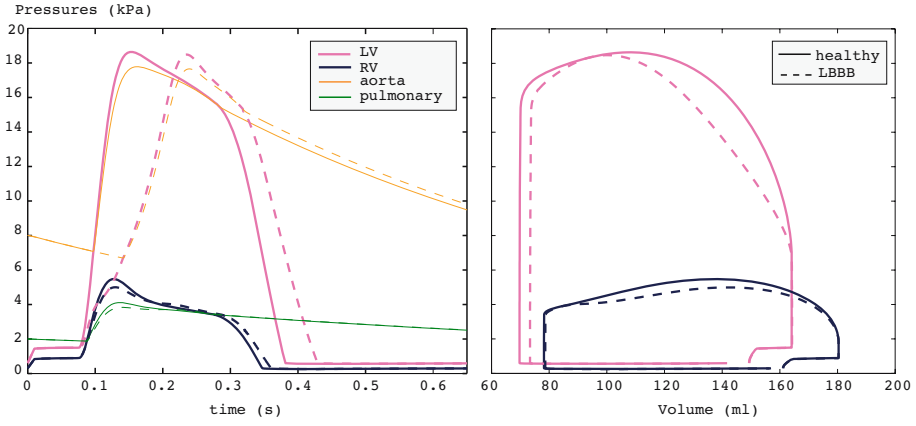

Fig. 4. Mechanical indicators: pressures (left) and pressure-volume curves (right)

has a physiological orientation, duration (70 ms) and amplitude, in each of the 12 leads. We deduce that the heart axis lies around 6.5 degrees, which is also within the normal range (between 0 and 90 degrees). Note that – since our anatomical model does not include the atria (Section 2.3) – the P-waves are missing.

This electrical simulation was used to simulate the mechanical phenomena over a complete heart beat. The resulting indicators – pressures and volumes in the various compartments – are displayed in Figure 4, in solid lines. The main quantitative indicators – in particular ejected fractions and maximum ventricular pressures – have physiological values.

3.2 A Pathological Case

Figure 3 shows (in blue lines) the numerical ECG obtained when simulating a Left Bundle Branch Block (LBBB), *i.e.* the initial activation starts only in the right ventricle. We emphasize that this is the only change in the model with respect to the previous healthy case. As expected, the QRS duration is larger (about 140 ms) and the time interval between the beginning of the QRS and its latest positive peak in V6 is larger than 40 ms (about 60 ms), which are recognized criteria in the diagnosis of a LBBB.

The corresponding mechanical indicators are displayed in Figure 4, in dashed lines. Compared to the healthy case, we can see that the ejection fraction is slightly reduced in the left ventricle, and that the left ventricular pressure increases much more slowly during systole. Note that this is only supposed to represent a partial and short term effect of the LBBB, as no change was introduced in the mechanical parameters (contractility, stiffness, preload, in particular), whereas of course an accompanying pathology such as a septal infarct on the one hand, and longer-term adaptation effects on the other hand, would definitely have an impact on these parameters. In Figure 5 we also show some snapshots of the simulated electrical activation and mechanical deformed

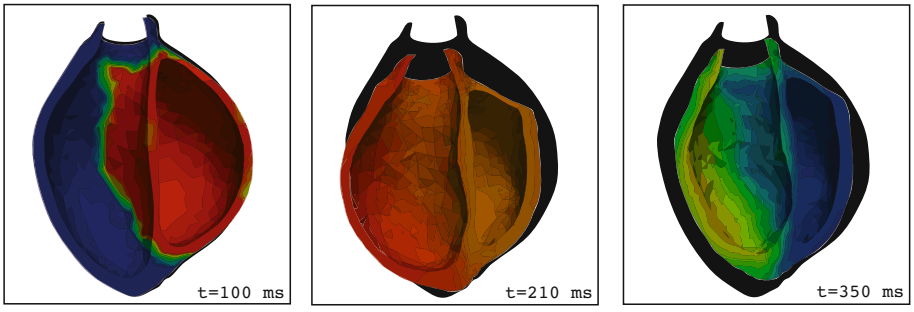

Fig. 5. Simulation of a LBBB: Snapshots of the electrical activation V_m (in colors) and mechanical deformed configurations (black outline for reference configuration)

configurations during a cardiac cycle, and the dissynchrony of the activation and contraction is clearly visible.

4 Conclusions

We have presented numerical simulations of the electromechanical activity of the heart based on an integrated 3D mathematical model of cardiac electrophysiology and mechanics, without mechano-electrical feedback. Typical medical indicators – such as pressures, volumes and ECGs – showed physiological values in a healthy case. The predictive capabilities of the model have been illustrated with a numerical simulation of a pathological condition (LBBB). Indeed, the resulting medical indicators provided physiological values, by a simple recalibration of the model parameters directly affected by the pathology (initial activation).

Further developments will include the incorporation of mechano-electrical feedback, ventricular flows and valve mechanics, see *e.g.* [1].

Acknowledgments

The research leading to these results has received funding from the European Community's Seventh Framework Program (FP7/2007-2013) under grant agreement number 224495 (euHeart project). The authors also acknowledge support by INRIA through its large scope initiative CardioSense3D. In addition, they wish to thank Elsie Phé (INRIA) for her work on the anatomical models and meshes, and Dr. Serge Cazeau for his helpful comments on the ECGs.

References

1. Astorino, M., Gerbeau, J.-F., Pantz, O., Traoré, K.: Fluid-structure interaction and multi-body contact. Application to aortic valves. Comp. Meth. Appl. Mech. Engng., doi:10.1016/j.cma.2008.09.012

2. Baerentzen, J., Aanaes, H.: Signed distance computation using the angle weighted pseudo-normal. IEEE Trans. Visual. Comput. Graph. 11(3), 243–253 (2005)
3. Bestel, J., Clément, F., Sorine, M.: A biomechanical model of muscle contraction. In: Niessen, W.J., Viergever, M.A. (eds.) MICCAI 2001. LNCS, vol. 2208. Springer, Heidelberg (2001)
4. Boulakia, M., Fernández, M.A., Gerbeau, J.-F., Zemzemi, N.: Mathematical modelling of electrocardiograms: a numerical study (submitted)
5. Boulakia, M., Fernández, M.A., Gerbeau, J.-F., Zemzemi, N.: Towards the numerical simulation of electrocardiograms. In: Sachse, F.B., Seemann, G. (eds.) FIMH 2007. LNCS, vol. 4466, pp. 240–249. Springer, Heidelberg (2007)
6. Chapelle, D., Fernández, M.A., Gerbeau, J.-F., Moireau, P., Zemzemi, N.: A 3D model for the electromechanical activity of the heart (in preparation, 2009)
7. Ciarlet, P.G.: Mathematical Elasticity. In: Three-Dimensional Elasticity. Studies in Mathematics and its Applications, vol. I. North-Holland, Amsterdam (1988)
8. Frey, P.: Yams: A fully automatic adaptive isotropic surface remeshing procedure. Technical report 0252, Inria, Rocquencourt, France (November 2001)
9. George, P.L., Hecht, F., Saltel, E.: Fully automatic mesh generator for 3D domains of any shape. Impact of Comp. in Sci. ans Eng. 2, 187–218 (1990)
10. Hill, A.V.: The heat of shortening and the dynamic constants in muscle. Proc. Roy. Soc. London (B) 126, 136–195 (1938)
11. Huxley, A.F.: Muscle structure and theories of contraction. In: Progress in Biophysics and Biological Chemistry, vol. 7, pp. 255–318. Pergamon Press, Oxford (1957)
12. Kerckhoffs, R.C.P., Healy, S.N., Usyk, T.P., McCulloch, A.D.: Computational methods for cardiac electromechanics. Proc. IEEE 94(4), 769–783 (2006)
13. Lab, M.J., Taggart, P., Sachs, F.: Mechano-electric feedback. Cardiovasc. Res. 32, 1–2 (1996)
14. Le Tallec, P.: Numerical methods for nonlinear three-dimensional elasticity. In: Ciarlet, P.G., Lions, J.-L. (eds.) Handbook of Numerical Analysis, vol. 3. Elsevier, Amsterdam (1994)
15. MacDonald, D.A.: Blood Flow in Arteries. Edward Harold Press (1974)
16. Mitchell, C.C., Schaeffer, D.G.: A two-current model for the dynamics of cardiac membrane. Bulletin Math. Bio. (65), 767–793 (2003)
17. Pullan, A.J., Buist, M.L., Cheng, L.K.: Mathematically modelling the electrical activity of the heart. From cell to body surface and back again. World Scientific, Singapore (2005)
18. Sachse, F.B.: Computational Cardiology: Modeling of Anatomy, Electrophysiology, and Mechanics. Springer, Heidelberg (2004)
19. Sachse, F.B., Frech, R., Werner, C.D., Dossel, O.: A model based approach to assignment of myocardial fibre orientation. Computers in Cardiology, 145–148 (1999)
20. Sainte-Marie, J., Chapelle, D., Cimrman, R., Sorine, M.: Modeling and estimation of the cardiac electromechanical activity. Computers & Structures 84, 1743–1759 (2006)
21. Sundnes, J., Lines, G.T., Cai, X., Nielsen, B.F., Mardal, K.-A., Tveito, A.: Computing the electrical activity in the heart. Springer, Heidelberg (2006)
22. Tung, L.: A bi-domain model for describing ischemic myocardial D–C potentials. PhD thesis, MIT (1978)

A Global Sensitivity Index for Biophysically Detailed Cardiac Cell Models: A Computational Approach

Sanjay Kharche[1], Niklas Lüdtke[2], Stefano Panzeri[3], and Henggui Zhang[1]

[1] Biological Physics Group, University of Manchester, Manchester, M13 9PL, UK
[2] MPI for Biological Cybernetics, Spemannstrasse 38, D-72076, Tübingen, Germany
[3] Italian Institute of Technology, Robotics, Brain and Cognitive Sciences Department, I-16163, Genoa, Italy

Abstract. Biophysically detailed cardiac cell models are based upon stiff ordinary differential equations describing ionic channels and intracellular dynamics aiming at reproducing experimental action potentials (APs) and intracellular calcium ($[Ca^{2+}]_i$) transients. Channel blocking and bifurcation analyses are local sensitivity analyses in model parameter space. However, all parameters influence model behaviour and require a global sensitivity index quantifying the influence of parameters on model responses. Identification of the influence of individual parameters increases our understanding of models. A global parameter sensitivity index for assessing the sensitivity of model responses to parameters in cardiac cell models is proposed. The robust index was applied to four widely used models. The analysis revealed that whilst models have common sets of parameters influencing AP and $[Ca^{2+}]_i$ transients, there are subtle differences. This sensitivity analysis offers a systematic method for quantifying the influence of individual parameters on model behaviour to assist in model reduction, refinement or development.

Keywords: Cardiac simulation, global sensitivity analysis, high throughput computing, modelling and simulation tool.

1 Introduction

Systems biology offers increasingly powerful tools for the simulation of complex biological processes [1]. In particular cardiac cell models consist of stiff coupled ordinary differential equations (ODEs) describing cell membrane and intracellular electrophysiology [2, 3, 4, 5]. These models consist of many variables (> 10) with large numbers of parameters (>10^2) and aim to simulate experimentally observed membrane action potentials (APs) and the intracellular calcium ($[Ca^{2+}]_i$) transients. Although the contribution of individual ionic channels and intracellular ionic sequestration processes to the electrical activity is apparent, the exact function of parameters may not be obvious. Electrophysiological data on which modelling parameter estimates are based are often incomplete, have large variability and impede mathematical modelling. Such shortcomings necessitate intuitive estimation of modelling parameters whilst validating the response, *i.e.* APs and $[Ca^{2+}]_i$ transients, against experimental measurements.

N. Ayache, H. Delingette, and M. Sermesant (Eds.): FIMH 2009, LNCS 5528, pp. 366–375, 2009.
© Springer-Verlag Berlin Heidelberg 2009

Parameter sensitivity analysis is the process of evaluating the sensitivity of model responses to parameter perturbations [6, 7]. Traditionally, sensitivity analysis of cardiac models is physiologically motivated and often involves simulation of ion channels blocking [8] or bifurcation analysis [9]. With such methods, although one or few parameters like conductances are varied simultaneously to evaluate their effects on overall model behaviour, all other non-linear interactions and parameters are generally left intact. Thus, such studies only identify the *local* sensitivity of model responses in parameter space, *i.e.* the influence of one or a few parameters on model responses. In addition, channel blocking and bifurcation analyses are insensitive to the inherent multi-model behaviour of cardiac models. From a modeling perspective, cardiac cell models are coupled ODEs wherein all parameters simultaneously impact response to varying degrees. In addition, Hodgkin-Huxley type cardiac models are primarily a collation of multi-compartmental models of sarcolemmal ion channel and intracellular ionic homeostasis models, rendering them over determined in the modelling parameter space. Due to such over determined nature of modern cardiac models, corresponding parameters among different models simulating the same phenomenon, e.g. pacemaking in the sino-atrial node (SAN) of the rabbit, may not influence model responses to the same degree.

An immediate and relevant application of the proposed robust global indexing scheme is that of parameter estimation in cardiac cell models. Parameter estimation [10] has previously been applied to allow simulation of APs where all parameters in a ventricular cell model were estimated. Such an approach increases computational overheads due to undue estimation of redundant parameters that do not impact model response. Quantifying the influence of parameters will assist in reducing such overheads whilst allowing focused estimation in models that have a large number of parameters. Other algorithms for identifying parameter influence on AP responses have been developed [11, 12] and successfully implemented to estimate parameters in simple models [13], but a universally applicable method has not been developed to the best of our knowledge.

In the present study, we propose a novel global information-theoretic parametric sensitivity indexing scheme that assesses the sensitivity of model responses to parameters. This method is based on repeated simulations of a model with randomly selected parameter configurations. A large number of such simulations provides with sufficient sampling of the global parameter space to allow computation of correlation between individual parameters and modelling responses. Due to parameter configurations being selected randomly, the model responses are also random, and the proposed sensitivity index measures statistical relationships between randomized model parameters and responses. The index is based on a robust mutual information theoretic approach, which captures any form of non-linear correlation between parameters and model responses without making any implicit assumptions about the underlying distributions of the responses like normality and modality [7]. The index is applied to four well established models to demonstrate identification of individual parametric influence on model responses.

2 Methods

Models considered in this study consist of stiff coupled non-linear ODEs with Hodgkin-Huxley formulations of ionic currents with model specific intracellular ionic

Table 1. List of modelling parameters from the four models found to be relevant to this study. Notational consistency with original models [2, 3, 4, 5] is maintained, with paramters relevant to this study being described.

Parameter	Description
$[K^+]_o$, $[Na^+]_o$	Extracellular potassium and sodium concentrations respectively.
$[Ca^{2+}]_i$	Intracellular calcium concentration.
C_m	Cell sarcolemmal membrane capacitance.
I_{Na}	Sodium ion channel.
I_{CaL}	L-type calcium ion channel.
I_{CaT}	T-type calcium ion channel.
I_{Kr}	Rapid delayed rectifier potassium ion channel.
I_{K1}	Time-independent inward rectifier potassium ion channel.
$\overline{m}_{0.5}$	Steady state half-activation voltage of I_{Na}.
$\overline{f}_{L,0.5}$	Steady state half-inactivation voltage of I_{CaL}.
$\overline{f}_{T,0.5}$	Steady state half-inactivation voltage of I_{CaT}.
$I_{K1,0.5}$	Half-deactivation voltage of I_{K1} conductance.
g_{Kr}	Maximal conductance of I_{Kr}.
g_{K1}	Maximal conductance of I_{K1}.
E_{CaL}	Reversal potential of I_{CaL}.
$\tau_{dL} = (dL_\alpha + dL_\beta)^{-1}$	I_{CaL} activation time kinetics in Kurata *et al.* [3]
$dL_\alpha =$ $-\frac{0.02839(V + p_{K1})}{e^{-(V+p_{K2})/2.5} - 1} - \frac{0.0849V}{e^{-V/4.808} - 1}$	with $p_{K1} = 35$ and $p_{K2} = 35$.
$\tau_{fL} = (fL_\alpha + fL_\beta)^{-1}$	I_{CaL} inactivation time kinetics in Zhang *et al.* [4], with $p_{Z1} = 25$.
$fL_\beta = \frac{p_{Z1}}{1 + e^{-(V+28)/4}}$	
$\tau_m =$ $[\frac{0.32(V+p_{CRN1})}{1-e^{-0.1(V+47.13)}} + 0.08e^{-V/11}]^{-1}$	I_{Na} activation time kinetics in the Courtemanche *et al.* [5] with $p_{CRN1} = 47.13$.

homeostasis mechanisms. To allow comparison among models with varying underlying dynamics, four well established cardiac cellular models were considered. As examples of auto-oscillatory pacemaking cardiac cellular systems, two rabbit SAN models were considered. These were the models by Kurata *et al.* [2] and by Zhang *et al.* [3]. As examples of excitable cardiac cellular systems, two models with vastly differing AP profiles were considered including the human atrial cell model by Courtemanche *et al.* [4] and the rat ventricular cell model by Pandit *et al.* [5]. In all models, independent variables were identified and numbered serially with no specific order of numbering. Due to their substantial influence, initial conditions (*i.c.*s) were also considered as parameters influencing model responses. This gave 194 independent parameters in Kurata *et al.* [2], 176 in Zhang *et al.* [3], 207 in Courtemanche *et al.* [4], and 223 in Pandit *et al.* [5] models. Notational consistency with the original models is maintained as far as possible. Model parameters relevant to results of this study are tabulated in Table 1.

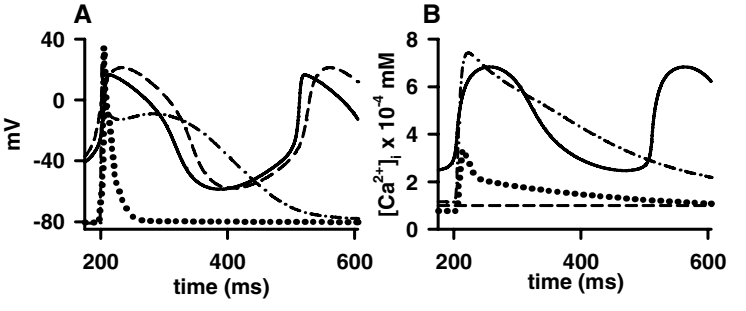

Fig. 1. Standard model AP (**A**) and $[Ca^{2+}]_i$ transients (**B**) in the Kurata *et al.* [2] (solid lines), Zhang *et al.* [3] (dashed lines), Courtemanche *et al.* [4] (dashed-dotted lines) and Pandit *et al.* [5] (dotted lines) models. All models show differing AP and $[Ca^{2+}]_i$ transients indicating the temporal characteristics of such AP and $[Ca^{2+}]_i$ transients as described in the Methods section.

Standard AP and $[Ca^{2+}]_i$ transient profiles from the four models are shown in Fig. 1 to illustrate the definition of typical maximal, minimal and temporal characteristics taken to be model responses. In particular, maximum diastolic potential (MDP) was defined as the minimum potential (V) during steady oscillations, overshoot potential (OS) was defined as the peak potential reached during an AP, upstroke velocity (dV/dt_{max}) was defined as the maximum positive rate of change of V during an AP upstroke, cycle length (CL) was defined as the duration between two consecutive upstrokes, AP duration (APD_{90}) was defined as the time interval between a MDP and the consequent 90% repolarization of V. Take off potential was defined as the V at which slope of AP became the same as the slope of line join between MDP and OS. The diastolic depolarization rate (DDR) was defined as slope of the line segment joining MDP and the take off potential. OS, dV/dt_{max} and APD_{90} were defined as in the SAN models. Due to the increasing experimental and modelling relevance of $[Ca^{2+}]_i$, diastolic $[Ca^{2+}]_i$ ($[Ca^{2+}]_{i,\min}$) and systolic $[Ca^{2+}]_i$ ($[Ca^{2+}]_{i,\max}$) have

Table 2. Standard responses of the four models. Row A shows data for Kurata *et al.* [2], row B for Zhang *et al.* [3], row C for Courtemanche *et al.* [4] and row D for Pandit *et al.* [5] models. In case of non-pacemaking excitable models [4, 5], CL and DDR are not relevant. In Zhang *et al.* [3], $[Ca^{2+}]_i$ is constant at 0.1 μM.

Model	MDP (mV)	OS (mV)	dV/dt_{max} (mV/ms)	APD_{90} (ms)	CL (ms)	DDR (mV/ms)	$[Ca^{2+}]_{i,min}$ (μM)	$[Ca^{2+}]_{i,max}$ (μM)
A	-58.6	16.6	6.4	269.1	307.3	0.215	0.25	0.68
B	-58.0	21.1	2.7	174.4	327.2	0.249	0.10	0.10
C	-81.1	24.8	216.5	313.0	NA	NA	0.12	0.74
D	-80.6	34.6	117.2	41.2	NA	NA	0.08	0.32

been incorporated as responses in this study. A quantitative summary of the standard modelling responses of the four models is given in Table 2.

The global information-theoretic sensitivity index was developed in a previous study [14]. It constitutes deterministic quantification of the correlation between modelling parameters, which included initial conditions (*i.c.*s), to model responses. Through multiple evaluations of the model (more than 10^5) for randomly selected configurations of parameters including *i.c.*s, one obtains empirical samples of model responses, from which the underlying probability distributions of responses are computed. Thus, although the models under investigation are deterministic, parameters and responses are randomised. The sensitivity indexing consists of determining statistical relations between parameters and responses. The impact of individual parameters on a particular model response can be quantified in terms of the correlation between the sampling distributions of the parameters and the resulting responses distributions. In the information-theoretic approach, a universally applicable correlation measure, the mutual information index (MI), was chosen as the mutual information between an individual parameter X_i and a model response Y, and the total information, or response entropy, in the system as

$$MI_i = \frac{I(X_i;Y)}{H(Y)}. \tag{1}$$

where $I(X_i;Y)$ is the mutual information and $H(Y)$ is the response entropy. Further details for computing $I(X_i;Y)$ and $H(Y)$ are discussed elsewhere [14]. In brief, the entropy $H(Y)$ quantifies the sampling-induced uncertainty of the response values (i.e. the "spread" of the distribution of Y), and the mutual information is the portion of this uncertainty that parameter X_i accounts for. Thus, every model response is associated with several MI_i related to parameter i. This set of MI_i for every model response can be further normalised to the maximal value in that set of MI_i to uniformly reveal the relative influence of parameters on that particular response.

All models were integrated using an Euler integration scheme with a constant time step of 10^{-4} ms for the Kurata *et al.* [2], Zhang *et al.* [3] and Pandit *et al.* [5] models and

5×10^{-3} ms in the Courtemanche *et al.* [4] case. Solutions obtained using such time steps were found to be stable against perturbation of integration parameters. Parameter configurations were chosen with a 30% maximal random perturbation of each modelling parameter including *i.c.*s. All parameters were perturbed simultaneously to obtain such parameter configurations. Such perturbations have been found to give sufficient information for computation of correlation in several ODE models in systems biology [14]. For each parameter configuration, the models were integrated for 8 s before computing model responses. Each model was thus evaluated 10^5 times to give sufficient data for computing MI. The simulations were carried out on two Linux Condor clusters each with 200 processors, and on a distributed memory UK National Grid Service supercomputer, allowing efficient high throughput computation. Mersenne Twister random number generator was adopted in this study [15] due to its ability to reproduce large numbers of uniformly distributed unbiased random numbers with very low periodicity.

3 Results

Standard AP and $[Ca^{2+}]_i$ transients computed from the models considered are shown in Fig. 1. As can be seen, the rabbit SAN models (Kurata *et al.* [2] and Zhang *et al.* [3]) have different responses. AP for the human atrial cell (Courtemanche *et al.* [4]) is much longer than in the rat ventricle (Pandit *et al.* [5]). There are also differences in the $[Ca^{2+}]_i$ transients. The sensitivity indexing allowed quantified ranking of the influence of all model parameters on model responses. The results are summarized in Fig. 2, wherein the parameters with maximal MI have been identified. The higher the value of MI, the more relevant the parameter is for that particular model response. Redundant parameters with no influence on model responses, or with very low MI, can also be identified. Computed MI show that MDP in the SAN models is mainly regulated by components of the activation time kinetics of I_{CaL} (Kurata *et al.* [2]) or by g_{Kr} (Zhang *et al.* [3]). In the excitable cell models, MDP is regulated by $[K^+]_o$. In the SAN models, MI for E_{CaL} (~ 45 mV) is highest for OS. In case of the excitable cell models, , OS was seen to be regulated maximally by I_{Na}, either via components of the activation kinetics (Courtemanche *et al.* [4]) or the steady state voltage of activation, $\overline{m}_{0.5}$ (Pandit *et al.* [5]). dV/dt_{max} in the SAN models was seen to be largely dependent on I_{CaL} either via components of the activation time kinetics, p_{K2} (Kurata *et al.* [2]) or the half voltage of inactivation, $\overline{f}_{L,0.5}$ (Zhang *et al.* [3]). In the excitable cell models, cellular capacitance, C_m (Courtemanche *et al.* [4]) or the *i.c.* of V (Pandit *et al.* [5]) regulated OS. APD_{90} in the SAN models was regulated by components of I_{CaL} activation time kinetics, p_{K2} (Kurata *et al.* [2]) and inactivation time kinetics of I_{CaL}, p_{Zl} (Zhang *et al.* [3]). In the excitation models, APD_{90} was mainly regulated by I_{K1} parameters. CL in the SAN models is regulated by $\overline{f}_{T,0.5}$

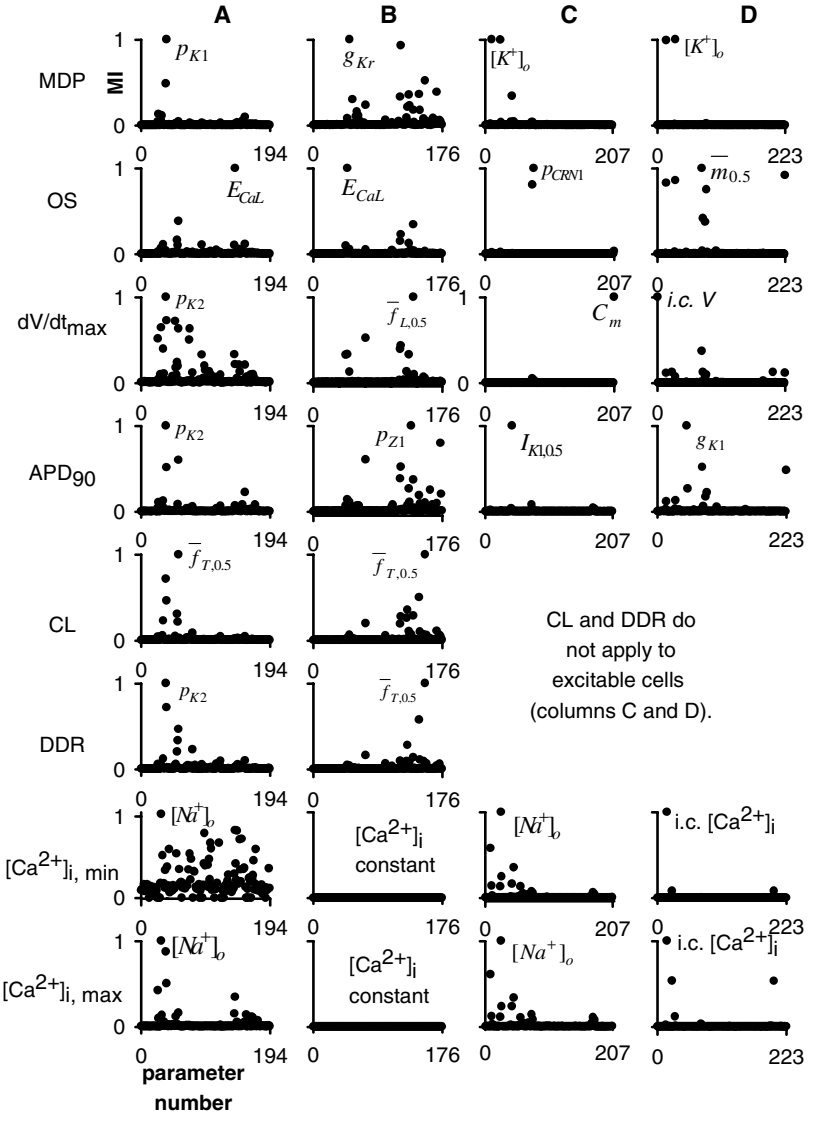

Fig. 2. Normalized MI giving the relative ranking of parametric influence on model responses. Column A shows data for Kurata *et al.* [2], column B for Zhang *et al.* [3], column C for Courtemanche *et al.* [4], and column D for Pandit *et al.* [5] models. Rows represent data for the 8 model responses as shown. In all panels, the vertical axis shows relative MI and the horizontal axis shown parameter number. Parameters affecting model responses maximally (relative MI = 1) are shown in the individual panels along with MI of all other parameters relative to the maximal parameter values.

whilst DDR is regulated by components of the activation time kinetics of I_{CaL} (Kurata *et al.* [2]) and $\overline{f}_{T,0.5}$ (Zhang *et al.* [3]). There is no CL and DDR in case of the excitable cell models. $[Ca^{2+}]_i$ is taken to be constant in the Zhang *et al.* [3] model. However, $[Ca^{2+}]_{i,\min}$ and $[Ca^{2+}]_{i,\max}$ are regulated by the extracellular $[Na^+]_o$ in Kurata *et al.* [2] and Courtemanche *et al.* [4], whilst the *i.c.* for $[Ca^{2+}]_i$ is important in Pandit *et al.* [5]. Along with identification of maximally influential parameters, the MI ranking also shows redundant parameters. It can be clearly seen from Fig. 2 that although several parameters affect MDP in the Zhang *et al.* [3] case, the same is regulated primarily by $[K^+]_o$ in the excitable cell models. Another example is in case of the diastolic $[Ca^{2+}]_i$ where almost all parameters affect its value in case of the Kurata *et al.* [2] model, whilst only a handful have play a significant role in case of the Pandit *et al.* [5] case. From all MI, it is clear that the underlying kinetics and steady state dynamics influence model behaviour to a greater extent than ion channel conductances.

The simulations were carried out using 200 processors on two Linux Condor pools and a UK National Grid Service supercomputer requiring between 10 hours and 6 days depending on the model, number of state variables, integration time step, and incidence of model break-down due to parameter perturbations.

4 Conclusions and Discussion

This MI analysis shows that although there is a common set of parameters regulating responses of the models (*e.g.* in the SAN models E_{CaL} regulates OS and $\overline{f}_{T,0.5}$ regulates CL; in the excitation models $[K^+]_o$ regulates MDP), often different models rely upon distinct mechanisms to reproduce various desired responses, *e.g.* the long and short APD_{90} in Courtemanche *et al.* [4] and Pandit *et al.* [5] respectively. Notwithstanding, MI analysis demonstrates that it is a much smaller subset of parameters that influence model behaviour substantially. It can also be seen that models (Pandit *et al.* [5]) in which there are very fast processes (like activation of I_{Na}) along with very slow processes (relaxation of $[Ca^{2+}]_i$), *i..c.*s play an important role in model behaviour. Along with relevant parameters, the MI also allows identification of redundant parameters. It can be seen from Fig. 2 that there are more modelling parameters affecting systolic $[Ca^{2+}]_i$ in the Kurata *et al.* [2] than in the Pandit *et al.* [5] model. One of the implications would be that manipulation or adjustments to the several remaining parameters in the Pandit *et al.* [5] $[Ca^{2+}]_i$ dynamics would not necessarily lead to desired changes in systolic $[Ca^{2+}]_i$. An interesting aspect of cardiac models that MI reveals is related to channel conductances. It can be seen from the MI of most model responses that time kinetics,

steady state dynamics and ionic concentrations regulate model behaviour to a greater extent than ion channel conductances. Thus, during model development and refinement, all aspects of ion channel models impinge on obtaining desired model behaviour.

Several new models are based on previous parent models [8]. Knowledge of MI of the parent model during such development will compliment experimental data. Indeed, the universally applicable MI proposed here indentifies exactly parameters influencing model responses. Thus, assuming the dynamics of the model is reliable, MI ranks the parameters objectively. Therefore, a few parameters could be considered simultaneously to affect any given response. If a complete set of responses is identified, a subset consisting of relevant parameters can be identified. The apparent parametric over determination of models studied stems from the fact that the dimensionality of the parameter space and number of ODEs in such models is usually determined by the amount of inbuilt physiological detail, rather than by considerations of model responses. This sensitivity analysis uncovers the degree of redundancy in the parameter set of a given model and can guide a subsequent step of model reduction. During model construction the inherent redundancy is not obvious, since there is no explicit mapping from the parameter space to the responses. Only numerical procedures, such as the sensitivity analysis demonstrated, can determine the relevant parameters. The sensitivity index obtained is based on random sampling of the parameter space, due to which the model responses become random variables. Global parameter sensitivity analysis consists of a break-down of the response variability, induced by the random sampling, into contributions by the different parameters. Thus, the chosen measure of response variability is crucial for the outcome of the analysis.

One key motivation for choosing an information-theoretic form of sensitivity analysis was the general applicability of the mutual information measure to non-linear systems. As in many other non-linear models [16], responses in cardiac models also show multi-modality. The parameter sensitivity index proposed in this study has the ability to accommodate such complex features and give accurate ranking of parameters. In contrast, the variance based global sensitivity indices [7], are not suitable for the analysis of multi-modal models since variance is inherently a uni-modal measure of variability. In the information-theoretic approach, the underlying measure of variability is the Shannon entropy, which is calculated directly from the response probability distribution, as estimated from multiple model evaluations. Hence, there is no presumption of model behaviour and responses.

In conclusion, a novel indexing scheme to quantify the influence of modelling parameters objectively has been introduced. The robust global index provides quantitative insight into the underlying dynamics of models, allowing model reduction and objective manipulation. It can further contribute to parameter estimation and eventually novel model development techniques.

Acknowledgment. This work was supported by Wellcome Trust (UK) (WT/081809/Z06/Z).

References

1. Robertson, S., Smith, C., Langhans, A., McLinden, S., Oberhardt, M., Jakab, K., Dzamba, B., DeSimone, D., Papin, J., Peirce, S.: Multiscale computational analysis of Xenopus laevis morphogenesis reveals key insights of systems-level behavior. BMC Systems Biology 1, 1–46 (2007)
2. Kurata, Y., Hisatome, I., Imanishi, S., Shibamoto, T.: Dynamical description of sinoatrial node pacemaking: improved mathematical model for primary pacemaker cell. Am. J. Physiol. 283, H2074–H2101 (2002)
3. Zhang, H., Holden, A.V., Kodama, I., Honjo, H., Lei, M., Varghese, T., Boyett, M.R.: Mathematical models of action potentials in the periphery and center of the rabbit sinoatrial node. Am. J. Physiol. 279, H397–H421 (2000)
4. Courtemanche, M., Ramirez, R.J., Nattel, S.: Ionic mechanisms underlying human atrial action potential properties: insights from a mathematical model. Am. J. Physiol. 275, H301–H332 (1998)
5. Pandit, S.V., Clark, R.B., Giles, W.R., Demir, S.S.: A Mathematical Model of Action Potential Heterogeneity in Adult Rat Left Ventricular Myocytes. Biophys. J. 81, 3029–3051 (2001)
6. Shin, S.-Y., Choo, S.-M., Woo, S.-H., Cho, K.-H.: Cardiac systems biology and parameter sensitivity analysis: Intracellular Ca2+ regulatory mechanisms in mouse ventricular myocytes. In: Seitz, H., Werther, M. (eds.) Advances in Biochemical Engineering and Biotechnology - Protein-Protein Interaction, pp. 25–45. Springer, Heidelberg (2008)
7. Saltelli, A., Ratto, M., Tarantola, S., Campolongo, F.: Sensitivity Analysis for Chemical Models. Chem. Rev. 105(7), 2811–2828 (2005)
8. Wilders, R.: Computer modelling of the sinoatrial node. Medical and Biological Engineering and Computing 45(2), 189–207 (2007)
9. Kurata, Y., Matsuda, H., Hisatome, I., Shibamoto, T.: Regional Difference in Dynamical Property of Sinoatrial Node Pacemaking: Role of Na^+ Channel Current. Biophys. J. 95(2), 951–977 (2008)
10. Dokos, S., Lovell, N.H.: Parameter estimation in cardiac ionic models. Prog. Biophy. Mol. Biol. 85(2-3), 407–431 (2004)
11. Bueno-Orovio, A., Cherry, E.M., Fenton, F.H.: Minimal model for human ventricular action potentials in tissue. J. Theo. Biol. 253(3), 544–560 (2008)
12. Oliver, R.A., Krassowska, W.: Reproducing cardiac restitution properties using the Fenton–Karma membrane model. Ann. Biomed. Eng. 33, 907–911 (2005)
13. Fenton, F.H., Karma, A.: Vortex dynamics in three-dimensional continuous myocardium with fiber rotation: Filament instability and fibrillation. Chaos 8(20) (1998)
14. Lüdtke, N., Panzeri, S., Brown, M., Broomhead, D.S., Knowles, J., Montemurro, M.A., Kell, D.B.: Information-theoretic sensitivity analysis: a general method for credit assignment in complex networks. J. R Soc. Interface 5(19), 223–235 (2008)
15. Matsumoto, M., Nishimura, T.: Mersenne twister: a 623-dimensionally equidistributed uniform pseudo-random number generator. ACM Trans. Model. Comput. Simul. 8(1), 3–30 (1998)
16. Naess, A., Dimentberg, M.F., Gaidai, O.: Lotka-Volterra systems in environments with randomly disordered temporal periodicity. Phys. Rev. E 78, 021126 (2008)

Cardiac Motion Recovery and Boundary Conditions Estimation by Coupling an Electromechanical Model and Cine-MRI Data

Florence Billet*, Maxime Sermesant, Hervé Delingette, and Nicholas Ayache

INRIA Sophia-Antipolis, 2004 route des lucioles – BP 93,
FR-06902 Sophia Antipolis, France
florence.billet@inria.fr

Abstract. We present a method for cardiac motion recovery using the adjustment of an electromechanical model of the heart to cine MRI. This approach is based on a proactive model which consists in a constrained minimisation of an energy coupling the model and the data. The presented method relies on specific image features in order to constrain the motion of the endocardia and epicardium and impose boundary conditions at the base. Thus, image intensity and gradient information are used to constrain the motion of the myocardium surfaces while a 3D block matching technique leads to the motion estimation of base vertices. Finally, we show that the implicit time integration of those forces and personalised boundary conditions lead to a better cardiac motion recovery from cine-MR images.

1 Introduction

Cardiovascular diseases are the number one cause of death in the industrialised world and is projected to remain so. That's why the modeling of the heart's electromechanical activity is an active research area [1,2,3]. Moreover, the coupling of these models and clinical data allows us to personalise them and then to simulate a number of pathologies or the effect of therapeutic actions, and to analyse the cardiac function of the considered patient.

There exist several approaches in the literature to create such patient-specific models of the heart from clinical images. The concept of deformable models is often used to adjust a geometrical model of the heart on time series of medical images [4,5,6]. In such approaches, the surface or the volumetric mesh is fitted to the apparent boundaries of the heart in the image by minimising the sum of an image energy and a regularising or internal energy. Those models may produce proper segmentations and are rather efficient, however they rely on little *a priori* knowledge of the heart motion which limits their ability to recover tangential motion due to the aperture problem.

Other approaches strongly constrain the estimation of motion by coupling an electromechanical heart model using data assimilation methods. In such a framework, dynamical systems representing electromechanical models of the heart are

* Corresponding author.

N. Ayache, H. Delingette, and M. Sermesant (Eds.): FIMH 2009, LNCS 5528, pp. 376–385, 2009.
© Springer-Verlag Berlin Heidelberg 2009

adjusted to time series of images by adding a filter that constrain the state variables (*i.e* the position and the velocity) and the model parameters to match the available observations. P.C Shi *et al.* introduced such techniques by integrating cardiac models and Kalman filters [7,8]. However, the use of extended Kalman filtering is often limited since they implies the use of full covariance matrices whose size are equal to the square of the number of state variables augmented by the number of parameters to estimate. To avoid the curse of dimensionality, some authors [9] have devised non optimal filters which do not involve any matrix inversion (unlike Kalman filtering). This approach leads to much faster computations and has been the inspiration of the work presented in this paper.

We showed in [14] the equivalence under some hypothesis between the method proposed in [9] and the use of a proactive deformable model introduced in [13]. In this paper, we use the proactive deformable model which extends the concept of deformable models by adding an active electromechanical model of the heart motion as the regularising energy term. In this paper, we improve from our previous work with two additional contributions. First, we provide an implicit formulation of image forces that can better predict the image forces between two time steps. Second, we estimate the motion of the base of the ventricles, where the ventricles are connected to the atria and outflow tracts. This represents a significant advance since most previous work on electromechanical modelling of the heart consider that ventricle bases are fixed or linked to fixed points through springs. To recover the base motion from image, we use a block matching technique at the base points that uses intensity correlation to track points along the cardiac cycle.

2 Electromechanical Model

As we want the complexity of the model to match the relatively sparse measures available from imaging data, we consider in this paper a fairly reduced electromechanical model. For instance, our model relies on linear elasticity for myocardium mechanics although a nonlinear material undergoing large strain would be better suited. However, we found the current reduced model to be a good trade-off in terms of computational efficiency and physiological realism. Furthermore, this coarse level of modeling makes the estimation of the mechanical state and parameters tractable and allows us to test the behaviour of the model on several heart beats. Our cardiac model couples two biophysical components : electrophysiology and biomechanics. Due to its efficiency, we use a multi-front anisotropic Eikonal approach solved with a Fast Marching algorithm on a volumetric tetrahedral mesh [10].

The depolarisation time t_d of the electrical wave for a given vertex of the volumetric mesh is computed by solving the anisotropic Eikonal equation $v^2(\nabla t_d^T D \nabla t_d) = 1$, where v is the local conduction velocity parameter and D is the tensor defining the conduction anisotropy. In the fibre coordinates, $D = diag(1, \rho, \rho)$, where ρ is the conduction anisotropy ratio between longitudinal and transverse directions.

The biomechanical model, derived from a multi-scale modelling of the myocardium detailed in [11], is composed of an active contractile element controlled by the electrophysiology and a parallel one which represents the properties of the tissue and is anisotropic linear visco-elastic.

The active contractile element is controlled by the depolarisation time t_d computed with the Eikonal equation and creates a stress tensor $\sigma_C \boldsymbol{f} \otimes \boldsymbol{f}$ where $\boldsymbol{f}$ is the 3D fibre orientation, $\otimes$ the dyadic product and σ_C the strength of the contraction defined by the equation 1:

$$\sigma_C(t) = \begin{cases} \sigma_0 \left(1 - e^{k_{ATP}(t_d - t)}\right) & \text{during depolarisation } t_d \leq t < t_r \\ \sigma_C(t_r) e^{k_{RS}(t_r - t)} & \text{during repolarisation } t_r \leq t < t_d + HP \end{cases} \quad (1)$$

where $t_r = t_d + APD$ is the repolarisation time with APD the active potential duration, σ_0 the maximum of the contraction, k_{ATP} and k_{RS} the contraction and relaxation rates respectively and HP the heart period. This tensor results in a 3D contraction force $\boldsymbol{f}_C$ for each vertex of each element.

Finally, the simplified dynamic law is: $M\ddot{Y} + C\dot{Y} + KY = F_{PV} + F_C + F_B$ where M, C are the mass, Rayleigh damping matrices, K the stiffness matrix, F_C, F_PV, F_B the force vectors respectively created by the active contractile elements, corresponding to the pressure forces in the ventricles and corresponding to other boundary conditions and Y, $\dot{Y} = dY/dt$, $\ddot{Y} = d^2Y/dt^2$ respectively the position, velocity and acceleration.

The four cardiac cycles (filling, isovolumetric contraction, ejection, isovolumetric relaxation) were simulated as presented in [13]. We compute the arterial pressures using a 3-element Windkessel model described in [12].

The pressure forces are computed differently in the cardiac phases. In the filling phase, they are set to the values of the pressures in the atrias. In the ejection phase, they are set to the arterial pressures computed with the 3-element Windkessel model. In the isovolumetric phases, the ventricular pressures are computed in order to counterbalance the contraction forces and to keep the ventricle volumes constant.

3 Cine MR Image Processing

Cine-MRI data consists in a sequence of 20 to 30 high resolution MR images of the heart that describes a whole cardiac cycle. We build a myocardium mesh that fits the mid-diastolic MRI image of the sequence when the filling of the ventricles is almost finished, just before the atrial contraction. As described in [14], we select this mid-diastole image based on blood pool volumes curves. Then, an interactive tool is used to delineate the epicardium and left and right ventricles endocardia in order to create three binary masks of the epicardium and the endocardia. We combined these masks to obtain the binary mask of the myocardium and create the mesh with an isosurface extraction and tetrahedral mesh generation.

Furthermore, synthetic fibre orientations are computed by linearly interpolating the elevation angle between the fibre and the short axis plane, from 80^o on the endocardium to -80^o on the epicardium.

4 Proactive Deformable Model

4.1 Image Forces

In deformable model approaches, the optimal shape corresponds to the minimization of the sum of an image energy and a regularizing energy. The use of an electromechanical model as a regularising term allows us to introduce some *a priori* knowledge about the active cardiac motion and thus to recover some movement (like the tangential motion) which cannot be obtained from classical geometrical tracking methods. Thus, we add to the previous dynamic equation $M\ddot{Y} + C\dot{Y} + KY = F_{PV} + F_C + F_B$ an image force F_{img} that derives from an image energy.

Of course, the image forces have no physiological meaning, and then the estimated motion is not physiological. But by coupling the model and the data and by estimating the model parameters (which is the next step of this work), the motion generated by the model should converge to the one observed in the images. Thus, the intensity of image forces should decrease along the estimation and the estimated motion should be more and more physiological.

The image energy is a metric that compares the simulated motion and the observed one. Thus, for each vertex Y_i of the epicardium or endocardium surfaces, if we define as Z_i the closest point on the apparent image boundary along the normal direction N_i at Y_i, then the image force at Y_i is $F_{img} = 2\gamma_i(Z_i - Y_i)$ (see [14,13]). In this equation γ_i is the image gain that depends on the confidence we have in the corresponding image point Z_i. In fact, with high gains, the estimated state will rely more on image data information than in the electromechanical model. Conversely, with gains equal to 0, the estimation does not take into account the data and is equivalent to the electromechanical model alone. Thus, the choice of the gains depends on the relative confidence in the model and the data. Furthermore, we showed in [14] how to set these gains in order to ensure convergence. For each vertex Y_i of the epicardium or endocardium surfaces, the definition of Z_i is a function of the image intensity and image gradient. More precisely, as shown in Fig. 1 (a) and (b), we first extract the intensity profile at Y_i along N_i and then determine the closest voxel Z_i whose image gradient norm is greater than a threshold and whose intensity is within a given range value. Those threshold and range value are set on the first image and kept constant during the cardiac cycle. In Fig. 1 (a) and (b), the way to find the point Z_i is shown in 2D for more simplicity, but it is performed using the all 3D image.

4.2 Implicit Image Forces

The image forces then may be temporally integrated either with an explicit or implicit scheme. In [14], we used an explicit scheme for time integration. Thus, at each time step t, we solved the approximated equilibrium equation $\tilde{K}Y^{t+dt} = F + F^t_{img}$ to compute the position Y^{t+dt} of the mesh at the following time step, where $\tilde{K}$ is the generalised stiffness matrix, F the external physical forces and F^t_{img} the image force as $2\gamma_i(Z^t_i - Y^t_i)$ if Y_i belongs to the heart surfaces

and 0 otherwise. As we know the position of the mesh at time t, we could find the point Z_i^t as explained above. This explicit scheme is computationally efficient since the generalised stiffness matrix does not change other time. However with such scheme, the proactive deformable model tends to lag behind the image observation which introduces a bias especially for large time steps.

Therefore, in this paper, we introduce an implicit scheme solving $\tilde{K}Y^{t+dt} = F + F_{img}^{t+dt}$, which requires predicting the next image force F_{img}^{t+dt}. To this end, we use a Taylor expansion of the image point Z_i^{t+dt}:

$$Z_i^{t+dt} = Z_i^t + \left(\frac{\partial Z_i}{\partial Y_i}\right)^t (Y_i^{t+dt} - Y_i^t) = Z_i^t + B(Y_i^{t+dt} - Y_i^t) \tag{2}$$

The B matrix is a 3×3 matrix that indicates how point Z_i moves as a function of Y_i. We provide here a first order approximation of this matrix by discarding the effect of surface curvature. Thus, we consider that Y_i lies on a plane with normal N_i while Z_i lies on a plane oriented by normal N_i^{img}. With those hypotheses, upon a displacement dY_i, Z_i is determined as the intersection of the line passing through $Y_i + dY_i$ and directed by N_i through the plane P_i^{img}. Obviously, only components of dY_i orthogonal to N_i entails a change in the point Z_i. Similarly, only components orthogonal to N_i^{img} would entail a change in point Z_i. Thus, skipping a detailed proof, one can show that the matrix B can be written as :

$$B = \frac{1}{cos^2\beta}(I_{3\times3} - N_i^{img} \otimes N_i^{img})(I_{3\times3} - N_i \otimes N_i) \tag{3}$$

where β is the angle between N_i and N_i^{img}, $I_{3\times3}$ is the identity matrix and $a \otimes b = ab^T$ is the dyadic product between the vectors a and b.

Finally, we need to solve the following equation: $(\tilde{K} + K_{img})Y^{t+dt} = F + \tilde{F}_{img}$ with $\tilde{F}_{img}$ a vector of size $3 \times N$ whose 3D component $\tilde{\boldsymbol{f}}_{img,i}$ is equal to $2\gamma_i(Z_i^t - Y_i^t) + 2\gamma_i(I_{3\times3} - B)Y_i^t$ if Y_i belongs to the myocardium surfaces, and 0 otherwise and with K_{img} a block diagonal matrix whose 3×3 component $(K_{img})_i$ is equal to $2\gamma_i(I_{3\times3} - B)$ if Y_i belongs to the myocardium surfaces, and the null matrix otherwise.

5 Boundary Constraints Estimation

Due to the modeling of the electromechanical behaviour of the heart, we have a lot of *a priori* knowledge on the motion of the ventricles. But for the base of the ventricles, near the atria, we have little *a priori* knowledge of the motion, and boundary constraints are set simply by attaching base vertices to fixed springs. Thus, we introduce here a way to estimate these boundary constraints by using a more complex external energy.

We cannot rely on intensity profiles to find Z_i as described in the previous section. Indeed this would only estimate displacement of base vertices along its normal direction which is ill-defined and physically incorrect. Instead, we use a 3D search method based on 3D block matching algorithm, as in [15]. We hope

therefore to better recover the real motion of the base, and not only its apparent one. Finally, we can use the similarity measure between the image blocks as a way to control the confidence in the point Z_i.

Therefore, we attach to each base vertex of the initial mesh a surrounding block of voxels from the reference image, which is the first image of the simulation (see section 3). Then, we search at each time step the most similar block around the current position in the following image of the cardiac cycle (the target image) (see Fig. 1 (c) and (d)). This is based on the assumption that the intensity around a given vertex of the base of the mesh should be similar in the two images, the difference coming from noise and from the movement of the vertex between the two images, which is not very important at the base of the heart, near the valve. The matching voxel selected is the center of the block in the target image maximising the chosen similarity criterion. Then, in order to take into account that the motion at the base is mainly a vertical one, we project the vector connecting the current point and the marching voxel on the normal of the mesh at this current point. The external force is then proportional to the norm of this projection and directed from the normal of the mesh at the considered point. The search range and the search step can be changed in a coarse to fine approach, as in [15]. In this paper, we used a similarity based on the sum of square differences, but several other similarity measures can be used depending of the noise and the used image modalities. Moreover, these estimated boundary constraints could be set as inputs in further simulations with the personalised model.

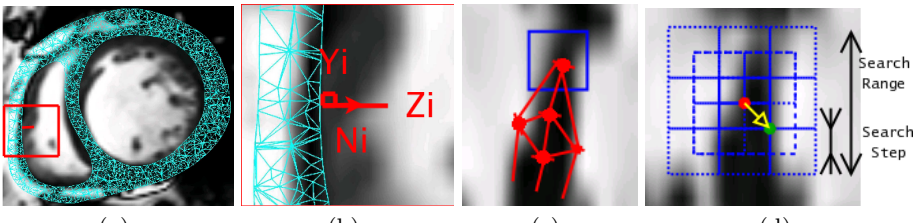

Fig. 1. (a, b) Surface image forces and corresponding Z_i point in the image. (c,d) Block matching algorithm (c) Reference image: initialisation in the reference image of the 3D block. (d) Target image: most similar block search around the current position.

6 Results

6.1 Validation on Synthetic Data

We generated synthetic cine-MR images using the electromechanical model with standard values. We considered 29 instants of the second simulated cycle and we generated the corresponding segmented 3D images, using tetrahedra rasterisation. We use for the different state estimation a cardiac model with same parameters as the model used to generate the synthetic data except for the reference position and the damping value.

We choose to estimate the state using a low damping because the effect of the implicit forces is more visible with low damped systems. Indeed in a highly damped system all applied forces are smoothed to a large extent which entails a delay in the reaction of the cardiac model to new image information.

We then compare the state vector estimation (position and velocity) with no image forces and with an explicit and implicit time integration of image forces. The gain γ of the image forces is set to the same value for the two estimations. For each method, we computed the root mean squared error (RMSE) between the estimated positions and the positions of the reference simulation (see Fig. 2 (a)). The RMSE with implicit forces is lower than the one with explicit forces (15% lower), and much lower than the one computed without image forces. Indeed, the average of all RMSE without image forces, with explicit and implicit image forces are respectively 14.9mm, 4.5mm and 3.6mm. Furthermore, explicit integration with low damping leads to large oscillation in the right ventricle (see Fig.2 (b)) due to undamped high frequencies in image forces. Finally, we can see that the mesh obtained with implicit forces better fits the segmented contour than the mesh obtained with explicit forces.

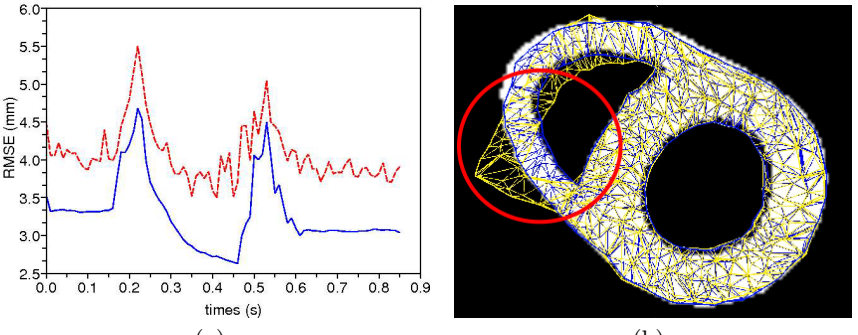

(a) (b)

Fig. 2. (a) RMSE between the positions of the reference simulation and the positions estimated with implicit forces (solid) and explicit forces (dashed). (b) Image and superimposed meshes estimated with implicit (blue) and explicit (yellow) image forces.

6.2 Results on Clinical Data

We used cine-MRI data of a patient with a left bundle branch block (LBBB) to test the effect of the block matching forces. The sequence consists in 30 images that describe a total heart cycle. The resolution of this dataset is $1.56 \times 1.56 \times 10\text{mm}^3$. In order to increase the robustness of the algorithms on clinical routine cardiac MRI, images are pre-processed. First, images are trilinearly resampled to get isometric voxel spacing (and then the resolution becomes $1.56 \times 1.56 \times 1.56\text{mm}^3$). Next, the contrast is enhanced by removing the extrema quantiles of the grey-level histogram. Finally, the histogram is linearly rescaled between 0 and 255 to have consistent intensities between images.

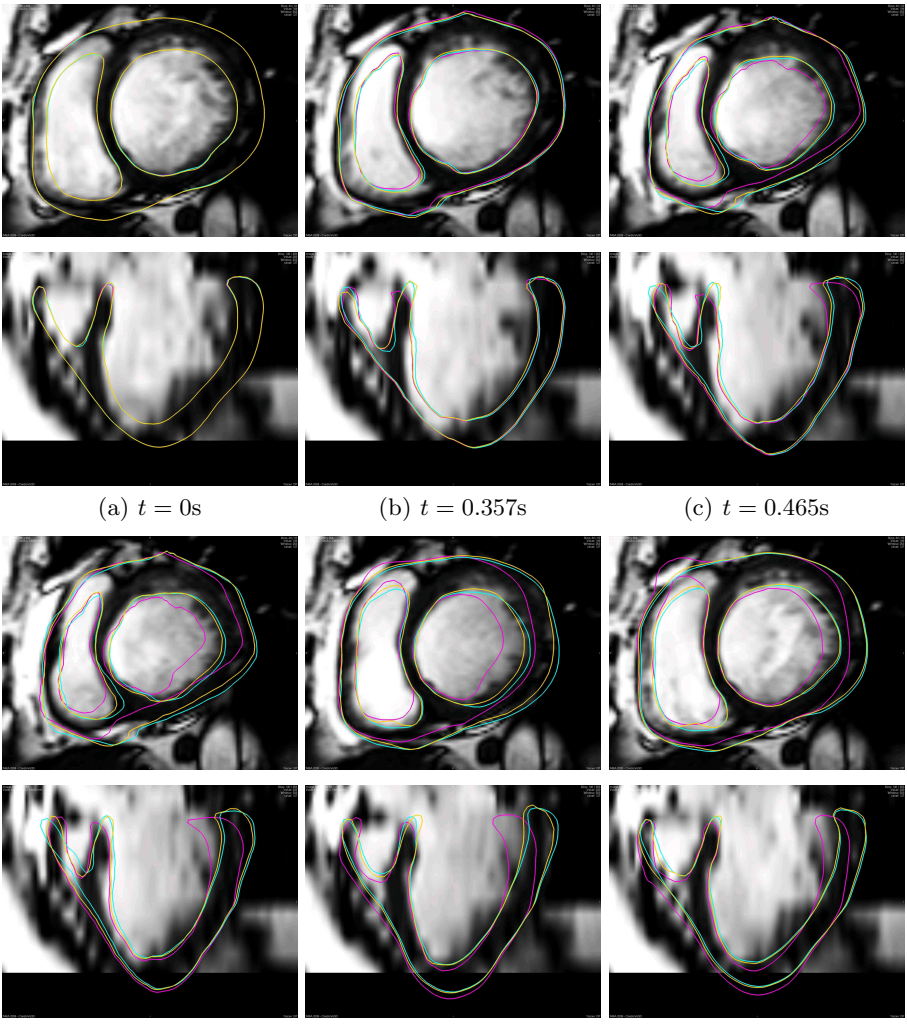

(a) $t = 0$s (b) $t = 0.357$s (c) $t = 0.465$s

(d) $t = 0.574$s (e) $t = 0.743$s (f) $t = 0.961$s

Fig. 3. MR image short axis (top) and long axis (bottom) slices at different times of the heart cycle, with the contrours of the estimated model position without boundary constraints (magenta), with boundary constraints (cyan) and with a block matching algorithm (yellow)

We manually adjusted the electrical parameters using the ECG and, in this case, with some clinically measured propagation times of the patient. If we have no measures of this propagation times, we initialize the electrical model with the volumes curves extracted from the images, as shown in [14]. The passive mechanical parameters used are taken from the literature [7]. In order to calibrate the active mechanical parameters, we use the volume curve to compute the

ejection fractions, wich are closely related to these parameters. For our data, σ_0 was set to 0.09 MPa/mm^2 for the left ventricle, 0.07 MPa for the right ventricle and 0.06 for the scars. The cardiac cycle duration is 1.035s.

We did three different estimations, all using the implicit forces described above for the epicardium and the endocardium surfaces. The first estimation uses no image forces applied to the base and no boundary constraints. The second one uses no image forces applied to the base, but applies boundary constraints involving fixed springs. The last one applies block matching forces on the base and image forces in the endocardium and epicardium surfaces.

Fig. 3 shows some short and long axis views with the contours of the three estimated positions superimposed with the corresponding MR image.

With no boundary constraints and no image forces there is no attach points in the model of the heart which entails that the generalised stiffness matrix may become singular. Also we have no *a priori* knowledge of the base motion. Thus, large errors in the estimation may occur, as shown in Fig. 3 (d, e and f) (the motion of left part of the left ventricle and of the top of the right ventricle is not well recovered).

With boundary constraints on the base, the model may be too much constrained, specially during the contraction as shown in Fig. 3 (c and d). For instance, the motions of the septum (see the short axis views of Fig. 3 (c and d)) and at the top of the lateral part of the right ventricle (see the long axis views of Fig. 3 (c and d)) are not well recovered.

Finally, the block matching forces achieve a good compromise between these two approaches. The motion of the base vertices are determined by block matching instead of being fixed with springs. We can see that the right ventricle motion has been well recovered, even during the contraction of the heart, as shown in Fig. 3 (b, c and d). However, we can see that the motion of the top of the septum is not well recovered, due to a not so good intitial segmentation of the top of the septum. This segmentation error makes the initialisation of the block matching algorithm not good, and then, the founded appariements try to keep this error. We can see here the need of a good segmentation for the use of the block matching approach.

7 Conclusion

We presented a method which relies on specific image features to recover the motion of the myocardium and estimate boundary constraints at the base. The use of implicit time integration of image forces allows us to ensure a better accuracy and smoother motion tracking for low damped systems. Furthermore, the use of a 3D block matching algorithm for the estimation of the boundary constraints at the base appears to be a good trade off between cardiac motion recovery with no boundary constraints and with classical boundary constraints consisting of fixed vertices or fixed springs and set manually. Finally, these promising results must be extended in order to perform parameter estimation of the model which would lead to a patient-specific electromechanical model of the heart.

Acknowledgements. INRIA Research Action CardioSense3D, European project euHeart (FP7/2007-2013 no 224495), Microsoft Research.

References

1. Hunter, P.J., Nash, M.P., Sands, G.B.: Computational Electromechanics of the Heart. Computational biology of the heart, 345–407 (1997)
2. Sachse, F., Seemann, G., Werner, C., Riedel, C., Dössel, O.: Electro-mechanical modeling of the myocardium: Coupling and feedback mechanisms. Proc. Comp. Cardiol. 28, 161–164 (2001)
3. Frangi, A., Niessen, W., Viergever, M.: Three-Dimensional Modeling for Functional Analysis of Cardiac Images: A Review. IEEE Trans. on Med. Im. 1, 2–25 (2001)
4. Papademetris, X., Sinusas, A.J., Dione, D.P., Duncan, J.S.: 3D Cardiac Deformation from Ultrasound Images. In: Taylor, C., Colchester, A. (eds.) MICCAI 1999. LNCS, vol. 1679, pp. 420–429. Springer, Heidelberg (1999)
5. Montagnat, J., Delingette, H.: 4D Deformable Models with temporal constraints: application to 4D cardiac image segmentation. Med. Im. Anal. 9, 87–100 (2005)
6. Qian, Z., Metaxas, D., Axel, L.: A Learning Framework for the Automatic and Accurate Segmentation of Cardiac Tagged MRI Images. Comp. Vis. for Bio. Im. App., 93–102 (2005)
7. Shi, P., Liu, H.: Stochastic finite element framework for simultaneous estimation of cardiac kinematic functions and material parameters. Med. Im. An. 7, 445–464 (2003)
8. Wong, K.C.L., Zhang, H., Liu, H., Shi, P.: Physiome Model Based State-Space Framework for Cardiac Kinematics Recovery. In: Larsen, R., Nielsen, M., Sporring, J. (eds.) MICCAI 2006. LNCS, vol. 4190, pp. 720–727. Springer, Heidelberg (2006)
9. Moireau, P., Chapelle, D., Le Tallec, P.: Joint state and parameter estimation for distributed mechanical systems. Computer Methods in Applied Mechanics and Engineering 197, 659–677 (2008)
10. Sermesant, M., Konukoglu, E., Delingette, H., Coudiere, Y., Chinchaptanam, P., Rhode, K.S., Razavi, R., Ayache, N.: An anisotropic multi-front fast marching method for real-time simulation of cardiac electrophysiology. In: Sachse, F.B., Seemann, G. (eds.) FIMH 2007. LNCS, vol. 4466, pp. 160–169. Springer, Heidelberg (2007)
11. Bestel, J., Clément, F., Sorine, M.: A Biomechanical Model of Muscle Contraction. In: Niessen, W.J., Viergever, M.A. (eds.) MICCAI 2001. LNCS, vol. 2208, pp. 1159–1161. Springer, Heidelberg (2001)
12. Stergiopulos, N., Westerhof, B., Westerhof, N.: Total arterial inertance as the fourth element of the windkessel model. Am. J. of Phys. 276, H81–H88 (1999)
13. Sermesant, M., Delingette, H., Ayache, N.: An Electromechanical Model of the Heart for Image Analysis and Simulation. IEEE TMI 25, 612–625 (2006)
14. Billet, F., Sermesant, M., Delingette, H., Ayache, N.: Cardiac Motion Recovery by Coupling an Electromechanical Model and Cine-MRI Data: First Steps. In: Proc. of the Workshop on Comp. Biom. Med. MICCAI (2008)
15. Ourselin, S., Roche, A., Prima, S., Ayache, N.: Block Matching: A General Framework to Improve Robustness of Rigid Registration of Medical Images. In: Delp, S.L., DiGoia, A.M., Jaramaz, B. (eds.) MICCAI 2000. LNCS, vol. 1935, pp. 557–566. Springer, Heidelberg (2000)

Atrioventricular Blood Flow Simulation Based on Patient-Specific Data

Viorel Mihalef[1], Dimitris Metaxas[1], Mark Sussman[2], Vassilios Hurmusiadis[3], and Leon Axel[4]

[1] CBIM Center, Rutgers University, NJ, USA
[2] Department of Mathematics, Florida State University, FL, USA
[3] Primal Pictures Ltd, London UK
[4] Department of Radiology, New York University, NY, USA

Abstract. We propose a new framework for simulating blood flow inside the heart, usable with geometric models of the heart from patient-specific data. The method is geared toward realistic simulation of blood flow, taking into account not only heart wall motion but also valve motion. The simulator uses finite differences to discretize a domain that includes a functional model of the left ventricle and the left atrium of the heart. Navier-Stokes equations are robustly solved throughout the simulation domain, such that one-way momentum transfer between the heart model and the blood is enforced. The valve motion was timed to correspond to valve motions obtained from MRI. The final simulation results are qualitatively consistent to those from MR phase contrast velocity mapping, including high-velocity flow to the aorta during systole and toroidal vortex formation past the mitral valve during diastole.

1 Introduction

As a result of a continuous increase in computational and imaging resources, blood flow simulation inside the heart is becoming a more and more precise scientific endeavor, greatly enhancing its possible use as a clinical application. This paper presents a framework for blood flow simulation in the heart that is flexible but simple enough to be part of a future clinical application suite. The method has been already introduced to computer graphics by [7] and here we present some enhancements and its application to heart blood flow simulation.

One of the first papers to tackle patient-specific simulation of left ventricular blood flow was [2]. The heart model used was only including the left ventricle and was imposing boundary conditions in the valve regions. Our method takes as input a sequence of full 3D heart meshes (including valves, atria and ventricles), then generates, as an intermediary step, a velocity field to be used as a boundary condition for the simulation, and then runs our proprietary Navier-Stokes solver to generate the blood flow dynamics. Such an approach is usually characterized as one-way momentum transfer. We are also working on a two-way momentum transfer approach, that will take into account the response of the flow on the heart walls, to be presented in the near future.

N. Ayache, H. Delingette, and M. Sermesant (Eds.): FIMH 2009, LNCS 5528, pp. 386–395, 2009.
© Springer-Verlag Berlin Heidelberg 2009

For obtaining realistic simulations our method relies on the use of a fairly complete heart model (in this case the left side), based on the one proposed by [1], that is immersed in a 3D computational box and allowed to transfer its momentum to the fluid inside and/or outside the heart model (our focus in this paper is the inside). Some advantages of this approach are relative computational simplicity while allowing geometric and topologic complexity, and also the possibility of using predefined models obtained from high quality MR data, or artificial heart models.

One of the main appeals of our method is that it allows for more complex/realistic setups than previous frameworks like [5,6,9], while also offering a comprehensive simulation platform that could take into account heart wall deformation as well. This is due to our use of the Standard Coupler Interface (SCI) framework which decouples fluid and (possibly deformable) solid simulation/implementation and our use of a "cartesian grid" (embedded boundary) method for treating the embedded heart. With such an approach one has less to worry about how to design boundary conditions or prescribe inflow/outflow velocity or pressure profiles for variable moving surfaces as in [5] or [9], and can (and should) focus on the geometric model of the heart, with the possibility of considering in more depth its mechanical deformation properties. Our method proved to be robust, regardless of the specified motion of the heart walls and valves.

In our work, the valves open and close progressively rather than instantaneously. This, combined with the presence of the mitral valve, led in our simulations to the formation of an annular vortex ring during early diastole. We note that [9] did not observe such a vortex formation, using only a circular ventricular inflow opening.

In this work we use a geometrically more realistic (MRI based) model than the simple one used by [6]. However, we should underline that an even more realistic simulation would have to use a twisting ventricle model obtained from tagged MRI, as reported by [10], with appropriately well resolved ventricular walls that can ensure the delivery of the wall rotational momentum to the blood. Finally, our model could be enhanced by the consideration of the mechanical deformation properties of the cardiac walls and of the valves.

In the following we present our simulation framework in section 2, along with the results obtained using it in section 3.

2 Simulation Method

Our simulation framework embeds the heart model in a rectangular box domain and solves the Navier-Stokes with a variable density throughout the domain, by prescribing the velocity in the solid/fluid cells as a boundary condition affecting directly the pressure Poisson solver. The domain outside the heart may be thought of as a passive body circulatory system. In this work the heart motion is completely predefined, and, as a consequence, fluid flow does not influence its motion. Our solver setup uses the so called Standard Coupler Interface (SCI)

framework which decouples Fluid and Solid simulation and implementation. In this paper the Solid code has quite simple tasks to handle, namely to pass at the appropriate time step the position and velocity of the heart and vessel stubs walls to the Fluid code, which uses this info to enforce the appropriate boundary conditions. This transfers in effect the heart kinematics to the blood flow. In a future model, which the SCI framework can handle naturally, we will also transfer momentum back from the fluid to the heart walls. The SCI framework works thus as follows: at any computational step

- the Fluid code advances flow calculation
- the Solid code advances body and passes velocity and position information to the Fluid code

In the rest of this section we present the fluid computation and the solid representation in more detail.

2.1 Fluid Flow Simulation

The governing equations consist of the Navier-Stokes equation, and continuity condition:

$$\rho \frac{D\mathbf{u}}{Dt} = -\nabla p + \mu \triangle \mathbf{u}$$

$$\nabla \cdot \mathbf{u} = 0$$

The physical parameters are here the blood density $\rho_{liquid} = 1050 kg/m^3$ and the dynamic viscosity $\mu = 4mPa \cdot s$. $\mathbf{u}$ is the velocity, p the internal pressure, and $\frac{D}{Dt}$ is the material (advective) derivative,

$$\frac{D}{Dt} \equiv \frac{\partial}{\partial t} + \mathbf{u} \cdot \nabla$$

At the beginning of each time step, we are given the velocity of the liquid $\mathbf{u}$ and the velocity of the solid $\mathbf{u}^{solid}$. We define a solid/fluid level set function ψ that will be used to distinguish between the solid and the liquid phase. The face centered density is defined (given here in 2D, for simplicity, but the 3D extension is trivial) as

$$\rho = \begin{cases} \rho_{liquid} & \text{if } \psi_{i+1/2,j} > 0 \\ 10^{15} & \text{otherwise} \end{cases}$$

For each time step, one does the following:

1. calculate provisional advective states for cell centered variables,

$$\frac{D\mathbf{u}}{Dt} = 0 \quad \frac{D\psi}{Dt} = 0$$

2. pressure correction step, in which we take into account the solid velocity.

$$\mathbf{u}^*_{i+1/2,j} = \begin{cases} \mathbf{u^{solid}}_{i+1/2,j} & \text{if } \psi_{i+1/2,j} \leq 0 \\ \mathbf{u}_{i+1/2,j} & \text{otherwise} \end{cases} \tag{1}$$

A pressure is derived which minimizes the quantity:

$$|dt\nabla \cdot \frac{\nabla p}{\rho} - \nabla \cdot \mathbf{u}^*|. \tag{2}$$

3. update the density using the current values of the level set, then update the liquid velocity

$$\mathbf{u}_{i+1/2,j} = \begin{cases} \mathbf{u^{solid}}_{i+1/2,j} & \text{if } \psi_{i+1/2,j} \leq 0 \\ \mathbf{u}_{i+1/2,j} - \frac{\nabla p}{\rho} & \text{otherwise} \end{cases} \tag{3}$$

2.2 Solid Wall Treatment

Each solid mesh corresponds to a specific time step in a 1Hz cardiac cycle. The left side of the heart chambers and vessel stubs geometry has been obtained from high resolution MRI imaging, as reported by [1]. A volume variation graph for both the left atrium and the left ventricle shows behaviour consistent with the classical physiological curves, and is presented in figure 2. In the same work, approximate fiber orientations from the University of Auckland canine fiber dataset were used to approximate the tangential motion of the ventricular wall. Corresponding valve geometry was modeled as well, and for this paper it has been modified and synchronized to better correspond to the cardiac cycle, as summarized in figure 1.

We used the doubly-wetted specification (as defined by [7]) for the description of the solid. This means, in short, that the original solid mesh is replaced inside the solver by another mesh defined as the dx level of the distance function of the mesh. In effect, this displaces the mesh dx away from the original one in both directions along the normals, and the smaller the grid size dx becomes, the better the approximation of the original geometry is. A geometric advantage of such a setup is that one can afford overlapping or holes of size less than dx inside the original mesh. A limitation is that one drops to first order accuracy when it comes to approximating the original mesh, and any sharp or small features (like ventricular wall creases) may be smoothed out for large grid steps.

2.3 Numerical Considerations

We used free-slip conditions along the computational box boundary. The heart walls impose automatically a no-slip condition on the fluid by means of equations (1) and (3). When both valves are closed our geometry does exhibit some volume variation, however our solver is robust. In order to accomplish this, we relax the incompressibility condition so that we fulfill $\nabla \cdot \mathbf{u} = A$, where A is a small nonzero constant. From the divergence theorem we have for example that

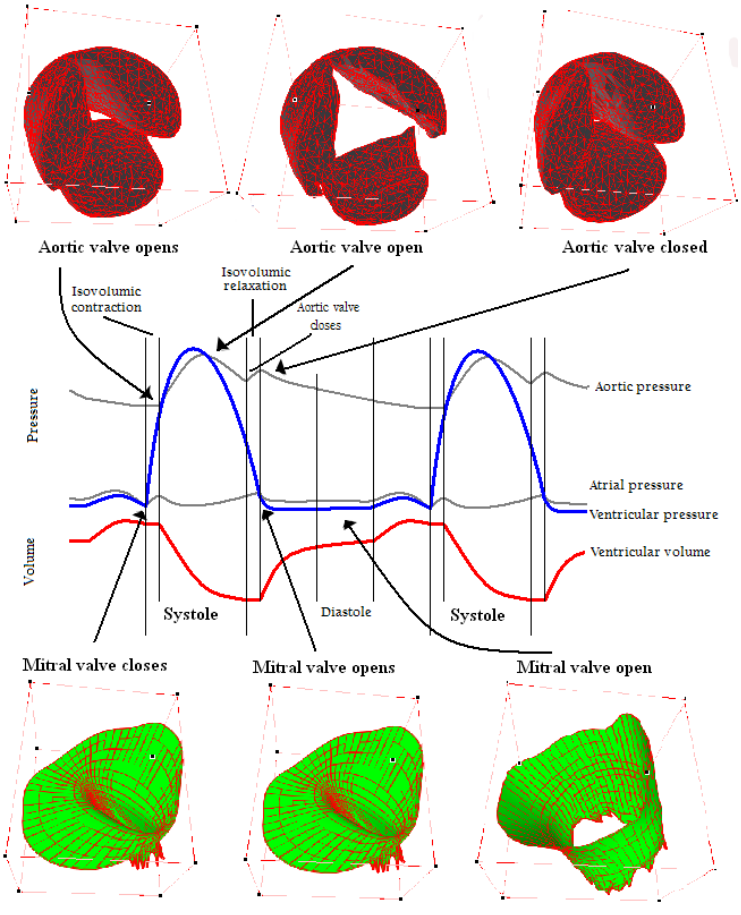

Fig. 1. A general heart cycle and specific keyframes of our aortic and mitral valves

$A = \frac{1}{vol(D)} \int_{\partial D} \mathbf{u} \cdot \mathbf{n}$, where $vol(D)$ is in our case the volume of the closed ventricular domain. We therefore solve a modified Poisson equation, namely $dt\nabla \cdot (\frac{1}{\rho}\nabla p) = \nabla \cdot \mathbf{u}^* - A$.

The projection method that we use for solving the Navier-Stokes equations does not include tracking the pressure in time. This, together with the possible gauge shift in the pressure values induced by the topological changes of the heart wall, complicates the issue of computing temporally coherent pressure values. We did notice however that during the various topologically stable stages, the pressure did behave as expected. For example, the pressure rose during the isovolumic contraction, and went down during the isovolumic relaxation. Similarly, the pressure remained fairly constant during diastole and rose and then dipped during systole.

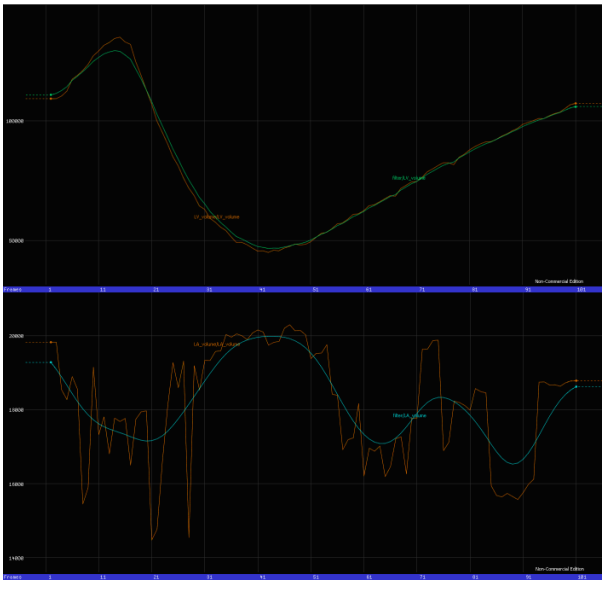

Fig. 2. Volume variation over one cardiac cycle of the left ventricle and atrium

3 Results

To perform our heart simulation we set up a model of the inner side of the left ventricle connected with the aorta and with the left atrium and its associated vessel stubs. Both aortic and mitral valves were in place, timed to open and close as visible in Figure 1. In particular, they were both closed during the isovolumic phases, and were smoothly interpolated from the closed positions to their full open extent (as noted, this is in contrast with previous work like [5,9], but similar to [6]). Our code spent an average of 6 hours to compute each cardiac cycle, computing 200 time steps in about 1.8 minutes per time step, on a 2.4GHz Quad Core PC. The grid size was $96 \times 96 \times 96$ for the results presented here. We have also run a $64 \times 64 \times 64$ simulation with qualitatively similar results, although it also showed the possible limitations of the doubly-wetted approach. Namely, when using the coarser mesh, the strong grid dependence of the small holes, including the vessel stubs, led to partial occlusion of the smaller vessels, and to diameter reduction of the aorta, so that the ventricular pressure increased greatly during systole, and led to too large aortic velocities. This is a numerical rather than a methodological artifact, and can be completely avoided once the grid spacing is chosen small enough. In our specific case for example, 96^3 was a fine enough grid, as proved by numerically consistent results obtained subsequently on a 128^3 grid.

Figure 3 shows several representative images from the main simulation. The images tell a story consistent with the MR velocity analysis from classic papers

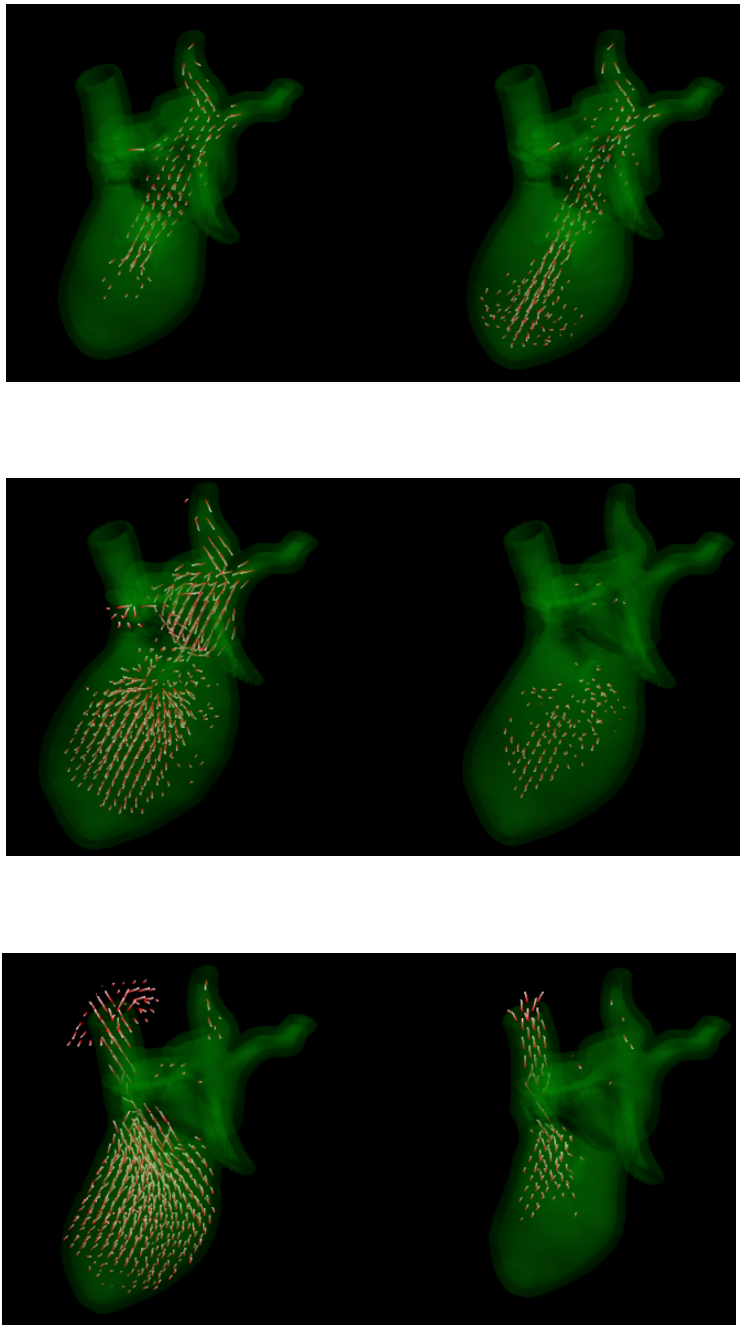

Fig. 3. Our heart cycle simulation in different stages. From left to right, top row: early diastole, diastole with annular vortex formation. Middle row: atrial systole, isovolumic contraction. Bottom row: early systole, late systole.

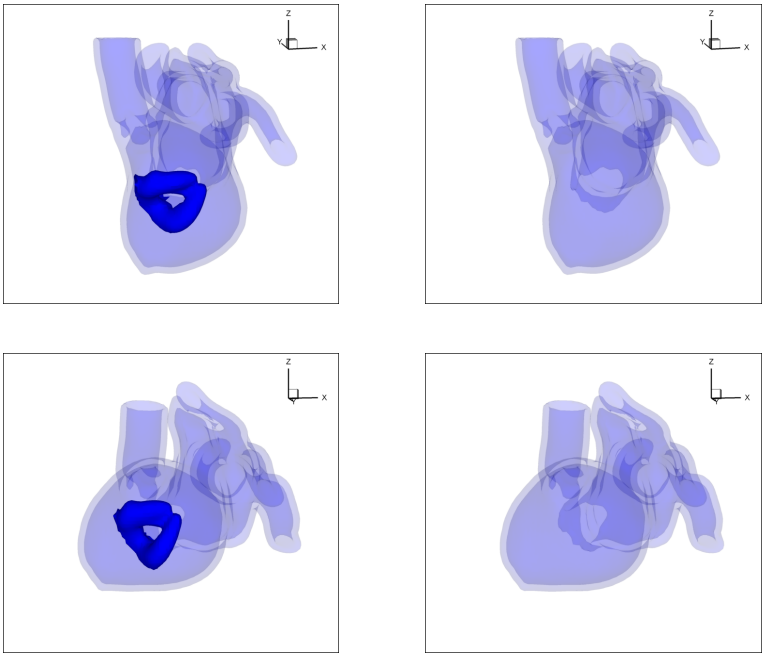

Fig. 4. Ring vortex formation at a given step early diastolic stage (t=0.625sec, in a 1 second cycle). From left to right, and top to bottom: view 1, with ring, view 1 without ring, view 2, with ring, view 2 without ring. The ring is visualized as a fixed vorticity isosurface right below the mitral valve, with all other vorticity isosurfaces (present mainly on the mitral valve and the atrial vessels) removed for clarity.

like [4], or [3] (who used phase contrast MRI). One sees several vortex formations during early diastole, with a main annular vortex shooting toward the apex, and subsiding in strength right before the atrial systole. The formation mechanism of the main vortex seems to be determined by the blood shear induced by the valve itself, as indicated by [4]. In figure 4 we show the vortex position at an early diastolic time step. Next, the atrial systole increases again the ventricular inflow velocities and contributes to short-lived new vortex formation. After an instant of isovolumic calm, the pressure buildup forces strong ejection of blood through the aorta, once the aortic valve opens. In the beginning of the systolic phase, the velocities (especially the ones inside the aorta) are the largest across the whole cycle. Towards the end of the systole, the ventricular velocities subside in magnitude, while the ones in the aorta remain quite high. During the subsequent isovolumic relaxation, the velocities decrease greatly, only to increase again with the start of a new cycle.

In terms of validation, the use of magnetic resonance imaging (MRI) methods for 3D mapping of velocities within the heart, at multiple phases of the cardiac cycle, is already possible with conventional MRI systems and their associated software (or with relatively minor modifications). Although the time required

for acquiring the large amount of associated imaging data is currently too long for routine incorporation within clinical cardiac MRI examinations, it is already feasible for research purposes. Thus, we will be able to obtain suitable in-vivo 7D velocity data in the same subjects from whom the 4D cardiac structural data is acquired for use in the CFD calculations, for comparison with and validation of the theoretical velocity fields computed from the MRI-derived boundary conditions. With the ongoing and expected continual advances in the speed of cardiac MRI, it is likely that this method of blood flow mapping will become faster and more accurate, and that it will find increasing clinical application. Thus, the insights into the physics of the blood flow patterns that can potentially be provided by these CFD results will be expected to be useful both for advancing our understanding of normal and abnormal physiologic process and for improving the care of individual patients.

4 Conclusion

We have presented a novel computational approach for simulating blood flow inside the heart that is simple yet versatile. We have used it to perform a medium size numerical simulation using a relatively complete model of the left side of the heart, including animated models of the aortic and mitral valves, and aortic and left atrial vessel stubs. We found the main characteristics of the resulting simulation to be consistent with the ones published in the literature, from general flow direction and relative size, to specific vortex formation. We are working on extending our framework with a two-way momentum transfer mechanism, and on updating the heart model with smaller intraventricular structures from MRI data, as well as more realistic twisting motion based on tagged MRI.

Acknowledgments. The authors want to thank the reviewers for their very useful suggestions and questions that led to substantial improvement of the original exposition. The first author thanks Iuliana Radu for her help in generating Figure 1. The first two authors were supported by NSF grant 0702591.

References

1. Hurmusiadis, V., Briscoe, C.: A functional heart model for medical education. In: Frangi, A.F., Radeva, P.I., Santos, A., Hernandez, M. (eds.) FIMH 2005. LNCS, vol. 3504, pp. 85–91. Springer, Heidelberg (2005)
2. Jones, T., Metaxas, D.: Patient-Specific Analysis of Left Ventricular Blood Flow. In: Wells, W.M., Colchester, A.C.F., Delp, S.L. (eds.) MICCAI 1998. LNCS, vol. 1496, pp. 156–166. Springer, Heidelberg (1998)
3. Jung, B., Schneider, B., Markl, M., Saurbier, B., Geibel, A., Hennig, J.: Measurement of left ventricular velocities: phase contrast MRI velocity mapping versus tissue-doppler-ultrasound in healthy volunteers. J. Cardiovasc. Magn. Reson. 6(4), 777–783 (2004)

4. Kim, Y.H., Walker, P.G., Pedersen, E.M., Poulsen, J.K., Oyre, S., Houlind, K., Youganathan, A.P.: Left ventricular blood flow patterns in normal subjects: a quantitative analysis by 3-D magnetic resonance velocity mapping. J. Am. Coll. Cardiol. 26, 224–238 (1995)
5. Long, Q., Merrifield, R., Yang, G.Z., Kilner, P.J., Firmin, D.N., Xu, X.Y.: The Influence of Inflow Boundary Conditions on Intra Left Ventricle Flow Predictions. Journal of Biomechanical Engineering 125, 922–927 (2003)
6. McQueen, D., Peskin, C.: A three-dimensional computer model of the human heart for studying cardiac fluid dynamics. Computer Graphics 34(1) (2000)
7. Mihalef, V., Kadioglu, S., Sussman, M., Metaxas, D., Hurmusiadis, V.: Interaction of Multiphase Flow with Animated Models. Graphical Models 70, 33–42 (2008)
8. Peskin, C.S., McQueen, D.M.: Cardiac fluid-dynamics. Crit. Rev. Biomed. Eng. 20, 451–459 (1992)
9. Saber, N., Wood, N., Gosman, A.D., Merrifield, R., Yang, G.-Z., Charrier, C., Gatehouse, P., Firmin, D.: Progress Towards Patient-Specific Computational Flow Modeling of the Left Heart via Combination of Magnetic Resonance Imaging with Computational Fluid Dynamics. Annals of Biomedical Engineering 31(1), 42–52 (2003)
10. Qian, Z., Metaxas, D., Axel, L.: Learning Methods in Segmentation of Cardiac Tagged MRI. In: Proceedings of ISBI (2007)

A Software Platform for Real-Time Visualization and Manipulation of 4D Cardiac Images

Qi Zhang, Roy Eagleson, and Terry M. Peters

Imaging Research Laboratories, Robarts Research Institute
London, Ontario, Canada, N6A 5K8
{qzhang,eagleson,tpeters}@imaging.robarts.ca

Abstract. Current capabilities of computerized radiology equipment have made three-dimensional (3D) and 4D (3D + time) medical images available for cardiac diagnosis, as well as for planning and guidance of therapy. Real-time display and interaction with these images plays an important role. To address this need, we have developed a graphics processing unit (GPU) accelerated 4D medical image visualization and manipulation platform, in which different levels of image representation and operation are employed, and anatomical volume of interest (VOI) can be efficiently enhanced. In addition, a new "depth texture indexing" algorithm is described to allow virtual surgical tools to be included in this environment, and a preliminary user study is performed to test the clinical usefulness and user performance enhancement when using the new techniques implemented in this software platform. The aim of this work is to supply cardiologists and surgeons with a comprehensive visualization software framework for cardiac disease preoperative diagnosis, treatment planning, and surgery guidance.

Keywords: Dynamic volume rendering, cardiac imaging, graphics processing unit (GPU), volume of interest (VOI), virtual surgical tools, depth texture indexing.

1 Introduction

Image-guided minimally invasive cardiac interventions have the potential to greatly reduce patient trauma and improve the procedure outcomes [1]. The progressive trend toward using intraoperative image-guidance techniques makes real-time image visualization an important component in these procedures [2,3]. However, the applications of advanced radiology equipment and computer aided medical imaging technologies create extremely large datasets, especially for 4D cardiac images. Such complex datasets can overwhelm the users, unless an appropriate intuitive and interactive environment is available to visualize them [4,5].

A 4D real-time cardiac image display and interactive analysis platform can provide physicians and cardiologists with an intuitive appreciation of both cardiac anatomy and physiology [6,7]. This clinical requirement and corresponding technical challenges have attracted researches' attention in recent years. Levin et al. [8] exploited consumer graphics hardware to display 4D cardiac magnetic resonance (MR) images in near real time, and interactive 4D motion segmentation and multi-modality data fusion were also implemented in the display system. This texture mapping based volume visualization

N. Ayache, H. Delingette, and M. Sermesant (Eds.): FIMH 2009, LNCS 5528, pp. 396–406, 2009.
© Springer-Verlag Berlin Heidelberg 2009

technique was also exploited by Lehmann and his colleague [9] to display a series of multi-slice computed tomography (MSCT) cardiac data. However, these cardiac renderings were based on a 3D texture mapping algorithm, which suffers from intermixing artifacts between different texture slices and imaging modalities, resulting in the image quality insufficient for clinical requirement.

To improve image quality while maintaining high rendering performance, we implemented a programmable graphics process unit (GPU) accelerated raycasting algorithm for cardiac rendering [12]. The general strategy of exploiting a GPU for raycasting computation was first proposed by Krüger and Westermann [10] and Purcell et al. [11], who described a stream model that exploits the intrinsic parallelism and efficient communication on modern GPUs. In our implementation, we proposed a novel dynamic texture binding scheme and included it into our GPU-accelerated raycasting algorithm for 4D cardiac MR image real-time rendering [12]. At the same time, the heart rate can be synchronized with the patient's electrocardiogram (ECG). Furthermore, we extended our 4D image visualization system for dual-modality volume rendering, and applied it to the real-time display of registered 4D cardiac MR and ultrasound images [13].

In the cardiac visualization software platform, volume of interest (VOI) enhancement of the beating heart can be employed to efficiently distinguish anatomical structures and physiological behavior [14]. The application of advanced image processing and analysis techniques can extract clinical useful information, and virtual surgical tool inclusion can provide surgeons with an effective method for surgical training and guidance [15]. The work described in this paper is aimed at building a real-time 4D cardiac image visualization and intervention system using our new medical image rendering, manipulation, enhancement, analysis, along with virtual tool inclusion techniques, to provide an efficient diagnostic and surgical planning platform through a user-friendly graphics user interface (GUI) and the underlying image processing and visualization techniques.

2 Platform Description

The system is designed with an object-oriented approach, and is implemented using C++, OpenGL, OpenGL Shading Language (GLSL), Visualization Toolkit (VTK), and

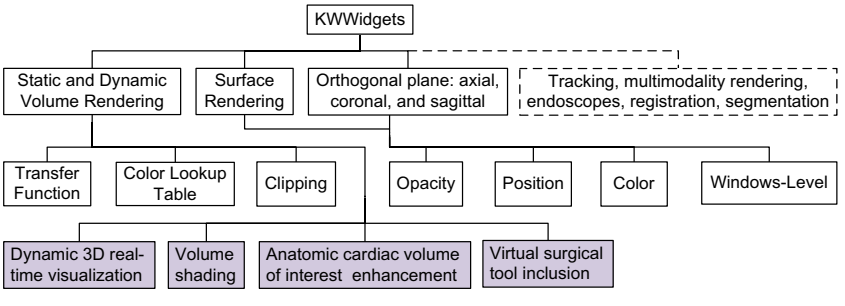

Fig. 1. The software platform workflow and the corresponding image visualization, processing, manipulation, and enhancement modules

KWWidgets. As shown in Fig. 1, it supplies functions for GUI and I/O management, and multiple real-time image volume rendering, processing, and manipulation methods. To simplify data navigation and interaction, this platform provides users with interactive transfer functions and clipping planes for different cardiac anatomical structures. In addition, the color, opacity, cross-volume navigation plane and window-level adjustments are synchronized with the corresponding 2D views. This platform also supplies new functions such as 4D cardiac rendering, VOI enhancement, GPU-based shading, and virtual tool inclusion.

3 GPU-Accelerated Raycasting

The advantage of volume rendering is that, unlike surface rendering, it maintains the entire data within the visualization volume. However, when rendering typical medical volumes, software-based raycasting is usually noninteractive, while algorithms based on texture-mapping produce "striping" or "flipping" artifacts, which consequently reduce their suitability for clinical applications. We therefore developed a real-time raycasting technique that takes advantage of both the programmability and parallelism of GPUs. The algorithm is presented below:

(1) Volumetric raw data and corresponding lookup table are loaded into the GPU graphics memory as a 3D and 2D texture, respectively.
(2) In the GPU vertex shader, the texture coordinates are first transferred from object space to local texture space. Next, these coordinates are interpolated and transformed to the fragment shaders.
(3) In the fragment shader, the algorithm obtains the camera position using the model view transformation, and the viewing direction is calculated based on the camera position and the coordinates of the input 3D texture. Next, the actual ray casting computation is performed, in a manner similar to the software-based algorithm.

4 Dynamic Cardiac Data Rendering

4D cardiac data are rendered using a dynamic texture-binding technique. A series of cardiac volumes is first loaded into the GPU graphics memory as a set of 3D target textures, and a unique texture name (unsigned integer) is created for each of them. A time trigger derived from the electrocardiogram (ECG) is employed to control the rendering speed of the beating heart. At each time point, a specific 3D texture is activated and linked to the real-time raycasting-based volume rendering engine on GPU fragment shader, which is managed by the dynamic texture binding and ECG synchronization. The activated 3D texture is constantly updated during the visualization procedure, resulting in real-time rendering of the beating heart.

5 VOI Enhancement

It is often desirable to be able to manipulate the image characteristics of a specific anatomical structure of interest independent of the remainder of the volume. The first

step is to identify the VOIs in the dataset V, and then segment the specified VOIs to create binary mask volumes MV_i ($i = 1, \cdots, n$) with the same size as V. The MV_i are first processed with dilating and filtering operations, and then used to extract texture information from the original volume V. Finally, both V and MV_i are loaded into the GPU graphics memory as 3D textures, while the corresponding lookup tables are also loaded to GPU as 2D textures.

During the rendering process on the GPU fragment shader, at every sampling point k on the casting ray, a set of scalar values v_k^i are fetched from V ($i = 0$) and MV_i ($i > 0$), then the corresponding transfer functions are used to map them to color and opacity. Finally, the derived optical values are blended together to created the final feature-enhanced images.

6 Virtual Tool Inclusion

We have developed a new technique that allows solid objects (such as representations of surgical instruments) to be manipulated and visualized within dynamic volume-rendered images. The workflow is described below:

6.1 Framebuffer Object

The framebuffer object (FBO) is used for render-to-texture operation in real time. It is a window system independent off-screen rendering technique that allows the rendered results in a framebuffer to be read directly as texture.

In our application, we have created two vertex and fragment shader pairs $\mathbb{S}_1$ and $\mathbb{S}_2$. $\mathbb{S}_1$ is used for rendering the virtual surgical tools, while $\mathbb{S}_2$ is employed to display the volume with the virtual tools included. $\mathbb{F}_1$ and $\mathbb{F}_2$ are employed to represent the corresponding fragment shaders. The following three FBOs are created, each of which has a unique color and depth texture pair attached:

(1) The front face color and depth of the volume object.
(2) The back face color and depth of the volume object.
(3) The color texture of the virtual tools, and the depth texture of the front face of these tools.

Finally, the 3D dataset along with the corresponding color lookup table are loaded to the GPU fragment shader $\mathbb{F}_2$ as a 3D and 2D texture respectively, and the three 2D texture pairs created above are also loaded to this fragment shader.

6.2 Depth Texture Indexing

For a given point in graphics memory, the associated depth is dependent on the near and far clipping planes, and is nonlinearly related to its texture coordinate in the depth buffer, so it is difficult to precisely compute its depth value. We therefore propose a new method to solve this problem, which is referred to as “depth texture indexing”. Here the GLSL components *gl_FragCoord·stp* is used with the texture fetch operation *shadow2DRect* to acquire the texture color coordinate and depth value of the front and

back faces of the object, returning tex_{cf}, tex_{cb} and tex_{df}, tex_{db}. Then we calculate the casting ray segment length len within the volume: $v = tex_{cb} - tex_{cf}$ and $len = |v|$. An adjustable sampling number n_s is set according to the final image quality requirement, which is further used to calculate sampling steps of the color- and depth-texture: $sp_c = len/n$ and $sp_d = |tex_{db} - tex_{df}|/n_s$. Here, sp_d acts as the "depth texture indexing" step size.

However, the actual ray entry and exit point may be not the same as the volume boundaries because of clipping, so we calculate the intersections of the ray $r(t)$ with the six clipping planes $clip_i$ ($i = 0, 1, \cdots 5$), finding the two shortest distances as the ray's new starting and ending points $\widehat{tex}_{cf}$, $\widehat{tex}_{cb}$ respectively. Then, we compute the number of skipped samplings n_{sp}:

$$n_{sp} = \left[\frac{|tex_{cf} - \widehat{tex}_{cf}| \times n_s}{sp_c} + 0.5 \right] \tag{1}$$

Here, $[t]$ is the closest integer that dose not exceed t, and n_{sp} is used to find the new start points $\widehat{pt}_{cs}$ and $\widehat{pt}_{ds}$: $\widehat{pt}_{cs} = tex_{cf} + n_{sp} \times sp_c$, and $\widehat{pt}_{ds} = tex_{df} + n_{sp} \times sp_d$.

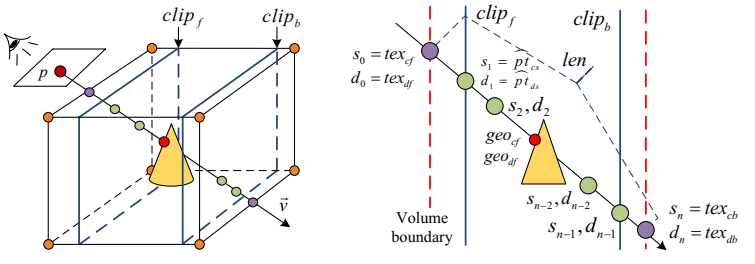

Fig. 2. The raycasting pipeline with virtual tool inclusion. Left, 3D explanation. Right, 2D illustration of the procedure.

6.3 Raycasting with Virtual Tool Inclusion

The following items describe the GPU-accelerated raycasting algorithm with the virtual tools included.

(1) As illustrated in Fig. 2, compute the color texture coordinates of the front and back face of the texture volume on the GPU fragment shader tex_{cf} and tex_{cb}, then for every pixel p on the display plane, calculate the casting ray $r(t)$ direction v and its segment length len within the volume.

(2) Check len, if it is zero, stop the processing of this ray; otherwise, compute the sampling steps of color coordinate and corresponding depth value. Then calculate the intersections of $r(t)$ with the six clipping planes $clip_i$ ($i = 0, 1, \cdots 5$) to find the ray $r(t)$ entry and exit points $\widehat{tex}_{cf}$, $\widehat{tex}_{cb}$, and next compute the skipping number n_{sp} using Eq. 1. $n_{sp} = 1$ is the case described in Fig. 2.

(3) Compute the new ray $r(t)$ starting point $\widehat{pt}_{cs}$ and the depth comparison point $\widehat{pt}_{ds}$, and then calculate the texture color and depth of the virtual tool's front face geo_{df} and geo_{cf}.

(4) At each sampling point, map the scalar value to color and opacity, updating the texture coordinate $\widehat{pt}_{cs}$ and depth $\widehat{pt}_{ds}$ using the step size sp_c and sp_d respectively.
(5) Compare the updated depth with the depth of the virtual tool's front face geo_{df}. If the depth is equal to or greater than geo_{df}, or the accumulated opacity is larger than the preset threshold α_{max} (α_{max} = 0.98 in our implementation), or if the accumulated sampling length is greater than len, stop the sampling process along this ray. Otherwise, continue the sampling process.
(6) After a ray $r(t)$ is stopped, compute the output color $c_f = c_r + \left[1.0 - c_r.a \times (1.0 - \lambda)\right] \times geo_{cf}$. Here, c_r is the accumulated opacity-associated color, and geo_{cf} is the fetched color texture of the geometry objects. λ ($\lambda \in [0, 1]$) is the transparency adjustment factor.

7 Experimental Results and Discussion

Fig. 3 shows two examples of the system: real-time volume rendered 4D CT human cardiac data (left), and dynamic MR cardiac image with myocardium (myo), and right atrium and ventricle (RAV) enhanced (right). The manipulation console is on the left, providing image operating functions, such as transfer functions, clipping planes, navigation planes with corresponding 2D slice views, color and opacity adjustment editors, as well as windows-level adjustment editor.

A MR cardiac dataset D_1 with the dimension $75 \times 170 \times 115$ and voxel size $1.5 \times 1.5 \times 1.5$ m^3 was used to test our GPU-accelerated raycasting algorithm (GPU-RC), and compared it with 2D texture mapping (2D-TM), 3D texture mapping (3D-TM), and software-based raycasting (SOFT-RC) algorithms. Fig. 4 shows the rendering results, from which it can be seen that the image quality of GPU-RC is similar to SOFT-RC, both of which are superior to texture mapping based methods, avoiding the "flipping" and "striping" artifacts commonly associated with these two approaches.

Next, we compared the rendering efficiency of the four algorithms on two hardware systems. The first is an Intel Pentium D 820, 2.8GHz, Dual Core, 2G DDR 533 Memory, Nvidia 6600 PCI Express graphics card, while the second is an Intel P4 2.8GHz,

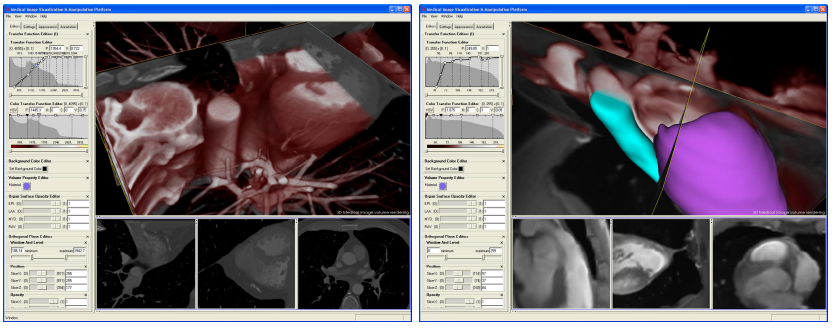

Fig. 3. Snapshot of 4D cardiac image volume rendering and manipulation software platform

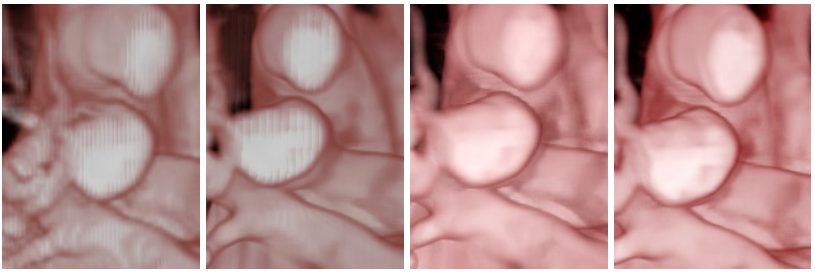

(a) (b) (c) (d)

Fig. 4. Image quality comparison: (a) 2D-TM; (b) 3D-TM; (c) SOFT-RC; (d) GPU-RC

Table 1. Volume rendering speed (frames per second, fps) comparisons of the four volume rendering algorithms using two hardware systems

	2D-TM	3D-TM	SOFT-RC	GPU-RC
Hardware System 1 (fps)	15.2	13.5	3.2	8.5
Hardware System 2 (fps)	15.0	31.4	2.0	22.3
Performance Increase (update System 1 to 2, %)	−1.3	132.6	−37.5	162.4

2G DDR 400 Memory, Nvidia 6800 GT AGP. The first system has a more powerful CPU, while the second has a more efficient GPU. Table 1 shows the results, demonstrating that the rendering speeds of texture mapping (TM) and GPU-based algorithms are mainly dependent on the GPU. When updating to a more powerful GPU, the performance increases are around 132% and 162% respectively for 3D-TM and GPU-RC, however, there is no speed improvement for 2D-TM, which we attribute to a graphics driver issue. The rendering speed of SOFT-RC is determined by the CPU, and a performance decrease of 37% was observed when running the algorithm on a less powerful GPU. As illustrated in Fig. 4 and Table 1, the GPU-RC has a high image quality similar to that obtained with SOFT-RC, but offers almost 20 times increase in performance.

We also evaluated our system for displaying the MR cardiac image of human heart with enhanced segmented anatomical structures. Fig. 5 (a) shows the volume shaded MR image with the left atrium and aorta (LAA), myocardium (myo), and right atrium and ventricle (RAV) emphasized with different colors, while in (b), these three cardiac structures are outlined. In (c), only LAA, myo and RAV are visualized, while in (d), the whole cardiac volume is rendered semi-transparently, providing a whole volume context to the enhanced cardiac sub-structures.

As demonstrated in Fig. 6, the virtual surgical tools are seamlessly incorporated in the volume rendered cardiac images, which can be displayed in real time and manipulated interactively. The visibility of the virtual tools inside the volume can be dynamically changed by adjusting the transparency factor λ. As illustrated in Fig. 6 (b) and (d), when λ is larger than 0.3, the rendered cardiac volume becomes semi-transparent with respect to the virtual tools, so the tools can be clearly seen within the heart. In addition,

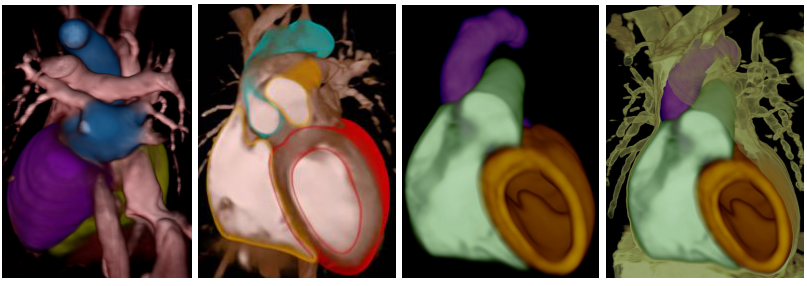

(a) (b) (c) (d)

Fig. 5. Volume rendered cardiac MR images of human heart with the segmented anatomical structures enhanced

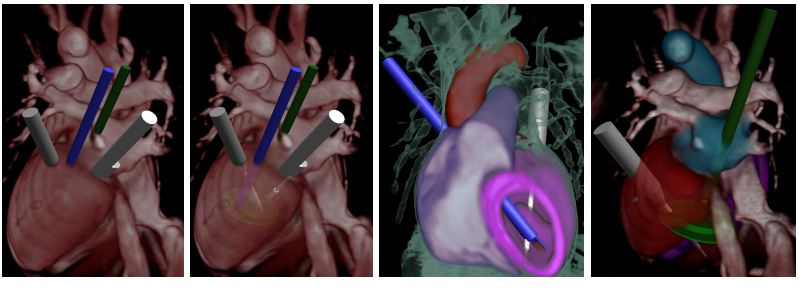

(a) (b) (c) (d)

Fig. 6. Cardiac image volume rendering with surgical tool inclusion. (a) and (b) with different transparency factor λ setting: (a) $\lambda = 0$, (b) $\lambda = 0.3$. (c) feature enhancement ($\lambda = 0$), and (d) feature enhancement with shading ($\lambda = 0.32$).

the anatomical structures can be enhanced with different colors and transparencies (c), and volume shading can be added to increase the depth information (d).

Finally, we compared the efficiency of the dynamic and static volume rendering of the 4D cardiac images using an Nvidia 8800 GTS GPU. To simulate clinical environment, the rendering window is set 800×800. Three set of 4D cardiac datasets are used in this experiment, each of which is acquired from a GE Healthcare Lightspeed volume CT scanner, having 10 volumes equally spaced within the cardiac R-R interval: beating heart phantom (dimension 148×133×214, voxel size 0.89×0.89×0.63 mm^3), canine data (512×512× 87, 0.35×0.35×1.25 mm^3), and human heart (200×200×281, 1.0×1.0×1.0 mm^3).

Fig. 7 describes the rendering performance. The average speed of static rendering is 51fps with the standard deviation 17.6, while the average performance for the dynamic rendering is 26 fps with the standard deviation 4.6. The static rendering is about 100% faster than the corresponding 4D display, while the 4D rendering has narrower performance deviation than the static visualization. We attribute the performance of the dynamic algorithm to be related to the computational resource consumption required to update the volume in real time during the 4D rendering process.

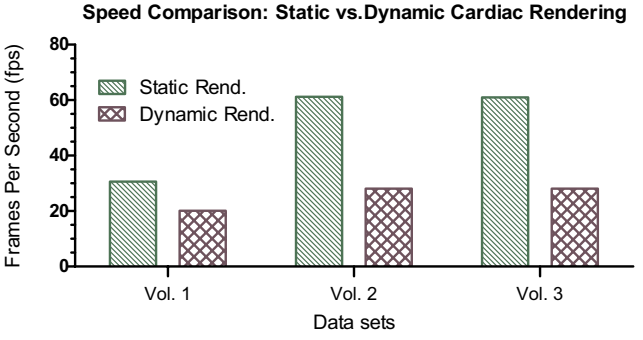

Fig. 7. Speed comparisons of static and dynamic volume rendering of 4D cardiac volumes

We also performed a preliminary user study to test the user performance improvements when using our new 4D cardiac image visualization, manipulation, enhancement, and virtual surgical tool inclusion techniques in a simulated clinical environment. Two cardiologists and three graduate students in medical imaging were asked to perform the following tasks. They first observed the myocardium and right ventricle structure details and motions on volume rendered 4D cardiac images without feature enhancement. During this time the users were able to interact with the 4D cardiac volumes by rotating, zooming, clipping, window-level adjustment, and transfer function tuning. Next, they were asked to perform the same tasks on the volume rendered heart with anatomical structure enhancement (as illustrated in Fig. 5). The three graduate students reported performance enhancement in detecting the myocardium and right ventricle, as well as the motion during ventricular contractions. The cardiologists also reported improvement in these factors, but to a less extent than the graduate students. As for the dynamical cardiac visualization, we compared it with surface rendering, two of the observers reported that volume rendering provided them with more information. Then we included the virtual tools into the 4D cardiac display environment (as described in Fig. 6), all the operators reported that the virtual tools improved their performance on cardiac volume manipulation.

We therefore conclude that, when compared with traditional visualization methods, such as surface rendering, or volume rendering without "tissue of interest" enhancement and virtual tool inclusion, our new 4D cardiac image display, enhancement, and manipulation environment can provide an improved visualization for both diagnosis and image-guided cardiac interventions.

8 Conclusion

High-quality real-time dynamic visualization, feature enhancement, and manipulation act as an important role in the image-guided minimally-invasive cardiac interventions. In this paper, we describe the development of a software platform, in which our research results on dynamic volume rendering, volumetric image processing, anatomical structure of interest enhancement, and virtual surgical tool inclusion are seamlessly integrated and their performance are evaluated. Moreover, a preliminary user study is

performed in a simulated clinical environment to test the user performance improvement when using our new technologies. In this software framework, new application modules can be easily integrated, and the existing software modules can be reused. We believe that our software system can be considered as the first step to obtain solutions totally integrated with the surgical instrumentation and of ease use in several fields of cardiac surgery.

Acknowledgments. This project was supported by the funding from Canadian Institutes for Health Research (Grant MOP 74626), the National Science and Engineering Research Council of Canada (Grant R314GA01), the Ontario Research and Development Challenge Fund, the Canadian Foundation for Innovation and Ontario Innovation Trust, as well as the scholarships from the Ontario Ministry of Education.

References

1. Wierzbicki, M., Drangova, M., Guiraudon, G., Peters, T.M.: Validation of dynamic heart models obtained using non-linear registration for virtual reality training, planning, and guidance of minimally invasive cardiac surgeries. Medical Image Analysis 8(3), 387–401 (2004)
2. Gasparovic, H., et al.: Three dimensional computed tomographic imaging in planning the surgical approach for redo cardiac surgery after coronary revascularization. Eur. J. Cardiothorac. Surg. 28, 244–249 (2005)
3. Vidal, F., et al.: Principles and applications of computer graphics in medicine. Comput. Graph. Forum 25(1), 113–137 (2006)
4. Lawler, L.P., Ney, D., Pannu, H.P., Fishman, E.K.: Four-Dimensional Imaging of the Heart Based on Near-Isotropic MDCT Data Sets. Am. J. Roentgenol. 184(3), 774–776 (2005)
5. O'Brien, J.P., Srichai, M.B., Hecht, E.M., Kim, D.C., Jacobs, J.E.: Anatomy of the Heart at Multidetector CT: What the Radiologist Needs to Know. RadioGraphics 27, 1569–1582 (2007)
6. Saito, K., Saito, M., Komatu, S., Ohtomo, K.: Real-Time Four-dimensional Imaging of the Heart with Multi–Detector Row CT. RadioGraphics 23, e8 (2003)
7. Robb, R.A., Hanson, D.P.: Biomedical image visualization research using the Visible Human Datasets. Clinical Anatomy 19(3), 240–253 (2006)
8. Levin, D., Aladl, U., Germano, G., Slomka, P.: Techniques for efficient, real-time, 3D visualization of multi-modality cardiac data using consumer graphics hardware. Computerized Medical Imaging and Graphics 29(6), 463–475 (2005)
9. Lehmann, H., Ecabert, O., Geller, D., Kiefer, G., Weese, J.: Visualizing the beating heart: interactive direct volume rendering of high-resolution CT time series using standard PC hardware. In: Proc. of SPIE Med. Imaging, 614109-1–12, pp. 59–70 (2006)
10. Krüger, J., Westermann, R.: Acceleration Techniques for GPU-based Volume Rendering. In: Proc. of the 14th IEEE Visualization 2003 (VIS 2003), pp. 287–292 (2003)
11. Grimm, S., Bruckner, S., Kanitsar, A., Gröller, E.: A refined data addressing and processing scheme to accelerate volume raycasting. Computers & Graphics 28(5), 719–729 (2004)
12. Zhang, Q., Eagleson, R., Peters, T.M.: Real-rime visualization of 4D cardiac MR images using graphics processing units. In: Proc. of IEEE ISBI, pp. 343–346 (2006)

13. Zhang, Q., Huang, X., Eagleson, R., Guiraudon, G., Peters, T.M.: Real-time dynamic display of registered 4D cardiac MR and ultrasound images using a GPU. In: Proc. of SPIE Med. Imaging, 65092D-1–11 (2007)
14. Bullitt, E., Aylward, S.: Volume rendering of segmented image objects. IEEE Trans. on Medical Imaging 21(8), 998–1002 (2002)
15. Bühler, K., Neubauer, A., Hadwiger, M., Wolsfberger, S., Wegenkittl, R.: Interactive 3D techniques for computer aided diagnosis and surgery simulation tools. In: Hruby, W. (ed.) Digital Revolution in Radiology - Bridging the Future of Health Care, 2nd edn. Springer, Heidelberg (2005)

euHeartDB: A Web-Enabled Database for Geometrical Models of the Heart

Daniele Gianni, Steve McKeever, and Nic Smith

Computing Laboratory
Oxford University
Parks Road, OX1 3QD, Oxford, UK
{daniele.gianni,steve.mckeever,nic.smith}@comlab.ox.ac.uk

Abstract. Achieving patient specific treatments is of fundamental importance in the future provision of cost and patient effective health care services for cardiovascular diseases. Implementing this view requires that software and data are reused and shared over the investigation process and within each single process phase. Within the heart modeling and simulation phase, geometrical models can be reused and shared with interoperable markup languages and a central repository. A markup language has been recently proposed to describe such models whereas a repository is still needed. In this paper we introduce *euHeartDB*, a publicly accessible database that aims to satisfy this role by providing the functionalities to upload, to search and to integrate geometrical models. The database is web-enabled and allows the visualization of the models which functionality is fundamental to human users. In addition, *euHeartDB* uses the Foundational Model of Anatomy ontology to classify the models and to support semantic-based queries.

Keywords: Database, heart, geometrical model, web application.

1 Introduction

Our longevity and the quality of our lives is heavily dependant on the conditions of the vital organs composing the human body, and in particular of the *heart* and cardiovascular system [1]. Nowadays, *cardiovascular diseases* cause over two million deaths each year in Europe alone and are estimated to become the primary cause of death in western countries by 2010 [2]. Tackling this future scenario requires that the whole investigative process, from the patient data acquisition to the monitoring of treatment, is optimized and supported by software tools. In addition, sharing and reuse of software components and data among the tools operating in each phase are also essential for the construction of more complex systems. In this paper, we specifically focus on the heart modeling and simulation phase, in which considerable efforts are needed to build the *geometrical models*. Moreover, a vast variety of models can be obtained depending on the species, the measurement process, the model structure and data fitting procedure. Well-established geometrical models in the community are: the Auckland canine model [3], the San Diego model [4], the Johns Hopkins model [5], the INRIA model [6], the UPF model [7], and the Auckland porcine model [8]. All

N. Ayache, H. Delingette, and M. Sermesant (Eds.): FIMH 2009, LNCS 5528, pp. 407–416, 2009.
© Springer-Verlag Berlin Heidelberg 2009

the six models are based on a similar mathematical structure and present a comparable average approximation of the geometry, of the fiber and of the sheet orientation, when modeled. The *Auckland canine model* was the first model to establish a compact and realistic finite element model of the geometry and of the fibrous organization for heart simulations. The model is obtained with histological techniques using a measurement ring tool on blunt dissections of the epicardium in diastole [3]. In the following years, the most suitable experiments for validating geometrical models were conducted on rabbits and this motivated the introduction of the *San Diego rabbit model*. The model maintains the Auckland structure and its data are obtained from image-based measurements on slices of myocardium cast in dental rubber [4]. Three years later, advancements of computer technologies in medical imaging stimulated the introduction of the *Johns Hopkins model*, which measures San Diego model data directly on Magnetic Resonance Images (MRIs) of formaline-fixed epicardium tissue [5]. This technique was further exploited in the *INRIA model* and in the *UPF model* with the design of sophisticated image analysis techniques that automatically derive model data from the MRI by inferring statistical properties of the diffusion tensors [6] and by building cardiac atlas on samples of human population [7], respectively. Finally, the *Auckland porcine model* was last introduced to exploit increased computational power – sheet orientation is modeled along a higher degree of continuity on the geometry and fiber field; and to suit the available porcine experimental data [8].

Reusing these models, or part of them, to validate functional models is fundamental to advancing the in silico investigation in cardiovascular diseases. Besides the inherent complexity of model characterization, considerable technical issues must be addressed to achieve model sharing and reuse. This includes the model exchange format and the accessibility of the models. Such issues can be dealt with the adoption of interoperable formats based on Markup Languages (ML) and with by the use of an accessible repository [9]. The *FieldML* specification has been recently introduced as a ML [10] to describe the models and to facilitate their reuse; however, a repository for such models has not been developed yet. In this paper we present *euHeartDB*, a database that aims to satisfy this role by automating model sharing and reusing, and by facilitating model integration. To achieve this, euHeartDB incorporates a web interface, which can be publicly accessed through the home page of the euHeart project [11], and the *Foundational Model of Anatomy* ontology [12]. The interface allows web-enabled user to access the models without human assistance; and the ontology provides the semantic basis for model classification, semantic queries, and integration checking.

The paper is organized as follows: a related work section positions this paper and compares its contributions to related work. We then proceed with a section illustrating our system. It includes the system architecture with emphasis on the web application, and the visualization of the current database content. Finally, we conclude with a discussion on future euHeartDB work.

2 Related Work

The use of software technologies to support health care is not new and the objectives and guidelines have been formulated in several projects and conferences [13] and

more specifically proposed in [14] for model databasing. However, the implementation of this view has not been achieved to date. Many tools have been introduced to support the various needs and treatment stages [15], such as simulation [16], visualization [16][17], and image analysis [6]. However, very few of these deal with the sharing and reuse of geometrical models, which enable the simulation results and input data. The closest projects to *euHeartDB* are: the *Cardiac Anatomic Database (CAD)* [18] and the *Cardiovascular Model Repository (CMR)* [19].

CAD consists of a standard Java local interface to load, to list, to search with programmatic query languages, and to visualize the models stored in a local database in a VTK format. *euHeartDB* differs from CAD in four ways: it is web-enabled and potentially accessible to everybody in the web, it integrates with FieldML [10], it enables natural language searches, and finally it uses a well-established ontology for the model classification.

CMR is currently a web-accessible page that provides links to cardiovascular geometrical models such as aorta or arterio-femoral system in VTK format. In contrast, *euHeartDB* offers a dynamic environment where geometrical models of the heart can be loaded, searched, visualized and next integrated.

3 euHeartDB

The objective of *euHeartDB* is to automate the sharing and the reuse of geometrical models in the entire cardiovascular community, and to facilitate their integration within simulations of functions. We achieve this goal in three steps. First, we identify the requirements that the system must satisfy, in cooperation with *euHeart partners*. Second, we formulate the system description. Third, we show the current and future uses of *euHeartDB* within the community.

3.1 Requirements

The goal of euHeartDB of automating model sharing and reuse translates into the definition of functional and non functional requirements. The functional requirements are divided into those for model users and for model creators. For model users, these include (R1) searching, (R2) downloading, (R3) commenting and (R4) curating of models. Similarly for model creators, the requirements are (R5) uploading, (R6) activity monitoring (e.g. who downloads what), and (R6) accessibility setting of models. In addition, the integration of bibliographic references (R7) (e.g. linking models to publications that illustrate, cite or use them) is highly recommended as it allows one to trace all the studies related to a given model. These functional requirements demand minimal description and, therefore, are directly addressed in the design of the system. Conversely, the non functional requirements have to be addressed in conjunction with the functional requirements and deserve more attention. These non functional characteristics include:

- Decentralised control of database content (R8)
- Web accessibility (R9)
- Secure control access (R10)
- Semantic-based search of models (R11)
- Graphical methods (R12)

- Interoperable and standard XML data format for model exporting (R13)
- Support for popular model data formats (R14).

A *decentralized control of the database content* means that users can autonomously access the database to upload, search and download their models. While the search and download are generally decentralized by exposing these resources on a distributed environment, the uploading is sometimes managed centrally by individuals charged with managing the database data entry phase.

To achieve the automation, a decentralized control of the database content is needed. This decentralized control, however, requires that users can connect to the system independently from the peculiarities of the user systems. In technical terms, this requires the use of web technologies, which overcome platform heterogeneity and location issues, and therefore *euHeartDB* functionalities must be *web accessible*. The universal accessibility offered by the web also implies that non authorized and non authenticated web users could access the interface services or could sample the database content when transmitted over the network. *euHeartDB* must avoid this by implementing a *secure control access*. In particular, the interface access must be restricted to solely authenticated and authorized users and all the database content must be transmitted over encrypted connections.

The fundamental database functionality for the sharing and reuse is the model search. This should be supported by *semantic-based* criteria, such as a specified structural part of heart for instance, in order to obtain more effective model retrieval. In addition, the search should also be supported by *graphical methods* because they allow a comprehensive view of the models to human users, who eventually check the model before downloading it in an *interoperable and standard XML data format*, such as FieldML [10], that allows reusing on any user system.

Finally, other popular model data formats, such as VTK, must be supported to effectively promote the use of *euHeartDB* within the entire cardiovascular community.

3.2 System Description

In this section we describe the main characteristics of our system. These are the architecture and the web interface.

3.2.1 System Architecture

The system architecture can be described horizontally, for the cross domain functionalities, and vertically for specific roles inside the system. The horizontal structure conforms to the *Model-View-Control (MVC)* architecture [20], which consists of three layers: one for the data model (*Model*), one for the user interface (*View*), and one for the business logic that determines the action flows and the respective action logic (*Control*). The vertical structure consists of a client and a server sides connected through the Internet. On the client side, a user accesses the server side resources with a Zinc-enabled web-browser [21], whereas on the server side the following components are operating:

1. FMA ontology [12]
2. Database
3. Web application.

The *FMA ontology* provides the semantic foundations for inferences, model checking and semantic-based queries on the database, thus fulfilling requirement R11. Each model stored in *euHeartDB* is classified by one or more concepts that are parts or subparts of the FMA Heart frame. Through the use of the FMA ontology models can be searched and integrated based on the semantic they represent.

The *database*, which is located at the *Model* layer, is Object-Oriented and is accessed through object persistence technologies [22]. The database stores all the data concerned with the models, which includes field data (such as the mesh and field values over the mesh) and field meta-data (such us field name, type and keywords).

The *web application* implements *View* and *Control* layers by respectively providing the interfaces to access the *database* and by defining the logic behind the sequence of actions to insert, to search, to download, to visualize, and to manage the models.

3.2.2 Web Application

The *web application* provides a user interface to access the model data and the business logic that enables decentralized insertion (R5, R8), searching (R1), downloading (R2), and visualization of the geometrical models (R12). The interface layer is implemented in standard web technologies [22] – thus fulfilling R9, and therefore can be downloaded and visualized by any Internet browser-enabled user. The business logic is also Java-based and develops in three access areas depending on the security and privacy issues [23], as indicated by requirement R10. The most external area is public, i.e. accessible to everybody on the web, and is delivered without any form of encryption. This area includes only the web interface home page and does not contain any sensitive data. The inner area, which includes the login page, is still public but introduces encryption to protect the user authentication data, user name and password. The inner most area is the core of the application. It is accessible solely by authenticated users and only on encrypted connections, i.e. unauthenticated users are filtered through standard practices and non-secure URLs are redirected to the respective secure URLs.

The application flow is driven by user clicks along the possible browsing paths. From the main menu page, currently, three types of operations can be activated:

1. Bibliographic references
2. Geometrical models
3. myEuHeartDB.

The first concerns all the operations needed to manage the bibliographic references – requirement R7. These are rather standard and include: insertion or updating of author data, uploading of publications, insertion and automatic extraction of publication metadata (i.e. authors, title, and references).

The second regards the operations related to the use of geometrical models. Currently, the system provides:

- Insert Model
- Show All Models
- Search Model.

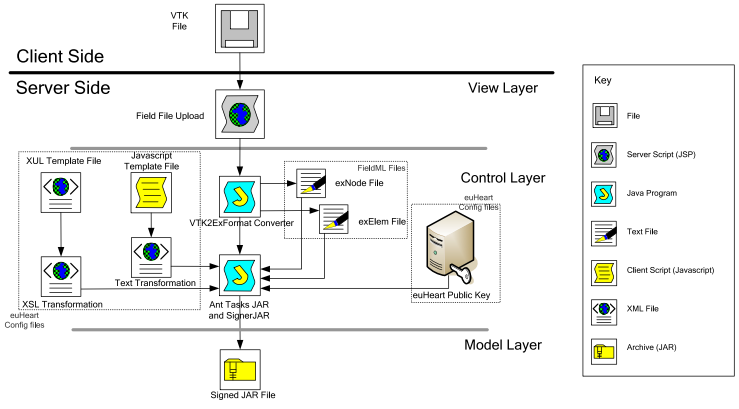

Fig. 1. VTK File Uploading and Preparation for Visualization

The *Insert Model* operation allows the uploading of the model data, e.g. field file and metadata describing it. After specifying the format of the field file being uploaded – the system currently satisfies requirements R13 and R14 by respectively supporting an early version of the FieldML format [10], the CMGUI *ex Format*, and a subset of VTK format; the system proceeds to the uploading procedure. Since the FieldML format is being used internally, we shall illustrate the VTK format case only because it includes the steps required when uploading FieldML files. Figure 1 details the steps involved in the uploading of a VTK file.

On the client side, the user inserts the model metadata and selects the VTK file to be uploaded in the respective forms. On the server side, the Struts framework [24] retrieves all the data from the form and activates the *Field File Upload* script. The script determines whether subsequent transformations are needed for visualization purposes before packaging the files as required by the Zinc plugin [21]. The plugin, which currently operates in Mozilla-based browsers, requires that four configuration files, for the XML description of the interface (XUL file), for the interface event handling (Javascript file), and the mesh and field files (exNode and exElem); are packaged and signed with a public key in a Java Archive (JAR) file.

Once the FieldML files are available for the uploaded model, the server script operates two transformations to produce respectively the XUL file and the Javascript associated to the model. The former consists of an XSL transformation [23] that takes in a preloaded XUL template and customizes it with the model specific data. The second transformation consists of text-based customization of a preloaded template script for generic settings of model visualization. Once both XUL and Javascript files have been produced, the script packages the four files into a JAR file and signs it. The file is thus stored into the database and is available in the authenticated area for visualization as much like any standard Zinc application. The model insert logic, however, does not end with the JAR packaging. This action is followed by the model description in terms of FMA concepts. This consists of browsing the OWL version of the FMA ontology [12] through Protégé [26] and of letting the user select to which anatomical parts of the heart, or the whole heart, the model represents. The heart as a whole can be selected or explored in its anatomically significant subparts. If the

explore option is selected, its subparts will be displayed and available for selection, further exploration or ignoring (default choice). The procedure ends when no subparts of the heart are selected for further explorations.

The *Show All Models* and *Search Model* operations display on the user interface the list of the models matching the search criteria. For the *Show All Models* operation the criteria is equivalent to all models and for the *Search Model* the filtering can be specified in terms of keywords to be searched in the model metadata, such as heart subpart or keyword. The search results are displayed as a list of links to the model pages. Each of the model pages can be reached with a script and contains all the model data, model metadata, download link and comments (requirement R3), besides from a link for the graphical visualization. This link consists in the secure downloading of the model JAR produced at uploading time and in the activation of the Zinc plugin in the user browser. The plugin thus accesses the *FieldML* files packaged in the archive and visualizes them as conventional geometrical models.

Finally, the *myEuHeartDB* option provides a personalised view on the *euHeartDB* content. This includes the list of the one's own recent activities in the system, the list of recent activities of other euHeartDB users on the owned models (e.g. downloads or visualisations) – requirements R6, and list of one's own models. This list, moreover, contains the references to the personal model pages, in which the model access settings in euHeartDB can be configured.

3.3 Current and Future Use of euHeartDB

Currently the database is available for use only to euHeart partners and is populated with four heart models: the Auckland canine model [3], the ASCLEPIOS model [7], the CILAB model [6], and the Philips model [27]. Once logged in, the four models can be retrieved using either the *Search Model* or *Show All Model* options from the main menu. By listing all the models and then clicking on the page of any of the above models, the visualization link is available in the page for displaying the selected model in the browser. In Figure 2, the Auckland, ASCLEPIOS, CILAB, and Philips models are shown inside the browser visualization interface in (a), (b), (c), and (d) respectively. The interface is composed of two vertically adjacent panels. On the left panel, some basic scene control options are available to adjust the visualization settings to the user preferences. In addition to the currently stored geometrical models, further models can be uploaded by users who have been granted access to the system. Currently, only euHeart partners are enabled to do this, and they are in the process of uploading their models. In spite of such dynamicity in the operational scenario, the system self manages the changes of the database content and does not require further maintenance for searching, listing and visualisation of the new models. Also, the access settings of the models are configured by the model owners, therefore inappropriate or undesired use of the private scientific data is prevented when the system will be made publicly accessible.

In the future, *euHeartDB* will have a much wider scope and be more extensively integrated with the implementation of patient specific treatments. In particular, euHeartDB will: 1) support *coupling of geometrical models* – which is recommended to exploit model reuse by assembling available models; 2) enable the *solution of simulations within different geometries* – which is necessary to obtain extensive and

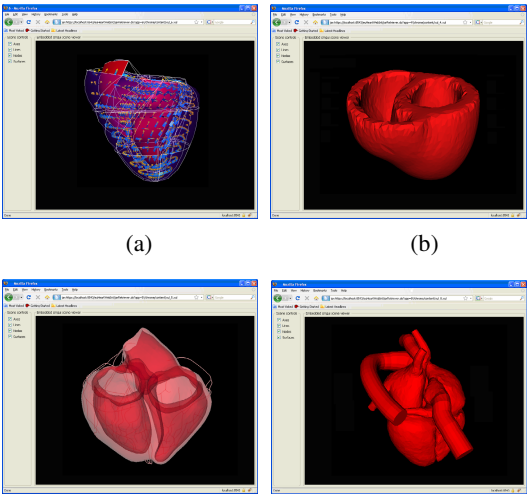

(a) (b)

(c) (d)

Fig. 2. euHeartDB Visualization of the Heart Models in [3] – (a), [7] – (b), [6] – (c), [27] – (d)

more accurate validations of functional models; 3) allow *benchmarking of simulation results* – which is needed to establish correlations between simulation output data and pathologies; 4) support *anatomical surveys on models of the heart* – which is needed to improve statistical analysis of the clinical data upon which the models are based; and 5) store *documentation of different diseases on the heart geometry* – which aims to ease statistical inferences of correlation between geometries and diseases, such as heart malformation and arrhythmia.

4 Future Work

In our vision, the current release of the *euHeartDB* constitutes only a preliminary step in the implementation of a Web-accessible and ontology driven database. Several major issues remain. First, the use of an updated version of *FieldML* is required to better integrate this work with the current standards in the computational biology heart community. Second, the semantic-based retrieval and integration of the models need to be implemented to effectively enable the sharing and reuse of the geometry and fiber fields. Third, performance issues need to be dealt with in order to guarantee optimal access to the data. Finally, current web technologies should be exploited to make the application more interactive and more usable. For example, the following functionalities will be introduced: curation of additional models (such as coronary, atrial, or purkinje) – requirement R4; linking to data and publications using the models and support for simulation benchmarking.

5 Conclusions

Sharing and reusing models is the key to achieve patient specific investigations in the future health care services, in particular for cardiovascular diseases. In this paper we

introduced *euHeartDB*, a database that automates the sharing of geometrical models of the heart and facilitates the reuse through integration with standards formats. The models, which are in the form of meshes and fields, can be uploaded and searched through a conventional web interface. The interface also allows the visualization of the models to human users in an interactive and intuitive manner. In addition, *euHeartDB* connects with the *Foundational Model of Anatomy* ontology to classify the models and to prepare the foundations for semantic-based searches and integration model checking. Currently, the database stores four comprehensive geometrical models and is in the process of being uploaded with further models.

Acknowledgements

This work has been supported the European Commission (FP7-ICT-2007-224495: euHeart). The authors would like to thank the Auckland Bioengineering Institute, the ASCLEPIOS team, at INRIA Sophia-Antipolis, the CILAB, at Universitat Pompeu Fabra, and the X-ray Imaging Systems department of Philips Research Aachen for providing the first geometrical models uploaded in euHeartDB.

References

1. Allender, S., Scarborough, P., Peto, V., Rayner, M., Leal, J., Luengo-Fernandez, R., Gray, A.: European cardiovascular disease statistics (2008), `http://www.heartstats.org`
2. The World Health Organization, The world health report (2003), `http://www.who.int`
3. LeGrice, I.J., Hunter, P.J., Smaill, B.H.: Laminar Structure of the Heart: a Mathematical Model. American Journal of Physiology 272(5), H2466–H2476 (1997)
4. McCulloch, A.D., Vetter, F.J.: Three-dimensional Analysis of Regional Cardiac Function: a Model of Rabbit Ventricular Anatomy. Progress in Biophysics and Molecular Biology 69, 157–183 (1998)
5. Winslow, R.L., Scollan, D.F., Holmes, A., Yung, C.K., Zhang, J., Jafri, M.S.: Electrophysiological Modeling of Cardiac Ventricular Function: From Cell to Organ. Annual Review of Biomedical Engineering 2, 119–155 (2000)
6. Ordas, S., Oubel, E., Sebastian, R., Frangi, A.F.: Computational Anatomy Atlas of the Heart. In: Proceedings of the 5th International Symposium on Image and Signal Processing and Analysis (ISPA 2007), September 2007, pp. 338–342 (2007)
7. Peyrat, J.M., Sermesant, M., Pennec, X., Delignette, H., Xu, C., McVeigh, E., Ayache, N.: A Computational Framework for the Statistical Analysis of Cardiac Diffusion Tensors: Application to a Small Database of Canine Hearts. IEEE Transaction on Medical Imaging 26(10), 1500–1514 (2007)
8. Stevens, C., Remme, E., LeGrice, I., Hunter, P.: Ventricular Mechanics in Diastole: Material Parameter Sensitivity. Journal of Biomechanics 36, 737–748 (2003)
9. Hunter, P.J., Li, W.W., McCulloch, A.D., Noble, D.: Multiscale Modeling: Physiome Project Standards, Tools, and Databases. IEEE Computer 36(11), 48–54 (2006)
10. Christie, G.R., Nielsen, P.M., Blackett, S.A., Bradley, C.P., Hunter, P.J.: FieldML: Concepts and Implementations. Philosophical Transactions of the Royal Society, special issue on Computational Biology: Tools & Applications (to appear, 2009)
11. euHeart Project Home Page, `http://www.euheart.eu`

12. Rosse, C., Mejino, J.V.L.: A reference ontology for biomedical informatics: the Foundational Model of Anatomy. Journal of Biomedical Informatics 36, 478–500 (2003)
13. Towards virtual physiological human: multilevel modelling and simulation of the human anatomy and physiology, White Paper (November 2005)
14. Smith, N.P., Crampin, E.J., Niederer, S.A., Bassingthwaighte, J.B., Beard, D.A.: Computational Biology of Cardiac Myocytes: Proposed Standards for the Physiome. Journal of Experimental Biology, 1576–1583 (May 2007)
15. Shortliffe, E.H., Cimino, J.J.: Computer Applications in Health Care and Biomedicine, 3rd edn. Springer, Heidelberg (2006)
16. CMISS – CMGUI Projects, http://www.cmiss.org/cmgui
17. MedINRIA Project, http://www-sop.inria.fr/asclepios/software/MedINRIA/
18. Cardiac Anatomic Database, http://www.ccbm.jhu.edu/software/card.php
19. SimBIOS Cardiovascular Model Repository, https://simtk.org/home/cv-gmodels
20. Fowler, M.: Patterns of Enterprise Application Architecture. Addison Wesley, Reading (2002)
21. Stevens, C., Blackett, S.A., LeGrice, I.J., Hunter, P.J.: Internet Applications for Computational Biology, the CMISS Web Browser Extension and Use in Education. In: Proceedings of the 2005 IEEE Engineering in Medicine and Biology 27th Annual Conference, September 2005, pp. 849–850 (2005)
22. J2EE, http://java.sun.com/javaee/
23. Win, K.T., Susilo, W.: Information security and privacy of health data. International Journal of Healthcare Technology and Management, Inderscience 7(6), 492–505 (2006)
24. Apache Group, http://www.apache.org/
25. XSL Transformation specifications, W3C, http://www.w3.org/TR/xslt
26. Protégé project, http://protege.stanford.edu
27. Ecabert, O., Peters, J., Schramm, H., Lorenz, C., Von Berg, J., Walker, M.J., Vembar, M., Olszewski, M.E., Subramanyan, K., Lavi, G., Weese, J.: Automatic Model-Based Segmentation of the Heart in CT Images. IEEE Transaction on Medical Imaging 27(9) (September 2008)

GIMIAS: An Open Source Framework for Efficient Development of Research Tools and Clinical Prototypes

Ignacio Larrabide[1,2,⋆], Pedro Omedas[2,1], Yves Martelli[2,1], Xavier Planes[2,1], Maarten Nieber[2,1], Juan A. Moya[2,1], Constantine Butakoff[2,1], Rafael Sebastián[2,1], Oscar Camara[2,1], Mathieu De Craene[1,2], Bart H. Bijnens[3,2,1], and Alejandro F. Frangi[2,1,3]

Center for Computational Imaging and Simulation Technologies in Biomedicine (CISTIB)
[1] Networking Biomedical Research Center on Bioengineering, Biomaterials and Nanomedicine (CIBER-BBN), Barcelona, Spain
[2] Universitat Pompeu Fabra, Barcelona, Spain
[3] Institució Catalana de Recerca i Estudis Avançats (ICREA), Barcelona, Spain
{ignacio.larrabide,pedro.omedas,alejandro.frangi}@upf.edu

Abstract. GIMIAS is a workflow-oriented environment for addressing advanced biomedical image computing and build personalized computational models, which is extensible through the development of application-specific plug-ins. In addition, GIMIAS provides an open source framework for efficient development of research and clinical software prototypes integrating contributions from the Virtual Physiological Human community while allowing business-friendly technology transfer and commercial product development. This framework has been fully developed in ANSI-C++ on top of well known open source libraries like VTK, ITK and wxWidgets among others. Based on GIMIAS, in this paper is presented a workflow for medical image analysis and simulation of the heart.

Keywords: Biomedical imaging, cardiovascular modeling, Virtual Physiological Human, personalized simulations, open source software.

1 Introduction

The integrative multi-scale and multi-disciplinar community that tries to understand the human patho-physiology is internationally known as "IUPS Physiome Project" [1,2] or, in the European context as "Virtual Physiological Human" (VPH) [3]. Besides the strategic character that it has regarding the priorities of the 7^{th} Framework Programme of the EU, the VPH is of great relevance in the current context given its integrative vision of the physiological and computational knowledge. In this perspective, a key challenge in the development of integrative and predictive models for the human physiology is the creation of

⋆ Corresponding author.

N. Ayache, H. Delingette, and M. Sermesant (Eds.): FIMH 2009, LNCS 5528, pp. 417–426, 2009.
© Springer-Verlag Berlin Heidelberg 2009

computational tools that enable the collaborative work between scientists, industry and health care to bridge the gap between scientific discovery and clinical treatment.

An essential condition for the success of the VPH is the development of software tools that ensure methodology integration. As examples we can site all multi-scale integration, access and exploitation of large repositories and databases, processing of data with state-of-the-art algorithms, creation of personalized models, data fusion and visualization.

In this paper we present GIMIAS (Graphical Interface for Medical Image Analysis and Simulation), a workflow-oriented environment that has been specially tailored for fast development of biomedical imaging and modeling software prototypes. GIMIAS provides an open source framework for the development of research tools and clinical prototypes, allowing the integration of contributions from the Physiome community while allowing business-friendly technology transfer.

2 Related Work

Current tools (see Table 1) have their own strengths and weaknesses, mainly linked to the core skills of the research group behind it. However, there is not currently, a single application that fulfills all the requirements of all possible VPH applications. For this reason, the VPH community is steadily progressing towards establishing data, modeling and communication standards that ensure interoperability between different tools rather than creating a single application that accounts for all possible needs. Furthermore, there is also a need for a Free Open Source Software platform that allows efficient development of prototypes, that requires minimal training time or prior knowledge to get started.

What GIMIAS brings to the community is a common framework to help on data manipulation and visualization in which processing algorithms can be easily integrated. In this environment new algorithms and models (developed by the user or provided by an existing library) can be easily integrated in more complex processing workflows. Furthermore, GIMIAS and all the libraries on which it relies are Free Open Source Software. In this way, different teams using the platform, either from academia or industry, can interact and share modules easily. The main goal of this platform is to transfer novel technologies into clinical environment by the fast development of prototypes.

3 Specifications

Taking into account all the requirements for the platform, GIMIAS architecture has been designed to accomplish the following specifications. The following non-functional requirements, i.e., criteria usable to judge the system other than its functionalities, should be addressed by GIMIAS:

– *Modularity*: its functionalities should be modular allowing flexibility in the way that they are combined to facilitate exchangeability and reuse.

Table 1. Summarized list of current software development projects focused on medical image processing and end-user software for model personalization. The brief feature list is based on the description provided by their distributors. The following list contains the corresponding websites for the tools described above where further details can be found: www.brainvisa.info, www.cmiss.org/cmgui, www-sop.inria.fr/asclepios/software/MedINRIA, www.mevislab.de/, www.openmaf.org/, www.paraview.org, www.slicer.org.

Name	Distribution license	Brief list of features
BrainVISA	Open source software. CeCILL License.	- scientific visualization - signal and image processing
CMGUI	Open source software. Mozilla Public License.	- scientific visualization - scripting capabilities - model personalization - signal and image processing
MedINRIA	Free for non-commercial use.	- scientific visualization - model personalization - signal and image processing
MeVisLab	Basic version free for non-commercial use. SDK version requires a commercial license.	- scientific visualization - scripting capabilities - plug-in architecture - image processing
OpenMAF	Open source software. BSD-style License.	- generic application framework - scientific visualization - model personalization - image processing
ParaView	Open source software. BSD-style License.	- scientific visualization - scripting capabilities - plug-in architecture
Slicer 3D	Open source software. BSD-style License.	- scientific visualization - plug-in architecture - image processing

- *Simplicity*: to allow technologists and scientists to easily integrate their algorithms in the platform in with small amount of time and effort.
- *Flexibility*: to support the development of research and clinical prototypes with different degrees of complexity. Also, binary (compiled) and/or interpreted (script-based) plug-in development should be possible requiring an even smaller amount of prior knowledge to integrate new features.
- *Interoperability*: to cope with the increasing amount of image processing and modeling tools available and to ensure maximum reuse, it is of crucial importance that this software is capable of inter-operating with others.

In order to illustrate how GIMIAS can be used for the implementation of a particular workflow, let us use as an example an application for cardiac modeling. On this regard, the treatment of biomedical data often involves (sometimes large) work-flows that require different data processing tools. This is particularly important in the case of cardiac modeling, where the use of computational tools

for image and signal processing, surface and volume mesh editing, creation of numerical models and data visualization is required.

GIMIAS framework users

GIMIAS, as a fast prototyping open source framework, has been developed thinking in two different user profiles:

1. *Researchers* who want to test methodologies and easily create prototypes for validating the practical feasibility of research concepts. Using the proposed framework, they can create new plug-ins that incorporate their methods and algorithms, allowing potential end-users (e.g., medical doctors, clinical scientists, among others) to assess them.
2. *Scientific developers (from academic or industrial environment)* that need to create fast and cheap prototypes for research tools and/or clinical products. Moreover, by having a BSD licence, GIMIAS is appropriate for promoting interaction between industrial and academic software development teams.

GIMIAS provides a simple Application Programming Interface (API) that permits, with minimal effort, to trial methodologies and algorithms in the form of end-user applications. Also, prototypes developed within/for GIMIAS can be tested by end users in real scenarios and with real data at early development stages, providing very useful feedback as well as reducing the time required to get new concepts from research to the clinical environment.

4 The GIMIAS Architecture

GIMIAS has been designed to be extended via the addition of plug-ins. Plug-ins are extension units (e.g., dynamic link libraries or shared objects depending on the platform) for an application whose architecture allows functionalities to

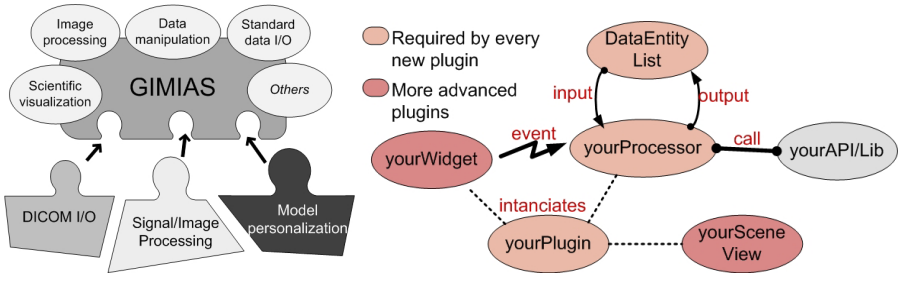

Fig. 1. Left: Schematic overview of the plug-in based architecture of GIMIAS. General infrastructure services are used by the different plug-ins according to the specific application. Plug-ins can be changed to create new workflows. Right: Classes to be developed, and their associated complexity and interaction, for the creation of a new plug-in. For the classes Widget and DataView the developer can choose either implementing them or using the standard implementation provided by the framework.

be introduced by users or programmers at well-defined places after it has been installed. In GIMIAS, plug-ins are software entities that can be created with minimal experience in programming for extending the application by providing specific features in a modular way.

Plug-in based software architecture

GIMIAS provides an API for the plug-ins to interact with the application core and with other plug-ins. The classes that can be extended for the creation of a new plug-in are: `Widget`, `SceneView`, `DataEntityList`, `FrontEndPlugin` and `Processor` (see Figure 1). Depending on the complexity of the desired plug-in, not all these classes need to be developed. The minimal set of classes needed to create a plug-in with new behavior are `WorkingData` (containing the data used by the plug-in), `FrontEndPlugin` (which describes the main functionality of the plug-in) and `Processor` (executes an algorithm given one or more input data and generates one or more output data). Very briefly, the classes that need to be used and/or extended for the creation of plug-ins are (see Fig. 1):

- `DataEntity`: This class stores and encapsulates a single data object (e.g., medical image, transformation, surface mesh, model simulation result, etc.).
- `DataHolder`: This class allows objects to register as observers of data, for instance, to be notified when the data is changed.
- `WorkingData`: This class holds a reference to the `DataHolders` associated to the data required and is currently used by the plug-in (selected input, output, etc.).
- `DataEntityList`: This class contains a list populated with the data entities currently available for processing in the application. The input data that will be processed by the plug-in and also their outputs are stored in this list.
- `FrontEndPlugin`: This is the base class for all the plug-ins, every new plug-in must extend this class. This base class provides access to the rendering classes, but delegates the creation of the rendering scene to the extending class' implementation.
- `Processor`: This class executes one algorithm and given on or more input data and generates one or more output data (usually coming from the `DataEntityList`). A plug-in may contain more than one `Processor` class. No data is stored inside the `Processor`.

Regarding data processing, each plug-in uses its own (one or more) `Processor` classes that encapsulate the application logic indicating which algorithm needs to be executed on the data. External algorithms (user defined or furnished by a library) are called by a `Processor` after the required input data have been specified. After the execution of an algorithm, the `Processor` notifies (through the `DataHolder`) the corresponding observers that new data is available. These data can be rendered or processed depending on the application. It is the responsibility of the plug-in to determine how the processing pipeline continues. In this way, the plug-in developer is responsible for defining how the end-user operates over the data and visualizes it. `DataEntity` encloses and represents 4D

working data in a single entity that can be modified, transformed and rendered by any plugin. This class allows plugins to share data, encapsulating its format conversion thus facilitating the exchange and flow data.

For its simple architecture, the sole specialization/implementation of three classes is enough for creating new plug-ins. In this way, new features can be integrated very fast. The architecture is flexible to support plug-ins with different complexity, going from simple (e.g., data is processed with a specific algorithm and the results are visualized with standard viewers) to complex (e.g., the entire user interface can be refurbished to create a new data interaction and visualization application). In addition to its plug-in API, the framework provides basic services which can be used by the plug-ins:

- scientific visualization through standard screen layout (i.e., 3D plus orthogonal slicing),
- multimodal (MRI, SPECT, MSCT, US, PET) image processing,
- heterogeneous data management (images, polylines, surface geometries, volumetric meshes),
- standard I/O formats (others can be added by the users).

All these services are accessed trough the `FrontEndPlugin` class. Further details on other features and plug-ins provided by the framework can be found at www.gimias.org.

Regarding interoperability with external tools, the framework allows to easily integrate different format readers and writers. A closer integration (e.g., in runtime) with other tools is possible by developing a specific plug-in for this matter.

Third-party libraries

GIMIAS has been entirely developed in ANSI-C++ and is distributed under BSD-licence. The reason to make the software open source is to facilitate and foster the cooperation and interaction between different research groups and with industry for technology transfer. This licence model together with its plug-in architecture make it ideal for this kind of interaction.

A proper selection of third party libraries is crucial for the long term continuity of the software. For this reason only BSD-licensed libraries with consolidated and active user communities where selected. For the graphical user interface, wxWidgets[1] was considered. The mesh manipulation is based on The Visualization Toolkit (VTK)[2], an open source, freely available software system for 3D computer graphics, image processing, and visualization with a large and established user community around the world. For user interaction and visualization of data, the Medical Imaging Interaction Toolkit (MITK) [4] is used. For handling data in DICOM standard, DCMTK library is used[3]. For image processing operations The Insight Toolkit (ITK)[4] was chosen.

[1] www.wxwidgets.org
[2] www.vtk.org
[3] dicom.offis.de/dcmtk
[4] www.itk.org

5 Example Workflow in GIMIAS

In this section we analyze in detail a case study based on image analysis and modeling of the heart. The objective of this case study is to show the capability of GIMIAS to integrate different algorithms in a single workflow. To this end, patient images in DICOM format are loaded. Next the images are segmented using an anatomical atlas of the heart. The last step involves generating a personalized computational model of the heart containing myocardial fiber orientation, the Purkinje system and different mesh labels (endo- and epicardium) for the subsequent electrophysiological simulation. This is addressed in a single user application that goes from the image to the personalized simulation model.

DICOM reading plug-in

The objective of the DICOM plug-in is to let the user browse medical images stored in DICOM format, allowing to load 2D, 3D and 4D data (Fig. 2). Once the data is loaded, it is organized using a tree viewer to facilitate visualization of patient, study, series and time point data. Using this plug-in, the user can inspect different studies and navigate through the slices and corresponding time points. The DICOM plug-in creates a volumetric or 3D+t image from the selected DICOM data including the slices and time points selected by the user. After that, the image can be easily rendered or located in the `DataEntityList` where it becomes visible to the rest of the application for further processing.

Cardiac image analysis plug-in

In order to obtain a personalized geometry of the heart from a medical image, image segmentation based on an anatomical heart atlas is used [5]. This atlas is first initialized using anatomical landmarks such as the left ventricle apex, the aorta and mitral valve ring (Fig. 2). Once the heart atlas has been positioned within the image, the plug-in allows the user to adjust the shape of the atlas using the image as reference and thus, semi-automatically segment the heart. Using this feature, the user can deform the heart model (by simply dragging the surface interactively by using the mouse) and adjust the shape to the image. Automatic segmentation using active shape and image appearance models is currently under development and will be integrated in the prototype in the future. In the case of 4D images, it is possible to segment the whole sequence of images starting from any given time frame. The plug-in allows the user to obtain a number of quantitative measurements of the heart including the ejection fraction, wall motion, wall thickness, wall thickening, among others, during the manual segmentation process to give immediate feedback to the user. After the segmentation, the result can be analyzed using Bull's eye plots (AHA 17-segment model) for the different variables such as wall thickening, radial wall motion, among others. As will be shown below, the resulting geometrical models are used for the generation of personalized simulations of the cardiac electrophysiology.

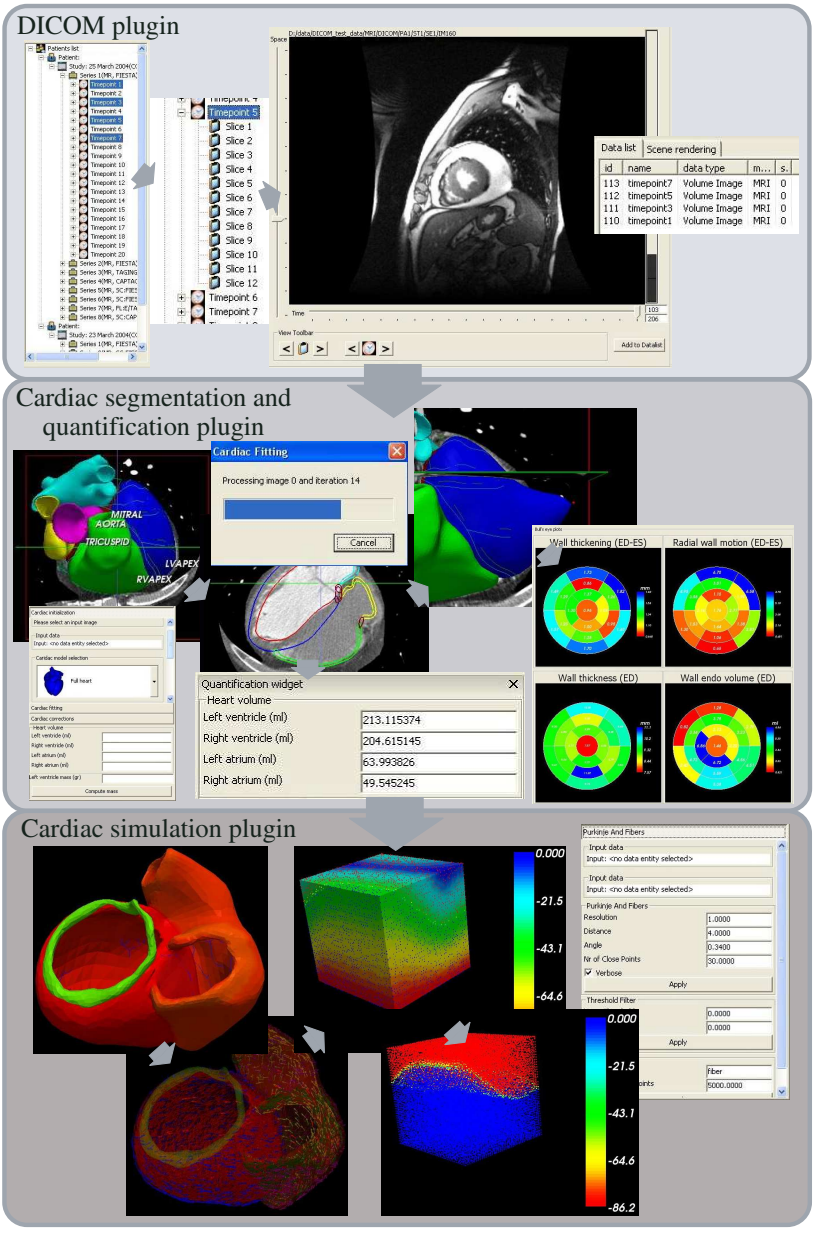

Fig. 2. Cardiac modeling workflow as implemented in GIMIAS. From top to bottom are presented the DICOM, the Cardiac segmentation and quantification, and the Cardiac simulation plug-ins. After desired images are selected from the time sequence, an atlas is used to segment the images and adjust the segmentation result where required. Then, from the resulting heart geometry, a model for simulation of the heart electrophysiology is created. Finally, the propagation front in a selected region of the cardiac muscle is presented.

Cardiac modeling plug-in

Before being able to use the anatomical model to perform electrophysiological or electromechanical simulation it is necessary to generate a proper FEM model. It is necessary to mesh the surface obtained from the segmentation step, and produce a volumetric fine mesh which will be made up of tetrahedral elements. Volumetric mesh quality is ensured by controlling both the maximum distance between neighboring nodes and the radius-to-edge ratio to assure regularly-shaped elements. In keeping with recommendations from literature high-resolution meshes with inter-node distance $\leq$ 500 μm to avoid physiologically inaccurate numerical effects such as wavefront warping and other artifacts.

Excitation and recovery sequences are influenced by the direction of myocardial fibers, which determine the longitudinal and transversal orientation of the anisotropic conductivity of intra- and extra-cellular media. As current imaging techniques are unable to non invasively extract myocardial fiber orientation from the beating heart, mathematical models are used to replicate the rotation of fibers across the ventricular wall. In GIMIAS, the fiber orientation is calculated for every element of the mesh, using a mathematical formulation based on the work of Streeter [6]. In this way, the familiar helical structure of fibers was reproduced, with orientations rotating from 50° at the endocardium to $-60°$ at the epicardium.

The Purkinje System (PS) is also an important part of the system that helps the fast and synchronous electrical propagation of the impulse coming from the sinus node. Since the reconstruction of the PS from specific patients is not feasible, a fiber network has been defined according to the descriptions by Durrer. The PS is represented as a 1D cable model that is placed upon the endocardial surface, containing the bundle branches and 100 Purkinje cables that expanded from the bundle terminals towards the ventricular apex continuing onto the left and right free walls. The procedure to include the PS consists in a manual delineation of the fibers in the heart atlas, and subsequently a propagation of the network to each mesh. The propagation is done during the segmentation of the ventricles, where the atlas is deformed to match the specific geometry of the patient heart, fitting at the same time the PS embedded in the atlas.

6 Conclusions

GIMIAS is an environment specially tailored for the creation of work-flow applications in the field of biomedical image computing and personalized simulation. The architecture of the underlying framework is based on plug-ins through which its core functionalities can be extended. Other services such as PACS connection, parallel computation through grid middleware, and scripting are in the development roadmap of the framework. In this work we presented a cardiac image analysis and simulation application developed within this environment. In the presented workflow, GIMIAS provides the capability of segmenting images of the heart and allows improving the outcome manually when the segmentation is not perfect.

GIMIAS provides an open source framework for efficient development of research and clinical software prototypes within the Physiome community while allowing business-friendly technology transfer and commercial product development.

Acknowledgements

A complete list of contributors to the analysis, design and implementation of this platform can be found at www.gimias.org. This research has been partly funded by CIBER-BBN (VPHTk project), the industrial and Technological Development Center (CDTI) under the CENIT programme (CDTEAM project) and the European Community's Seventh Framework Programme (FP7/2007-2013) under the grants agreement n.224495 (euHeart Project) and n.223920 (VPH NoE). Dr. O. Camara and R. Sebastian acknowledge grant support from the Spanish Ministry of Research and Innovation, under a Ramon y Cajal and Juan de la Cierva Research Fellowship, respectively.

References

1. Hunter, P., Robbins, P., Noble, D.: The IUPS Human Physiome Project. Eur. J. Physiol. 445(1), 1–9 (2002)
2. Hunter, P., Borg, T.: Integration from Proteins to Organs: The Physiome Project. Nature 4(3), 237–243 (2003)
3. Fenner, J., Brook, B., Clapworthy, G., Coveney, P., Feipel, V., Gregersen, H., Hose, D., Kohl, P., Lawford, P., McCormack, K., Pinney, D., Thomas, S., Jan, S.V.S., Waters, S., Viceconti, M.: The EuroPhysiome, STEP and a roadmap for the virtual physiological human 366, 2979–2999 (2008)
4. Wolf, I., Vetter, M., Wegner, I., Böttger, T., Nolden, M., Schöbinger, M., Hastenteufel, M., Meinzer, H.P.: The Medical Imaging Tookit 9, 594–604 (2005)
5. Ordas, S., Oubel, E., Leta, R., Carrera, F., Frangi, A.: A statistical shape model of the heart and its application to model-based segmentation. In: Proc. SPIE Medical Imaging, San Diego, CA, USA, vol. 6511 (2007)
6. Streeter, D.: Handbook of Physiology, Section 2: The Cardiovascular System. In: Gross morphology and fiber geometry of the heart. The Heart, ch. 4, vol. I, pp. 61–112. American Physiological Society (1979)

Maximum Likelihood Motion Estimation in 3D Echocardiography through Non-rigid Registration in Spherical Coordinates

Andriy Myronenko[1], Xubo Song[1], and David J. Sahn[2]

[1] Department of Science and Engineering, School of Medicine
Oregon Health and Science University
20000 NW Walker Road, Beaverton, OR 97006, USA
[2] Cardiac Fluid Dynamics and Imaging Laboratory
Oregon Health and Science University
20000 NW Walker Road, Beaverton, OR 97006, USA
myron@csee.ogi.edu, xubosong@csee.ogi.edu, sahnd@ohsu.edu

Abstract. Automated motion tracking of the myocardium from 3D echocardiography provides insight into heart's architecture and function. We present a method for 3D cardiac motion tracking using non-rigid image registration. Our contribution is two-fold. We introduce a new similarity measure derived from a maximum likelihood perspective taking into account physical properties of ultrasound image acquisition and formation. Second, we use envelope-detected 3D echo images in the raw spherical coordinates format, which preserves speckle statistics and represents a compromise between signal detail and data complexity. We derive mechanical measures such as strain and twist, and validate using sonomicrometry in open-chest piglets. The results demonstrate the accuracy and feasibility of our method for studying cardiac motion.

1 Introduction

Quantitative analysis of 3D echo images can provide mechanical measurements such as strain, wall thickening, twist, volume and ejection fraction, which can be used to evaluate the elasticity and contractility of the myocardium [1]. In this paper, we describe a method to estimate the myocardial motion, from 3D ultrasound image sequence. The idea is to consecutively align 3D images one onto another and track the motion field using non-rigid image registration [2,3]. Spatially-dense displacement field can be derived, from which we compute quantitative measures such as strain and twist.

Applications of non-rigid image registration for quantitative analysis from 3D echocardiography have been recently proposed by several researchers including Elen et al. [3], Leung et al. [4], Ledesma-Carbayo et al. [5] and Sanchez-Ortiz et al. [6]. Despite significant algorithmic advances, registration of 3D ultrasound images remains challenging due to multiple intensity artifacts, low image quality, speckle and large computation load.

N. Ayache, H. Delingette, and M. Sermesant (Eds.): FIMH 2009, LNCS 5528, pp. 427–436, 2009.
© Springer-Verlag Berlin Heidelberg 2009

The novelty of this paper is two-fold. First, we introduce a new similarity measure for ultrasound image registration. We derive it from a maximum likelihood (ML) perspective taking into account the physical properties of ultrasound image acquisition and formation. Second, we use envelope-detected 3D echo images in the raw *spherical coordinates* format, which preserves speckle statistics and represents a compromise between signal detail and data complexity. We validate the algorithm-derived measures to those derived from sonomicrometry on open chest pigs.

Maximum likelihood approach: Registration of 3D echocardiogram has several specifics compared to general non-rigid registration techniques, which can be taken into account using the ML approach. Cohen and Dinstein [7] derived a CD_2 similarity measure using the ML approach. They assumed that two consecutive ultrasound images are both corrupter by multiplicative noise with Rayleigh pdf and that noise pdfs are independent of each other.

Here, we derive a new similarity measure assuming that Rayleigh noise in consecutive images is correlated and that speckle is blurred. The speckle noise is a random signal, but has implicit dependence on the underlying imaging object structure. If the static object is imaged twice, the speckle remains the same [8]. This is in contrast to other noise sources, e.g. electrical noise, which always has a random nature. Several researchers showed the dependence of speckle correlation on the motion of imaged area [9,10]. If two consecutive images are taken with sufficiently high frame rate, which is the case for modern ultrasound devices, the speckle noise formation between the consecutive frames is similar, and two speckle noise variables are correlated [8]. Finally, during data acquisition, the speckle is not measured at an ideal point, but rather integrated over some area of detector element. The speckle pattern motion, caused by imaging area motion, makes the measurement quantity integrated over some part of ideal speckle pattern. This results in *blurred speckle* effect, which modifies the density function [11].

Spherical coordinates: A typical digital ultrasound processing chain consists of the following four steps: 1) Multiple analog-to-digital converters convert the analog radio frequency (RF) signal from the ultrasound transducer to a digital RF signal; 2) Beamforming is applied to individual RF signals by applying time delays and summations as a function of time and transformed into a single RF signal, which is often called "beamformed RF" data; 3) The RF signal is filtered, is run through an envelope detector and is log compressed into a gray scale format. At this stage the data is represented as a sequence of 3D arrays, each of which is a 3D image in the raw spherical coordinate system; 4) Finally, the envelope-detected signal is scan converted to Cartesian coordinate system and interpolated at the regular grid to form the digital 3D image (also called B-mode data). The data corresponding to the third and fourth steps (spherical vs. Cartesian coordinates of post-converted image) is shown in Figure 1.

We shall use envelope-detected 3D echo image in the raw spherical coordinates (step 3), before the final conversion to the Cartesian coordinates. In other words,

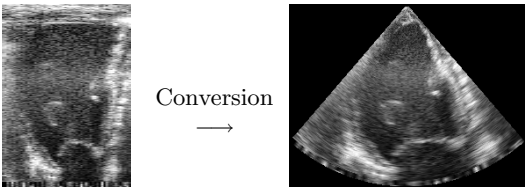

(a) Spherical (b) Cartesian

Fig. 1. (a) An example of spherical data displayed as a 2D array ($416 \times 62 \times 56$). (b) The spherical data is converted to the Cartesian data ($208 \times 297 \times 269$).

we take one step back in 3D echo image formation. We note that our approach differs significantly from the registration methods [12] that build a spherical or cylindrical transformation model along the heart orientation axis, using Cartesian post-converted images (step 4). Whereas, we use envelope-detected images in raw spherical coordinates (step 3), which may or may not be in alignment with heart orientation.

The main benefits of using envelope-detected image in spherical coordinates, in contrast to the final Cartesian coordinates, is the preservation of speckle statistics and avoidance of information loss associated with scan conversion and interpolation. The envelope-detected data has higher resolution in vicinity of transducer and lower resolution away from the transducer. Also, the axial resolution is much higher than the lateral. After conversion to the Cartesian system some information is lost, including high axial resolution and high resolution closer to the transducer, and additional errors are introduced, for instance, the new voxels that appear after regular grid interpolation in the areas far from the transducer. Even though the envelope-detected data in spherical coordinates still contains less information than RF data, it represents a reasonable compromise between level of the signal details and computational complexity.

2 Maximum Likelihood Motion Estimation

Consider two 3D ultrasound images I and J acquired at consecutive time instances. The maximum likelihood (ML) approach to estimate the transformation $\mathcal{T}$ between the images is to maximize the conditional probability [7,13], $p(J(\mathcal{T})|I, \mathcal{T})$, or equivalently minimize the following energy function

$$E(\mathcal{T}) = \sum_{n=1}^{N} -\log p(J_n(\mathcal{T})|I_n, \mathcal{T}) \tag{1}$$

where we assumed that all voxelwise conditional probabilities are i.i.d. and $J_n(\mathcal{T})$ denotes the intensity values of n^{th} voxel after applying the transformation $\mathcal{T}$.

In ultrasound imaging, the image intensities are the log-compressed values of the envelope amplitudes (denoted as a and b) [8]:

$$I_n = D\log(a) + G; \quad J_n(\mathcal{T}) = D\log(b) + G \tag{2}$$

where G and D are the linear gain and the dynamic range constants.

When the speckle is fully developed the noise is multiplicative and follows the Rayleigh pdf [8,11]:

$$p(n) = \frac{n}{\sigma^2} \exp \frac{-n^2}{2\sigma^2}, \quad n \geq 0 \tag{3}$$

If $a = sn_1$ and $b = sn_2$ are the realizations of the informative signal s corrupted by multiplicative Rayleigh noise n_1 and n_2 respectively, and $\eta = \frac{n_1}{n_2}$ is the division of two random variables [14], then

$$p(J_n(\mathcal{T})|I_n, \mathcal{T}) = \frac{\eta}{D} p(\eta) = \frac{\eta}{D} \int n_2 p(\eta n_2, n_2) dn_2 \tag{4}$$

2.1 Independent Rayleigh Noise Assumption

Cohen and Dinstein [7] assumed that the noise at consecutive ultrasound images is independent and has equal variances, then $p(J_n(\mathcal{T})|I_n, \mathcal{T}) = \frac{1}{D} \frac{2\eta^2}{(\eta^2+1)^2}$ and the similarity function takes the form[1]

$$E(\mathcal{T}) = \sum_{n=1}^{N} -\log \frac{e^{2d_n}}{(e^{2d_n}+1)^2} + const; \quad d_n = \frac{J_n(\mathcal{T}) - I_n}{D} \tag{5}$$

where by d_n we defined a scaled difference between the intensities of corresponding image voxels. Cohen and Dinstein derived this similarity function and called it CD_2 similarity measure[2]. This similarity measure showed superior performance comparing to other similarity measure for ultrasound image tracking, and was widely used in tracing and block matching algorithms [15,16,17,18].

2.2 Correlated Rayleigh Noise Assumption

Here we do not assume that Rayleigh noise n_1 and n_2 are independent. If two consecutive images I and J are taken with sufficiently high frame rate, which is the case for modern ultrasound devices, the speckle noise formation between the consecutive frames is similar, and the random variables n_1 and n_2 are correlated [8]. The bivariate Rayleigh distribution [11] of two random variable n_1 and n_2 with equal variance σ^2 is

$$p(n_1, n_2) = \frac{n_1 n_2}{(1-\rho)\sigma^4} e^{-\frac{n_1^2+n_2^2}{2\sigma^2(1-\rho)}} I_0 \left[\frac{\sqrt{\rho} n_1 n_2}{(1-\rho)\sigma^2} \right]; \quad I_0(z) = \sum_{k=0}^{\infty} \frac{z^{2k}}{2^{2k}(k!)^2} \tag{6}$$

where I_0 is a modified Bessel function of the first kind with zero order, $0 \leq \rho < 1$ is a correlation coefficient and $n_1 \geq 0$, $n_2 \geq 0$. Substitution Eq. 6 in Eq. 4, we have to take a non-trivial integral

[1] Usually, the ultrasound log-compression is done with decimal logarithm function, which results in $10^{2d_n} = e^{2d_n \ln 10}$ terms instead of e^{2d_n}. We absorb the scaling $\ln 10$ into the constant D for convenience.

[2] In its original derivation,Cohen and Dinstein do not account for scaling constant D, which is equivalent to assume $D = 1$.

$$p(\eta)=\int_0^\infty n_2 p(\eta n_2, n_2)dn_2=\int_0^\infty \frac{\eta n_2^3}{(1-\rho)\sigma^4} e^{-\frac{n_2^2(1+\eta^2)}{2\sigma^2(1-\rho)}} \cdot I_0\left(\frac{\sqrt{\rho}\eta n_2^2}{(1-\rho)\sigma^2}\right) dn_2 =$$
$$\frac{2(1-\rho)\eta}{(1+\eta^2)^2}\sum_{k=0}^{\infty}\left(\frac{\eta^2\rho}{(1+\eta^2)^2}\right)^k \frac{(2k+1)!}{(k!)^2} = \frac{2(1-\rho)\eta}{(1+\eta^2)^2}\left(1-\frac{4\rho\eta^2}{(1+\eta^2)^2}\right)^{-\frac{3}{2}} \quad (7)$$

To simplify, we exchanged the integration and summation and used the formula for integration of definite integrals and for infinite series summation [19] (for $m=1$):

$$\sum_{k=0}^{\infty} z^k \frac{(2k+2m-1)!}{(k+m-1)k!} = \frac{(2m-1)!}{(m-1)!}(1-4z)^{-\frac{2m+1}{2}} \quad (8)$$

Thus the new similarity function takes the from

$$E(\mathcal{T}) = \sum_{n=1}^{N} -\log\frac{e^{2d_n}}{(e^{2d_n}+1)^2} + \frac{3}{2}\log(1-\frac{4\rho e^{2d_n}}{(e^{2d_n}+1)^2}) =$$
$$\sum_{n=1}^{N}\frac{3}{2}\log(\cosh^2(d_n)-\rho) - \frac{1}{2}\log(\cosh^2(d_n)) + const \quad (9)$$

By convention, we shall call this similarity function MS similarity measure. As a check on this result, if the correlation coefficient $\rho = 0$, then MS simplifies to CD_2 in Equation 5.

2.3 Blurred Speckle

The probability density function of speckle noise at an ideal point in space is quite idealistic. During data acquisition, the speckle is not measured at an ideal point, but rather integrated over some area of detector element. Also, the speckle pattern motion, caused by imaging area motion, makes the measurement quantity integrated over some part of ideal speckle pattern. This results in *blurred speckle* effect, which modifies the density function [11]. To deal with the problem in optical imaging, Goodman [11] showed that a Gamma density is a good approximation to speckle intensity pdf. In ultrasound imaging, the detector is pressure sensitive, which means that we measure the amplitude (square root of intensity). Using a change of variable for the Gamma pdf, we achieved that the blurred speckle has a Nakagami distribution

$$p(n) = \frac{m^m}{2^{m-1}\sigma^{2m}\Gamma(m)} n^{2m-1} e^{-\frac{mn^2}{2\sigma^2}}, \quad n>0 \quad (10)$$

which is also called a generalized Rayleigh distribution [20]. For $m=1$ the distribution reduces to the Rayleigh distribution (Eq. 3). The application of the Nakagami distribution in ultrasound imaging has been popularized by Shankar [21]. He showed that the Nakagami distribution fits the real speckle distribution superior to Rayleigh and K-distributions.

We assume that two speckle variables are correlated, and their joint pdf is a bivariate Nakagami distribution [22]

$$p(n_1, n_2) = \frac{m^{m+1}(n_1 n_2)^m}{2^{m-1}\sigma^{2(m+1)}(1-\rho)\rho^{\frac{m-1}{2}}\Gamma(m)} e^{-\frac{m(n_1^2+n_2^2)}{2(1-\rho)\sigma^2}} I_{m-1}\left(\frac{m\sqrt{\rho}n_1 n_2}{(1-\rho)\sigma^2}\right) \tag{11}$$

Here, we assumed that the distribution widths σ^2 are equal, ρ is a squared correlation coefficient $0 \leq \rho < 1$ and I_{m-1} is a modified Bessel function of the first kind of order $m-1$. Substitution Eq. 11 in Eq. 4, we obtain

$$p(\eta) = 2(1-\rho)^m \frac{\Gamma(2m)}{\Gamma(m)^2} \frac{\eta^{2m-1}}{(\eta^2+1)^{2m}} \left(1 - \frac{4\rho\eta^2}{(1+\eta^2)^2}\right)^{-\frac{2m+1}{2}} \tag{12}$$

To simplify, we exchanged the integration and summation and used the formula for integration of definite integrals and for infinite series summation [19] (Eq. 8). Thus, the similarity function, based on blurred and correlated speckle assumptions, is

$$f = -m \log \frac{e^{2d}}{(e^{2d}+1)^2} + \frac{2m+1}{2} \log(1 - \frac{4\rho e^{2d}}{(e^{2d}+1)^2}) + const = \frac{2m+1}{2} \log(\cosh^2(d) - \rho) - \frac{1}{2} \log(\cosh^2(d)) + const. \tag{13}$$

which, we shall call the MS_2 similarity measure. As a check, for $m = 1$, MS_2 simplifies to MS (Eq. 9).

2.4 Analysis of the CD_2, MS and MS_2 Similarity Measures

The CD_2 similarity measure, we believe, is of general interest for image registration. We can rewrite the Eq. 5 in different but equivalent form as $E(\mathcal{T}) \propto \sum_n -\log \operatorname{sech}^2(d_n)$, where sech is a hyperbolic secant function. Thus, we could have achieved the same similarity measure by simply assuming an additive image noise with logistic pdf. The logistic distribution resembles the Gaussian distribution, but has heavier tails (higher kurtosis) and thus belongs to the class of super-gaussian distributions.

From the optimization perspective, we can analyze the shape of the voxel-wise similarity function and its derivative (influence function), rather than the distribution itself. The shape of CD_2 similarity function resembles the shape of the absolute value function (L_1 norm between the images), but is also differentiable at the origin. The derivative of the CD_2 function is *tanh*, which approximates the step function. Figure 2(a,b) shows the plot of CD_2 similarity function and its derivative versus $L1$ norm ones. $L1$ norm belongs to the family of robust similarity measures with many applications in statistics, machine learning and computer vision areas. This supports the robust and accurate performance of CD_2 measure for image registration.

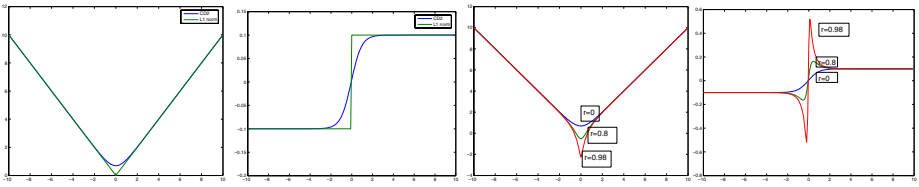

a) CD_2 vs L_1 b) derivatives CD_2,L_1 c) MS d) derivative MS

Fig. 2. The plot of $CD2$ similarity function and its derivative versus L1 norm function

The MS similarity measure generalizes the CD_2 measure. Figure 2(c,d) shows the plot of MS similarity function and its derivative for different values of correlation coefficient ρ. For $\rho = 0$, the MS simplifies to CD_2. For the larger values of correlation coefficient, MS has a sharper peak in a vicinity of the origin and otherwise asymptotically approaches the $L1$ norm function. From the optimization perspective, the higher the correlation value, the higher weight is assigned to the closer intensity differences, which makes the similarity function more robust to outliers (large differences in intensity). Furthermore, the extra parameter m, in the MS_2 similarity measure, introduces a change of slopes compared to the MS ones, which adds a balance control on weights for closer and further intensity differences. The behavior of MS and MS_2 function becomes similar to the behavior of functions in the robust M-estimator approach. The robustness to outliers are crucial in registration of ultrasound images, which typically includes multiple intensity artifacts.

3 Validation by Sonomicrometry

Sonomicrometers implanted on open chest piglets were used for validation. An array of seven sonomicrometers (sono crystals) was implanted as two sets: three sonomicrometers at apex level and four sonomicrometers closer to the base level in the LV myocardium. Using Sonometrics software, we computed off-line the pair-wise crystal distances. From these distances, we computed pairwise strains and between-plane twist, which were used as ground truth for validation.

To compare strain and twist derived from the registration algorithm to those from the sonomicrometry, we visually located, based on anatomical markers, the sono crystals positions on the myocardium in the end diastole volume. These locations were propagated across time by the displacement field obtained from the nonrigid registration algorithm.

4 Results

We acquired the 3D echo sequences using Philips iE33 with EKG gating. Twenty different sequences were taken from 5 piglets. The animals were anesthetized and subjected to midline sternotomy to expose the heart. The spatial resolution

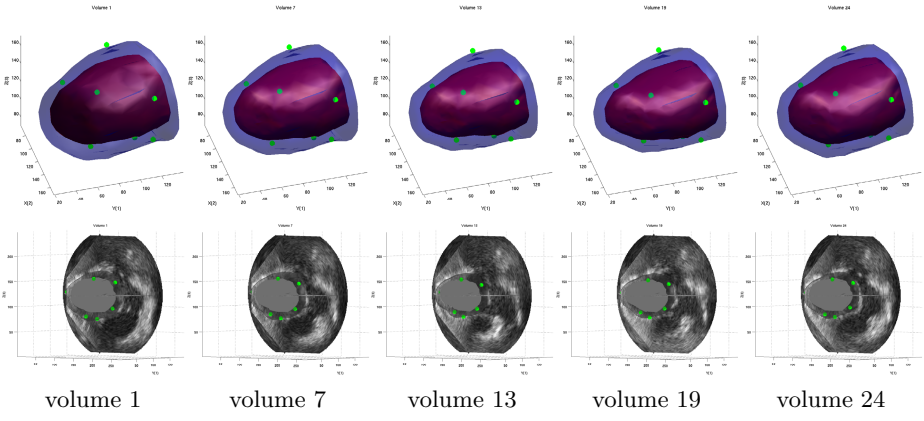

Fig. 3. The LV contour and sonomicrometer motion found during the cardiac cycle (24 consecutive volumes). LV achieves the maximum contraction at volume 13, then the LV dilates (diastolic phase) up to the volume 22 and starts contracting again (systolic phase).

for envelope-detected images in spherical coordinates was $384 \times 62 \times 56$, with 24 volumes per sequence on average. For the given temporal resolution, the motion between the two consecutive images is small, and the correlated speckle assumption holds.

For every scan, we consecutively register 3D images one onto the previous, starting from the first two images. We model the transformation $\mathcal{T}$ using the Free Form Deformation (FFD) [23] with regularization. We put the FFD control points uniformly with 10 voxels spacing. The transformation estimated in spherical coordinates were then converted to Cartesian coordinates. For the comparison we used the SSD, CD_2, MS and MS_2 similarity measures. We set $D = 1$,$\rho = 0.8$ and $m = 0.5$, which we empirically found to give the best performance. We implemented the algorithm in Matlab, and tested on a Pentium4 CPU 3GHz with 4GB RAM. On average, the tracking algorithm between two volumes requires around 10 minutes. The computational time can be significantly reduced, for instance, using the dedicated implementation (e.g., in C++ instead of Matlab), parallel processing, optimization only around the myocardium, etc.

To visualize the LV motion, we also pre-aligned the endocardium and epicardium contours, and found their motion (displacement field) [2]. Figure 4 shows the estimated motion of LV endocardium, epicardium contours and sonomicrometers. Figure 4(a,b) shows the displacement vector field visualized at the LV endocardium position between end diastole and end systole volumes at different viewing angles.

For validation, we computed correlation coefficients (CC) between algorithm- and sonomicrometry-derived strains and twists, which were averaged over all pairs (for strain) and across all volumes of all piglets. Figure 4(c,d) illustrates a typical strain plot between a single pair of crystals and a typical twist (in degrees) during the cardiac cycle. The average CC achieved with SSD, CD_2, MS and MS_2 is shown in the table.

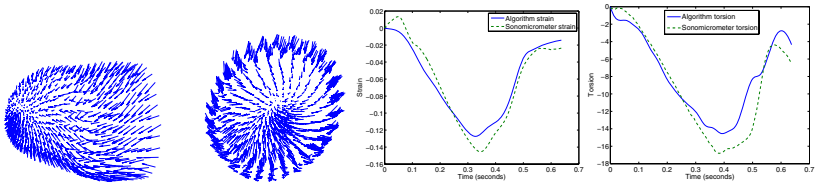

(a) (b) (c) (d)

Fig. 4. (a,b) The displacement vector fields on LV endocardium between end diastole and end systole volumes at two different viewing angles. (c) A comparison between the algorithm- and sonomicrometry-derived measures. Strain between a single pair of crystals through time. (d) Torsion between the apex and base planes (in degrees).

	SSD	CD_2	MS	MS_2
strain CC	0.882 ± 0.053	0.913 ± 0.018	0.927 ± 0.021	0.929 ± 0.019
twist CC	0.934 ± 0.026	0.951 ± 0.012	0.958 ± 0.010	0.961 ± 0.012

On average, MS and MS_2 outperform both SSD and CD_2 similarity measures, which demonstrates their accuracy in ultrasound image registration.

5 Discussion and Conclusion

We present a method for automated processing of 3D echo images, which includes two main contributions: a) we introduce a new similarity measure for sequential non-rigid registration of ultrasound images, derived from the maximum likelihood perspective, b) we register images in spherical coordinate system instead of Cartesian coordinates.

The MS and MS_2 similarity measures explicitly considers the correlated speckle noise between the consecutive frames, its formation and acquisition process in ultrasound imaging. We use sonomicrometry to validate the algorithm. We found a strong correlation, between the algorithm- and sonomicrometry- derived strain and twist. The new similarity measures demonstrated accurate and robust performance compared to other similarity measures.

Image processing in raw spherical coordinates benefits from high resolution in axial direction without the interpolation artifacts resulted from conversion to Cartesian coordinates. The pre-converted data preserves speckle statistics, modeled for ML estimation. Finally, the convertion to the Cartesian system of a single 3D images, even by sacrificing the half of axial resolution, takes several magnitudes more operative memory, which greatly slows down the processing. Thus, processing the images directly in raw spherical format before conversion benefits both in resolution and computation speed.

References

1. Lang, M., Mor-Avi, V., Sugeng, L., Nieman, P., Sahn, D.J.: Three-dimensional echocardiography. Jour. of the Am. Coll. of Cardiology 48(10), 2053–2069 (2006)

2. Myronenko, A., Song, X., Sahn, D.J.: LV motion tracking from 3D echocardiography using textural and structural information. In: Ayache, N., Ourselin, S., Maeder, A. (eds.) MICCAI 2007, Part II. LNCS, vol. 4792, pp. 428–435. Springer, Heidelberg (2007)
3. Elen, A., Choi, H.F., Loeckx, D., Gao, H., Claus, P., Suetens, P., Maes, F., D'hooge, J.: Three-dimensional cardiac strain estimation using spatio–temporal elastic registration of ultrasound images: A feasibility study. TMI 27(11), 1580–1591 (2008)
4. Leung, K., van Stralen, M., Nemes, A., Voormolen, M., Voormolen, M., van Burken, G., Geleijnse, M.J.t., Reiber, J., de Jong, N., van der Steen, A., Bosch, J.: Sparse registration for 3D stress echocardiography. Medical Imaging 27(11), 1568–1579 (2008)
5. Ledesma-Carbayo, M., Kybic, J., Desco, M., Santos, A., Sühling, M., Hunziker, P., Unser, M.: Spatio-temporal nonrigid registration for ultrasound cardiac motion estimation. IEEE Transactions on Medical Imaging 24(9), 1113–1126 (2005)
6. Sanchez-Ortiz, G., Wright, G., Clarke, N., Declerck, J., Banning, A., Noble, J.: Automated 3-D echocardiography analysis compared with manual delineations and spect muga. IEEE Transactions on Medical Imaging 21(9), 1069–1076 (2002)
7. Cohen, B., Dinstein, I.: New maximum likelihood motion estimation schemes for noisy ultrasound images. Pattern Recognition 35(2), 455–463 (2002)
8. Cobbold, R.S.C.: Foundations of Biomedical Ultrasound. Biomedical Engineering Series. Oxford University Press, Oxford (2006)
9. Burckhardt, C.B.: Speckle in ultrasound b-mode scans. IEEE Trans. on Sonics and Ultrasonics 25(1) (1978)
10. Meunier, J.: Tissue motion assessment from 3D echographic speckle tracking. Physics in medicine and biology 43(5), 1241–1254 (1998)
11. Goodman, J.W.: Speckle Phenomena in Optics. Theory and Applications (2006)
12. Chandrashekara, R., Mohiaddin, R.H., Rueckert, D.: Daniel rueckert. In: Ayache, N., Delingette, H. (eds.) IS4TM 2003. LNCS, vol. 2673, pp. 88–99. Springer, Heidelberg (2003)
13. Roche, A., Malandain, G., Ayache, N.: Unifying maximum likelihood approaches in medical image registration. IJIST 11, 71–80 (2000)
14. Papoulis, A.: Probability, Random Variables, and Stochastic Processes (1991)
15. Boukerroui, D., Noble, J.A., Brady, M.: Velocity estimation in ultrasound images: A block matching approach. IPMI 2732, 586–598 (2003)
16. Revell, J., Mirmehdi, M., McNally, D.: Combined ultrasound speckle pattern similarity measures. In: MIUA, pp. 149–153. BMVA Press (2004)
17. Song, X., Myronenko, A., Sahn, D.J.: Speckle tracking in 3D echocardiography with motion coherence. In: Comp. Vision and Patt. Recognition (CVPR) (2007)
18. Linguraru, M.G., Vasilyev, N.V., Marx, G.R., Tworetzky, W., Nido, P.J.D., Howe, R.D.: Fast block flow tracking of atrial septal defects in 4D echo. MIA (2008)
19. Sloane, N.: Online enc. of integer sequences. A002457, A002802, A020918 (2008)
20. Miller, K., Bernstein, R., Bluemenson, L.: Generalized rayleigh processes. Quarterly of Applied Mathematics 16, 137–145 (1958)
21. Shankar, P.M.: A general statistical model for ultrasonic backscattering from tissues. IEEE T. Ultr., Ferr. and Frequency Control 47(3), 727–736 (2000)
22. Tan, C.C., Beaulieu, N.C.: Infinite series representations of the bivariate rayleigh and nakagami-m distributions. IEEE Trans. Communications 45(10) (1997)
23. Rueckert, D., Sonoda, L.I., Hayes, C., Hill, D.L.G., Leach, M.O., Hawkes, D.J.: Nonrigid registration using free-form deformations: Application to breast MR images. IEEE Trans. Image Processing 18(8), 712–721 (1999)

Large Diffeomorphic FFD Registration for Motion and Strain Quantification from 3D-US Sequences

Mathieu De Craene[1,2], Oscar Camara[2,1], Bart H. Bijnens[3,2,1], and Alejandro F. Frangi[2,1,3]

Center for Computational Imaging and Simulation Technologies in Biomedicine (CISTIB),
[1] Networking Biomedical Research Center on Bioengineering, Biomaterials and Nanomedicine (CIBER-BBN), Barcelona, Spain
[2] Universitat Pompeu Fabra, Barcelona, Spain
[3] Institució Catalana de Recerca i Estudis Avançats (ICREA), Barcelona, Spain
{mathieu.decraene,oscar.camara,bart.bijnens,alejandro.frangi}@upf.edu

Abstract. This paper proposes a new registration method for the *in vivo* quantification of cardiac deformation from a sequence of possibly noisy images. Our algorithm has been applied to 3D ultrasound (3D-US) images, which currently give a reasonable spatial and time resolution, but suffer from significant acquisition noise. Therefore, this modality requires the design of a robust strategy to quantify motion and deformation with the clinical aim of better quantifying cardiac function e.g. in heart failure. In the proposed method, referred to as Large Diffeomorphic Free Form Deformation (LDFFD), the displacement field at each time step is computed from a smooth non-stationary velocity field, thus imposing a coupling between the transformations at successive time steps. Our contribution is to extend this framework to the estimation of motion and deformation in an image sequence. Similarity is captured for the entire image sequence using an extension of the pairwise mutual information metric. The LDFFD algorithm is applied here to recover longitudinal strain curves from healthy and Left-Bundle Branch Block (LBBB) subjects. Strain curves for the healthy subjects are in accordance with the literature. For the LBBB patient, strain quantified before and after Cardiac Resynchronization Therapy show a clear improvement of cardiac function in this subject, in accordance with clinical observations.

1 Introduction

Quantification of cardiac deformation provides insight about cardiac function by quantifying how a given pathology affect global or local contractility of the myocardium. In clinical routine, myocardial motion is usually derived from ultrasound images that were, until recently, restricted to 1D+t or 2D+t acquisitions. The improvements in transducer technology some years ago allowed the acquisition of real-time 3D-US images, thus opening up the possibility of better

N. Ayache, H. Delingette, and M. Sermesant (Eds.): FIMH 2009, LNCS 5528, pp. 437–446, 2009.
© Springer-Verlag Berlin Heidelberg 2009

capturing myocardial motion, which naturally has a complex 4D nature. On the other hand, 3D-US images have lower signal-to-noise ratio (SNR) and temporal resolution than the 2D ones, making the extraction of motion information even more challenging.

The quantification of motion and strain can be obtained from two types of techniques, namely Doppler myocardial imaging and speckle tracking. In the first one, velocities are measured by comparing changes in US pulses on a line. The drawback is that velocities can only be measured in the direction of the probe. In the second, motion is estimated by local registration techniques, e.g. block matching, that exploits the local consistency of speckle noise over time. If the input images have a high spatial and temporal resolution, strain quantification relies on the accuracy of the registration technique employed to estimate the displacements.

Several approaches have been proposed to extend 2D speckle tracking techniques to 3D and recover myocardial motion from a sequence of 3D US image. Duan *et al.* [3] used an optical flow technique to quantify myocardial deformations but limited their validation to simulated US images. Grau *et al.* [5] proposed a new similarity measure based on local orientation and phase differences to minimize the effect of artifacts intrinsic to 3D-US sequences, obtaining registration errors smaller than 2mm with a non-automatic initialization. Elen *et al.* [4] recently applied a B-spline registration technique guided by mutual information to estimate 3D myocardial strains from 3D-US sequences, obtaining absolute errors up to 21% for the radial strain and up to 4% for the longitudinal and circumferential strains on simulated US images and having expected strain curves on *in vivo* clinical data. One of the drawbacks of these techniques is that they do not make use of the temporal information embedded in the 4D-US datasets to compensate for the low quality of these images.

Temporal continuity can be achieved by the use of 4D transformation models. Such models have for instance been applied to 2D ultrasound images by Ledesma-Carbayo *et al* [7]. However, applying a 4D model to the displacement field does not render properly temporal consistency. The displacement field at each time point should be related to all previous displacements. This is not correctly approximated by a 4D model of the displacement field that only ensures smoothness of the recovered mapping in the spatiotemporal domain.

In the last few years, the development of diffeomorphic registration algorithms has gained a significant interest (e.g. [1,10,9]). Diffeomorphic registration algorithms ensure a continuous, differentiable and invertible correspondence between the images to register [1]. The diffeomorphic registration framework naturally embeds a temporally consistent representation of the transformation by computing the displacement field from a continuous velocity field in space and time. It can indeed be shown that if the velocity field is continuous and differentiable, the resulting displacement field will produce an invertible mapping with a continuous inverse. Recently, Khan *et al.* [6] proposed to exploit this feature of diffeomorphisms by extending the Large Diffeomorphic Metric Mapping (LDDMM) approach [1] to monitor growth processes by estimating the diffeomorphic flow of a baseline image

passing through a sequence of follow-up images. In their approach, the transformation chain was modeled using dense displacement fields which limits the optimization to a gradient descent based on the functional gradient.

In this paper, we take a similar registration approach, called LDFFD, where a set of Free-Form Deformations (FFD), each one capturing the motion between consecutive image frames, is jointly optimized to obtain the consistent temporal transformation that maximizes the joint alignment of all images in the sequence. This strategy ensures that the transformation at each time step is coherent with the transformation of previous temporal phases, and consequently increases the robustness of the alignment procedure. While existing diffeomorphic registration approaches use a dense displacement field representation of the velocity field, the FFD representation was chosen here because of the natural regularization embedded in the B-Spline basis functions. Whereas dense approaches require the computation of the displacement at each voxel, FFD can be accelerated by sampling randomly the image domain for the computation of the joint histogram [8].

We have applied the LDFFD registration technique to estimate *in vivo* myocardial motion and strain from 3D-US sequences in two healthy subjects and one patient suffering form electrical conduction abnormalities before and after Cardiac Resynchronization Therapy (CRT). Results show that strain curves get closer to the healthy subjects after CRT, in accordance with clinical observations.

2 Algorithm

2.1 Transformation Model

In the pairwise diffeomorphic registration framework, invertible mappings are obtained by introducing an additional temporal dependency to the spatial dependency of the displacement field. The temporal dimension is introduced into the registration problem by relating the displacement field $\boldsymbol{u}(\boldsymbol{x};t)$ to a velocity field $\boldsymbol{v}(\boldsymbol{x};t)$ with $t \in [0,1]$. Hence, the first order differential equation that relates velocity and displacement is

$$\frac{\mathrm{d}}{\mathrm{d}t}\boldsymbol{u}(\boldsymbol{x};t) = \boldsymbol{v}(\boldsymbol{x}+\boldsymbol{u}(\boldsymbol{x};t);t), \text{with } \boldsymbol{u}(\boldsymbol{x};0) = 0. \tag{1}$$

In order to obtain the displacement $\boldsymbol{u}$ from Eq. 1, the velocity field $\boldsymbol{v}$ must be integrated over time. The integration path in the spatio-temporal domain depends on the location $\boldsymbol{x}(t)$ and therefore on the velocity field itself. This temporal integration, illustrated in Fig. 1, can be discretized as

$$\boldsymbol{u}_k(\boldsymbol{x},\boldsymbol{\omega}|_1^k) = \boldsymbol{u}_{k-1}(\boldsymbol{x},\boldsymbol{\omega}|_1^{k-1}) + \boldsymbol{v}_k(\boldsymbol{x}+\boldsymbol{u}_{k-1}(\boldsymbol{x},\boldsymbol{\omega}|_1^{k-1}),\boldsymbol{\omega}_k)\,\delta t_k \tag{2}$$

where $\boldsymbol{\omega}_k$ parameterize the velocity field at each time step k, $\boldsymbol{\omega}|_1^k$ is the concatenation of all transformation parameters up to time step k, and being δt_k the time interval associated to the discretization point k, which can be assumed to be equal to 1 without loss of generality.

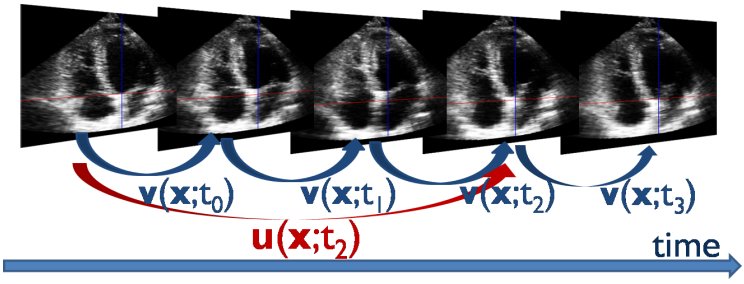

Fig. 1. Chaining of the velocity fields to produce the displacement field at each time step

The main motivation behind the use of our transformation model is to decompose the transformation as a chain of small and smooth deformations. Indeed, decomposing the total transformation into a composition of small amplitude invertible transformations guarantees the invertibility of the total transformation. In the case of an image sequence, this also has the advantage of ensuring temporal consistency between successive time steps. The smoothness of each transformation is guaranteed by the implicit regularization embedded in the FFD basis functions whereas the invertibility of each time step is ensured by the small magnitude of the deformation provided that the temporal resolution of the input sequence is satisfactory. Acquisition protocols in clinical practice offer nowadays a temporal resolution of 20 frames per second. It is assumed here that, even if this resolution is still low for capturing the full complexity of heart dynamics, it is high enough to guarantee invertibility of the transformation between consecutive time steps.

The image metric gradient estimation requires to compute the derivative of the displacement field at spatial samples of the fixed image domain with respect to all transformation parameters, here defined as parametric Jacobian. This computation of the parametric Jacobian is a key component of our algorithm since it introduces a coupling between the different time steps and enables the optimization of all transformation parameters simultaneously. This coupling raises from the fact that acting on the transformation parameters at a given time step t_k modifies the transformation of the evaluated point at all subsequent instants. Hence, we want to compute the derivative of the displacement at a time step t_M regarding the transformation parameters of all time steps $t_m < t_M$, the derivative regarding posterior time step parameters being null by definition. Eq. 2 brings the following expression for the derivatives.

It can be observed from Eq. that this derivative can be written as

$$\frac{\mathrm{d}\boldsymbol{u}_M(\boldsymbol{x},\boldsymbol{\omega}|_1^M)}{\mathrm{d}\boldsymbol{\omega}_m} = \frac{\mathrm{d}\boldsymbol{u}_{M-1}(\boldsymbol{x},\boldsymbol{\omega}|_1^{M-1})}{\mathrm{d}\boldsymbol{\omega}_m} \left(\boldsymbol{I} + \frac{\mathrm{d}\boldsymbol{v}_M(\boldsymbol{y},\boldsymbol{\omega}_M)}{\mathrm{d}\boldsymbol{y}} \bigg|_{\boldsymbol{y}=\boldsymbol{x}+\boldsymbol{u}_{M-1}\left(\boldsymbol{x},\boldsymbol{\omega}|_1^{M-1}\right)} \right), \tag{3}$$

where $\boldsymbol{I}$ stands for the identity matrix. Applying the recurrence in Eq. 2 on $\frac{\mathrm{d}\boldsymbol{u}_{M-1}(\boldsymbol{x})}{\mathrm{d}\boldsymbol{\omega}_m}$ leads to

$$\frac{\mathrm{d}\boldsymbol{u}_M(\boldsymbol{x},\boldsymbol{\omega}|_1^M)}{\mathrm{d}\boldsymbol{\omega}_m} = \frac{\mathrm{d}\boldsymbol{u}_m(\boldsymbol{x},\boldsymbol{\omega}|_1^m)}{\mathrm{d}\boldsymbol{\omega}_m} \prod_{l=m+1}^{M-1} \left(\boldsymbol{I} + \frac{\mathrm{d}\boldsymbol{v}_l(\boldsymbol{y},\boldsymbol{\omega_l})}{\mathrm{d}\boldsymbol{y}}\bigg|_{\boldsymbol{y}=\boldsymbol{x}+\boldsymbol{u}_l(\boldsymbol{x},\boldsymbol{\omega}|_1^l)} \right). \quad (4)$$

At time step t_m, the derivative of the displacement field $\boldsymbol{u}_{m-1}$ with respect to the transformation parameters $\boldsymbol{\omega}_m$ is canceled. Therefore, $\mathrm{d}\boldsymbol{u}_m(\boldsymbol{x},\boldsymbol{\omega}|_1^m)/\mathrm{d}\boldsymbol{\omega}_m$ is equal to $\mathrm{d}\boldsymbol{v}_m(\boldsymbol{y},\boldsymbol{\omega}_m)/\mathrm{d}\boldsymbol{\omega}_m$ at $\boldsymbol{y} = \boldsymbol{x} + \boldsymbol{u}_m(\boldsymbol{x})$ which is the parametric Jacobian of a classic FFD transformation. We can observe two different terms in the right-side of Eq. 4: the derivative with respect to the transformation parameters (outside parenthesis); and the derivative with respect to the spatial coordinates of the transformation input point (within parenthesis). The latter term contains the transformation Jacobian in the classical sense (i.e. local volume change) and propagates the derivative of the m^{th} transformation to the subsequent time steps. A similar term appears in the LDDMM approach [1] that uses the mean squared error as similarity metric and a variational analysis for optimization. The similarity between our approach and LDDMM directly raises from the joint optimization of all time steps, in contrast with sequential optimization at each time step [9].

2.2 Application to Image Sequence Registration

In the context of image sequence registration, the transformation model described in Section 2.1 can be used to map information available in the first image to the posterior images in the sequence. Each image I_j in the sequence is thus associated with a time step j in the transformation. For addressing the image sequence registration problem globally, a multi-image similarity metric capable of quantifying the joint alignment of all images in the sequence must be defined. In this paper, we propose to use a simple extension of the mutual information (MI) metric.At each iteration, the joint alignment of the image sequence is measured by averaging the joint intensity histograms between the first image and each subsequent image in the sequence. Mutual information is then computed from this averaged joint intensity distribution. Each sample in the space of the first image in the sequence generates $N-1$ samples in the joint histogram. The advantage of this approach is to maintain the estimation of probability densities in a space of low dimension where the efficiency and the accuracy of histogram-based estimation are guaranteed. Beg *et al.* [1] showed that the use of a joint alignment metric improves the robustness in case of missing data in one of the images in the sequence.

MI was chosen as similarity measure to compensate possible artifacts or low image correlation between the first and subsequent images in the sequence. Similarity is measured in this paper to the first image, mainly for simplifying the computation of the metric derivative. Measuring similarity between consecutive frames should however be a better strategy for exploiting speckle correlation between successive images.

The derivation of MI regarding the transformation parameters requires to compute the intensity variation of a sample mapped from the first to the j^{th} image I_j. This variation can be expanded, similarly to classic pairwise registration algorithms, as

$$\frac{\mathrm{d}I_j(\boldsymbol{x}, \boldsymbol{\omega}_{1,\ldots,j})}{\mathrm{d}\boldsymbol{\omega}_m} = \nabla_{\boldsymbol{x}} I_j \left(\boldsymbol{x} + \boldsymbol{u}_j(\boldsymbol{x}, \boldsymbol{\omega}|_1^j) \right) \cdot \frac{\mathrm{d}\boldsymbol{u}_j(\boldsymbol{x}, \boldsymbol{\omega}|_1^j)}{\mathrm{d}\boldsymbol{\omega}_m} \tag{5}$$

where $\boldsymbol{\omega}_m$ parametrize the displacement of a control point in a transformation at a time step anterior or equal to j and where the second term in the right hand side Eq. 5 is given by Eq. 4. In our implementation, MI was optimized using the Limited memory Broyden - Fletcher - Goldfarb - Shanno (L-BFGS) [11] algorithm. This Quasi-Newton method has been applied to non-rigid registration based on mutual information [8] and includes an iterative sparse estimate of the Hessian matrix. The limited memory version is specially adapted to handle problems with high dimensionality, as it is the case here. We used the implementation provided by the ITK and VNL toolkits.

2.3 Strain Computation

After performing non-rigid registration, the resulting spatio-temporal transformation is applied to a mesh in the space of coordinates of the first time point and strain is computed on the sequence of deformed meshes. In this paper, an active appearance model trained on simulated ultrasound data [2] was used to segment the left ventricle in the first time frame of the image sequence. The original left ventricular geometry was obtained from CT data and is warped to match the ultrasound image using the shape and appearance modes learned from the simulated population.

For each triangular cell in the mesh, the displacement to the first time point is computed at each node, and the spatial derivatives are computed at the center of the triangle using linear shape functions. If F is the gradient of the displacement field, the strain tensor can be computed using

$$\sigma = \frac{1}{2}(F^t F + F + F^t) \tag{6}$$

The strain can further be projected on a direction $\boldsymbol{d}$ using $\sigma_{\boldsymbol{d}} = \boldsymbol{d}^t \sigma \boldsymbol{d}$. Strain curves in this paper were obtained by projecting the strain on the longitudinal direction.

3 Joint Alignment of 3D-US Images

3.1 Strain Quantification in Healthy Subjects

In this experiment, the LDFFD algorithm was applied for quantifying strain in two healthy patients. The spatial image resolution is $1.28 \times 1.28 \times 0.88\mathrm{mm}^3$ and 16 phases have been reconstructed over one cardiac cycle. The two volunteers

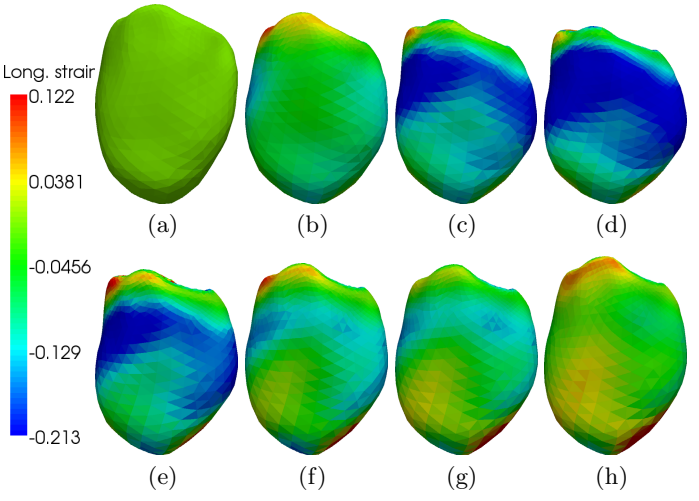

Fig. 2. Longitudinal strain over the cardiac cycle (the complete sequence has 16 time points) for a healthy volunteer. This view is oriented so that the septum appears on the left of the figure.

using a GE Vivid 7 system in a 4 chambers apical view. The fact that all data was acquired in apical view induces a higher spatial resolution in the longitudinal direction. For this reason, we chose to focus our analysis on the longitudinal component of the strain.

Longitudinal strain was computed on the propagated mesh as described in Section 2.3. As computations are obtained from a healthy subject, the observed strain pattern is expected to be mostly constant over the entire ventricle at each time point. Fig. 2 plots the recovered longitudinal strain for the first volunteer and shows that strain is globally constant at a given time point. Minor inhomogeneities appear around the base and the apex. In the apex, this can be numerically explained by the fact that the smaller magnitude of the displacement makes the computation of strain (i.e. a spatial derivative) more difficult for a given level of noise.

Longitudinal strain curves were computed and averaged over each of the AHA 17 segments of the left ventricle. Figure 3 plots the longitudinal strain curves for the two healthy subjects over each of the remaining 12 regions. The temporal evolution of strain shows a similar pattern in most regions apart from two outliers in the first subject. This two outliers correspond to basal anterior and basal anterolateral segments. Since the sequence was acquired from an apical view, it is logical that low image quality hampers accurate strain estimation in the basal regions. It can be observed that the curves do not go back to zero since the input sequences do not cover the entire cardiac cycle. A possible bypass of this problem would be to wrap the cycle by appending the first set of frames at the end of the sequence to ensure the recovery of cyclic strain curves.

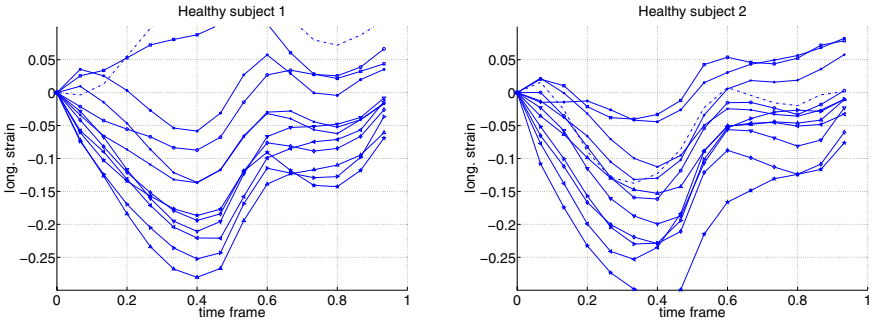

Fig. 3. Longitudinal strain plotted for 12 segments of the left ventricle for two volunteers

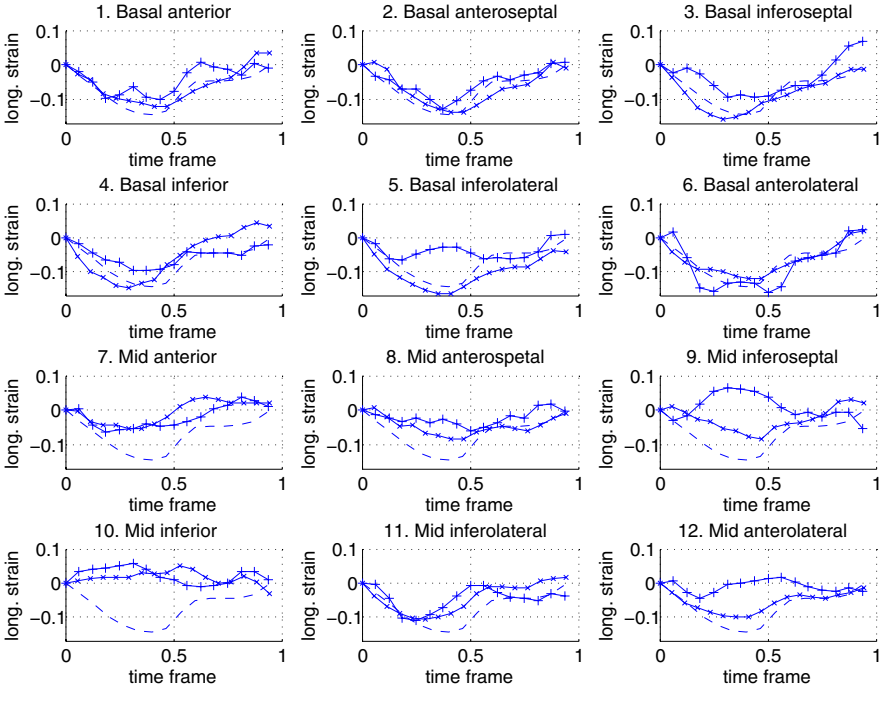

Fig. 4. Longitudinal strain plotted for 12 segments of the left ventricle for a patient with LBBB before (+) and after (×) CRT. An average strain curve obtained by averaging longitudinal strain over all segments in the two healthy volunteers is plotted for comparison in dashed.

3.2 Comparison of Longitudinal Strain Curves for Healthy and LBBB Subjects

In this experiment, strain curves before and after CRT are plotted for one LBBB patient and compare to the healthy curves plotted in Fig. 3. The patient showed before CT severe dilation of the left ventricle, abnormal septum wall motion, and a severe intra-ventricular asynchrony. 3D US images were acquired using a Philips 7500 SONOS system in a 4 chambers apical view with a similar temporal resolution as the healthy cases quantified in the previous section. Figure 4 plots the longitudinal strain in the same left ventricular regions for a patient suffering from LBBB before (+) and after (×) CRT. For comparison, the average of all strain curves in the healthy subjects is plotted with a dashed line. It can be observed that in a majority of regions (apart from 7, 8 and 10), the strain curves shows an improved temporal evolution after CRT.

4 Conclusion

This paper proposes a new registration algorithm for the robust estimation of a spatio-temporal velocity field from an image sequence. The method is generic and can be applied to any modality but is particularly relevant in presence of noisy sequences as in the case of the 3D ultra-sound modality. The robustness of our method raises from the coupling between time steps, as enforced by the transformation model, and the joint alignment of all images in the sequence using a single cost function. Results show that strain can be accurately estimated from in-vivo 3D-US sequences, both in healthy and diseased patients, as illustrated here for a LBBB case. The computation time is currently high (in the order of 5 hours per patient). Acceleration of the algorithm will be considered in future work by implementing a multi-threaded version of the algorithm for fast execution on shared memory architectures. The multiplication of Jacobian matrices appearing in the metric derivative would as well benefit of a parallelization on GPU architectures, specially optimized for such matricial products.

References

1. Beg, M.F., Miller, M.I., Trouvé, A., Younes, L.: Computing Large Deformation Metric Mappings via Geodesic Flows of Diffeomorphisms. Int. J. Comput. Vision 61(2), 139–157 (2005)
2. Butakoff, C., Balocco, S., Ordas, S., Frangi, A.F.: Simulated 3D ultrasound lv cardiac images for active shape model training, vol. 6512, p. 65123U. SPIE (2007)
3. Duan, Q., Angelini, E., Homma, S., Laine, A.: Validation of optical-flow for quantification of myocardial deformations on simulated RT3D ultra-sound. In: ISBI, pp. 944–947. IEEE, Los Alamitos (2007)
4. Elen, A., Choi, H.F., Loeckx, D., Gao, H., Claus, P., Suetens, P., Maes, F., D'hooge, J.: Three-dimensional cardiac strain estimation using spatio-temporal elastic registration of ultrasound images: a feasibility study. IEEE T Med. Imaging 27(11), 1580 (2008)

5. Grau, V., Becher, H., Noble, J.A.: Registration of multiview real-Time 3-D echocardiographic sequences. IEEE T Med. Imaging 26(9), 1154–1165 (2007)
6. Khan, A.R., Beg, M.F.: Representation of time-varying shapes in the large deformation diffeomorphic framework. In: ISBI, pp. 1521–1524 (2008)
7. Ledesma-Carbayo, M.J., Kybic, J., Desco, M., Santos, A., Suhling, M., Hunziker, P., Unser, M.: Spatio-temporal nonrigid registration for ultrasound cardiac motion estimation. IEEE T Med. Imaging 24(9), 1113–1126 (2005)
8. Mattes, D., Haynor, D.R., Vesselle, H., Lewellen, T.K., Eubank, W.: PET-CT image registration in the chest using free-form deformations. IEEE T Med. Imaging 22(1), 120–128 (2003)
9. Rueckert, D., Aljabar, P., Heckemann, R.A., Hajnal, J.V., Hammers, A.: Diffeomorphic Registration using B-Splines. In: Larsen, R., Nielsen, M., Sporring, J. (eds.) MICCAI 2006. LNCS, vol. 4191, pp. 702–709. Springer, Heidelberg (2006)
10. Vercauteren, T., Pennec, X., Perchant, A., Ayache, N.: Non-parametric diffeomorphic image registration with the demons algorithm. In: Ayache, N., Ourselin, S., Maeder, A. (eds.) MICCAI 2007, Part II. LNCS, vol. 4792, pp. 319–326. Springer, Heidelberg (2007)
11. Zhu, C., Byrd, R.H., Nocedal, J.: L-BFGS-B: Algorithm 778: L-BFGS-B, FORTRAN routines for large scale bound constrained optimization. ACM Transactions on Mathematical Software 23(4), 550–560 (1997)

Random Forest Classification for Automatic Delineation of Myocardium in Real-Time 3D Echocardiography

Victor Lempitsky[1], Michael Verhoek[2], J. Alison Noble[2], and Andrew Blake[1]

[1] Microsoft Research Cambridge
victlem@microsoft.com, ablake@microsoft.com
[2] University of Oxford
mverhoek@robots.ox.ac.uk, noble@robots.ox.ac.uk

Abstract. Automatic delineation of the myocardium in real-time 3D echocardiography may be used to aid the diagnosis of heart problems such as ischaemia, by enabling quantification of wall thickening and wall motion abnormalities. Distinguishing between myocardial and non-myocardial tissue is, however, difficult due to low signal-to-noise ratio as well as the efficiency constraints imposed on any algorithmic solution by the large size of the data under consideration. In this paper, we take a machine learning approach treating this problem as a two-class 3D patch classification task. We demonstrate that solving such task using *random forests*, which are the discriminative classifiers developed recently in the machine learning community, allows to obtain accurate delineations in a matter of seconds (on a CPU) or even in real-time (on a GPU) for the entire 3D volume.

1 Introduction

Fast and accurate automatic delineation of the myocardium in echocardiograms can be a valuable aid in the assessment of heart-related diseases and abnormalities. Such a visual aid is particularly important in 3D echocardiography, where the visualization and comprehension of the data can be especially hard. 3D cardiography is however a challenging modality to work with due to low signal-to-noise ratio, unpredictable speckle patterns, and large variability in shape and appearance between different subjects. A large number of tissues that have similar appearance to the myocardium such as adjacent muscles or bright vessel walls complicate the discrimination even more. Finally, the sheer amount of the data contained in a 3D echocardiography study should ideally be processed in a matter of a few seconds (ideally in real-time), in order for an algorithm to be useful in clinical practice. Most (if not all) methods (such as [1]) in the published literature fail to meet this criterion.

Automatic delineation of the myocardium in 3D echocardiograms can be regarded as a binary classification problem, where each voxel should be assigned to either myocardium or non-myocardium. In the paper, we investigate a discriminative approach to this classification task. Thus, our classifier is trained to model the

N. Ayache, H. Delingette, and M. Sermesant (Eds.): FIMH 2009, LNCS 5528, pp. 447–456, 2009.
© Springer-Verlag Berlin Heidelberg 2009

posterior probability of the class given the data directly, without explicit modeling of either the statistics of the shape of the heart or the physics of the imaging process. Furthermore, the non-parametric nature of the classifier we use means that no restrictive assumptions are made about the form of the posterior. Our system is thus much simpler than many of the competing approaches. Importantly, as the output of our method is "soft" (posterior probability for each voxel), it could be used as an input for a more complex algorithm which can incorporate richer geometric information, such as deformable templates, level sets, or graph cuts.

The particular discriminative classifier that we use is the Random Forest classifier [2,3]. Our choice is motivated by the computational efficiency that random forests exhibit at both runtime and training time, as well as their growing popularity for similar segmentation tasks in computer vision (see e.g. [4,5,6]). Capitalizing on the efficiency of random forests, the current CPU implementation of our system is able to accomplish delineation of the full 3D volume in a few seconds. A GPU implementation along the lines of [7] is highly likely to achieve real-time speed for the full 3D volume.

In terms of accuracy, Random Forests have an excellent track record for various machine learning problems on a par or even better than boosting method or max-margin classifiers like SVMs [8]. Towards this end, our approach achieves a considerable delineation accuracy (92% true positive rate at 8% false positive rate).

2 Related Work

Traditional segmentation methods have been applied to cardiac chambers [9], including level sets [10] and active contours [11]. However, the literature on segmentation of the myocardium is limited. Myocardial segmentation has been performed [12] by first finding the endocardium in 2D+T echocardiographic slices, then locating the epicardium by searching outward along normals to the endocardium, using PCA shape and motion models. Others used level sets [1] in 2D MRI slices to find two coupled contours, one for the endocardium and one for the epicardium. Coupled evolving contours were also employed in [13], on 3D+T echocardiography data, using an incompressibility constraint. Compared to our proposed method, these segmentation algorithms are far from real-time.

A useful feature when segmentating myocardium from blood pool in echocardiography is tissue characterization, by fitting a distribution to the histogram of a given signal, which may be either the RF (radio frequency) signal or the intensity in the B-mode image. The results of fitting to several different distributions have been compared, for the RF signal [14], and for B-mode images [15].

Many researchers have investigated the delineation of tissues in ultrasound using discriminative classifiers, typically SVMs or neural networks [16,17]. These machine learning techniques have an inherent limitation for the tissue classification tasks, as each patch has to be described by low- to moderate-dimensional descriptor. This means that a preliminary, typically hand-crafted, feature selection step leading to the loss of information has to be performed. Furthermore, these methods tend to use features that are too expensive to compute for 3D images (e.g. Gabor filters).

Recently, a number of machine learning approaches have been developed, which are able to work with very high-dimensional representations by unifying the feature selection and supervised learning tasks. The most widely known learning framework of this kind is boosting [18], and several papers on ultrasound image segmentation have considered this learning framework (e.g. [19,20]). In this paper, we focus on another framework called *random forests* [3], and investigate the use of this framework for tissue classification in 3D echocardiograms. Compared to boosting, random forests have been demonstrated to achieve a comparable accuracy, while being faster [8]. Random forests also proved to be more robust to significant overlaps between classes and noise in the training labels [3], which is a scenario that is highly relevant to ultrasound classification. Finally, random forests can be effortlessly applied to multi-class classification, whereas boosting methods typically resort to binary classification reductions (such as training several *one-vs-all* binary classifiers). Although we do not investigate multi-class feature classification in this work, this may be useful when several types of cardiac tissues are considered.

Random forests [2,3] have been used for a large number of classification as well as regression tasks. A typical random forest consists of a set of binary decision trees [21]. During training, each non-leaf node in each tree is assigned a binary test that is applicable to any data sample. Depending on the result of the test, a sample can go to one of the two children of a given non-leaf node. This way, a sample can be passed through each of the trees, starting from its root and ending up in one of its leaves.

Random forests are trained in a supervised way. Training involves tree construction as well as assigning to each leaf node the information about the training samples reaching this leaf node, e.g. the class distribution in the case of classification tasks. At runtime, a test sample is passed down all the trees of the forest, and the output is computed by averaging the distributions recorded at the reached leaf nodes.

It has been shown [2,3,8] that assembling (bagging) together several trees trained in a randomized way achieves superior generalization and stability compared to a single deterministic decision tree. The randomization is achieved, firstly, by training each tree on a random subset of the training data, and, secondly, by considering a random subset of possible binary tests at each non-leaf node. Among this random subset, the training procedure picks the binary test that splits the training samples in the optimal way.

To the best of our knowledge, random forests have seen a very limited use in medical imaging so far [22,23,24]. However, in the computer vision community, several groups of authors [5,6,4] have recently proposed to use random forests for semantic segmentation of photographs, and our method has a lot of similarities with those approaches.

3 Delineation Using Random Forests

Problem setting. We formalize our problem as a binary classification of voxel samples. Each voxel sample $\mathcal{V}$ is thus described by the voxel coordinates

$\mathbf{x} = (x_1, x_2, x_3)$ in the 3D echocardiogram $\mathbf{I}$ it is drawn from. At runtime, each voxel sample is classified into myocardium or non-myocardium based on the appearance of the fixed-size 3D neighborhood around it as well as its position in the image. Incorporation of the position information is important (as demonstrated in the experiments below) as a cardiologist positions the heart with respect to the echo-volume roughly in the same way. In our approach, the meaning of *"roughly in the same way"* is to be learned from training data. The position information only acts very weakly as a shape model. Note that a sophisticated shape model derived from healthy hearts will not necessarily represent the shape of a diseased heart. We are also bound to learn the inter-dependencies between the position and the appearance, as the typical appearance of myocardial tissue tends to change with the position in an echocardiogram.

As we learn to classify voxels in a supervised setting, we assume that in the training step we are given a collection of labeled voxels $\{\mathcal{V}^i = (\mathbf{I}^i, \mathbf{x}^i, c^i)\}$, where $\mathbf{I}$ is one of the training echocardiograms, $\mathbf{x}^i$ is the position of the i-th training voxel, whereas c^i is its *class label* provided by an expert, which can be either 1 (if the voxel is annotated as myocardium) or 0 (if the voxel is annotated as non-myocardium).

At test time, the position $\mathbf{x}$ and the appearance of the echocardiogram $\mathbf{I}$ around the voxel are observed, and our goal is to infer the class label c. In this way, given an echocardiogram, we can assign a label c to each voxel according to the prediction of our classifier. As the classifier we use has a probabilistic nature, the labels assigned at run-time would span the interval $[0; 1]$ rather than being binary. Such "soft" labeling conveys the information uncertainty when used to highlight the myocardium during visualization. The uncertainty information is also likely to boost the performance if labeling is used as an input to some further geometric integration step (e.g. level sets, graph cuts, deformable template fitting, etc.). However, if the "hard" binary labeling is required straight away, the voxel labels can be thresholded at some fixed value (e.g. 0.5).

Trees construction. Our random forests consist of a collection of randomized binary trees and below we discuss how these trees are constructed. The construction proceeds in a top-down fashion, starting from the root. At each node, a *training collection* of labeled voxels received from its parent is considered (the root node receives a randomly drawn subset of the size N_{train} of our full training set). A *binary test* is then chosen to minimize the uncertainty of the class labels in the subsets, it splits the training collection into (the exact choice method is discussed below). Once the binary test is chosen, the training collection of voxels is split in the two subsets according to this binary test. The two children nodes are then created and the two subsets are passed to them as their training collections, so that the recursion proceeds.

The recursive tree construction stops either when a certain maximal tree depth $D_{\max}$ is reached or when all voxels in the training collection have the same label. At this point, the node is declared a leaf. Once the tree is constructed (based on the drawn subset of the labeled voxels), we take all available labeled voxels and pass each of them through the tree. For each leaf node, we then record

the average class label of the labeled voxels that have reached this node. This average class label can be interpreted as the posterior probability of a voxel being myocardium, given the fact that this voxel falls into the leaf.

Binary tests. Let us now discuss the way the binary tests are chosen. As the voxel description has two components, namely, the position in the volume and the neighborhood appearance, we consider two types of tests. The *appearance tests* are defined as:

$$t^{a_1,a_2,a_3,\tau_a}_{\text{appearance}}(\mathbf{x},\mathbf{I}) = \begin{cases} 0, & \text{if } \sum\limits_{p_1=x_1-a_1}^{x_1+a_1} \sum\limits_{p_2=x_2-a_2}^{x_2+a_2} \sum\limits_{p_3=x_3-a_3}^{x_3+a_3} \mathbf{I}(p_1,p_2,p_3) > \tau_a \\ 1, & \text{otherwise.} \end{cases} \tag{1}$$

An appearance test thus compares a sum of the intensities over an axis-aligned box of the size $(2a_1{+}1) \times (2a_2{+}1) \times (2a_3{+}1)$ centered at the voxels with some threshold τ_a, where the parameter values a_1, a_2, a_3, τ_a are chosen in a randomized fashion as discussed below. Note that such box sums can be evaluated extremely efficiently using just 7 additions and subtractions irrespective of the size of the box using the *integral image* technique [25].

The second type of the tests is the *position test* defined as:

$$t^{i,\tau_p}_{\text{position}}(\mathbf{x}) = \begin{cases} 0, & \text{if } x_i > \tau_p \\ 1, & \text{otherwise.} \end{cases} \tag{2}$$

This test, thus, simply compares the ith coordinate of the voxel with a threshold τ_p, where i, τ_p are chosen randomly as discussed below.

Given a collection of labeled voxels $\mathcal{C} = \{\mathcal{V}^i, c^i\}$, we define the *uncertainty* of its labels as:

$$U(\mathcal{C}) = |\mathcal{C}| \cdot \mathit{Entropy}\left(\{c^i\}\right) = |\mathcal{C}| \left(\bar{c} \cdot \log \bar{c} + (1-\bar{c}) \cdot \log(1-\bar{c})\right) \tag{3}$$

where $\bar{c}$ denotes the average class label over collection. Thus, the uncertainty is maximal for the collections where all voxels are from the same class and minimal (for a given size) for the collections where class labels are split into equal halves.

When choosing a split for a training collection $\mathcal{C}$, we generate N_{tests} random tests. We choose two thirds of our tests to be the appearance tests and one third to be the position tests. When generating an appearance test, we sample a_1, a_2, a_3 independently and uniformly from the interval $[0; R]$ from zero to the neighborhood radius R. We then pick the threshold τ_a by averaging the respective box sums from (1) for the two randomly chosen samples from the training collection. When generating a position test, we pick one of the three dimensions with equal probability and we pick the threshold τ_p equal to the respective coordinate of a randomly chosen sample from the training collection.

For each of the generated tests, we consider the two subsets, it splits the training collection into. We then pick a test, which has the smallest sum of the uncertainties (3) for these subsets. Such a choice ensures that the uncertainty in labels decreases quickly towards the leaves of the tree.

There are two properties worth noting. Firstly, despite the extreme simplicity of the position tests the superposition of such tests at different depths of the tree allows to learn a non-trivial shape prior. Secondly, as the position and appearance tests are interleaved within a tree, we are able to learn the inter-dependencies between the shape and appearance.

Annotating a voxel using a random forest. Given a random forest, i.e. several trees that were independently trained as discussed above, we can classify a new voxel $\mathcal{V}$ located at the position $\mathbf{x}$ in a previously unseen echocardiogram $\mathbf{I}$. To do that we simply pass the voxel $\mathcal{V} = (\mathbf{x}, \mathbf{I})$ through every tree. Given a set of leaves the voxel ends up in different trees, we simply average the class probabilities recorded in these leaves.

4 Experiments

Experimental protocol. We have evaluated the developed method on several 3D echocardiograms (Figure 1). Towards this end, we have obtained 14 3D+T echocardiograms from different healthy subjects with the myocardium for left and right ventricles delineated by an expert. The echocardiograms were recorded at the Oxford John Radcliffe Hospital, using a Philips iE33 ultrasound system. The echocardiograms had a spatial resolution of 0.93 mm $\times$ 0.94 mm $\times$ 0.85 mm or 0.82 mm $\times$ 0.84 mm $\times$ 0.76 mm, depending on the settings of the ultrasound system. We chose to use the end-systolic frame out of each sequence. In these 3D echocardiograms, every fifth short-axis slice was annotated, using a Wacom Cintiq interactive pen display and a Matlab script to record an endocardial and an epicardial contour in each slice. Papillary muscle was regarded as belonging to the blood pool. In places where wall data appeared to be missing due to attenuation or being parallel to the beam, the expert used their knowledge of the shape of the myocardium to construct the contours. The expert could view orthogonal long-axis slices simultaneously to judge the manual segmentation in those views. As the echocardiograms contained significant variations in brightness, we performed a histogram equalization step, so that histograms of all echocardiograms were approximately matched to the histogram of one of the examples. This pre-processing step was beneficial for our method, as the appearance tests (1) employed in our implementation are not invariant to brightness changes.

There are four major parameters in our method that have to be adjusted: the number of training samples for each tree N_{train}, the maximal tree depth $D_{\max}$, the number of random binary tests generated for each node N_{tests}, and the radius of the neighborhood R. Therefore, we singled out the three last echocardiograms and used them for validation, while the first eleven echocardiograms were used for training. As a result of the validation step, the values of parameters were set as follows: $N_{\text{train}} = 100000$, $D_{\max} = 16$, $N_{\text{tests}} = 30$, $R = 32$.

After the parameter tuning, we have evaluated our method on the first eleven echocardiograms. We tested the method on each of the eleven echocardiograms, training a random forest containing 20 trees on the remaining ten datasets (so

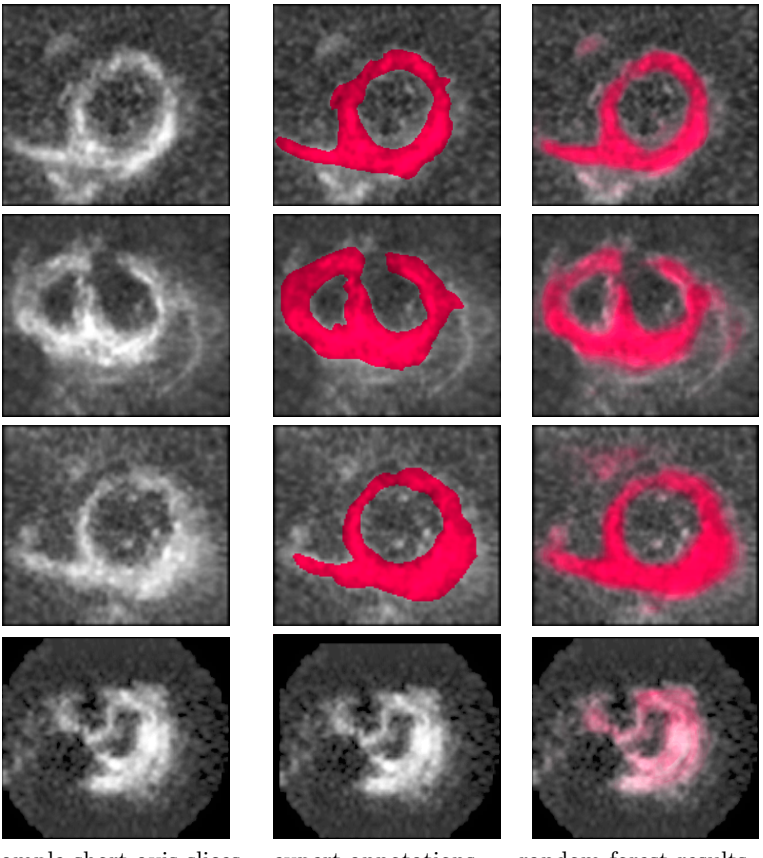

Fig. 1. Qualitative results. For the examples of short-axis slices, the random forest predicts "soft" delineations that closely match the delineations performed by an expert. As the bottom row demonstrates, our classifier still "fires" on the bright vessel walls, yet the response is relatively weak.

that training and test data are not mixed). Using the trained forests, we obtained a "soft" segmentation for every voxel in each of the eleven datasets. We then evaluated the accuracy of the hard segmentation obtained with a sequence of thresholds. For each value of threshold, we summed up the number of true positives (voxels correctly labeled as myocardium) and the number of all positives (voxels labeled as myocardium). In Figure 2, we present the results of our method in the form of a recall-precision and ROC-curves [26], generated by varying the probability threshold.

As a baseline, we provide the recall-precision curve for thresholding the raw values of the intensity (note, that this simple approach is likely to benefit a lot from the histogram equalization pre-processing). Although the muscular myocardial tissue has a tendency to be brighter than the surrounding tissues, it can

be clearly seen that brightness is not a powerful enough cue in this case (one may wonder if a simple intensity thresholding would benefit from prefiltering the image with a low-pass filter, but in our experiments such prefiltering only worsened the performance of thresholding). We have also tried thresholding of the shifted Rayleigh parametric image obtained by estimating the σ^2 parameter in the shifted Rayleigh distribution, which was used previously [13] to characterize the blood pool and myocardium in B-mode images. We estimated the parameter in a neighborhood of 5^3 voxels around each voxel. The thresholding of the shifted Rayleigh parameter performed slightly better than raw intensity thresholding.

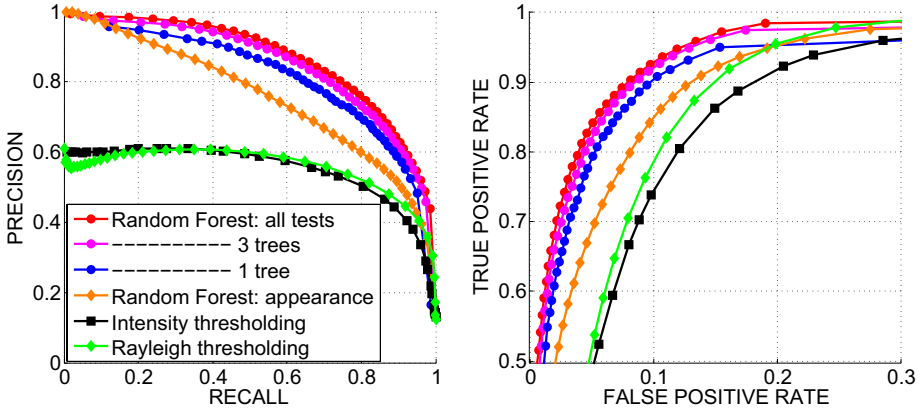

Fig. 2. Quantitative results. Recall-precision (left) and ROC (right) curves demonstrate the significant advantage of our method over the thresholding of raw intensity and of the shifted Rayleigh parameter. As an aside, removing the position tests (Random Forest-A curve) deteriorates the performance of our method much more than reducing the number of trees.

Variations of our method. Figure 2 also demonstrates the recall-precision and ROC curves for the variation of our method, where only appearance tests (1) were allowed, while position tests (2) were not considered. As can be seen (*Random Forest-A* curve), the performance of our method degraded considerably, suggesting that the rough knowledge about the positioning of the myocardium in the echo-volume was picked up and utilized by the training algorithm. It can be observed at the same time that even without the position tests, random forest based classification performs significantly better than thresholding, which suggests that a sophisticated model of appearance can be learned using random forests.

Finally, we demonstrate the performance of our method using a different number of trees smaller than 20. As can be seen, while the performance of a single tree is considerably worse than that of the whole forest, this performance quickly saturates as the number of trees is increased, achieving the comparable accuracy already for 3 trees.

Computational performance. The 3D echocardiograms in our experiments had the size $218 \times 202 \times 272$; around 45% of voxels were inside the echo-cone and, hence, classified with the random forest. For a modern CPU (2.4 GHz), the time required to delineate the entire echocardiogram was around 2.1 seconds for a forest with 3 trees and around 22 seconds for a forest with 20 trees. The GPU implementation as described in [7] is highly likely to run at several frames per second ([7] reported hundred-fold acceleration). The training procedure was also remarkably fast taking around 15 seconds per one tree on a CPU.

5 Conclusions and Future Work

We have evaluated random forests, which are one of the most accurate and computationally efficient discriminative classifiers, on the problem of automatic myocardial tissue delineation in 3D echocardiograms. A significant boost in accuracy compared to thresholding of raw intensities or Rayleigh parameters has been demonstrated on a dataset of real data. Importantly, the developed method is fast (potentially real-time), which distinguishes it from most (if not all) other methods published for this problem.

The future work would include a more thorough evaluation on a larger amount of data as well as assessing the clinical applicability of the algorithm as an aid for myocardium volume estimation and, potentially, regional wall thickening and motion abnormalities detection. We also plan to investigate the use of the output labelings within more sophisticated, higher-level algorithms, such as deformable template fitting, graph cuts, or level sets. However, a care should be taken that the acceptable speed is maintained.

References

1. Lynch, M., Ghita, O., Whelan, P.: Left-ventricle myocardium segmentation using a coupled level-set with a priori knowledge. Computerized Medical Imaging and Graphics 30(4), 255–262 (2006)
2. Amit, Y., Geman, D.: Shape quantization and recognition with randomized trees. Neural Computation 9(7), 1545–1588 (1997)
3. Breiman, L.: Random forests. Machine Learning 45(1), 5–32 (2001)
4. Winn, J.M., Shotton, J.: The layout consistent random field for recognizing and segmenting partially occluded objects. In: CVPR (1), pp. 37–44 (2006)
5. Shotton, J., Johnson, M., Cipolla, R.: Semantic texton forests for image categorization and segmentation. In: CVPR (2008)
6. Schroff, F., Criminisi, A., Zisserman, A.: Object class segmentation using random forests. In: BMVC (2008)
7. Sharp, T.: Implementing decision trees and forests on a GPU. In: Forsyth, D., Torr, P., Zisserman, A. (eds.) ECCV 2008, Part IV. LNCS, vol. 5305, pp. 595–608. Springer, Heidelberg (2008)
8. Caruana, R., Niculescu-Mizil, A.: An empirical comparison of supervised learning algorithms. In: ICML, pp. 161–168 (2006)
9. Noble, J., Boukerroui, D.: Ultrasound image segmentation: a survey. IEEE Trans. Med. Imaging 25(8), 987–1010 (2006)

10. Yan, J., Zhuang, T.: Applying improved fast marching method to endocardial boundary detection in echocardiographic images. Pattern Recognition Letters 24(15), 2777–2784 (2003)
11. Angelini, E.D., Homma, S., Pearson, G., Holmes, J.W., Laine, A.F.: Segmentation of real-time three-dimensional ultrasound for quantification of ventricular function: A clinical study on right and left ventricles. Ultrasound in Medicine & Biology 31(9), 1143–1158 (2005)
12. Jacob, G., Noble, J., Behrenbruch, C., Kelion, A., Banning, A.: A shape-space-based approach to tracking myocardial borders and quantifying regional left-ventricular function applied in echocardiography. IEEE Trans. Med. Imaging 21(3), 226–238 (2002)
13. Zhu, Y., Papademetris, X., Sinusas, A., Duncan, J.S.: Segmentation of myocardial volumes from real-time 3D echocardiography using an incompressibility constraint. In: Ayache, N., Ourselin, S., Maeder, A. (eds.) MICCAI 2007, Part I. LNCS, vol. 4791, pp. 44–51. Springer, Heidelberg (2007)
14. Nillesen, M.M., Lopata, R.G., Gerrits, I.H., Kapusta, L., Thijssen, J.M., de Korte, C.L.: Modeling envelope statistics of blood and myocardium for segmentation of echocardiographic images. Ultrasound in Medicine & Biology 34(4), 674–680 (2008)
15. Tao, Z., Tagare, H., Beaty, J.: Evaluation of four probability distribution models for speckle in clinical cardiac ultrasound images. IEEE Trans. Med. Imaging 25(11), 1483–1491 (2006)
16. Chang, R., Wu, W., Moon, W.K., Chou, Y., Chen, D.: Support vector machines for diagnosis of breast tumors on US images. Academic Radiology 10(2), 189–197 (2003)
17. Drukker, K., Giger, M.L., Vyborny, C.J., Mendelson, E.B.: Computerized detection and classification of cancer on breast ultrasound1. Academic Radiology 11(5), 526–535 (2004)
18. Freund, Y., Schapire, R.E.: Experiments with a new boosting algorithm. In: ICML, pp. 148–156 (1996)
19. Pujol, O., Rosales, M., Radeva, P., Nofrerias-Fernández, E.: Intravascular ultrasound images vessel characterization using adaboost. In: Magnin, I.E., Montagnat, J., Clarysse, P., Nenonen, J., Katila, T. (eds.) FIMH 2003. LNCS, vol. 2674, pp. 242–251. Springer, Heidelberg (2003)
20. Georgescu, B., Zhou, X.S., Comaniciu, D., Gupta, A.: Database-guided segmentation of anatomical structures with complex appearance. In: CVPR (2) (2005)
21. Quinlan, J.R.: Induction of decision trees. Machine Learning 1(1), 81–106 (1986)
22. Andres, B., Köthe, U., Helmstaedter, M., Denk, W., Hamprecht, F.A.: Segmentation of SBFSEM volume data of neural tissue by hierarchical classification. In: Rigoll, G. (ed.) DAGM 2008. LNCS, vol. 5096, pp. 142–152. Springer, Heidelberg (2008)
23. Hope, T.A., Gregson, P.H., Linney, N.C., Schmidt, M.H., Abdolell, M.: Selecting and assessing quantitative early ultrasound texture measures for their association with cerebral palsy. IEEE Trans. Med. Imaging 27(2), 228–236 (2008)
24. Vibha, L., Harshavardhan, G.M., Pranaw, K., Shenoy, P.D., Venugopal, K.R., Patnaik, L.M.: Lesion detection using segmentation and classification of mammograms. In: AIAP 2007, pp. 311–316 (2007)
25. Viola, P.A., Jones, M.J.: Robust real-time face detection. In: ICCV, p. 747 (2001)
26. van Rijsbergen, C.: Information Retrieval. Butterworth (1979)

Discriminative Joint Context for Automatic Landmark Set Detection from a Single Cardiac MR Long Axis Slice

Xiaoguang Lu[1], Bogdan Georgescu[1], Arne Littmann[2], Edgar Mueller[2], and Dorin Comaniciu[1]

[1] Siemens Corporate Research, Princeton, NJ, USA
[2] Magnetic Resonance, Siemens Healthcare, Erlangen, Germany

Abstract. Cardiac magnetic resonance (MR) imaging has advanced to become a powerful diagnostic tool in clinical practice. Automatic detection of anatomic landmarks from MR images is important for structural and functional analysis of the heart. Learning-based object detection methods have demonstrated their capabilities to handle large variations of the object by exploring a local region, context, around the target. Conventional context is associated with each individual landmark to encode local shape and appearance evidence. We extend this concept to a landmark *set*, where multiple landmarks have connections at the semantic level, e.g., landmarks belonging to the same anatomy. We propose a joint context approach to construct contextual regions between landmarks. A discriminative model is learned to utilize inter-landmark features for landmark set detection as an entirety. This helps resolve ambiguities of individual landmark detection results. A probabilistic boosting tree is used to learn a discriminative model based on contextual features. We adopt a marginal space learning strategy to efficiently learn and search a high dimensional parameter space. A fully automatic system is developed to detect the set of three landmarks of the left ventricle, the apex and the two basal annulus points, from a single cardiac MR long axis image. We test the proposed approach on a database of 795 long axis images from 116 patients. A 4-fold cross validation results show that about 15% reduction of the errors is obtained by integrating joint context into a conventional landmark detection system.

1 Introduction

In cardiology, precise information on both the dimensions and functions of the left ventricle (LV) and other heart chambers is essential in clinical applications for diagnosis, prognostic, and therapeutic decisions. Magnetic Resonance (MR) imagery provides a complete morphological LV characterization. The precision on the measures extracted from MR images has been demonstrated and makes MR imagery a standard for LV analysis [1]. Although cardiac MR imaging technologies have rapidly advanced [2,3], due to considerable amount of available

N. Ayache, H. Delingette, and M. Sermesant (Eds.): FIMH 2009, LNCS 5528, pp. 457–465, 2009.
© Springer-Verlag Berlin Heidelberg 2009

data, analysis such as segmentation of cardiac images for functionality quantification is time consuming and error-prone for human operators. Automated analysis tools are in great need.

In MR scans, long axis slices are not only used as scout images for acquisition planning, but also are complementary to the short axis stack [4]. Long axis slices captures left ventricle's shape information and can also be used to correct mis-registration of the short axis stack. Long axis acquisitions can be an image sequence or a single slice during acquisition planning, when the short stack and temporal information may not be available. Anatomic landmarks can be used for higher level segmentation, such as initialization of deformable model based approaches [5], and for accelerating acquisition time by facilitating the fully automatic planning of Cardiac MR examinations [6]. Therefore, we are focused on detecting a set of three landmarks from a single cardiac MR long axis slice, containing the apex and two basal annulus points of LV as shown in Fig. 1.

Learning based object detection approaches have been demonstrated successful in many applications [7,8]. However, they still encounter challenges in a cluttered environment, such as landmark detection in MR long axis slices, due to large anatomy shape and appearance variations across populations along with different acquisition parameters. A number of different anatomies other than the heart also appear in the same slice. For the same patient, time sampling across the entire heart beat cycle, with ED and ES as two ends, also leads to significantly different myocardium contour shape changes. These variations and ambiguities result in challenges for each individual landmark detector to identify

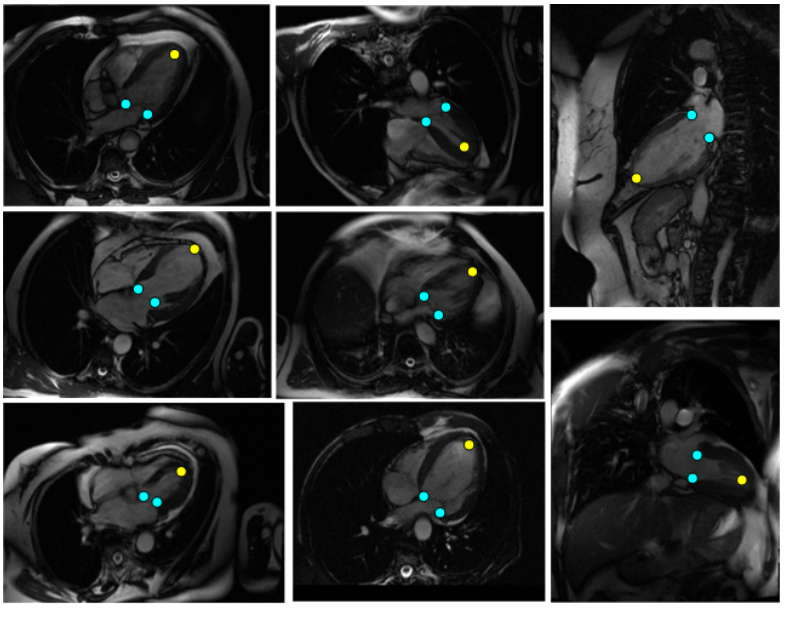

Fig. 1. Examples of cardiac long axis images and three landmarks of interest, which are the apex (yellow) and two basal annulus points (cyan) of LV

correct landmarks. Cardiac MR long axis image examples along with the three target landmarks in our experiments are shown in Fig. 1.

Context of a landmark is considered as its local evidence such as shape and appearance. Each individual landmark has limited local evidence to identify. However, a set of landmarks are not independent to each other. Correlation in shape and appearance among landmarks can be crucial to identify a landmark set as an entirety. For example, each basal annulus point of LV has limited context, but joint context of the two basal annulus points contains the base plane region, which has a more discriminative power than each individual annulus point to distinguish from other anatomic structures. For those anatomic landmarks that have semantic connections, such as the two basal annulus points and the apex of the left ventricle, joint contextual information (around LV region) captures the correlation of the shape and appearance constructed from the landmark set, which includes more evidence and helps resolve the ambiguities in detecting each landmark individually. Therefore, we propose a joint context based approach under a learning-based object detection framework to automatically identify a landmark set. We define a mapping calculated from a landmark set to derive contextual region, where features are automatically learned to build a discriminative model/classifier. We apply joint context to two scenarios: one for the two basal annulus points, and the other for the set of the apex and the base plane (defined by the two basal annulus points).

2 Methodology

2.1 Overall Workflow

For a cardiac MR long axis image, our joint context based landmark set detection framework includes the following steps (see Fig. 2):

(1). Apply an apex detector and select the top M candidates.
(2). Apply a base plane detector and select the top N candidates.
(3). For each possible candidate pair of <apex, base plane> from the candidate pool (M apex candidates and N base plane candidates), construct joint context.
(4). Apply the joint context classifier to determine the best pair of <apex, base plane> with the highest probability.
(5). A local search can be applied to further improve the estimation accuracy of the detected landmarks.

2.2 Joint Context

We define a context operator C to represent context of an object O, whose parameters are denoted by θ, i.e., $C(O|\theta)$. For concise representation purposes, we use $C(\theta)$. The operator C is applied to extract features (context information) from contextual appearance. For example, a series of Haar-wavelet like features [7] can be computed and selected by C.

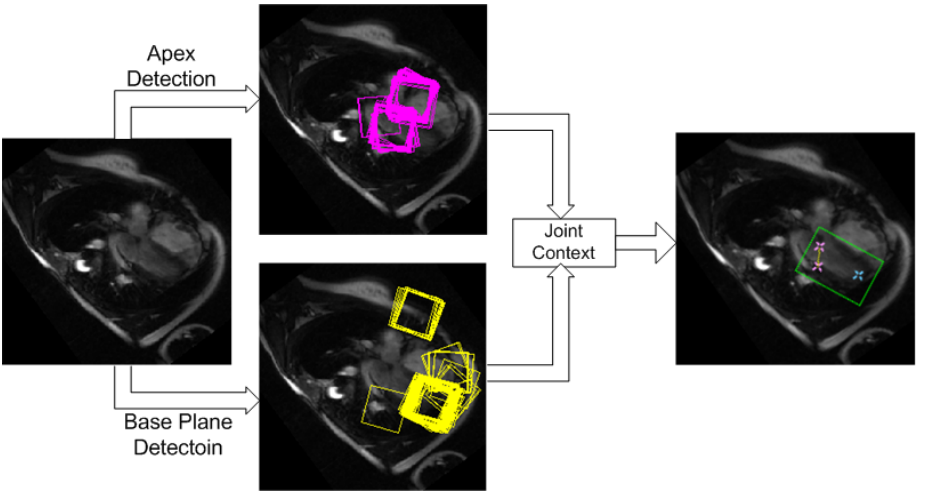

Fig. 2. Joint context based detection workflow

Joint context is defined across a set of landmarks. For two objects O_1 and O_2, which are represented by their respective parameters θ_1 and θ_2, the joint context (JC) is defined as:

$$JC = C(f(\theta_1, \theta_2)). \tag{1}$$

JC is represented as appearance and encodes the shape by computing geometric relationship through the mapping f, which derives a geometric region based on θ_1 and θ_2.

2.3 Joint Context Based Landmark Set Detection

Context Construction. We associate a two-dimensional bounding box with each target landmark object and their derived context. Each bounding box is specified by a five-parameter set θ, containing two positions $< x, y >$, one orientation $< \phi >$, and two scales $< sx, sy >$. The original landmark detection task can then be formulated into estimating this set of parameters. Although only positions are used as the output, orientation and scales are useful in encoding proper and consistent context learned during offline training process, where a set of contextual models/classifiers are obtained.

To learn contextual models, we collect a set of cardiac long axis images and annotate the landmark positions. Based on this annotated training set, we build a contextual model for each target object and a joint contextual model for the pair of <apex, base plane>. Let $< x_a, y_a >$, $< x_{b1}, y_{b1} >$, and $< x_{b2}, y_{b2} >$ denote the positions of the apex, and two basal annulus points, respectively. The joint contextual parameter sets derived from this landmark set are constructed as shown in Table 1.

Table 1. Context construction (mapping f in Eq. (1)). $< x_a, y_a >$, $< x_{b1}, y_{b1} >$, and $< x_{b2}, y_{b2} >$ denote the positions of the apex, and two basal annulus points, respectively. Base Plane (BP) context is obtained from two basal annulus points. Joint context of <Apex, Base Plane> depends on the apex and the two basal annulus points.

	Positions	Orientation
Apex	$x_a = x_a$ $y_a = y_a$	$phi_a = \arctan \frac{(y_a-(y_{b1}+y_{b2})/2)}{(x_a-(x_{b1}+x_{b2})/2)}$;
Joint context BP	$x_b = (x_{b1} + x_{b2})/2$ $y_b = (y_{b1} + y_{b2})/2$	Orthogonal to the line segment connecting the two basal annulus points, and pointing toward the apex
Joint context <Apex, BP>	$x_{jc} = (x_a + x_b)/2$ $y_{jc} = (y_a + y_b)/2$	$\phi_{jc} = \arctan \frac{y_a-(y_{b1}+y_{b2})/2}{x_a-(x_{b1}+x_{b2})/2}$

	Scales
Apex	$sx_a = \sqrt{(y_{b2} - y_{b1})^2 + (x_{b2} - x_{b1})^2} * 1.8$[1] $sy_a = sx_a$
Joint context BP	$sx_b = \sqrt{(y_{b2} - y_{b1})^2 + (x_{b2} - x_{b1})^2} * 1.8$ $sy_b = sx_b$
Joint context <Apex, BP>	$sx_{jc} = \sqrt{(y_a - y_b)^2 + (x_a - x_b)^2} * 1.5$ $sy_{jc} = \sqrt{(y_{b2} - y_{b1})^2 + (x_{b2} - x_{b1})^2} * 1.8$

2.4 Learning Discriminative Context

To utilize context for object detection, we build a discriminative model to differentiate the true object from background by calculating the probability of given context (of a candidate) being a target object, denoted as $P(O|C)$. Our joint context based landmark set detection approach follows the database-driven knowledge-based framework, which has been demonstrated effective in object detection and medical applications [7,8]. Landmark detection is formulated as a two-category classification problem, i.e., true object vs. background. Discriminative features from context are extracted and learned by a machine algorithm based on the experts' annotations, resulting in a probabilistic model for each landmark context or a joint context of a landmark set. The online detection algorithm searches through multiple hypotheses in the parameter space to identify the ones with high probabilities.

Context-based landmark detection is to estimate the parameter set, θ, of an object target from a given image. There are five parameters for each context in our framework, including 2 positions (x, y), 1 orientation (ϕ), and 2 scales along each axis (sx, sy). Because exhaustively searching in this five-dimensional parameter space is expensive for online applications, we adopt a search strategy similar to the marginal space learning based approach, which was proposed by Zheng et al. [9] for 3D object detection. These detectors are trained using positive samples based on the position, orientation, and size of the annotated object

[1] The magnifier 1.8 is used to include more context.

context, while the negative set is generated by extracting sub-images that are further from the positive samples in the parameter space.

For each learning/classification task, we use a probabilistic boosting tree (PBT) proposed by Tu et al. [10] as the classifier. The classifier is a tree-based structure with which the posterior probabilities of the presence of the landmark of interest are calculated from candidate context in given images. Following the marginal space learning strategy, we designed a series of classifiers that estimate parameters at a number of sequential stages in the order of complexity, i.e., position, orientation, and scale. Different stages utilize different features computed from image intensities. Multiple hypotheses are maintained between algorithm stages, which quickly removes false hypotheses at the earlier stages while propagates the right hypothesis to the final stage. Only one hypothesis is selected as the final detection result.

A set of discriminative features are selected to distinguish the positive target from negatives from a large pool of features at each stage. For the classifiers at the position stage, we choose Haar wavelet-like features [7], which are efficiently calculated using integral image-based techniques. For the classifiers at the orientation and scale search stages, steerable features [9] are applied, because their computation does not require image rotation and re-scaling, which are computationally expensive.

3 Experiments

We collected 253 long axis sequences from 116 patients (ages range from 11 to 72 years old), from which slices were selected to cover a large range of dynamic heart motion from end diastole to end systole. In total, there are 795 long axis slices (images) in our database. For each slice, three landmarks of LV (two basal annulus points and the apex) were manually annotated by experts and used as groundtruth for evaluation.

For each long axis slice, we applied the proposed joint context based algorithm to detect the landmark set, i.e., two basal annulus points and the apex, in a fully automatic fashion. We computed Euclidean distance between the detected landmark position and its corresponding groundtruth as the detection error for each landmark. The average error of all three landmarks was used as the metric to evaluate the system performance.

A 4-fold cross-validation scheme was applied for evaluation. The entire dataset of 795 images was randomly partitioned into four quarters. For each fold evaluation, three quarters were combined for training and the remaining one quarter was used as unseen data for testing. This procedure was repeated four time so that each image has been used once for testing. Examples of the detection results are shown in Fig. 3. Performance is summarized based on all 4 folds and provided in Table 2. Both individual landmark detectors and joint context based approach are evaluated under the same experimental protocol. It shows that the overall mean errors are reduced by about 15 percent with the proposed joint context based approach integrated. While the median error is not reduced as much as

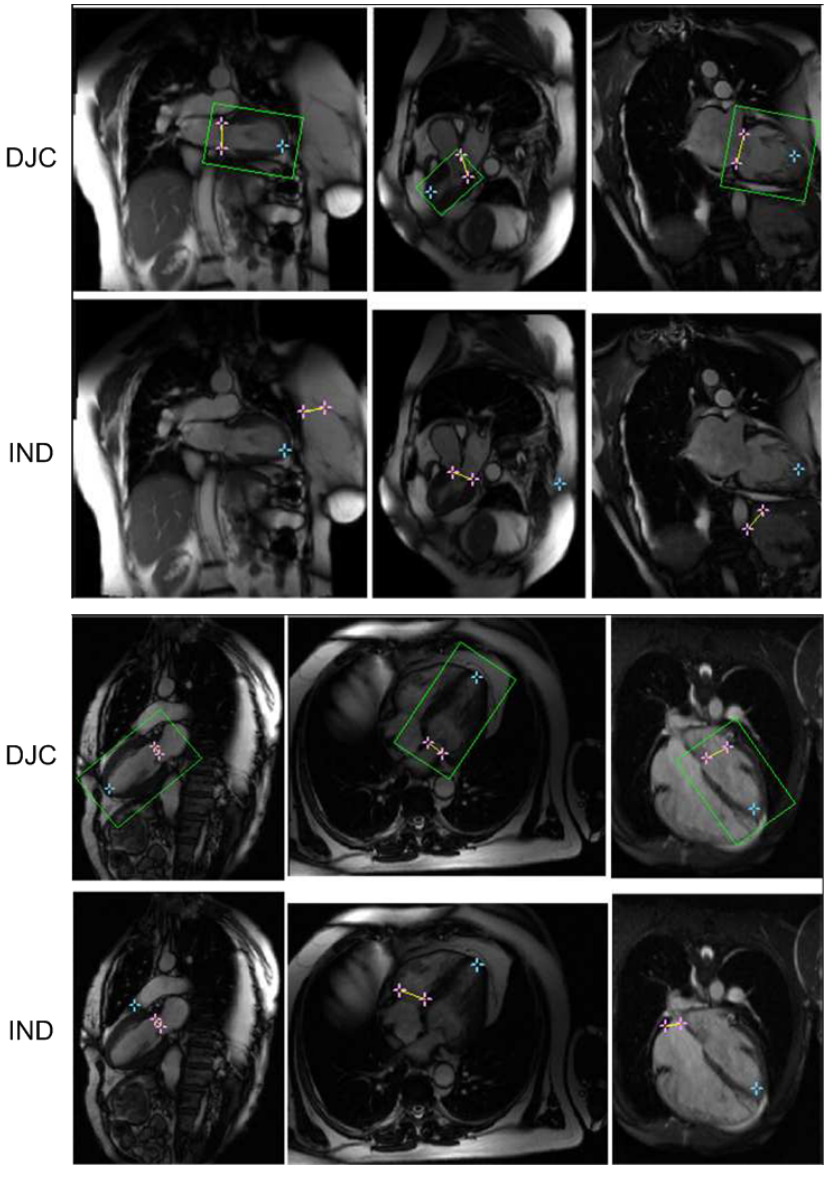

Fig. 3. Bottom ('IND' group): detection results of the base plane detector and the apex detector individually. Top ('DJC' group): landmark set detection results after applying the discriminative joint context (DJC) based approach. The green region represents joint context that provides the highest likelihood value of a pair of <apex, base plane>. Pink: detected two basal annulus points; blue: detected apex.

the mean, this indicates that the proposed approach significantly reduces the outliers generated by the individual landmark detectors. Cardiac MR images in a large population present a large variations of appearance intensities along with

Table 2. Statistics of the average error of all three landmarks (two basal annulus points and the apex) in a 4-fold cross validation. Errors are measured in *mm*.

	Mean	Std	Median
Individual landmark detector	9.4	15.9	5.4
Joint context based landmark set detection	8.0	13.9	5.2

the anatomy shape changes across the heart beat cycle, leading to difficulties for accurate identification. Large errors still occur when all individual detectors fail to locate correct landmarks, resulting in zero correct candidate for joint context. On the average, it took about 1.5 seconds to detect the three landmarks from a 400×400 image on a duo core 2.8GHz CPU.

4 Conclusions

We have proposed a joint context based approach that is integrated into a learning-based object detection framework. We have applied joint context and developed a fully automatic system to detect a landmark set from cardiac MR long axis images. The target landmark set contains the apex and the two basal annulus points. The proposed joint context based approach is not dependent on any specific learning algorithms. To account for both scout and diagnosis images, we are focused on a single MR long axis slice. However, for image sequences, the cue of temporal coherence can be integrated to further improve the landmark set detection accuracy.

Acknowledgements

We would like to thank Haibin Ling for helpful discussion and Yefeng Zheng for providing marginal space learning implementation.

References

1. Cousty, J., Najman, L., Couprie, M., Clement-Guinaudeau, S., Goissen, T., Garot, J.: Automated, accurate and fast segmentation of 4D cardiac MR images. In: Sachse, F.B., Seemann, G. (eds.) FIMH 2007. LNCS, vol. 4466, pp. 474–483. Springer, Heidelberg (2007)
2. Frangi, A., Niessen, W., Viergever, M.: 3D modeling for functional analysis of cardiac images: a review. IEEE Trans. on Medical Imaging 20(1), 2–25 (2001)
3. Finn, J.P., Nael, K., Deshpande, V., Ratib, O., Laub, G.: Cardiac MR imaging: State of the technology. Radiology 241(2), 338–354 (2006)
4. Koikkalainen, J., Pollari, M., Lotjonen, J., Kivisto, S., Lauerma, K.: Segmentation of cardiac structures simultaneously from short- and long-axis MR images. In: Barillot, C., Haynor, D.R., Hellier, P. (eds.) MICCAI 2004. LNCS, vol. 3216, pp. 427–434. Springer, Heidelberg (2004)

5. Jolly, M.P.: Automatic segmentation of the left ventricle in cardiac MR and CT images. International Journal of Computer Vision 70(2), 151–163 (2006)
6. Young, A., Cowan, B., Thrupp, S., Hedley, W., Dell'Italia, L.: Left ventricular mass and volume: Fast calculation with guide-point modeling on MR images. Radiology 216(2), 597–602 (2000)
7. Viola, P., Jones, M.J.: Robust real-time face detection. International Journal of Computer Vision 57(2), 137–154 (2004)
8. Georgescu, B., Zhou, X., Comaniciu, D., Gupta, A.: Database-guided segmentation of anatomical structures with complex appearance. In: Proc. IEEE CVPR (2005)
9. Zheng, Y., Barbu, A., Georgescu, B., Scheuering, M., Comaniciu, D.: Fast automatic heart chamber segmentation from 3D CT data using marginal space learning and steerable features. In: Proc. ICCV (2007)
10. Tu, Z.: Probabilistic boosting-tree: Learning discriminative models for classification, recognition, and clustering. In: Proc. ICCV, pp. 1589–1596 (2005)

Cardiac Imaging and Modeling for Guidance of Minimally Invasive Beating Heart Interventions

Terry M. Peters[1,2,3], Cristian A. Linte[1,2], John Moore[1], Andrew Wiles[1,3], Jennifer Lo[1,2], Danielle Pace[1,2], Chris Wedlake[1], Daniel Bainbridge[1,2], Douglas L. Jones[1,2], and Gerard M. Guiraudon[1,2]

[1] Robarts Research Institute, London ON Canada
[2] University of Western Ontario, London ON Canada
[3] Canadian Surgical Technologies and Advanced Robotics, London ON Canada
{clinte,tpeters}@imaging.robarts.ca

Abstract. Minimally invasive beating heart intracardiac surgery is an area of research with many unique challenges. Surgical targets are in constant motion in a blood-filled environment that prevents direct line-of-sight guidance. The restrictive workspace requires compact, yet robust tools for proper therapy delivery. Our novel method for approaching multiple targets inside the beating heart allows their identification and access under augmented reality-assisted image guidance. The surgical platform integrates real-time ultrasound imaging with virtual models of the surgical instruments, along with virtual cardiac anatomy acquired from pre-operative images. Extensive *in vitro* studies were performed to assess the operator's ability to "deliver therapy" to dynamic intracardiac targets via both transmural and transluminal access, and demonstrated significantly more accurate targeting under augmented reality guidance compared to ultrasound image guidance alone, accompanied by a reduction of procedure time by half. Moreover, preliminary *in vivo* acute studies on porcine models showed successful prosthesis positioning for beating-heart septal defect repair and mitral valve implantation via direct surgical access. While still in its infancy, this work emphasizes the promise of ultrasound-enhanced model-guided environments for minimally-invasive cardiac therapy, whether delivered via a catheter introduced into the vascular system or a cannula inserted through the heart wall.

1 Introduction

Intracardiac procedures have challenged surgeons and researchers ever since the pioneers of modern cardiac surgery performed the first interventions on the beating heart [1,2], as their outcome was compromised by inadequate visualization of intracardiac structures. Thanks to recent developments in image-guided surgical techniques, cardiac surgery has benefited from reduced trauma and shorter recovery times for patients [3]. Nevertheless, minimizing invasiveness has inevitably led to more limited visual access to the target tissues. While incision sites have been reduced, and robotic and laparoscopic technologies have been introduced to minimize tissue exposure, most intracardiac interventions are still performed under cardiopulmonary bypass, which may lead to adverse effects [4,5].

N. Ayache, H. Delingette, and M. Sermesant (Eds.): FIMH 2009, LNCS 5528, pp. 466–475, 2009.
© Springer-Verlag Berlin Heidelberg 2009

Image-guided surgery (IGS) relies on the assumption that pre-operatively acquired images provide a sufficiently accurate representation of the intra-operative anatomy to guide the procedure. However, this assumption is not necessarily valid for most soft tissues, and it definitely poses a significant issue in cardiac applications. Considering the large myocardial deformations encountered during interventions, intra-operative imaging is indispensable to provide real-time information on the anatomical changes, and is often employed in the operating room (OR). Moreover, stereoscopic, virtual (VR) and augmented reality (AR) techniques have been implemented to enhance visualization and surgical guidance.

We have developed a novel surgical guidance package to facilitate therapy delivery on the beating heart. Our platform relies on trans-esophageal echocardiography (TEE) for real-time intra-operative guidance, pre-operative cardiac models for anatomical enhancement, and magnetic tracking technology for real-time tracking of surgical instruments [6]. As a result, clinicians can explore the intracardiac environment in real-time via US, using the registered pre-operative models as guides, and navigate tracked surgical tools intuitively relative to the 3D cardiac anatomy [7]. We envision that VR-enhanced ultrasound (US) guidance will eliminate the need for intra-operative fluoroscopic imaging and allow the fusion of surgical planning and guidance [8,9].

This paper provides an overview of our VR/AR-based surgical guidance platform, the development and integration of various components, the evaluation of the environment, and finally its translation from the image-guided surgery laboratory into the operating room.

2 Surgical Platform

2.1 Architecture

Our surgical guidance platform integrates a wide variety components for IGS applications, including multi-modality image visualization, anatomical modeling, and surgical tracking. Moreover, given the lack of visualization during off-pump surgery, we used this system to build an AR environment to provide surgeons with a virtual display of the surgical field that resembles the real intracardiac environment.

2.2 Augmented Reality Environment

The origins of our augmented reality surgical platform arose from the desire of our surgeon colleagues to develop a procedure for implanting a prosthetic mital valve inside the beating heart. Not only did they require a means of introducing multiple tools into the cardiac chambers, they also needed to manipulate and visualize these devices in real time.

Ultimately, transmural surgical access was enabled via the Universal Cardiac Introducer(UCI)©- a device that is attached to the heart chamber and acts as

an "air-lock" between the blood-filled cavity and the chest, enabling the positioning of surgical instruments, introduced into the throacic cavity via a mini-thoracotomy, inside the beating heart. Moreover, we proposed an intracardiac visualization approach that relied on intra-operative echocardiography for real-time imaging, augmented with representations of the surgical tools tracked in real-time and displayed within anatomical context available from pre-operative images. By carefully integrating all components, such an environment is capable to provide reliable tool-to-target navigation, followed by accurate on-target positioning.

Intra-operative Imaging: Echocardiography. Ultrasound is widely employed as a standard interventional imaging modality. Specifically, 2D TEE provides good-quality images and eliminates the interference between probe manipulation and surgical work-flow. However, the main drawback is its inability to depict sufficiently crisp representations of the anatomical targets and surgical tools. While such limitations may be tolerable in *in vitro* studies performed in a laboratory environment under ideal conditions, they are highly amplified in a clinical setting by the complexity and variability of the anatomy, image quality, and orientation of the US beam with respect to the anatomy (Fig. 1). To address these problems, we augment the 2D intra-procedure images with anatomical context supplied by the pre-operative models generated from CT or MR images acquired prior to the intervention.

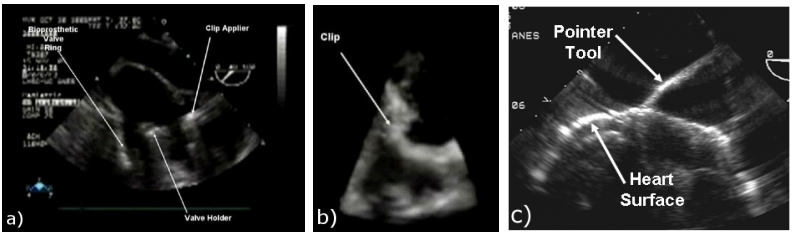

Fig. 1. a) 2D TEE image of the valve tool and clip applier inside a beating porcine heart; b) 3D US image of a similar scene; 2D TEE image of *in vitro* phantom study. Note the difficulty in interpreting the anatomical features and surgical tools.

Pre-operative Modeling. For *in vitro* studies involving cardiac phantoms, we rely primarily on pre-operative CT images for model building, given their good image contrast and temporal resolution, and make use of automatic techniques for image segmentation, such as the Vascular Modeling Toolkit[1]. On the other hand, once translating to clinical porcine studies, the insufficient contrast between cardiac structures provided by CT without contrast enhancement forced us to resort to the use of MR images. Their excellent soft tissue characterization facilitated the of anatomical feature identification, leading to better quality

[1] VMTK: http://www.vmtk.org

subject-specific models. We first model each cardiac component, then assemble them together according to the complexity of the procedure. Typically, the main features of interest include the left ventricle myocardium (LV), the left atrium (LA), the right atrium and ventricle (RA/RV), and aorta (Ao).

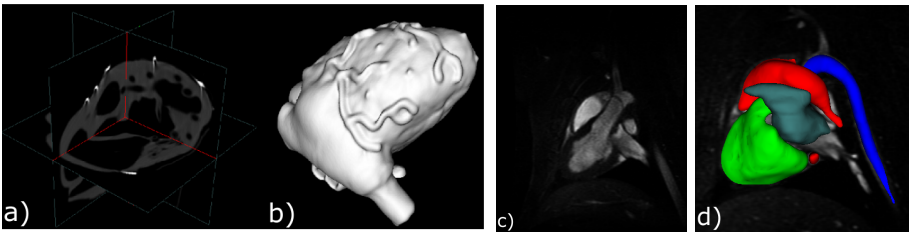

Fig. 2. a) CT image of beating heart phantom; b) Surface model of phantom extracted from CT image; c) Pre-operative cardiac MR image of porcine subject at mid-diastole; d) Heart model showing various chambers extracted from MR image

A common obstacle encountered is the extraction of fine anatomical structures (i.e. mitral or aortic valve) from low-resolution, thick-slice, clinical MR data. To address this issue, we have developed and tested a technique on human MR data that relies on fitting a high-resolution, average heart model to clinical-quality MR datasets of new subjects via non-rigid registration, leading to reasonably accurate subject-specific models. Nevertheless, for the time being, porcine cardiac models are generated via manual segmentation, as we are in the process of building a porcine heart atlas similar to that employed for humans.

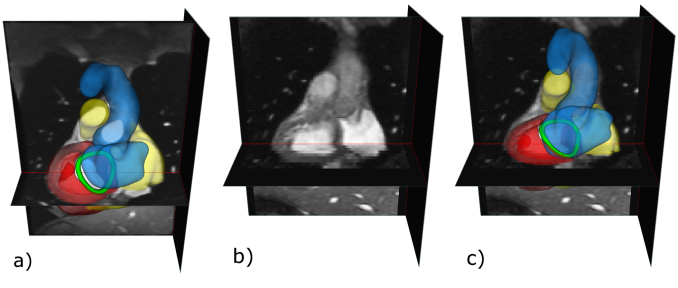

Fig. 3. a) Prior cardiac model at MD, containing segmented LV, LA/Ao, RA/RV, MVA, and AVA; b) Clinical quality subject MR image at MD; c) Clinical quality subject MR image segmented using the prior model

Ultimately, a dynamic cardiac model depicting the heart at different time points in the cardiac cycle is obtained by sequentially propagating the static model throughout the cardiac cycle with the motion estimated via non-rigid image registration [10] and rendered to portray the dynamics of the heart.

Model-to-Subject Registration. We employ a peri-operative feature-based registration technique to augment the intra-operative US images (Fig. 4a) with the pre-operative cardiac models (Fig. 4b). Easily identifiable targets in both datasets, the mitral (MVA) and aortic (AVA) valve annuli, are chosen to drive the registration. The pre-operative annuli are segmented manually from the cardiac MR image using a custom-developed spline-based segmentation tool (Fig. 4b). The intra-operative annuli are extracted from "pseudo" 3D US volumes generated by assembling 2D TEE images acquired at finite angular increments, according to their spatial and temporal time-stamps encoded by the tracking system and ECG-gating. The algorithm first aligns the centroids (translational component) and normal unit vectors (rotational component) corresponding to the homologous annuli, and ultimately refines the alignment via an iterative closest point approach, minimizing distance between homologous features.

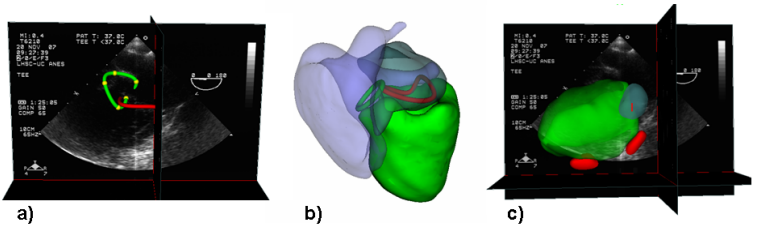

Fig. 4. a) Intra-operative US image, and b) pre-operative model, showing the MVA and AVA; c) Pre- and intra-operative datasets fused via feature-based registration

This mapping technique is suitable for cardiac interventions, as it does not significantly lengthen procedure time, the selected valvular structures are easily identifiable in both datasets, and they also ensure a good alignment of the pre- and intra-operative surgical targets. Furthermore, given the location of the features used to drive the registration, we expect good anatomical alignment in the surrounding regions, enabling us to employ this technique for a variety of image-guided intracardiac interventions.

Surgical Tool Tracking. For all off-pump interventions, the surgeon must to know the position and orientation of the instruments with respect to the intrinsic surrounding anatomy at all times during the procedure. We integrate this feature via surgical tool tracking using the NDI Aurora (Northern Digital Inc., Waterloo, Canada) magnetic tracking system. Virtual representations of the instruments, registered to their physical counterparts, are tracked in real time relative to the pre- and intra-operative anatomy within the AR environment. In addition, a reference sensor is attached to a stationary region of the subject to avoid the need to recalibrate the "world" coordinate system in case of accidental motion of the subject or field generator.

As an example, for a MV implantation, we need virtual representations for the TEE transducer, valve-guiding tool and valve-fastening tool Fig. 5. A more

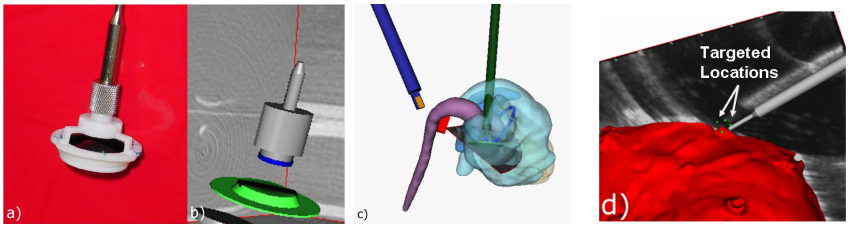

Fig. 5. a) Physical and b) virtual representation of a prosthetic mitral valve attached to the valve-guiding tool; c) AR environment specific to an *in vivo* porcine study, and d) *in vitro* beating heart phantom study

sophisticated model is required for the US probe, as it incorporates the video feed from the scanner and the image plane must be automatically adjusted to changes in rotation angle and depth as manipulated by the sonographer.

3 Assessing Therapeutic Feasibility

3.1 Endocardial Interventions in Phantoms

To assess the feasibility of surgical navigation under augmented reality-assisted guidance, we performed extensive tests *in vitro* on a beating heart phantom, mimicking left or right atrial endocardial procedures, where the surgeons would use a tracked instrument (i.e. ablation catheter) to "deliver therapy" to intracardiac targets in absence of direct vision. Moreover, we compared AR-guided targeting accuracy and procedure duration with those achieved under US image guidance alone (i.e., typical guidance modality employed for similar procedures), and endoscopic guidance. Although the latter is not a guidance option for intracardiac procedures, it nevertheless provides similar visualization to that available under direct vision, and therefore allows us to establish a positive control in terms of both accuracy and duration.

Three users conducted the *in vitro* catheter navigation on four surgical targets, whose positions were tracked simultaneously using 5 DOF magnetic tracking sensor coils. Each user attempted the targets in 4 trials (i.e., 4 consecutive target sequences, each with a different target order) under each guidance modality (endoscopic, VR-US, and 2D US image guidance). The procedure outcome was assessed according to the targeting accuracy — distance between the tip of the catheter and the surgical target at the time of contact, as well as the duration of each trial (Fig. 7).

3.2 Initiating Clinical Translation

Direct access to the cardiac chamber was achieved using the Universal Cardiac Introducer (UCI) [11]. The AR environment consisted of the pre-operative model

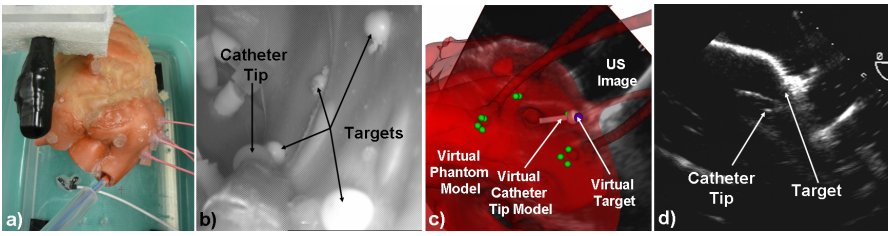

Fig. 6. Graphical representation of targeting accuracy and procedure duration achieved under endoscopic, VR-US, and 2D US image guidance, respectively. Note a significant improvement in both targeting accuracy and procedure duration under VR-US guidance with respect to 2D US image guidance.

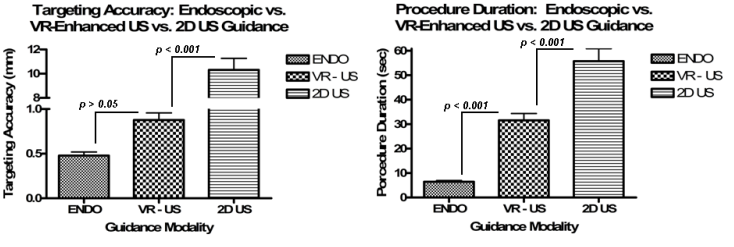

Fig. 7. Graphical representation of targeting accuracy and procedure duration achieved under endoscopic, VR-US, and 2D US image guidance, respectively. Note a significant improvement in both targeting accuracy and procedure duration under VR-US guidance with respect to 2D US image guidance.

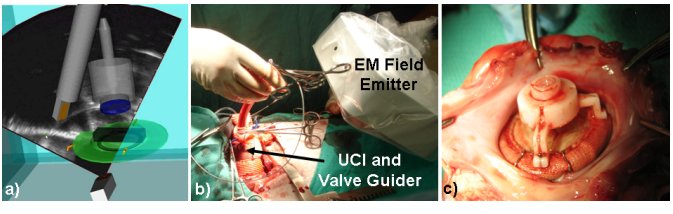

Fig. 8. a) AR environment showing virtual models of the US probe and surgical tools; b) OR setup during AR-guided interventions; c) Post-procedure assessment image

registered to the intra-procedure US, and virtual representations of the valve-guiding tool and valve-fastening tool, in this case a laparoscopic clip applier. The procedure involves the positioning and fastening of the valve onto the native mitral annulus. Both steps entail navigating the tools to the target under guidance provided by the virtual models, followed by the correct positioning and attachment of the valve via surgical clips, guided via US (Fig. 8). Intra-operative assessment using Doppler imaging confirmed a successful valve placement, also observed in the post-procedure analysis. Nevertheless, one of the applied surgical clips failed to properly secure the valve due to poor penetration into the tissue.

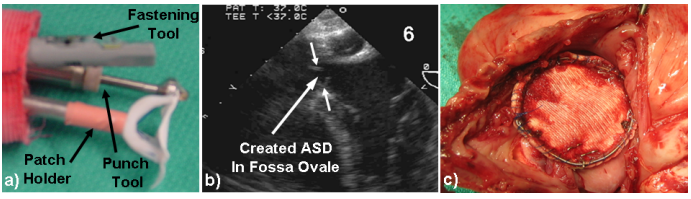

Fig. 9. a) Tools employed during the ASD creation and repair; b) 2D US image showing the septal defect; c) Post-operative image showing the successful ASD repair

The atrial septal defect (ASD) repair procedure entails similar tasks as the MV implantation, however the surgical target does not exist naturally in the porcine heart. The septal defect was therefore created by removing a circular disc of tissue from the fossa ovale under US guidance, using a "hole-punching" tool. The blood flow through the ASD was identifiable on Doppler US, and the repair patch was guided to the target under virtual reality guidance. Once on target, US imaging was used to correctly position the patch onto the created ASD and anchor it to the underlying tissue. Correct ASD repair was confirmed in the post-procedure assessment (Fig. 9b). While the VR-enhanced US guidance provided significant assistance in both navigation and positioning, this study also raised the need to improve tool design to better suit the limited intracardiac space.

4 Challenges and Lessons Learned

In spite of our recent successes, the translation from the lab to the clinic has helped us identify several roadblocks that had not posed major concerns within the *in vitro* laboratory conditions. Here we summarize some of these the issues.

One must keep in mind that cardiac IGS will always be prone to higher inaccuracies, mainly due to the high degree of rapid movement of cardiac tissue and the limitations of working in a blood filled environment. These challenges are further amplified by the difficulty of building perfect models of a subject's heart and the limited accuracy to register the model to the subject. In our work, we have studied model accuracy in predicting surgical target location [12], quantified the alignment of the pre- and intra-operative anatomy [13,14], and assessed the augmented reality-assisted targeting accuracy [15]. For the purpose of the applications of interest, our system proves clinically feasible, considering the magnetic surgical tracking accuracy on the order of 1-2 mm and the scope of the pre-operative models as aids to enhance intra-operative anatomical context.

Surgical tool design and manufacture, when subject to constraints imposed by the cardiac anatomy, interventional application, and surgical environment, is another challenge. To accommodate our needs, we built various prototypes (i.e., valve- or ASD patch-guiding tools) or adapt previous tools (i.e., laparoscopic abdominal stapler used as fixation device), embedded the MTS sensors within the tools, and tested their compatibility with the surgical environment. However,

the most efficient approach would be to involve a medical device manufacturer in the project and have them build tools that will help us achieve the millimetre accurcy goal for this project.

Over the years, surgeons have become used to "standard views" of human anatomy. However, minimal invasiveness restricts both visual and surgical access, and moreover, in off-pump intracardiac interventions, surgeons cannot "see" what they do; rather, the AR guidance platform **is** their eyes. Hence, we have learned that it is often best to maintain intuitive guidance by making use of displays most familiar to surgeons. The optimal approach is to make the new look as much like the old, and instead of overwhelming them with a lot of new technology at once, rather give them the time to get accustomed to the new environments, and let them tell you how impressed they are. For the time being, our surgical team has reported great comfort using both overhead monitors and head-mounted display (HMD) units for visualization, which allow the surgeons to directly "navigate" within a virtual volume [16].

5 Conclusions

We have briefly described several IGS components developed and validated in our laboratory and outlined the path to translate traditional cardiac surgery into an AR environment in a clinical setting. Some of the lessons learned while paving the road to the clinic have proved to be rather harsh and we still expect several other surprises down the road, given the increased complexity of the procedures attempted. Nevertheless, new image guidance tools are being developed continuously, a new cohort of surgeons is recruited annually, so is not unreasonable to expect that operating rooms of the future will be routinely equipped with image-guidance systems such as the system described here.

Acknowledgments. The authors thank Drs. Marcin Wierzbicki, Usaf Aladl and David Gobbi, and Jaques Milner for assistance with software development, and Sheri VanLingen and Karen Siroen for support with the animal studies. In addition, we acknowledge funding for this work provided by the NSERC, CIHR, HSFC, ORF and CFI.

References

1. Harken, D.E., Ellis, L.B., Ware, P.F.: The surgical treatment of mitral stenosis: valvuloplasty. N. Engl. J. Med. 239, 801–809 (1948)
2. Gibbon, J.R.: Application of a mechanical heart and lung apparatus to cardiac surgery. Minn Med. 37, 171–185 (1954)
3. Lutter, G., Ardehali, R., Cremer, J., Bonhoeffer, P.: Percutaneous valve replacement: current state and future prospects. Ann. Thor. Surg. 78, 2199–2206 (2004)
4. Downing, S.W., Edmunds, L.H.: Release of vasoactive substances during cardiopulmonary bypass. Ann. Thorac. Surg. 54, 1236–1243 (1992)

5. Zeitlhofer, J., Asenbaum, S., Spiss, C., Wimmer, A., Mayr, N., Wolner, E., Deecke, L.: Central nervous system function after cardiopulmonary bypass. Eur. Heart J. 14, 885–890 (1993)
6. Linte, C.A., Moore, J., Wiles, A.D., Wedlake, C., Peters, T.M.: Virtual reality-enhanced ultrasound guidance: A novel technique for intracardiac interventions. Comput. Aided Surg. 13, 82–94 (2008)
7. Sauer, F.: Image registration: Enabling technology for image-guided surgery and therapy. In: Proc. of IEEE Eng. Med. Biol. Soc., pp. 7242–7245 (2005)
8. Wilson, K., Guiraudon, G.M., Jones, D.L., Peters, T.M.: 4D shape registration for dynamic electrophysiological cardiac mapping. In: Larsen, R., Nielsen, M., Sporring, J. (eds.) MICCAI 2006. LNCS, vol. 4191, pp. 520–526. Springer, Heidelberg (2006)
9. Wilson, K., Guiraudon, G.M., Jones, D.L., Linte, C.A., Wedlake, C., Moore, J., Peters, T.M.: Dynamic cardiac mapping on patient-specific models. In: Metaxas, D., Axel, L., Fichtinger, G., Székely, G. (eds.) MICCAI 2008, Part I. LNCS, vol. 5241, pp. 947–974. Springer, Heidelberg (2008)
10. Wierzbicki, M., Peters, T.M.: Determining epicardial surface motion using elastic registration: Towards virtual reality guidance of minimally-invasive cardiac interventions. In: Ellis, R.E., Peters, T.M. (eds.) MICCAI 2003. LNCS, vol. 2878, pp. 722–729. Springer, Heidelberg (2003)
11. Moore, J., Guiraudon, G.M., Jones, D.L., Hill, N., Wiles, A.D., Bainbridge, D., Wedlake, C., Peters, T.M.: 2D ultrasound augmented by virtual tools for guidance of interventional procedures. In: Proc. Medicine Meets Virtual Reality. Stud. Health Technol. Inform., vol. 125, pp. 322–327 (2007)
12. Linte, C.A., Wierzbicki, M., Moore, J., Guiraudon, G.M., Little, S.H., Peters, T.M.: Towards subject-specific models of the dynamic heart for mitral valve surgery. In: Ayache, N., Ourselin, S., Maeder, A. (eds.) MICCAI 2007, Part II. LNCS, vol. 4792, pp. 94–101. Springer, Heidelberg (2007)
13. Wiles, A.D., Linte, C.A., Moore, J., Wedlake, C., Peters, T.M.: Object identification accuracy under ultrasound enhanced virtual reality for minimally invasive cardiac surgery. In: Medical Imaging 2008: Visualization, Image-Guided Procedures and Modeling. Proc. of SPIE, vol. 6918 (2008) (in press)
14. Linte, C.A., Moore, J., Wedlake, C., Bainbridge, D., Guiraudon, G.M., Jones, D.L., Peters, T.M.: Inside the beating heart: An in vivo feasibility study on fusing pre- and intra-operative imaging for minimally invasive therapy. Int. J. CARS (2008), doi:10.1007/s11548-008-0278-6 (in press)
15. Linte, C.A., Wiles, A., Moore, J., Wedlake, C., Peters, T.M.: Virtual reality-enhanced ultrasound guidance for atrial ablation: In vitro epicardial study. In: Metaxas, D., Axel, L., Fichtinger, G., Székely, G. (eds.) MICCAI 2008, Part II. LNCS, vol. 5242, pp. 644–651. Springer, Heidelberg (2008)
16. Birkfellner, W., Figl, M., Matula, C., Hummel, J., Hanel, R., Imhof, H., Wanschitz, F., Wagner, A., Watzinger, F., Bergmann, H.: Computer-enhanced stereoscopic vision in a head-mounted operating binocular. Phys. Med. Biol. 48, 49–57 (2003)

Computer-Assisted Open Heart CABG: Image-Guided Navigation for All Target Vessels

Claudia Gnahm[1], Christine Hartung[1], Reinhard Friedl[2], Martin Hoffmann[3], and Klaus Dietmayer[1]

[1] Institute of Measurement, Control and Microtechnology, University of Ulm
[2] Department of Cardiac Surgery, University Hospitals of Ulm and Lübeck
[3] Department of Diagnostic Radiology, University Hospital of Ulm

Abstract. During open heart coronary artery bypass grafting (CABG), optimal placement of the bypass graft on the diseased target vessel is of utmost importance. To assist the heart surgeon in this matter, a surgical navigation system has been developed. The concept includes preprocedural planning of the optimal position for the distal anastomosis (surgical target) on the target vessel and intraoperative image-guided navigation to that position. Navigation is enabled by registration of pre- and intraoperative data. The registration mechanism was validated retrospectively. Promising results justified subsequent intraoperative live application of the system during 11 open heart CABG surgeries enabling navigation on 21 target vessels on the anterior, lateral and inferior wall of the heart. In each case, the employed registration mechanism ensured good alignment of preoperatively planned and intraoperatively identified surgical targets. The system is very well applicable for in-vivo navigation and allows for bypass grafting precisely at a preoperatively planned position.

1 Introduction

CABG is the standard treatment for advanced coronary heart diseases. In this revascularisation procedure, sufficient blood flow to the heart muscle distal to a stenosis is restored by a blood vessel graft. Optimal placement of the bypass graft on the diseased vessel is of great importance. To assist the surgeon in this matter and to facilitate navigation on the coronary vessels, a surgical assistance system has been developed within the Cardio-Pointer project. The system has been validated retrospectively on patient data from CABG surgeries. Yielding good results with sufficient accuracies, this validation led to successful in-vivo application of the navigation system during several bypass grafting procedures.

In surgical disciplines such as neurosurgery and orthopaedic surgery, navigation systems are widely used nowadays [1],[2]. Concerning cardiac interventions, valuable research has been done in the field of minimally invasive surgery [3]. In open heart surgery, the development of surgical assistance systems is still at the beginning, the Cardio-Pointer project being the first approach to develop a surgical assistance system for open heart CABG with navigation at the beating [4] and the arrested heart. This work focuses on navigation at the arrested heart.

N. Ayache, H. Delingette, and M. Sermesant (Eds.): FIMH 2009, LNCS 5528, pp. 476–485, 2009.
© Springer-Verlag Berlin Heidelberg 2009

2 Methods

On the medical side, the live application of the navigation system comprises a preoperative planning step during which the position of the optimal anastomosis site on the diseased target vessel is planned and an intraoperative navigation step during which the heart surgeon uses a surgical pointing device (Cardio-Pointer) to perform image-guided navigation to the planned position. For preoperative planning, a cardiac MSCT (multi slice computed tomography) is analysed, while an optical tracking system is used to acquire intraoperative data directly prior to bypass grafting. Intraoperative navigation on the surface of the heart is facilitated by registration of both data sets. This is illustrated in Fig. 1. Intraoperative setup and Cardio-Pointer are depicted as well.

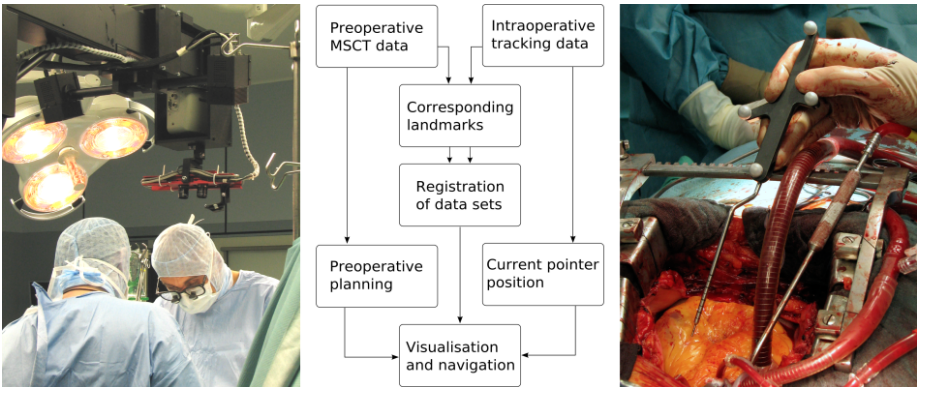

Fig. 1. *Left:* Intraoperative setup showing an optical tracking system mounted on a video robot arm; *Centre:* Schematic view of the usage of pre- and intraoperative data for navigation; *Right:* Cardio-Pointer on the heart surface as used by the surgeon

On the technical side, facilitating navigation on the surface of the arrested heart comprises four steps, one of them prior to surgery and three during surgery:

1. Preoperative Data Recording and Processing: During the last few years, MSCT has rapidly advanced and evolved as reliable modality for non-invasive coronary imaging [5]. Here, MSCT data were acquired post contrast-enhancement with Imeron 400 using a post-threshold-delay of 11 s. In the MSCT images, lumen information and wall plaque formations are very well visible allowing for preoperative planning of the optimal position for each bypass graft (distal anastomosis). This is done jointly by operating heart surgeon and diagnostic radiologist. Then, the planned 3D position for each distal anastomosis is extracted together with plaque positions inside the target vessels. The preprocedural cardiac MSCT also builds the first half of the data basis used for registration. To establish this data basis, the 3D positions of potential anatomical point landmarks and vessel path centrelines

are extracted from the CT data. Potential anatomical point landmarks are vessel bifurcations, crossing points of arteries and veins and other distinctive points which might be visible during surgery. That means, all landmarks which could be useful are extracted, whereas not all of them are actually available during surgery because of possible coverage with epicardial fat. Which landmarks are available for registration turns out intraoperatively. Preprocedural extraction of all potential landmarks helps keeping time need during ischaemia as short as possible. For intraoperative visualisation and image-guidance, a map of the coronaries including planned anastomosis sites and plaque positions is generated from the MSCT images.

2. Intraoperative Data Recording: During surgery, the arrested heart is repositioned prior to grafting each bypass. As it is intended to represent the operating situs, intraoperative data have to be recorded after positioning the heart for subsequent bypass grafting. Intraoperative data is recorded with an infrared optical tracking system. Therefore, the surgeon uses a surgical pointing device (Cardio-Pointer) which is trackable via reflective markers. The 3D position of the tip of the pointer is continuously recorded while the surgeon points at anatomical point landmarks actually visible on the heart surface and retraces visible parts of the target vessel path and neighbouring arteries and veins. The positions of point landmarks and vessel paths obtained that way build the second half of the data basis used for registration.
3. Registration of the Pre- and Intraoperative Data Sets: The position for the planned anastomosis site is extracted from preoperative data while the arrested heart as currently positioned in the operating field is represented by intraoperative data. Successful matching of both data sets facilitates navigation on the arrested heart. For registration, corresponding landmarks and vessel paths available in both, the pre- and the intraoperative data set are used. The registration mechanism is described below.
4. Visualisation and Navigation: After registration, the map of the coronaries around the target vessel is visualised on a video screen showing both, the preoperatively planned anastomosis site and the current position of the tip of the pointer. The position of the pointer is continuously updated, reflecting the movement of the pointer. This way, the surgeon can navigate with the pointer on the arrested heart and is guided to the intraoperative position of the sugical target: the preoperatively planned anastomosis site.

Being cannulated, relaxed and not beating, the arrested heart is considerably deformed compared to its preoperative shape. Moreover, severe deformations occur as soon as the heart is manually brought into a position which exposes the target vessel in the centre of the operating field. In most patients, large parts of the heart surface are covered with epicardial fat which diminishes the number of landmarks available for registration as only a few of the potential point landmarks and vessel paths are actually visible on the heart surface. Thus, the registration mechanism has to cope with two challenges arising during open heart bypass grafting at the arrested heart: The significant deformation of the heart between pre- and intraoperative data recording and the limitation of corresponding

landmarks. The multi-step registration mechanism presented here is able to deal with both challenges: A deformation correction mechanism completes the registration process and the generation of additional landmarks based on the unaltered length of the target vessel path is provided. The multi-step registration mechanism for the arrested heart consists of three consecutive steps:

1. Rigid Registration of pre- and intraoperative data sets using corresponding point landmarks. This step provides coarse alignment of the data sets. Subsequently, this is used as initialisation for the ICP (iterative closest point) algorithm in step 2.
2. An Enhanced Weighted ICP Algorithm is applied to refine the matching using corresponding vessel paths. Usable are all parts of vessel paths which are visible in the target region. The enhanced weighted ICP is an improved version of the basic ICP algorithm [6]. A basic ICP would not be applicable as it has difficulties with considerable changes in the shape of preoperative and intraoperative data. For open heart CABG at the arrested heart, the trajectory of any vessel path is not preserved between pre- and intraoperative data acquisition because of connection to the heart lung machine and manual positioning of the heart, and the registration process has to take that into account. Thus, a subsequent deformation correction is performed in step 3. The enhanced, weighted ICP developed for the arrested heart allows for individual weighting of the data and provides optimal preparation of the data for this deformation correction. In contrast to a basic ICP which aims at the best overall matching of the data, the desired outcome from the enhanced, weighted ICP is the best matching of less deformed areas in which the shape of the vessel path is preserved to some extent. For that purpose, larger weighting factors are assigned to little deformed parts of the vessel path, while smaller weighting factors are assigned to strongly deformed parts. Hence, matching of less deformed parts is favoured. This leaves the strongly deformed areas not optimally matched but in the best possible initial position for the subsequently applied deformation correction mechanism. The deformation correction step then corrects the shape of the vessel path according to its deformations. For more details see [7].
3. Correction of Major Deformations resulting from positioning of the arrested heart for bypass grafting and thus further improvement of the matching. Deformation correction is done along the target vessel path. The correction mechanism is based on the heart being modelled as rotationally symmetric object with regard to an heuristically estimated central axis of the heart. The estimation of the torsion axis is based on the anatomy of the patient's heart. The heart region where the major vessels connect the heart with the body is not moveable during surgery but remains in the same anatomical position as prior to surgery. Therefore, one point of the axis is chosen in the centre of a cross section of this area. The cardiac apex is chosen as the other axis point. The torsion angle of the tracking data in comparison to the MSCT centreline is calculated with respect to this axis for each tracking data point of the vessel path. Then, the variation of the torsion angle along the vessel is approximated

using either polynomial curve fitting or piecewise linear approximation. The resulting function of torsion angle difference along the torsion axis is used to un-distort the tracking data after rescaling the vessel length accordingly (see Fig. 3). Likewise employed is the surface of the rotationally symmetric object which serves as a model for the heart as a point on a vessel path always is situated on the surface of the heart.

Using this mechanism, registration is possible for patients which exhibit a minimum of three corresponding point landmarks and one part of the target vessel path. To incorporate even more patients and lower the minimally required amount of landmarks, a method for the generation of additional landmarks is provided. To establish the generation method, the length of known parts of vessel paths has been analysed at the beating and the arrested, manually positioned heart. As no change in the length was found, the retained vessel length is used for the generation of additional landmarks. This is viable as soon as one part of the target vessel adjacent to one landmark but not necessarily including the preoperatively planned anastomosis site is visible. Additional landmarks are generated in cases where the multi-step registration mechanism could otherwise not be used by reason of to the shortage of visible landmark points, i.e. in cases where only 1 or 2 point landmarks are visible. After generation, the additional landmarks are used together with the recorded landmarks in the multi-step registration mechanism.

The unaltered length of the vessel path has another benefit: an alternative registration and navigation method can be considered based on the retained length of corresponding parts of the vessel path. If the relevant part of the vessel path is visible during surgery, it has to exhibit only one corresponding point landmark to facilitate navigation along the visible vessel path. This alternative registration method is only usable when the target vessel path is both visible in the relevant region and exhibiting one reliable landmark. Note that in comparison, the multi-step registration mechanism - with or without additionally generated landmarks - enables navigation not only on the vessel path itself but in the region around the relevant vessel as well. For that, the target vessel neither has to be visible at the target position nor has it to exhibit one landmark as long as the minimum prerequisites are fulfilled. However, the alternative registration method is a valuable tool and was successfully used during several CABG procedures, especially for target vessels on the lateral and inferior wall of the heart.

3 Results

The registration mechanism developed for the arrested heart has been validated in two phases: At first, intraoperative tracking data sets recorded during bypass grafting procedures have been registered retrospectively with preoperative CT data. The registration results obtained this way were very promising and justified subsequent in-vivo testing of the registration mechanism. Thus, the intraoperative modus operandi was altered to enable not only data recording but also immediate registration and subsequent navigation on the arrested heart.

3.1 Retrospective Registration

A preoperative MSCT scan and intraoperative tracking data were recorded for 20 patients undergoing CABG surgery. Intraoperative data was recorded after the heart was manually brought into an appropriate position exposing the target vessel in the centre of the operating field. Retrospective registration was performed on data sets from target vessels on the anterior, lateral and inferior wall of the heart including the LAD (left anterior descending artery), branches of the LAD (D1 and D2), LCX (left circumflex artery), RIM (ramus intermedius), RMS (ramus marginalis sinister, i.e. left marginal artery), RCA (right coronary artery) and PDA (posterior descending artery). Per patient, data from 1 to 3 target vessels were recorded. Even though considerable deformations of the heart were observed for each target vessel, the multi-step registration mechanism for the arrested heart - where required using additionally generated landmarks - provided matching of pre- and intraoperative data with sufficient accuracy in all cases. This means, the registration accuracy reached the intraoperative spatial measurement inaccuracy (see below). Retrospective registration was performed on a total of 35 target vessels. 16 of the data sets provided at least the minimum of 3 corresponding anatomical point landmarks, while the remaining data sets provided only 1-2 corresponding point landmarks. The latter data sets are not qualified directly for the multi-step registration mechanism. In these cases, additional landmarks were generated and then used in the multi-step registration mechanism together with the recorded landmarks. Hence, the generation of additional landmarks enabled the registration of many data sets which could otherwise not have been matched. The average amount of available corresponding point landmarks was 2.4, on average 0.9 landmarks had to be generated additionally to allow for registration of the pre- and intraoperative data sets. In summary, 3 to 5 point landmarks (including recorded and generated ones) were used per data set for registration. Whether or not additional landmarks had to be used in the registration mechanism did not affect the resulting accuracies. This means, the generation of additional landmarks makes it possible to include patient data sets with less than 3 corresponding point landmarks in the multi-step registration mechanism without foregoing sufficient precision. The RMS registration errors of the corresponding point landmarks and the distances of corresponding vessel paths were calculated to evaluate the retrospective registration result. In the calculation of the error of the corresponding landmarks, each corresponding landmark pair was regarded independent of their possible usage in the registration process. This proceeding results from two facts. First, in most cases all available pairs of corresponding point landmarks had to be used to facilitate registration so that no other corresponding point landmarks remained for the calculation of the error alone. Second, all corresponding point landmarks are used only for rough matching in the first step of the registration process and their position is changed as the matching is refined in the following steps. For the calculation of the RMS distance of the vessel paths, all available vessel paths in the target region were considered. For all 35 target vessels, an average RMS

Table 1. Retrospective Registration: Target vessels and errors

Target vessels for retrospective registration	
Number of anterior wall target vessels (LAD, D1, D2)	20
Number of lateral wall target vessels (LCX, RIM, RMS)	10
Number of inferior wall target vessels (RCA, PDA)	5
Registration errors	
RMS error of corresponding point landmarks (in mm)	2.1 ± 1.1
RMS error of corresponding vessel paths (in mm)	1.2 ± 1.0

of 2.1 ± 1.1 mm was obtained for the corresponding point landmarks, while the average RMS distance of the vessel paths after registration amounted to 1.2 ± 1.0 mm (see Table 1). As expected, the average RMS distance of the vessel paths is smaller than the average RMS of the corresponding landmark points. This results from the fact, that the RMS distance considers the vessel displacement perpendicular to the vessel path but cannot include displacements alongside the vessel path. The good results from the retrospective utilisation of the registration mechanism led to intraoperative live application of the assistance system for navigation on all target vessels for bypass grafting.

3.2 Intraoperative Registration and Navigation

Live application of the computer assistance system was realised during 11 bypass grafting procedures with in-vivo navigation on a total of 21 target vessels on the anterior, lateral and inferior wall of the heart. Both, the complete registration mechanism and the alternative vessel length registration were used for matching of the preoperative CT data and the intraoperative optical tracking data. Results indicated no preference for either method. For each target vessel, intraoperative data recording, registration of data sets and navigation to the preoperatively planned position were performed consecutively, the whole process taking 3-4 minutes. During this short period of time any movement of the heart has to be avoided. Due to unintended movement of either heart or operating table the successful registration was not long enough valid for navigation in two cases. Such incidents are attributed to the learning curve and are expected to become rarer. As re-registration was not performed with regard to the ischaemic time both cases are not considered further in this context. Intraoperative navigation was performed on 21 target vessels including LAD, D2, RIM, RMS, LCX, RCA and PDA. On a video screen in the OR, the patient's coronary map including the optimal anastomosis site as preoperatively planned by the heart surgeon and cardiac radiologist was displayed. After registration, the current position of the Cardio-Pointer was displayed as well. This pointer position was continuously updated while the surgeon moved the pointer along the target vessel until current pointer position and planned anastomosis site coincided. This position resulting from the image-guided navigation was marked with a clip right beside the vessel

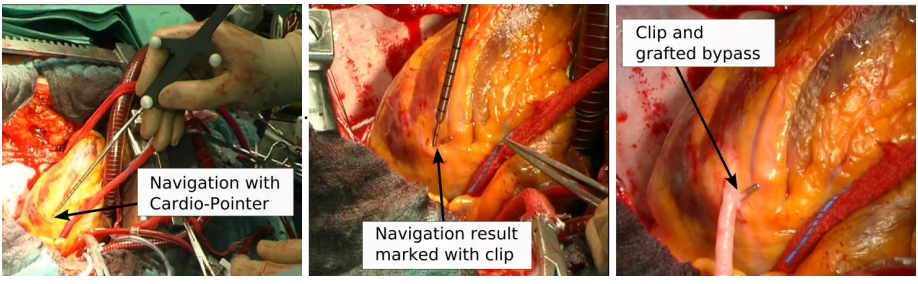

Fig. 2. Intraoperative navigation, operating field: navigation on the heart; navigation result is marked with a clip; bypass is grafted next to the clip, at the planned site

and then the bypass was grafted. The operating field is shown in Fig. 2, the intraoperative visualisation during navigation in Fig. 3 (left).

The precision of intraoperative navigation results was evaluated by comparison of pre- and postoperative CT data of the patients (see Fig. 3 (right)). In both CT data sets, the same reference point on the target vessel was chosen. From this point, the distance along the target vessel path to the planned and grafted anastomosis respectively was calculated and compared, yielding how precisely the bypass was grafted to the preoperatively planned position. Measurement inaccuracies at the most ± 1 mm may occur when determining the centre of the grafted anastomosis and the centre of the reference point in the CT data sets. This results in a measurement inaccuracy not exceeding ± 2 mm for the distance calculations and thus the accuracy assessment for the intraoperative navigation. In two cases, the bypass was not grafted to the preoperatively planned position because of medical reasons and thus the clip marking the navigation result was used for postoperative evaluation. In all other cases, the centre of the anastomosis which usually has an extension of several mm was used. For the 21 target vessels, the resulting navigation accuracy was 2.3 ± 1.4 mm, proving good accordance of the preoperatively planned position and the navigation result. This achieved

Fig. 3. *Left:* Intraoperative navigation, CT visualisation: planned anastomosis site (violet +) and current pointer position (green x) are displayed in the coronary map; *Right:* Evaluation: Preoperative and postoperative CT with distances from the same bifurcation to the planned (left) and grafted (right) anastomosis respectively

Table 2. Intraoperative navigation: Target vessels and errors

Target vessels	
Number of anterior wall target vessels	8
Number of lateral wall target vessels	9
Number of inferior wall target vessels	4
Navigation results	
Mean distance of planned and grafted anastomosis (in mm)	2.3
Standard deviation of the distances (in mm)	1.4
Maximum distance (in mm)	4.9
Minimum distance (in mm)	0.0

accuracy actually reaches the limiting spatial measurement accuracy at the arrested heart which amounts to ± 2.2 mm. This limiting measurement accuracy was evaluated by multiple recording of the same point landmark and deviation of data from point landmarks situated on a vessel path from the recorded vessel path. It mainly arises from the spatial extension of anatomical point landmarks and the lateral extension of vessels but includes also inaccuracies of tracking system and surgical pointer and effects of the breathing motion of ± 0.6 mm. The target vessels and navigation results are outlined in Table 2.

The accuracy of the computer-assisted intraoperative navigation during open heart CABG at the arrested heart could not be compared to the results from traditional open heart CABG surgery. Unfortunately, such a comparison is not possible as no comparable data exist from traditional open heart surgery. This results mainly from the fact that in current clinical practise CABG anastomoses are not grafted at the position on the target vessel they would have been situated best according to preoperative plans but either where the target vessel is visible best or where the surgeon believes may be the best alternative depending on his experience and skills. The aim in computer-assisted surgery is quite different. Here, the purpose is to identify the position of a preoperatively planned surgical target during CABG surgery and to graft the bypass exactly at that planned position on the target vessel path. An intraoperative navigation accuracy of 2.3 ± 1.4 mm was achieved for the 21 cases. Moreover, the incision for the bypass graft which is several mm long included the preoperatively planned position in all 21 cases. This shows that grafting a bypass precisely at a preoperatively planned position was successfully enabled with the developed system.

4 Discussion

The surgical assistance system developed within the Cardio-Pointer project is capable of providing precise navigation assistance during open heart CABG. The underlying registration mechanisms have been developed on patient data sets from CABG surgeries and the performance of the system has been evaluated during 11 bypass grafting procedures. The system successfully enabled

computer-assisted navigation on 21 target vessels for bypass grafting on the anterior, lateral and inferior wall of the heart. After successful registration, the heart surgeon efficiently performed navigation to the preoperatively planned position. Postoperative evaluation of the navigation results shows good accordance of preoperatively planned and intraoperatively identified positions for the distal anastomosis. Hence, the developed system facilitates image-guided navigation during open heart CABG and allows the heart surgeon to precisely graft the bypass to a preoperatively planned optimal anastomosis site. This increases not only the precision of open heart bypass grafting but also patient safety by providing a precise and low-risk method to identify a preoperatively defined surgical target on the deformed and possibly fat-covered surface of the heart.

Acknowledgements

This work is supported by the Federal Ministry of Education and Research (BMBF), project 01EZ0614. Thanks to Sabine Wuchenauer for preprocessing of the CT data.

References

1. Grimson, E., et al.: Clinical Experience with a High Precision Image-Guided Neurosurgery System. In: Wells, W.M., Colchester, A.C.F., Delp, S.L. (eds.) MICCAI 1998. LNCS, vol. 1496, pp. 63–73. Springer, Heidelberg (1998)
2. DiGioia, A., et al.: Computer Assisted Navigation Systems for Hip and Knee Reconstructive Surgery. In: DETEC. ASME 2001 Design Engineering Technical Conferences and Computers and Information in Engineering Conference (2001)
3. Mourgues, F., Vieville, T., Falk, V., Coste-Manière, E.: Interactive Guidance by Image Overlay in Robot Assisted Coronary Artery Bypass. In: Ellis, R.E., Peters, T.M. (eds.) MICCAI 2003. LNCS, vol. 2878, pp. 173–181. Springer, Heidelberg (2003)
4. Hartung, C., Gnahm, C., Friedl, R., Hoffmann, M., Dietmayer, K.: Computer-Assisted LAD Bypass Grafting at the Open Heart. In: Proc. SPIE Med. Imaging (2009)
5. Raff, G.L., Gallagher, M.J., O'Neill, W.W., Goldstein, J.A.: Diagnostic Accuracy of Noninvasive Coronary Angiography using 64-slice Spiral Computed Tomography. J. Am. Coll. Cardiol. 46(3), 552–557 (2005)
6. Besl, P.J., McKay, N.D.: A Method for Registration of 3-D Shapes. IEEE Trans. Pattern Anal. Mach. Intell. 14(2), 239–256 (1992)
7. Gnahm, C., Hartung, C., Friedl, R., Hoffmann, M., Dietmayer, K.: Towards Navigation on the Heart Surface during Coronary Arterty Bypass Grafting. Int. J. CARS (2008), http://www.springerlink.com/content/88161p22p6743754

Extraction of Coronary Vascular Tree and Myocardial Perfusion Data from Stacks of Cryomicrotome Images

Pepijn van Horssen[1], Jeroen P.H.M. van den Wijngaard[1], Froukje Nolte[1], Imo Hoefer[2], Rene Haverslag[2], Jos A.E. Spaan[1], and Maria Siebes[1]

[1] Dept. of Biomedical Engineering & Physics, Academic Medical Center, University of Amsterdam, Meibergdreef 9
1105 AZ, Amsterdam, The Netherlands
[2] Dept. of Experimental Cardiology, Utrecht Medical Center, Heidelberglaan 100, 3584 CX, Utrecht, The Netherlands
P.vanHorssen@amc.uva.nl

Abstract. Computational models of myocardial perfusion in normal as well as pathological conditions have contributed to recent advances in the personalized diagnosis and treatment of cardiovascular disease.. For the coronary circulation we attempt to develop a vascular tree model based on realistic replicas from the intramural vessels in hearts from animals and man. These virtual replicas are obtained by means of a novel imaging cryomicrotome producing a stack of 4000 images of 2000x2000 pixels. This paper describes the methods developed for segmentation of the images resulting in a 3D virtual vascular model. Also the methods for fluorescent microsphere detection are described used to validate the models in prediction of flow distribution over the walls of the heart chambers. Special attention is provided to the detection of collaterals and collateral flow.

Keywords: Myocardial perfusion, imaging cryomicrotome, coronary collateral flow, centerline extraction.

1 Introduction

Coronary Artery Disease (CAD) accounts for almost 2 million deaths within the EU on an annual basis. As a consequence, improved diagnosis and treatment of CAD may significantly benefit patients as well as reduce economic cost. A recently started European research initiative, euHeart (www.euHeart.eu) targets the personalized diagnosis and treatment of cardiovascular disease through the use of computational models. An important step in the development of computational predictive models of myocardial perfusion is the accurate estimation of physiological parameters and validation of coronary and microvascular resistances. Subsequently, such models may be used for improved diagnosis in the form of patient-specific personalized computational models of myocardial perfusion.

In case the perfusion of a certain area of the heart becomes compromised by a coronary stenosis, flow is increased through collateral arteries connecting the distal tissue at risk for ischemia with an area that receives sufficient flow. As a consequence

N. Ayache, H. Delingette, and M. Sermesant (Eds.): FIMH 2009, LNCS 5528, pp. 486–494, 2009.
© Springer-Verlag Berlin Heidelberg 2009

of enhanced flow, the fluid shear stress at the vascular wall is increased which drives outward growth of the collateral vessel. To stimulate collateral development, several pharmaceutical and stem cell therapies have been developed and tested [1]. Evaluation of these therapies is essential to establish cause and effect relations in patients. However, success in human subjects has been limited, in contrast to animal models.

A simplified scheme illustrating collateral flow in a model of coronary stenosis is shown in Fig. 1.

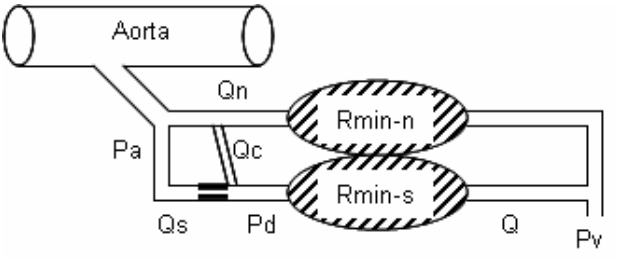

Fig. 1. Schematic overview of coronary collateral flow between two perfusion territories. From a main coronary branch with blood pressure Pa (mmHg), flow divides into two vessels. One vessel with normal flow, Qn (ml/min), perfuses the normal microvascular bed with resistance Rmin-n (mmHg/ml·min). The second vascular bed lies downstream of a stenosed artery with reduced flow (Qs) and distal pressure (Pd). The resulting pressure difference between the two branches causes collateral flow (Qc) which adds to Qs to yield the total flow, Q, to the vascular bed supplied by the stenotic vessel.

Such lumped models are widely used for the interpretation of clinical data [2], however, inherent simplifications may prevent rather than produce improved insight into underlying mechanisms. It is frequently assumed that the microvascular resistances at full vasodilation are constant and that the simple measurement of Pd would be sufficient to parameterize the model. However, vessels are not rigid tubes but compliant, making coronary resistance a function of distending pressure [3, 4, 5]. Moreover, because of cardiac contraction related compression of intramural vessels, resistance per unit mass differs strongly between tissue layers close to the ventricular cavity (subendocardium) and those close to thoracic space (subepicardium). It is obvious that the intramural position of the collateral vessel is relevant as well.

A computational model of myocardial perfusion that takes these dependencies into account may greatly enhance our understanding of the limits of applicability of these parameters, and may suggest additional clinical parameters to assess coronary or microvascular dysfunction. In order to arrive at such a model, data of myocardial perfusion acquired during various states of induced perfusion limitation are necessary. Measurements of blood pressure and flow velocity distal to an artificially created stenosis may provide necessary data for computational models of myocardial perfusion. A 3-dimensional reconstruction of the coronary arterial tree can be obtained by means of our imaging cryomicrotome [6] together with microsphere distributions for perfusion measurements.

In this paper we outline the methodology of especially the image processing aspects of the imaging cryomicrotome in relation to vascular bed reconstruction and microsphere detection.

2 Material and Methods

2.1 Experimental Protocol

Animal experiments were carried out in which normal coronary perfusion and conditions where perfusion was limited by balloon occlusion were evaluated during infusion of five different colors of microspheres. The experiments were conducted in accordance with the local institute's ethical regulations for animal research.

Infusion catheters were used to selectively deliver a dose of approximately 100.000 fluorescent microspheres (15µm, Invitrogen, The Netherlands) into the left anterior descending artery, LAD, and left circumflex artery at different levels of balloon inflation.

After the experiment, the heart was removed and flushed with a buffer solution containing adenosine. A cast replica material of Batson no. 17 (Polysciences, USA) consisting of a monomer base solution, a catalyst and a promoter was infused throughout the arterial system as described previously [6]. Potomac Yellow (Radiant Colour, Belgium) provided the fluorescent base for the replica plastic. The cast material was then allowed to harden over a period of 24 hours at ambient temperature. The fully prepared heart was embedded in a solution of carboxymethylcellulose sodium solvent (Brunschwig Chemie, Amsterdam, Netherlands) and Indian ink (Royal Talens, Apeldoorn, Netherlands) and frozen at minus 20 degrees Celsius [6]. Structural information on the geometry of the vascular tree and the distributions of the microspheres was retrieved by using a specially developed imaging cryomicrotome [7].

The hemodynamic measurement are not analyzed in this report and therefore not further described.

2.2 The Imaging Cryomicrotome

In the imaging cryomicrotome (Fig. 2), the frozen heart was cut sequentially with 40 µm slices. After each slice, the surface of the remaining bulk material was imaged using a 2048x2048 pixel camera equipped with a 70-180 mm lens [1]. Filter wheels for excitation and emission, containing five filters each, allowed a specific bandwidth of light to be imaged. A high-resolution digital reconstruction of the sample was created from the image stack based on 40 µm voxels.

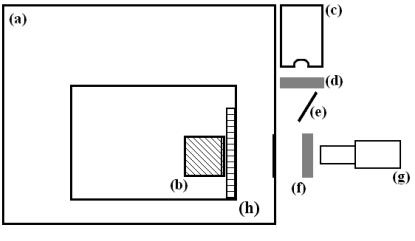

Fig. 2. Schematic overview of the imaging cryomicrotome. (a) Cryostat at minus 20 degrees Celsius. (b) Embedded sample. (c) 250W Xenon lamp. (d) Excitation filterwheel. (e) Mirror. (f) Emission filterwheel. (g) Camera with lens (h) Cutting mechanism.

2.3 Extraction of the Vessel Centerlines

After acquiring the three dimensional data set, a series of filters was applied to retrieve the centerlines of the vascular tree. First, the image stack was checked for inconsistencies in continuity in the longitudinal direction. This is necessary since small remnants of previously cut tissue may have stuck to the cutting plane. At slice *n*, the correlation between slices *n* and *n+1* was compared to that between slices *n-1* and *n+1*. In case of a higher correlation between *n-1* and *n+1* (Eq. 1), the *n*th slice was replaced by a maximum intensity projection (MIP) of its neighboring slices.

$$\sum_{i=1}^{h}\sum_{j=1}^{w} abs\left(I(i,j)_{n-1} - I(i,j)_{n+1}\right) > \sum_{i=1}^{h}\sum_{j=1}^{w} abs\left(I(i,j)_{n} - I(i,j)_{n+1}\right), \qquad (1)$$

$$n \in \{2,..,N-1\}$$

with *I* the pixel intensity at spatial coordinates *i, j; h* and *w* the height and width of the images and *n* an image at corresponding depth from the stack with length *N*.

Subsequently, the dark current, an artifact produced by the camera at large exposure times, was removed from the data with custom designed software. If the intensity of consecutive pixels in the axial direction remained above a user defined threshold (typically 100 on a 0-255 scale) for more than 30 percent of the stack depth, those pixels were identified as dark current. A median filter was then applied to remove the dark current, while preserving the structural information.

Fig. 3. Cropped section (300^3 pixels) of a volume representation of the raw data (a). The restored data by deconvolution (b) and the extracted centerpoints (c).

The data were then de-convolved with a kernel consisting of an anisotropic point spread function [8], specific to the cryomicrotome setup (Fig. 3a/b). This was necessary to correct for the blurring introduced by the lens and for detection artifacts introduced by the transparency of the tissue, causing fluorescent light from layers up to 200 µm deep to be visible at the cutting plane, and to enhance the smaller vasculature in the images. A custom-made macro was used that adapts the deconvolution algorithm available in the software package ImageJ (National Institutes of Health, USA) to very large data sets such as these by piece-wise processing. The maximum size of the data blocks processed was limited by the internal memory of the computer used. For each block, an iterative Fourier-based algorithm for deconvolution was used [9]. The kernel was provided as a stack of images digitally reconstructed from the point spread function as proposed by Rolf [8].

The centerlines of the restored data were then obtained using a topology-preserved thinning algorithm, written in custom software with Delphi Architect 2005 (Borland, Austin, USA). Centerline extraction is widely used in medical images of e.g. the colon, the pulmonary system [10] and the coronary arteries [11]. A set of matching templates as deletion conditions was used as proposed by Palagyi [12]. Similar to the deconvolution, the data were processed piece-wise by using overlapping blocks of interest. The resulting centerpoints (Fig. 3c) were labeled according to their Euclidean distances from each other. Each centerpoint was classified by the number of its connections with surrounding pixels. This yields end-points, i.e. centerpoints with only one neighbor, mid-points, i.e. points that have two neighbors, and points with three or more connections. Segments connecting multiple points can subsequently be formed between endpoints and points of higher connecting order than midpoints. From these segments, the thinned representation of the tree was build. Non-connected points were omitted and over-connected regions at single pixel scale were reduced to bifurcations only, without loss of connectivity. Finally, spurious branches as a result of perturbations on the vessel surface were removed (Fig. 4).

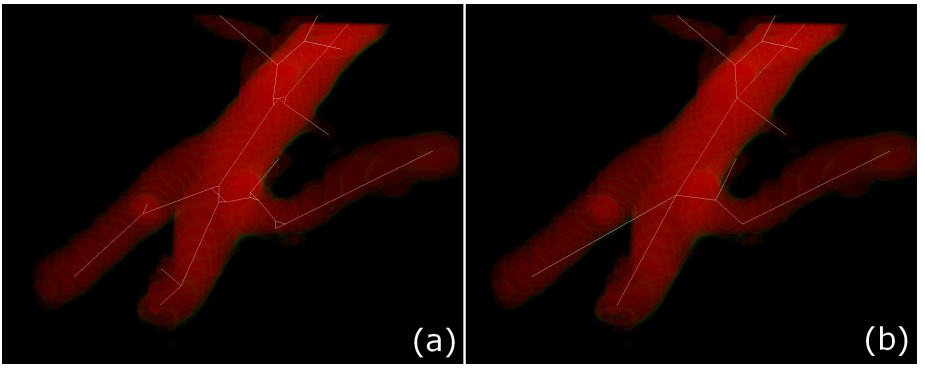

Fig. 4. Cropped region (100^3 pixels) of a 3D data set, showing vessels of approximately 500 microns in diameter with the segments after the thinning algorithm (a) and after correction for over-connected regions and spurious branches (b)

2.4 Extracting the Microsphere Distributions

After obtaining image stacks at different filter settings, the locations of the separate microspheres can be retrieved. However due to spectral overlap (Fig. 5) between the different fluorescent colors it was necessary to filter the data.

A linear combination of images acquired at different filter settings was used per color to achieve separation into the different fluorescent microsphere groups. In brief, e.g. the red microspheres were retrieved from a stack containing red and carmine simultaneously, images that contain scarlet and carmine microspheres are subsequently subtracted. Similar combinations were used to acquire the other unique colors: carmine, scarlet, yellow and green. Since different exposure times were used per setting, the image to subtract is multiplied by a factor. This factor was retrieved by fitting the intensity of the unwanted microspheres in the raw data to microspheres in the subtracting image.

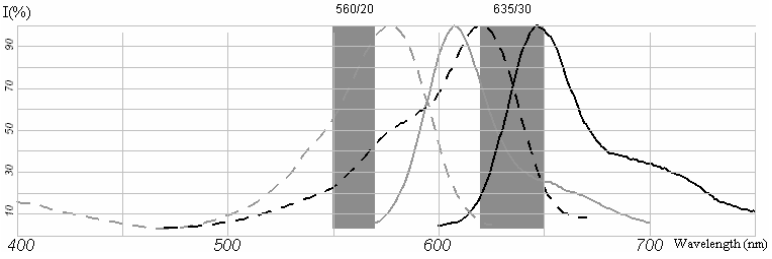

Fig. 5. Excitation (*dotted line*) and emission (*solid line*) spectra of red and carmine microspheres. The gray areas represent the filters for excitation (*560/20*) and emission (*635/30*). (Image from Invitrogen, Fluorescence SpectraViewer).

The transparency of the tissue leads to false positive identifications of microspheres. However, with both the point spread function of the system known, as well as the amount of attenuation of the light at slice depth, the succeeding images can be used to correct for excess light in the current slice. Also, a tophat-filter with a circular mask of similar size as the microspheres is used to remove the light from possible auto-fluorescence of the tissue (Fig. 6).

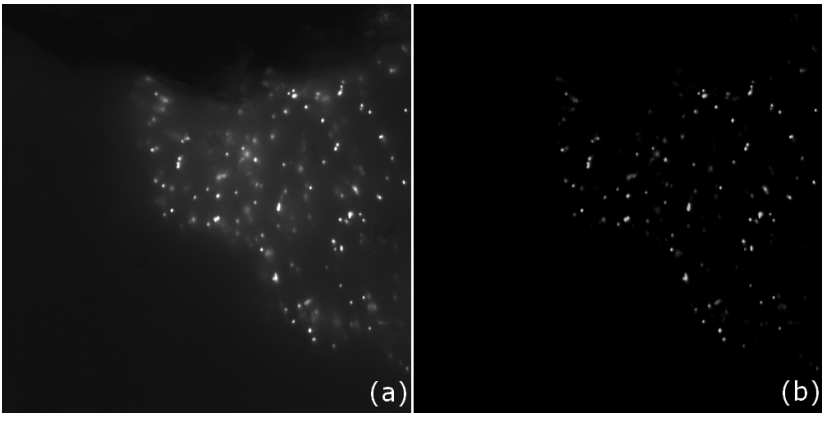

Fig. 6. A cropped section (500x500 pixels) of one slice of raw data showing red microspheres (a), along with the same area after tophat-filtering (b)

Bright areas in the images exceeding a threshold for intensity and size are counted as one observation, resulting in a 3 dimensional distribution for each of the five colors of microspheres. The intensity level of the background noise serves as a threshold, and the area of a microsphere at the imaging surface as predicted by the point spread function defines the size limit for detection.

3 Preliminary Results

The feasibility of the study is illustrated by Figure 7 where the combination of vascular reconstruction and microsphere detection is illustrated. Figure 7a demonstrates a

MIP projection of the virtual cast in a plane oriented along the axis from base to apex. Figure 7b is a MIP of 8 mm thick tissue. In this example microspheres where injected in the LAD while the LCX was open as well. The demarcation of the LAD perfusion territory is clear. The distributions for partial and full occlusion show a change in perfusion territory as expected but are not further reported here. The topology of the vascular tree was retrieved from the cast images as described and allows the interpretation of the microsphere distribution in relation to the structural information.

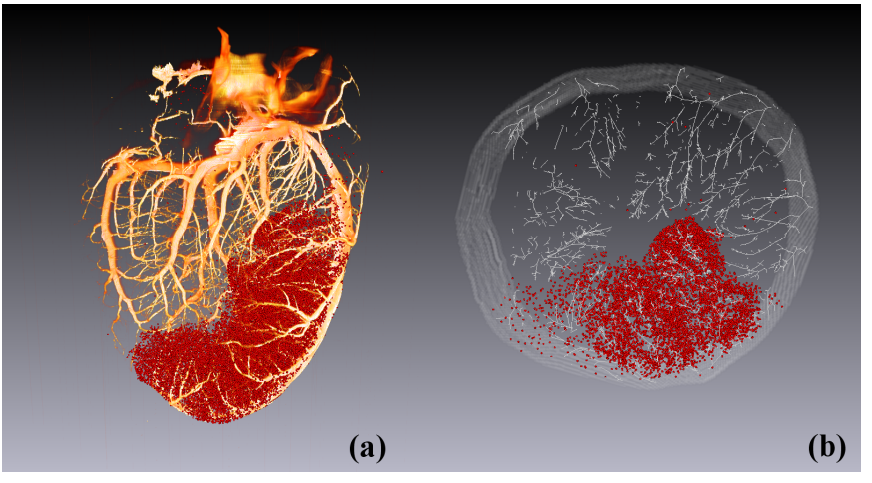

Fig. 7. Distributions of microspheres, with the vasculature retrieved from the cast material. Red microspheres injected into the LAD demarcating the area of perfusion in normal conditions (a). Short axis view showing a cross-section of 8mm thickness with the same microsphere distribution as in (a), along with the thinned representation of the vascular tree (b) and the outline of the cardiac wall.

4 Discussion

4.1 Contributions of the Study

Experiments involving microspheres in order to determine collateral flow have been done in the past [13]. In these experiments, however, tissue had to be manually cut into small pieces, often with a weight of several grams, which reduces spatial resolution and prevents gathering information about the perfusion boundary. Those microsphere measurements therefore lack spatial resolution which can be greatly improved by use of the imaging cryomicrotome.

Our results indicate the feasibility of obtaining perfusion measurements from microsphere distributions. Based on microsphere distributions under conditions of normal cardiac perfusion, separation was demonstrated of perfusion areas belonging to the different major coronary arteries. From future experiments we expect to obtain vascular tree reconstructions in which the perfusion boundaries are crossed by collateral vessels, as identified by the fluorescent filling of the intramural vessels. Moreover, the flow through these collaterals will be quantified by the microspheres that will have crossed these demarcation planes.

4.2 Methodological Considerations

In order to image the smaller vessels down to 50 micron in diameter, a sufficient exposure time is needed. This introduces overexposure at the larger vessels, resulting in an intensity cut-off in the images. The current algorithm for deconvolution is not capable of correcting the saturated pixels, because of the plateau profile of intensity. Consequentially, this will result in dark patches within the data that lead to thinning artifacts, since the tree will be thinned from within. Other artifacts such as spurious branches can be removed; however, this is done by using the diameter information to separate true branches from artifacts, at the cost of increased computational time.

Cluster forming of several microspheres can pose a problem in estimating the number of microspheres. This is especially the case since the point spread function of the system causes the microspheres to appear larger in the images than their actual size. Hence, two or more microspheres together will result in a connected region of high intensity. After processing the data, these areas are counted as one observation, essentially yielding an underestimation of the number of microspheres.

4.3 Future Prospect

To further enhance the quality of the retrieved vascular tree, a pre-processing step can be introduced to smooth the raw data, along with a morphological operator to fill the dark patches. This may reduce the amount of spurious branches and artifacts. A feature detection scheme as proposed by Lindeberg [14] can improve the ability to separate microspheres that are clustered together. More importantly however, by using this method, high spatial resolution measurements can be obtained of the distinct perfusion areas of the heart.

4.4 Conclusion

This study demonstrated the feasibility of the presented approach to arrive at high-resolution spatial measurements of perfusion during conditions of normal and altered coronary flow. Importantly this kind of analysis retains information between local tissue perfusion and feeding vessels.

Acknowledgements. This study was further supported in part by the Netherlands Heart Foundation (grants 2006B145 and 2006B226) and by The Netherlands Organization for Scientific Research (ZON-MW 911-05-008) and the European Community's Seventh Framework Program (FP7/2007-2013) under grant agreement n° 224495 (euHeart project).

References

1. Molin, D., Post, M.J.: Therapeutic angiogenesis in the heart: protect and serve. Curr. Opin. Pharmacol. 7, 158–163 (2007)
2. Kern, M.J., Lerman, A., Bech, J.W., De Bruyne, B., Eeckhout, E., Fearon, W.F., Higano, S.T., Lim, M.J., Meuwissen, M., Piek, J.J., Pijls, N.H., Siebes, M., Spaan, J.A.E.: Physiological assessment of coronary artery disease in the cardiac catheterization laboratory: a scientific statement from the American Heart Association Committee on Diagnostic and Interventional Cardiac Catheterization, Council on Clinical Cardiology. Circulation 114, 1321–1341 (2006)

3. Siebes, M., Verhoeff, B., Meuwissen, M., de Winter, R.J., Spaan, J.A.E., Piek, J.J.: Single-wire pressure and flow velocity measurement to quantify coronary stenosis hemodynamics and effects of percutaneous interventions. Circulation 109(6), 756–762 (2004)
4. Verhoeff, B.J., Siebes, M., Meuwissen, M., Atasever, B., Voskuil, M., de Winter, R.J., Koch, K.T., Tijssen, J.G., Spaan, J.A., Piek, J.J.: Influence of percutaneous coronary intervention on coronary microvascular resistance index. Circulation 111, 76–82 (2005)
5. Spaan, J.A.E., Piek, J.J., Hoffman, J.I.E., Siebes, M.: Physiological basis of clinically used coronary hemodynamic indices. Circulation 113(3), 446–455 (2006)
6. Spaan, J.A.E., ter Wee, R., van Teeffelen, J.W.G.E., Streekstra, G., Siebes, M., Kolyva, C., Vink, H., Fokkema, D.S., VanBavel, E.: Visualisation of intramural coronary vasculature by an imaging cryomicrotome suggests compartmentalisation of myocardial perfusion areas. Med. Biol. Eng. Comput. 43, 4 (2005)
7. Kelly, J.J., Ewen, J.R., Bernard, S.L., Glenny, R.W., Barlow, C.H.: Regional blood flow measurements from fluorescent microsphere images using an Imaging Cryomicrotome. Rev. Sci. Int. 71, 1 (2000)
8. Rolf, M.P., ter Wee, R., van Leeuwen, T.G., Spaan, J.A.E., Streekstra, G.J.: Diameter measurements from images of fluorescent cylinders embedded in tissue. Med. Biol. Eng. Comput. 46, 589–596 (2008)
9. Dougherty, R.P.: Extensions of DAMAS and benefits and limitations of deconvolution in beamforming, AIAA Paper 2005-2961 (2005)
10. Palágyia, K., Tschirren, J., Hoffman, E.A., Sonka, M.: Quantitative analysis of pulmonary airway tree structures. Computers in Biology and Medicine 36, 974–996 (2006)
11. Lee, J., Beighley, P., Ritman, E., Smith, N.: Automatic segmentation of 3D micro-CT coronary vascular images. Medical Image Analysis 11, 630–647 (2007)
12. Palágyi, A., Kuba, A.: 3D 6-subiteration thinning algorithm for extracting medial lines. Pattern Recognition Letters 19, 613–627 (1998)
13. Buckberg, G.D., Fixler, D.E., Archie, J.P., Hoffman, J.I.: Experimental Subendocardial Ischemia in Dogs with Normal Coronary Arteries. Circ. Res. 30, 67–81 (1972)
14. Lindeberg, T.: Feature detection with automatic scale selection. Int. J. of Computer Vision 30, 2 (1998)

Intravoxel Fibre Structure of the Left Ventricular Free Wall and Posterior Left-Right Ventricular Insertion Site in Canine Myocardium Using Q-Ball Imaging

Hans Dierckx[1], Alan P. Benson[2,4], Stephen H. Gilbert[2,4], Michael E. Ries[3,4], Arun V. Holden[2,4], Henri Verschelde[1], and Olivier Bernus[2,4]

[1] Department of Mathematical Physics and Astronomy, Ghent University, Belgium
[2] Institute of Membrane and Systems Biology, University of Leeds, United Kingdom
[3] School of Physics and Astronomy, University of Leeds, United Kingdom
[4] Multidisciplinary Cardiovascular Research Centre, University of Leeds, United Kingdom

Abstract. Q-ball imaging (QBI) is an established high-angular resolution diffusion MRI technique enabling to resolve intravoxel fibre structure. Here, we present a detailed study of myocardial fibre orientation using QBI. We compare standard diffusion tensor MRI (DTI) versus QBI in the canine left ventricular free wall (LVFW) and posterior left-right ventricular insertion site. Most voxels within the LVFW show high fractional anisotropy (FA), Gaussian diffusion profiles, and a single population of aligned fibres. In these, the difference between fibre helix angles estimated by DTI and QBI is below 5°. However, we show that reduced FA near the anterior papillary muscle in the LVFW and in most of the left-right ventricular fusion site correlates with non-Gaussian diffusion. The QBI orientation distribution functions (ODF) in these regions reveal complex intravoxel fibrous structure, which cannot be inferred using DTI. Extensive ODF maps of myocardial fibre orientation are presented and discussed for the first time to our knowledge.

1 Introduction

The fibrous structure of the heart plays an important role in cardiac contraction (e.g. [1]) and physical quantities such as conduction velocity of myocardial activation waves have long been known to depend strongly on fibre orientation [2]. Hence, the accurate knowledge of the heart's fibre architecture is not only essential for understanding cardiac function but also necessary for realistic electrophysiological and electromechanical simulations of cardiac activity.

In the present study, we make use of a high-angular resolution diffusion MRI technique, called Q-Ball Imaging (QBI), to map the complex fibre architecture in selected regions of the canine ventricles. The sensitivity of myofibre structure to diffusion MRI resides in the preferential orientation of collagenated layers and

N. Ayache, H. Delingette, and M. Sermesant (Eds.): FIMH 2009, LNCS 5528, pp. 495–504, 2009.
© Springer-Verlag Berlin Heidelberg 2009

cell membranes within fibrous tissue, rendering the occuring diffusion processes anisotropic. Numerous studies have used diffusion tensor imaging (DTI, [3]) to map local fibre and sheet structure based on the assumption that the water diffusion, although anisotropic, has Gaussian character. However, in voxels with fibres that diverge, rotate abruptly or belong to different ill-aligned subpopulations, the Gaussian model – and hence DTI itself – is a poor estimate. QBI does not rely on a Gaussian diffusion model and can hence be used to map such complex intravoxel fibre structures. Shi et al. recently demonstrated the feasibility of QBI in cardiac tissue [4]. However, their study was conducted at low angular and spatial resolution and did not quantify the deviation from Gaussian diffusion, which would justify the use of QBI over DTI.

We present an extensive comparison of DTI with QBI in two equatorial tissue wedges, which were cut from intact canine ventricles as depicted in Fig. 1. The first transmural wedge (A) was obtained from the lateral left ventricular free wall (LVFW) and contained part of the anterior papillary muscle (APM). The second wedge (B) consisted of the posterior insertion of the RV onto the LV and septum. Using high angular resolution MRI data, we quantify the deviation from Gaussian diffusion to localize regions where the tensor formalism can no longer describe diffusion of water accurately. In both tissue samples, regions were identified in which diffusion is non-Gaussian and where complex intravoxel fibre organisation was observed using QBI.

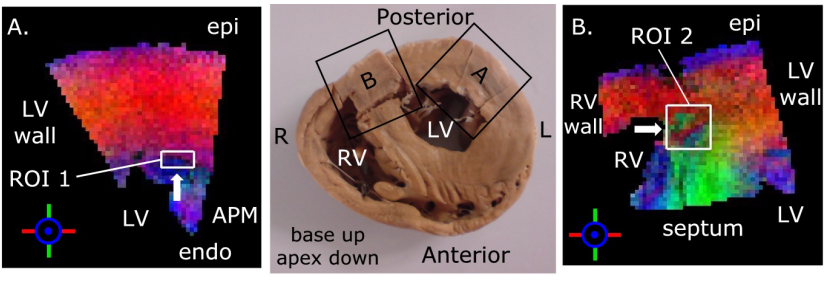

Fig. 1. Anatomical loci of the samples and ROIs. The central picture shows the equatorial section of canine heart from which tissue samples A (lateral left ventricular free wall) and B (posterior LV-RV insertion) were cut. The outer panels mark different ROIs in which itensity represents FA. The red/green/blue colours encode the dominant fibre direction as circumferential/axial/axial, respectively. Reconstruction from 42 gradient directions using DTI ($b = 3000\,\mathrm{s/mm^2}$). The thick white arrows signal viewing directions for the ODF-maps in Fig. 4.

2 Methods

2.1 Short Review of Q-Ball Imaging

Soon after the inability of DTI to resolve intravoxel fibre bundle crossing had been acknowledged (see, e.g. [5]), efforts were undertaken to estimate the net spin

displacement function $P(\mathbf{r})$ itself. It had already been noticed by Stejskal and Tanner [6] that this function is Fourier-conjugated to the diffusion MRI signal $E(\mathbf{q})$, where $\mathbf{q} = (2\pi)^{-1}\gamma\delta\mathbf{g}$ expresses the direction and amplitude of the applied diffusion gradient $\mathbf{g}$. Furthermore, δ denotes the diffusion gradient duration and the gyromagnetic ratio for protons $\gamma/2\pi = 42.58\,\mathrm{MHz/T}$. Diffusion Spectrum Imaging (DSI) aims to sample $E(\mathbf{q})$ in the entire 'q-space', after which a Fourier transform yields the full diffusion function $P(\mathbf{r})$. However, due to reconstruction problems, long scan times and high technical demands, this method has been abandoned in favour of QBI as initially developped by Tuch [7] to image local fibre orientation in brain white matter. Tuch demonstrated that restricting the data acquisition to a spherical shell in q-space preserves enough information to reconstruct the radially integrated displacement function in all directions, which is called the Orientation Distribution Function (ODF).

The preceding definition introduces the ODF as quantifying, for each direction, the probability that a proton has displaced itself in that direction during the echo time of the acquisition (15 ms in our case). For a voxel containing a single population of well-aligned fibres, the net proton displacement exhibits a maximum for the direction parallel the fibres' axis, and so will the ODF. In the case where multiple fibre populations are present in a voxel, the ODF arises as the linear superposition of singe-fibre ODFs, with the partial volume coefficients serving as weighting factors. In a sense, the ODF surface generally 'points' in the direction where alignment of a fibre bundle in the voxel is more probable. That is why voxels containing a single fibre population have peanut-shaped ODFs, and crossing fibre bundles will generate a single X-shaped ODF.

The ODF can be readily estimated from the diffusion MRI signal as measured on a ball with radius q in q-space using a Funk-Radon Transform (FRT). The price one pays for not measuring the entire q-space is convolution of the local ODF with a zeroeth order Bessel function of the first kind, whose effective width follows from the Rayleigh resolution criterion, yielding $\Delta r = 0.383/q$ [7]. Hence, one is urged to work with high gradients strengths q if one wants good angular resolution. On the other hand, a Stejskal-Tanner spin echo sequence with rectangular gradients yields $b = q^2(\Delta - \delta/3)$, with Δ the time lag between the diffusion encoding gradients. Since the signal attenuates exponentially according to b, the optimal b-value arises as a trade-off between diffusion constrast and signal-to-noise ratio.

The two major advantages of QBI over DTI are (i) the linear superposition of sources and (ii) the independence of the underlying diffusion process. The latter allows to visualize non-Gaussian diffusion, whereas the former enables to map multiple populations of fibres within a single voxel.

2.2 Imaging Experiment

From an isolated formaldehyde (4% in saline) fixed dog heart two equatorial wedge-shaped samples were cut, corresponding to the left ventricular free wall and posterior merging site of left and right ventricle with the septum, as depicted in Fig. 1. Prior to imaging, both wedges were submerged in Fomblin (Aldrich

317942-100G) to supress the surrounding MRI signal. Imaging was done on a Bruker 9.4 T spectrometer (Bruker BioSpin, Ettlingen, Germany).

A standard DTI spin-echo sequence was used for diffusion weighted imaging, of which the gradient table was expanded to accommodate $N_g = 162$ gradient directions. These were obtained by twofold tesselation of a regular icosahedron. In both samples we imaged three axial slices of thickness 1 mm, with an in-plane isotropic resolution of 0.4 mm (FOV 2.56 cm×2.56 cm, matrix size 64 × 64). A single scan took 5h17m to collect, and they were repeated for three b-values: 1500 s/mm^2, 3000 s/mm^2 and 4500 s/mm^2. Although QBI does not require a reference image with $b = 0$ s/mm^2, we nevertheless took three such images for use in DTI estimation. Table 1 summarizes imaging parameters and resulting quantities for these scans. As in DTI, the total scan time simply equals the acqusition time needed for one diffusion-weighted image, multiplied with the desired number of diffusion encoding directions.

Table 1. QBI parameters for different b-values. Echo time was 15 ms for all scans.

b	δ	Δ	q	Δr	$\mathrm{SNR}_{\mathrm{LVFW}}$	$\mathrm{SNR}_{\mathrm{LVRV}}$
1500 s/mm^2	2 ms	7 ms	$0.775\,10^3$ cm^{-1}	4.9 μm	17.6	15.3
3000 s/mm^2	2 ms	7 ms	$1.095\,10^3$ cm^{-1}	3.5 μm	8.3	7.5
4500 s/mm^2	3 ms	7 ms	$1.378\,10^3$ cm^{-1}	2.8 μm	5.0	4.6

2.3 Data Processing

We compared the performance of DTI for various numbers of directions used for reconstruction: diffusion tensors were reconstructed for $N_g = 12$, 42 and 162 directions, corresponding to subsequent tesselations of a regular icosahedron. The unweighted image S_0 was calculated as the geometric mean of three scans with $b = 0$ s/mm^2. We computed the diffusion tensor using the standard technique of six-dimensional linear regression on the logarithm of the diffusion MRI signal S_i [3]. During regression, the correlation coefficient R^2 was stored, for each voxel, as a measure to non-Gaussianity of the diffusion profile. With $y_i = \log(S_i/S_0)$ representing the logarithmic attenuation of the signal in the i-th of N_g gradient directions, the correlation coefficient from a linear regression reads

$$R^2 = \left(\sum_{i=1}^{N_g} (\hat{y}_i - \bar{y})^2 \right) \cdot \left(\sum_{i=1}^{N_g} (y_i - \bar{y})^2 \right)^{-1}, \tag{1}$$

where $\hat{y}_i$ denotes the linear fit to y_i and $\bar{y}$ expresses the arithmetic mean of the y_i. The tensors resulting from linear regression were diagonalised and the eigenvalues were ordered: $D_1 \geq D_2 \geq D_3$. The unique dominant fibre direction was taken to lie along the eigenvector $\boldsymbol{e}_1$ corresponding to the largest eigenvalue, and we calculated fractional anistropy (FA) as in [8].

For QBI post-processing, we have implemented the signal conversion procedure from [7], with ODF calculation in $N_{\mathrm{rec}} = 642$ reconstruction directions,

which were found by threefold tesselation of a regular icosahedron. The interpolation kernel with optimal condition number (see [7]) has width $\sigma = 6°$. Prior to further processing, the obtained ODFs were smoothed by a discrete Gaussian filter, averaging over nearest and second-to-nearest neighbouring directions. The dominant fibre orientation, i.e. the direction in which the ODF takes its maximal value, was used for fibre helix angle computation. Subsidiary peaks in the ODF (local maxima) were taken to correspond to the orientations of subpopulations of fibres.

3 Results

Figure 2 depicts the FA and R^2 maps for both tissue samples, at $b = 1500\,\mathrm{s/mm^2}$. From correlation plots such as panel (e) we conclude that local reduction in FA is due to non-Gaussianity of the diffusion process. The midwall part of the LV free wall has high R^2 values, demonstrating that the diffusion tensor is a good fit to the observed diffusion pattern. Gaussianity is also present in the inner region of the anterior papillary muscle ($R^2 > 0.7$). However, in the border zone between these regions, the correlation coefficient R^2 is significantly smaller (Fig. 2c). In the LV-RV insertion sample shown in Figs. 2b,d one can appreciate the continuing zone of voxels where FA remains high and Gaussianity is preserved, when turning from LV to septal wall. In contrast, the onset with the RV wall has slightly lower R^2 and FA and moreover, a small triangular tissue slab in the insertion shows a significant decrease in tensor correlation.

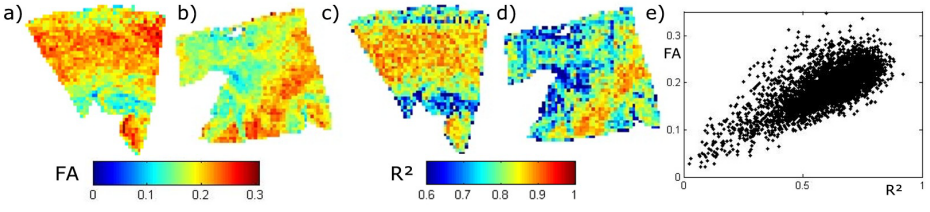

Fig. 2. Quantification of FA (a,b) and Gaussianity (c,d) of the diffusion profile, at $b = 1500\,\mathrm{s/mm^2}$. Panel (e) correlates FA to R^2 for all voxels from the LVFW sample, yielding a Pearson's r^2 coefficient of 0.7.

Fibre direction results from DTI and QBI can only be compared meaningfully in voxels where DTI is valid, for QBI does not rely on a diffusion model. Thus, we impose a threshold $R^2 > 0.7$ to mask all voxels in which DTI might produce an erroneous outcome. Table 2 shows the mean angular difference between DTI and QBI for the remaining data points. As more gradient directions are used, the difference in predicted fibre orientation between the two techniques decreases to about 5°, irrespective of the b-value. Note that this angular difference is of the same order as our QBI angular resolution (6°) and hence denotes an almost perfect match between QBI and DTI in those regions where $R^2 > 0.7$. At high

Table 2. Average angle (in degrees) spanned between the main fibre direction estimated by DTI and QBI, for different b-values (in s/mm^2). Only voxels with $R^2 > 0.7$ were counted. Deviations are represented by standard error of the mean (SEM).

sample	LVFW	LVFW	LVFW	LV-RV	LV-RV	LV-RV
N_g	12	42	162	12	42	162
$b = 1500$	6.53 ± 0.06	5.07 ± 0.05	4.59 ± 0.04	7.62 ± 0.08	5.68 ± 0.05	5.01 ± 0.05
$b = 3000$	9.22 ± 0.12	5.69 ± 0.07	4.64 ± 0.05	10.44 ± 0.15	6.29 ± 0.10	4.87 ± 0.07
$b = 4500$	12.29 ± 0.16	6.51 ± 0.11	4.71 ± 0.12	14.89 ± 0.22	6.74 ± 0.16	5.05 ± 0.18

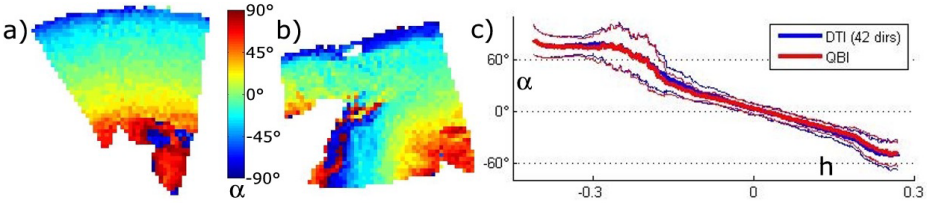

Fig. 3. QBI based fibre helix angle measurement for lateral LVFW (a) and posterior LV-RV insertion (b), at $b = 3000\,\mathrm{s/mm^2}$. Panel c depicts the transmural profile for LVFW helix angle. The dimensionless transmural coordinate h was taken from Geerts [9], with $h = 0$ corresponding to mid-wall and $h = -1$ at the slice centroid. Thinner lines mark standard deviation of the moving average. No R^2 thresholding was used.

b-value and low number of gradient directions ($N_g = 12$), the difference between DTI and QBI is largest, probably due to low SNR (see Table 1) and a non-robust tensor fit when unsufficient reconstruction directions are used. Figure 3 shows fibre helix angle maps and profiles for DTI ($N_{rec} = 42$) and QBI, for $b = 3000\,\mathrm{s/mm^2}$. From this figure one can appreciate the excellent spatial and quantitative correlation between DTI and QBI in those voxels with $R^2 > 0.7$.

Since the ODFs act as distribution functions on a sphere, they are mostly rendered as sphere-like surfaces, where both radius and colour correspond to ODF magnitude. In each tissue sample, we chose a region of interest (ROI) where non-Gaussian diffusion profiles, i.e. $R^2 < 0.7$, were observed (see Figs. 1, 2). The ODF fields in these ROIs are presented in Fig. 4 for high diffusion weighting ($b = 4500\,\mathrm{s/mm^2}$). They have been min-max normalized for clarity, as in [7].

The first ROI displays fibre organisation in the onset of the anterior papillary muscle, viewed in endo- to epicardial direction (Fig. 4, upper panel). In the outer left and right transmural profiles (marked as 1a, 1b), fibres are seen to turn smoothly in the tangential plane, with helix angles α ranging roughly from $+80°$ to $+50°$. In the central part of the FOV (1c), however, fibre orientation changes rapidly, turning $-45°$ over a distance of only two voxel sizes (0.8 mm), as can be inferred from the elongated ODFs on either side of this transition. Within this border zone, the ODFs show no single dominant fibre orientation, and the fibre orientation probability grows wider. We attribute these fan-shaped

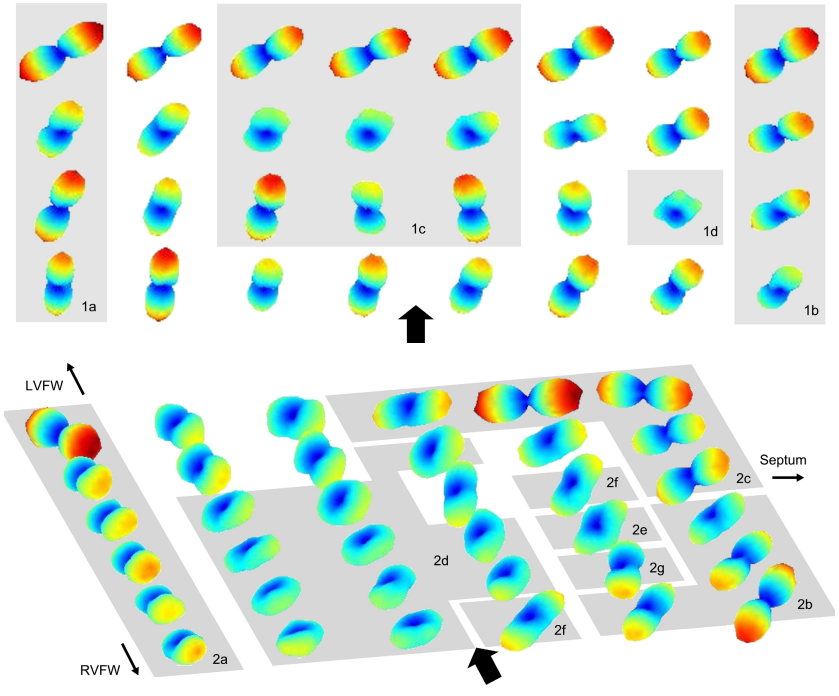

Fig. 4. Min-max normalised ODFs for ROI 1 (above) and ROI 2 (below); the thick black arrows correspond to the viewing directions, as was indicated in Fig. 1. For ROI 1, the viewing direction is endo- to epicardial and the circumferential direction runs left-right. FOV equals 3.2 mm × 1.6 mm. ROI 2 represents an axial plane viewed from inside the RV, the far left corresponding to RV wall (2a) and the voxels on the right-hand side connecting to the septal wall (2b, 2c). For ROI 2, only every second voxel is shown in each direction (FOV = 4.4 mm × 4.4 mm). Both maps were taken at $b = 4500\,\mathrm{s/mm^2}$; labelled grey areas refer to the main text.

ODFs to rapid but continuous intravoxel fibre rotation. The opposite case of discontinuous fibre rotation may be suspected in the lower right corner (1d), where a cross-shaped ODF can be observed.

We equally calculated ODFs in the LV-RV insertion sample. The results for ROI 2 are presented in the second panel of Fig. 4, viewed from the RV towards the fusion site. The outer left row, which is tagged as 2a, originates from the endocardial RVFW (lower part) and connects to the left ventricular wall (top). This zone is designated by aligned fibres running almost circumferentially in the axial plane. The rightmost voxels show fibers bundles starting from the midwall septum, which subsequently split in two tracks that join the RV (2b) and LV wall (2c), beyond the scope of this image frame. The region in between these main branches is filled with mostly fan-shaped ODFs (2d), similar to the central ones (1c) from ROI 1, which we ascribe to fast but gradual intravoxel fibre rotation as well. Label (2e) indicates a voxel whose ODF exhibits secondary

bulging. It is worth noting that the two dominant fibre orientations present in this voxel's cross-shaped ODF are each found in neighbouring voxels (2f, g), and belong to two of the aforementioned major fibre branches, i.e. septum to LV (2f) and LV to RV (2g). Hence the q-ball image allows us to infer that there might be two distinct fibre populations present within this particular voxel (2e), and simulaneously grants us these directions. Moreover, based upon the relative intensity of the ODF peaks, we deduce that the fibre subpopulation running from septum to LV occupies the largest volume within the voxel.

4 Discussion

The macroscopic myocardial fibre architecture not only governs cardiac contraction, but also affects wave propagation and re-entrant dynamics, as has been assessed both numerically [10] and experimentally [11]. However, one point of view is that sub-millimeter structure plays a subsidiary role in wave propagation, as the wave front is typically about 1-2 millimeters thick. Nevertheless, regions with rapidly varying fibre orientation (e.g. at the onset of the papillary muscles) are known to behave as anchoring points for rotor filaments [11]. Additionally, the geometric interpretation of conduction anisotropy, as proposed in [12] and elaborated on in [13,14], also hints that small-scale changes in fibre direction could invoke strong curvature effects that act on rotor filaments and thereby affect their dynamics. Further investigations on the dynamical role of fibrous fine-structure will require the synergy of realistic computer simulations using biophysical electrophysiological models and detailed anatomical and structural data sets.

Detailed imaging of fibrous structure in the heart should ideally couple high spatial with high angular resolution. However, smaller voxel sizes contain less signal and therefore high static fields have been used, for they intrinsically increase SNR and allow small echo times TE for a given b-value. Conversely, with high field imaging come stronger eddy currents, which could lead to misregistration between images taken in different diffusion weighting directions. However, our diffusion gradient duration δ lies below typical eddy current decay constants of few tens of milliseconds, and thereby avoids malign eddy current accumulation. Moreover, a recent phantom study indicated the feasibility of QBI using similar protocols in a 9.4T Bruker scanner, without noticeable artefacts in the reconstruction [15]. Finally, in this study we have not used echo planar readout, which suffers critically from eddy current induced image distortion [16]. Still, if one would wish to image larger (whole-heart) volumes in feasable measurement times using echo-planar imaging, one needs to adopt eddy-current compensated radiofrequent protocols, such as offered in [16] and applied in, a.o., [7].

QBI has been developed for brain white matter imaging and has, in that context, proven to be a valuable method for fibrous tissue imaging, even at field strengths as high as 7 T [17]. A first validation of QBI in a cardiac context is the reproduction of tensor imaging results in regions with well-aligned fibres. From Table 2 we conclude that cardiac QBI does perform well within the limits set by

the number of diffusion encoding directions. However, further validation against reference methods such as histology or confocal scanning will be required in those regions where we observed non-Gaussian diffusion profiles. It would allow to discriminate between abrupt transitions in fibre orientation [11] and interwoven fibrous meshes [18] in regions where the ODFs exhibit a typical cross-shape.

5 Conclusion

In the present study we have conducted an extensive comparison between DTI and QBI in a myocardial context. To this aim, we mapped local fibre orientations in the canine left ventricular free wall and the left-right ventricular insertion site using both techniques. We found that voxels of decreased fractional anisotropy generally coincide with reduced diffusion tensor fit correlation (R^2), indicating that the Gaussian diffusion model, and hence DTI, is not appropriate to reconstruct myocardial fibre orientation in these regions. Using QBI we have gathered arguments supporting that in regions of low R^2 complex intravoxel fibrous structure is present. Examples have been provided where the imaging technique could discriminate between rapid fibre rotation and the co-existence of multiple populations of fibres with distinct orientations. Although, due to imaging times, DTI is still the preferred technique in regions with a single, slowly varying fibre population (such as the left ventricular mid-myocardium), we found that QBI has the potential to significantly advance our understanding of cardiac microstructure in regions of complex fibre organisation, such as the left-right ventricular fusion sites, or the insertion sites of the papillary muscles.

Acknowledgements

H.D. would like to express special thanks to Steven Delputte, who introduced him to the QBI formalism. A.P.B. and S.H.G. are supported by MRC Fellowships. H.D. is a PhD fellow of the Research Foundation - Flanders (Belgium). O.B. acknowledges support from the EPSRC (EP/F065574/1). This work was also supported by the European Union through the BioSim network of Excellence (contract No. LSHB-CT-2004-005137). The authors would like to thank the referees for helpful suggestions.

References

1. Chen, J., Liu, W., Zhang, H., Lacy, L., Yang, X., Song, S., Wickline, S., Yu, X.: Regional ventricular wall thickening reflects changes in cardiac fiber and sheet structure during contraction: quantification with diffusion tenor MRI. Am. J. Physiol. Heart Circ. Physiol. 289, H1898–H1907 (2005)
2. Clerc, L.: Directional differences of impulse spread in trabecular muscle from mammalian heart. J. Physiol. 255, 335–346 (1976)
3. Basser, P., Mattiello, J., LeBihan, D.: MR Diffusion tensor spectroscopy and imaging. Biophys. J. 66, 259–267 (1994)

4. Shi, Y., Jiang, Y., Hsu, E.: Comparison of diffusion tensor and Q-ball imaging of the canine myocardium. Proc. Intl. Soc. Magn. Reson. Med. 15, 1470 (2007)
5. Frank, L.: Anisotropy in high angular resolution diffusion-weighted MRI. Magn. Reson. Med. 45, 935–939 (2001)
6. Stejksal, E., Tanner, J.: Spin diffusion measurements: spin echoes in the presence of a time-dependent field gradient. J. Chem. Phys. 42, 288–292 (1965)
7. Tuch, D.: Q-ball imaging. Magn. Reson. Med. 52, 1358–1372 (2004)
8. Basser, P., Pierpaoli, C.: Microstructural and physiological features of tissues elucidated by quantitative-diffusion-tensor-MRI. J. Magn. Reson. B 111, 209–219 (1996)
9. Geerts, L., Bovendeerd, P., Nicolay, K., Arts, T.: Characterization of the normal cardiac myofiber field in goat measured with MR-diffusion tensor imaging. Am. J. Physiol. Heart Circ. Physiol. 283, H139–H145 (2002)
10. Fenton, F., Karma, A.: Vortex dynamics in three-dimensional continuous myocardium with fiber rotation: filament instability and fibrillation. Chaos 8(1), 20–46 (1998)
11. Kim, Y., Xie, F., Yashima, M., Wu, T., Valderrabano, M., Lee, M., Ohara, T., Voroshilovsky, O., Doshi, R., Fishbein, M., Qu, Z., Garfinkel, A., Weiss, J., Karagueuzian, H., Chen, P.: Role of papillary muscle in the generation and maintenance of reentry during ventricular tachycardia and fibrillation in isolated swine right ventricle. Circ. Res. 100(13), 1450–1459 (1999)
12. Wellner, M., Berenfeld, O., Jalife, J., Pertsov, A.: Minimal principle for rotor filaments. Proc. Nat. Ac. Sc. 99(12), 8015–8018 (2002)
13. Verschelde, H., Dierckx, H., Bernus, O.: Covariant stringlike dynamics of scroll wave filaments in anisotropic cardiac tissue. Phys. Rev. Lett. 99(16), 168104–1–168104–4 (2007)
14. Dierckx, H., Verschelde, H., Bernus, O.: A geometric theory for scroll wave filaments in anisotropic excitable media. Physica D (in press)
15. Tournier, J., Yeh, C., Calamante, F., Cho, K., Connelly, A., Lin, C.: Resolving crossing fibres using constrained spherical deconvolution: Validation using diffusion-weighted imaging phantom data. NeuroImage 42, 617–625 (2008)
16. Reese, T., Heid, O., Weisskoff, R., Wedeen, V.: Reduction of Eddy-current-induced distortion in diffusion MRI using a twice-refocused spin echo. Magn. Reson. Med. 49, 177–182 (2003)
17. Mukherjee, P., Hess, C., Wu, D., Han, E., Kelley, D., Vigneron, D.: Development and initial evaluation of 7-T q-ball imaging of the human brain. Magn. Res. Imag. 26, 171–180 (2008)
18. Anderson, R., Smerup, M., Sanchez-Quintana, D., Loukas, M., Lunkenheimer, P.: The three-dimensional arrangement of the myocytes in the ventricular walls. Clin. Anat. 22(1), 64–76 (2009)

Relationship between Maximal Upstroke Velocity of Transmembrane Voltage and Minimum Time Derivative of Extracellular Potential

Kwanghyun Sohn, Bonnie B. Punske, and Frank B. Sachse

Nora Eccles Harrison Cardiovascular Research and Training Institute and
Bioengineering Department, University of Utah, Salt Lake City, Utah, USA
http://www.cvrti.utah.edu, http://www.bioen.utah.edu

Abstract. The purpose of this computational study was to test the pertinence of the magnitude of the minimum time derivative of the extracellular potential, $|dV_{es}/dt_{min}|$, measured in a thin, conducting solution layer adjacent to the tissue, as an index of cardiac excitability. For this purpose, we performed computational studies characterizing the relationship between $|dV_{es}/dt_{min}|$ and the maximum upstroke velocity of transmembrane voltage, dV_m/dt_{max}, which has been used in previous studies as an index of excitability. A three-dimensional bidomain model of electrical conduction in cardiac tissue was used based on the Noble-Varghese-Kohl-Noble model of ventricular myocytes. The spatial domain included a slab of cardiac tissue with intra- and extracellular anisotropic conductivities surrounded by a layer of solution. The simulations showed linear relationships between $|dV_{es}/dt_{min}|$ and dV_m/dt_{max} for reduction of maximum sodium current conductance (G_{Na}) from 100% to 20%. The relationship was dependent on location and propagation direction. However, when both parameters were normalized, those dependencies disappeared. In summary, our study demonstrated that normalized $|dV_{es}/dt_{min}|$ is linearly related to normalized dV_m/dt_{max}. The results support our hypothesis that normalized $|dV_{es}/dt_{min}|$ can be used as an index of cardiac excitability.

Keywords: Extracellular Potential, Excitability, Bidomain Model, Cardiac Electrophysiology.

1 Introduction

Cardiovascular diseases are the major cause of mortality and morbidity. Mortality is often a consequence of ventricular arrhythmias [1, 2]. Abnormal cardiac excitability predisposes the heart to arrhythmias [2, 3]. Excitability has been defined as "the ease with which cells undergo individual and regenerative depolarization and repolarization, communicate with each other, and propagate in a normal and abnormal manner" [4, 5].

The maximum upstroke velocity of the transmembrane voltage, dV_m/dt_{max}, has been reported as an index of cardiac excitability [6, 7]. This measure indicates a significant role of sodium currents in excitability. A proportional relationship between upstroke velocity of transmembrane voltage and sodium current has been established

N. Ayache, H. Delingette, and M. Sermesant (Eds.): FIMH 2009, LNCS 5528, pp. 505–512, 2009.
© Springer-Verlag Berlin Heidelberg 2009

for the case of single myocyte activation [8]. Assuming instantaneous whole cell depolarization, the sodium current flows into the cytosol and depolarizes the membrane. The magnitude of capacitive current is equal to the magnitude of sodium current with opposite direction:

$$i_m = i_c + i_{Na} = 0$$

with transmembrane current density i_m, capacitive current density i_c, and sodium current density i_{Na}. In this case, dV_m/dt is linearly proportional to i_{Na}:

$$c_m \frac{dV_m}{dt} = i_c = -i_{Na} \cdot$$

with c_m: capacitance per unit area, and V_m: transmembrane voltage. However, in case of inter-myocyte coupling, due to currents from the depolarized myocytes to those in rest, i_m is not zero during activation. The cardiac action potential propagates by interactions between the transmembrane ionic and capacitive currents as well as intercellular currents. When sodium channels open, sodium ions flow into a myocyte driven by the electrochemical potential difference across the cell membrane. This inward i_{Na} depolarizes the myocyte. Subsequently, current flows to the downstream resting myocytes inducing capacitive current. This outward i_c depolarizes the membrane of the downstream myocytes. If the membrane voltage reaches the activation threshold of sodium ion channels, those open allowing additional current to flow and initiate activation. The assumption that the magnitude of the fast sodium current is much greater than other currents at the time of action potential upstroke, supports dV_m/dt being greatly dependent on the i_{Na} [8]. Therefore the primary driving force of activation and propagation is i_{Na}, which suggests that excitability can also be characterized by i_{Na}.

In our previous experimental studies [9], we used the minimum time derivative of the extracellular potentials, $|dV_{es}/dt_{min}|$, measured close to the surface of the heart to characterize effects of glucose transport rate on the electrical activity of isolated, perfused mouse hearts during hypoxia. A cylindrical 64-electrode array was slipped over the heart to measure unipolar extracellular potentials V_{es}. Our experimental results showed that values of $|dV_{es}/dt_{min}|$ were strongly correlated with other measures used to assess changes in electrical activity during hypoxia. The attenuation of $|dV_{es}/dt_{min}|$ during hypoxia showed a strong dependency on the level of glucose transport rate. Based on these results, we hypothesized that $|dV_{es}/dt_{min}|$ could be applied an index of cardiac excitability.

The purpose of this computational study was to test our hypothesis of a linear relationship between the magnitude of the minimum time derivative of extracellular potential $|dV_{es}/dt_{min}|$ and dV_m/dt_{max} as suggested by our experimental work. The study aims at characterizing $|dV_{es}/dt_{min}|$ measured outside the tissue as an index of cardiac excitability by seeking its relationship to dV_m/dt_{max} at different levels of sodium current.

2 Methods

We tested the hypothesis with computational simulations using a three-dimensional bidomain model of conduction in cardiac tissue [10, 11]. The spatial domain was a hexahedron with a size of 2.7 mm × 3.4 mm × 3.4 mm and discretized with an isotropic spatial resolution of 0.1mm (Fig. 1). The domain included a slab of cardiac

tissue with a size of 2.7 mm ×3.0 mm ×1.4 mm surrounded by a finite bath of solution. The slab represents a segment of the left ventricle of a small mammal. Myocyte orientation was parallel to the y-axis direction. Myocyte electrophysiology was modeled with the Noble-Varghese-Kohl-Noble model [12]. The sodium current I_{Na} was controlled by changing the maximum sodium conductance G_{Na} [13]:

$$I_{Na} = G_{Na}(V_m - E_{mh})m^3h$$

with E_{mh}: reversal potential based on intra- and extracellular K and Na concentrations, m: the fraction of m-particles in the open state, and h: the fraction of non-inactivated channels.

The ordinary differential equations underlying the cell models were solved using the forward Euler method with a time step of 5 μs. Intercellular currents and the extracellular were calculated every 5μs based on the finite-element method. Assigned intra- and extracellular conductivities are listed in Table 1 [14].

In case of z-directional (endo to epi, transmural) propagation, a stimulus current of -5nA with a frequency of 1 Hz and a duration of 4 ms was injected in the myocytes at z values between 0.8 and 1.0 mm. For y-directional (apex to base) propagation, the stimulus current was applied to myocytes at values of y between 0 and 0.2 mm. In the simulations, values G_{Na} were varied from 0.5 to 2.5 μS with 2.5 μS considered to be 100% G_{Na}.

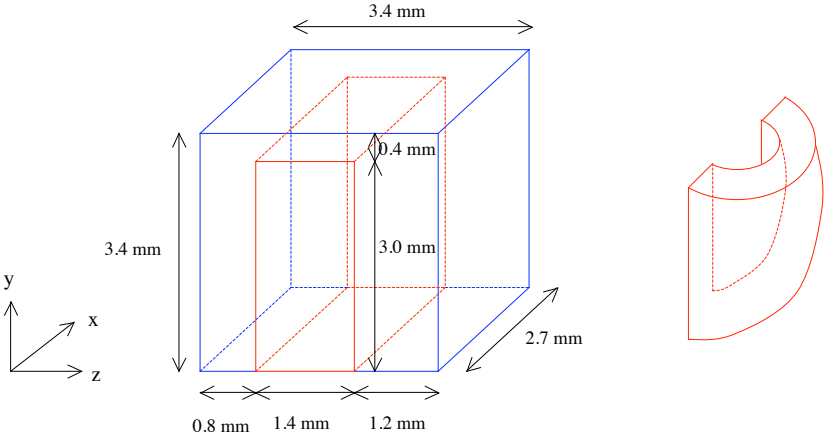

Fig. 1. Spatial model. The inside hexahedron depicts a slab of cardiac tissue which models a portion of the left ventricular freewall shown in the figure at the right. The slab is surrounded by conducting solution on the epicardial and endocardial sides and at the base. Epicardial and endocardial surfaces are located at z=2.2 and 0.8mm, respectively.

Table 1. Tissue and Bath Conductivities

Intracellular longitudinal conductivity, σ_{il}	0.375 S/m
Intracellular transversal conductivity, σ_{it}	0.0375 S/m
Extracellular longitudinal conductivity, σ_{el}	0.375 S/m
Extracellular transversal conductivity, σ_{et}	0.214 S/m
Bath (solution) conductivity, σ_{es}	1.5 S/m

3 Results

We performed simulations of electrical conduction through cardiac tissue varying the maximal sodium conductance G_{Na} and direction of propagation. Extracellular potentials and transmembrane voltages computed after the tenth beat were used for analysis. The simulations were carried out on a Mac OSX cluster (Intel processors, 16 cores, 3 GHz).

Fig. 2 shows dV_m/dt_{max} distributions in the tissue along the z-direction for different values of G_{Na} and propagation directions. In case of y-directional propagation (Fig. 2a), there is little variation in the transmural dV_m/dt_{max} except for small increases at both the endocardial and epicardial surfaces. Z-directional propagation also showed constant transmural dV_m/dt_{max} and slightly increased dV_m/dt_{max} at the epicardial and endocardial surfaces (Fig. 2b). The increased values at the tissue surfaces can be explained by boundary effects. Furthermore, stimulation applied in proximity to the endocardial surface contributes to higher dV_m/dt_{max} values in this region (Fig. 2b).

Further analysis focused on the center of the tissue in the x direction, x = 1.35mm. Figs. 3, 4 and 5 present the relationship between $|dV_{es}/dt_{min}|$ and dV_m/dt_{max} for changes in G_{Na} using values of dV_m/dt_{max} from the subepicardial region at a depth of 0.15mm inside the epicardial surface (z=2.05mm). We chose this position as a reference, because dV_m/dt_{max} at this position is very similar to the transmural (but not surface) dV_m/dt_{max} values. Fig. 3 shows $|dV_{es}/dt_{min}|$ versus dV_m/dt_{max} for increased values of G_{Na} at increasing distances from the epicardial surface and at different locations along the y-direction in the surrounding solution. In case of y-directional propagation, $|dV_{es}/dt_{min}|$ and dV_m/dt_{max} show a linear relationship with large variations in slope at different distances from the epicardial surface (Fig. 3a) and for different y values (Fig. 3b). After $|dV_{es}/dt_{min}|$ and dV_m/dt_{max} are normalized to their values at 100% G_{Na}, all graphs of $|dV_{es}/dt_{min}|$ versus dV_m/dt_{max} exhibit the same slope (Fig. 3c and 3d). Similar relationships are shown in Fig. 4 for z-directional propagation.

Fig. 5 compares $|dV_{es}/dt_{min}|$ versus dV_m/dt_{max} for y- and z-directional propagation. $|dV_{es}/dt_{min}|$ values for z-directional propagation are much larger than for y-directional propagation (Fig. 5a). Hence the value of the slope of the graph of $|dV_{es}/dt_{min}|$ versus dV_m/dt_{max} for z-directional propagation is also larger (Fig. 5a). However, once $|dV_{es}/dt_{min}|$ and dV_m/dt_{max} values are normalized, the y- and z-directional propagation graphs overlap (Fig. 5b).

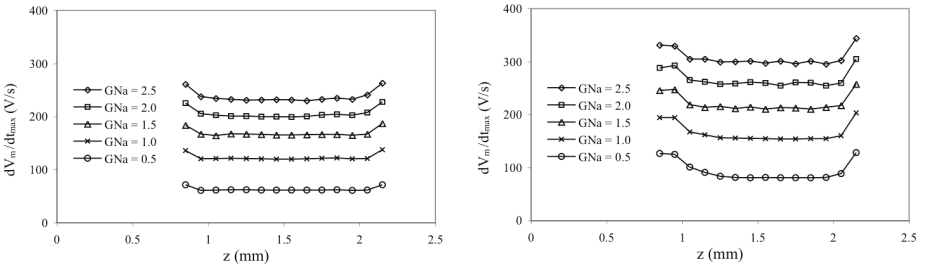

Fig. 2. Distributions of dV_m/dt_{max} at x=1.35mm, y=1.05mm and z=0.8-2.2mm for (a) y-directional and (b) z-directional propagation. The conductance G_{Na} is in S/m^2. Maxima are found at the endo- and epicardial surfaces.

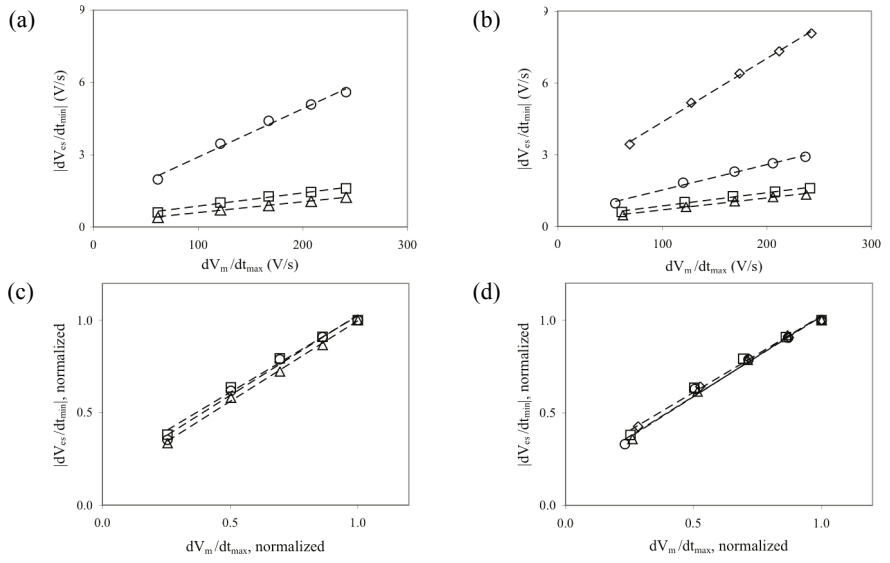

Fig. 3. $|dV_{es}/dt_{min}|$ versus dV_m/dt_{max} for y-directional propagation. (a) At a distance of 0.15 (circle), 0.65 (square), and 1.15mm (triangle) from the epicardial surface (x = 1.35mm, y = 1.05mm). (b) At y=0.35 (circle), 1.05 (square), 1.75 (triangle) and 2.55mm (diamond) (x = 1.35mm, epicardial distance d = 0.65mm). (c,d) Normalized data from (a,b).

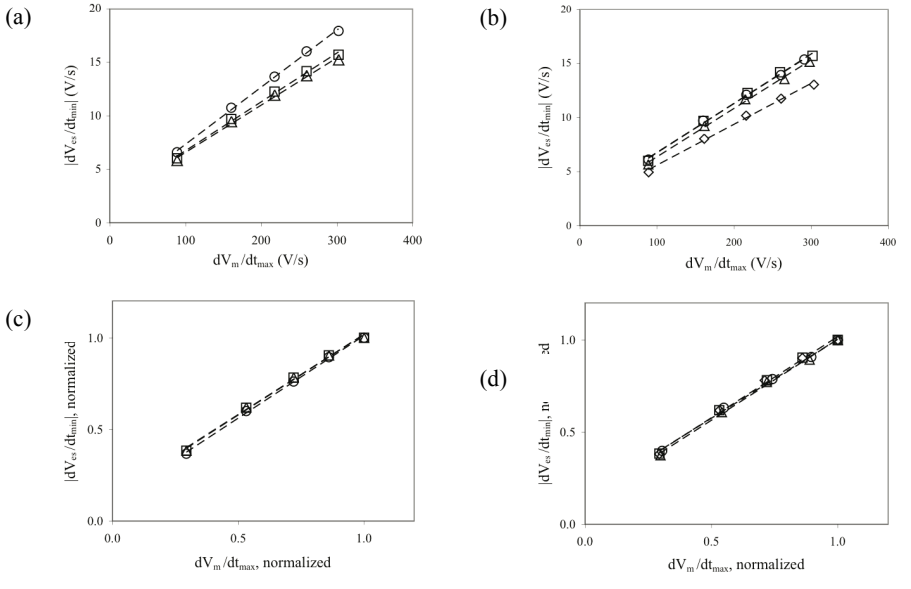

Fig. 4. $|dV_{es}/dt_{min}|$ versus dV_m/dt_{max} for z-directional propagation. (a) At a distance of 0.15 (circle), 0.65 (square), and 1.15mm (triangle) from the epicardial surface (x = 1.35mm, y = 1.05mm). (b) At y=0.35 (circle), 1.05 (square), 1.75 (triangle) and 2.55mm (diamond) (x = 1.35mm, epicardial distance d = 0.65mm). (c,d) Normalized data from (a,b).

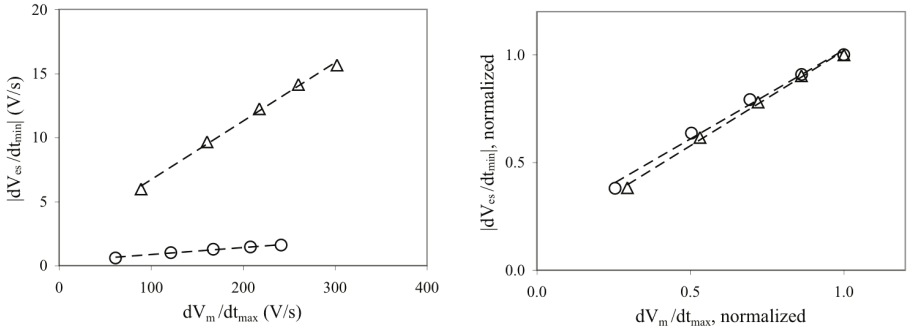

Fig. 5. (a) $|dV_{es}/dt_{min}|$ versus dV_m/dt_{max} for y- (circle) and z-directional (triangle) propagations. Data is from position x=1.35mm, y=1.05mm, and epicardial distance d=0.65mm. (b) Normalized data from (a).

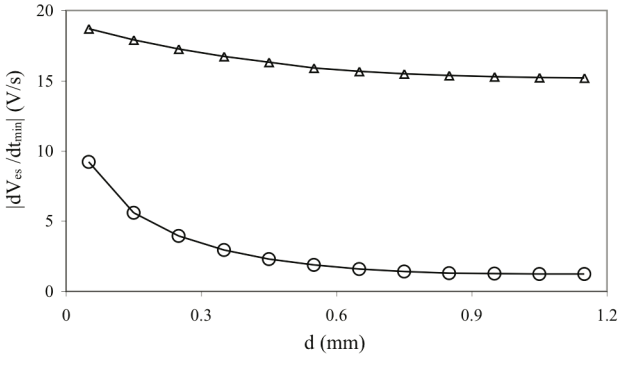

Fig. 6. $|dV_{es}/dt_{min}|$ as a function of distance from the epicardial surface into the solution, d, for y- (circle) and z-directional (triangle) propagation. Data is from position x = 1.35mm, y = 1.05mm, and z=0.1-1.1mm.

4 Discussion

The computational simulations presented here showed that for y-directional propagation, the time of $|dV_{es}/dt_{min}|$ at any location y occurs at the moment when the activation wave front passes y. For z-directional propagation, the time of $|dV_{es}/dt_{min}|$ at any location in the solution on the epicardial side of the bath corresponds to the moment when the wave front reaches the epicardial surface. Fig. 6 shows a rapid decrease in $|dV_{es}/dt_{min}|$ as a function of distance from the epicardial surface for y-directional propagation (open circles). However, for z-directional propagation, $|dV_{es}/dt_{min}|$ shows far less attenuation. We suggest that these differences can be explained by the orientation of the activation wave plane with respect to the measurement sites.

For G_{Na} varying from 20 to 100% of the control value, the slopes of $|dV_{es}/dt_{min}|$ versus dV_m/dt_{max} depended on the location in the bath and propagation direction. After normalization of $|dV_{es}/dt_{min}|$ and dV_m/dt_{max}, the relationships overlap and are

independent of both parameters. This finding indicates that relative changes of dV_m/dt_{max} can be determined from relative changes of $|dV_{es}/dt_{min}|$. Other simulations (data not shown) we have conducted showed that this finding holds in various cases of point stimulation. The finding is of particular importance for experimental studies where G_{Na} decreases are known to be associated with acidosis. Previous computational studies showed that after the onset of ischemia, over time excitability attenuates via reduced sodium current as a result of increased intercellular acidosis [7].

These computational results are complementary to our previous experimental study [9], in which we characterized cardiac electrical activity based on $|dV_{es}/dt_{min}|$. We measured extracellular potentials from isolated perfused mouse hearts during hypoxia. Measured $|dV_{es}/dt_{min}|$ values were averaged and normalized to the value at the beginning of the hypoxia. Attenuation of the normalized $|dV_{es}/dt_{min}|$ value was inversely related to the glucose transport rate which was controlled by the concentrations of insulin and glucose in perfusate. Our computational results support our hypothesis that $|dV_{es}/dt_{min}|$ measured from the surface of the heart can provide a useful index of excitability.

Limitations. Several limitations are associated with the presented computational study. The aim of the study was to provide insights in basic electrical properties of cardiac tissue in a bath. We only modeled a portion of the ventricle and did not attempt a realistic description of the geometry of a whole heart as used in our previous experimental study [9]. We applied a geometrically simple spatial model to facilitate the analysis and interpretation of the results. With the same intent, heterogeneity of cellular electrophysiology and the cardiac conduction system were neglected. We tested our hypothesis with a single cell model including a standard sodium channel description. We expect that simulations with other models produce quantitatively different data. However, because of the rather basic parameter adjustment, we do not expect significant differences in the presented normalized relationships.

We focused on characterizing effects of G_{Na} on $|dV_{es}/dt_{min}|$ as a marker of excitability. We did not investigate effects of alteration of ion concentrations, ion channel and gap junction channel currents on $|dV_{es}/dt_{min}|$. We expect a contribution of ion concentrations and ion channel currents to affect $|dV_{es}/dt_{min}|$. This might be caused e.g. by modulation of the resting voltage, which would affect sodium channel availability in addition to modulations of G_{Na}. Furthermore, excitability and $|dV_{es}/dt_{min}|$ are affected indirectly by experimentally documented closure of gap junction channels. However, gap junction closure is reported to occur much later in the time course of ischemia as compared to the changes in excitability which we focused on in this study.

Acknowledgments. This research was supported by grants from the Nora Eccles Treadwell Foundation and the Richard A. and Nora Eccles Harrison Fund for Cardiovascular Research.

References

1. Kokolis, S., Clark, L.T., Kokolis, R., Kassotis, J.: Ventricular arrhythmias and sudden cardiac death. Prog. Cardiovasc. Dis. 48, 426–444 (2006)
2. Marban, E.: Cardiac channelopathies. Nature 415, 213–218 (2002)

3. Arnsdorf, M.F.: Membrane factors in arrhythmogenesis: concepts and definitions. Prog. Cardiovasc. Dis. 19, 413–429 (1977)
4. Arnsdorf, M.F.: Cardiac excitability and antiarrhythmic drugs: a difference perspective. J. Clin. Pharmcal. 29, 395–404 (1989)
5. Arnsdorf, M.F., Schmidt, G.A., Sawicki, G.J.: Effects of encainide on the determinants of cardiac excitability in sheep Purkinje fibers. J. Pharmacol. Exp. Ther. 232, 40–48 (1985)
6. Shaw, R.M., Rudy, Y.: Electrophysiologic effects of acute myocardial ischemia: a theoretical study of altered cell excitability and action potential duration. Cardiovasc. Res. 35, 256–272 (1997)
7. Shaw, R.M., Rudy, Y.: Electrophysiologic effects of acute myocardial ischemia. A mechanistic investigation of action potential conduction and conduction failure. Circ. Res. 80, 124–138 (1997)
8. Walton, M., Fozzard, H.A.: The relation of Vmax to INa, GNa, and h infinity in a model of the cardiac Purkinje fiber. Biophys. J. 25(3), 407–420 (1979)
9. Sohn, K., Sutherland, D.R., Liang, Q., Punske, B.B.: Experimental measures of the minimum time derivative of the extracellular potentials as an index of electrical activity during metabolic and hypoxic stress. In: Sachse, F.B., Seemann, G. (eds.) FIMH 2007. LNCS, vol. 4466, pp. 250–259. Springer, Heidelberg (2007)
10. Henriquez, C.S.: Simulating the electrical behavior of cardiac tissue using the bidomain model. Crit. Rev. Biomed. Eng. 21, 1–77 (1993)
11. Sachse, F.B., Moreno, A.P., Seemann, G., Abildskov, J.A.: A model of electrical conduction in cardiac tissue including fibroblasts. Ann. Biomed. Eng., EPub. (March 13, 2009)
12. Noble, D., Varghese, A., Kohl, P., Noble, P.: Improved guinea-pig ventricular cell model incorporating a diadic space, Ikr and Is, and length- and tension-dependent processes. Can. J. Cardiol. 14, 123–134 (1998)
13. Hodgkin, A.L., Huxley, A.F.: A quantitative description of membrane current and its application to conduction and excitation in nerve. J. Physiol. 117, 500–544 (1952)
14. Roth, B.J.: Action potential propagation in a thick strand of cardiac muscle. Circ. Res. 68, 162–173 (1991)
15. Spach, M.S., Miller III, W.T., Miller-Jones, E., Warren, R.B., Barr, R.C.: Extracellular potentials related to intracellular action potentials during impulse conduction in anisotropic canine cardiac muscle. Circ. Res. 45, 188–204 (1979)
16. Plonsey, R.: Bioelectric phenomena, pp. 221–275. McGrawHill, New York (1969)

Effects of Anisotropy and Transmural Heterogeneity on the T-Wave Polarity of Simulated Electrograms

Piero Colli Franzone[1], Luca F. Pavarino[2], Simone Scacchi[2], and Bruno Taccardi[3]

[1] Dipartimento di Matematica, Universitá di Pavia and IMATI-CNR
Via Ferrata 1, 27100 Pavia, Italy
colli@imati.cnr.it
[2] Dipartimento di Matematica, Universitá di Milano,
Via Saldini 50, 20133 Milano, Italy
pavarino@mat.unimi.it
[3] Cardiovascular Research and Training Institute, University of Utah,
Salt Lake City, Utah
taccardi@cvrti.utah.edu

Abstract. The major determinants of the T wave polarity in electrocardiograms (ECGs) are still a debated issue. The aim of this work is to investigate the effects of tissue anisotropy, cellular action potential duration (APD) heterogeneities and excitation wavefront shape on the T wave polarity in unipolar and bipolar ECGs, simulated in a conducting medium surrounding the cardiac tissue at some distance fom endo to epicardium. The study is based on three-dimensional anisotropic Monodomain simulations of the entire depolarization and repolarization phases of propagating action potentials in a parallelepipedal slab. The results show that the T wave of unipolar ECGs is positive at all sites explored and its shape and polarity are mainly determined by the anisotropy of the cardiac tissue, irrespective of cellular APD heterogeneities and shape of the excitation wavefront. On the other hand, bipolar ECGs are mainly affected by their isotropic component and their T wave turns out to be positive for single site stimulations in the presence of transmural APD heterogeneity, while it becomes always negative in case of multiple sites stimulation generating large activation wavefronts, regardless of the considered cellular APD heterogeneities.

1 Introduction

The factors determining the shape and polarity of the T wave in electrocardiograms (ECGs) are still a matter of debate. According to the classical theory based on the double layer source model (see e.g. [19] and the classical references therein), an activation sequence starting from the endocardium and proceeding towards the epicardium generates ECG waveforms at leads facing the epicardium with an R wave. By applying the heart surface model (see e.g. [17,19]), it is generally believed that if the repolarization sequence follows the activation one,

N. Ayache, H. Delingette, and M. Sermesant (Eds.): FIMH 2009, LNCS 5528, pp. 513–523, 2009.
© Springer-Verlag Berlin Heidelberg 2009

then a negative T wave is expected, due to opposite direction of the transmembrane potential gradients during the downstroke phase of the action potential. On the contrary, measured human Einthoven leads II exhibit QRS complex and T wave with the same positive polarity. In order to explain this discrepancy, a different transmural repolarization sequence within the ventricular wall has been proposed, where the epicardium recovers before the endocardium based on the assumption that the action potential duration (APD) of epicardial cells is considerably shorter than the APD of endocardial cells. Experimental evidence of transmural APD heterogeneity and of transmural repolarization gradients has been established in [21] for isolated cells and in vitro wedge preparations of canine left ventricles. Computational studies on isotropic ([1,12,8,10]) or anisotropic cardiac tissue ([2,20]), with transmural APD cell heterogeneity, have been able to reproduce concordant R and T waves. Nevertheless, a repolarization sequence directed from epicardium to endocardium has never been observed in *in vivo* animal models; see [9,14,11,18]. In alternative to transmural repolarization gradients, apico-basal APD heterogeneities have been proposed as a determinant of the T wave polarity. The aim of this work is to provide some insight on how the tissue anisotropy, cellular APD heterogeneities and shape of excitation wavefronts influence the polarity of the T wave in unipolar and bipolar ECGs. The study is based on three-dimensional anisotropic Monodomain simulations of the entire depolarization and repolarization phases of propagating action potentials in a slab embedded in an unbounded homogeneous conducting medium.

2 Methods

The anisotropic Monodomain model. The evolution of the transmembrane potential $v(\mathbf{x},t)$, extracellular/extracardiac potential ϕ, gating variables $w(\mathbf{x},t)$ and ionic concentrations $c(\mathbf{x},t)$, is described by the reaction-diffusion system

$$\begin{cases} c_m \partial_t v - \operatorname{div}(D_m \nabla v) + i_{ion}(v,w,c) = i_{app} \ \text{ in } H, \qquad \mathbf{n}^T D_m \nabla v = 0 \ \text{ on } \partial H \\ \partial_t w - R(v,w) = 0, \qquad \partial_t c - S(v,w,c) = 0 \ \text{ in } H \\ -\operatorname{div} D \nabla \phi = \begin{cases} \operatorname{div} D_i \nabla v & \text{in } H \\ 0 & \text{in } \mathbb{R}^3 \setminus H \end{cases} \qquad \text{where } D = \begin{cases} D_i + D_e & \text{in } H \\ \sigma_0 I & \text{in } \mathbb{R}^3 \setminus H \end{cases} \end{cases} \tag{1}$$

with appropriate initial conditions. Here H is the cardiac volume, c_m and i_{ion} denote the capacitance and the ionic current of the membrane per unit volume, i_{app} represents the applied current per unit volume, and σ_0 is the conductivity coefficient of the extracardiac medium.

The conductivity tensors $D_i(\mathbf{x})$ and $D_e(\mathbf{x})$ at any point $\mathbf{x} \in H$ are defined as $D_{i,e}(\mathbf{x}) = \sigma_l^{i,e}\, \mathbf{a}_l(\mathbf{x})\mathbf{a}_l^T(\mathbf{x}) + \sigma_t^{i,e}\, \mathbf{a}_t(\mathbf{x})\mathbf{a}_t^T(\mathbf{x}) + \sigma_n^{i,e}\, \mathbf{a}_n(\mathbf{x})\mathbf{a}_n^T(\mathbf{x})$. Here $\sigma_l^{i,e}, \sigma_t^{i,e}, \sigma_n^{i,e}$ are the conductivity coefficients along $\mathbf{a}_l(\mathbf{x})$, $\mathbf{a}_t(\mathbf{x})$, $\mathbf{a}_n(\mathbf{x})$, a triplet of orthonormal principal axes with $\mathbf{a}_l(\mathbf{x})$ parallel to the local fiber direction, $\mathbf{a}_t(\mathbf{x})$ and $\mathbf{a}_n(\mathbf{x})$ both transversal to the fiber axis and, based on the laminar organization of the cardiac tissue, tangent and orthogonal to the laminae, respectively. For

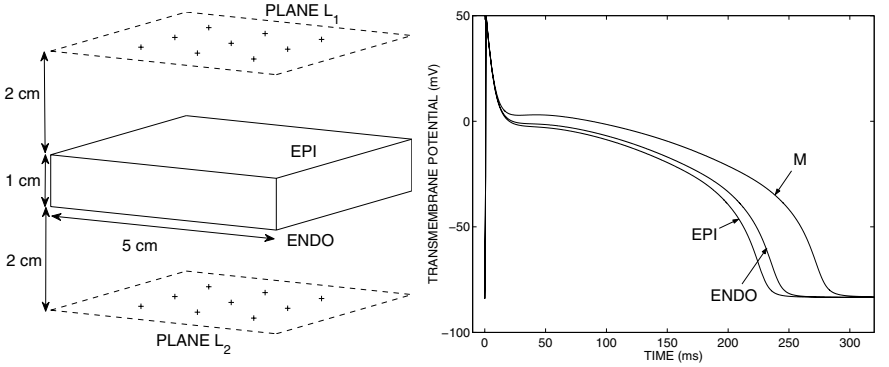

Fig. 1. Left: cardiac slab and location of the 3×3 transmural ECG electrode array 2 cm above the epicardial surface (plane L_1) and 2 cm below the endocardial surface (plane L_2). Right: Epicardial, Midmyocardial and Endocardial action potentials in the transmural heterogeneous **3-slab** calibration.

intra- and extracellular media with unequal anisotropic ratio, the Monodomain conductivity tensor D_m is given by $D_m = D_e(D_i + D_e)^{-1}D_i$, see [6,3].

The fibers rotate intramurally linearly with the depth for a total amount of 120^o and when the point of view is from the epicardial side, the rotation is counterclockwise proceeding from the epicardium to endocardium. More precisely, in the canonic reference system $(\mathbf{e}_1, \mathbf{e}_2, \mathbf{e}_3)$, the fiber direction $\mathbf{a}_l(\mathbf{x})$ and the other two principal axes at a point $\mathbf{x}$ are given by

$$\mathbf{a}_l(\mathbf{x}) = \mathbf{e}_1 \cos\alpha(r) + \mathbf{e}_2 \sin\alpha(r),\ \ \mathbf{a}_t(\mathbf{x}) = \mathbf{e}_3,\ \ \mathbf{a}_n(\mathbf{x}) = \mathbf{e}_1 \sin\alpha(r) - \mathbf{e}_2 \cos\alpha(r)$$
$$\alpha(r) = \tfrac{2}{3}\pi(1-r) - \tfrac{\pi}{4}, \quad \text{with } r \in [0,1].$$

The conductivity tensors are assumed orthotropic with conductivity coefficients along the principal axis given in the Table 1 (right) below.

Table 1. Parameter calibration for modeling the transmural heterogeneities (left) and conductivity coefficients in $mScm^{-1}$ (right)

slab type	H-slab	3-slab		
number of layers	1	3		
		endo	mid	epi
layer thickness (cm)	1	0.33	0.34	0.33
fact_I_K	1	2.62	1.95	2.88
APD (ms)	266	235	272	225

conductivity coefficients		
	intra	extra
σ_l	3	2
σ_t	0.3152	1.3514
σ_n	0.0315	0.6757
$\sigma_0 = 6$		

Transmural heterogeneity. The membrane model employed is the Luo-Rudy phase I (LR1) ionic membrane model (see [16]), requiring six gating variables and one calcium concentration variable. We consider two different types of transmural distribution of the intrinsic APDs of the cells, one homogeneous (**H-slab**) and one heterogeneous (**3-slab**). The transmural intrinsic APD heterogeneity is

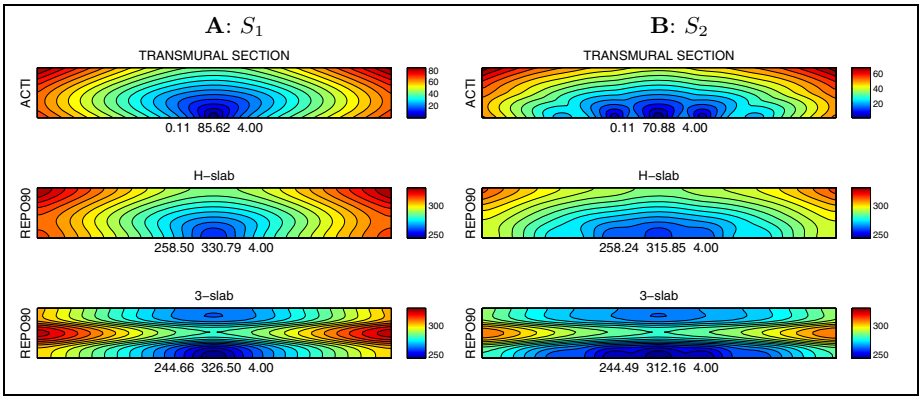

Fig. 2. A: Single site stimulation (S_1), isochrones of activation time ACTI (first row) and repolarization time REPO90 (second and third row) on a transmural diagonal section of **H-slab**, **3-slab**. **B**: Multiple sites stimulation (S_2), same format as in **A**.

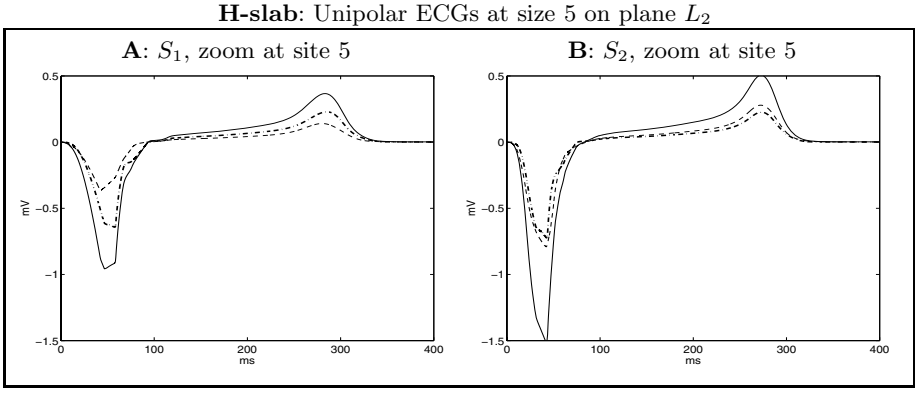

Fig. 3. H-slab: Unipolar ECGs at site 5 on plane L_2 (site 5 is the central one in the 3×3 array, see Fig. 4). **A**: Single site stimulation (S_1). **B**: Multiple sites stimulation (S_2). Continuous line: full unipolar ECG. Dashed line: HS component. Dashed-Dotted line: AS component.

assumed to be the same along any transmural epi-endocardial straight line, i.e. in any plane parallel to the epicardium all cells have the same intrinsic APD. In the heterogeneous slab, the intrinsic APD of the cells is obtained by multiplying the potassium current I_K in the LR1 model by a factor fact_{I_K}. This modulation factor is chosen in order to introduce a transmural APD profile with M-cell layers; see Table 1, Fig. 1-right and [7,12] for more details.

Computation of unipolar and bipolar electrograms. Unipolar ECGs ϕ are computed at an array of 3×3 points on planes located 2 cm (1 cm, not shown) above the epicardium (plane L_1) and 2 cm (1 cm, not shown) below the

endocardium (plane L_2), see Fig. 1-left. In order to investigate the qualitative behavior of the T wave of ECGs for sites at some distance from the active tissue, we disregard the anisotropic conduction effects of the bulk tissue, but we take into account the anisotropic cardiac source structure. Thus, the ECGs far away from the tissue slab are computed by assuming $D_i + D_e \approx \sigma_0 I$, hence according to the formula (see e.g. [15,17,5,4,13])

$$\phi(\mathbf{x}, t) = -\frac{1}{4\pi\sigma_0} \int_H D_i(\mathbf{y}) \nabla v(\mathbf{y}, t) \cdot \nabla \left(\frac{1}{|\mathbf{y} - \mathbf{x}|} \right) d\mathbf{y}, \tag{2}$$

where $D_i(\mathbf{y})\nabla v(\mathbf{y}, t)$ represents the anisotropic cardiac electric sources generating the extracardiac potential field.

Decomposition of the ECG waveform. In order to study the contribution of the anisotropic cardiac sources to the T wave morphology, we introduce an additive splitting of the intracellular conductivity tensor $D_i = D_{HS} + D_{AS}$ given by

$$D_{HS} = \sigma_t^i \mathbf{I} \quad \text{and} \quad D_{AS} = (\sigma_l^i - \sigma_t^i)\mathbf{a}_l(\mathbf{x})\mathbf{a}_l^T(\mathbf{x}) + (\sigma_n^i - \sigma_t^i)\mathbf{a}_n(\mathbf{x})\mathbf{a}_n^T(\mathbf{x}).$$

This splitting of D_i induces an analogous splitting of the cardiac sources into the so called double layer or heart surface (HS) source model (see [19,17]) and into a residual anisotropic source (AS). Consequently, the source term is decomposed as $D_i \nabla v = D_{HS} \nabla v + D_{AS} \nabla v$ and since ϕ depends linearly on $D_i \nabla v$ in eq. (2), the full unipolar ECG is decomposed as the sum of an isotropic (heart surface) and anisotropic components $\phi = \phi_{HS} + \phi_{AS}$. Given two points $\mathbf{x}_{epi}$ 2 cm above the epicardium (plane L_1) and $\mathbf{x}_{endo}$ 2 cm below the endocardium (plane L_2), we introduce also the transmural bipolar ECG ψ given by $\psi(\mathbf{x}_{epi}, \mathbf{x}_{endo}, t) = \phi(\mathbf{x}_{epi}, t) - \phi(\mathbf{x}_{endo}, t)$. Using the same splitting as before, we also decompose the full bipolar ECG ψ into the HS component $\psi_{HS}(\mathbf{x}_{epi}, \mathbf{x}_{endo}, t)$ and the anisotropic component $\psi_{AS}(\mathbf{x}_{epi}, \mathbf{x}_{endo}, t)$.

Numerical methods. The cardiac domain H considered is a cartesian slab of dimensions $5 \times 5 \times 1$ cm^3 modeling a portion of the left ventricle; see Fig. 1-left. In all computations, a structured grid of $500 \cdot 500 \cdot 100$ hexahedral isoparametric Q_1 elements of size $h = 0.1$ mm is used in space. The time discretization is based on an Euler Imex method. We used the PETSc parallel library (http://www.mcs.anl.gov/petsc) in order to ensure the parallelization and portability of our code, run on a Linux Cluster at the IMATI-CNR institute of Pavia; see e.g. [6] for more details.

3 Results

We consider two endocardial stimulation protocols: a single (ectopic) site stimulation (S_1), eliciting a twisted semi-ellipsoidal excitation front, or multiple (12) sites stimulation (S_2), modeling a simplified Purkinje network, eliciting a large

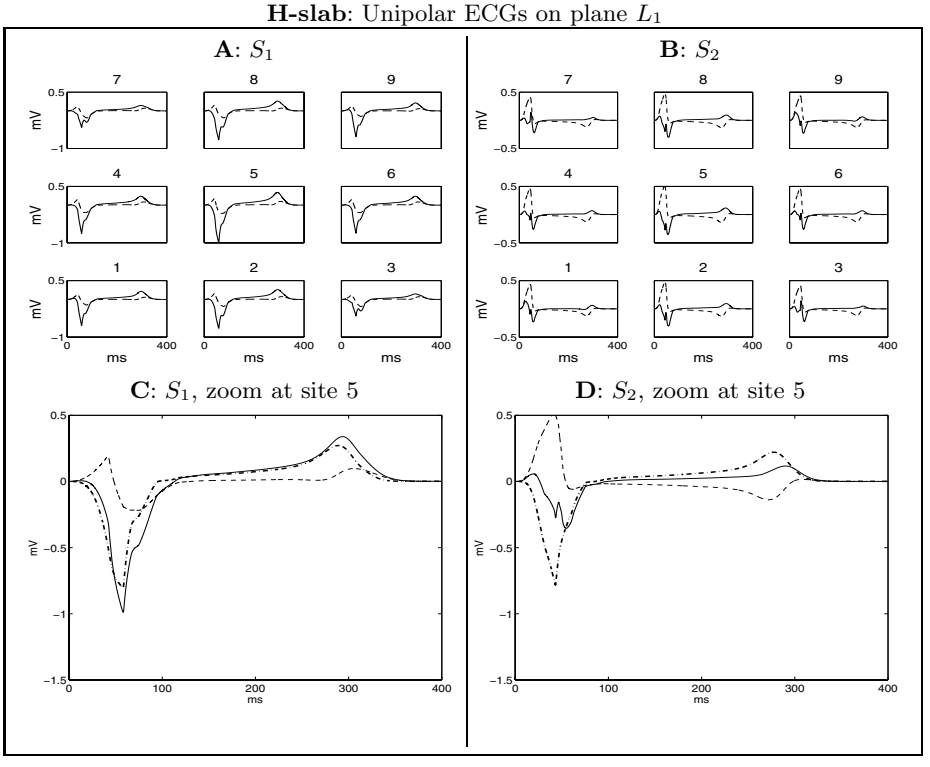

Fig. 4. **H-slab**: Unipolar ECGs on plane L_1. Continuous line: full unipolar ECG. Dashed line: HS component. Dashed-Dotted line: AS component (only in zoom). **A**: Single site stimulation (S_1). **B**: Multiple sites stimulation (S_2). **C, D**: zoom at site 5.

excitation front spreading transmurally mainly across fiber. These two protocols are applied to both **H-slab** and **3-slab**, for a total of four simulations.

S_1: unipolar ECGs. The activation (ACTI) and repolarization (REPO90) isochrones on a transmural section of the tissue are reported in Fig. 2 **A**. The HS components of all unipolar ECGs on plane L_2 (2 cm below the endocardium) for **H-slab** (see Fig. 3 **A**) display a Q wave and a positive T wave, as expected. The same behavior is also observed in 3-slab case (not shown), where the intramural repolarization sequence displays a primary and a secondary fronts coming from the endocardial and epicardial surfaces, respectively. Instead, the HS components on plane L_1 (2 cm above the epicardium) display a QRS complex with R and S waves and, unexpectedly for a tissue without transmural heterogeneities, a positive T wave, see Fig. 4 **A, C**. The AS components of unipolar ECGs on both planes L_1 and L_2 display a Q wave and a positive T wave. The same morphology is shared by the full unipolar ECGs on both planes L_1 and L_2 (Fig. 3 **A**, 4 **A, C**). This fact indicates that the full unipolar ECGs are dominated by their anisotropic AS components. The HS components have little influence on the full ECGs, since their positive T waves reinforce those of the full ECGs but

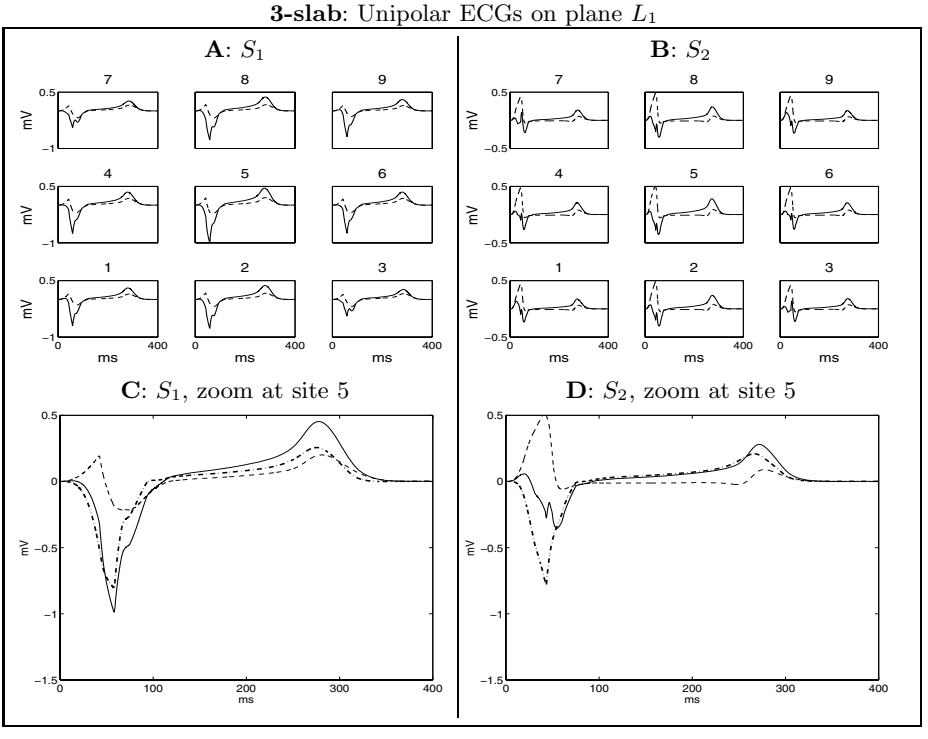

Fig. 5. 3-slab: Unipolar ECGs on plane L_1. Same format as Fig. 4.

their R waves at almost all sites on plane L_1 are absent in the QRS complex of the full ECGs. Analogous morphological considerations hold for the **3-slab** (Fig. 5), although with slight differences in magnitude.

S_2: unipolar ECGs. The isochrones of ACTI and REPO90 on a transmural section of the tissue are reported in Fig. 2 **B**. The excitation wavefronts are larger than those elicited by the ectopic stimulation. On plane L_2, the morphology of the unipolar ECGs is the same as in the ectopic case described before; see Fig. 3 **B**. On plane L_1, all the AS components have Q waves and positive T waves, while the HS components exhibit R waves and negative (**H-slab**, Fig. 4 **B, D**) or positive (**3-slab**, Fig. 5 **B, D**) T waves. Nevertheless, the larger magnitude of the AS components prevail in the full unipolar ECGs and they still exhibit a positive T wave and QRS complex entirely negative or with RS configuration (small R and large S wave) and positive T wave. Therefore, the full unipolar ECGs are still dominated by their AS components.

S_1: bipolar ECGs. Unlike unipolar waveforms, the bipolar ECGs (Fig. 6 and 7 **A, C**) appear to be dominated by their HS components, all with R and S waves and biphasic (for **H-slab**) or positive (for **3-slab**) T waves. Since the AS components of the unipolar ECGs on planes L_1 and L_2 are almost identical, the bipolar AS component has a very small magnitude in comparison with the

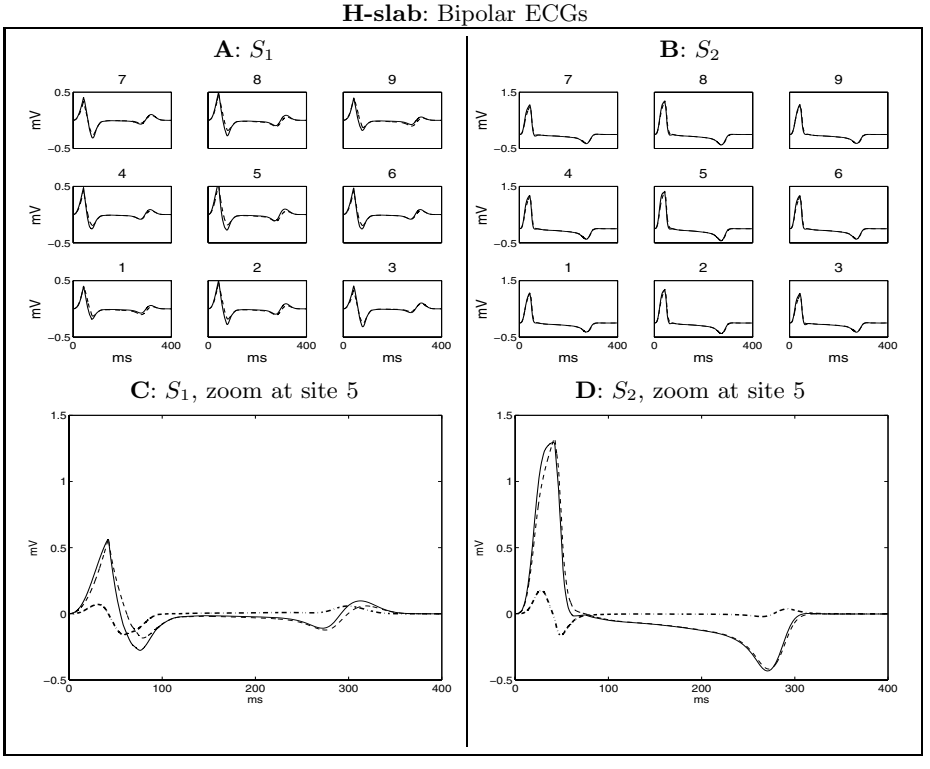

Fig. 6. **H-slab**: Bipolar ECGs on plane L_1. Continuous line: full unipolar ECG. Dashed line: HS component. Dashed-Dotted line: AS component (only in zoom). **A**: Single site stimulation (S_1). **B**: Multiple sites stimulation (S_2). **C, D**: zoom at site 5.

bipolar HS component, hence they have a negligible influence on the full bipolar ECGs. The negative minimum of the biphasic T wave appearing in the bipolar ECGs in the **H-slab** case is due to the T peak of the unipolar HS components at sites on plane L_2 preceding the T peak of the symmetric sites on plane L_1.

S_2: bipolar ECGs. Bipolar ECGs now display a QRS complex with a large R wave and negative T wave (Fig. 6 and 7 **B, D**), similarly to their HS components. The bipolar AS components have little influence because of their much smaller magnitude and therefore, as in the ectopic case, the full bipolar ECGs are dominated by their HS components.

4 Discussion

By means of three-dimensional simulations based on the anisotropic Monodomain model, we have studied the influence of tissue anisotropy, cellular APD heterogeneities and the shape of the excitation wavefront on the T wave polarity. The simulation results have shown that: i) unipolar ECGs exhibit a positive T wave mainly determined by the anisotropy of the cardiac tissue, irrespective of

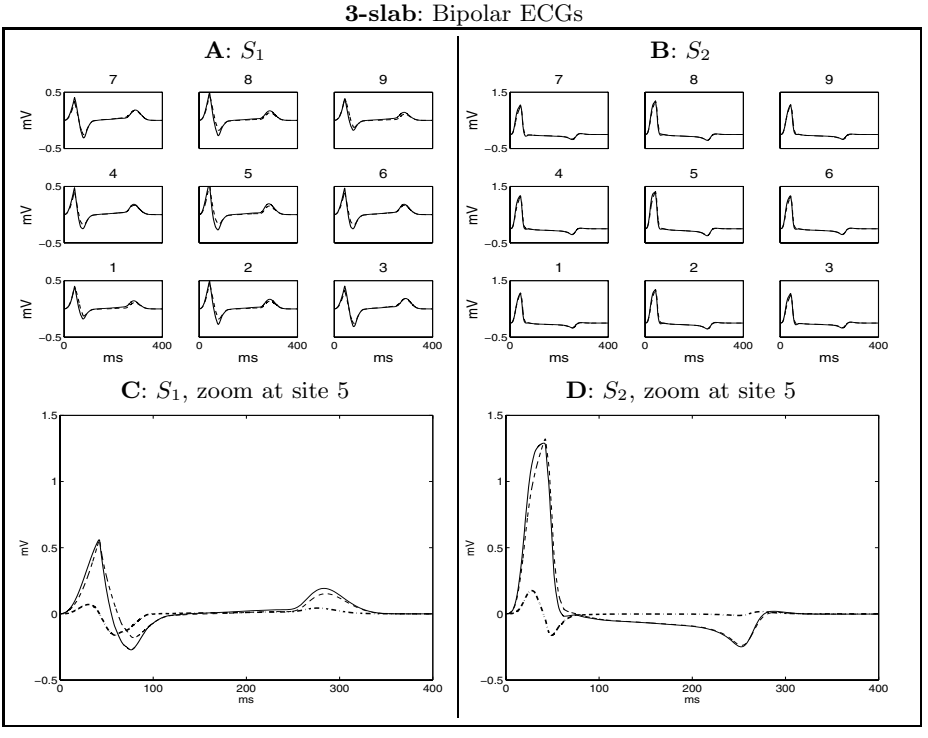

Fig. 7. 3-slab: Bipolar ECGs. Same format as Fig. 6.

cellular APD heterogeneities and the shape of the excitation wavefront; ii) on the other hand, bipolar ECGs are mainly determined by their isotropic component and their T wave turns out to be positive only for a single stimulation in presence of transmural APD heterogeneity, while it becomes always negative in case of multiple stimulation generating large activation wavefronts, regardless of the considered cellular APD heterogeneities. We remark that in our ECG computation, we have used an idealized cardiac geometry taking into account anisotropic cardiac sources but considering the widely used assumptions of the same isotropic properties for bulk tissue and for the surrounding infinite extracardiac medium. Previous studies ([5,4]) have shown that including anisotropic bulk tissue affects the ECGs magnitude far away from the cardiac surface but it does not alter their QRS morphology. The extension of our conclusions on T wave polarity to real 12-lead ECGs will require considering realistic geometries for both cardiac tissue and torso, as well as the anisotropy of the bulk tissue. Nevertheless, the real 12-lead ECGs are far-field signals and we expect that the full ECG and the isotropic/ anisotropic ECG components will be smoothed out due to the greater distance from the active tissue. Since each ECG is the sum of its isotropic and anisotropic components, we should still be able to apply our conclusions on the dominant role played by these components in determining the polarity of the T wave for unipolar or bipolar signals.

References

1. di Bernardo, D., Murray, A.: Computer model for study of cardiac repolarization. J. Cardiovasc. Electrophys. 11(8), 895–899 (2000)
2. Boulakia, M., et al.: Towards the Numerical Simulation of Electrocardiograms. In: Sachse, F.B., Seemann, G. (eds.) FIMH 2007. LNCS, vol. 4466, pp. 240–249. Springer, Heidelberg (2007)
3. Clements, J.C., et al.: Activation Dynamics in Anisotropic Cardiac Tissue via Decoupling. Ann. Biomed. Engrg. 32(7), 984–990 (2004)
4. Colli Franzone, P., et al.: On the polyphasic character of simulated and experimental electrograms. Biomedizin. Tech. 46(2), 16–19 (2001)
5. Colli Franzone, P., et al.: Anisotropic mechanism for multiphasic unipolar electrograms. Simulation studies and experimental recordings. Ann. Biomed. Engrg. 28, 1–17 (2000)
6. Colli Franzone, P., et al.: Simulating patterns of excitation, repolarization and action potential duration with cardiac bidomain and monodomain models. Math. Biosci. 197(1), 35–66 (2005)
7. Colli Franzone, P., et al.: Effects of transmural electrical heterogeneities and electrotonic interactions on the dispersion of cardiac repolarization and action potential duration: A simulation study. Math. Biosci. 204(1), 132–165 (2006)
8. Clayton, R.H., Holden, A.V.: Propagation of normal beats and re-entry in a computational model of ventricular cardiac tissue with regional differences in action potential shape and duration. Progr. Biophys. Mol. Biol. 85(2–3), 473–499 (2004)
9. Conrath, C.E., Opthof, T.: Ventricular repolarization: An overview of (patho)physiology, sympathetic effects and genetic aspects. Progr. Biophys. Mol. Biol. 92(3), 269–307 (2006)
10. Fish, J.M., et al.: Epicardial activation of left ventricular wall prolongs QT interval and transmural dispersion of repolarization - Implications for biventricular pacing. Circulation 109(17), 2136–2142 (2004)
11. Franz, M.R., et al.: Monophasic action potential mapping in human subjects with normal electrocardiograms: direct evidence for the genesis of the T wave. Circulation 75, 379–386 (1987)
12. Gima, K., Rudy, Y.: Ionic current basis of electrocardiographic waveforms: A model study. Circ. Res. 90, 889–896 (2002)
13. Huiskamp, G.: Simulation of depolarization in a membrane-equation-based model of the anisotropic ventricle. IEEE Trans. Biomed. Engrg. 45, 847–855 (1998)
14. Janse, M., et al.: Repolarization gradients in the canine left ventricle before and after induction of short-term cardiac memory. Circulation 112, 1711–1718 (2005)
15. Leon, L.J., Horacek, B.M.: Computer model of excitation and recovery in the anisotropic myocardium. I. Rectangular and cubic arrays of excitable elements. J. Electrocardiol. 24(1), 1–15 (1991)
16. Luo, C., Rudy, Y.: A model of the ventricular cardiac action potential: depolarization, repolarization, and their interaction. Circ. Res. 68, 1501–1526 (1991)
17. Simms Jr., H.D., Geselowitz, D.B.: Computation of Heart Surface Potentials Using the Surface Source Model. J. Cardiovasc. Electrophys. 6(7), 522–531 (1995)
18. Taggart, P., et al.: Transmural repolarization in the left ventricle in humans during normoxia and ischaemia. Cardiovasc. Rer. 50(3), 454–462 (2001)

19. van Oosterom, A.: Genesis of the T wave as based on an equivalent surface source model. J. Electrocard. 34, 217–227 (2001)
20. Weiss, D.L., et al.: Modeling of heterogeneous electrophysiology in the human heart with respect of ECG genesis. Proceed. Comput. in Cardiol. 34, 49–52 (2007)
21. Yan, G.-X., Antzelevitch, C.: Cellular basis for the normal T wave and the electrocardiographic manifestations of the Long-QT syndrome. Circulation 98, 1928–1936 (1998)

From Intracardiac Electrograms to Electrocardiograms: Models and Metamodels

Géraldine Ebrard[1], Miguel A. Fernández[1], Jean-Frédéric Gerbeau[1], Fabrice Rossi[2], and Nejib Zemzemi[1,3]

[1] INRIA Paris-Rocquencourt BP 105, F–78153 Le Chesnay Cedex, France
[2] Institut TELECOM, TELECOM ParisTech, LTCI – UMR CNRS 5141, 46, rue Barrault, F–75013 Paris
[3] Université Paris 11, Laboratoire de mathématiques d'Orsay, Bâtiment 425, F-91405 Orsay Cedex, France

Abstract. We consider the problem of building a standard electrocardiogram (ECG) from the electrical potential provided by a pacemaker in a few points of the heart (electrogram). We use a 3D mathematical model of the heart and the torso electrical activity, able to generate "computational ECG", and a "metamodel" based on a kernel ridge regression. The input of the metamodel is the electrogram, its output is the ECG. The 3D model is used to train and test the metamodel. We illustrate the performance of the proposed strategy on simulated bundle branch blocks of various severities and a few clinical data.

1 Introduction

In this work, we show how an ECG simulation tool can be used to address an industrial problem raised by a pacemaker manufacturer. A typical modern pacemaker with implantable defibrillator can provide the measurements of the electrical potential in several points of the heart. Instead of these raw data, the pacemaker manufacturer would like to provide the clinician with something more familiar, namely, a standard electrocardiogram (ECG). Of course, given the small number of measurements in the heart, this "pseudo-ECG" is not expected to be very accurate. The idea is rather to get a rough instantaneous ECG, just by remotely questioning the pacemaker, without setting up all the leads needed to get a real standard ECG. Of course, this cannot replace a genuine ECG but since the data are available for free, one can find it interesting to use them for a simple routine clinical examination.

To formalize a little bit the problem at hand, we denote by $x(t) \in \mathbb{R}^{m_P}$ the vector representing the intracardiac potential measured by the pacemaker in m_p points in the heart at time t. A typical value for m_P is five. The quantity $x(t)$ will be called an electrogram (EGM). We denote by $y(t)$ a lead of a standard ECG, for example the first lead, known as DI, which is the difference of potential between the left and the right arms. The data $(x(t), y(t))_{t\in T}$ define a *training set*. With the training set, we try to build a function f such that $y(t) \approx f(x(t))$ (as a matter of fact the argument of f will be slightly more complicated, see below). After a while, say a few months later, the same patient will probably

N. Ayache, H. Delingette, and M. Sermesant (Eds.): FIMH 2009, LNCS 5528, pp. 524–533, 2009.
© Springer-Verlag Berlin Heidelberg 2009

have a different EGM $\tilde{x}(t)$. Nonetheless, $\tilde{y}(t) = f(\tilde{x}(t))$ is expected to give a good approximation of the first lead of the ECG. The purpose of this work is to propose a possible approach to actually build function f.

The construction of a function f that satisfies $y(t) \approx f(x(t))$ on the training set is a relatively easy task. The difficulty is to build an f able to reconstruct a good ECG $\tilde{y}$ from an EGM $\tilde{x}$ which is not in the training set. Several methods have been developed in the machine learning community to address this kind of problem. In this work, we propose to use the so-called *kernel ridge regression* and a simple treatment of the time series defined by the EGM. We present this method in §3.

Another difficulty of the problem is that the function f has to be patient specific (for the obvious reason for example that the location of the points where the EGM is measured varies from a patient to another). The training set corresponds to a certain state of the patient and it is not easy to test the reconstruction algorithm on different situations. Another contribution of this work is to show that a numerical simulation tool can be convenient to address this issue. In §2, we briefly present this simulation tool. Of course, many simplifications are done to model the complex electrophysiology of the heart in a tractable way. Nevertheless, in spite of these simplifications, the model has been built in order to provide realistic ECGs. It is therefore a good candidate to test the reconstruction algorithm, as shown in §4.

2 Model

The mathematical model used to generate the computational ECGs has been presented in other works ([1,2]) but to keep this paper as self contained as possible, we briefly recall it in this section.

We denote by Ω_{T} a 3D domain representing the torso and by Ω_{H} a 3D domain representing the heart. The model consists of two degenerate parabolic reaction-diffusion partial differential equations (PDE), known as the *bidomain equations* (see *e.g.* [7,11]), coupled to a system of ordinary differential equations (ODE):

$$\begin{cases} A_{\mathrm{m}}\big(C_{\mathrm{m}}\partial_t v_{\mathrm{m}} + I_{\mathrm{ion}}(v_{\mathrm{m}}, w)\big) - \operatorname{div}(\boldsymbol{\sigma}_{\mathrm{i}}\boldsymbol{\nabla} u_{\mathrm{i}}) = I_{\mathrm{app}}, & \text{in} \quad \Omega_{\mathrm{H}} \times (0,T), \\ A_{\mathrm{m}}\big(C_{\mathrm{m}}\partial_t v_{\mathrm{m}} + I_{\mathrm{ion}}(v_{\mathrm{m}}, w)\big) + \operatorname{div}(\boldsymbol{\sigma}_{\mathrm{e}}\boldsymbol{\nabla} u_{\mathrm{e}}) = I_{\mathrm{app}}, & \text{in} \quad \Omega_{\mathrm{H}} \times (0,T), \\ \partial_t w + g(v_{\mathrm{m}}, w) = 0, & \text{in} \quad \Omega_{\mathrm{H}} \times (0,T). \end{cases} \tag{1}$$

The two PDEs describe the dynamics of the averaged intra- and extracellular potentials u_{i} and u_{e}, whereas the ODE is related to the dynamics of the myocardium cell membrane. The unknown w represents the ion concentrations and gating variables, $v_{\mathrm{m}} = u_{\mathrm{i}} - u_{\mathrm{e}}$ is the transmembrane potential, C_{m} is the membrane capacitance, A_{m} stands for the volume density of membrane surface, $\boldsymbol{\sigma}_{\mathrm{i}}, \boldsymbol{\sigma}_{\mathrm{e}}$ are the intra- and extracellular conductivity tensors and I_{app} is an external applied volume current. The potentials are defined up to an additive constant. We get rid of this undetermination by enforcing a zero mean value to u_{e}.

The nonlinear reaction term $I_{\text{ion}}(v_{\text{m}}, w)$ and the function $g(v_{\text{m}}, w)$ depend on the ionic model. Several ionic models have been proposed for decades, either based on physiological or phenomenological considerations (see [7,11] for a review). In our works, we use the Mitchell-Schaeffer equations [4] which is a two-current phenomenological model. The unknown w, which is scalar is this case, is a gate variable. This model is defined by

$$I_{\text{ion}}(v_{\text{m}}, w) = -\frac{w}{\tau_{in}} v_{\text{m}}^2 (1 - v_{\text{m}}) + \frac{v_{\text{m}}}{\tau_{out}}, \tag{2}$$

$$g(v_{\text{m}}, w) = \begin{cases} \dfrac{w - 1}{\tau_{open}} & \text{if } v_{\text{m}} < V_{gate}, \\ \dfrac{w}{\tau_{close}} & \text{if } v_{\text{m}} > V_{gate}, \end{cases} \tag{3}$$

where τ_{in}, τ_{out}, τ_{open}, τ_{close} and V_{gate} are given parameters. The complexity of the Mitchell-Schaeffer ionic model is comparable to the well-known FitzHugh-Nagumo equations [5] but it is more convenient to parametrize and gives more realistic results for cardiac cells. It has been shown to be well-suited to obtain computational ECG [1].

The numerical simulation of the ECG signals, which are measurements of voltages (*i.e.* potential differences) on the body surface [3], requires a description of how the surface potential is related to the electrical activity of the heart. Such as description is based on the coupling of (1) with a diffusion equation in Ω_{T}:

$$\text{div}(\boldsymbol{\sigma}_{\text{T}} \boldsymbol{\nabla} u_{\text{T}}) = 0, \quad \text{in} \quad \Omega_{\text{T}}, \tag{4}$$

where u_{T} stands for the torso potential and $\boldsymbol{\sigma}_{\text{T}}$ for the conductivity tensor of the torso tissue. The boundary Γ_{ext} can be supposed to be insulated, which corresponds to the condition

$$\boldsymbol{\sigma}_{\text{T}} \boldsymbol{\nabla} u_{\text{T}} \cdot \boldsymbol{n}_{\text{T}} = 0 \text{ on } \Gamma_{\text{ext}},$$

where $\boldsymbol{n}_{\text{T}}$ stands for the outward unit normal on Γ_{ext}.

The following coupling conditions between (1) and (4) are enforced on the interface Σ separating the heart Ω_{H} and the torso Ω_{T}:

$$\begin{cases} u_{\text{e}} = u_{\text{T}}, & \text{on} \quad \Sigma, \\ \boldsymbol{\sigma}_{\text{e}} \boldsymbol{\nabla} u_{\text{e}} \cdot \boldsymbol{n} = \boldsymbol{\sigma}_{\text{T}} \boldsymbol{\nabla} u_{T} \cdot \boldsymbol{n}, & \text{on} \quad \Sigma. \end{cases} \tag{5}$$

These relations can be simplified replacing the second equation by $\boldsymbol{\sigma}_{\text{e}} \boldsymbol{\nabla} u_{\text{e}} \cdot \boldsymbol{n} = 0$ on Σ. This does not affect dramatically the ECG and saves a lot of computational time. In this work, all the tests are performed with this simplification. In Fig. 1 is given an example of ECG obtained with this model. For futher details, we refer to [1].

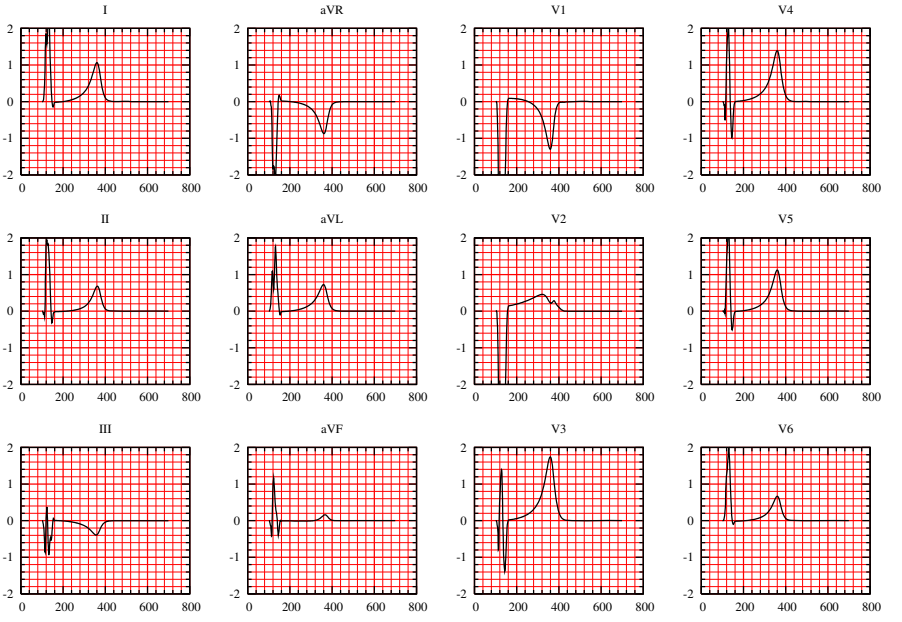

Fig. 1. An example of a computational ECG obtained with the model of §2; x-axis: time (milliseconds), y-axis: potential (millivolts)

3 Metamodel

As explained in the introduction, our purpose is to build a "metamodel", denoted by f which takes in input an EGM and provides in output the first lead (for example) of a standard ECG. More precisely, the EGM is made of the measurements $(x_i)_{i=1..n} \in (\mathbb{R}^{m_P})^n$ of the potential u_e in m_P points $(P_k)_{k=1..m_P}$ of the heart at times $t_1, \ldots, t_n$. The first lead of the ECG $(y_i)_{i=1..n}$ is made of the difference of the potential u_T between two points of the torso denoted by P_L and P_R. For simplicity, we first assume that $t_1, \ldots, t_n$ correspond to *one* heart beat (see Remark 1 below). For $k \in \mathbb{N}$, $0 \leq k < n$, we define by periodicity $x_{n+k} = x_k$. and $x_{-k} = x_{n-k}$.

The model presented in the previous section will be used to train and test the metamodel f. With the above notations, we have:

$$x_i = (u_\mathrm{e}(t_i, P_j))_{j=1..m_P} \in \mathbb{R}^{m_P},$$

and

$$y_i = u_\mathrm{T}(t_i, P_L) - u_\mathrm{T}(t_i, P_R) \in \mathbb{R}.$$

3.1 Temporal Dynamics

Searching a function f such that $y_i \approx f(x_i)$ would assume the relationship between the torso potential and the extracellular potential in the myocardium

be static, which is obviously not the case (see Remark 3 below). To take into account in a simple way the time dynamics of the problem, we define a temporal window of length m_W and we build the metamodel f such that $y_i \approx f(\mathbf{x}_i)$, with

$$\mathbf{x}_i = (x_i, \ldots, x_{i+m_W-1}) \in \mathbb{R}^{m_P \times m_W}. \tag{6}$$

In the sequel, we denote by m the dimension of the variable in the data space. We have $m = m_P \times m_W$.

Remark 1. When several heart beats are used to train the algorithm, we first build the vectors $\mathbf{x}_i$ according to (6) for each heart beat and we put together all the $\mathbf{x}_i$ in the training set. ♢

3.2 Kernel Ridge Regression

The proposed method is known as *kernel ridge regression* (KRR, see [8]). It is an alternative to *Support Vector Regression*, an adaptation of the *Support Vector Machine* principle to regression problems (see *e.g.* [9]). In KRR, the regression function depends on all the training examples and not only on a subset (the support vectors). This typically makes the kernel ridge regression function more expensive to use but less difficult to construct than support vector regression models.

Function f is looked for in a Hilbert space $(\mathcal{H}, \langle\cdot,\cdot\rangle_{\mathcal{H}})$, using a least square method with a regularization term ensuring that the norm $\|f\|_{\mathcal{H}} = \langle f, f\rangle_{\mathcal{H}}^{\frac{1}{2}}$ remains "small". We choose the space $\mathcal{H}$ as the *Reproducing Kernel Hilbert Space* (RKHS) based on a Gaussian kernel $K(\mathbf{x},\mathbf{y}) = \exp(-\frac{|\mathbf{x}-\mathbf{y}|^2}{2\sigma^2}), \forall \mathbf{x},\mathbf{y} \in \mathbb{R}^m$. The kernel is said to be reproducing on $\mathcal{H}$ because of the following property:

$$f(\mathbf{x}) = \langle f(\cdot), K(\cdot,\mathbf{x})\rangle_{\mathcal{H}}, \quad f \in \mathcal{H}, \quad \forall \mathbf{x} \in \mathbb{R}^m, \tag{7}$$

where $\langle\cdot,\cdot\rangle_{\mathcal{H}}$ is the inner product in $\mathcal{H}$. The use of the Gaussian kernel can be motivated by the following property (see [10]): given a compact subset K of $\mathbb{R}^m$, the set of the restriction to K of functions from $\mathcal{H}$ is dense in the set of continuous functions from K to $\mathbb{R}$. In other word, $\mathcal{H}$ is rich enough to approximate any possible continuous mapping from the EGM to a given lead of the ECG.

Consider in $\mathcal{H}$ the following regularized least square problem: given a training set $\{(\mathbf{x}_i, y_i)\}_{i=1}^n \in (\mathbb{R}^m \times \mathbb{R})^n$, solve

$$\min_{f\in\mathcal{H}} \left\{ \frac{1}{n}\sum_{i=1}^{n} (f(\mathbf{x}_i) - y_i)^2 + \lambda \|f\|_{\mathcal{H}}^2 \right\}, \tag{8}$$

where $\lambda > 0$ is a given regularization coefficient. The representer theorem ([9]) states that the solution to (8) can be written as $\sum_{i=1}^n \alpha_i K(\cdot,\mathbf{x}_i)$ where $\alpha = (\alpha_i)_{i=1\ldots n} \in \mathbb{R}^n$ is the new unknown. Defining the Gram matrix $\mathrm{K} = (K_{ij})_{i,j=1\ldots n}$ with $K_{ij} = K(\mathbf{x}_i,\mathbf{x}_j)$, the training problem (8) is equivalent to solving:

$$\min_{\alpha\in\mathbb{R}^n} \left\{ \frac{1}{n}(\mathrm{K}\alpha - y)^T(\mathrm{K}\alpha - y) + \lambda \alpha^T \mathrm{K}\alpha \right\},$$

whose solution is simply given by

$$\alpha = (\mathrm{K} + \lambda n \mathrm{I})^{-1} y. \tag{9}$$

Remark 2. If the eight independent leads of the standard ECG are to be reconstructed, one should solve eight least square problems of this kind, with different right-hand sides but with the same matrix. In other words, the training phase of the algorithm consists in solving $\mathrm{A} = (\mathrm{K} + \lambda n \mathrm{I})^{-1}\mathrm{Y}$, with $\mathrm{A} \in \mathbb{R}^{n\times 8}$ and $\mathrm{Y} \in \mathbb{R}^{n\times 8}$. Each column of A and Y corresponding, respectively to the coefficient α and to the values of a given lead of the ECG. ♢

Once the training phase is completed, the reconstruction of an ECG from a given one beat EGM $(\tilde{x}_i)_{i=1..\tilde{n}} \in (\mathbb{R}^{m_P})^{\tilde{n}}$ is obtained, according to (7), by $\widetilde{\mathrm{Y}} = \widetilde{\mathrm{K}}\mathrm{A}$, with $\widetilde{\mathrm{K}}_{ij} = K(\tilde{\mathbf{x}}_i, \mathbf{x}_j)$, $i = 1 \dots \tilde{n}$, $j = 1 \dots n$, where the $\tilde{\mathbf{x}}_i$ are defined from the $\tilde{x}_i$ as explained in (6).

3.3 Parameters Optimization

The proposed algorithm depends on a relatively small number of parameters: the regularization coefficient λ, the width of the Gaussian kernel σ and the size of the temporal window m_W. Assuming that m_W is fixed, we determine parameters λ and σ with a *leave-one-out* procedure: we train the metamodel with all the examples but one and we assess its performance on the example which has been removed from the training set. In other words, we use of cross validation with a singleton as testing set. We repeat the procedure with all the singletons of the training set. The brute force leave-one-out may be extremely expensive. Fortunately, there exists formulae to compute the leave-one-out mean-squared error using the results of a single training on the whole training set. This is one of the advantages of the kernel ridge regression over support vector regression. We refer for example to [6] for more details.

4 Results

4.1 Synthetic Data

We use the mathematical model presented in §2 to generate "synthetic" data. We consider the extracellular potential in $m_P = 5$ points in the heart (corresponding roughly to a distal RV, distal LV, proximal RV, distal coil and proximal coil) and the DI lead of the corresponding computational ECG. The versatility of the numerical model allows to test the reconstruction algorithm in various situations more easily than with clinical data. All the examples of this section are obtained with the following parameters: $\sigma = 150$, $\lambda = 10^{-4}$, $m_W = 6$ (σ and λ being automatically given by the leave-one-out procedure briefly described in §3.3).

We focus on a pathological case called right bundle branch block (RBBB). Starting from the healthy situation presented in Fig. 1, we simulate a RBBB by artificially delaying the activation of the right ventricle. For example, a delay of

10 ms will be denoted by RBBB-10. A larger delay of course corresponds to a situation which is farther from the healthy state.

First suppose the test case is a part of the training set. In that case, the reconstruction of the ECG is, as expected, very good. In Fig. 2 (top), we see that increasing the size of the training set does not deteriorate significantly the result.

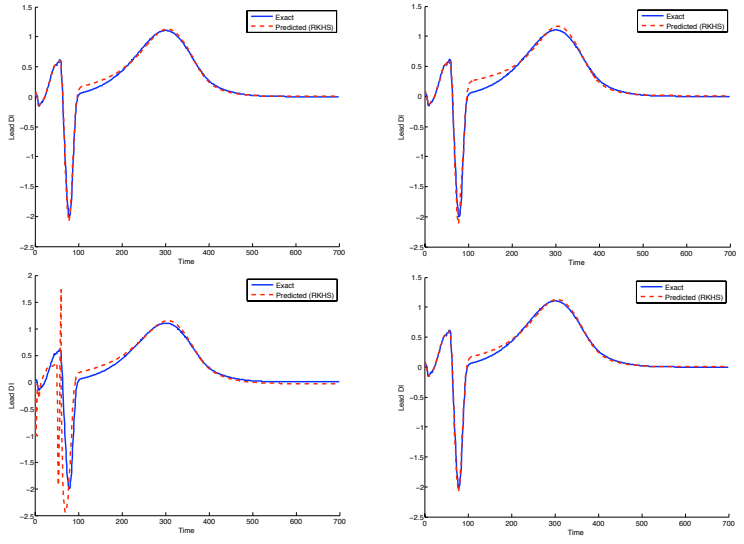

Fig. 2. Reconstruction of a RBBB-50 when the training set is RBBB-{10, 50, 100, 200} (top left) and RBBB-{10, 50, 100, 200, 400, 700} (top right), and using different time window parameters: $m_W = 1$ (bottom left) $m_W = 6$ (bottom right)

Remark 3. We show in Fig. 2 (bottom) that the results obtained with $m_W = 6$ are clearly better than those obtained with $m_W = 1$. This confirms that the relationship EGM/ECG is not static and that the technique of temporal windows is a possible solution to handle the dynamic of the problem. The optimal length of the temporal window could be determined, as for σ and λ, using the leave-one-out procedure. ♢

Next consider a test case which does not belong to the training set. In practice, this corresponds for example to the following situation: the patient has a slight right bundle branch block when the algorithm is trained, but when he comes back a few months later, the pathology is getting worse. Fig. 3 (top left) shows what happens if we train the algorithm with a RBBB-10, and if we try to reconstruct the ECG corresponding to a RBBB-50. We can see that the result is poor. Since we get good results with larger training sets, a natural idea is to enrich the training set so that the new situation be close to a training case. For the sake of illustration, suppose a patient has a RBBB-10 and suppose the numerical model can be parametrized to reproduce the patient's ECG. With the simulation tool,

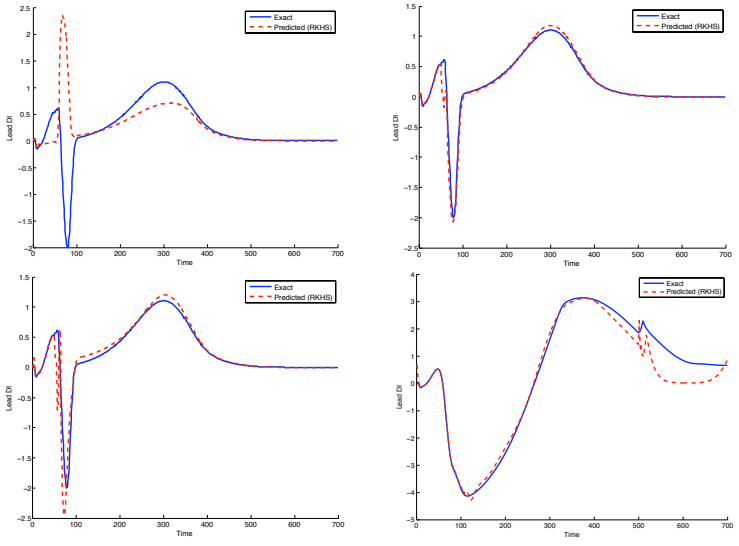

Fig. 3. Reconstruction of a RBBB-50 from RBBB-10 (top left) and from RBBB-{10,40,60} (top right). Reconstruction of a RBBB-50 (bottom left) and a RBBB-500 (bottom right) from RBBB-{10, 20, 40, 60, 70, 80, 100, 150, 200, 300, 400, 700}.

we can investigate possible situations the patient may encounter in the future. For example, assume we compute a RBBB-40 and a RBBB-60. Thus we build a training set made of RBBB-{10,40,60}. We show in Fig. 3 (top right) that the prediction obtained if the patient has a RBBB-50 is then much better.

In Fig. 3 (bottom left), we show the result obtained with a much larger training set {RBBB-10, 20, 40, 60, 70, 80, 90, 100, 120, 150, 200, 300, 400, 700}. In that case the result for a RBBB-50 is slightly less accurate than with the training set of only 3 cases, but the resulting metamodel is more robust and can be used in a wide range of situations. This is illustrated in Fig. 3 (bottom right), where we report the reconstruction of a RBBB-500 with the same training set.

4.2 Clinical Data

In this paragraph we use our method to reconstruct ECGs from clinical EGMs. In Fig. 4 (top left) we reconstruct the ECG of a myocardial ischemia disease patient ("patient 1"), with a training done on a Tachycardia heart disease patient ("patient 2"). As expected the reconstruction is totally wrong which confirms that the metamodel has to be patient specific. In Fig. 4 (top right), the data of "patient 1" is added to the training set and the reconstruction becomes very good. Again, if we add more cases, for example an atrial fibrillation disease ("patient 3") and a LBBB disease ("patient 4") in the traning data set, the reconstruction of the ECG remains acceptable (Fig. 4, bottom left). This confirms on clinical data the trend observed with numerical simulations. We have

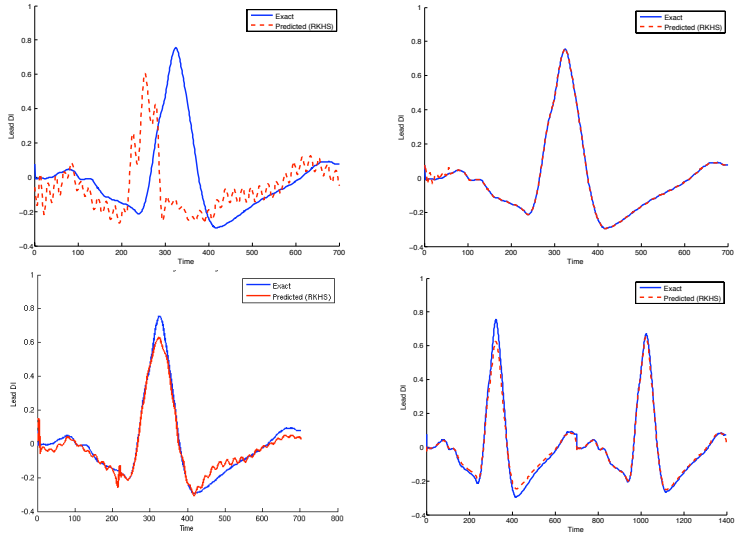

Fig. 4. Reconstruction of "patient 1" ECG from: "patient 2" (top left), "patient 1 & 2" (top right), "patient 1, 2, 3 & 4" (bottom left). Two heart-beat of "patient 1" when the training is performed on different heart beats of the same patient (bottom right).

also observed that the results are usually very good when the reconstruction is performed on a heart beat different from those used for the training on the same patient (Fig. 4, bottom right).

5 Conclusion

In this work we have considered a machine learning approach, based on the kernel ridge regression method, in order to provide ECG information from a set of EGM measurements.

The procedure has been trained using synthetic data from numerical simulations, based on a 3D mathematical model of the ECG involving a quite complete description of the electrical activity of the heart and the torso. A few clinical data have also been considered for illustration. Several examples showed the method is able to reconstruct conveniently the ECG information included in the training data set, and is robust when reconstructing situations close to the training data set. In the proposed approach, the solution depends on all training examples, which may be too expensive. This point could be improved in future works.

We have also illustrated that a possible use of the numerical simulation could be to *enrich* available clinical data to conveniently investigate a wider range of situations. This strategy nevertheless relies on the capability to adapt the model to a specific patient, which is the topic of ongoing researches.

Acknowledgment. This work was partially supported by ELA Medical[1], a Sorin group company, and by the CardioSense3D[2] project (INRIA). We are thankful to Alain Ripart and Renzo Dal Molin for introducing us to this problem and for many interesting discussions.

References

1. Boulakia, M., Fernández, M.A., Gerbeau, J.-F., Zemzemi, N.: Towards the numerical simulation of electrocardiograms. In: Sachse, F.B., Seemann, G. (eds.) FIMH 2007. LNCS, vol. 4466, pp. 240–249. Springer, Heidelberg (2007)
2. Boulakia, M., Fernández, M.A., Gerbeau, J.-F., Zemzemi, N.: A coupled system of PDEs and ODEs arising in electrocardiograms modelling. Applied Math. Res. Exp. (2008), doi:10.1093/amrx/abn002
3. Malmivuo, J., Plonsey, R.: Bioelectromagnetism. Principles and applications of bioelectric and biomagnetic fields. Oxford University Press, New York (1995)
4. Mitchell, C.C., Schaeffer, D.G.: A two-current model for the dynamics of cardiac membrane. Bulletin Math. Bio. (65), 767–793 (2003)
5. Nagumo, J.S., Arimoto, S., Yoshizawa, S.: An active pulse transmission line stimulating nerve axon. Proc. IRE (50), 2061–2071 (1962)
6. Opper, M., Winther, O.: Advances in Large-Margin Classifiers. In: Gaussian Processes and SVM: Mean Field and Leave-One-Out, ch. 17. MIT Press, Cambridge (2000)
7. Sachse, F.B.: Computational Cardiology: Modeling of Anatomy, Electrophysiology, and Mechanics. Springer, Heidelberg (2004)
8. Saunders, C., Gammerman, A., Vovk, V.: Ridge regression learning algorithm in dual variables. In: Proceedings of the Fifteenth International Conference on Machine Learning (ICML1998), Madison, Wisconsin, USA, July 1998, pp. 515–521 (1998)
9. Scholkopf, B., Smola, A.J.: Learning with Kernels: Support Vector Machines, Regularization, Optimization, and Beyond. MIT Press, Cambridge (2001)
10. Steinwart, I.: On the influence of the kernel on the consistency of support vector machines. Journal of Machine Learning Research 2, 67–93 (2001)
11. Sundnes, J., Lines, G.T., Cai, X., Nielsen, B.F., Mardal, K.-A., Tveito, A.: Computing the electrical activity in the heart. Springer, Heidelberg (2006)

[1] http://www.elamedical.com
[2] http://www.inria.fr/CardioSense3D

Author Index

Al-Owais, Moza 172
Angelini, Elsa D. 104, 211
Arridge, Simon 239, 182
Arts, Theo 58, 249
Ashikaga, Hiroshi 114
Aslanidi, Oleg V. 154
Axel, Leon 386
Ayache, Nicholas 1, 201, 239, 376

Bainbridge, Daniel 466
Balocco, Simone 330
Becher, Harald 134
Benson, Alan P. 49, 172, 495
Bernus, Olivier 49, 495
Bijnens, Bart H. 21, 68, 417, 437
Billet, Florence 239, 376
Bishop, Martin J. 87, 268
Blake, Andrew 447
Blanc, Julie 201
Bosch, Johan G. 295
Boudjemline, Younes 201
Bovendeerd, Peter 58
Boyett, Mark R. 154
Boyle, Patrick M. 68
Burton, Rebecca 268
Butakoff, Constantine 417

Cai, Xing 11
Camara, Oscar 21, 330, 417, 437
Cannell, Mark B. 11
Carillo, Paola 144
Chabiniok, Radomir 239
Chapelle, Dominique 220, 239, 357
Chinchapatnam, Phani 182, 239
Colli Franzone, Piero 513
Comaniciu, Dorin 457
Connelly, Kim 339
Croisille, Pierre 39, 78
Crystal, Eugene 1

De Craene, Mathieu 21, 330, 417, 437
Delhaas, Tammo 58, 249
Delingette, Hervé 201, 239, 376
Detsky, Jay 1
Dick, Alexander 1, 339
Dierckx, Hans 495
Dietmayer, Klaus 476
Donal, Erwan 258
Dössel, Olaf 30, 144
Duan, Qi 211
Duchêne, Cédric 277

Eagleson, Roy 396
Ebrard, Géraldine 524
Ecabert, Olivier 191, 312

Fanton, Laurent 78
Fefer, Paul 1
Fernández, Miguel A. 357, 524
Fleureau, Julien 258
Frangi, Alejandro F. 21, 68, 330, 417, 437
Friedl, Reinhard 476
Frindel, Carole 39

Garreau, Mireille 258
Gavaghan, David J. 87
Georgescu, Bogdan 457
Gerbeau, Jean-Frédéric 357, 524
Gianni, Daniele 407
Gibb, Matthew 268
Gilbert, Stephen H. 49, 495
Ginks, Matthew 182, 239
Gnahm, Claudia 476
Grass, Michael 191
Grau, Vicente 87, 134, 268
Guiraudon, Gerard M. 466
Gurm, Sandeep 30
Gutierrez, Luis 321

Hales, Patrick 87
Hartung, Christine 476
Haverslag, Rene 486
Hawkes, David J. 303
Hernández, Alfredo 258
Hoefer, Imo 486
Hoffmann, Martin 476
Holden, Arun V. 11, 49, 172, 495

Holmes, Jeffrey W. 211
Homma, Shunichi 211
Howe, Robert D. 97
Hurmusiadis, Vassilios 386

Jain, Ameet 321
Jones, Douglas L. 466

Katouzian, Amin 104
Kelm, Malte 312
Kharche, Sanjay 366
Kneser, Reinhard 312
Kohl, Peter 268
Kroon, Wilco 58
Krueger, Martin W. 144
Kühl, Harald 312
Kuijpers, Nico 285

Laine, Andrew F. 104, 211
Lambiase, Pier 239
Larrabide, Ignacio 417
Leclercq, Christophe 258
Lehmann, Helko 312
Lelieveldt, Boudewijn P.F. 295
Lemay, Mathieu 277
Lempitsky, Victor 447
Li, Pan 11
Liénard, Jean 124
Linte, Cristian A. 466
Littmann, Arne 457
Lo, Jennifer 466
Lorenz, Cristian 30
Lorsakul, Auranuch 104, 211
Lu, Xiaoguang 457
Lu, YingLi 339
Lüdtke, Niklas 366
Lumens, Joost 249

Ma, Meng 295
Mansi, Tommaso 1, 201, 239
Martelli, Yves 417
McKeever, Steve 407
McVeigh, Elliot R. 1, 114
Metaxas, Dimitris 386
Mihalef, Viorel 386
Moireau, Philippe 220, 239, 357
Mont, Lluis 21
Moore, John 466
Moya, Juan A. 417

Mueller, Edgar 457
Myronenko, Andriy 427

Nair, Prasanth 182
Neizel, Mirja 312
Nieber, Maarten 417
Niederer, Steven 348
Noble, J. Alison 134, 447
Nolte, Froukje 486

Oeltze, Steffen 21
Omedas, Pedro 417
Oubel, Estanislao 330
Ourselin, Sebastien 303

Pace, Danielle 466
Panzeri, Stefano 366
Pavarino, Luca F. 513
Peters, Jochen 191, 312
Peters, Terry M. 466, 396
Peyrat, Jean-Marc 201, 239
Piella, Gemma 330
Planes, Xavier 417
Plank, Gernot 87, 268
Pop, Mihaela 1
Punske, Bonnie B. 505

Radau, Perry 339
Rajpoot, Kashif 134
Rapacchi, Stanislas 78
Razavi, Reza 182, 239, 303, 348
Reiber, Johan H.C. 295
Rhode, Kawal 182, 239, 303, 348
Ries, Michael E. 495
Rinaldi, C. Aldo 239
Robini, Marc 39
Rodriguez, Blanca 268
Romero, Daniel 68
Rossi, Fabrice 524

Sachse, Frank B. 505
Sahn, David J. 427
Sainte-Marie, Jacques 357
Scacchi, Simone 513
Schaerer, Joël 39
Scheider, Jürgen 87
Schilling, Christopher 30
Schmitt, Holger 191
Scholz, Eberhard P. 144
Sebastian, Rafael 21, 68, 417
Seemann, Gunnar 30, 144

Sermesant, Maxime 1, 182, 201, 239, 376
Shi, Pengcheng 162, 229
Siebes, Maria 486
Silva, Etel 21
Sitges, Marta 21
Smith, Nic 348, 407
Soeller, Christian 11
Sohn, Kwanghyun 505
Song, Xin 78
Song, Xubo 427
Sorine, Michel 239
Spaan, Jos A.E. 486
Stanton, Douglas 321
Straub, Dorothee 30
Sturm, Bernhard 104
Sussman, Mark 386
Szmigielski, Cezary 134

Taccardi, Bruno 513
Tamborero, David 21
ten Eikelder, Huub 285
Tong, Wing C. 172

Vaillant, Régis 124
van den Wijngaard, Jeroen P.H.M. 486
van Horssen, Pepijn 486
van Oosterom, Adriaan 277
van Stralen, Marijn 295
Verheule, Sander 285
Verhoek, Michael 447
Verschelde, Henri 495
Vesin, Jean-Marc 277
Vidal, Camille 114
Vigmond, Edward J. 68

Wang, Linwei 162, 229
Weber, Frank M. 30
Wedlake, Chris 466
Weese, Jürgen 191, 312
Wei, Wenjie 11
Weiss, Daniel L. 144
Wiles, Andrew 466
Wong, Ken C.L. 162, 229
Wright, Graham A. 1, 339

Yang, Feng 78
Yang, Yuesong 1
Yvinec, Mariette 220

Zemzemi, Nejib 357, 524
Zhang, Henggui 154, 366
Zhang, Heye 162
Zhang, Qi 396
Zhu, Yue-Min 39, 78
Zhuang, Xiahai 303
Zimmerman, Viviana 68